MERD'16

31 March 2016
Kampus Teknologi UTeM, Melaka

PROCEEDINGS *of*

Mechanical Engineering Research Day 2016

www3.utem.edu.my/care/proceedings

Edited by
Mohd Fadzli Bin Abdollah
Mohd Azli Bin Salim
Tee Boon Tuan

Jointly organized by
Faculty of Mechanical Engineering
Centre for Advanced Research on Energy

UTeM
اونيۏرسيتي تيكنيكل مليسيا ملاك
UNIVERSITI TEKNIKAL MALAYSIA MELAKA

© Universiti Teknikal Malaysia Melaka

FOREWORD BY THE EDITORS-IN-CHIEF

This Open Access e-Proceeding contains a compilation of 105 selected papers from the Mechanical Engineering Research Day 2016 **(MERD'1**6) event, which is held in Kampus Teknologi, Universiti Teknikal Malaysia Melaka (UTeM) - Melaka, Malaysia, on 31 March 2016. The theme cho**sen for this event is '**IDEA. INSPIRE. INNOVATE**'.**

It was gratifying to all of us when **the response for MERD'16 is overwhelming as** the technical committees received more than 200 submissions from various areas of mechanical engineering. After a peer-review process, the editors have accepted 105 papers for the e-proceeding that cover 7 main themes. This open access e-Proceeding can be viewed or downloaded at www3.utem.edu.my/care/proceedings. We hope that these proceeding will serve as a valuable reference for researchers.

With the large number of submissions from the researchers in other faculties, the event has achieved its main objective which is to bring together educators, researchers and practitioners to share their findings and perhaps sustaining the research culture **in the university. The topics of MERD'**16 are based on a combination of fundamental researches, advanced research methodologies and application technologies.

As the editor-in-chief, we would like to express our gratitude to the editorial board and fellow review members for their tireless effort in compiling and reviewing the selected papers for this proceeding. We would also like to extend our great appreciation to the members of the Publication Committee and Secretariat for their excellent cooperation in preparing the proceeding **of MERD'1**6.

Thank you

Mohd Fadzli Bin Abdollah
Mohd Azli Bin Salim
Tee Boon Tuan

EDITORIAL BOARD

REVIEWERS

Abd Salam Bin Md Tahir – FKM, UTeM, Malaysia
Abdul Munir Hidayat Syah Lubis – FTK, UTeM, Malaysia
Ahmad Rivai – FKM, UTeM, Malaysia
Amrik Singh A/L Phuman Singh – FKM, UTeM, Malaysia
Azma Putra – FKM, UTeM, Malaysia
Faiz Redza Bin Ramli – FKM, UTeM, Malaysia
Fatimah Al-Zahrah Binti Mohd Sa'at – FKM, UTeM, Malaysia
Ghazali Bin Omar – FKM, UTeM, Malaysia
Hidayat Bin Zainuddin – FKE, UTeM, Malaysia
Imran Syakir Mohamad – FKM, UTeM, Malaysia
Jaharah Binti A. Ghani – UKM, Malaysia
Kamarul Ariffin Bin Zakaria – FKM, UTeM, Malaysia
Mariam Binti Md Ghazaly – FKE, UTeM, Malaysia
Md. Fahmi Bin Abd. Samad – FKM, UTeM, Malaysia
Mohd Ahadlin Bin Mohd Daud – FKM, UTeM, Malaysia
Mohd Asyadi 'Azam Bin Mohd Abid – FKP, UTeM, Malaysia
Mohd Azli Bin Salim – FKM, UTeM, Malaysia
Mohd Azman Bin Abdullah – FKM, UTeM, Malaysia
Mohd Basri Bin Ali – FKM, UTeM, Malaysia
Mohd Fadzli Bin Abdollah – FKM, UTeM, Malaysia
Mohd Haizal Bin Mohd Husin – FKM, UTeM, Malaysia
Mohd Khairi Bin Mohamed Nor – FKM, UTeM, Malaysia
Mohd Nizam Bin Sudin – FKM, UTeM, Malaysia
Mohd Warikh Bin Abd Rashid – FKP, UTeM, Malaysia
Mohd Zaid Bin Akop – FKM, UTeM, Malaysia
Mohd Zulkefli Bin Selamat – FKM, UTeM, Malaysia
Muhammad Ilman Hakimi Chua Bin Abdullah – FTK, UTeM, Malaysia
Noraiham Binti Mohamad – FKP, UTeM, Malaysia
Norfariza Binti Ab Wahab – FTK, UTeM, Malaysia
Nurin Wahidah Binti Mohd Zulkifli – UM, Malaysia
Olawale Ifaye Funmi – FTK, UTeM, Malaysia
Omar Bin Bapokutty – FKM, UTeM, Malaysia
Rafidah Binti Hasan – FKM, UTeM, Malaysia
Rainah Binti Ismail – FKM, UTeM, Malaysia
Reduan Bin Mat Dan – FKM, UTeM, Malaysia
Roszaidi Bin Ramlan – FKM, UTeM, Malaysia
Siti Hajar Binti Sheikh Md Fadzullah – FKM, UTeM, Malaysia
Sivakumar A/L Dhar Malingam – FKM, UTeM, Malaysia
Suhaila Binti Salleh – FKM, UTeM, Malaysia
Suhaimi Bin Misha – FKM, UTeM, Malaysia
Tee Boon Tuan – FKM, UTeM, Malaysia
Zairulazha Bin Zainal – FKM, UTeM, Malaysia
Zaleha Binti Mustafa – FKP, UTeM, Malaysia

TABLE OF CONTENTS

Theme 1: Automotive

Theme 2: Computer Modelling and Simulation

Theme 3: Design and Optimization

Theme 4: Energy Conversion and Management

Theme 5: Structure and Materials

Theme 6: Thermal and Fluids

Theme 7: Vibration and Control

The effect of temperatures and extraction time on bio oil extracted from banana peel wastes

H.A. Hamid[1], N.A.B. Masripan[1,2,*], M.F.B. Abdollah[1,2], R. Hasan[1,2], G. Omar[1,2]

[1] Faculty of Mechanical Engineering, Universiti Teknikal Malaysia Melaka,
Hang Tuah Jaya, 76100 Durian Tunggal, Melaka, Malaysia
[2] Centre for Advanced Research on Energy, Universiti Teknikal Malaysia Melaka,
Hang Tuah Jaya, 76100 Durian Tunggal, Melaka, Malaysia

*Corresponding e-mail: norazmmi@utem.edu.my

Keywords: Oil; extraction; banana peel

ABSTRACT – Bio oil extracted from various part of edible and non-edible plants offer several potential applications such as a biodegradable lubricant. In this study, banana peels which known as waste and often ignored was subjected to solven extraction via *soxhlet* method. Moreover, the extraction of oil from banana peels wastes of *Musa aluminata balbis*iana (MBS) was performed and optimized. The effects of temperatures and extraction time were investigated in order to optimize the extraction conditions for achieving maximum oil obtained. The optimum conditions using *n*-hexane as a solvent of extractor was found at the temperatures of 68°C and 7 hours of reaction times whereby the extraction recovery was 62.42% with 3.6 mL of oil obtained.

1. INTRODUCTION

Banana, which is scientifically known as *Musa sapientum* is a herbaceous plant of the family *Musaceae*. It is known to have originated from the tropical regions of Southern Asia. The *Musa sapientum* grows up to height of about 2-8 metre with leaves of about 3.5 metre in length. The stem which also known as pseudostem produces a single bunch of banana before dying and replace by new pseudo stem. The fruits is grows in hanging cluster, which 20 fruits to a tier and 3-20 tiers to a bunch. The fruit is protected by its peel, which is discarded as a waste after the inner fleshy portion is eaten [1].

Solvent extraction is the preferred method as it is cost- effective and requires no further purification of the product [2, 3, 4]. Solvent extraction is the ability of a solute to distribute itself between an aqueous solution and an immiscible organic solvent. The organic solvent separates and purifies the solutes by extracting into the organic phase, leaving undesirable substances in the aqueous phase [5]. Hexane is the most extensively used solvent for oil extraction because of its high stability, high ability to dissolve oil, low greasy residual effects as well as low boiling point and corrosiveness [6, 7]. The properties of the organic solvent require that the dissolved species be electrically neutral. Species that prefer the organic phase particularly organic compounds are lipophilic.

The objective of this study was to evaluate the oil recovery through solvent extraction process. The influence of various extraction parameters were investigated and optimized. These parameters includes extractions temperatures from temperatures of 40 to 80°C and extraction time ranges from 3-13 hours. The results provides basis for solvent extraction process from non-edible of banana peel waste.

2. METHODOLOGY

2.1 Chemical and instrumentations

Analytical grade hexane was purchased from Polyscientific Enterprise Sdn.Bhd (Melaka, Malaysia) and was used as solvent. An electrical grinder was used at its fine grind setting to grind the dried banana peel wastes. An electrical oven (Memmert, UM200, Germany) was used to dry the samples and measure the moisture content. A universal soxhlet extraction system (B-811 / B-811 LSV, Buchi, Switzerland) was used extract the oil from the banana peel wastes. Rotary vacuum evaporator (N - 10004 - W, Eyela, USA) was used to dry the samples.

2.2 Raw material preparation

A banana peel waste of MBS was collected at the pisang goreng stall in Klebang Area, Melaka Malaysia. Botanist from Pejabat Pertanian Cawangan Melaka Tengah, Melaka Malaysia, then identified the sample. The peel was cleaned and cut into a smaller size before subjected to dryness using universal oven. The dried peel was grinded prior to extraction process.

2.3 Oil extraction from banana peel waste of MBS.

A standard weight of crushed banana peel wastes was placed in a 5 L three neck flask. Hexane was used as solvent to extract oil. The volume of hexane needed was determined by the ratio of 6:1. A reflux condenser was fitted and the mixture was heated at desired temperatures and hours. The resulting oil and solvent mixture were filtered to remove the suspended solids. Then, the mixture was placed in a rotary vacuum evaporator to evaporate the solvent and to obtain oil. The percentage of extraction recovery was calculated.

2.4 Effect of temperatures

The experiments were conducted to determine the optimum temperatures for oil extraction from waste of banana peel. The temperatures were varied from 40 to 80 °C.

2.5 Effect of extraction time

Extraction was performed at various times ranging from 3 to 13 hours.

2.6 Determination of oil extraction yield

The oil from the solvent extraction was determined with respect to time fro various test. The oil extraction yields, Oy (% w/w) was calculated using equation 1 below:

$$Oy = 100(M_o / M_p) \tag{1}$$

Where M_o is mass of oil in grams, M_p is mass of banana peel wastes in grams.

3. RESULTS AND DISCUSSION

The effect of the extraction temperatures was investigated at different temperatures which were 40, 68 and 80 °C. The experiments were conducted in order to determine the optimum temperatures for oil from MBS. In this study, higher temperatures were not tested. It is obviously due to the solvent vaporization at high temperatures. Besides, the temperatures, which lower than atmospheric temperatures, were also not investigated as it was observed at ambient temperatures no oil is recovered [8]. The result obtained from the process is depicted in Figure 1.
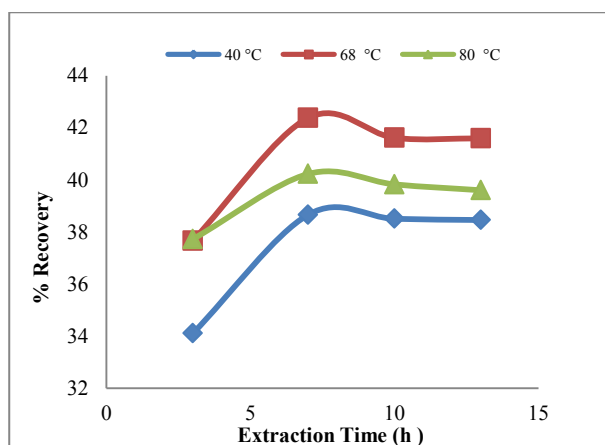
Figure 1 The Effect of Temperature on extraction recovery in *soxhlet* extraction method.

The Figure 2 shows that increasing the time for reaction do exhibit a signifcant increament in oil extraction from 3 to 7 hours at all the temperatures. However, there are no increament or decrement of oil yield after 10 to 13 hours of reaction time.
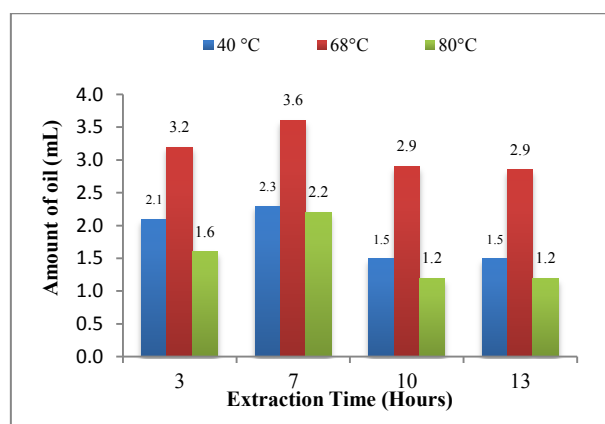
Figure 2 The effect of extraction time on oil extraction from peel waste of MBS by solvent extraction Operations

4. CONCLUSION

The results obtained in this study shows that an extraction time and extraction temperature affects the extraction recovery and oil obtained. The temperature of 68 °C and 7 hours of extraction was found to be an optimum condition for oil extraction process with 42.38% of extraction recovery and 3.6 mL of oil obtained.

REFERENCES

[1] Anhwange, B.A., 2008. Chemical Composition of Musa sapientum (Banana) Peels. *Journal of Food Technology* 6(6): 263-266.

[2] Coulson, J.M. and Richardson, J.F., 2002. Chemical Engineering. 5th Edition

[3] Forson, F.K., Oduro, E.K., and Hammond-Donkoh, E., 2004. Performance of jatropha oil blends in a diesel engine. Renew. Energ., 29: 1135-1145. DOI: 10.1016/j.renene.2003.11.002

[4] Sugunya, T. and Renganathan, S., 2012. Optimization and Kinetic Studies on Algal Oil Extraction from Marine Macroalgae Ulvalactuca. Bioresource Technology vol.107, 319-329.

[5] Rincon, J., Canizares, P., and Garcia, M.T., 2005. "Regeneration of Used Lubricant Oil by Polar Solvent Extraction," Ind. Eng. Chem. Res., vol. 44, pp. 4373 – 4379.

[6] Amin, S. K., Hawash, S., El Diwani, G. and El Rafei, S., 2010. "Kinetics and thermodynamics of oil extraction from Jatrophacurcas in aqueous acidic hexane solutions," J. Am.Sci. vol. 6, pp. 293–300.

[7] Sayyar, S. Zainal Abidin, Z., Ynunus, R. and Muhammad, A., 2009. Extraction of Oil from Jatropha Seeds-Optimization and Kinetics. American Journal of Applied Science 6(7), 1390-1395.

[8] Diphare, M. and Muzenda, E., 2014. The Effect of Extraction Conditions on Oil Yield from Waste Lubricating Grease. International Journal of Research in Chemical, Metallurgical and Civil Engg. (IJRCME) vol 1(1), 75-78.

Field test of regenerative suspension system on an actual vehicle

J.F. Jamil[1,*], M.A. Abdullah[1,2,*], A.E. Mohan[1,3]

[1] Faculty of Mechanical Engineering, Universiti Teknikal Malaysia Melaka,
Hang Tuah Jaya, 76100 Durian Tunggal, Melaka, Malaysia
[2] Centre for Advanced Research on Energy, Universiti Teknikal Malaysia Melaka,
Hang Tuah Jaya, 76100 Durian Tunggal, Melaka, Malaysia
[3] Middle Euphrates University, Al-Mussaib Technical College, Al-Mussaib, Babil, Iraq

*Corresponding e-mail: jazlifirdaus@yahoo.com, mohdazman@utem.edu.my

ABSTRACT – The technology of hybrid and electric vehicle are rapidly developed in the past few years because the main resource of vehicle energy is not renewable which is known as fossil fuel. It will be depleted in the future. This research emphasizes the test of the energy regenerative suspension system (EReSS) that uses as the alternative energy resource for the vehicle. It can be used on the vehicle as it can produce voltage output for charging the vehicle battery or other electronic components. The EReSS is attached to the stock vehicle suspension system and the test is done on a road with low traffic situation with various conditions. The voltage produced by the EReSS is maximized by optimizing the resistor in the circuit of half bridge which converts the alternate current (AC) to direct current (DC). The maximum voltage produced by the EReSS during the test is recorded and discussed.

1. INTRODUCTION

All vehicles have suspension system installed that uses to isolate the car from road disturbance and balance the contact between the tyre and the road. This system used on vehicle to achieve comfort driving and road holding [1,2]. Most of the mechanical energy on the suspension system is converted to heat and it is believe that the energy can be harvested and uses for other usage. The research on harvesting energy from suspension system is getting popular and taken much interest by many researchers [3,4].

They introduce several types of regenerative system that can be use on the vehicle suspension system as a harvesting device. There are several types of system introduced such as piezoelectric, electromagnetic and hydraulic. From all the research, mostly their regenerative system can harvest energy but different in results which some is small value and some is high value of voltage produces [5,6]. The energy harvested from the suspension can be used for the vehicle itself for electronics usage and charging the battery. This will reduce the workload of the alternator which is the main resource of charging the vehicle battery [7,8].

In this paper, an electromagnetic regenerative suspension system [9] that is self operates is tested on an actual vehicle. This is to predict the function and voltage generated by the regenerative system.

2. METHODOLOGY

The electromagnetic regenerative suspension system is designed and the system does not disturb the vehicle original suspension system where the regenerative system is only attached to suspension system as shown in Figure 1.

Figure 1 Regenerative system is attached to the vehicle.

The diameter of the coil is changed when each type of diameter of coil test is completed. The diameter of the coil for test is 0.29 mm, 0.4 mm and 0.8 mm using copper. The magnet uses for the test remain the same which is permanent magnet (NdFeb) grade N35 with Ni coating. The length, width and thickness of the magnet is 30 mm, 15 mm and 5 mm respectively which six (6) pieces used in the regenerative system. The regenerative system is attached to the rear left vehicle suspension system. The test is made in a low traffic road with various road conditions such as corner, slope and bump. The test goes through the road for three (3) times to see the reading different of voltage produces by the regenerative system for a long driving maneuver.

3. RESULTS AND DISCUSSION

The test is completely done for all of the parameters set. The test data is recorded by using a multi-meter and a half bridge circuit to convert the AC voltage to DC voltage. The data is recorded from the output of the bridge. The data is then analyzed to get the maximum voltage generated by the regenerative system. By using the different value of resistor, the voltage produced can be maximized and the parameters used can be optimized. This is to ensure that the system generated the best voltage charge for the vehicle usage.

The maximum voltage generated by the regenerative system by using the electromagnetic principle is shown in Table 1 with different value of resistor in the bridge and different diameter of the coil used for the each test.

Table 1 Voltage generated by the regenerative system.

Diameter of coil (mm)/	Voltage (V)			
Resistor value (Ohm)	1 M	2 M	3 M	700 k
0.8	8.6	9	8.7	8.4
0.4	7.9	11.3	13.1	9.8
0.29	17.2	17.2	14.7	13

The maximum voltage produced by the regenerative system is 17.2 Volts by using the 0.29 mm diameter of the coil and 2 M Ohm resistor. Thus, the resistor that is suitable to be used on the car test is 2 M Ohm where most of the voltage produced is the highest. Highest voltage generated will be more useful for the vehicle. From the results, it is get that the diameter of the coil also plays important role for the regenerative system where the smaller the diameter of the coil the higher the voltage generated. This is because smaller diameter can maximize the number of windings of the copper coil in the regenerative system. The highest value shown is when the car is taking a corner in an upward slope followed by downward slope. During this time, the vehicle suspension system movement maximized the regenerative system displacement thus highest voltage is generated. The other value that is higher is when the vehicle is in braking and moving through a bump but the voltage is not as high as taking the corner with a slope. In a normal cornering, the voltage higher than only moves in a straight road. A slalom type of driving maneuver will give out more voltage where the frequency of the suspension system is higher.

In a constant driving in a straight road, the voltage reading is slightly lower but with a constant charge. This voltage generated by the regenerative system can be used for vehicle electronics system such as lighting and electronic control unit (ECU). Other than that, the voltage can be uses as alternative source of energy for charging the vehicle battery. Thus, the main source of power supply unit which is the alternator usage can be reduced. As the alternator usage is reduced, the workload on the vehicle engine is also reduced and the fuel consumption will be also reduced.

As a result, the natural fuel fossil used can be reduced. Moreover, the fuel can be used efficiently to give more power to the vehicle engine and achieved the energy efficient vehicle (EEV).

4. CONCLUSION

The test of the regenerative suspension system on the vehicle proved that the system can harvest the vertical energy on the vehicle suspension system where voltage is generated. The electromagnetic system is a system that is simple and save the cost better than other systems. Moreover, the regenerative system can be used in the hybrid and electric vehicle as an additional feature for alternative source of energy different than the current features used in the vehicle. This regenerative suspension system has a bright future usage on the vehicle to achieve the world requirement on automotive industry where fuel consumption of a vehicle should be reduced and maximized the vehicle power with optimized fuel fossil usage.

REFERENCES

[1] M. Jonasson. Wang and F. Roos, "Design and evaluation of an active electromechanical wheel suspension system," *Elsevier Journal of Mechatronics*, vol. 18, pp. 218–230, 2008.

[2] M. A. Abdullah, J. F. Jamil, N. Basrah, A. Putra and M. A. Salim, "Noise analysis in Malaysian passenger car cabin," *Proceedings of Mechanical Engineering Research Day 2015*, pp. 105-106, 2015.

[3] S. Zhu, W. Shen and Y Xu, " Linear electromagnetic for vibration damping and energy harvesting : modeling and testing," *Elsevier Journal of Engineering Structures*, vol. 34, pp. 198-212, 2012.

[4] K. Nakano, Y. Suda and S. Nakadai, "Self-powered active vibration control using a single electric actuator," *Academic Press Journal of Sound and Vibration*, vol. 260, pp. 213-235, 2003.

[5] J. F. Jamil, M. A. Abdullah, N. Tamaldin and A. E. Mohan, "Fabrication and testing of electromagnetic energy regenerative suspension system," *Jurnal Teknologi (Sciences and Engineering)*, vol. 77:21 pp. 97-102, 2015.

[6] X. Tang and L. Zuo, "Enhanced vibration energy harvesting using dual-mass system," *Elsevier Journal of Sound and Vibration*, vol. 330, pp. 5199-5209, 2011.

[7] M. A. Abdullah, J. F. Jamil, M. A. Mohamad, R. S. Rosdi and M. N. I. Ramlan, "Design selection and analysis of energy regenerative suspension," *Jurnal Teknologi (Sciences and Engineering)*, vol. 76:10, pp. 27-31, 2015.

[8] D. Corona, A. Giua and C. Seatzu, "Optimal control of hybrid automata: design a semiactive suspension," *Elsevier Journal of Control Engineering Practice*, vol. 12, 2004.

[9] M. A. Abdullah, J. F. Jamil and N. S. Muhammad, "Fabrication and testing of energy regenerative suspension," *Proceedings of Mechanical Engineering Research Day 2015*, pp. 19-20, 2015.

The improvement and laboratory testing of regenerative suspension system

A.E. Mohan[1,3], M.A. Abdullah[1,2,*], J.F. Jamil[1]

1) Faculty of Mechanical Engineering, Universiti Teknikal Malaysia Melaka,
Hang Tuah Jaya, 76100 Durian Tunggal, Melaka, Malaysia
2) Centre for Advanced Research on Energy, Universiti Teknikal Malaysia Melaka,
Hang Tuah Jaya, 76100 Durian Tunggal, Melaka, Malaysia
3) Middle Euphrates University, Al-Mussaib Technical College, Al-Mussaib, Babil, Iraq

*Corresponding e-mail: mohdazman@utem.edu.my

Keywords: Regenerative, suspension; energy harvesting; energy efficient vehicle

ABSTRACT – Nowadays, the requirement for more efficient vehicle is essential in the field of alternative energy and very crucial for automation industry. The aim of this paper is to ensure the enhancement of regenerative suspension system (EReSS) in order to obtain energy efficient vehicle (EEV). Accomplishment of laboratory testing was to ensure the improvement in the suspension system. Consequently, the output voltage can be increased if an improvement in the materials has been occurred. The results indicated that the proposed system can minimize the vibration's energy wastage and result in an effective vehicle in terms of electrical and electronic utilization.

1. INTRODUCTION

A vehicle suspension system can be defined as a system that connect the vehicle tires and springs to vehicle wheels to enable vehicle motion. The main function of suspension system is to act as a mechanical system which enhnces the sprung and communicate with un-sprung masses of the vehicle and offer a conveninent vehicle stabilty, where the sprung mass refered to the vehicle body ,while the un-sprung mass refered to the vehicle wheel [1]. The vehicle suspension system comprises of damper and spring, the damper utilized to absorb the vibration generated and distributes the energy to the encirclement. This type of energy can be gained with assistance of a modified suspension system called as energy regenerative suspension system. In addition, the fuel consumption can be minimized by utilizing the regenerative shock absorber [2], since the gained energy is utilized to charge the battery of the vehicle as well as enable the battery to start up instead powering up the vehicle battery using alternator [3]. Various researches have been conducted in the field regenerative suspension system where the main focus of all the studies is to produce noticeable improvement in the suspension system [4]. However, the improvement has been accomplished still not suffice the requirements of the commercial applications [5]. Hence, the requirement for producing an improved and sufficient regenerative suspension system is very important in order to fit the power demand and produce an enhanced final output demanding.

2. METHODOLOGY

The flow of this research begins by opting the EReSS [6]. This opted system considered as the best system that can produce the highest voltage reading in terms of theoretical. Apart from that, the opted EReSS system is very easy to be fabricated, where it utilizes a single barrel housing that consists all the necessary part for the electromagnetic regenerative suspension system [7]. The EReSS opted system is verified via testing on the laboratory by utilizing parameters variations, such as the number of windings which were (100, 250, 400), also the diameter of the coil (0.29, 0.4, 0.8) mm, and the magnetic utilized is NdFeb (grade N35). The system implementation is achieved by conducting an experiment on the laboratory utilizing a testing rig which moves in vertical orientation similar to the suspension system of a vehicle as presented in Figure 1.

Figure 1 Test rig for the EReSS testing on laboratory.

During testing in the laboratory, the frequency was varied to fall in the range from 10 Hz to 50 Hz. As well as the rectifier bridge is installed as a simple power electronic circuit in order to convert AC to DC Current. The produced output voltage of the EReSS is measured by utilizing multi meter in which the measurement is conducted and recorded for each part in the system with respects to parameters variation as mentioned earlier.

3. RESULTS AND DISCUSSION

The regenerative energy suspension has been designed and tested in the laboratory and the result of the testing was recorded and analyzed .As shown in Figure 2 and presented in Table 1 the results of the testing is demonstrated in a graphical manner. As the aim of this research indicates the testing was done with respect to parameters variation in which the number of winding and diameter of the coil result in impacts on the voltage reading of the EReSS. As can be seen from the tabulated results show in table 1 the power reading is decreasing when the number of windings is increased where ,the highest reading of the test is 30.5W at 30Hz for 0.8mm diameter, 2.8W at 10Hz for 0.4 mm diameter and 1.4W at 10Hz for 0.29 mm diameter. As well as an obvious observation can be seen that 30Hz frequency produces higher power output from the test. Therefore, large amount of power utilized in order to reduce the engine loading produced by usage also minimizes of the alternator, increase fuel efficiency, reduce vehicle emissions and fuel consumption.

Table 1 Power reading for the EReSS with different number of windings and coil wire diameter.

No of windings/ coil wire diameter (mm)/ Frequency (Hz)	Power (W)		
	400	250	100
	0.29	0.4	0.8
10	1.41	2.08	18.61
20	0.91	1.82	22.87
30	1.04	1.18	30.51
40	1.35	1.6	12.38
50	1.35	1.65	21.3
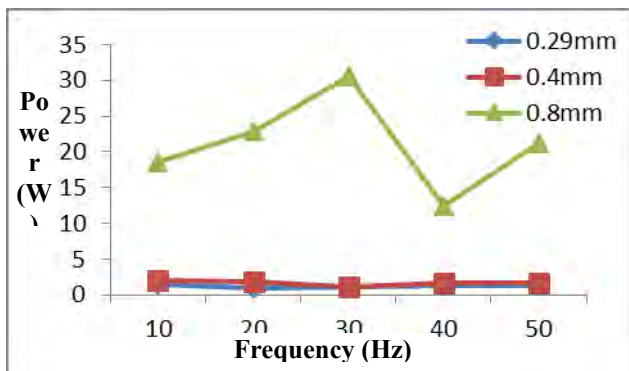
Figure 2 Graph plot of EReSS test with different diameter of coil.

4. CONCLUSIONS

In conclusion this study, concern in developing a harvest device for suspension system. The proposed suspension system utilizes the EReSS and tested on the laboratory test rig. According to the test results, it is observed that the maximum power reading for parameters variation for the system testing is 30.51W. In addition, the output power could be enhanced by improving the materials utilized in the electromagnetic system of the EReSS. Measuring instruments must be utilized in order to read the value of frequency of the

test rig so that the produced output power can be recorded with respect to frequency variation Moreover, from the obtained results, it is noticed that, the output power of the EReSS is affected by varying the number of windings and coil wire diameter. Apart from that, varying the frequency during the test is also plays important role in producing better performance of the system. Lastly the proposed system utilizes the regenerative shock absorber to act as reduction tool of the fuel consumption in which the gained energy can charge the battery of the vehicle and help to start up the battery instead of using the alternator on the vehicle.

REFERENCES

[1] M.A. Abdullah, N. Tamaldin, M.A. Mohamad, R.S. Rosdi and M.N.I. Ramlan, "Energy Harvesting and Regeneration from the Vibration of Suspension System," *Applied Mechanics and Materials*, Vol. 699, pp. 800-805, 2015

[2] X. Tang and L. Zuo, "Enhanced vibration energy harvesting using dual-mass system," *Elsevier Journal of Sound and Vibration*, vol. 330, pp. 5199-5209, 2011.

[3] R.H. Patil and S.S. Gawade, "Design and Static Magnetic Analysis of Electromagnetic Regenerative Shock Absorber," *International Journal of Advanced Engineering Technology*, vol. III, April-June, 2012, 54-59.

[4] B.L.J. Gysen, P.J. Tom and J.J.H. Paulides, "Efficiency of a Regenerative Direct-Drive Electromagnetic Active Suspension," *IEEE Transaction on Vehicle Technology*, vol. 60, no. 4, pp. 1384-139, 2011.

[5] X. Lin, Y. Bo, G. Xuexun, and Y. Jun, "Simulation and Performance Evaluation of Hydraulic Transmission Electromagnetic Energy-Regenerative Active Suspension," in *Second WRI Global Congress on Intelligent System*, 2010: p. 58-61.

[6] M. A. Abdullah, J. F. Jamil, M. A. Mohamad, R. S. Rosdi and M. N. I. Ramlan, "Design selection and analysis of energy regenerative suspension," *Jurnal Teknologi (Sciences and Engineering)*, vol. 76, no. 10, pp. 27-31, 2015.

[7] J. F. Jamil, M. A. Abdullah, N. Tamaldin and A. E. Mohan, "Fabrication and testing of electromagnetic energy regenerative suspension system," *Jurnal Teknologi (Sciences and Engineering)*, vol. 77, no. 21, pp. 97-102, 2015.

Performance of compressed natural gas (CNG) engine with pre chamber

M.S. Ali[1,*], M.T. Musthafah[1], A.M. Mohd Shafei[1], A.M.T. Khairil[1], N.F.M. Nor[1], R.A. Bakar[2]

[1] Faculty of Mechanical Engineering, Universiti Teknikal Malaysia Melaka,
Hang Tuah Jaya, 76100 Durian Tunggal, Melaka, Malaysia
[2] Faculty of Mechanical Engineering, Universiti Malaysia Pahang,
26600, Pekan, Pahang, Malaysia

*Corresponding e-mail: syahir9610@gmail.com

Keywords: Pre chamber; CNG; performance

ABSTRACT – Pre chamber is use to extend lean limit of mixture and improve combustion efficiency. Pre chamber used in this study was pre chamber without auxiliary fuel. Then, this pre chamber was applied to single cylinder compressed natural gas engine. The effects of pre chamber on CNG performance are increase in power and torque starting at engine speed 3000 rpm. However, disadvantage by the pre chamber had been discovered on the brake specific fuel consumption (BSFC). It caused the BSFC by CNG was higher than a CNG without pre chamber.

1. INTRODUCTION

Original design of pre chamber was found on 2-stroke Ricardo Dolphin engine [1]. Based on this original design, many studies were carried out with different design of pre chamber. The pre chambers are divided by two types which are pre chamber with auxiliary fuel and pre chamber without auxiliary fuel. Pre chamber with auxiliary fuel is the pre chamber equip with injector inside pre chamber volume [2,3]. Pre chamber without auxiliary fuel is the pre chamber does not have any injector inside pre chamber volume[4,5]. In this study, pre chamber without auxiliary fuel was selected because it easy to fabricate and install to the engine. Then, the single cylinder spark ignition engine fuel with CNG is tested with the pre chamber. The effects of pre chamber to the CNG engine are focus on power, torque, and BSFC.

2. METHODOLOGY

The engine was tested using hydraulic dynamometer and data acquisition. The engine used in this study is single cylinder spark ignition engine. Fuel types used is CNG fuel. The complete setup for all these equipments are shown in Figure 1.

Figure 1 Complete experiment setup.

The experiment was conducted based on SAE International standard (J1349). The pre chamber was installed in front of spark plug. This pre chamber located at top of engine head. Figure 2 shows the location of pre chamber and spark plug on the engine.
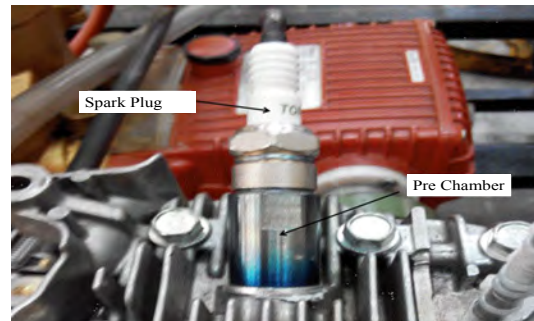
Figure 2 Location for pre chamber installed.

This methodology was illustrated by using flow chart in Figure 3.
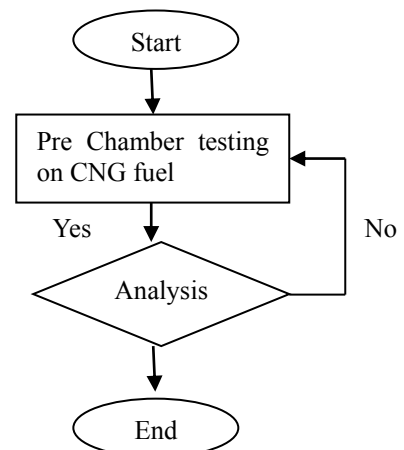
Figure 3 Flow chart for methodology.

2.1 Mathematical equation

The performance effects by the pre chamber were observer on power, torque, and BSFC. Mathematical equation for the power and torque is described based on the Equation (1):

$$\text{Torque} = \frac{\text{Power} \times 60}{2 \times \pi \times N} \tag{1}$$

Equation (1) represents the relation between the power and torque. When the powers increase, theoretically the torque should be increase. The equation for BSFC is shown in Equation (2):

$$BSFC = \frac{\dot{m}}{Power} \tag{2}$$

Based on Equation (2), main parameter for the BSFC in mass flow rate ($\dot{m}$). The power in the Equation (2) is relate with Equation (1).

3. RESULT AND DISSCUSSION

The results for this study are power, torque, and BSFC. The effect of pre chamber on the power by CNG fuel is shown in Figure 3.
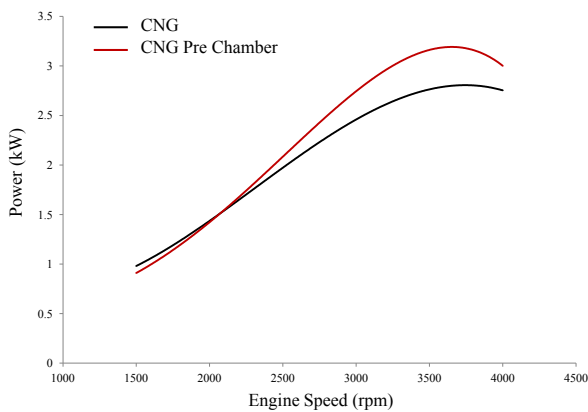
Figure 3 Effect of pre chamber on the power by CNG at various engine speeds.

Based on Figure 3, below engine speed 2000 rpm, the pre chamber caused power decrease. However, start at engine speed 2500 rpm until 4000 rpm, the pre chamber increased power by CNG fuel. The improvement by pre chamber on the power by CNG fuel is about 16%-20% improvement. This improvement also founded in torque as shown in Figure 4.
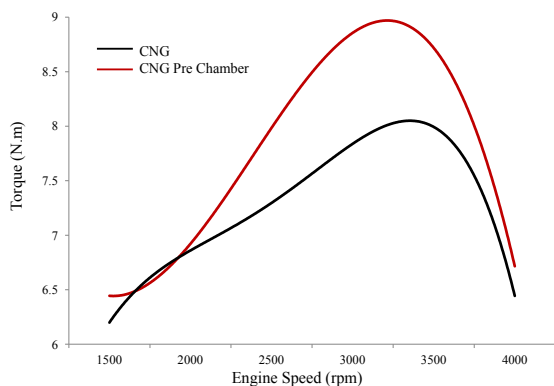
Figure 4 Effect of pre chamber on torque by CNG fuel at various engine speeds.

The pre chamber also improve the torque by CNG fuel same as power. This improvement occurred start at engine speed 2500 rpm. This improvement occurs at

same engine speed for both results are support by Equation (1). Final result is BSFC as shown in Figure 5.
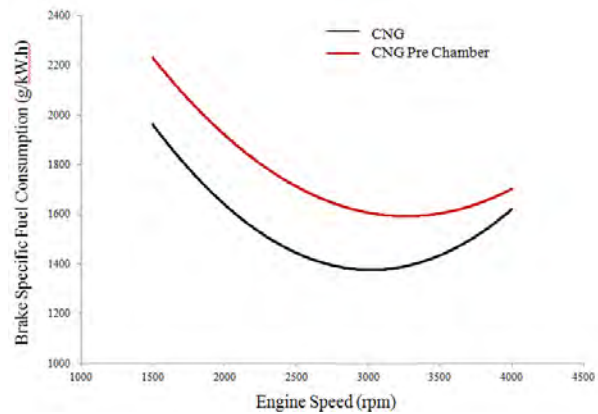
Figure 5: Effect of pre chamber on the BSFC by CNG at various engine speeds.

The pre chamber somehow increases the BSFC by CNG fuel. This is because of increase in mass flow rate and power by CNG fuel with pre chamber.

4. CONCLUSION

Application of pre chamber on CNG engine caused CNG performance increase in power and torque. However, it only starts to increase at engine speed 2500 rpm for both. Besides that, this pre chamber also gives disadvantage on the BSFC by CNG fuel. It caused BSFC increase at all engine speeds.

ACKNOWLEDGEMENT

REFERENCES

[1] E. Toulson, H. J. Schock, and W. P. Attard, "A Review of Pre-Chamber Initiated Jet Ignition Combustion Systems," *SAE International*, 2010-01-2263, 2010.
[2] C. Zuo and K. Zhao, "A Study on the Combustion System of a Spark Ignition Natural Gas Engine," *SAE Technical Paper Series*, 981386, 1998.
[3] W. P. Attard and P. Parsons, "Flame Kernel Development for a Spark Initiated Pre-Chamber Combustion System Capable of High Load, High Efficiency and Near Zero NOx Emissions," *SAE International,* 2010-01-2260, 2010.
[4] R. M. Kettner M., Velji A., Spicher U., Kuhnert D., and Latsch R., "A New Flame Jet Concept to Improve the Inflammation of Lean Burn Mixture in SI Engine.," *SAE Technical Paper,* 2005-01-3688, 2005.
[5] K. Yamanaka, Y. Shiraga, and S. Nakai, "Development of Pre-chamber Sparkplug for Gas Engine," *SAE International*, 2011-01-1870, 2011.

Validation of automotive passive engine mount system

M. Hafiz Harun[1,3,*], M.Z. Sariman[2,3], A.K. Mat Yamin[2,3], R. Yunos[1,3], M.A. Azhari[1,3], F. Ahmad[2,3]

1) Faculty of Engineering Technology, Universiti Teknikal Malaysia Melaka,
Hang Tuah Jaya, 76100 Durian Tunggal, Melaka, Malaysia
2) Faculty of Mechanical Engineering, Universiti Teknikal Malaysia Melaka,
Hang Tuah Jaya, 76100 Durian Tunggal, Melaka, Malaysia
3) Centre for Advanced Research on Energy, Universiti Teknikal Malaysia Melaka,
Hang Tuah Jaya, 76100 Durian Tunggal, Melaka, Malaysia

*Corresponding e-mail: mohamadhafiz@utem.edu.my

Keywords: Engine mount; passive system; frame structure

ABSTRACT – Engine mount has been designed to improve the engine vibration by providing unwanted vibration isolation from engine to the driver. There are three types of engine mount systems which consist of passive, semi-active and active engine mount system. This study emphasizes on the validation of mathematical equation derived from Newton Second Law of Motion with real time experiment. The engine mount characteristic generated using a 3-degree of freedom (DOF) mathematical modelling simulated in Matlab Simulink software. Finally, the mathematical model was verified by using experimental approach. The result from the experiment and simulation shows that the model is enables to generate the similar response as in the experimental result.

1.   INTRODUCTION

In automotive industry, noise, vibration and harshness (NVH) have become the critical issues concerned. Unwanted vibration generated from several sources that cause uncomfortable situation to the driver while manoeuvres the vehicle. These unwanted vibrations are caused by the road condition and the engine itself. The engine vibrations generated from the unbalance mass in the engine components. Engine mounts system was discovered to minimize the vibration transfer to the driver. There are three types of engine mounting system that had been discovered, namely passive, semi-active and active engine mount [1].

Rubber engine mount is a passive engine mounting where it usually affects by the single frequency. The passive system depends on the damping coefficient of the rubber materials used. However, rubber mount are still being used for passenger cars due to the simplicity of the design and low maintenance cost. On the other hand, Hydraulic Engine Mount (HEM) has become the main focus for bigger engine such as diesel engine vehicle. However, modern cars and trucks have become lighter from time to time whereas the performance of engine increases, thus the vibration produced is much higher [2].

In order to study the characteristic of the engine mount, the mathematical equation of frame structure system has been derived by using Newton Second Law of Motion. The frame structure proposed in this work is

considered as a small-scaled intermediate structure which has the dominant elastic modes in the frequency range of 20 Hz. The method used was referred from previous researcher in his publication [3].The main contribution of this work is to validate the mathematical model to be used before developing the control structure of semi active engine mount. In order to achieve this, the appropriate experiment on the frame structure was designed and fabricated. The vibration characteristic is filtered after the experiment to eliminate the noise and other disturbance. The passive system is used to the frame structure and subjected to vibration source which is up to 15 Hz. After establishing the sensors on the right position, the body acceleration and force transmitted was formulated. The control response such as acceleration and transmitted force at each mount are presented.

2.   METHODOLOGY

The model validation experiment is illustrated in Figure 1 contains two parts where it represents the engine and passenger compartment of passenger car while the steel frame structure represents the vehicle chassis. The electrical motor is fixed on the test rig generates the engine motion where it provides the vibration source. The frequency setting on the electrical motor will be alternately changed to generate the unbalance motion. There are two types of sensors embedded with the data acquisition device which is accelerometer and gyro sensor. Gyro sensor used to obtain the pitch and roll moment data while the accelerometer is used to collect the vertical acceleration data. The data acquisition device used in this experiment was LEGO Mindstorm EV-3. It converts the data from analog to digital data before restore in the computer.

3.   RESULTS AND DISCUSSION

This section discusses the comparison between simulation data and experimental data results. Both comparison data uses 9 Hz frequency input and the physical parameter for simulation and experiment such as length, mass and height. From the data, the trend of simulation and experimental were tremendously in correlation between each other for vertical acceleration as depicted in Figure 2.
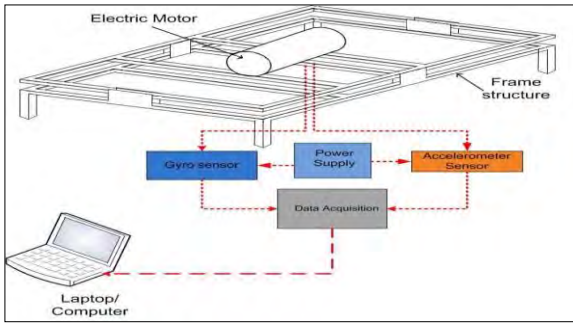
Figure 1 Experimental setup descriptions.
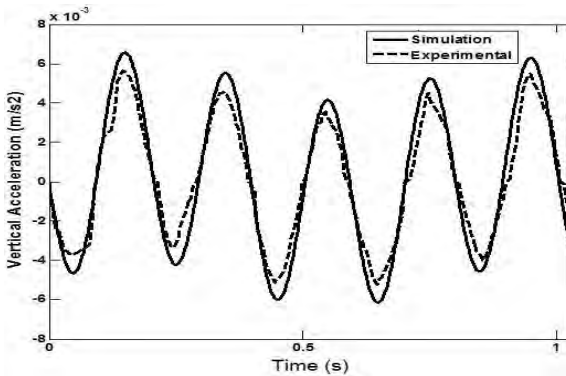
Figure 2 Comparison between the simulation results with the experiment results for the vertical acceleration with frequency input 9 Hz.

Meanwhile, Figure 3 shows the value of pitch moment acceleration for experiment is slightly higher compared to simulation results. Likewise, Figure 4 illustrates the value of roll moment acceleration for experiment is higher compared to simulation result. It is because the effect of mass and length of the frame structure. When the length of frame structure increases, the moment inertia of the structure also increases. Thus the pitch moment acceleration value also increases.
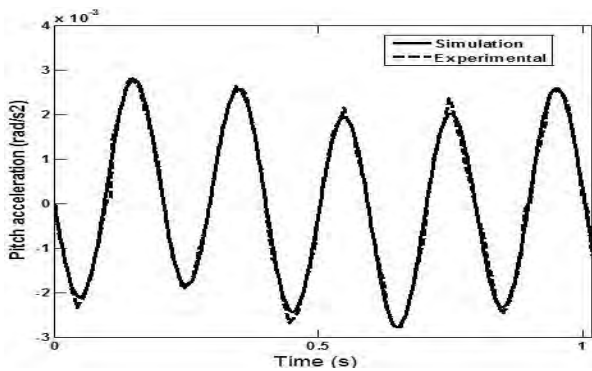
Figure 3 Comparison between the simulation results with the experimental results for the pitch moment acceleration with frequency input 9 Hz.
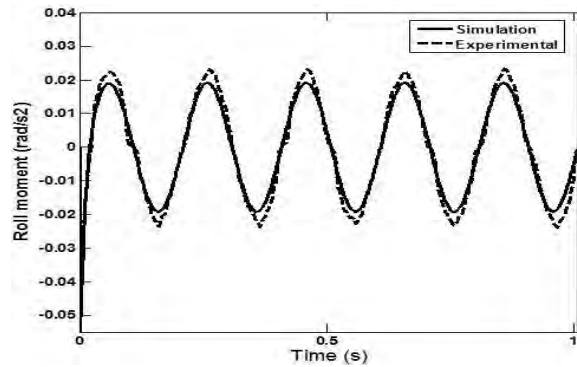
Figure 4 Comparison between the simulation results with the experimental results for the roll moment acceleration with frequency input 9 Hz.

4. CONCLUSION

As summary, the three engine mounts located on the designed test rig are able to represent the passenger vehicle engine's compartment. The engine was represented by the Direct Current (DC) motor while the chassis of the vehicle represent by the structural steel frame. The simulink model created from 3-DOF mathematical equation had been performed by using Newton Second Law of motion. The actual values of the engine mount such as damping (Cs) and the stiffness (Ks) have been used in the Simulink model. The 3-DOF passive engine mount was validated by experimental using a passive engine mount test rig and it shows that similarity trend in vertical acceleration, pitch moment acceleration and roll moment acceleration.

REFERENCES

[1] M. Elahinia, C. Ciocanel, T.M. Nguyen, and S. Wang, "MR-and ER-based Semiactive Engine Mounts: A Review," *Smart Materials Research*, p. 21, 2013.

[2] G.J. Stelzer , M.J. Schulz, J. Kim, and R.J. Allemang, "A Magnetorheological Semi-Active Isolator to Reduce Noise and Vibration Transmissibility in Automobiles," *Journal of Intelligent Materials Systems and Structures*, vol. 14, pp. 743-765, 2003

[3] S.R. Hong, S.B. Choi, and M.S. Han, "Vibration Control of a Frame Structure using Electrorheological Fluid Mounts," *International Journal of Mechanical Sciences*, vol. 44, pp. 2027-2045, 2002.

Optimization of friction coefficient of kenaf/epoxy composites as an alternative friction material using Taguchi method

A. Mustafa[1], M.F.B. Abdollah[1,2,*], H. Amiruddin[1,2], F.F. Shuhimi[1], N.A.M. Tahir[1], N. Muhammad[1,2], S.E. Mat Kamal[1,2], N. Ismail[1,2,3]

[1] Faculty of Mechanical Engineering, Universiti Teknikal Malaysia Melaka,
Hang Tuah Jaya, 76100 Durian Tunggal, Melaka, Malaysia
[2] Center for Advanced Research on Energy, Universiti Teknikal Malaysia Melaka,
Hang Tuah Jaya, 76100 Durian Tunggal, Melaka, Malaysia
[3] Department of Surface Technology and Tribology, Faculty of Engineering Technology, University of Twente,
P.O. box 217, 7500 AE Enschede, The Netherlands

*Corresponding e-mail: mohdfadzli@utem.edu.my

Keywords: Kenaf; polymer composite; friction coefficient

ABSTRACT – This paper introduces the application of Taguchi optimization methodology in optimizing the design factors for obtaining high friction coefficient of kenaf/epoxy composites under dry sliding condition. An orthogonal array of the Taguchi method was set-up and used to analyse the effect of the design parameters on the friction coefficient. Tribological testing was conducted using a pin-on-disc tribometer. For the highest friction coefficient, 45wt.% non-treated kenaf fiber sliding at 19.62N, 500rpm and 100°C is found to be the optimized combination of levels of all the six control factors. The confirmation test proves that the optimized friction coefficient is within the range of friction coefficient of conventional friction material.

1. INTRODUCTION

Recently, the interest in using natural fibers as a reinforcement for polymeric composites is increased due to their properties such as less weight, renewability, low density, high specific strength, non abrasivity, combustibility, non-toxic, low cost and biodegradability [1,2].

Kenaf fibers have a long history of cultivation in Asia and southeast Europe. The fiber has been mainly used in rope, twine, coarse cloth and paper. However, nowadays, there is demand for the fibers to be used as reinforcement for polymers.

However, the potential of using high interfacial adhesion kenaf fibers as reinforcement for tribo-composites based polymer has not been explored yet. This motivates the current work in determining the optimal design parameters for high friction coefficient of kenaf/epoxy composites under dry sliding condition using Taguchi method.

2. METHODOLOGY

2.1 Design of experiment

In this study, Taguchi method consists of L18 orthogonal array was selected using Minitab statistical software. The 18 total runs with 6 factors and 2-3 mixed levels are shown in Table 1 and 2. The response in this study is friction coefficient, where larger value is better.

A confirmation test was carried out to verify the quality characteristic using optimal levels of each factor.

2.2 Sample preparation and tribological test

The kenaf polymer composite was prepared by mixing several weight percentages of kenaf with epoxy, as a resin, where the ratio of epoxy to hardener is 4:1. The sample was fabricated as a pin with 10mm diameter using hot-cold compression machine.

Table 1 Design parameters at 2-3 mixed levels.

Level	Factors					
	Types	**Tr**	**wt. %**	**Load (N)**	**Speed (rpm)**	**Temp (°C)**
1	P	NT	30	19.62	200	24
2	F	T	45	49.05	500	100
3	-	B	60	98.1	1000	150

P:Powder; **F**:Fibers; **Tr**:Treatment; **NT**:Non-treated; **T**:Treated; **B**:Bleached; **wt**:Kenaf weight composition

Table 2 Taguchi L₁₈ orthogonal arrays.

Run	Types	Tr	wt.%	Load	Speed	Temp
1	1	1	1	1	1	1
2	1	2	1	2	2	2
3	1	3	1	3	3	3
4	1	1	2	1	2	2
5	1	2	2	2	3	3
6	1	3	2	3	1	1
7	1	1	3	2	1	3
8	1	2	3	3	2	1
9	1	3	3	1	3	2
10	2	1	1	3	3	2
11	2	2	1	1	1	3
12	2	3	1	2	2	1
13	2	1	2	2	3	1
14	2	2	2	3	1	2
15	2	3	2	1	2	3
16	2	1	3	3	2	3
17	2	2	3	1	3	1
18	2	3	3	1	1	2

Eighteen run (L_{18}) of tribological tests, as shown in Table 2, were carried out using a pin-on-disc tribometer according to the ASTM G99-10 standard. The sample was slided against polished JIS-SKD 11 steel disc. The friction coefficient, μ was calculated using Equation (1):

$$\mu = \frac{F_f}{F_n} \qquad (1)$$

Where F_f is the frictional force and F_n is the normal load. Both loads are in unit N.

3. RESULTS AND DISCUSSION

Friction coefficient obtained range from 0.21-0.52. The response was analysed using combination methods of signal-to-noise (S/N) ratio, means and Analysis of Variance (ANOVA) in order to identify the optimal design parameters. Table 3 shows the percentage of contribution, obtained from ANOVA, for S/N ratio and means of each factor. A higher contribution is required in determining the optimal design parameters either using S/N ratio or means value.

From Figure 2, a greater S/N ratio or means value corresponds to a better performance, where high friction coefficient can be obtained. For the highest friction coefficient, 45wt.% non-treated kenaf fiber sliding at 19.62N, 500rpm and 100ºC is found to be the optimized combination of levels of all the six control factors. This is believed due to the presence of waxy layers and impurities of non-treated kenaf fiber [2]. Besides, rougher surfaces may produce larger variations in the contact area and, thereby exhibit more friction. The experimental study proved that the arithmetic mean surface roughness, Rz of non-treated sample (Rz=0.105) is larger than treated sample (Rz=0.089).

Table 3 Percentage of contribution obtained from ANOVA for S/N ratio and means of each factor.

Source	DOF	SS S/N	SS Mean	S/N Cntrb. (%)	Mean Cntrb. (%)
Types	1	6.956	0.00761	7.68	5.742
Wt.%. Kenaf	2	10.41	0.01730	11.50	13.048
Treatments	2	2.477	0.00471	2.74	3.554
Load (N)	2	16.44	0.03613	18.16	27.245
Speed (rpm)	2	13.52	0.01820	14.94	13.721
Temperature (ºC)	2	16.26	0.02022	17.97	15.2461
Error	6	24.47	0.02844		
Total	17	90.55	0.13264		

A confirmation test, as shown in Figure 3, can successfully verify the friction coefficient of 45wt.% non-treated kenaf fiber is within the range of 0.40 to 0.44 of conventional friction materials. This friction coefficient value is recommended for friction material performance [3].

4. CONCLUSION

In this study, Taguchi method was applied to determine the optimal parameters leading to the maximum friction coefficient of kenaf/epoxy composites. It was found that the friction coefficient of 45wt.% non-treated kenaf fiber sliding at 19.62N, 500rpm and 100ºC is within the range of conventional friction material (0.35-0.45).
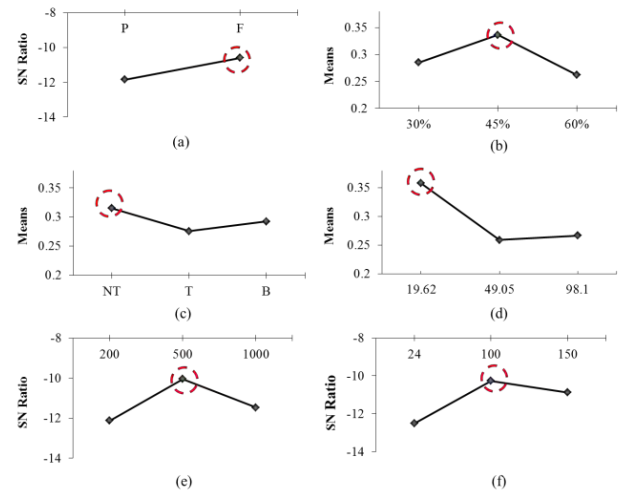
Figure 1 The selected optimal design parameters for (a) type of kenaf, (b) wt.% kenaf, (c) treatment method, (d) normal load, (e) speed and (f) temperature.
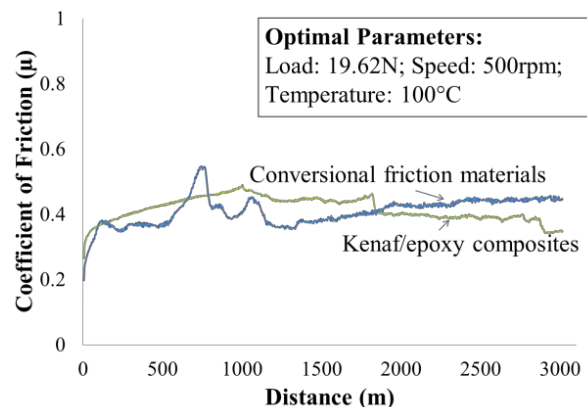
Figure 2 A confirmation test results by comparing the friction coefficient of kenaf/epoxy composites and conventional friction material using optimal design parameters.

REFERENCES

[1] U. Nirmal, J. Hashim, S.T.W. Lau, M.Y. Yuhazri, B.F. Yousif, "Betelnut fibres as an alternative to glass fibres to reinforce thermoset composites: a comparative study," *Textile Research Journal*, vol. 82, pp. 1107–20, 2012.

[2] B.F. Yousif, N.S.M. El-Tayeb. Adhesive wear performance of T-OPRP and UT-OPRP composites.Tribology Letter, vol. 32, pp. 199–208, 2008.

[3] A.E. Anderson. *Friction and wear of automotive brakes*, ASM handbook, vol. 18, 1992.

Application of waste chicken fat in base catalyzed (potassium hydroxide) biodiesel production

N.H. Razak[1,2,*], M.I.A.K.M. Safari[1], H.A. Merican[3], F. Ghafar[3], N.I. Zulkafli[1,2,4]

1) Faculty of Mechanical Engineering, Universiti Teknikal Malaysia Melaka,
Hang Tuah Jaya, 76100 Durian Tunggal, Melaka, Malaysia

2) Centre for Advanced Research on Energy, Universiti Teknikal Malaysia Melaka,
Hang Tuah Jaya, 76100 Durian Tunggal, Melaka, Malaysia

3) Section of Chemical Engineering Technology, Universiti Kuala Lumpur Malaysia Institute of Chemical
& Bioengineering Technology (UniKL MICET), Vendor City, 78000 Taboh Naning, Alor Gajah, Melaka, Malaysia

4) School of Energy, Environmental Technology and Agrifood, Cranfield Campus,
Cranfield University, MK43 0AL Bedfordshire, United Kingdom

*Corresponding e-mail: nurulhanim@utem.edu.my

Keywords: Biodiesel; waste chicken fat; base catalyzed transesterification

ABSTRACT – The objective of this research was to analyze the effect of temperature, catalyst ratio and methanol ratio on biodiesel yield from waste chicken fat. The optimum yield were 95.4% with 0.006 w/w catalyst and 0.3 w/w alcohol at 50°C. The product density was 873.4 kg/m^3, the iodine value, 117 g I/100g and the acid value, 0.561 mg KOH/g. The compositions of fatty acids were 0.22% of methyl laurate, 19.98% of methyl palmitate, 41.08% of methyl stearate and 0.17% of methyl linoleate. Consequently, the biodiesel obtained under these conditions had characteristics very similar to those described in the ASTM standards.

1. INTRODUCTION

Nowadays, the alternative lipids waste residues as waste frying cooking oil and inedible waste animal fats have also majoring considerable attention from green fuel sector. Consequently, a recycled program, which has to reuse residues in order to take advantage of these low cost and low quality resources, and hence successfully integrate the sustainable energy supply and waste management in food processing facilities. The waste chicken fat (WCFs) have a great potential as feedstocks for biofuel industry, because they are not commodities, having a lower market value.

Darunde [1] claimed that the saturated fatty acids from WCF are the source of high CN and the values over 60 are common. Soybean oil based biodiesel usually has a CN about 48-52 and petroleum-based diesel fuel is usually between 40 and 44. As a result, the WCF with a higher CN, indicating a shorter ignition delay time, more complete combustion of the fuel and hence should improve the fuel efficiency.

Furthermore, the WCF biodiesel could bring a number of environmental, economic and social advantages. Biodiesel is free from sulfur, hence less sulfate emissions, and reduced particulate matters (PM) in the engine exhaust. Due to the near absence of sulfur in the WCF, it helps reduce the problem of acid rain caused by emission of pollutant from fuels burning. The lack of aromatic hydrocarbon (benzene, toluene etc.) in

biodiesel reduces unregulated emissions as well as ketone, benzene etc. Breathing particulate matter has been found to be hazardous for human health, especially in terms of respiratory system problems. PM consists of elemental carbon (~31%), sulfates and moisture (~14%), unburnt fuel (~7%), unburnt lubricating oil (~40%) and potential remaining metals and others substances [2].

2. MATERIALS AND METHODOLOGY

2.1 Transesterification reaction and separation process

The chicken fat was heated up till desired temperature. The temperatures are 50°C, 60°C and 70°C. As the oil has reached the desired temperature, the mixture of potassium hydroxide and methanol was poured into the beaker containing the waste chicken oil. The speed of the stirring was kept at 200 rpm throughout the experiment. The reaction time is kept constant for one hour. The time allocated for the product to separate was six hours. The top product is biodiesel while the bottom product in the separator funnel is glycerol. The glycerol is removed from the separator funnel and discarded.

2.2 Analysis of biodiesel

In order to determine the characteristic of the biodiesel sample was analyzed by using four different analyses such as acid value test, iodine value test, density test and Fatty Acid Methyl Ester (FAME) analysis.

3. FINDINGS AND DISCUSION

3.1 Effect of temperature to biodiesel

The rate of reaction is influenced by the reaction temperature as per kinetics of reaction. Generally the reaction is conducted close to the boiling point of the methanol at the atmospheric pressure [3]. The maximum yield of esters was observed at temperature ranging from 50 ± 5°C. Figure 1 shows the highest percentage of yield at 50°C.
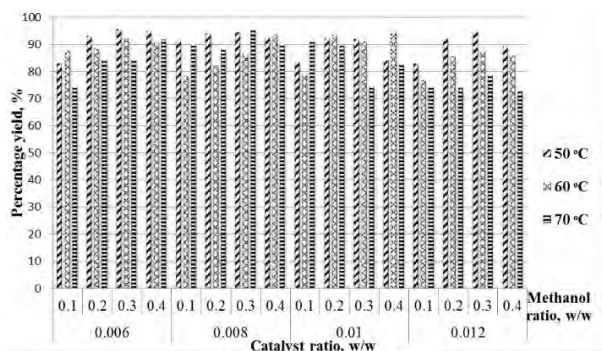
Figure 1 Effect of temperature, catalyst ratio and methanol ratio on biodiesel yield.

3.2 Effect of methanol ratio to biodiesel

Based on Figure 1, the optimum alcohol ratio for transesterification is at 0.3 w/w as it yields the highest biodiesel up to 95.4%. This situation shown concluded that as when the methanol ratio is high, the biodiesel yield decreases. According to Komintarachat and Chuepeng [3], at higher methanol amount, the free fatty acid (FFA) conversion increased but the yield decreased. This is due to the transesterification reaction which is reversible as the additional methanol accelerates considerably an adjustment of the new equilibrium. A high amount of methanol interferes the separation of glycerol due to an increase in solubility while the glycerol remaining in the solution drives the reaction equilibrium back, resulting in the lower yield of biodiesel.

3.3 Effect of catalyst ratio to biodiesel

A catalyst functions to accelerate the reaction rates. Catalyst is an important factor in transesterification of waste chicken fat into biodiesel. The catalysts that are commonly used are KOH and sodium hydroxide (NaOH). According to the obtained data, it can be seen that the more catalyst being used, the more yield is obtained but the reaction decreases. This is because, if too much catalyst is being used, the reaction might change to saponification reaction that produces soap. Soap is the undesired product. Therefore it can be said that the optimum catalyst ratio that yield the most biodiesel is 0.01 w/w with the biodiesel conversion of 95.4%. The same trend was discovered by Komintarachat and Chuepeng [3], which mentioned that an increasing amount of catalyst will caused the slurry which is a mixture of catalyst to reactant to occur problem in mixing thus a demand of higher power is required for adequate stirring.

3.4 FAME analysis

The composition of biodiesel was determined using gas chromatography (GC) with retention time was 20 minutes. There are four fatty acids in the biodiesel that was able to be identified which are methyl laurate, methyl palmitate, and methyl stearate and methyl linoleate. The percentage composition for methyl laurate is 0.22%, methyl palmitate is 19.98%, methyl stearate is 41.08% and methyl linoleate is 0.17% as shown in Table 1.

Table 1 Experimental value of biodiesel with the standard value.

Characteristic	Experimental Value	EN 14214	ASTM standard
Density, kg/m^3	873.4	860-900	860-900
Acid Value, mgKOH/g	0.561	< 0.5	< 0.8
Iodine Value g I/100g	117.0	< 120	< 120

4. CONCLUSION

Transesterification reaction involves WCF to react with alcohol with the presence of base catalyst (KOH) to yield biodiesel and glycerol. The optimum parameters for producing biodiesel in this project is at 50°C with the ratio of catalyst to oil 0.006 w/w and methanol to oil ratio of 0.3 w/w. The yield obtained at this parameter is 47.7 g of biodiesel and the percentage of yield is 95.4%. The organic compounds in the biodiesel produced consist 0.22% methyl laurate, 19.98% methyl palmitate, 41.08% methyl stearate and 0.17% methyl linoleate. The iodine value of the biodiesel produced is 117 gI/100g while the density obtained is 873.4 kg/m^3 and the acid value of 0.561 mgKOH/g that met EN 14214 and ASTM D6751 biodiesel specifications.

REFERENCES

[1] Darunde Dhiraj S, and Deshmukh Mangesh M., "Biodiesel Production from Animal Fats and its Impact on the Diesel Engine with Ethanol-Diesel Blends: A Review", *International Journal of Emerging Technology and Advanced Engineering*, vol. 2, no. 10, pp. 179-185, 2012.

[2] Agarwal AK., "Biofuels (alcohols and biodiesel) applications as fuels for internal combustion Engines", *Progress in Energy and Combustion Science*, vol. 33, pp. 233–271, 2007.

[3] Komintarachat, C., and Chuepeng, S. "Methanol-Based Transesterification Optimization of Waste Used Cooking Oil Over Potassium Hydroxide Catalyst", *American Journal of Applied Science*, vol. 7, no. 7, pp. 1073-1078, 2010.

Brake insulator analysis in reducing internal brake squeal noise

M.A. Abdullah[1,2,*], A.R. Efariani[1]

[1] Faculty of Mechanical Engineering, Universiti Teknikal Malaysia Melaka,
Hang Tuah Jaya, 76100 Durian Tunggal, Melaka, Malaysia
[2] Centre for Advanced Research on Energy, Universiti Teknikal Malaysia Melaka,
Hang Tuah Jaya, 76100 Durian Tunggal, Melaka, Malaysia

*Corresponding e-mail: mohdazman@utem.edu.my

ABSTRACT – Brake functions when two different materials are in contact to reduce a motion. Due to surface irregularity, this contact at high revolution and contact force produce irritating noise called brake squeal noise. This paper presents the study of introducing brake insulator into the brake assembly in order to reduce the noise. Different configurations of insulators are used in the Finite Element Analysis (FEA). The squeal is shown by positive real part of the baseline graph. The accompanied slip rate in the baseline model of the insulator increases the brake squeal noise significantly.

1. INTRODUCTION

There are few terminologies for brake noise such as squeal, groan, chatter, judder, moan, hum and squeak that can be found in literature. However, the terminology that often be used is squeal. The phenomenon of squeal is probably the most common, disturbing to users and environment, and its cost the manufacturer in term of warranty. There are no precise definitions for brake squeal, but it is frequently agreed that squeal occurred at frequency above 1000 Hz [1,2]. Drum brake (Figure 1) produces significant amount of noise compared to disc brake. Motorcycle brake which is using the drum brake type is used for this study.

Brake is one of the most important things that need to be considered when producing a vehicle. The squealing sound that produced from the brake not only contributed to the noise pollution, but also make the users are not comfortably used the vehicle. They thought that the brake might be broken down and the vehicle are not safely be used which will lead them to claim a warranty from the company that produced the vehicle.

2. METHODOLOGY

There are two stages have been followed to achieve the objective, which are: i) develop the finite element model of the rear drum brake system that based on the real system components, ii) run the stability analysis with and without insulator to analyze the effectiveness of the insulator in squeal suppression. The stress analysis performed [3-6] using ABAQUS software through complex eigenvalue analysis (CEA), the positive real part of the (CEA) indicate unstable frequency (the propensity of squeal occurrence).

Different types of material for the insulators (Figure 1) have been proposed to reduce the squeal generation and it was found that the method is efficient to suppress the squeal occurred but it does not fully eliminate the squeal generated.
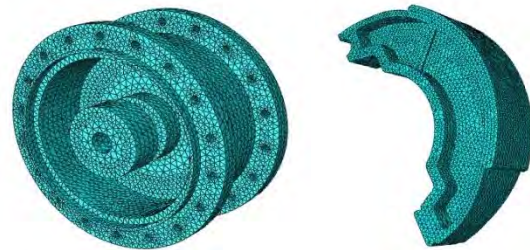
Figure 1 Drum brake and shoe insulator.

There are a few approaches used in predicting the probability of the squeal occurrence which are theoretical, experimental and Finite Element (FE) approaches. Besides, there are several methods also proposed to suppress or reduce the squeal occurrence which are; structural modifications, active control and adding damper. From the three methods, adding damper is the most efficient method and it may be applied by changing the material with high damping material or by adding insulator to the pad or shoe, which depend on what type of brake that will be used (Figure 2 and Table 1). Finite element (FE) method of drum brake system for motorcycle will be used to predict the squeal occurrence from 1 kHz until 10 kHz and insulator will be used to reduce the noise.
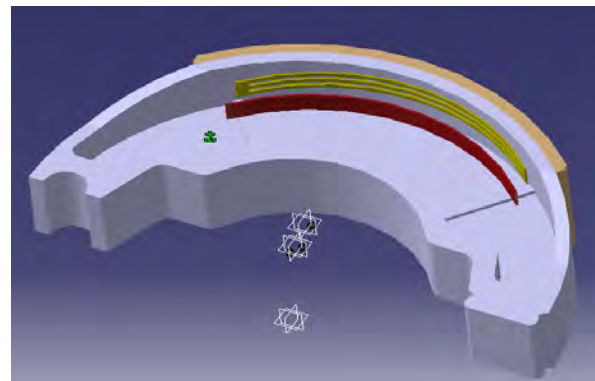
Figure 2 Insulator configuration.

Table 1 Sample insulator configuration.

Sample	Configuration
1	Frame rubber 0.5 mm thickness & steel plate 0.5 mm thickness
2	Frame ABS 0.5 mm thickness & steel plate 0.5 mm thickness
3	Rubber plate 0.5 mm thickness & aluminum plate 0.5 mm thickness.
4	Frame ABS 0.5 mm thickness & aluminum plate 0.5 mm thickness
5	Rubber plate 0.5 mm thickness & composite plate 0.5 mm thickness
6	Frame ABS 0.5 mm thickness & composite plate 0.5 mm thickness

3. RESULTS AND DISCUSSION

Figure 3 shows the predicted result of the squeal occurrence of the FE model of the drum brake system. The result of the project will be compared between the baseline models which have a static coefficient of friction without slip rate and another one is baseline models with the presence of slip rate. The complex eigenvalue analysis performed by setting a set of boundary condition, where the frequency of interest is between 1 to 10 kHz, the rotational speed of drum is set to be 40 rad/s, the displacement of the cam for brake applying is set to be 4 mm and the coefficient of friction, μ is varied from 0.3 to 0.5. It is clearly can be seen that baseline model without slip rate that contains coefficient of friction, $\mu=0.30$ have no squeal generation. However, the squeal is detected when the coefficient of friction, μ is 0.4 and 0.5. There is one squeal detected for $\mu=0.4$ at frequency 5677.7 Hz and $\mu=0.5$ at frequency 5659.9 Hz. Previously in literature review, it is stated that this phenomenon occurred is due to the magnitude of stiffness matrix with increasing friction coefficient. The addition of the friction coupling forces at the friction interface result in the stiffness matrix for the system containing unsymmetrical off-diagonal coupling term. From this stability point of view, this coupling is considered as the reason of brake squeal occurred.
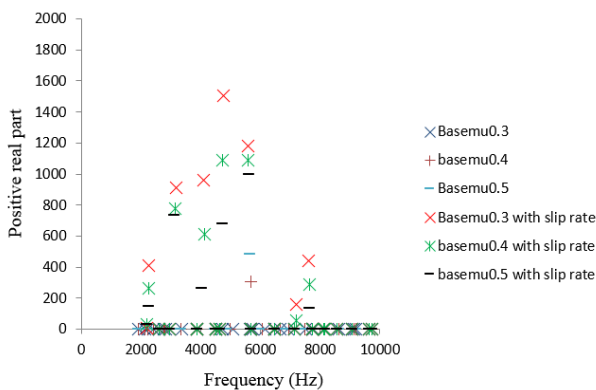
Figure 3 Baseline graph results at different coefficient of friction.

4. CONCLUSION

Complex eigenvalue analysis is the tool that has been used successfully to predict the squeal noise in a drum brake system. Using complex eigenvalue analysis may help in reducing the cost of the experimental tests and shorten the time of the experimental test by just doing analysis, and also it will provide a clear vision about which design could be more successful. Based from the result in previous section, it is clearly can be seen that brake insulator could help in reducing brake squeal. Although all the pair of materials has a potential to reduce the brake squeal, however, the pairs of iron material with rubber show more detail and precise result compare to the pairs of iron material with ABS.

REFERENCES

[1] M.K. Abdul Hamid, N.I. Shamsudin, A.R. Mat Lazim, A.R. Abu Bakar, "Effect of Brake Pad Design On Friction and Wear with Hard Particle Present," *Jurnal Teknologi*, Vol 71, No 2, 135-138, 2014.

[2] A. R. Mat Lazim, A. R. A. Bakar, M. Kchaou, "The Study of Disc Brake Noise on Three Different Types of Friction Materials", *Applied Mechanics and Materials*, Vol. 663, pp. 113-118, 2014.

[3] Abdullah, Mohd Azman, Tamaldin, Noreffendy, Ramli, Faiz Redza, Sudin, Mohd Nizam And Mohamed Muslim, Abdul Mu'in, "Design and Development of Low Cost All-Terrain Vehicle (ATV)," *Applied Mechanics and Materials*, Vols. 663, pp 517-521, 2014.

[4] M.A. Abdullah, A.H. Mohamad and F.R. Ramli, "Design Analysis and Fabrication of Fixed-Base Driving Simulator Frame," *Journal of Engineering and Technology*, Vol. 4, No. 2, 2013.

[5] M. A. Abdullah, M. R. Mansur, N. Tamaldin and K. Thanaraj, "Development of Formula Varsity Race Car Chassis," *IOP Conference Series: Materials Science and Engineering*, Vol. 50, No. 1, 2013.

[6] Mohd Azman. Abdullah, Muhd Ridzuan. Mansor, Musthafah. Mohd Tahir, Syahibudil Ikhwan. Abdul Kudus, Muhammad Zahir. Hassan and Mad Nasir. Ngadiman, "Design, Analysis and Fabrication of Chassis Frame for UTeM Formula Varsity™ Race Car," *International Journal of Mining, Metallurgy & Mechanical Engineering,* Vol. 1, No. 1, 75-77, 2013.

Influence of tire stiffness and sprung mass on ride quality

A. Md Saad[1,2,*], M.A. Salim[1,2], M.H. Harun[1], M.R. Mansor[1,2], M.Z. Akop[1,2], M.T. Musthafah[1,2]

[1)] Faculty of Mechanical Engineering, Universiti Teknikal Malaysia Melaka,
Hang Tuah Jaya, 76100 Durian Tunggal, Melaka, Malaysia
[2)] Green Technology Vehicles Research Group, Centre for Advanced Research on Energy, Universiti Teknikal Malaysia Melaka, Hang Tuah Jaya, 76100 Durian Tunggal, Melaka, Malaysia

*Corresponding e-mail: adzni@utem.edu.my

Keywords: Tire stiffness; sprung mass; ride quality

ABSTRACT – Automobile ride quality is a vehicle characteristic of great importance. It is a factor that consumer is very sensitive to, and which can have a profound influence on passenger comfort. The purpose of this study is to investigate the effects of tire stiffness and sprung mass on ride quality. Numerical simulation is used by representing ideal physical of vehicle quarter car model into Bond Graph. By lowering tire stiffness, it reduces the worst frequency response due to external force but the natural frequency of the system remains the same. However, by increasing the sprung mass, it reduces the natural frequency of the system but the worst frequency due to external forces is comparably same.

1. INTRODUCTION

With the purpose of producing customer oriented products, comfort is becoming one of the most important aspect in designing a vehicle. Comfort is perhaps the most obvious attribute to ride quality.

A harsh riding vehicle subjects the passengers to significant acceleration levels. In some cases, for example in trucks and off-road construction equipment, these acceleration levels can cause chronic medical conditions. An overly soft riding vehicle can cause passengers to develop motion sickness.

Safety is an issue from the standpoint of driver fatigue, which may be accelerated in cars with poor ride quality characteristics. However, safety can also be compromised by poor stability and maneuverability characteristics, which can result from a car designed solely to improve ride quality. This can be seen in cars designed as luxury sedans, which handle much worse than sport cars in which suspensions have been designed for handling at the expense of ride quality. Additionally, a harsh riding vehicle may also affect reliability. Car components as well as the driver are subjected to higher forces in a car with poor ride quality. This can limit the life expectancy of the components.

The objectives of this study is to investigate the effects of tire stiffness and sprung mass in ride quality. The changes of these two properties have strong relation to our everyday driving. For the purpose of this study, tire is assumed to be deflated and the stiffness reduces by 35%. For the effect of sprung mass, the car is assumed to have 5 passenger with average mass of 70kg. It increases total sprung mass of the vehicle by 350kg.

2. RESEARCH METHODOLOGY

This study was conducted by using 20sim software. Firstly, a quarter car model was used and represented as Bond Graph as shown in Figure 1. Model parameters used for this simulation were shown in Table 1.
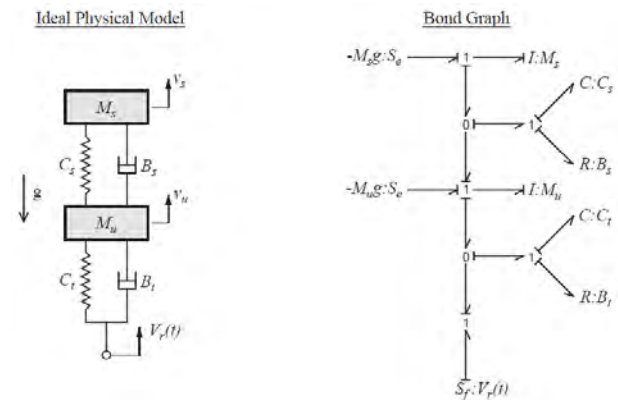
Figure 1 Quarter car model.

Table 1 Model parameters.

Parameters	Values
Sprung Mass, M_s (kg)	1068
Suspension Stiffness, K_s (N/m)	74968
Suspension Damping, B_s (Ns/m)	2800
Unsprung Mass, M_u (kg)	146.4
Tire Stiffness, K_t (N/m)	775660
Tire Damping, B_t (Ns/m)	800

Model input to the system was determined by roughness of the road. Idealized road profile was used and it represented by sinusoidal bumps of wavelength, L and amplitude, R (road roughness) as shown in Figure 2. The road profile can be described by Equation (1).

$$y_r(x) = R \sin\left(\frac{2\pi}{L}x\right) \tag{1}$$

For the purpose of this study, constant forward velocity used was 25m/s with road roughness, R of 0.05m. Wavelength, L used were 0.5m, 1m, 2m, 2.5m, 6m, 10m, 12m, 15m, 20m, 23m, 30m and 50m.
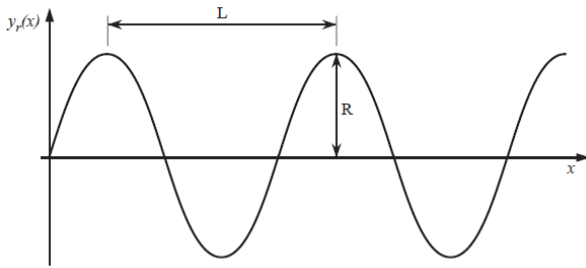
Figure 2 Rough road model.

3. RESULTS AND DISCUSSION

In this section, results of the test will be discussed in details. Initial response of the system with original tire stiffness and without any changes of sprung mass obtained from Bode plot showed that the system had two worst bump frequencies. Natural frequency of the system was 8.035 rad/s with magnitude of 29.825 dB. Worst frequency due to input road roughness was 73.621 rad/s with magnitude of 18.054 dB.

For the effect of tire stiffness, it was assumed that the tire was deflated and the stiffness reduced by 35%. Response of the system by having lower tire stiffness was shown on Figure 3 below. It has 2 worst bump frequencies with corresponding amplitudes. Frequency with highest corresponding amplitude was the natural frequency of the system. Based on the plot, the natural frequencies of the system showed minor changes. Natural frequency was 7.852 rad/s with magnitude of 30.242 dB. But, by having lower tire stiffness, it reduced the worst frequency response of the system due to the sinusoidal road profile input. Worst frequency response recorded was 59.566 rad/s with corresponding magnitude of 16.296 dB.
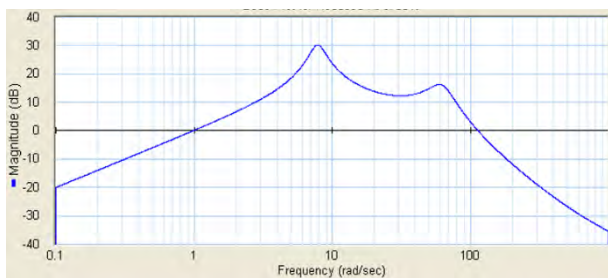
Figure 3 Bode plot of the system with 35% reduction of tire stiffness.

For the effect of sprung mass, it was modeled with the assumption that the vehicle had 5 passengers with average mass of 70kg. It increased total sprung mass by 350kg. The frequency response of the system was shown on Figure 4 below. The system had two worst frequencies with corresponding magnitudes. Frequency with highest magnitude was the natural frequency of the system and the other frequency was the worst frequency response

due to external force that acting on the system. Based on the plot, by increasing the sprung mass it reduced the natural frequency of the system. The new natural frequency was 6.966 rad/s with magnitude of 29.705 dB. But, the worst frequency of the system due to the external forces was comparably same with initial condition. By increasing the value of sprung mass also increased tire deformation. Tire deformation response was shown in Figure 5 below. The steady state value of the deformation was 0.02m.
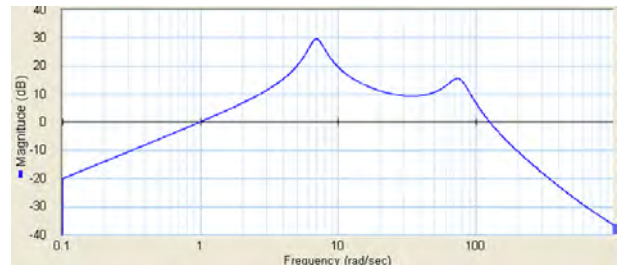
Figure 4 Bode plot of the system with 350 kg additional sprung mass.
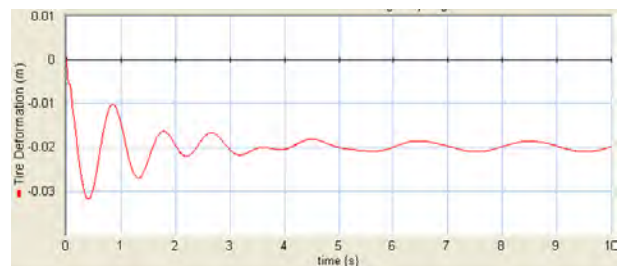
Figure 5 Tire deformation of additional 350 kg of sprung mass.

4. SUMMARY

This study was carried out to determine the effects of tire stiffness and sprung mass on ride quality. Numerical simulation by utilizing 20sim software was used as tool for this investigation. Ideal physical quarter car model was represented by using Bond Graph. Results showed that by lowering tire stiffness, it reduced the worst frequency response but the natural frequency of the system remained the same. However, by increasing the sprung mass, it reduced the natural frequency of the system but the worst frequency due to external forces was comparably same.

REFERENCES

[1] D.C. Karnopp, D.L. Margolis and R.C. Rosenberg, Sytems Dynamics; Modeling and Simulation of Mechatronic System, 4th Edition John Wiley & Sons Inc; 2005

[2] T.D. Gillespie, Fundamental of Vehicle Dynamics, Society of Automotive Engineers;1999.

Driving behaviour analysis of young vehicle drivers

M.A. Abdullah[1,2,*], M.A.H. Abdul Rahim[1]

[1] Faculty of Mechanical Engineering, Universiti Teknikal Malaysia Melaka,
Hang Tuah Jaya, 76100 Durian Tunggal, Melaka, Malaysia
[2] Centre for Advanced Research on Energy, Universiti Teknikal Malaysia Melaka,
Hang Tuah Jaya, 76100 Durian Tunggal, Melaka, Malaysia

*Corresponding e-mail: mohdazman@utem.edu.my

ABSTRACT – Different driver carries different driving behaviour and style. The most dangerous behaviour is the aggressive behavior, normally for young drivers. This behaviour can cause danger to the driver and other people. The driving behaviour can be detected from the way they control the vehicle during cornering, through uneven road and during accelerating and decelerating. How they handle the vehicle can be seen from the values of roll, pitch and yaw moments and *x, y, z* accelerations. The driving behaviour can be identified and classified according to the data collected. Usually at a higher value of moments and accelerations, the vehicle was controlled by the driver with quite aggressive driving style. In this paper, a number of young vehicle drivers are selected to perform driving test. From the test data, they will be classified based on the range of values.

1. INTRODUCTION

Driving behaviour is the behaviour when the driver drives a car or vehicle and the ways he or she control the car or any other vehicle in accelerating, braking, taking a corner, out of a junction and many more. The behaviour of the driver can be considered in many ways. It can easily be said that whether the driver is a good driver or bad driver based on when he or she control the vehicle on the road [1]. The behaviour also can be based on the driving ability, driving environment, demographic factor personal characteristic and perceived environment that influence the behaviour become a good or bad behaviour [2,3].

Teenagers nowadays can get their driving license as early as 17 years old. At this earliest of age, there are many types of behaviour among these young drivers. This behaviour of the young drivers will affect the traffic safety and increasing of traffic accident that happen almost every day. There were drivers that have a good skill in driving and not. The behaviour of the drivers also was change by time. The driving behaviours were influenced by many factors. The behaviour of the drivers has been determined from all the force from the vehicle that had been driven by the driver. The main objective of this project is to analysis the driving behaviour among teenagers. The behaviours of the drivers relate to the skill of the drivers. The behaviour of the drivers also can be analysed from the way there were control the car at various situations on the road taken.

2. METHODOLOGY

The scopes that need to be done on this project is needed to collect the data of horizontal, vertical, lateral vibrations and pitch, yaw, roll moments of the car using Lego Mindstorms EV3 [4] (Figure 1). Before that the vehicle has been weighed using the DAQ system. From the data taken, graph of these data were made and the graph was analyzed to determine the behavior of the driver [5,6]. In this project, LEGO Mindstorm as shown in Figure 1 will be used as the DAQ in order to determine the values of the moments and accelerations of a vehicle [7]. Five number of drivers (male, 21 years of age) are randomly selected for the experiment.

Figure 1 Lego Mindstorms DAQ and sensors.

Vehicle that makes a journey on the road tend to have a force when they are travelling through various types of road conditions such as go through a bumpy road, taking a cornering, exit of the junction and also when accelerating and decelerating. The force that the vehicle will be having is vibration or acceleration between x, y and z axis and moments that are roll, pitch and yaw moments. Figure 2 shows the driving route for the experiment.
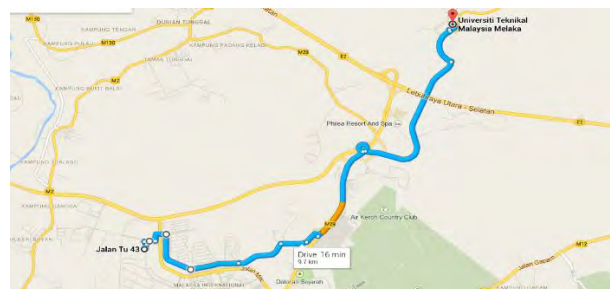
Figure 2 Driving route.

3. RESULTS AND DISCUSSION

Figure 3 and 4 show the vertical vibrations and roll of the vehicle and the offset (idle) value is 10 m/s^2 for the vibration and 0 rad/s for the roll. For Figure 3, the value above the offset is upward motion and the value below the offset is the downward motion of the vibrations. Above and below the dotted horizontal line are considered aggressive. For Figure 4, the value above the offset is moment to the right and the value below the offset is the moment to the left of the vehicle. Above and below the dotted horizontal line are considered aggressive. The highest value is at the point which the time is 401.73 sec that is when the vehicle is taking a corner. The highest value recorded is 87 rad/s with the speed of 52 km/h. As been analyzed, the roll moments are high when the driver is taking a corner and enter a junction. For the Z-accelerations, the highest value recorded at time 577.98 with the value of 7.51 m/s^2 and the speed of 70 km/h. Data Z-acceleration record the high data when the vehicle passing through bumpy roads.
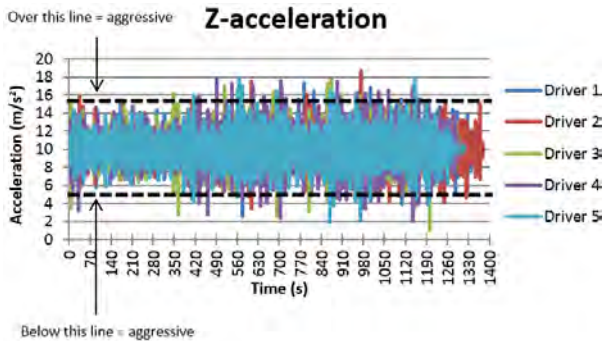
Figure 3 Vehicle vertical vibration.
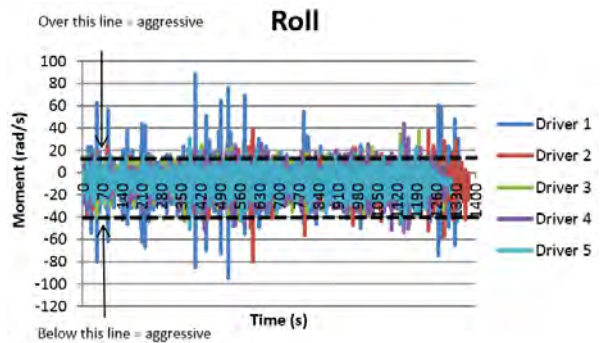
Figure 4 Vehicle roll moment.

4. CONCLUSION

From the experiment that has been done, it can be concluded that the force acting on the car represents the behavior of the driver. For this project, the driver that is doing the driving experiment is from the teenagers and then the driving behavior of these young drivers is being analyzed to know each driver behavior. The driver which has high experience in driving has more skill when driving and manage to control the vehicle with good manner to prevent the car experience a high force. Thus, this experiment has achieved their objectives successfully despite having some problem to analyze the result. This experiment also can be used by the car manufacturer. Vehicle system such as a suspension system has influenced the vehicle movement to avoid the accelerations and moments acting on the vehicle. This experiment also can be done again with the different type of vehicle and different objective to further the study to prevent the bad behaviour of the driver acting on the car that can lead a danger to the driver, passenger and also to other people.

REFERENCES

[1] M. Casucci, M. Marchitto and P.C. Cacciabue, "A numerical tool for reproducing driver behaviour: Experiments and predictive simulations." *Applied Ergonomics*, vol. 41, no. 2, pp. 198-210, 2010.

[2] A. Doshi & M.M. Trivedi, "Tactical driver behavior prediction and intent inference: A review," *in 2011 14th International IEEE Conference on In Intelligent Transportation Systems (ITSC)*, 2011, pp. 1892-1897.

[3] A. Calvi and M. De Blasiis, "Driver behavior on acceleration lanes: driving simulator study," *Journal of the Transportation Research Board*, vol. 2248, 96-103.

[4] M.A. Abdullah, J.F. Jamil, N. Ismail, M.Z.M. Nasir, M.Z. Hassan, "Formula varsity race car-Roll dynamic analysis," in *Proceedings of Mechanical Engineering Research Day 2015*, 2015, pp. 23-24.

[5] M.A. Abdullah, J.F. Jamil, M.A. Salim, "Dynamic performances analysis of a real vehicle driving," *IOP Conference Series: Materials Science and Engineering*, vol. 100, no. 1, 2015.

[6] M.A. Abdullah, M.A. Salim and M. Z. Mohammad Nasir, "Dynamics Performances of Malaysian Passenger Vehicle," *in Proceeding of International Conference on Automotive, Innovation and Green Energy Vehicle (AiGEV)*, 2014.

[7] M.A. Abdullah, F.R. Ramli, C.S. Lim, "Railway Dynamics Analysis Using Lego Mindstorms," *Applied Mechanics and Materials*, 465-466, pp. 13-17, 2013.

Effect of hydrogen injection on diesel engine performance intake: Preliminary result

M.N.M. Norani[1,2,*], B.T. Tee[1,2], M.Z. Zulfattah[1,2], M.N.A. Saadun[1,2], A. Hussain[1], M.N. Mansor[3]

[1] Faculty of Mechanical Engineering, Universiti Teknikal Malaysia Melaka,
Hang Tuah Jaya, 76100 Durian Tunggal, Melaka, Malaysia
[2] Centre for Advanced Research on Energy, Universiti Teknikal Malaysia Melaka,
Hang Tuah Jaya, 76100 Durian Tunggal, Melaka, Malaysia
[3] Faculty Of Mechanical and Manufacturing Engineering, Universiti Tun Hussein Onn Malaysia
86400 Parit Raja, Batu Pahat, Johor, Malaysia

*Corresponding e-mail: mohamadnordin91@gmail.com

Keywords: Diesel hydrogen; fuel efficiency; diesel engine.

ABSTRACT − In automotive industry, diesel engine knows as a compression ignition engine plus was a better performance compared to gasoline engines. However, it contributes to environmental problem by causing global emission. In order to reduce the emission, hydrogen injection has been introduced on diesel performance intake. Thus, this research was about analyzed the effect of hydrogen gas inside the intake of a single cylinder diesel engine. Two conditions with and without hydrogen will be analyzed by comparing the diesel fuel consumption on different rotational speed of the crankshaft. Based on the preliminary result, hydrogen injection to the diesel engine can saved the fuel up to 16.82% from 200RPM until 2000RPM.

1. INTRODUCTION

The issue of large amounts of exhaust gas produced by diesel engine has received considerable critical attention. Exhaust gases contained hydrocarbons, nitrogen oxides and carbon monoxide, which are harmful to the environment and mankind [1]. Besides, the exhaust emission also released the carbon dioxide gas that can cause the greenhouse effect. Based on the studies by Jailani [2], the earth's temperature will rise by 2°C if the content of carbon dioxide in the atmosphere doubled. The pollution effects of diesel engine will encourage researchers to find the proper solutions in solving this issue. Injected a small amount of hydrogen gas into diesel can be one of the alternative methods to improve fuel efficiency during the process of combustion in diesel engines. Compression ignition (CI) provides better thermal efficiency than spark ignition because of the higher compression ratio. Under optimum conditions, SI engine only uses 30% of heat liberated to turn the crankshaft, but with CI engines can attain more thermal efficiency which is above 40%. Compressing the air, rather than a mixing the air and fuel as the piston approach top dead centre (TDC), help in improving the engine thermal efficiency [3].

Although most of the research has been focused on hydrogen by modification the diesel engine, there is very little investigation on supplied hydrogen without changing the diesel engine. So, this paper examined the effects of non altered diesel engine consumption efficiency in the supply of hydrogen gas as an additive based on the different rotational speed of the crankshaft.

2. METHODOLOGY

The single cylinder, 4 stroke engine was used for this investigation. The specification of the diesel engine was given in Table 1, and Figure 1 shows the experimental set-up.

Table 1 Specification of diesel engine.

Engine type	Single cylinder, 4-stroke, direct injection
Maximum power (Hp)	5.5
Maximum engine speed (RPM)	3700
Bore (mm)	76
Stroke (mm)	62
Displacement (ml)	296
Compression ratio (CR)	20:1

Figure 1 Diesel engine set-up.
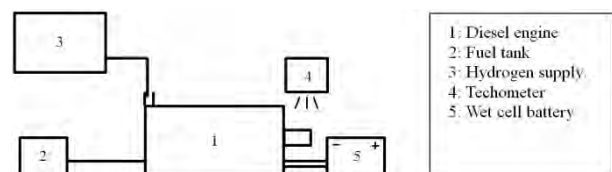
Figure 2 Schematic diagram of apparatus.

1: Diesel engine
2: Fuel tank
3: Hydrogen supply
4: Techometer
5: Wet cell battery

Figure 2 shows the general schematic diagram for this experiment. Other components required includes lubrication oil tachometer, hydrogen supply, syringe, wet cell battery and measuring beakers. The experiment was conducted to measure the required time for diesel engine with fuel capacity of 40 ml at different speed (RPM). The hydrogen was supplied at the intake air section of the engine. Measuring beakers were used to estimate the rate of hydrogen per minute before being supplied to the engine. The flow rate of hydrogen was 1.17×10^{-8} m^3/s. As the crankshaft rotates, the speed was measured by a tachometer.

3. RESULTS AND DISCUSSION

Further result is being compared by adding an additive with and without hydrogen gas inside diesel engine at different RPM towards fuel consumption. Table 2 and Table 3 shows the results for different engine speed (RPM) without and with hydrogen injection. Both tables consist of time duration with limited fuel capacity. Based on that data, the flow rate at each RPM will be calculated.

Table 2 Results without hydrogen injection.

Rotational Speed (RPM)	Volume (m^3)	Time Taken (s)	Diesel Fuel Flow Rate, D_0 (m^3/s)
1000	4 x 10^{-5}	741.9	5.316 x 10^{-8}
1500	4 x 10^{-5}	670.3	5.9675 x 10^{-8}
2000	4 x 10^{-5}	591.4	6.7636 x 10^{-8}
2500	4 x 10^{-5}	486.5	8.222 x 10^{-8}
3000	4 x 10^{-5}	398.8	1.003 x 10^{-7}
3500	4 x 10^{-5}	318.3	1.2567 x 10^{-7}

Table 3 Results with hydrogen injection.

Rotational Speed (RPM)	Volume (m^3)	Time Taken (s)	Diesel Fuel Flow Rate, D_H (m^3/s)
1000	4 x 10^{-5}	879	4.5506 x 10^{-8}
1500	4 x 10^{-5}	737.5	5.4237 x 10^{-8}
2000	4 x 10^{-5}	602.4	6.6401 x 10^{-8}
2500	4 x 10^{-5}	487.5	8.2051 x 10^{-8}
3000	4 x 10^{-5}	399.1	1.0023 x 10^{-7}
3500	4 x 10^{-5}	322.3	1.2411 x 10^{-7}

Figure 3 Graph of the diesel fuel consumption.

$$Efficiency = \frac{(D_0 - D_H)}{D_H} \times 100 \qquad (1)$$
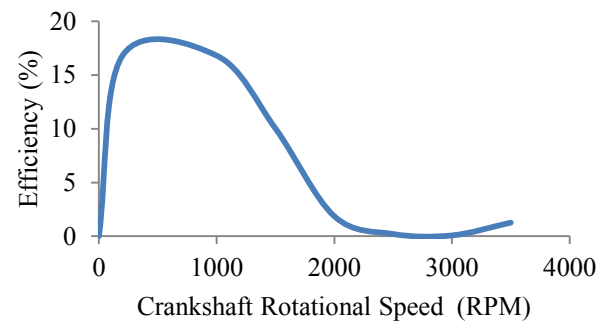
Figure 4 Efficiency diesel fuel

Figure 3 shows the graph of the diesel flow rate at different shaft rotational speed. Thus, the diesel flow rate increased correspondingly to the speed of the crankshaft. Equation (1) shows efficiency in Figure 4, at rotational speed 200RPM until 2000RPM, the diesel flow rate with hydrogen injection save approximately 16.82% compared to the one without hydrogen injection. This indicates that the hydrogen usage is being maximized at low speed. Young [1] proved that the suitable usage of hydrogen was only for lower load.

4. CONCLUSION

Hydrogen injection to the diesel engine can save the fuel up to 16.82% at lower load. The ideal engine combustion can be achieved by using hydrogen injection because the hydrogen auto-ignition is higher than other conventional fuel. Hydrogen can also decrease the excess fuel during combustion. When the ideal engine combustion occurred, the excess fuel will burn completely in the engine and contributing to high efficiency.

REFERENCES

[1] J. Young, "Hydrogen Injection In Diesel Engine For Fuel Efficiency Improvement.", Dissertation, Murdoch University, 2008.

[2] M. A. Jailani and M. N. M. Jaafar, "Emisi Ekzos Dari Kenderaan Bermotor, Kesannya Ke Atas Atmosfera Dan Kaedah Pengurangannya : Satu Kajian," Jurnal Mekanikal, 2nd ed, Johor, UTM, pp.14-15, 1999. [Online]. Avalilable: http://core.ac.uk/download/pdf/11784206.pdf. Accessed Sept. 3, 2015.

[3] P. Dempsey, "Troubleshooting and Repairing Diesel Engines", 4th ed. United States: McGraw Hill; 2008.

Influence of transient response on suspension damping

A. Md Saad[1,2]*, M.A. Salim[1,2], M.H. Harun[1], M.R. Mansor[1,2], M.Z. Akop[1,2], M.T. Musthafah[1,2]

[1] Faculty of Mechanical Engineering, Universiti Teknikal Malaysia Melaka,
Hang Tuah Jaya, 76100 Durian Tunggal, Melaka, Malaysia
[2] Green Technology Vehicles Research Group, Centre for Advanced Research on Energy, Universiti Teknikal Malaysia Melaka, Hang Tuah Jaya, 76100 Durian Tunggal, Melaka, Malaysia

*Corresponding e-mail: adzni@utem.edu.my

Keywords: transient response; suspension damping; ride quality

ABSTRACT – Suspension system is one the most important components that affects overall performance of a vehicle. Determination of proper suspension damping is crucial to improve ride quality. The purpose of this study is to investigate the effects of transient response on suspension damping. Numerical simulation is used by representing ideal physical of vehicle quarter car model into Bond Graph. By lowering suspension damping, it reduces magnitude of rapid acceleration of the vehicle when it hits a bump. But, it takes longer time for the response to die out. However, by increasing the suspension damping, it increases magnitude of rapid acceleration significantly.

1. INTRODUCTION

With the changing of customer demands on vehicle overall characteristics, the focus areas in designing a vehicle have changed over time. Customers not only require better performance in terms of powertrain, but also other aspects especially in comfort level. It is not only limited to have luxurious feel inside the cabin with high quality material used and perfect components fitting, but the ability of vehicle to absorb forces due to road load also attracts customer attention.

Because of that, suspension design has become more complex in order to meet customer demands. Suspension system not only affect vehicle performance in terms of ride and handling, but also in safety. More research works are focusing in this area to meet continuous improvement requirements in suspension characteristics. This can be improved not only by having good suspension geometry but also by applying appropriate values of suspension parameters. Moreover, this process needs to be carried out accurately including suspension damping because it directly contributes to overall suspension performance.

The objective of this study is to investigate the effects of suspension damping on ride quality. It can be improved by lowering the value of the suspension damping. However, if this value is lowered too much, the car will oscillate long after it encounters a transient input and makes the car difficult to control. At the same time, an increase in the value of suspension damping can produce larger increases in the peak vertical acceleration of the body due to transient inputs. This response will be transmitted to the body and passengers by the suspension.

2. RESEARCH METHODOLOGY

This study was conducted by using numerical simulation approach. Software used for analysis was 20sim by converting ideal physical model of quarter car to Bond Graph as shown in Figure 1. Table 1 represented model parameters that were used for this simulation.
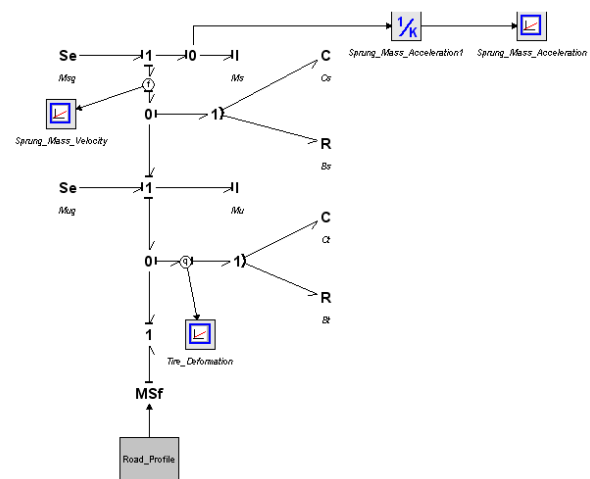
Figure 1 Bond Graph for quarter car model

Table 1 Model parameters.

Parameters	Values
Sprung Mass, M_s (kg)	1068
Suspension Stiffness, K_s (N/m)	74968
Suspension Damping, B_s (Ns/m)	2800
Unsprung Mass, M_u (kg)	146.4
Tire Stiffness, K_t (N/m)	775660
Tire Damping, B_t (Ns/m)	800

Analysis was carried by assuming that a car was hitting a single bump. Transient input to the system was represented by an idealized single bump as shown in Figure 2. For a constant forward velocity of V_F, the velocity input for bump was given by Equation (1).

$$V_r(t) = \begin{cases} 0 \ \forall t < t_1 \\ \frac{RV_F}{L} \ \forall t_1 \leq t \leq t_2 \\ 0 \ \forall t > t_2 \end{cases} \quad (1)$$

Where L is wavelength and R is road roughness.
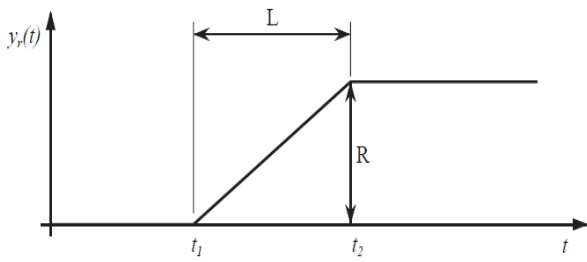
Figure 2 Single bump road model.

The time required to traverse the bump was given in Equation (2).

$$t_2 - t_1 = {L}/{V_F} \qquad (2)$$

For the purpose of this study, constant forward velocity used was 25m/s, road roughness, R of 0.05m and wavelength, L of 0.5m. The car hit the bump at t_1 of 10s to allow transients due to gravity input to die out. Simulation final time was set at 15s. Three stages of simulation were carried out. The initial stage was by using original suspension damping value. Later, one lower and higher values of suspension damping were used respectively for comparison purposes.

3. RESULTS AND DISCUSSION

In this section, results of the test will be discussed in details. Sprung mass acceleration response of the system using original value of suspension damping of 2800Ns/m was shown in Figure 3. The first part of the response oscillation was due to the effect of sprung weight of the system. It took about 5 seconds before it died out and the vehicle hit a bump at t=10 seconds. When the vehicle hit a bump, the sprung mass acceleration increased rapidly and reached about 9m/s^2 before it died out after 4 seconds.
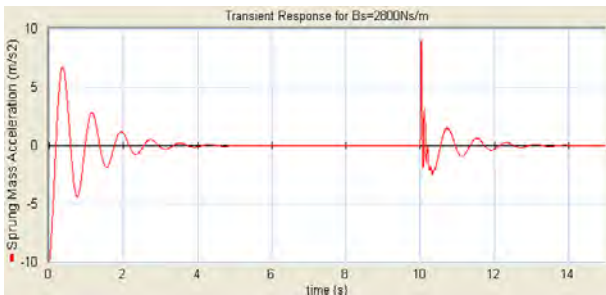
Figure 3 Sprung mass acceleration of B_s=2800Ns/m.

For the second stage of simulation, suspension damping was reduced to 1400Ns/m as shown in Figure 4. It displayed slightly different response compared to the original condition. The response took a longer time to die out because of the effect of gravity on the sprung mass. But once the vehicle hit the bump, magnitude of rapid acceleration of the vehicle was lower. It accelerated up to 7m/s^2 but the response took more than 5 seconds to die out. The longer response oscillation time improved ride quality but made the vehicle more difficult to control.
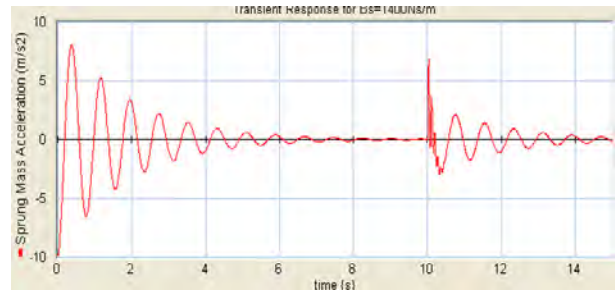
Figure 4 Sprung mass acceleration of B_s=1400Ns/m.

Suspension damping was increased to 5600Ns/m for the final stage of simulation. Time for the oscillation response to die out was shorter as shown in Figure 5. It took less than 3 seconds for the response due to sprung weight to completely vanish. Later, the plot showed no response when the vehicle hit the bump. In real condition, there was rapid acceleration response occurred with greater magnitude once the vehicle hit the bump. As the response died out almost instantaneously, the plot was unable to capture the acceleration response that transpired during that short period of time. By having higher suspension damping, it reduced the time for the response to die out but the system had to sustain higher magnitude of sprung mass acceleration.
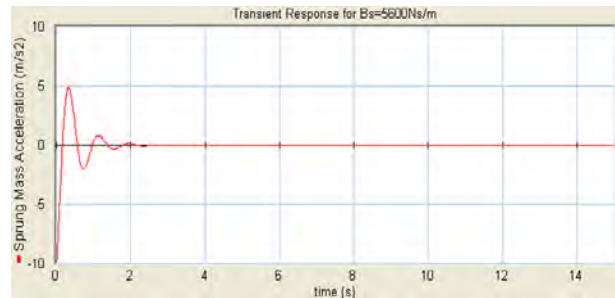
Figure 5 Sprung mass acceleration of B_s=5600Ns/m.

4. SUMMARY

This study was carried out to determine the effects of transient response on suspension damping. Software used for analysis was 20sim by converting ideal physical model of quarter car to Bond Graph. Results showed that by lowering suspension damping, it reduced magnitude of rapid acceleration of the vehicle when it hits a bump. But, it took longer time for the response to die out. However, by increasing the suspension damping, it increased magnitude of rapid acceleration significantly. But, the response died out almost instantaneously.

REFERENCES

[1] D.C. Karnopp, D.L. Margolis and R.C. Rosenberg, Sytems Dynamics; Modeling and Simulation of Mechatronic System, 4th Edition John Wiley & Sons Inc; 2005.
[2] T.D. Gillespie, Fundamental of Vehicle Dynamics, Society of Automotive Engineers;1999.

Experimental Investigation of engine performance and emission for biodiesel at various storage conditions

N. Tamaldin[1,2,*], A.S. Mohamad[1], Y. Humairak[1] , M.H.M. Husin[1,2], M.F.B. Abdollah[1,2]

[1] Faculty of Mechanical Engineering, Universiti Teknikal Malaysia Melaka,
Hang Tuah Jaya, 76100 Durian Tunggal, Melaka, Malaysia
[2] Centre for Advanced Research on Energy, Universiti Teknikal Malaysia Melaka,
Hang Tuah Jaya, 76100 Durian Tunggal, Melaka, Malaysia

[*]Corresponding e-mail: noreffendy@utem.edu.my

ABSTRACT – The aim of this paper is to evaluate the engine performance of high blending biodiesel. Biodiesel palm oil will be used as the main blending material. The types of biodiesel for this study are B7x, B8x and B9x. All biodiesel were blended and stored at three different storage conditions. Based on the best properties, one type of biodiesel is chosen to be tested to get the engine performance. Results, performance by using biodiesel B7x is slightly decreasing about 2-8% less of engine horse power and 4-10% less in torque. Biodiesel B7x can perform satisfactorily during diesel engine.

1. INTRODUCTION

Biodiesel is a biodegradable and nontoxic renewable fuel [1]. It has reduced the molecular weights, reduced viscosity and improves volatility [2]. Most of the combustion engines can run on biodiesel without modification [3]. Blending of biodiesel is one way to keep the performance of the fuel in combustion engine remaining great [4]. In 1895, Rudolf Diesel developed a new engine that can be run by using variety of fuels including vegetable oil [5]. Different types of biodiesel blends give different properties such as kinematics viscosity, flash point, water content and acid value.

The higher viscosity can leads to choking of injector tips which can cause the engine to lose its power [6]. Zakaria et al. [7] stated that in long storage duration, biodiesel fuel become oxidize, fuel degraded and microbial growth. The investtigation on power, torque, the brake specific fuel consumption (BSFC) and emission of the exhaust of both pure diesel fuel and different types of biodiesel of Sunflower Methyl Ester (SME) has been done by Moreno et al. [8]. While, in this study, the performance of high blending biodieslel (B7x) were evaluated and the standard biodiesel was used as benchmark.

2. METHODOLOGY

Three types of biodiesel will be used in these experiments which are B7x, B8x and B9x. B7x represents 70% of biodiesel and 30% of standard diesel (STD). Where, STD contains 5-7% of biodiesel. The fuel was mixed together and blended for an hour and heated around 70°C [9]. In this experiment, after biodiesel was blend, it will be stored in the storage box at three different conditions of temperatures which are low, ambient and high temperature. Then they are tested for parameter study which is the flash point. These fuels are then analyzed for the best condition to be tested on the engine.

Based on the data of the flash point, for standard diesel has the overall temperature of 90 °C flash points in all three conditions. Meanwhile, for blending biodiesel samples, B7x sample shows a precisely flash point result at lowest temperature compare to all storage condition samples. Thus, in this experiment, biodiesel B7x at ambient was selected for the diesel engine performance testing compare to the standard diesel.

The diesel engine performance testing was conducted by a single cylinder engine diesel engine model 170 F Single Cylinder Diesel Engines that runs at 3500 rpm to 1500 rpm. During this test, the engine will be connected to DAQ board such as the value for its power and torque which called. When the engine is running, all the data can be obtained from the device and the data will be recorded and analyzed.

3. RESULTS AND DISCUSSION

The performance of the engine can be defined into two types of performance which are horsepower and torque.
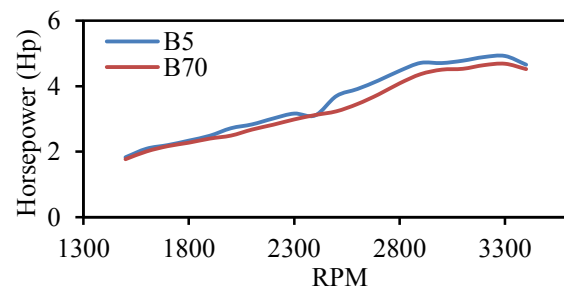
Figure 1 Horsepower (Hp) against rotation per minute (RPM).

Figure 1 shows the graph of horsepower against rotation per minute (RPM). The figure shows that all the values of horsepower have slightly decrease compared to performance of horsepower by standard diesel (STD). That means the used of biodiesel can decreasing the

performance of the engine. This is due to the ability of B7x to ignite for minimum temperature (flash point) is higher compare to standard diesel which is 120 ˚C and 90 ˚C respectively. . Table 1 below shows the percentage differences between the value of horsepower by B5 and B7x.

Table 1 Percentage of differences in horsepower between B5 and B7x.

RPM	HP for B5	HP for B7x	Differences	Percentage (%)
1500	1.8834	1.7844	0.0990	5.26
2000	2.7670	2.5778	0.1892	6.84
2500	3.6236	3.2770	0.3466	9.57
3000	4.6998	4.5228	0.1770	3.77
3400	4.7778	4.7690	0.0088	0.18

From the Table 1, decreasing of biodiesel engine performance for horsepower was up to 10% compared to standard diesel. For performance by horsepower, the lowest reduces percentage is 0.18%. A very small reduces percentage happens at the highest speed of the engine. This shows that the engine performance of biodiesel blend is slightly reduce compare to performance of engine by using a standard diesel. But at the speed of engine in 2500rpm, the highest percentage of reduced in horsepower is 9.57%. That means the use of biodiesel can reduces the performance of an engine by maximum of 10% or below.
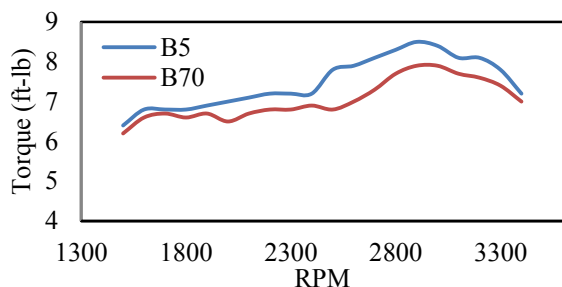
Figure 2 Torque (ft-lb) against rotation per minute (RPM).

Figure 2 shows the graph of torque against rotation per minute. The figure shows that there are no significant effects to the torque when the B7x is used in the diesel engine. In terms of values, the performance by torque for B7x is at the speed of 1500rpm until 2000rpm. After that, the values are always less than the values of performance by torque for standard diesel (B5). The value of torque is increasing as the speed is increase until it reach at the highest value of torque recorded which is at the speed of 3000rpm. Then, the performance by torque is decreasing as the speed continues to increase.

For the performance by torque, the lowest reduces in percentage is at the speed of 3000rpm which is 4.57% and the highest is at the speed of 2500rpm which is 9.47%. This shows that the performance of biodiesel is reduced by maximum of 10% compared to the uses of standard diesel on the engine. By combining the two

results, it can be concluded that the use of biodiesel on the engine can reduces its performance of power and torque by 5-10%. Other than that, the maintained data gained from the experiment proved that biodiesel can perform satisfactorily during diesel engine operation.

4. CONCLUSIONS

As conclusion, the performance of biodiesel is reducing from 5-10% compared to standard diesel. In addition with that, further investigation should be conducted to test all the blend level of the biodiesel to be compared to the conventional diesel.

REFERENCES

[1] M., Bowman, D., Hilligoss, S. Rasmussen and R. Thomas., "Biodiesel: a Renewable and Biodegradable Fuel Hydrocarbon Processing," 2006, Retrieved September 23, 2013 from, http://www.perkinelmer.com/pdfs/downloads/ATL _BiodieselHydrocarbProcessing.pdf.

[2] G. Knothe, "Biodiesel and renewable diesel: A comparison," *Progress in Energy and Combustion Science*, vol. 36, no. 3, pp. 364-373, 2010.

[3] R. Senthilkumar, K. Ramadoss and M. Prabu, "An effective experimental investigation on 4-stroke single cylinder C.I. engine using cottonseed biofuels," *International Conference on Advances in Engineering, Science and Management*, pp. 341-345, 2012.

[4] J.A. Kinast, "Production of Biodiesel from Multiple Feedstocks and Properties of Biodiesel and Biodiesel/Diesel Blends: Final Report, Report No. NREL/SR-510-31460," National Renewable Energy Laboratory, Golden [CO]: March 2003.

[5] A.C. Pinto, L.L.N. Guarieiro, M.J.C. Rezende, N.M. Ribeiro, E.A. Torres, W.A. Lopes, P.A.P. Pereira and J.B. Andrade, "Biodiesel: An Overview", *Journal of the Brazilian Chemistry Society*, vol. 16, no. 6B, pp. 1313-1330, 2005.

[6] G. Knothe, J.V. Gerpen and Krahl, *In the Biodiesel Handbook*. AOCS Press, Illinois, 2004.

[7] H. Zakaria, A. Khalid, M.F. Sies and N. Mustaffa, "Overview effect of biodiesel storage on properties and characteristics," *Applied Mechanics and Materials*, vol 465 – 466, pp. 260-264, 2014.

[8] F. Moreno, M. Munoz and J. Morea-Roy, "Sunflower Methyl Ester as a Fuel for Automobile Diesel Engines," *in Transaction of the ASAE, vol.* 42, no. 5, pp. 1181-1185, 1999.

[9] A. Khalid, N. Tamaldin, M. Jaat, M.F.M. Ali, B. Manshoor and I. Zaman, "Impacts of biodiesel storage duration on fuel properties and emissions," *Procedia Engineering,* vol. 68, pp. 225-230, 2013.

Effect of storage duration on the fuel properties of different biodiesel blends

N. Tamaldin[1,2,*], F. Harun[1], Y. Humairak[1], M.H.M. Husin[1,2], M.F.B. Abdollah[1,2]

[1] Faculty of Mechanical Engineering, Universiti Teknikal Malaysia Melaka,
Hang Tuah Jaya, 76100 Durian Tunggal, Melaka, Malaysia
[2] Centre for Advanced Research on Energy, Universiti Teknikal Malaysia Melaka,
Hang Tuah Jaya, 76100 Durian Tunggal, Melaka, Malaysia

*Corresponding e-mail: noreffendy@utem.edu.my

ABSTRACT – In this paper, the impacts of biodiesel properties are identified according to the storage condition and weight percentage of the fuel in a period of time. The samples used are standard diesel (STD), B7x, B8x and B9x were stored for 5 weeks. There are three fuel properties being tested which are flash point, density and water content. All experiment carried out are according to respective ASTM standard. The properties changes of biodiesel were not significant throughout five weeks" time due to the short time of storage except for water content.

1. INTRODUCTION

The global production of biodiesel has been rapidly grown about three to four decades back which major production comes from Indonesia and Malaysia in Southeast Asia [1]. Biodiesel is generally made up from the vegetables oils or animal fats with an addition of catalyst and alcohol [2-3]. The advantages of biodiesel over diesel fuel are higher cetane number, non-toxic, better lubricity and environmental friendly [4-5]. Whereas the disadvantages of biodiesel include cold kick start, low energy burst, higher copper strip corrosion and higher viscosity [5]. The productions of biofuesls are more costly than diesel because of insufficient animals and plants fat to totally replace fossil fuel [6].

On the other hand, the enrichment of oxygen in palm oil biodiesel promoted the further oxidation of carbon monoxide (CO) during combustion process [7]. However, the higher content of biodiesel could affect the engine for long use because of corrosion [8-9]. With all factors been stated, this study will analyze the properties effect of high blending biodiesel storage up to 5 weeks duration.

2. METHODOLOGY

There are three types of blend biodiesel need to be prepared which are B7x, B8x and B9x by using lab scale blending machine. The blending machine mechanism consists of rotating blade, motor to rotate the blade, heating coil and double layered tank. The mixture to be blend depends on the ratio given. The standard diesel used is from conventional fuel which consists of 7% of biodiesel. Therefore, the mixture of 70% of biodiesel (B100) and 30% of standard diesel

will produce B7x which x is uncertainty value between 5-7 % of biodiesel. The mixture was heated at 70°C before starting to blend for one hour [7]. This is to ensure the mixture is ready to blend. The process was repeated for B8x and B9x.

For flash point identification, the sample of 5ml fuel is put into the closed cup chamber of SETA Flash Point. Then, light up the fire source for a respective period until ‚Flash" appear on screen. Density of the biodiesel was determined by using hydrometer. While, to indicate the water content of biodiesel, Trivector Spectro machine was being used by pour the mixture of sample and solvent inside testing chamber and the water content result shown on the monitor.

3. RESULTS AND DISCUSSION

Properties of all samples were taken right after blending process. This is a reference data of the actual reading of each sample at ambient temperature (25°C).

Table 1 Properties of fuel sample for 0th week.

Fuel parameter	Types of fuel (week 0th)			
	STD	B7x	B8x	B9x
Flash point (°C)	90	120	128	138
Density (kg/m³)	850	870	870	875
Water content (%)	0	9	10	17.7
Acid value (mgNaOH/g)	0.20	12.01	13.03	14.02

As per theory, flash point will be decrease because the increment of alcohol in a fuel. In Figure 1 shows, graph is near to constant as the storage duration increase. It shows that the samples are stable and safe to be store because flash point is important parameter for biodiesel while handling, storage and safety when it used in transportation [10]. In Figure 2, density for all samples gives uneven trend but also near to constant. It explains that there is no significant effect to the density of high blending biodiesel as duration time increase.

Besides, water content gives increase trend as shown in Figure 3. It is because biodiesel content –OH

bonding and while storage the biofuels is react to the surrounding and the samples will oxidise. Consequently, the fuel will degrade and could effect to the component engine because of corrosion.
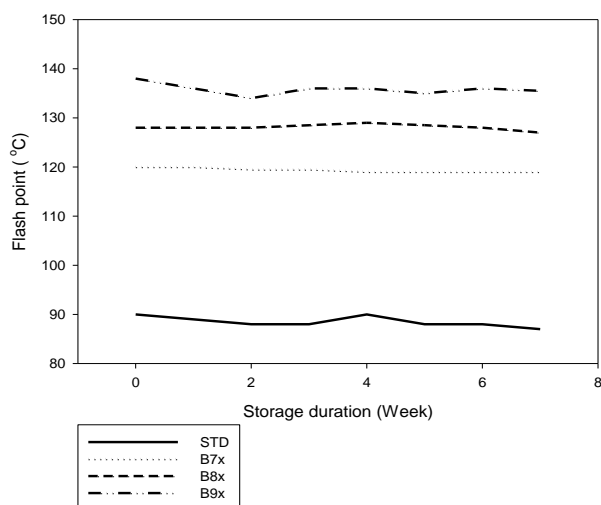
Figure 1 Flash point against storage.
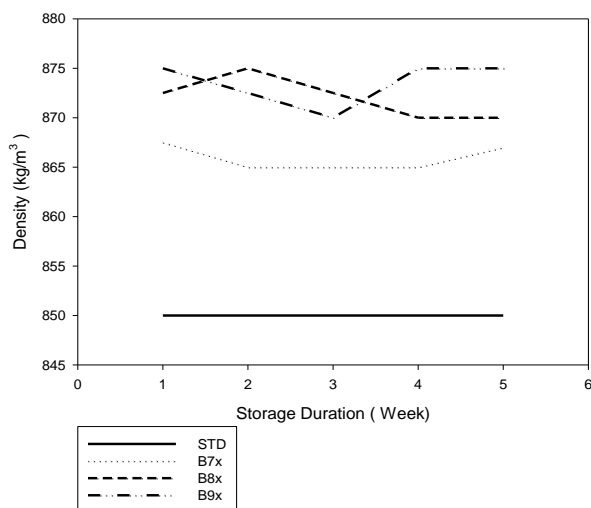
Figure 2 Density against storage duration.
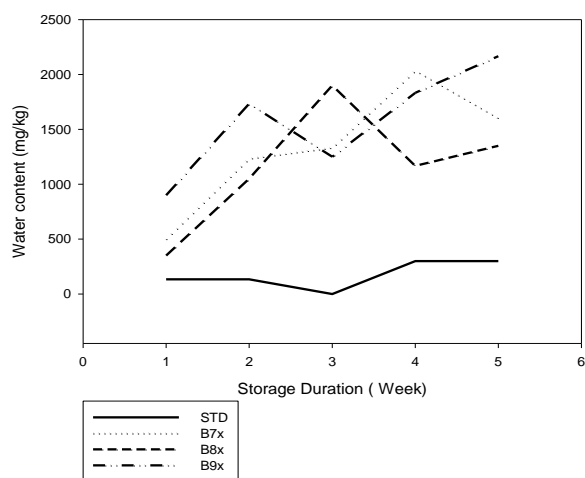
Figure 3 Water content against storage duration.

4. CONCLUSION

The properties changes of biodiesel were not significant throughout five weeks" time except for water content. As a conclusion, high blending biodiesel is stable and no degradation happens within storage duration.

ACKNOWLEDGEMENT

REFERENCES

[1] P. Oliver, J. Bhattacharya, C.H. Teoh (ed), *The palm oil controversy in Southeast Asia: A transnational perspective.* Mainland Press Pte. Ltd. Singapore; 2013.

[2] B.R. Moser. "Biodiesel production, properties and feedstocks," *Fuels*. pp 286-347, 2013.

[3] E. Christensen and R.L. McCornick, *Long-term storage stability of biodiesel and biodiesel blends*, Denver. United States; 2014.

[4] M.M. Noor, A. P. Wandel and T. Yusaf,. "Analysis of recirculation zone and ignition position of non-premixed bluff-body for biogas mild combustion," *International Journal of Automotive and Mechanical Engineering*, vol. 8, pp. 1176-1186, 2013

[5] P. Saxena, S. Jawale, M.H. Joshipura, "A review on prediction of properties of biodiesel and blends of biodiesel," *in Proceedings of 3rd Nirma University International Conference on Engineering*, 2013, pp. 395-402.

[6] S.A. Paes, "Production of edible mushroom and degradation of antinutritional factors in jatropha biodiesel residues," *LWT-Food Science and Technology*, pp. 575-580, 2013.

[7] A. Khalid, N. Tamaldin,, M. Jaat, M.F. Ali, B. Manshoor, I. Zaman, "Impacts of biodiesel storage duration on fuel properties and emission," *Procedia Engineering,* vol. 68, pp. 225-230, 2013.

[8] M.H. Mat Yasin, R. Mamat, A.F. Yusop, R. Rahim, A. Aziz, L.A. Shah, "Fuel physical characteristics of biodiesel blends fuels with alcohol as additive," *Procedia Engineering,* vol. 53, pp. 701-706, 2013.

[9] S.S. Wirawan, A.H. Tambunan, M. Djamin, and H. Nabetani, "The effect of palm biodiesel fuel on the performance and emission of the automotive diesel engine," *Agricultural Engineering International: the CIGR Ejournal*, Manuscript EE 07 005. Vol. X. April, 2008.

[10] A. Khalid, N. Mustaffa, B. Manshoor, H. Zakaria, A. J. Alimin, M. Leman and A. Sadikin., "The comparison of preheat fuel characteristics of biodiesel and straight vegetable oil," *Applied Mechanics and Materials*, vol 465-466, pp. 161-166, 2014.

The effect of increasing current to temperature of alternator

R.K. Mazlan[1,2,*], R.M. Dan[1,2], M.Z. Zulfattah[1,2], A.H.A. Hamid[1,2]

[1] Faculty of Mechanical Engineering, Universiti Teknikal Malaysia Melaka,
Hang Tuah Jaya, 76100 Durian Tunggal, Melaka, Malaysia
[2] Centre for Advanced Research on Energy, Universiti Teknikal Malaysia Melaka,
Hang Tuah Jaya, 76100 Durian Tunggal, Melaka, Malaysia

[*]Corresponding e-mail: rozdman.edir@gmail.com

ABSTRACT – Alternator is a major component in the charging system. Alternator act as main power source, providing current to power the electrical component in a vehicle. As more power demand, the more current is produced, and the more heat is generated. This heat has contributed an increase of under hood ambient temperature. An experiment has been done to investigate how the current and heat relate to each other. The car used is Proton Preve 1.6L Manual. The alternator has a rating of 12V/90A. The result shows that temperature increase exponentially with increase of current.

1. INTRODUCTION

Every automobile has a charging system. For a car, it consists of the alternator, regulator, and the interconnecting wiring. Charging system act as main source of electrical energy, and provide power to electrical components in the car while the engine is running. If there is no charging system, battery will be the source of power. But until the battery is weak, and there is no power source to charge the battery, then this will cause the engine to has less current to fire the spark plugs [1]. In this case, the engine will be forced to stop running.

The alternator, like most mechanical and electrical machinery, cannot withstand at maximum output for extended periods of time. Maximum output for a short period of time might be tolerable. But for most of the time, alternator operates at about three quarter of full output potential. Also, like any other machinery, alternators produce heat as a by-product of generating electrical power [2]. As the more power is produced, the more heat they make. During the 80's, the alternator can produced power up to 1500W. Then, as technology advancing and more research development, and due to increasing power demand, the alternator has been modified and designed so that it can produce power to 2000W. This has increased the under hood ambient temperature from 110 degrees C in 1980 to 130 degrees C nowadays [3]. But the alternator has been designed so that it can work well at temperature up to 300 degrees C.

One of the wastage or inefficiency that happen in the automotive engine is the unused current generated by the alternator. The electricity supply by the alternator is continuous when the engine is in operation, there will be surplus of energy generated by the alternator that will

be wasted in term of thermal energy. The higher the power demand, the more current is generated by the alternator. And the more heat is being produced. Whenever an electric current flows through a material that has some resistance, it creates heat. This resistive heating is the result of friction [4].

In this research, an energy audit is performed to find out how temperature is increasing in the cable at the alternator output, and at the alternator itself. The study will focus on the energy audit on the electricity produced by the alternator. The car used in this research is Proton Preve 1.6L manual. And the experiment is done at engine is at idle.

2. METHODOLOGY

Figure 1 shows how the experiment is done. An AC/DC Clamp is used to get the reading of alternator current output. It is being clamped at the current output cable. A K-Type thermocouple is being put inside the cable at the alternator output to get the reading of the wire temperature. A thermal imaging camera is used to take the temperature at the alternator coil. K-Type thermocouple is not used to take temperature at the coil to avoid it from melting, which will affect the reading. Thermal imaging camera cannot be used to take reading of temperature inside the cable as it only can take reading of temperature at the surface.
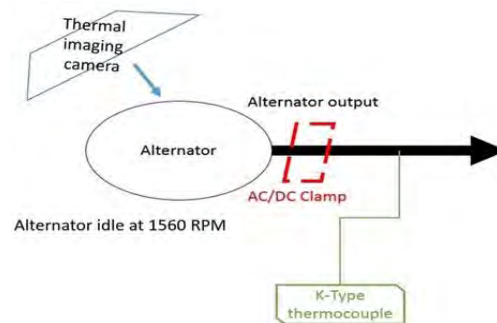
Figure 1 Schematic diagram of experiment.

The engine is idle at 1560 RPM, measured by a tachometer. All the available electrical components were turned on one after another by sequence. Table 1 shows how the electrical components were arranged and turned on by sequence. The reason for the arrangement and sequence was to get a constant result when doing repeating testing.

Table 1 Electrical components turned on in sequence.

No.	Electrical Component(s)
1	Radio
2	Front lamp
3	Rear lamp (brake)
4	Hi-beam
5	Spotlight (R)(L)
6	Interior lamp
7	Air-cond
8	Wiper, signal, hazard, power window, radiator fan

3. RESULTS AND DISCUSSION

Table 2 below shows the average data for the experiment. The experiment was repeated six times. Figure 2 and Figure 3 shows that both graph have same pattern, which tells that the heat at the wire and alternator have same behavior. As the current increase, the temperature rise. The line of the graph is increase exponentially. This prove that heat will increase as the current increase.

As shown in Figure 2 and Figure 3, there is a drastic increase of temperature at current 48.6A to 50.4A. At that point, by referring to Table 1, it shows that at that time, the right and left spotlight are being turned on. The spotlight may contribute in this sudden increase of temperature.

The more current is produced, the more heat generated. Electrical current is the flow of electrons through a substance that will permit that flow. The substance is called a conductor, which resist electron flow to some extent. The current transmitted is fast, causing more friction per unit time and therefore a higher resistance. When electron flow is resisted, some of the energy in the electrons does not travel through all the way. Because energy is conserved, the energy that was moving the electrons forward is converted to heat energy [5].

Table 2 Alternator output current and temperature.

Alternator Current output (Amp) (Approximately)	Wire Temperature (°C)	Alternator coil temperature (°C)
13.30	33.50	101.14
22.60	34.00	104.5
27.10	34.20	109.23
35.90	35.10	127.45
48.60	38.30	144.83
50.40	43.30	182.79
58.90	45.00	203.13
62.20	47.30	218.72

4. CONCLUSION

The car used in this experiment has an alternator rating of 12V/90A. The alternator can produce up to 90A of current. Without any external electrical component, the maximum power demand is 62.2A. And the maximum temperature for alternator output cable is 47.3°C, while maximum temperature at coil is 218.72°C. The more current is produced, the more heat generated. If there is any external electrical component

is being installed, the current and temperature may rise. This is not good for lifespan of the wire and the alternator itself.
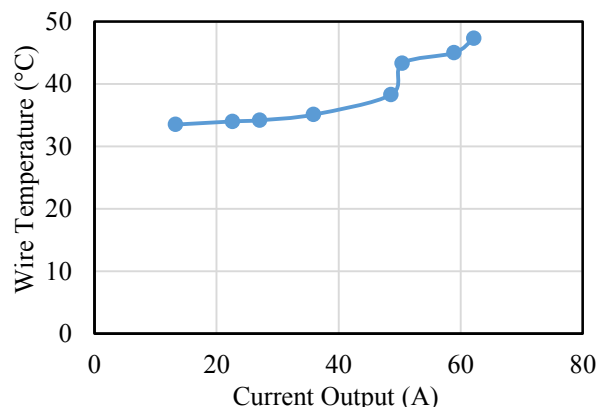
Figure 2 Current output against wire temperature.
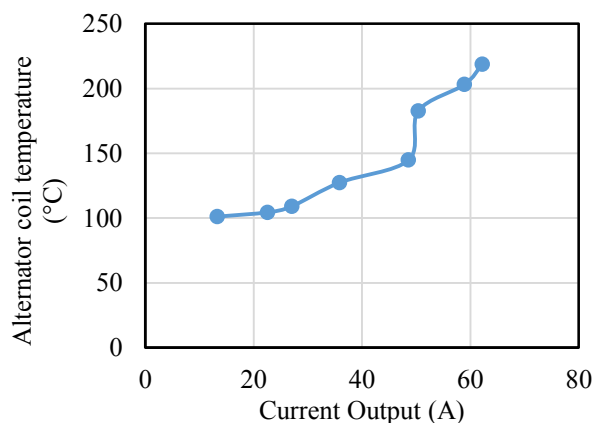
Figure 3 Current output against alternator coil temperature.

REFERENCES

[1] C. Ofria, "*A Short Course on Charging System*". [Online] Retrieved from http://www.carparts.com, 20 Dec 2015.

[2] M. Hamilton, "*Voltage Regulator, Alternator, and Battery Operation*" [Online] Retrieved from http://www.madelectrical.com, 20 Dec 2015.

[3] M. Bradfield, "*Thermal Design Challenges in Automotive Alternator Power Electronics*" [Online] Retrieved from http://www.electronics-cooling.com, accessed on 20 Dec 2015.

[4] E. Csanyi, "Resistive heating explained in details" [Online] Retrieved from http://electrical-engineering-portal.com, accessed on 20 Dec 2015.

[5] "Why does electrical current make heat?" [Online] Retrieved from http://www.qrg.northwestern.edu, accessed on 20 Dec 2015.

Experimental study of noise level for car engines

M.R. Rizainal[1,2], M.A. Salim[1,2,*], A. Md Saad[1,2], M.R. Mansor[1,2], M.Z. Akop[1,2], M.T. Musthafah[1,2], I.R.A. Rosszainily[1,2]

[1] Faculty of Mechanical Engineering, Universiti Teknikal Malaysia Melaka,
Hang Tuah Jaya, 76100 Durian Tunggal, Melaka, Malaysia

[2] Green Technology Vehicles Research Group, Centre for Advanced Research on Energy, Universiti Teknikal Malaysia Melaka,Hang Tuah Jaya, 76100 Durian Tunggal, Melaka, Malaysia

*Corresponding e-mail: azli@utem.edu.my

Keywords: Sound intensity; engine noise; noise level

ABSTRACT – In all driving conditions, engine will continuously generate unwanted noise and vibration. Excessive noise may cause discomfort to the driver and passengers. The purpose of this study is to investigate engine noise in two different engine operating conditions; engine loading and unloading. Simple approach is used to examine the noise level which is by using sound intensity probe that is integrated to a software. Test has been carried at different engine speed for both engine operating conditions; loading and unloading. Results show that noise level is higher when engine in loading condition.

1. INTRODUCTION

Throughout the century, automotive industry has been growing rapidly all over the world. Nowadays, every car manufacturer is trying to come out with products that able to meet customer demands and expectations in order to survive in this industry. With the change of our lifestyle, these demands and expectations are progressively changed. Other than safety and performance, comfort has become one of the most desirable criteria for car buyers. Because of that, most of the car manufacturers spend abundant amount of money and efforts to reduce any discomfort issues.

One of the main issue that relates to comfort is the unwanted noise. It is mainly produced by the engines. In this study, identified the noise level was identified by using sound intensity probe that is integrated with software. There are two engine conditions that are chosen for this study which are unloading and loading conditions. Unloading refers to the condition when the engine is operating ideally, and for loading condition is when the engine is operating by switching on the air conditioning system. Additionally, this test is carried at two different engine speeds; idle speed at 1000 revolution per minute (RPM) and 2000 RPM.

2. RESEARCH METHODOLOGY

This study was conducted at Faculty of Mechanical Engineering Laboratory. The procedure of this study is illustrated in Figure 1.
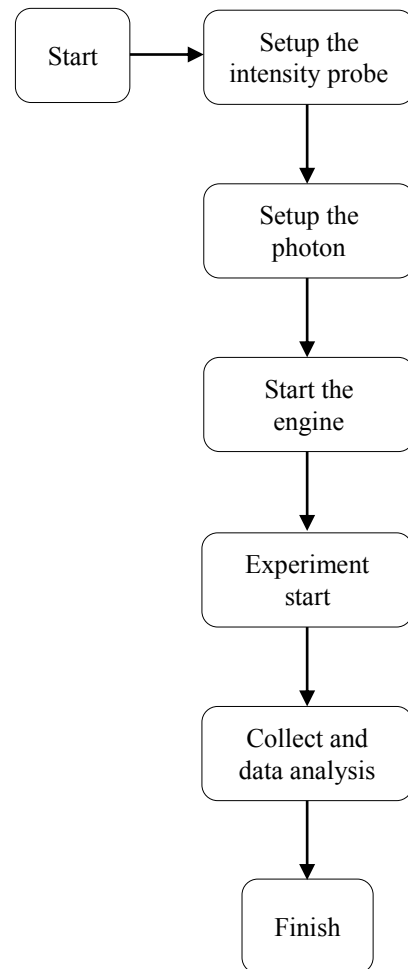
Figure 1 Procedure of this study

3. RESULTS AND DISCUSSION

In this section, results of the test will be discussed in details. Data for two different engine conditions; unloading and loading are taken at two different engine speeds which are at idle speed of 1000 RPM and 2000 RPM. Figure 2 and Figure 3 are the results of engine noise at different engine speeds with both engine conditions.

By referring to Figure 2, the loading condition produces higher noise level from frequency of 1 Hz up to 9 kHz compared to unloading condition. However, the significant difference of noise level between two engine loading conditions only occurs at low frequency. At higher frequency, the difference declines. It is because, during loading condition, engine needs to produce more power to support the air conditioning system but maintaining the same speed. The rate of combustion inside the chamber and the rate of air fuel intake are also increases. These factors may contribute to the increase of noise level.

This same phenomenon occurs at second measurement in which the engine operates at 2000 RPM as shown in Figure 3. The noise level is higher compared to when the engine is running at idle speed. But, it shows the same trend. The difference of noise level between two engine loadings decreases as the frequency increases.
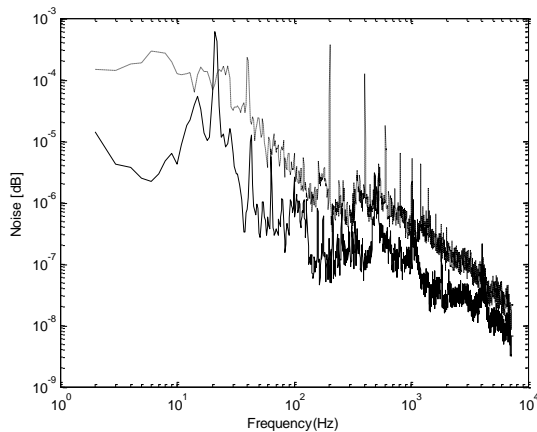
Figure 2 Noise levels at 1000 RPM; straight line for unloading and dotted line for loading.
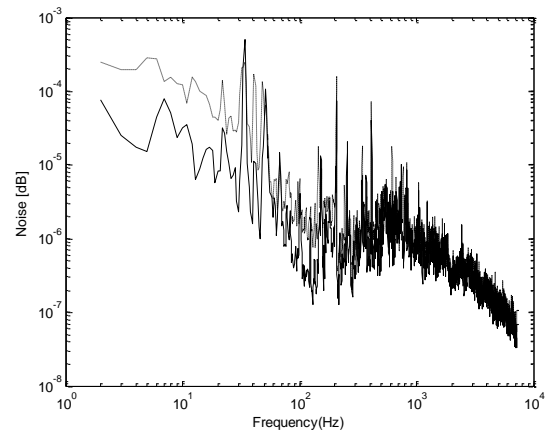
Figure 3 Noise levels at 2000 RPM; straight line for unloading and dotted line for loading

4. SUMMARY

At the end of the study, the objectives were achieved. The noise levels of car engine have been examined using sound intensity probe technique. On the other hand, the noise level is proportional with rotation speed of engine and also the loading condition of the car. In this study, the loading condition refers when the engine is loaded with air conditioning system.

REFERENCES

[1] V.W. Kallus, "Sound Quality of Turn Indicator Sounds," *Journal of Traffic and Transportation Engineering,* vol. 3, pp. 158-165, 2015.

[2] Kevin Bernard GINN, K. H., 2012. "Noise source Identify", in *Proceedings of the Acoustics Nantes Conference*, 2012.

Influence of halo and source/drain implant variations on the drive current in p-channel vertical double gate MOSFET

K.E. Kaharudin[1,2,*], F. Salehuddin[1,2], A.S.M. Zain[1,2], M.N.I.A. Aziz[1,2]

[1] Faculty of Electronics and Computer Engineering, Universiti Teknikal Malaysia Melaka,
Hang Tuah Jaya, 76100 Durian Tunggal, Melaka, Malaysia
[2] Centre for Telecommunication Research and Innovation, Universiti Teknikal Malaysia Melaka,
Hang Tuah Jaya, 76100 Durian Tunggal, Melaka, Malaysia

[*] Corresponding e-mail: khairilezwan@yahoo.com.my

Keywords: ANOVA; drive current; Taguchi

ABSTRACT – This paper describes an investigation on the influence of process parameters such as Halo and Source/Drain (S/D) implantation on drive current (I_{ON}) in p-channel vertical DG-MOSFET device was done by utilizing L_9 orthogonal array Taguchi method. The level of significance for each process parameters on I_{ON} were determined by using analysis of variance (ANOVA). The virtual fabrication and electrical characterization of the device were performed by using a process simulator (ATHENA) and a device simulator (ATLAS) respectively. This procedure was followed by Taguchi modeling to aid in optimizing the process parameters variation towards I_{ON}. Based on the final results, the most dominant factor that affecting I_{ON} value was found to be S/D implant energy with 99% of factor effects on signal-to-noise ratio (SNR). Meanwhile, the highest possible I_{ON} value was found to be 323.2 mA/μm.

1. INTRODUCTION

Over the past decades, a physical gate length (Lg) of MOSFET devices has been attempted to be reduced while keeping good electrical performance. For achieving a physical gate length (Lg) lower than 22nm with excellent device characteristics, a very careful design of channel doping profiles is required. Halo or pocket and source/drain implantation is widely utilized in deep submicron MOSFET technologies. These implant can be independently adjusted to prevent puchthrough effect. The dopant spread in the channel region can be suppressed by to reduce the body effect.

Optimization of the process parameters is a key step in the Taguchi method in order to achieve better device characteristics. The Taguchi method involves an analysis that is capable of identifying the most significant factors in achieving the higher I_{ON} value in which the level of these factors should be adjusted in term of their dosage and energy [1]. The optimization of process parameters using Taguchi method is insensitive to the variation of environmental conditions and noise factors [2]. Basically, the traditional process parameter design developed by Fisher [3], is very complex, especially when involving a large number of experiments. However, Taguchi method utilizes a special design of orthogonal arrays to analyze the entire process parameters space by using a small number of experiments. Besides that, Taguchi method utilizes a

signal-to-noise ratio (SNR) analysis to analyze the experimental data that could help in figuring out the optimal parametric combination [4].

In this work, an analytical model of two-dimensional p-channel Vertical DG-MOSFET device is developed by using Silvaco Technology Computer Aided Design (TCAD) simulation software, where the effects of halo and source/drain implant variation are investigated using Taguchi method. The Taguchi method is also utilized to reveal the ideal level of dosage and energy of halo and source/drain (S/D) implantation for the higher I_{ON} value of Vertical DG-MOSFET device.

2. MATERIALS AND METHODS

2.1 Process simulation

The completed structure of p-channel Vertical DG-MOSFET device is illustrated as in Figure 1.
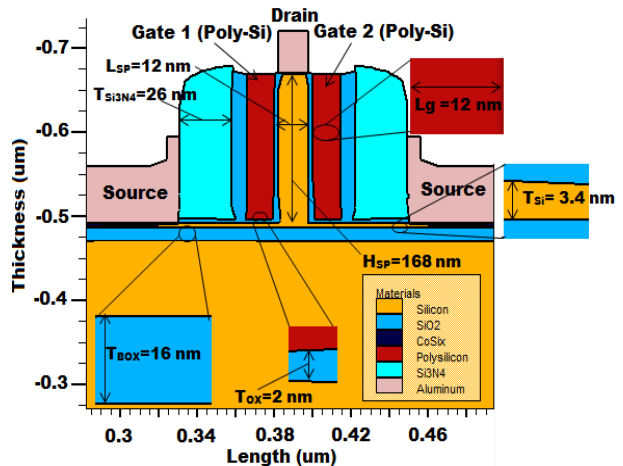
Figure 1 Structure of p-channel vertical DG-MOSFET.

3. RESULTS AND DISCUSSION

3.1 Characterization of p-channel vertical DG-MOSFET

Figure 2 shows the graph of subthreshold drain current (I_D) versus gate voltage (V_G) at drain voltage V_D = - 0.05 V and V_D = - 1.0 V for p-channel Vertical DG-MOSFET device. The value of off-leakage current (I_{OFF}) and drive current (I_{ON}) were extracted from the graph.
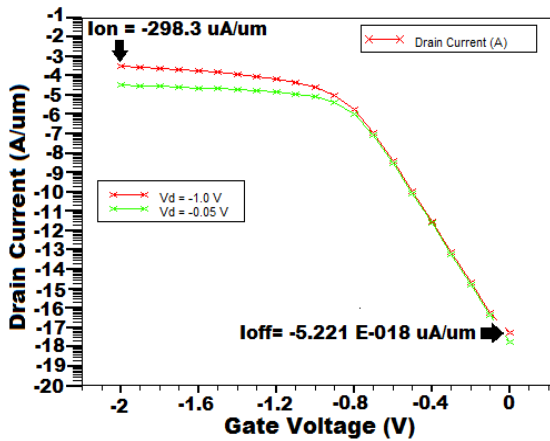
Figure 2 Graph of subthreshold drain current (I_D) versus gate voltage (V_G).

3.2 Signal-to-Noise ratio (SNR) analysis

The type of signal-to-noise (SNR) analysis that was assigned to analyze the I_{ON} values was higher-the-better. The SNR (higher-the-better), η can be expressed as [5]:

$$\eta = -10Log_{10}\left[\frac{1}{n}\sum_{i=1}^{n}\frac{1}{y^2}\right] \qquad (1)$$

The factor effects graph for SNR (Higher-the-better) was plotted as illustrated in Figure 3. The dashed horizontal lines in both graphs represent the overall mean of SNR (Higher-the-better) which is 49.71dB.
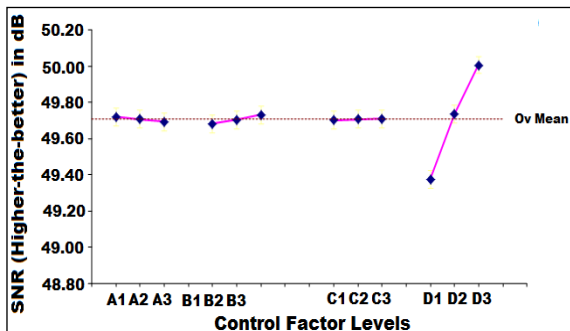
Figure 3 Factor effects graph for SNR (Higher-the-better).

3.3 Analysis of Variance (ANOVA)

The percent factor effect on SNR indicates the priority of a factor (process parameter) to reduce variation. For a factor with a high percentage of contribution and a small variance (mean square) will have a great influence on the device's performance. The percentages of factor effect on SNR of all factors are visualized in Figure 4.

4. CONFIRMATION TEST

The final step is to verify the improvement of the device's characteristic by simulating the device using the best setting of process parameters. The results of the final simulation of the device are shown in Table 1.
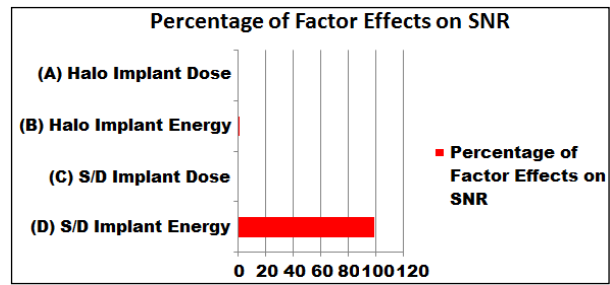
Figure 4 Pareto plot of factor effects on SNR for I_{ON}.

Table 1 Final result of confirmation test for drive current.

Drive Current, I_{ON} (mA/μm)				SNR (Higher-the-best)
I_{ON1} (U_1V_1)	I_{ON2} (U_1V_2)	I_{ON3} (U_2V_1)	I_{ON4} (U_2V_2)	
323.2	318.8	318.3	312.2	50.01 dB

5. CONCLUSIONS

As conclusions, the optimum solution in obtaining the highest possible value of drive current (I_{ON}) value was successfully predicted by L_9 orthogonal array Taguchi method. Drive current (I_{ON}) is the main response that has been investigated in this project as it is regarded as the main factor to decide the functionality of p-channel Vertical DG-MOSFET device. The level of significance of process parameters on I_{ON} is determined by using analysis of variance (ANOVA). Based on ANOVA method, the process parameter that has the major influence on I_{ON} was identified to be S/D implant energy with a percentage of 99% (factor effects on SNR). The highest possible drive current (I_{ON}) value was observed to be 323.2 mA/μm by using the optimized combination level of halo and S/D implantation predicted by Taguchi method.

REFERENCES

[1] F. Salehuddin, I. Ahmad, F. A. Hamid, A. Zaharim, H. A. Elgomati, B. Y. Majlis, P. R. Apte, "Influence of HALO and Source / Drain Implantation Variations on Threshold Voltage in 45nm CMOS Technology," *International Journal of Electronics Communication and Computer Technology*, Vol. 2, no. 3, pp. 27-33, 2012.

[2] K. Yang, E. C. Teo, F. Fuss, "Application of Taguchi Method in Optimization of Cervical Ring Cage," *International Journal of Biomechanics*, Vol. 40, no. 14, pp. 3251-3256, 2007.

[3] M. Nalbant, H. Gokkaya, G. Sur, "Application of Taguchi method in the optimization of cutting parameters for surface roughness turning," *International Journal Design*, Vol. 28, pp. 1379-1385, 2007.

[4] U. Esme, "Application of Taguchi Method for the Optimization of Resistance Spot Welding Process," *Arabian Journal for Science and Engineering*, Vol. 34, pp. 519-528.

[5] M. S. Phadke, *Quality Engineering Using Robust Design*, Pearson Education, Inc. and Dorling Kindersley Publishing, Inc; 2001.

Comparison of flow analysis between flat and ring plastic parts using moldflow software

Mohd Amran Md Ali[1,*], Mohd Faizal Khalik[1], Mariam Md Ghazaly[2], Zulkeflee Abdullah[1]

1) Faculty of Manufacturing Engineering, Universiti Teknikal Malaysia Melaka,
Hang Tuah Jaya, 76100 Durian Tunggal, Melaka, Malaysia
2) Faculty of Electrical Engineering, Universiti Teknikal Malaysia Melaka,
Hang Tuah Jaya, 76100 Durian Tunggal, Melaka, Malaysia

*Corresponding e-mail: mohdamran@utem.edu.my

Keywords: Injection moulding; simulation; moldflow; flow analysis

ABSTRACT – The flat and ring plastic part were designed using Solidwoks software to produce solid parts. Then the solid parts were imported in Autodesk Moldflow Insight (AMI) to analyze warpage deflection, fill time and weldline for both parts. Simulation result shows that the deflection for the flat plastic part is higher than the ring plastic part by 0.1466mm due to the bigger of volume and contact surface area for the flat plastic part. Meanwhile, fill time shows that the ring plastic part is longer 0.0458s then the flat plastic part due to the reduction of flow area. Finally, ring plastic part obviously shows weldline mark at flow front area however no weldline is observed at flat plastic part surface.

1. INTRODUCTION

It is important understand the flow of molten material filling the cavity area in an injection moulding process. To driving towards the fast, cost effective and reliable plastic manufacturing, simulation has taken part to achieving those goals [1]. Nowadays the simulation is one important element that must be done in order to get the best settings, parameters and preliminary results in the form of a contour image that show details needed. Recently, the simulation on an injection moulding plastic part has been studied by several researchers. Jian and Chuanyang have investigated the plastic flowing status during the circular plastic part by changing the melting temperature by simulation using MPI software. They find that productivity rate is the highest due to the maximum melting flow rate and the minimum injection time [2]. Xia investigated the flow and warpage simulation of mobile phone injection mould by using Moldflow software and found the application of the technology reduces the mould reworking time and increases the efficiency of the injection mould design [3]. Result from simulation can be compared with visualization where the parameters of machine injection can be optimized using various optimization methods such as using full factorial [4], response surface method and Taguchi method [5].

This project discusses the simulation mechanism of flat shape part and ring shape part that using the Autodesk Moldflow Insight (AMI) as the analyzer by looking at the warpage deflection, fill time difference and weld lines for both shapes.

2. METHODOLOGY

Figure 1 shows the simulation flow chart for flat and ring plastic part. To design the flat and ring plastic part, there are considerations that need to be look such as draft angle, part thickness, corner radius and it had been discussed in detail in our previous paper [6]. The solid modeling in CAD part is then imported into the AMI software to be analyzed both flat and ring part. The responses of this project selected are warpage deflection, fill time and weld line. Result responses in AMI for both parts are shown in the form of value and colour contour flow image. Finally, both results are compared which part shows less warpage, short fill time and obvious weldline mark.
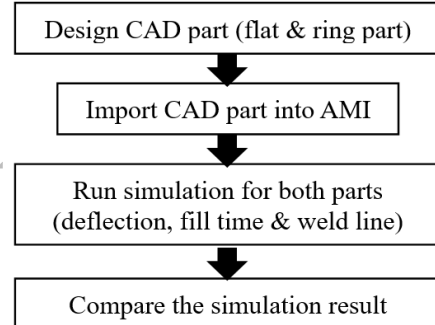
Figure 1 Simulation flow chart.

3. RESULT AND DISCUSSION

From the simulation, the results are display in a contour image of material flow filling the shape of the part. The material used in this analysis is polypropylene (PP) and the machine type Arburg alrounder 420c 80 tons. The results for both flat part and ring part are shows and discuss.

3.1 Flat part

Figure 2 shows the warpage deflection effect and fill time for the flat part in contour flow image. The maximum deflection for flat part is 0.38mm shows in the red area at the four edges. Meanwhile, the blue area is the areas that having the deflection only of 0.0204mm. Futher in Figure 2(b) the maximum fill time are at the end of the part with having 0.3081s. The flat part shows no weld lines due to its shape.

(a)   (b)

(c)
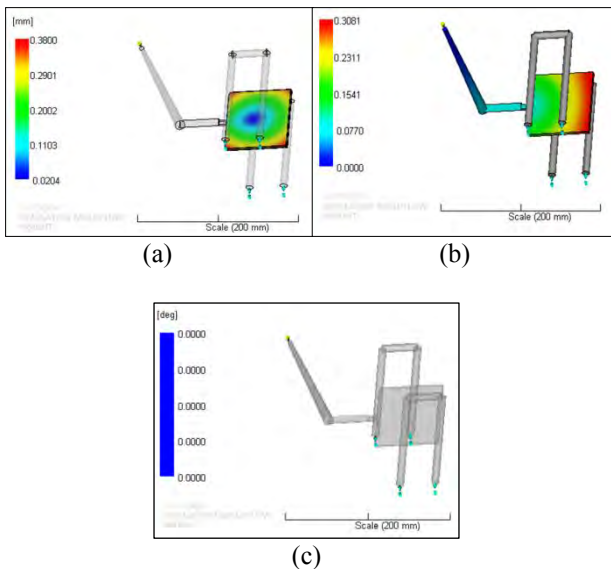
Figure 2 Flat plastic part; (a) warpage deflection of 0.3596mm (b) fill time in 0.3081s and (c) no sign of weldline.

3.2 Ring part

Figure 3 shows the warpage deflection, fill time and weld line for the ring part in contour flow image.

(a)   (b)

(c)
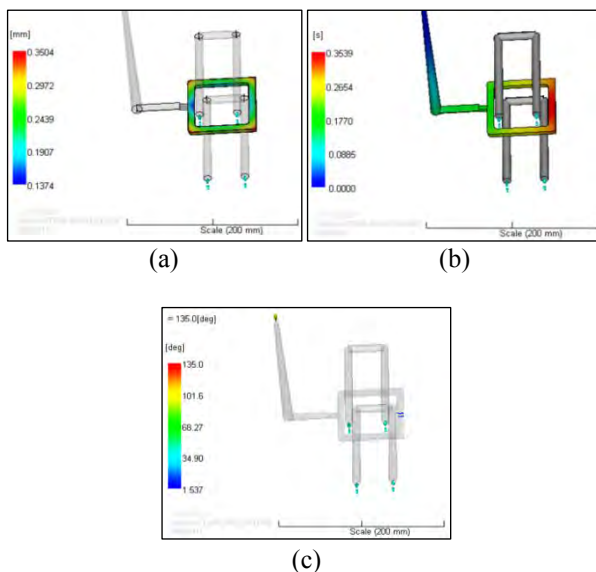
Figure 3 Ring plastic part; (a) warpage deflection of 0.213mm (b) Fill time of 0.3539s and (c) shows sign of weldline.

The maximum deflection for ring part is 0.3504mm shows in the red area at the far away edges. The blue area is the areas that having the minimum deflection of 0.1374mm. While in Figure 3(b) the maximum fill time is at the end of the part with having 0.3539s. Further, Figure 3(c) the ring part shows weld line at the meeting area at the end of the ring part.

From the simulation result, it shows that the maximum warpage deflection for flat part as compare to the ring part is 0.1466mm due to the shape of the flat part that consist more material and the contact surface area with the mould is bigger thus the heat dissipation from the part to the mould is slower than the ring part.

However, the fill time for the ring part is slower than the fill time of the flat part by 0.0458s because of the flow area that is smaller for the material to fill until the end of the part. The weld lines are formed in the ring part because of two flow fronts meets heads on. They give the part of the area local weakness because they act as stress concentrations. Although the weld lines cannot be eliminated, this flow analysis can show the location and the mould can either be redesign to position weld lines in the least sensitive area.

4. CONCLUSION

The comparison of simulation analysis for both flat and ring plastic part by using AMI is performed. The warpage deflection, fill time and weld lines for flat and ring plastic part are observed carefully by contour image result. It can be concluded that flat part shows more warpage deflection but lower fill time as compare to ring part. Further, flat part shows no weldline but obvious weldline for ring part. Thus, result shows that volume and shape are crucial factors for materials characteristics of plastic part.

REFERENCES

[1] J. Shoemaker, *Moldflow design guide,* Framingham: Hanser; 2006.

[2] Z. Jian and W. Chuanyang, "Flow analysis in injection moulding process based on moldflow," in *International Conference Mechanic Automation and Control Engineering (MACE)*, 2010, pp. 19-22.

[3] W. Xia. Flow and warpage simulation of mobile phone injection mold," in *International Symposium on Instrument and Measurement, Sensor Network & Automation (IMSNA),* 2012, pp. 491-493

[4] M. Amran, S. Salmah, M. Zaki, R. Izamshah, M. Hadzley, Sivarao, M. Shahir, and M. Amri, "The effect of pressure on warpage of dumbbell plastic part in injection moulding machine," *Advanced Materials Research*, vol. 903, pp. 61-66, 2014.

[5] M. Amran, S. Salmah, A. Faiz, R. Izamshah, M. Hadzley, B. Manshoor, M. Shahir, and M. Amri, "Effect of injection moulding machine parameters on the warpage by applying taguchi method," *Applied Mechanics and Materials*, vol. 699, pp. 20-25, 2014.

[6] M. Amran, M. Faizal, M. Syukor, M. Amri, and M. Effendi, "Design consideration for design a flat and ring plastics part using solidworks software" in *3rd International Conference on Mechanical Engineering Research (ICMER 2015*). *IOP Conf. Series: Materials Science and Engineering,* vol. 100, pp. 1-9, 2015.

Study of thinning effect from deep drawing process on crash analysis

R.M. Amman[1,*], M.F. Halim[2], D. Sivakumar[1], I. Abu-Shah[2], M.S. Sulaiman[2], H. Samekto[1]

[1] Faculty of Mechanical Engineering, Universiti Teknikal Malaysia Melaka,
Hang Tuah Jaya, 76100 Durian Tunggal, Melaka, Malaysia
[2] Faculty of Technology Engineering, Universiti Teknikal Malaysia Melaka,
Hang Tuah Jaya, 76100 Durian Tunggal, Melaka, Malaysia

*Corresponding e-mail: rosmiaamman@gmail.com

ABSTRACT – This study presents the effect of thinning on crash analysis results of a circular cup shape formed from deep drawing process. Forming and crash simulation of a circular cup was performed using Explicit Radioss code simulation solver. Circular cup shape formed from deep drawing with and without thickness effect was used to conduct explicit dynamic crash simulation. The effect of material thickness change from stamping process was studied. It was found that thinning effect from stamping causes the structural part to have a weaker crash response.

1. INTRODUCTION

Nowadays, many industrial fields tend to use numerical simulation to design and develop a product in order to reduce time and costs for the development. However, the simplicity of simulation approach in order to produce a product can cause negligence of important factor than can affect the simulation results. Crash simulation in automotive industries also has no exception. Traditionally, finite element (FE) crash simulation utilizes only the geometry of the structure without taking into consideration that the material of the single parts of the entire body structure may have changed their physical properties during the forming process [1]. In other words, the model is considered as virgin material. As a consequence from this assumption, the crash simulation will lead to inaccurate results.

Huh et al. [2] conducted a crash analysis on a front side member in an auto-body considering the effect of fabrication in order to quantify the forming effect on the crashworthiness assessment. Cafolla et al. [3] also studied about the forming to crash effect by including thickness change and plastic strain for the lower longitudinal (sub-frame extension). Recently, Zhang et al. [4] investigated the forming effects on crush response of tapered circular tube with graded thickness under axial loading and found that forming effects showed important influence on the increase of efficiency. All the above studies insisted that the crash analysis of auto-body structures should be carried out considering the forming effects for the purpose of reliable assessment of crashworthiness.

Due to the gap between the product design and the manufacturing process, the influences of manufacturing process on the material properties and thickness distribution is unknown and one would arbitrarily choose a high-value „safety factor" to uniformly increase the thickness across the entire part in order to be on the safe side [5]. The present study is focused on the influence of thinning effect from deep drawing process to the crash response of a simple cup structure model formed by using plastic deformation process. This study only covers numerical analysis using finite element.

2. METHODOLOGY

In this paper, finite element simulation studies are conducted for a simple structure in the shape of a cup. A small scale of a cup model is used instead of large scale of full vehicle because of its simplicity. The methodology of this work is highlighted in two steps of simulations which starts with forming simulation and subsequent crash simulation in order to quantify the effects of thickness change from preceding process.

The forming simulation was performed using single action draw since a small and medium size parts are generally formed using these type of draw forming process in normal practices. The desired circular cup shape is designed from a draw forming tools set up which consists of a sheet metal as deformable steel blank and three rigid parts (die, punch and blank holder) with zero die clearance. A deformable steel blank with 1.2 mm thickness and 85 mm in diameter is meshed using 4-node quadrilateral element type with fine and coarse mesh. The number of elements and nodes is 1620 and 1641 respectively. The material formability is evaluated in order to determine the success of draw forming process into the desired shape as shown in Figure 1.

Figure 1 Desired shape of circular cup.

Numerical simulations of crash tests were performed using explicit code Radioss solver to present dynamic response of crash simulation. The geometric modeling consists of three parts: (1) moving rigid body (Impactor), (2) fixed rigid body (Base) and (3) deformable body (Circular cup shape). The impactor was moved at a constant velocity of 50 km/h or equal to 13.9×10^3 mm/s towards the cup. The coulomb friction between the impactor and deformable cup is assumed frictionless.

---

3. RESULTS AND DISCUSSION

The results obtained between these two case studies is compared qualitative and quantitatively. The analysis results with and without thickness reduction from forming are showed in Figure 2. It is evident that there is change in thickness during forming process. There is thinning of 12.87% at the sidewall and 3.53% thickening at the flange. This is because the structural part undergoes deep drawing process.

The final deformed shape of the circular cup after impact for both cases are shown in Figure 3. Results shows that there is less significant difference in the collapse mode as both deformed in buckling mode. Since the circular cup model is set free to move and is not constrainted at any area, the upper surface of the circular cup moved downward while the flange area moved upward. The maximum and minimum displacement value displayed represented the distance of the upper surface and the flange of the cup respectively, as it is impacted. The reaction forces normal to the impactor are plotted with respect to the cup displacement in Figure 4.

(a)   (b)
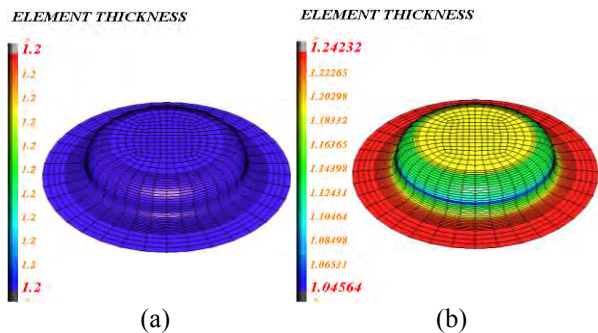
Figure 2 Thickness distribution for; (a) Without thinning effect (Uniform thickness), (b) With thinning effect (Non-uniform thickness).

(a)   (b)
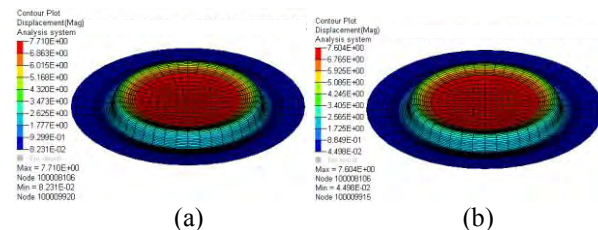
Figure 3 Circular cup deformation due to crash analysis; (a) Without thinning effect, (b) With thinning effect.
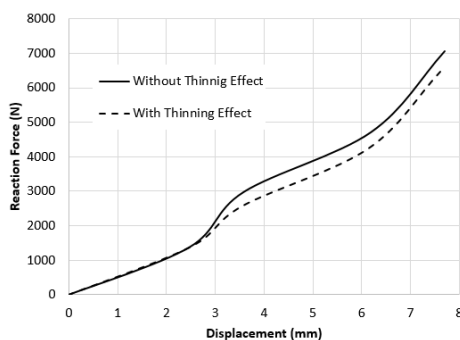
Figure 4 Reaction forces during the crash of the circular cup part.

Figure 4 shows that the reaction forces between the impactor and circular cup have high peak value when uniform thickness was considered in the crash analysis. The reaction force tends to decrease more with displacement in the case of analysis considering the thinning effects than without considering thinning effects. The results explain that the non-uniform thickness distribution with the thinned region can be considered as the initial defect of the circular cup part. This results also shows that the forming effects does influences the crash analysis results such as deformation and reaction force results.

4. CONCLUSIONS

Thickness distribution from thinning due to stamping plays a role as initial defects and could affect the crash response of a structural part. This would make a structure become weaker and the crash performance will significantly decrease. Even though the deformation mode gives less significant difference between the two cases studied, the reaction force between the impactor and circular cup part that consider thickness change was lower than other. This results shows that the structure became weaker and does proved that forming effects (thickness change) does affect the crash analysis results. Therefore, it is concluded that the forming effects need to be included in crash analysis in order to ensure the reliable assessment of crashworthiness.

ACKNOWLEDGEMENT

REFERENCES

[1] S.-H. Lee, C.-S. Han, S.-I. Oh, and P. Wriggers, "Comparative crash simulations incorporating the results of sheet forming analyses," *Eng. Comput.*, vol. 18, no. 5/6, pp. 744–758, 2001.

[2] H. Huh, K. P. Kim, S. H. Kim, J. H. Song, H. S. Kim, and S. K. Hong, "Crashworthiness assessment of front side members in an auto-body considering the fabrication histories," *Int. J. Mech. Sci.*, vol. 45, no. 10, pp. 1645–1660, Oct. 2003.

[3] J. Cafolla, R. Hall, and D. Norman, ",, Forming to Crash " Simulation in Full Vehicle Models," *4th Eur. LS-DYNA Users Conf.*, no. 0, pp. 17–26, 2003.

[4] X. Zhang, H. Zhang, and Z. Wen, "Axial crushing of tapered circular tubes with graded thickness," *Int. J. Mech. Sci.*, vol. 92, pp. 12–23, 2015.

[5] A. E. Tekkaya, J. M. Allwood, P. F. Bariani, S. Bruschi, J. Cao, S. Gramlich, J. Lueg-althoff, M. Merklein, W. Z. Misiolek, M. Pietrzyk, R. Shivpuri, and J. Yanagimoto, "CIRP Annals - Manufacturing Technology Metal forming beyond shaping : Predicting and setting product properties," vol. 64, pp. 629–653, 2015.

Design, simulation and analysis of disc rotor using anycasting software

N.F.B.W. Anuar[1,*], N. Jani[1], M.R.M. Kamal[1]

[1] Faculty of Engineering Technology, Universiti Teknikal Malaysia Melaka,
Hang Tuah Jaya, 76100 Durian Tunggal, Melaka, Malaysia.

*Corresponding e-mail: nurfarah@utem.edu.my

Keywords: AnyCasting; solidification time; casting defects

ABSTRACT – This project describes about the design and simulation of disc rotor in sand casting by using AnyCasting software. The analysis of this study is filling time, solidification time and defects on the three mold designs. The selected design in this study is design 2 referring the present defect that happened on the riser part. The filling time for design 2 is 7.6648 seconds and solidification time is 1452.6 seconds.

1. INTRODUCTION

Foundry sand is often used in the industry to make parts consisting of iron, bronze, copper and aluminum as well. The metal is poured into the mold cavity that formed by the sand when the metal melted in the furnace. The process is relatively simple and inexpensive, and this process had been applied in many industries. However, the weakness of sand casting is commonly in parts of cast sand and it can affect the properties of casting materials [1].

Gray cast iron is one of the most important casting materials and has many industrial applications because of its good castability properties and large variation in mechanical properties. Kumar and Kumar [2] stated that the variation of mechanical properties depends on the microstructure. The quality of the casting parts is depending on the percentage of the porosity in the product; the smaller percentage will lead to the better design.

The objective of the project is to analyze the casting defects on gray cast iron disc brake in AnyCasting software.

2. METHODOLOGY

2.1 Part selection

The part selection for an obsolete automotive part in this project was made based on several criteria. The part focused with produced by sand casting method. The chosen part is disc rotor. Disc rotor is a device is used for slowing or stopping the rotation of the tire wheels in automotive fields [3].

2.2 Design CAD

The CAD software that is used in this project was SolidWorks software. From this, the 3D CAD data of the disc rotor and the mold design of the sand casting can be generated. There are three molds are designed as shown in Figure 1 based on four criteria of parameters which are gating system, runner system, riser system and the position of sprue.

2.3 AnyPRE (Pre-processing)

In this stage, it is function to generate meshes by analyzing the CAD data. A fix mesh, which is hexahedron was used in simulation. The total mesh for design 1, design 2 and design 3 are 1164800, 931190, and 6349500, respectively. Materials properties and temperature condition were selected. The setting parameters gate conditions is to determine the pouring temperature and velocity of the molten metal.
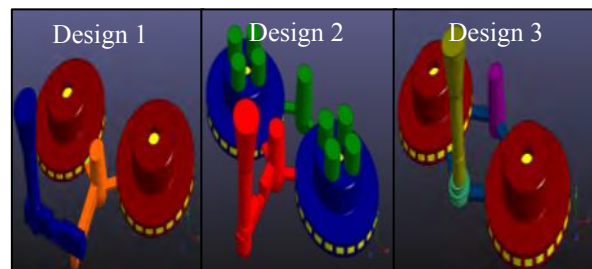
Figure 1 Three designs of sand casting mold.

2.4 AnySOLVER

Simulates the flow and temperature fields of the design proces. The solidification of the molten metal need to be starts when the casting completely filling with the molten metal.

2.5 AnyPOST (Post-processing)

Graphics function for analyzing the simulation results. The results that will be considered in this simulation are filling time, solidification time, and defects.

3. RESULTS AND DISCUSSION

The filling times for three designs were analyzed as shown in Figure 2. The velocity condition during filling for all designs are 45 cm/s while the pouring temperature is 1420 °C for gray cast iron. The longest filling time is 7.6648 seconds which is observed from Design 2 while Design 3 has the shortest filling time which is 1.5559 seconds. The solidification time as shown in Figure 3 for the molten metal of Design 2 to solidify is high, 1452.6 seconds while Design 1 is the shortest time to solidify which is 1172.8 seconds. The defects occur as shown in simulation was happened on product and mold for Design 1 and Design 3, while the

defects occur only on the riser of mold for Design 2 as shown in Figure 4. Thus, the product of the casting is not affected and the part product still in good castability shape for Design 2.
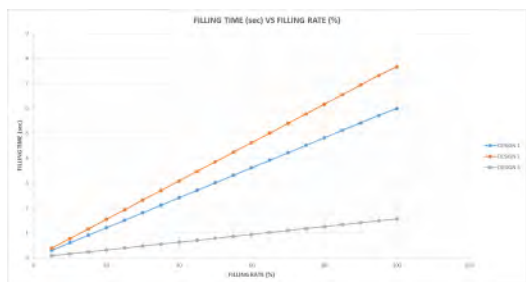
Figure 2 Filling time vs filling rate for three different of mold designs.
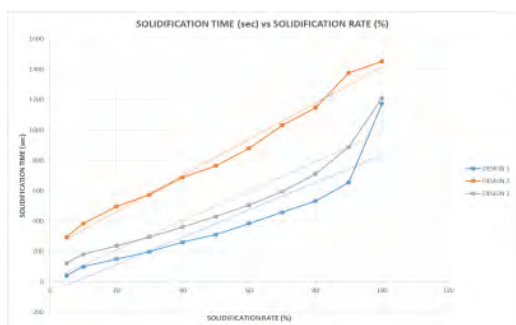
Figure 3 Solidification time vs solidification rate for three different of mold designs.

Shrinkage cavity will form when a large isolated region of liquid phase remains within solid and with it surrounding. Based on the feature of retained melt modulus for three designs, the formation and location of the defect of shrinkage cavity as shown in Figure 4.
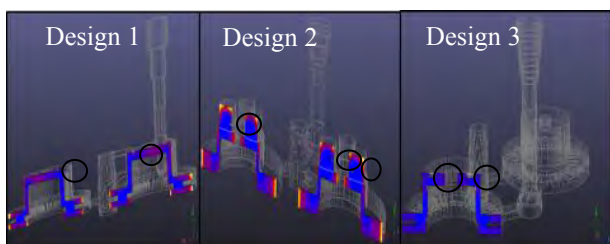
Figure 4 The defects of shrinkage cavity for three designs.

Component of disc rotor that has been analyzed and the value is shown in Table 1 for their retained melt volume. Retain Melt Volume indicates the volume of the residual melt for each grid when it reaches the critical solid rate. The increasing of retained melt volume, it will lead to better area for solidification and reducing the defect formation.

Table 1 Data analysis of retained melt volume.

Design	Retained melt volume, cm³
Design 1	5456.8066
Design 2	6486.7300
Design 3	5236.6099

Figure 5 shows the turblence occur at circles area due to the designs of the runner at the side of the cavity and the area of the top riser.
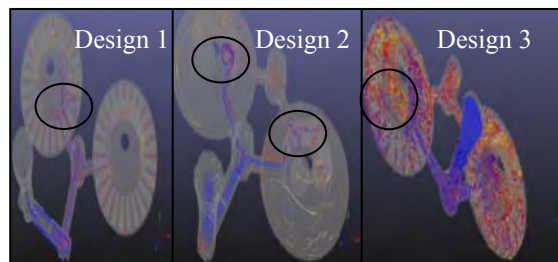
Figure 5 Analysis of particle tracing and position of turbulance for three designs.

Figure 6 shows the cooling curve for three designs and the pouring temperature state is at 1420°C. It is started to cooling until it is reached the freezing point and starting to become a semi-solid. After it reached the freezing point, it starting to become a solid state and the total time taken for deformation of solid state for design 1 is 1172.8 seconds, design 2 is 1452.6 seconds, and design 3 is 1209.3 seconds.
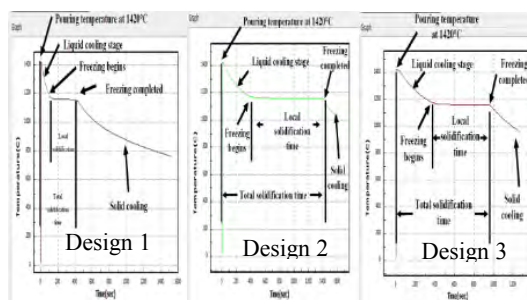
Figure 6 The cooling curve for three designs.

4. CONCLUSION

In a conclusion, the best design that have been selected is design 2. The design 1 and 3 have a defect of unfilling at the product. Eventhough the design 2 has the longest filling time that is 7.6648 seconds, the overall results from the simulation shows that the defects are happened on the mold and at the machining part for wheel stud only. For the solidification, it takes about 1452.6 seconds but the defects of casting as shown in analysis are occurs at the mold. The objective of this project is to analyze the simulation of sand casting and to find the optimum parameters based on quality reponse is successfully achieved.

REFERENCES

[1] E. Merten, *Sand Casting of Metal*, pp. 1-5, 2012.

[2] V. Kumar, A. Kumar, "Simulation of Cooling Rate of Gray Cast Iron Casting in a Sand Mold and its Experimental Validation", *Materials Science Forum*, Vol. 710, pp. 208-213, Jan. 2012

[3] M. Sasikumar, "Design and Thermo-structural Analysis of Disc Brake", *International Journal in Physical & Applied Sciences,* Vol.1, Issue-03, December 2014.

Linear and nonlinear dynamic model of a gantry crane system

H.I. Jaafar[1,*], Z. Mohamed[2], M.A. Ahmad[3], R. Ghazali[1], A.M. Kassim[1]

[1] Faculty of Electrical Engineering, Universiti Teknikal Malaysia Melaka,
Hang Tuah Jaya, 76100 Durian Tunggal, Melaka, Malaysia
[2] Faculty of Electrical Engineering, Universiti Teknologi Malaysia, 81310 Skudai, Johor, Malaysia
[3] Faculty of Electrical and Electronics Engineering, Universiti Malaysia Pahang,
26600 Pekan, Pahang, Malaysia

*Corresponding e-mail: hazriq@utem.edu.my

Keywords: Gantry crane system; linear; nonlinear

ABSTRACT – This paper investigates linear and nonlinear dynamic models for a Gantry Crane System (GCS). The system is a Single Input Multi Output (SIMO) system which a trolley displacement and payload oscillation as the outputs. The GCS is modeled by using the Lagrange Equation and both system responses are observed and analysed. The fundamental differences between the linear and nonlinear equations are presented. This analysis is beneficial for the development of efficient controllers for a GCS.

1. INTRODUCTION

A gantry crane system (GCS) is a machinery that is commonly used in industries for heavier materials (concrete, container, etc) that related to the process of transporting and carrying the load. GCS consists of a trolley and a payload is attached to the trolley by a cable vertically. The load with the cable is treated similar to a concept of a pendulum and free to oscillate in a 360 degree direction. For an analysis and development of controllers, the system has to be expressed by an accurate mathematical expression.

The development of mathematical concepts and techniques is aggressively implemented for all dynamic systems. The purpose is to represent the understanding of the actual phenomena system into theoretical for solving the problems that arise [1]. Normally, nature phenomena is always abounds with nonlinear systems due to material, inertia, body forces or friction [2]. However, this nonlinear system is quite difficult to be analysed due to the complex mathematical structure. Thus, nonlinear models can be linearized to a linear model in order to simplify the mathematical model to make it easier for controller designs.

2. MATHEMATICAL MODELING OF GCS

Several methods can be used to model the GCS. From several aspects of observations, the Lagrange's equation is more suitable and efficient to derive the mathematical expression, especially for a higher order system [3]. The GCS has two independent generalized coordinates, namely trolley displacement (x) and payload oscillation (θ). The structural model and all the parameter values of GCS are presented in Figure 1 and Table 1 respectively. Some assumptions have been made such as cable of trolley and hanged load are assumed to be rigid and massless.
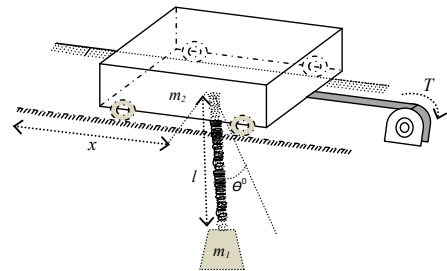
Figure 1 Structural model of GCS.

Table 1 System parameters [3].

Parameters	Values
Payload mass (m_1)	0.5 kg
Trolley mass (m_2)	2 kg
Cable length (l)	0.5 m
Gravitational (g)	9.81 m/s^2
Damping coefficient (B)	0.001 Ns/m
Resistance (R)	2.6 Ω
Torque constant (K_T)	0.007 Nm/A
Electric constant (K_E)	0.007 Vs/rad
Radius of pulley (r_P)	0.02 m
Gear ratio (z)	0.15

The standard form of Lagrange's equation is written as:

$$\frac{d}{dt}\left\lfloor \frac{\partial L}{\partial \dot{q}_i} \right\rfloor - \frac{\partial L}{\partial q_i} = Q_i \tag{1}$$

Where L, Q_i and q_i represent the Lagrangian function, nonconservative generalized forces and independent generalized coordinates respectively. The Lagrangian function can be written as:

$$L = T - P \tag{2}$$

Solving for Equation (1) and (2) yields differential equations as:

$$(m_1 + m_2)\ddot{x} + m_1 l\ddot{\theta}\cos\theta - m_1 l\dot{\theta}^2\sin\theta + B\dot{x} = F \qquad (3)$$

$$m_1 l^2\ddot{\theta} + m_1 l\ddot{x}\cos\theta + m_1 gl\sin\theta = 0 \qquad (4)$$

Where F is external force. By considering the dynamic of a DC motor is included in this GCS model, a complete nonlinear equation of the GCS can be obtained as:

$$V = \left[\frac{RBr_P}{K_T z} + \frac{K_E z}{r_P}\right]\dot{x} + \left[\frac{Rr_P}{K_T z}\right](m_1 l)\left[\ddot{\theta}\cos\theta - \dot{\theta}^2\sin\theta\right] +$$
$$\left[\frac{Rr_P}{K_T z}\right](m_1 + m_2)\ddot{x} \qquad (5)$$

$$m_1 l^2\ddot{\theta} + m_1 l\ddot{x}\cos\theta + m_1 gl\sin\theta = 0 \qquad (6)$$

Where V is an input voltage and all the parameters are presented in Table 1. In order to linearize the nonlinear model, small θ ($\sin\theta \approx \theta$ and $\cos\theta = 1$) during system operation is considered. Therefore, the linear equations can be obtained as:

$$V = \left[\frac{RBr_P}{K_T z} + \frac{K_E z}{r_P}\right]\dot{x} + \left[\frac{Rr_P}{K_T z}\right](m_1 l\ddot{\theta}) +$$
$$\left[\frac{Rr_P}{K_T z}\right](m_1 + m_2)\ddot{x} \qquad `(7)$$

$$l\ddot{\theta} + \ddot{x} + g\theta = 0 \qquad (8)$$

3. RESULTS AND DISCUSSION

Figure 2 shows the Simulink model of linear and nonlinear models of GCS. The linear and nonlinear equations in Equation (5), (6), (7) and (8) were applied in the Simulink model and the system responses are observed and analysed for their similarity. Figures 3 and 4 show the trolley displacement and payload oscillation responses with a pulse input.
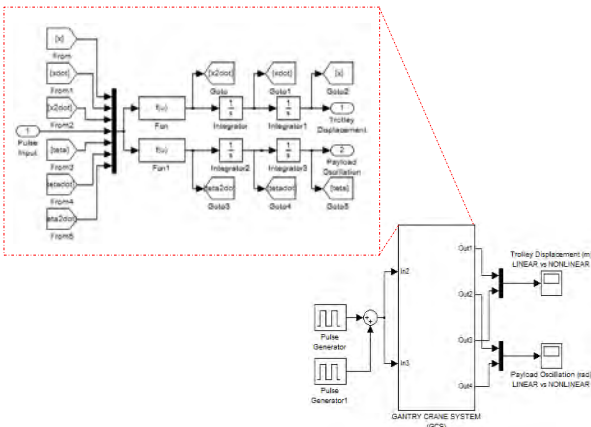
Figure 2 Simulink model of linear and nonlinear GCS.

It is noted that a very close agreement between the linear and nonlinear models have been obtained for both system responses (trolley displacement and payload oscillation). It can be further shown by the trolley displacement response in a selected time period as shown in Figure 3. It shows that, within a small angle, the linear model can represent a nonlinear model and provide a simpler equation for controller design.
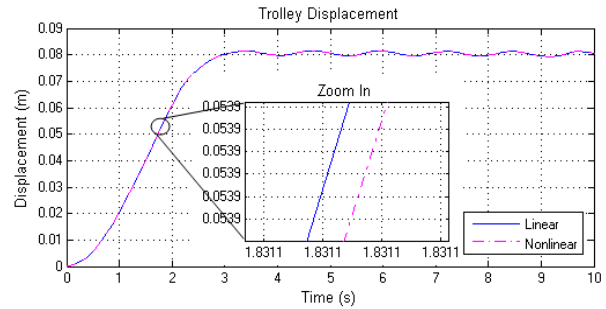
Figure 3 System response of trolley displacement.
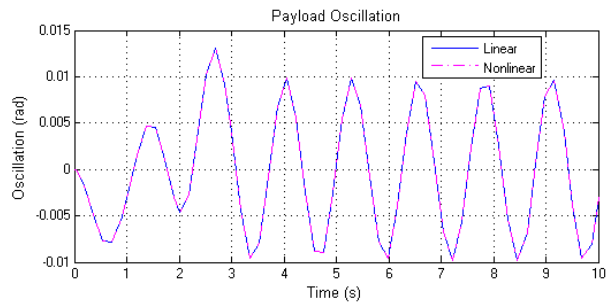
Figure 4 System response of payload oscillation.

4. CONCLUSION

Designing of controllers is easier by using a linear model as the derived mathematical models are less complicated. For the GCS, it has been proven that both linear responses (trolley displacement and payload oscillation) are in a good agreement with a natural response that present in a nonlinear system. Thus, it is reasonable to estimate or approximate all the nonlinear model parameters with the linear model.

REFERENCES

[1] G.B. Whitham, *Linear and nonlinear waves*, New York: John Wiley and Sons; 1974.

[2] Ali H. Nayfeh, and P. Frank Pai, *Linear and nonlinear structural mechanics*, New York: John Wiley and Sons; 2004.

[3] H.I. Jaafar, Z. Mohamed, J.J. Jamian, A.F.Z. Abidin, A.M. Kassim, and Z.A. Ghani, "Dynamic behaviour of a nonlinear gantry crane system," *Procedia Technology*, vol. 11, pp. 419-425, 2013.

Finite Element Modelling of microscale and macroscale on deformation of composite material

Ab Ghani Ahmad Fuad[1,2], Reduan Mat Dan[1,2], M.I. Shariff[1], Tan Joon Tak[1]

[1] Faculty of Mechanical Engineering, Universiti Teknikal Malaysia Melaka,
Hang Tuah Jaya, 76100 Durian Tunggal, Melaka, Malaysia
[2] Centre for Advanced Research on Energy, Universiti Teknikal Malaysia Melaka,
Hang Tuah Jaya, 76100 Durian Tunggal, Melaka, Malaysia

*Corresponding e-mail: ahmadfuad@utem.edu.my

Keywords: Finite Element Modelling; composite modeling; Microscale; RVE; FEA

ABSTRACT – Performance prediction is an important aspect in confirming the correct design specification of composite materials. Finite Element Modelling (FEM) approach enables to calculate stress and strain components of a structure for more realistic strength predictions. In this study numerical simulation is perform using FEM method to simulate composite materials through tensile test at micro and macro level. The geometric for tensile test were according to ASTM D3039 for GFRP and CFRP. Micromodelling of composites were simulated based on theory of Representative Volume Element (RVE). It is found that RVE able to predict deformation and mechanical properties extraction of composite in unidirectional.

1. FINITE ELEMENT MODELLING OF COMPOSITE

The finite-element method (FEM) has been found to be la powerful numerical tool for the analysis of composite structures under static loading [1-3]. In this study, different types of elements for composite have been used namely plane strain, plane stress, 3D Conventional Shell and 3D Continuum Shell. There are many ways in studying the effect of different element used for composite material simulation in accounting for through thickness shear deformation, normal stress and width influence.

2. METHODOLOGY

2.1 Composite solid elements in FEM

The use of composite solids is limited to three-dimensional brick elements that have only displacement degrees of freedom. Composite solid elements are primarily intended for modelling convenience.[2] They usually do not provide a more accurate solution than composite shell elements. The thickness, the number of section points required for numerical integration through each layer and the material name and orientation associated with each layer are specified as part of the composite solid section definition. The solid (or continuum) elements in Abaqus can be used for linear analysis and for complex nonlinear analyses involving contact, plasticity, and large deformations.

2.2 Creating conventional shell composite layups

Conventional shell composite layups are composed of plies made of different materials in different orientations. A layup can contain a different number of plies in different regions. Shell elements perform somewhat better than solid elements in modelling the transverse shear stress through the thickness. Since the transverse shear stresses in thick shell elements are calculated by Abaqus on the basis of linear elasticity theory, such stresses are often better estimated by thick shell elements than by solid elements.[6]

2.3 Stacked or layered continuum shells

The continuum shell model is a fully three-dimensional geometrical study of stress and displacement elements in composite which the thickness is defined as nodal geometry. The results in this method are more accurate and it can be used for all thickness.[6]

2.4 Material properties of the GFRP and CFRP Macroscale

The GFRP layups is builds up with 10 plies and stack with 0 degree fiber orientation. The CFRP layups is builds up with 2 plies and stack with 0 degree fiber orientation. The material properties of the GFRP and CFRP are listed in **Table 1**.

Table 1 Material properties of the GFRP and CFRP.

Property/ Material	GFRP	CFRP
Young's Modulus (GPa)	E_1= 37.6 E_2= 10.3	E_1= 120 E_2= 7.614
Poisson's Ratio	0.3	0.31
Shear Modulus (GPa)	5.85	4.8

2.5 Micromechanical modelling

Micromechanical of materials is the analysis on the level of individual constituents that represent the whole material of composite material or might as well defined as heterogeneous materials which is defined as non-uniform and composed of diverse parts that occupy the same volume [4].For heterogeneous material, it display a statistical arrangement of the constituent where it shows an orthotropic material symmetry which

---

the behaviour depends on the shape and orientation of the inclusions, instead of deterministic arrangement of the constituents such as homogeneous material. Thus, the concept of representative volume element (RVE) is used as the method of micromechanics where such task known as homogenization applied. In this study, the micromechanical modelling of RVE represents the unidirectional composite material [5].Besides that micromechanical representation on macrolevel is limited to corresponding volume fraction and fiber orientation which is 60 percent and 0 degree in longitudinal direction. Figure 1 shows the RVE modelling under longitudinal tensile loading with boundary condition involved. The size of RVE were modelled as accordance to real size in microscale and represents volume fraction of 60 percent which similar with real size. Meshing type used is swept mesh for matrix and fiber solid region with hexahedral 3D shape. This is based on other scholars' previous works. [4,5]
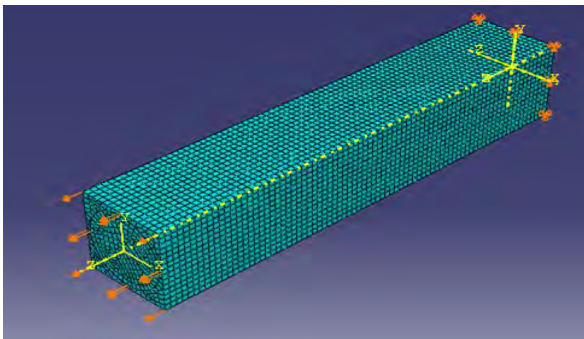
Figure 1 Unit cell of RVE for longitudinal tension.

3. RESULTS AND DISCUSSION

Predicting deformation using RVE for GFRP and CFRP shows consistent value of mechanical properties of macroscale unidirectional with volume fraction 60% under static loading. The young modulus were obtained by using relation of Eq 1.

$$E_{11} = \frac{\sigma_{11}}{\varepsilon_{11}} = \frac{F_1/A}{\varepsilon_{11}} \tag{1}$$

Where $_{11}$ notation apply to longitudinal similar with tensile loading direction. Figure 2 shows contour of von misses stress experienced by RVE under tensile loading. Meanwhile Figure 3 and Figure 4 depict stress against strain plot under similar direction of tensile shown by RVE after tensile loading. Gradient computed for CFRP is 115329MPa and 36086MPa for GFRP of the plot represents young modulus of macroscale GFRP and CFRP which match very closely as 120GPa for CFRP and 30-45 GPa for GFRP respectively.

4. CONCLUSION

RVE models have been developed and simulated to study the homogenization of FRP at macroscale using commercial finite element software Abaqus. Method of RVE based on specific volume fraction proved successful in predicting mechanical properties of young modulus E1 and poisson ratio. Further work could include the shear as well as compressive properties of composite. The result also limited to unidirectional

cases. Macroscale FEM on composite offer arrays potential of research work, from simple comparison of static loading deformation with analytical to predicting the strength and failure of composite during static loading. The feature of commercial software Abaqus have been explored and proven able to simulate real scenario and experimental with any composite layup and any orientation.
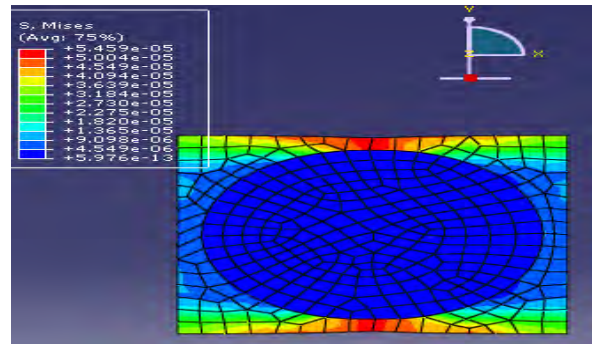
Figure 2 Stress, Von Misess Contour after longitudinal tensile loading of RVE GFRP.
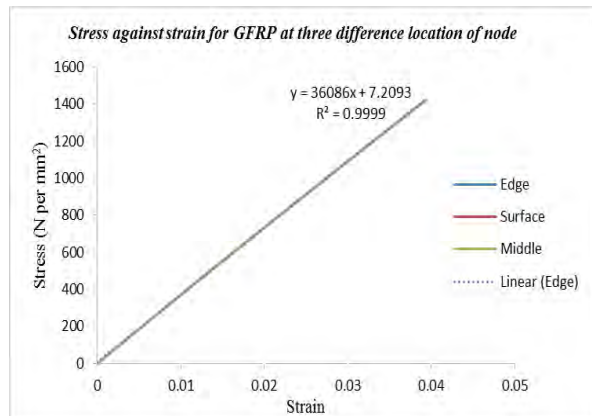
Figure 3 Stress against strain plot for GFRP model of RVE at 60 percent volume fraction.
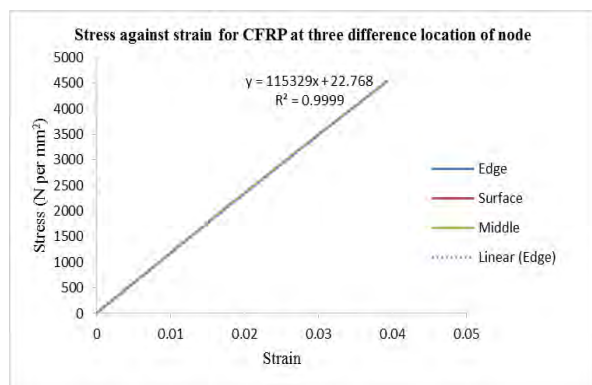
Figure 4 Stress against strain plot for CFRP model of RVE at 60 percent volume fraction.

REFERENCES

[1] N. Taniguchi, T. Nishiwaki and H. Kawada, Tensile strength of unidirectional CFRP laminate under high strain rate, *Adv. Compos. Mater.* Vol. 16, pp. 167–180, 2007.

[2] S. Wenbin, Experimental Investigation on Mechanical Behavior of Unidirectional CFRP Lamina

[3] W.J. Drugan, and J.R. Willis, „A micromechanics-based nonlocal constitutive equation and estimates of representative volume element size for elastic composites," *Journal of the Mechanics and Physics of Solids*, vol. 44, no. 4, 1996.

[4] S. Pimenta, S.T. Pinho, P. Robinson, "Micromechanics Of Recycled Composites For Material Optimisation And Eco-Design", in *18th International Conference On Composite Materials*.

[5] S.B.R. Devireddy and S. Biswas, "Effect of Fiber Geometry and Representative Volume Element on Elastic and Thermal Properties of Unidirectional Fiber-Reinforced Composites," *Journal of Composites*, vol. 2014, p1-12, 2014.

[6] ABAQUS Manual Documentation (2009), Dassault Systèmes, 2009.

Performance analysis of neural network models for sustainable manufacturing practices (SMP) and economy performances

N.H. Abu[1,*], A.S.M. Jaya[1], M.R. Muhamad[2]

[1] Faculty of Information Technology and Communication, Universiti Teknikal Malaysia Melaka,
Hang Tuah Jaya, 76100 Durian Tunggal, Melaka, Malaysia
[2] Faculty of Manufacturing Engineering, Universiti Teknikal Malaysia Melaka,
Hang Tuah Jaya, 76100 Durian Tunggal, Melaka, Malaysia

*Corresponding e-mail: norhashidahabu@gmail.com, m031420010@student.utem.edu.my

ABSTRACT – This study presents a development of neural network model based on the single hidden layer with 10, 12 and 15 neurons in the hidden layer. 150 data of sustainable manufacturing practices (SMP) were divided into 70% for training (104 data), 15% for validation (23 data) and 15% for testing (23 data). Two performance measures are used to validate the model which is mean square error (MSE) and R valued. It shows that neural network model with 10 neurons in hidden layer give better performance and can be used to predict the target output of sustainability performance.

1. INTRODUCTION

Sustainability is evolutionary concepts that expand to responses the issues of global inequality and arises as a consequence of adaptation to changing circumstances. The previous research focusing on manufacturing management faces a lot of difficulties in a way of gaining reliable data and analysis about manufacturing practices and the performances. Time and cost consuming become the highest problem and it follows by lack of knowledge about the manufacturing practices and performances by the manufacturing firms itself. Instead of applying all the manufacturing practices into the firms directly, it is wisely to provide the statistically evidences through mathematical modeling and analysis before the implementation.

Regarding the issues, ANNs have been recently developed as a powerful modeling tool in comparison to the statistical or numerical methods. ANNs have been used for many engineering applications such as prediction, optimization classification and pattern recognition. They have a highly interconnect structure similar to brain cells of human neural networks. There are eight inputs involves which are cleaner production (CP), eco-efficiency (EE), employee relation (ER), supplier relation (SR), customer relation (CuS), community relation (CoR), closed-loop production (CLP) and industrial ecology (IE). The target output is economic sustainability performance. The objective is to find relationship between SMP and economy performance using neural network approach.

2. METHODOLOGY

Neural network consisted of input, sum function, log-sigmoid activation function and output. Levenberg-Marquardt back propagation as training algorithm is reinforced by this neural network. The input values for neuron are obtained by multiplying the output that connected the neuron by strength of connection.

The structures consist of great number of processing elements call neuron and arranged in different layers of the network. Each network contains an input layer, an output layer and one or more hidden layers. The neurons in the networks are interconnect using weight factors, $c_{j,k}$. A neuron in given layer receives information (i_j) from all the neurons in the preceding layer. It sums up information (net_k) weighted by factors corresponding to the connection and the bias of the layer (θ_k) and transmit output values (y_k) computed through applying a mathematical function (f(.)) to net_k, to all the neurons of the next layer. This process is formulated in equation (1) and (2):

$$net_k = \sum_{i=1}^{n} C_{j,k} W_k + \theta_k \tag{1}$$

$$y_k = f(net_k) = \frac{1}{1 + e^{-net_k}} \tag{2}$$

The number of neurons in the ANN layer has an important effect to the network performances [1-2]. The number of neurons in input layer is same with the number of input (independent) variables. While number in neurons in output layer represent the number of output (dependent) variables. However, this situation happen based on cause and effect relationship because currently no explicit rule to detect the number of hidden neuron in the hidden layer(s). Both number of hidden layer and number of neurons in hidden layer are generally detected by process of trial and error.

The influence of the number of neurons in the hidden layer on the performance of the network is quite complicated. The trained network does not have sufficient ability to learn the relationship of inputs and outputs if the architecture of ANN model is too simple. While, if the architecture is too complex the training of the network will be over fitted or the model will not converge to the goal error.

In the abstract, the hidden layer was testing using three different numbers of neurons which are 10, 12,

and 15 neurons as previous study [2-5]. The chosen number of neuron must avoid overfitting and improve neural network generalization [2]. The aim of these steps is to improve the result of the neural network.

3. RESULTS AND DISCUSSION

There are two performance measures is used to validate the neural network model which are mean squared error (MSE) and R value. Mean squared error is the average squared difference between outputs and targets. The lower values the better and zero means no error. The regression R values measure the relationship between outputs and targets. The higher R values the better and value of 1 means that outputs and targets value is close in relationship. Table 1 until Table 3 show the MSE and R values for all the neural network models:

Table 1 Results of MSE and R value for neurons = 10.

Results	MSE	R value
Training	0.2482	0.6574
Validation	0.2228	0.4644
Testing	0.2249	0.5084

Table 2 Results of MSE and R value for neurons = 12.

Results	MSE	R value
Training	0.1377	0.7828
Validation	0.5351	0.0683
Testing	0.3456	0.5867

Table 3 Results of MSE and R value for neurons = 15.

Results	MSE	R value
Training	0.1249	0.8416
Validation	0.3662	0.3208
Testing	0.6089	0.2042

From the Table 1, Table 2 and Table 3, it shows the mean squared error (MSE) and R value for the neural network models. The lowest MSE for training data is the hidden layer with 15 neurons which is 0.1249. Then, the lowest MSE for validation data is the hidden layer with 10 neurons which is 0.2228. Lastly, for the testing data, the lowest MSE is also hidden layer with 10 neurons which is 0.2249 [2].

The R values shows that the highest for training data is hidden layer with 15 neurons which is 0.8416. For validation data is 10 neurons which is 0.4644 and for testing data, the hidden layer with 12 neuron is the highest which is 0.5867 [3].

From this two performance measure, it shows that training set data provide the best results with the lowest mean squared error (MSE) and highest R value [4]. While the best hidden layer is with 10 neurons because consist of average lower MSE and average higher R value [5].

4. CONCLUSION

In this research we have demonstrated the use of neural network analysis for the prediction of economy sustainability performance based on sustainable manufacturing practices (SMP). The analysis shows that the predicted model consists of all the manufacturing practices give a lot of information regarding the economy sustainability. It was concluded that neural network model can provide accurate prediction of economy sustainability performance from sustainable manufacturing practices (SMP).

Hence, the result can provide guidelines, statistical evidence and analysis for manufacturing engineers and firms. It is crucial before implementing sustainable manufacturing practices (SMP) into the manufacturing firms and management

REFERENCES

[1] T. Yang and Y. Shen, ―Computers & Industrial Engineering The dynamic transfer batch-size decision for thin film transistor – liquid crystal display array manufacturing by artificial neural-network,‖ *Comput. Ind. Eng.*, vol. 60, no. 4, pp. 769–776, 2011.

[2] A. K. Tsadiras, C. T. Papadopoulos, and M. E. J. O. Kelly, ―Computers & Industrial Engineering An artificial neural network based decision support system for solving the buffer allocation problem in reliable production lines,‖ *Comput. Ind. Eng.*, vol. 66, no. 4, pp. 1150–1162, 2013.

[3] D. Opritescu and W. Volk, ―Automated driving for individualized sheet metal part production—A neural network approach,‖ *Robot. Comput. Integr. Manuf.*, vol. 35, pp. 144–150, 2015.

[4] O. Duran, J. Maciel, and N. Rodriguez, ―Expert Systems with Applications Comparisons between two types of neural networks for manufacturing cost estimation of piping elements,‖ *Expert Syst. Appl.*, vol. 39, no. 9, pp. 7788–7795, 2012.

[5] C.C. Lee and C. Ou-Yang, ―A neural networks approach for forecasting the supplier's bid prices in supplier selection negotiation process,‖ *Expert Syst. Appl.*, vol. 36, no. 2 PART 2, pp. 2961–2970, 2009.

Multiobjective optimization of injection moulding process parameters using Grey Fuzzy method

Mohd Amran Md Ali[1,*], Noorfa Idayu Mohd Ali[1], Mariam Md Ghazaly[2], Zulkeflee Abdullah[1], Suhaila Yacob[1]

[1] Faculty of Manufacturing Engineering, Universiti Teknikal Malaysia Melaka,
Hang Tuah Jaya, 76100 Durian Tunggal, Melaka, Malaysia
[2] Faculty of Electrical Engineering, Universiti Teknikal Malaysia Melaka,
Hang Tuah Jaya, 76100 Durian Tunggal, Melaka, Malaysia

*Corresponding e-mail: mohdamran@utem.edu.my

ABSTRACT – Grey fuzzy method is used to find the multiobjective optimization of injection moulding process parameters. Various responses results are calculated by GRA for getting grey relational coefficients. Then values are used as input in MATLAB software by using FIS. It is found that optimum parameters for deflection, volumetric shrinkage, and residual stress are mould temperature at level 1, melt temperature at level 3, injection time at level 1 and cooling time at level 1.

1. INTRODUCTION

Injection moulding is a high-speed moulding of plastic parts. It works by injecting molten thermoplastic into a mould cavity. The advantage of this process is it can produce complex and intricate shapes of plastic products. It well known that factors that most influence injection moulding process parameters such as packing pressure and packing time on the post-moulding shrinkage and warping of parts made from polypropylene filled with calcium carbonate.

Annicchiarico and Alcock [1], critical processing parameters in injection moulding were temperatures, the packing parameters, cooling time, and injection speed, temperatures and packing parameters. In addition, at macro scale, they found that shrinkage was decreased by increasing the critical factors.

For multiple objective optimization, several researchers have implemented grey-fuzzy method in their research. In 2014, Yeh and Tsai [2] optimized copper wire bonding process with multiple quality characteristics using a grey-fuzzy Taguchi method. Pattnaik et al. [3] stated that as the optimal condition determined for each response was different, grey-fuzzy method was used to combine individual objective functions into a single objective function.

In this study, optimization of injection moulding parameters of multiobjective such as deflection, volumetric shrinkage and residual stress can be achieved by using a grey-fuzzy Taguchi method.

2. METHODOLOGY

In previous study, Md Ali et al. [4], optimized injection moulding parameters to get the lowest deflection, volumetric shrinkage at ejection and in cavity-residual stress of family mould part by using Taguchi method. It was found that each response has different optimum parameters. By using Grey-Fuzzy Taguchi method, process parameters optimization of multiobjective can be achieved.

3. RESULT AND DISCUSSION

3.1 Optimization using Grey Relational Analysis (GRA)

First of all, measured value of deflection, volumetric shrinkage at ejection and in-cavity residual stress ranging from „0‟ to „1‟ are normalized. This is called as Grey relational normalization. For all responses, 'smallest is the best‟ quality characteristics [4] have been implemented and expressed in Equation (1).

$$x_i(k) = \frac{max\ y_i(k) - y_i(k)}{max\ y_i(k) - min\ y_i(k)} \tag{1}$$

Where, $x_i(k)$ is the value after the grey relational generation, min $y_i(k)$ is the smallest value of $y_i(k)$ for the kth response, and max $yi(k)$ is the largest value of $y_i(k)$ for the *kth* response.

After that, from the normalized experimental data, the grey relational coefficient is calculated to represent the correlation between the desired and the actual experimental data. The grey relational coefficient $\boldsymbol{\xi_i}$ (k) is calculated as in Equation (2).

$$\xi_i(k) = \frac{\Delta min + \xi \Delta max}{\Delta 0_i(k) + \xi \Delta max} \tag{2}$$

Here, $\boldsymbol{\xi}$ is a distinguishing coefficient between 0 and 1 which is taken as 0.5, $\Delta 0i(k)$ the difference in absolute value between $y_0(k)$ and $y_i(k)$, $y_0(k)$ the ideal or reference sequence, Δmin the smallest value of $\Delta 0i$ and Δmax the largest value of $\Delta 0_i$. Table 1 shows the individual grey relational coefficient values of the responses.

3.2 Fuzzy Inference System (FIS)

According to Vasudevan et al. [5], FIS is used to couple grey relational coefficient into single performance index called as multi performance criteria index (MPCI). In this paper, Mamdani type fuzzy

system is implemented and the FIS consists of fuzzification, rules evaluation and defuzzification. The calculated MPCI together with their S/N ratio are as given in Table 2.

Table 1 Individual grey relational coefficient values of the responses.

Run	Deflection	Volumetric Shrinkage	Residual Stress
1	0.4034	1.0000	0.3333
2	0.4856	0.4798	0.5723
3	0.7011	0.3402	1.0000
4	0.3537	0.7981	0.3671
5	0.4494	0.4970	0.6253
6	1.0000	0.3333	0.7055
7	0.3333	0.7757	0.3913
8	0.5732	0.4770	0.4752
9	0.7807	0.3347	0.8710
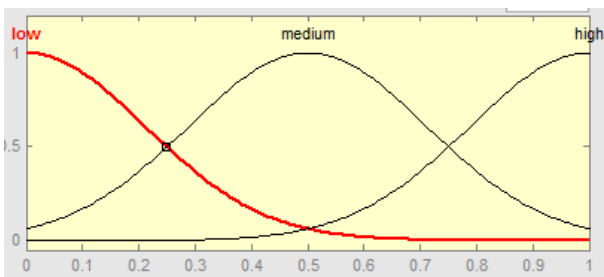
Figure 1 Membership functions of the inputs.
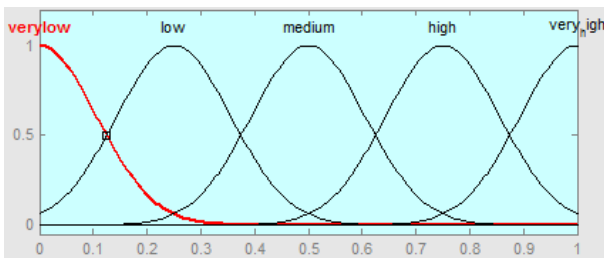
Figure 2 Membership functions of the output.

Table 2 Calculated MPCI and its S/N ratio.

Run	1	2	3	4	5	6	7	8	9
MPCI	0.61	0.52	0.66	0.56	0.53	0.66	0.54	0.51	0.61
S/N (-)	4.34	5.76	3.61	5.07	5.58	3.64	5.32	5.78	4.31

3.3 Taguchi optimization

According to Vasudevan et al. [5], the highest value of MPCI determined the optimal parameter setting. In addition, MPCI optimization was carried out using Taguchi method. By implementing higher-the-better characteristics of S/N ratio, optimal parameters combination can be determined. Table 2 shows the calculated value of MPCI and its S/N ratio.
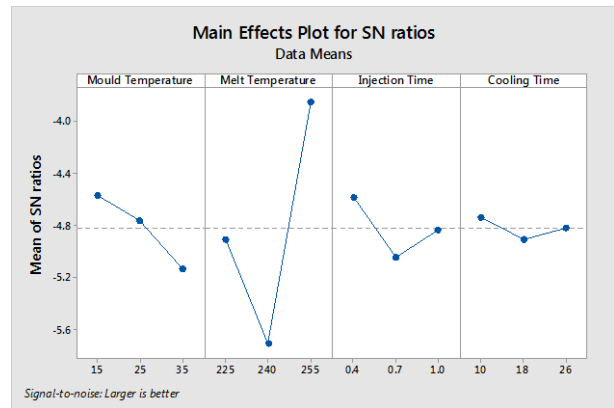
Figure 3 S/N ratio graph of MPCI.

Optimal parametric combination has been evaluated from the plot in Figure 3. The optimum parameter combinations have the highest S/N ratio value represent in the graph. It is found that the grey-fuzzy grade obtained at the optimal condition is 0.680 which is greater than all values obtained for L9 OA.

4. CONCLUSION

In this study, the process parameters optimization of multiobjective of family mould part is studied. The optimum parameter combinations are mould temperature of 15°C, melt temperature of 255°C, injection time of 0.4s and cooling time of 10s. It is found that the grey-fuzzy grade obtained at the optimal condition is 0.68 which is greater than all values obtained for L9 OA.

REFERENCES

[1] D. Annicchiarico and J.R. Alcock, "Review of factors that affect shrinkage of moulded part in injection moulding," *Mater. Manuf. Process.*, vol. 29, pp. 662-682, 2014.

[2] J. H. Yeh and T. N. Tsai, "Optimizing the fine-pitch copper wire bonding process with multiple quality characteristics using a grey-fuzzy Taguchi method," *Microelectron. Reliab.*, vol. 54, no. 1, pp. 287–296, 2014.

[3] S. Pattnaik, M.K. Sutar, and J. Rana, "Multi-objective optimization of the ems processed ic by grey-fuzzy method," *Mater. Today Proc.*, vol. 2, no. 4–5, pp. 2555–2561, 2015.

[4] M.A. Md Ali, N. Idayu, R. Jaafar, M. Hadzley, Y. Yaakob, A.R. Samsudin and M.R. Salleh, "Comparison between star and linear runner layout of family plastic injection mold," *ARPN Journal of Engineering and Applied Sciences,* vol. 10, pp. 6263-6268, 2015.

[5] H. Vasudevan, N.C. Deshpande, and R.R. Rajguru, "Grey fuzzy multiobjective optimization of process parameters for CNC turning of GFRP/epoxy composites," *Procedia Eng.*, vol. 97, pp. 85–94, 2014.

Force optimization of the permanent magnet switching flux (PMSF) and switching reluctance (SR) actuators using Finite Element Analysis

I. Yusri[1], M.M. Ghazaly[1,2,*], E.A. Alandoli[1], M.F. Rahmat[3], Z. Abdullah[4], M.A. Md Ali[4], R. Ranom[1,2]

[1] Faculty of Electrical Engineering, Universiti Teknikal Malaysia Melaka,
Hang Tuah Jaya,76100 Durian Tunggal, Melaka, Malaysia
[2] Center for Robotic and Industrial Automation, Universiti Teknikal Malaysia Melaka,
Hang Tuah Jaya,76100 Durian Tunggal, Melaka, Malaysia
[3] Faculty of Electrical Engineering, Universiti Teknologi Malaysia, 81310 UTM Johor Bahru, Johor, Malaysia
[4] Faculty of Manufacturing Engineering, Universiti Teknikal Malaysia Melaka,
Hang Tuah Jaya,76100 Durian Tunggal, Melaka, Malaysia

*Corresponding e-mail: mariam@utem.edu.my

Keywords: Electromagnetic; actuator; Finite Element method

ABSTRACT – This paper addresses the force optimization of a rotary motion type of electromagnetic actuator that compares two types of motor; i.e. the permanent magnet switching flux (PMSF) motor and the switching reluctance (SR) motor. The force optimization is accomplished by manipulating the actuator parameters using Finite Element Analysis (FEM). The best result was achieved by the permanent magnet switching flux (PMSF) actuator compared to the switching reluctance actuator (SR); i.e. 4.367 kN when the initial parameters are varied with the excitation current 2A.

1. INTRODUCTION

The switched reluctance motor is one of the electromagnetic actuators, which has established in 1838 and in the mid-1960, where it had a fresh start to raise its performance based on Aljaism et al. [1]. Moreover, the switched reluctance actuator is a newcomer to the electromagnetic actuators' family. The torque expression is the key to understand any actuator, which is derived from their principles. It has many advantages such as, cheaper in price, robust, can operate in high temperature, and has very high rotational speed. In addition, the switching reluctance does not consist of permanent magnet, and a high torque density of switching reluctance actuators has been developed extensively around the world for automotive propulsion as shown in previous study [2-6].

The switched reluctance motors have gone through remarkable efforts in research due to its advantages of having a simple structure, faulty tolerance and mechanical robustness, which are leading to be attractive for industrial applications. The advantages of the permanent magnet motors or doubly salient permanent magnet (DSPM) as compared to the reluctance motors are efficiency and power density. A permanent magnet switching flux (PMSF) motor has a doubly salient structure and a magnet imbedded in each pole of the stator. Therefore, it has the advantages of both motors' switched reluctance and permanent magnet. Therefore, in this paper, optimization is done by varying the actuator parameters for two types of electromagnetic actuator; i.e. the permanent magnet switching flux (PMSF) motor and the switching reluctance (SR) motor.

2. METHODOLOGY

There are two types of rotary electromagnetic actuators needed to be designed, which are the permanent magnet switching flux (PMSF), and the switching reluctance (SR). Maxwell 3D software is used to design and analyze the electromagnetic actuator. This is a high performance interactive software package, which uses finite element analysis to solve the magnetic, electric, eddy current, and transient problems.

The two types of the actuator designed with the initial parameters are shown and labelled in Table 1. The parameter to be varied for the two electromagnetic actuators are; a) winding turns & b) size. The difference is only in the presence of permanent magnet at the PMSF actuator. The force optimizations are done by varying the parameters; i.e.: a) winding turns & b) size. Figures 1 and 2 show the initial actuator's parameter for both PMSF & SR.

Table 1 Label and dimensions of the PMSF actuator.

Labelling		Dimensions	
Phase A		Stator outer diameter	60 mm
Phase B		Stator inner diameter	36 mm
Phase C		Air gap thickness (G)	0.1 mm
Stator		Winding number	100 Turns
Rotor		Stator and rotor height	36 mm
Magnet		S : R	6 : 5
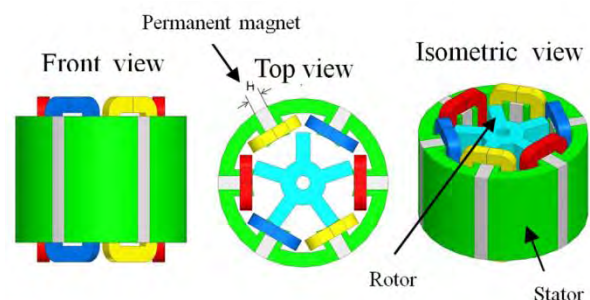
Figure 1 The PMSF actuator.
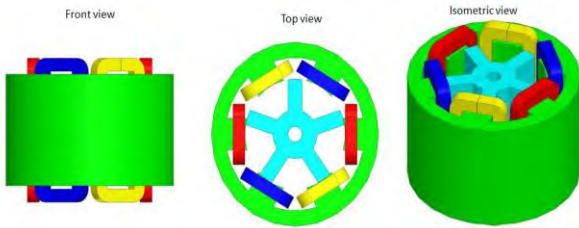
Figure 2 The SR actuator.

3. RESULT AND DISCUSSION

Varying the parameters of the permanent magnet switching flux and switching reluctance actuators resulted in different force performances. Varying the number of winding turns in switching reluctance actuator generated the largest force by the maximum number of winding turns (168.8507 μN) once the input current is 2A. Figure 3 shows the result based on FEM analysis for varying the winding turns on SR actuator. The magnetostatic force increases by increasing the number of winding turns, while in the PMSF actuator, increasing the number of winding more than 140 turns causes decreasing in the magnetostatic force.

The size of the PMSF and SR actuator has been analyzed with six different sizes. The greatest magnetostatic force (4.366316 kN) for PMSF produced by the largest size which is 100% scaled from the original size. Increasing the size of the actuator by 20%, causes a similar increased in the output force for each interval. Figure 4 shows the FEM result analysis with varying the size of PMSF actuator. The SR actuator also has been analyzed with the same method but the greatest magnetostatic force produced by the size of 20% scaled from the original size.
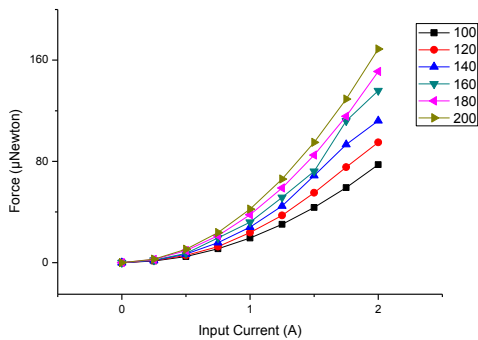
Figure 3 FEM result with varying winding turns for SR.
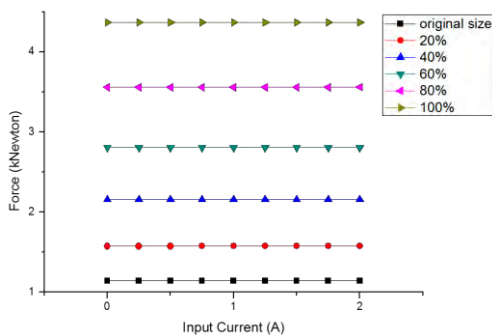
Figure 4 FEM result with varying the size for PMSF.

4. CONCLUSIONS

Two types of electromagnetic actuators, which are the permanent magnet switching flux (PMSF) flux and switching reluctance (SR) actuator have been designed and analyzed by Finite Element Analysis (FEM). As a conclusion, the FEM analysis results clarifies that the permanent magnet switching flux (PMSF) actuator shows a better performance. It shows a greater thrust force compared to the switching flux actuator (SR); i.e. 4.367 kN when the initial parameters are varied as shown in Table 2, with the excitation current 2A.

Table 2 Summary of the best parameter chosen for 2A excitation current.

No.	Varying Parameter	Designs	
		PMSF	SR
1	Actuator's size	100% larger	Original size
2	Number of winding turns	100	200
3	S:R poles ratio	6:5	6:5
4	Air gap thickness (mm)	0.1	0.1
	Maximum Force (N)	4.367kN	168.85μN

REFERENCES

[1] W. Aljaism, M. Nagrial and J. Rizk, "Investigation of torque development in SRM under single phase excitation", in *IEEE GCC Conference (GCC)*, pp.1, 2006.

[2] J.M. Miller, A.R. Gale, P.J. McCleer, F. Leonardi, and J. H. Lang, "Starter-alternator for hybrid electric vehicle: Comparison of induction and variable reluctance machines and drives", in *IEEE Ind. Appl. Soc. Annu. Meet*, vol. 1, pp.513–523, 1998.

[3] A. Chiba, K. Kiyota, N. Hoshi, M. Takemoto and S. Ogasawara, "Development of a Rare-Earth-Free SR Motor with High Torque Density for Hybrid Vehicles", *IEEE Transactions on Energy Conversion*, vol. 30 no.1, pp. 175-182, 2015.

[4] S. Wang, Q. Zhan, Z. Ma and L. Zhou, "Implementation of a 50-kW four-phase switched reluctance motor drive system for hybrid electric vehicle", *IEEE Transactions on Magnetics*, vol. 41, no. 1, pp. 501-504, 2005.

[5] N. Schofield, S.A. Long, D. Howe and M. McClelland, "Design of a Switched Reluctance Machine for Extended Speed Operation", *IEEE Transactions on Industry Applications*, vol. 45, no. 1, pp. 116-122, 2009.

[6] M.D. Hennen, M. Niessen, C. Heyers, H.J. Brauer, and R.W. De Doncker, "Development and Control of an Integrated and Distributed Inverter for a Fault Tolerant Five-Phase Switched Reluctance Traction Drive", *IEEE Transactions on Power Electronics*, vol. 27, no. 2, pp. 547-554, 2010.

Force optimizations of a tubular linear reluctance actuator (TLRA) and tubular linear permanent magnet actuator with Halbach array (TLPM)

A.H. Jamaludin[1], M.M. Ghazaly[1,*], T.A. Yahya[1], A.C. Amran[2], Z. Abdullah[3], M.A.M. Ali[3], N.M. Ali[1]

[1] Centre for Robotic and Industrial Automation, Faculty of Electrical Engineering,
Universiti Teknikal Malaysia Melaka, Hang Tuah Jaya, 76100 Durian Tunggal, Melaka, Malaysia
[2] Faculty of Engineering Technology, Universiti Teknikal Malaysia Melaka,
Hang Tuah Jaya, 76100 Durian Tunggal, Melaka, Malaysia
[3] Faculty of Manufacturing Engineering, Universiti Teknikal Malaysia Melaka,
Hang Tuah Jaya, 76100 Durian Tunggal, Melaka, Malaysia

*Corresponding e-mail: mariam@utem.edu.my

Keywords: Linear electromagnetic actuator; Halbach; reluctance

ABSTRACT – This paper presents a characterizing study of two novel electromagnetic actuators i.e. Tubular Linear Reluctance Actuator (TLRA) and Tubular Linear Permanent Magnet Actuator with Halbach array (TLPM). The study concentrated on the varying parameter i.e. the number of winding turns and the air gaps. The simulation of 3D FEM analysis is used to show the differences between two designs in force and the effects of parameters variations.

1. INTRODUCTION

Electromagnetic actuators are used in a vast variety of applications that require high thrust, high accuracy and variant working ranges. The tubular type has rugged mechanical structure, almost same like a piston structure. The tubular type minimised the elimination of stray magnetic field. For the same sizes and weights, the force density delivered by tubular actuator is greater than planar actuator as previous study [1]. Electromagnetic linear actuator consists of two main components, which are the stator (stationary part) and the mover (moving part). TLRA structure consists of coil at stator and non-magnetic mover while TLPM consists of coil at stator and permanent magnet mover. TLPM provides the highest efficiency and trust force. This has led to the increment of the use of tubular permanent-magnet actuators in manufacturing, medical tools, transportation, advance electronic devices, and robotics as stated in previous study. TLRA has advantages in terms of very simple structure, ruggedness, and inexpensive [2-4].

2. METHODOLOGY

Two types of linear electromagnetic i.e. TLRA and TLPM are designed with same initial parameters. The varying parameter i.e. air gap (between stator winding coil and mover) and number of turns has been analyzed with same input current (0A to 20A with interval of 2A). The initial parameters of TLRA and TLPM are shown in Table 1 and Table 2.

Table 1 Initial parameter of TLRA.

Parameter	Values		
	First Winding	Second Winding	Third Winding
Number of turns	17turns	33turns	66turns
Coil inner diameter		21mm	
Coil outer diameter	25mm	30mm	40mm
Mover outer diameter		20mm	
Length of the mover		90mm	
Air gaps		0.5mm	

Table 2 Initial parameter of TLPM.

Parameter	Values
Number of turns	66turns
Coil inner diameter	21mm
Coil outer diameter	40mm
Shaft outer diameter	12mm
Magnets outer diameter	20mm
Length of the mover	90mm
Air gaps	0.5mm

The designs of TLRA and TLPM are shown in Figure 1 and Figure 2. The differences between the two structures in this study are; i.e. TLPM consists of permanent magnet on the mover shaft and TLRA consists of 3 steps of coil windings.
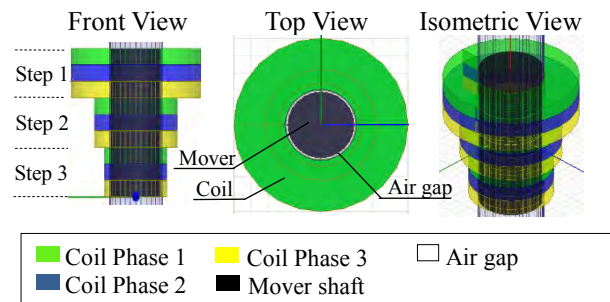
Figure 1 TLRA structure design.

Front View   Top View   Isometric View
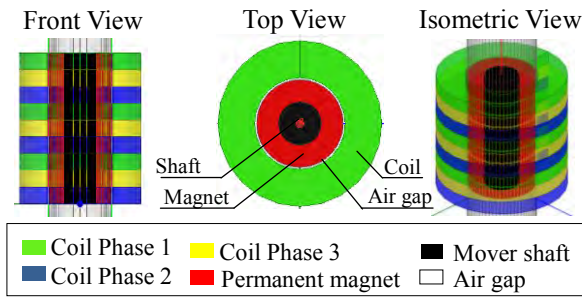
Figure 2 TLPM structure design.

3. RESULTS AND DISCUSSION

3.1 Varying winding turn

As TLRA consists of set of step winding coils, the winding numbers of turn details for step 1 and step 2 are shown in Table 3. Winding turns for step 3 TLRA and winding set for TLPM are varied from 100 to 500 turns with the interval of 100 turns. The highest force generated by varying winding turn for TLRA is 760 N with 500 turns and for TLPM is 134N also with 500 turns as shown in Figure 3 and Figure 4.

Table 3 Sets of TLRA number of turns.

Steps	Number of turns				
	Set 1	Set 2	Set 3	Set 4	Set 5
Step 1	25	50	75	100	125
Step 2	50	100	150	200	250
Step 3	100	200	300	400	500
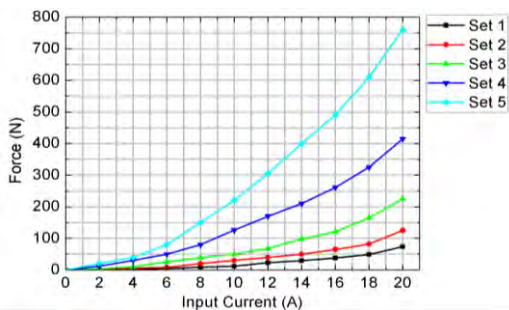
Figure 3 Forces vs number of turn variant for TLRA.
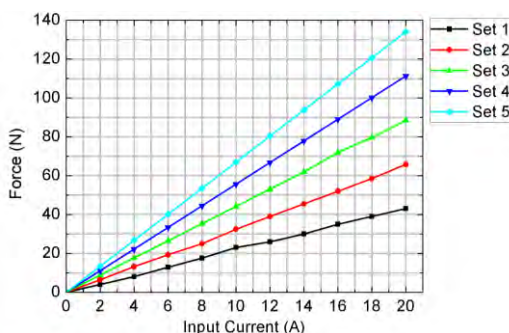
Figure 4 Forces vs number of turns variant for TLPM.

3.2 Varying air gap

The air gap dimensions are varied from 0.5mm to 1.5mm with interval of 0.2mm. The highest force generated by varying number of turns of TLRA is 55N with 0.5mm air gap, while TLPM is 85N with 1.5mm

air gap as shown in Figure 5 and Figure 6.
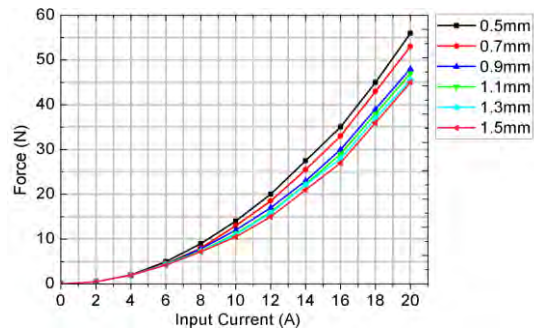
Figure 5 Forces vs air gap variant for TLRA.
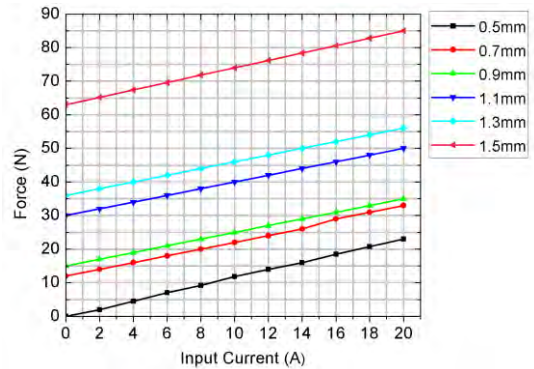
Figure 6 Forces vs air gaps variant for TLPM.

4. CONCLUSIONS

The FEM analysis proved that TLPM produced more force than TLRA due to the magnet and the Halbach array arrangement; however the cost of magnet is expensive. If larger number of step winding turns is used (500turns), TLRA can generate more forces (760N) compare to TLPM which is the optimum parameter for this study. The disadvantage of TLRA is high current consumption is required to generate high force.

REFERENCES

[1] W.J. Kim, D.L. Tumper and J,H, Lang, "Modelling and Vector Control of Planar Magnetic Levitator," *IEEE Trans. On Industry applications*, vol. 34, no.6, pp. 1254-1262, 1998.

[2] B. Lesquesne, "Permanent Magnet Linear Motors for Short Strokes," *IEEE Trans. On Industry applications*, vol. 32, no.1, pp. 161-168, 1996.

[3] N.Bianchi, S.Bolognani and F. Tonel, "Design Consideration for a Tubular Linear PM servo Motor," *EPE J.*, vol. 11, no.3, pp. 41-47, 2001.

[4] Z.Q. Zhu, P.J. Hor, D. Howe and J.R. Jones, "Novel linear Tubular Brushless Permanent Magnet Motor," *Int. Conf. Electr. Machines Drives*, Cambridge, MA, vol 144, pp 91-95, 1997.

Development of a RFID inter-office document's delivery system via mobile robot

M.M. Ghazaly[1,*], K.Y. Soo[1], Z. Abdullah[2], M.R. Yaacob[1], C.C. Ho[1], C.Y. Ng[1]

[1] Centre for Robotic and Industrial Automation, Faculty of Electrical Engineering,
Universiti Teknikal Malaysia Melaka, Hang Tuah Jaya, 76100 Durian Tunggal, Melaka, Malaysia
[2] Faculty of Manufacturing Engineering, Universiti Teknikal Malaysia Melaka,
Hang Tuah Jaya, 76100 Durian Tunggal, Melaka, Malaysia

*Corresponding e-mail: mariam@utem.edu.my

ABSTRACT – This paper presents an efficient method of a mobile robot navigation system in an indoor environment. The mobile robot able to reduce heavy lifting and the repetitive tasks by workers. However, the navigation of robot in an indoor environment is a challenging task due to the requirement to avoid obstacle when in motion. Therefore in this paper, the design and develop of a mobile robot for an inter-office environment using Radio Frequency Identification (RFID) tag is discussed. The motions of the mobile robot are validated using several the trajectory patterns. In addition, the mobile robot is able to avoid obstacles.

1. INTRODUCTION

Navigation of mobile robot has been widely discussed in the past few years and this issue can be considered as a huge challenge to be accomplished in the field of robotics. For localisation in outdoor environment, Global positioning System (GPS) has been widely used in tracking people and asset as well as a navigation system for transportation since it provides accurate coordinates and information about a certain place. However, GPS does not perform well in indoor localization because the satellite cannot penetrate through the building [1]. Based on the research, Radio Frequency Identification (RFID) is a most suitable system used for localization and navigation of mobile robot due to its ease of use, inexpensive cost and flexibility [2,3]. As a conclusion, two-wheeled chassis is design which is equipped with RFID system for evaluating the performances of the mobile robot.

2. EXPERIMENTAL SETUP & SYSTEM OVERVIEW

The overview of mobile robot is shown in Figure 1. The platform of the mobile robot is designed with two DC motor installed at the front of the platform and a castor installed at the back of the mobile robot to balance the robot structure. The mobile robot is equipped with RFID reader, ultrasonic sensor and line following sensor on the upperpart of the robot to follow the black line path while receiving commands from passive tag and to navigate the mobile robot to reach the destination. Acrylic board is used as the basic structure of the mobile robot to hold the circuit board, sensors,

and motors. In Figure 1, the document delivery tray is not shown.
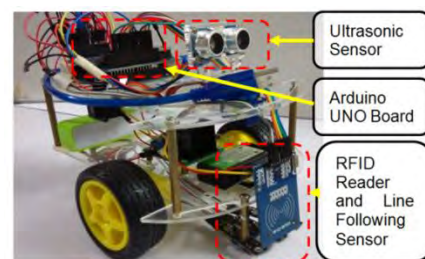
Figure 1 Overview of mobile robot prototype.

2.1 RFID system

The RFID system consists of three main components which are RFID reader (interrogators), RFID tags (transponders), and host computer with appropriate application software. The process flow of RFID system is shown in Figure 2.
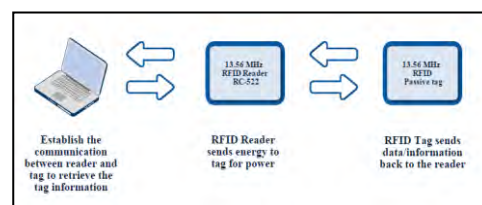
Figure 2 RFID system.

2.2 Navigation of mobile robot based on trajectory

In this setup, the mobile robot is equipped with the RFID reader and line following sensor on the upperpart of the robot which tracks the 18mm width black line path, while receiving commands from the passive tag to navigate the mobile robot to reach the destination. There are four types of trajectory patterns used for testing the performance of mobile robot; i.e. a) square-shaped, b) s-shaped, c) triangle-shaped and d) zigzag-shaped. Total of 25 passive RFID tags were install on the workspace in a grid-like pattern over an area measuring 120 cm × 120 cm, with a spacing of 20 cm. The experiments setup as shown in Figures 3.
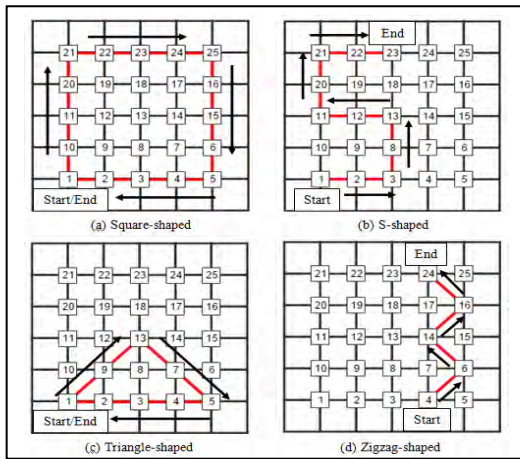
Figure 3 Trajectory pattern for mobile robot navigation.

2.3 Obstacle avoidance of mobile robot

In this setup, a stationary obstacle is placed in a particular location for the mobile robot to detect and avoid obstacle in order to reach the destination without collision. The experiment setup for obstacle avoidance is shown in Figure 4.
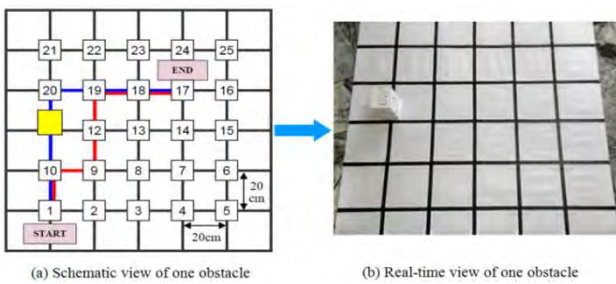
Figure 4 The workspace of mobile robot for one obstacle avoidance.

3. RESULTS & DISCUSSION

3.1 Analysis trajectory patterns

Figure 5 shows the bar chart illustrating the distance and average time taken to complete the path for different types of trajectory patterns; i.e. a) square-shaped, b) s-shaped, c) triangle-shaped and d) zigzag-shaped. This implies that that the farther the distance, the longer the average time takes for the mobile robot to complete the path and vice versa. Based on the findings, it can conclude that the mobile robot performed stably and consistently even in different types of trajectory patterns.

3.2 Obstacle avoidance

The results of obstacle avoidance are shown in Figure 6. The graphs show fluctuations in between period 2.2 seconds to 3.5 seconds due to the number of turning of mobile robot, thus the motor oscillation increases. The time take to reach the end point is 6.6 seconds. In conclusion, the mobile robot is able to navigate itself from the start to reach the target destination without collision with the obstacle.
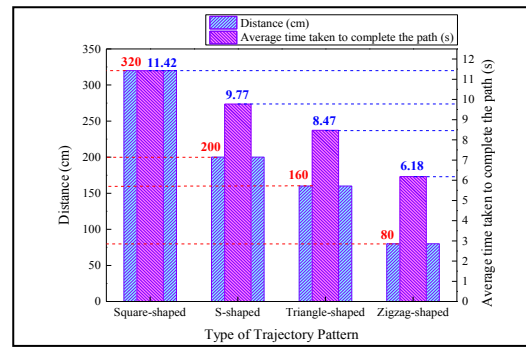
Figure 5 The distance and average time taken for different type trajectory pattern.
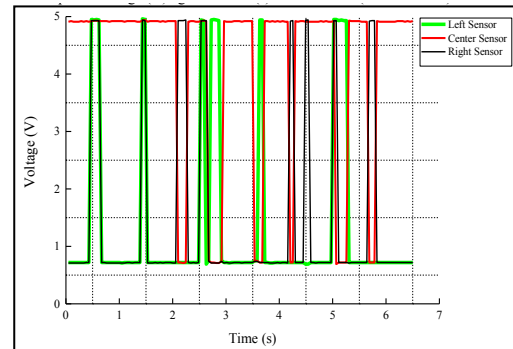
Figure 6 Test for one obstacle avoidance.

4. CONCLUSIONS

In this paper, an effective method to navigate the mobile robot in an inter-office environment using RFID tag was discussed. In addition, the results show that the mobile robot able to reach the target destination successfully without the collision with obstacles based on several trajectory patterns and avoiding obstacle. For future recommendations, the oscillation of the mobile robot can be eliminated by designing a Proportional-integral-derivative (PID) controller, which able to stabilize the motor performances of the mobile robot.

REFERENCES

[1] Y. Gu, A. Lo, and I. Niemegeers, "A survey of indoor positioning systems for wireless personal networks," IEEE Communications Surveys and Tutorials, vol. 11, no. 1, pp. 13–32, 2009.

[2] D. Stojanović, and N. Stojanović, Indoor Localization and Tracking: Methods, Technologies and Research Challenges. Facta Universitatis, Series: Automatic Control And Robotics, North America, 13, May. 2014.

[3] W. Gueaieb, and M.S. Miah, "An Intelligent Mobile Robot Navigation Technique Using RFID Technology," Instrumentation and Measurement, IEEE Transactions on, vol. 57, no. 9, pp.1908-1917, 2008.

Optimization using L9 Taguchi method toward threshold voltage of 18nm gate length SOI p-channel MOSFET

M.N.I.A. Aziz[1,2], F. Salehuddin[1,2,*], A.S.M. Zain[1,2], K.E. Kaharuddin[1,2], A.R. Hanim[1,2], H. Hazura[1,2], S.K. Idris[1,2]

[1] Faculty of Electronics and Computer Engineering, Universiti Teknikal Malaysia Melaka,
Hang Tuah Jaya, 76100 Durian Tunggal, Melaka, Malaysia
[2] Centre for Telecommunication Research and Innovation, Universiti Teknikal Malaysia Melaka,
Hang Tuah Jaya, 76100 Durian Tunggal, Melaka, Malaysia

*Corresponding e-mail: fauziyah@utem.edu.my

Keywords: MOSFET, SOI, Taguchi

ABSTRACT – Silicon on insulator (SOI) technology is proven to effectively counter the short channel effect. In this paper, the characterization of 18nm Gate Length of SOI p-channel MOSFET has been studied according to the latest prediction of the International Technology Roadmap Semiconductor (ITRS). The optimization approach is mainly focused on the threshold voltage (V_{TH}) of device through L_9 Taguchi method. There are four process parameters were varied into three different levels in order to conduct nine set of experiments. At the end of the experiments, the best setting of the process parameters that have been predicted by Taguchi method were used for verification. The result shows V_{TH} after optimization approaches is closer to the nominal value (-0.533V), which is well within the ITRS 2013 specifications.

1. INTRODUCTION

As the Metal Oxide Semiconductor Field Effect Transistor (MOSFET) becomes more minuscule, the number of atoms in the silicon that engender many of the transistor's properties is becoming fewer, with the result that control of dopant numbers and placement is more erratic [1]. The introduction of a method that called Buried oxide thickness deposition has brought the significant impact to the technology of MOSFET. With this improved method which is known as Silicon-on-insulator (SOI) MOSFET, the electrical characteristic of MOSFET can be further improved. This happens due to the advantage of SOI technology that can mitigate the short channel effect (SCE) problem [2].

The SCE is a crucial problem to a MOSFET when the dimension of the device is scaled down. It is assumed that the SOI device have the advantages of speed about 20 to 30 percent more expeditious and consume one-third to one-half the puissance of bulk MOSFET [2]. SCE has become the major threat in conventional MOSFET device structure. SCE occurs when the source and drain region become too proximate to each other. If the effective channel length (L_{eff}) is too short, the depletion region from drain will reach the source region and subsequently reduces the barrier for electron injection. As a result, the electrical characteristic of the device will be degraded.

In this paper, the virtual fabrication of the transistor device is done by utilizing ATHENA module, meanwhile the simulation for electrical examination is done by utilizing ATLAS module from SILVACO software [3]. For identify semiconductor process parameters whose variability would impact most on the device characteristics is realized using Taguchi Method. Taguchi method has become a potent implement for ameliorating productivity during research and development. Through the implementation of Taguchi method, the final product or process can enhance the quality at minimum time and cost [4,5].

2. METHODOLOGY

In this research, there are 3 stages such as designing stage, extraction of electrical characteristic stage and optimization of process parameter stage. For the designing stage Athena module from Silvaco TCAD tools been used while for the extraction stage Atlas module been use to tabulate the result [3]. The L_9 orthogonal array of Taguchi method been used for optimization process. Based on the Table 1, the process parameter and their level has been determined. Four process parameter among other parameters have been chosen.

Table 1 Process parameter and their level

Sym	Process parameter	Unit	Level 1	Level 2	Level 3
A	Halo implant Dose	Atom cm^{-3}	1.72e13	1.73e13	1.74e13
B	Halo Implant Energy	keV	157	158	159
C	S/D Implant Dose	Atom cm^{-3}	2.97e13	2.98e13	2.99e13
D	S/D implant Energy	keV	57	58	59

The four process parameters are halo implant energy, halo implant dose, Source/Drain (S/D) implant dose and S/D implant energy. Among all the process parameters, these four process parameters are parameters which give more impact on electrical characteristic [5]. Table 2 shows the noise factor that will be used in this optimization process parameter using L_9 Orthogonal Array Taguchi method.

Table 2 Noise factor and their level

Symbol	Noise Factor	unit	Level 1	Level 2
M	Sacrificial Oxide Temperature	°C	600	601
N	Annealing Process Temperature	°C	910	912

3. RESULT AND DISCUSSION

Figure 1 shows the S/N ratio (Nominal the best) graph where the dashed line is the value of the total mean of the S/N ratio. In this research, V_{TH} of the device belongs to the nominal-the-best quality characteristics. This S/N Ratio is selected to get closer or equal to a given target value, which is also known as nominal value The total mean for this V_{TH} is 51.25dB. V_{TH} is the main response to determine either the device work or not but the other characteristic also need to be keep as best as possible. Basically the larger the S/N ratio, the quality characteristic of V_{TH} is better [5,6].
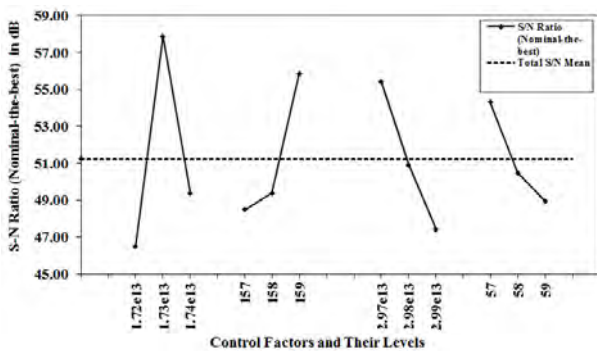
Figure 1 S/N graph of V_{TH} for SOI p-channel device
.

The results of analysis of variance (ANOVA) for the 18nm gate length SOI p-channel MOSFET device are shown in Table 3. According to these analyses, the major factor effecting the V_{TH} is halo implant dose (Factor A) with 47% whereas the second ranking factor was halo implant energy (Factor B) that is 22%. Percent factor effect on S/N Ratio indicates the relative power of a factor to reduce variation. For a factor with a high percent contribution, a small variance will have a great influence on the performance [6]. Based on the result of ANOVA, it clearly can be defined that, S/D implant energy (Factor D) as an adjustment factor because it has small effect on the variance (10%) and large effect on the mean (84%).

Table 3 Result of ANOVA for SOI p-channel MOSFET device

Symbol	Degree Freedom	Sum of Square	Mean Square	F-value	Factor Effects on SNR (%)	Factor Effects on Mean (%)
A	2	211	105	23	47[a]	2
B	2	98	49	11	22[a]	14
C	2	97	48	11	21	0
D	2	46	23	5	10	84

[a]At least 95% confidence.

The analysis of average performance showed that optimized levels of the process parameters that has been suggested by Taguchi method is $A_2B_3C_1$. Because Factor D was found as adjustment factor in V_{TH}, it could be set at any level [6]. The full recommendation for optimization is $A_2B_3C_1D_2$. The mean for V_{TH} after optimization approaches is -0.50V. This value is still in range ±12.7% from the nominal (target) value, -0.533V [7]. The value is also closer with ITRS prediction. This shows that Taguchi Method can predict the optimum solution in finding the 18nm gate length SOI p-channel MOSFET device with appropriate threshold voltage value.

4. CONCLUSION

As conclusion, this paper focuses on optimizing the process parameter of threshold voltage. Based on the ANOVA method, halo implant dose was identified as the most impact on the V_{TH} of the 18nm gate length SOI p-channel MOSFET device. Meanwhile, S/D implant energy was identified as an adjustment factor in the device. This adjustment factor has been used to get the value of V_{TH} closer to the target (–0.533V). The percent different of V_{TH} value from the target after the optimization approach are just ±6.19%. This value is within the range and closer with ITRS prediction. It can be shown that the optimum solution in achieving the desired transistor was successfully predicted by using Taguchi Method.

ACKNOWLEDGEMENT

REFERENCES

[1] F. Salehuddin, A.S.M. Zain, N.M. Idris, A.K. Mat Yamin, A.M. Abdul Hamid, I. Ahmad and P.S. Menon," Analysis of threshold voltage variance in 45nm n-channel device using L_{27} Orthogonal Array Method," *Advanced Materials Research*, vol. 903, pp. 297-302, 2014.

[2] B. Mehandia, "Study of Electrical Characteristics of SOI MOSFET Using Silvaco TCAD Simulator," vol. 1, pp. 15–18, 2012

[3] A. Kumar, N. Kar, A. Jaiswal, and A. Kar, "Characterization of SOI PMOSFET using Silvaco TCAD Tools," *IJAIEM org*, vol. 2, no. 6, pp. 540–546, 2013.

[4] K.E. Kaharudin, A.H. Hamidon and F. Salehuddin, "Implementation of Taguchi Modeling for Higher Drive Current (I_{ON}) in Vertical DG-MOSFET Device," *Journal of Telecommunication, Electronic and Computer Engineering,* vol. 6, no. 2, pp. 11-17, 2014.

[5] A.H. Afifah Maheran, P.S. Menon, I. Ahmad, S. Shaari, H.A. Elgomati, B.Y. Majlis and F. Salehuddin, "Design and optimization of 22nm NMOS transistor," *Australian Journal of Basic and Applied Sciences*, vol. 6, no. 7, pp. 1-8, 2012.

[6] M.S. Phadke, Quality Engineering Using Robust Design. Pearson Education, Inc. and Dorling Kindersley Publishing, Inc., 1998.

[7] ITRS 2013 report, http://www.itrs.net

Structural design and analysis of autonomous guided vehicle (AGV) for parts supply

Mohd Suffian Ab Razak[1,*], Khairul Hazwan Mohd Rasit[1], Nur Rashid Mat Nuri[1], M.Z.A Rashid[2]

[1] Faculty of Engineering Technology, Universiti Teknikal Malaysia Melaka,
Hang Tuah Jaya, 76100 Durian Tunggal, Melaka, Malaysia
[2] Faculty of Electrical Engineering, Universiti Teknikal Malaysia Melaka,
Hang Tuah Jaya, 76100 Durian Tunggal, Melaka, Malaysia

*Corresponding e-mail: suffian@utem.edu.my

ABSTRACT – The world economic growth rapidly and becomes very competitive. AGV is introduced to support the supply system, however the initial investment is very high and it cannot convince a certain company to invest such amount of money for the system. In this project, the focus research is more on a low cost, lightweight AGV development. Lightweight design leads to less energy consume to carry its body. The purpose of this study is design an AGV that to be used in parts supply using polyboxes. The structural strength analyses are performed through computer aided engineering (CAE) simulation.

1. INTRODUCTION

The main concept of an autonomous guided vehicle (AGV) grasps all transport systems which are capable of functioning without driver assistance. When its first introduced to industry, the AGV was in competition with driver operated material handling system such as pallet carts, fork lifts and tow tractors. However, since microcontroller technology has evolved, the capabilities and types of AGV system improved from time to time [1]. Nowadays AGV is now in direct competition with other forms of industrial transportation such as roller conveyors, belt conveyors and chain conveyors.
The objective of this project is to design and optimize economic lightweight AGV through structural strength analysis by CAE simulation

2. RESEARCH METHODOLOGY

2.1 Material properties of AGV structure

Steel ASTM 500 is being used in this project due to low cost and light. The material properties will influence the accuracy of virtual result when compared to physical prototyping [2].

Table 1 Material properties of AGV frame (ASTM 500).

Properties	Data
Modulus of Elasticity, E	14.0 E+03 MPa
Poisson Ratio, Nu	0.3
Tensile Strength	7.861E-09 t/mm^3
Yield Strength	315 MPa

2.2 Create design space

Figure 1 shows the design space of the AGV is basically a space where the material layout is allowed. This space is where the topology optimization process takes place.
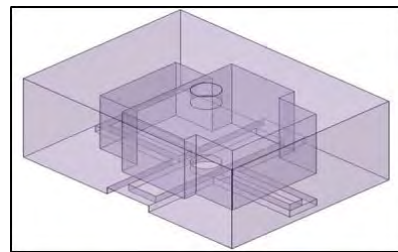
Figure 1 The AGV design space.

2.3 Topology optimization

The SolidThinking Inspire is an easy to use CAE software which runs the selected design space based on boundary conditions and generates optimized design (Figure 2).
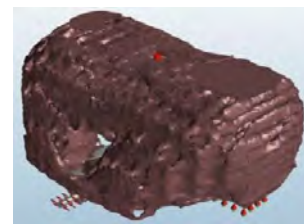
Figure 2 The optimized design space.

2.4 New structurally efficient conceptual design.

The model is then imported to Computer Aided Design (CAD) hybrid modelling software, SpaceClaim, in order to interpret the design based on the load path and design new conceptual model using the previous optimization result which is saved in STL file (Figure 3).

2.5 Result interpretation

The design is then runs through several design iterations in order to further reduce structure mass while retaining the Von Mises Stress below target 8.0 MPa. It is also important to ensure the design is feasible to manufacture. After the structural frame is optimized by the SolidThinking software, a new model, as in Figure 4, is

designed based on the previous optimization load path result.
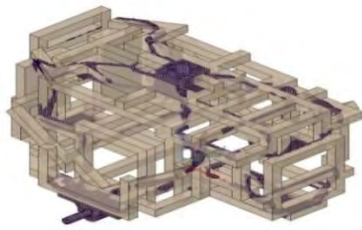
Figure 3 AGV design with load path iteration.
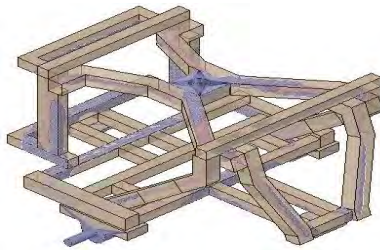
Figure 4 Final design iteration.

3. RESULTS AND DISCUSSION

Based on the results, the mass of the AGV structure, as in Figure 5, shows weight reduction after seven design iteration.
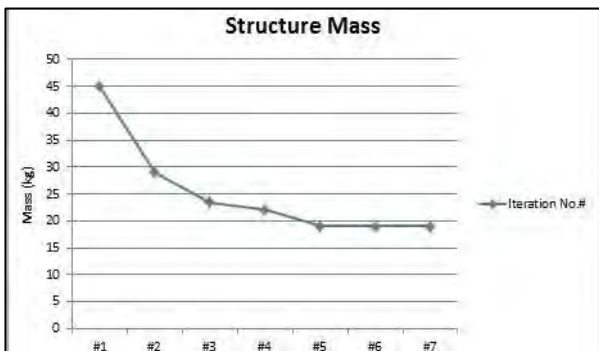
Figure 5 The AGV structure mass distributions.

The initial weight of 45 kg AGV structure mass is a massive value to move the AGV from stationary position. Therefore, the reduction of the mass after optimization phase helps the AGV to be more effective and the efficiency increase. The final mass obtained is 19 kg, which is total 58% total mass reduction from the original design. This result is based on solid structure, since the SolidThinking Inspire is only allows solid meshing instead of shell meshing. The actual product which is using hollow square would weigh only 20% ~ 25% of the mass based on cross section area calculation.

During the structural strength analysis of AGV structure, the maximum Von Mises Stress were obtained from each optimization results to determine the maximum stress level as shown in Figure 6.

From Figure 7, the Von Mises Stress distribution is not uniform through each stage of design iteration. The optimum value of the Von Mises Stress is at 4.50 MPa, which is at design iteration #6, not exceeding the limitation value of 8MPa. As the result is far below the

yield strength of 315 MPa, the design is safe to carry loads of 200kg based on its total tractive effort calculation and feasible to manufacture.
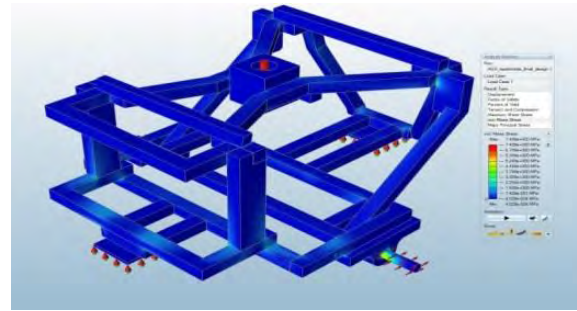
Figure 6 Von Mises stress analysis of AGV structure.
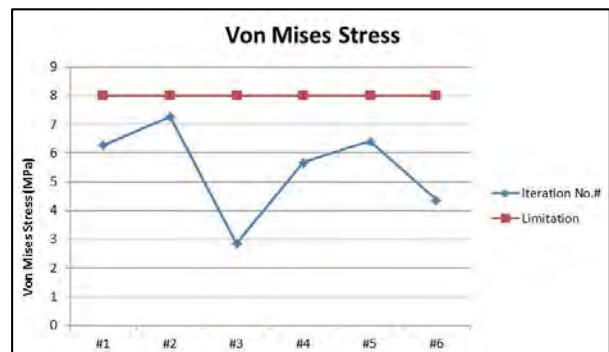
Figure 7 Von Mises Stress distribution.

4. CONCLUSION

The new concept structure was intended to replace the present bulky and heavy AGV structure with the same amount of ability to carry loads. By utilizing analyses and advanced techniques relative to material, and design, a unique, non-traditional structure which is 58% lighter frame from the original design space is successfully designed. The frame is 100% ASTM 500 steel and the overall complex structure was reduced to simpler design and meets the design requirement. In spite of current limitation of SolidThinking Inspire is for solid meshing only, the topology optimization result generated is suitable for CAE driven conceptual design.

REFERENCES

[1] J.L. Jones, A.M. Flynn and B.A. Seiger, *Mobile Robots: Inspiration to Implementation*, AK Peters, Ltd, 1998.

[2] M.Z. Hassan, M.R. Razali and M.S. Halid, "Design and Development of Amphibious Hybrid Vehicle Body Structure," *International Journal of Science and Research (IJSR),* vol. 2, no. 5, pp. 220-223, 2013.

Design strategy for concept design of hybrid bio-composite automotive anti-roll bar using TRIZ

M.T. Mastura[1,2], S.M. Sapuan[1,3,*], M.R. Mansor[2], A.A. Nuraini[1]

[1] Department of Mechanical and Manufacturing Engineering, Universiti Putra Malaysia
43400 UPM Serdang, Selangor, Malaysia
[2] Faculty of Mechanical Engineering, Universiti Teknikal Malaysia Melaka,
Hang Tuah Jaya, 76100 Durian Tunggal, Melaka, Malaysia
[3] Laboratory of Biocomposite Technology, Institute of Tropical Forestry and Forest Products (INTROP),
Universiti Putra Malaysia, 43400 UPM Serdang, Selangor, Malaysia

*Corresponding e-mail: sapuan@upm.edu.my

ABSTRACT – In this study, development of concept design of hybrid bio-composite automotive anti-roll bar (ARB) has been performed using TRIZ as its design strategy. Using Contradiction Matrix and 40 Inventive Principles, TRIZ suggested the concept design of the automotive ARB could consist of ribs for the reinforcement and multi diameter of ARB's arms in order to reduce weight. The new design improved the stiffness by reduces the maximum displacement by 22.5%. Thus, TRIZ has suggested a new concept design that could satisfy the properties of the materials without affecting its functions and performance.

1. INTRODUCTION

Function of automotive anti-roll bar (ARB) is to generate reactive force by compressing the suspension on the adjacent side of the vehicle when suspension on the other side is compressed. ARBs that made from steel are considered heavy and when they are configured in tubular shape, they are susceptible to breakage [1]. With recent awareness on environment-friendly products and sustainability, it shows that hybrid bio-composites could be one of the substitute materials of steel and could be used in many applications in automotive industry especially ARB [2]. A suitable design of ARB is needed due to the critical size and shape of ARB regarding on its functions and operation that linked to suspension in vehicle [3]. Hence, a suitable concept design including determination of geometry of lightweight ARB is the focus area in this study. Moreover, there is a study by Doody [4] that found hybrid carbon fiber could be used as a substitute material for lightweight ARB. However, the shape and size of ARB should be different from steel-based ARB. Therefore, conflict between the features of ARB and properties of hybrid bio-composite material that applied in the ARB is going to be solved by tools in TRIZ in order to generate an inventive solution for the improvement of the hybrid bio-composite automotive ARB.

2. METHODOLOGY

TRIZ was developed by Atlshuller to solve inventive problems using scientific approach from patents data analysis by identifying innovative solution [5]. TRIZ tools that are commonly practiced in product design and development are Contradiction Matrix and 40 Inventive Principles because of simplicity and direct approach in problem solving. Thus, in this study, application of both tools are selected for design development of hybrid bio-composite ARB.

Based on the operation and principle of ARB, the stiffness of the ARB is defined by the geometry and material properties and strongly depends on the diameter of the ARB as shown in the equation below:

$$c = \frac{G\pi d^4}{32a^2 b} \qquad (1)$$

where G is modulus of shear, a and b are defined as length for arm and centre respectively as in Figure 1 and d is diameter of the ARB.
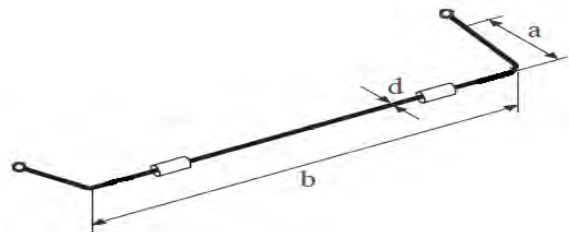
Figure 1 Anti-roll bar

From equation (1), the Engineering Contradiction in the form of improving parameter and worsening parameter is defined. In this case, Engineering Contradiction is *"If the diameter of the bar is increase, the stiffness of the bar is improved but it is ultimately gaining more weight"*. This means that in order to improve the stiffness of the bar, the diameter of the bar should be increased; however it would require more weight added on the bar. Thus, the improving parameter are volume of moving object (#7), strength (#14) and reliability (#27). The worsening parameter in this case is weight of moving object (#1).

3. RESULTS AND DISCUSSION

As mentioned in previous section, TRIZ has suggested a few possible general solutions to solve the contradiction. The selected Inventive Principles that are considered as the most appropriate solutions are #2

taking out, #3 local quality and #40 composite materials. In Table 1, specific solution strategies are developed in order to adopt in the problem of design ARB.

Table 1 Specific solution strategy based on the TRIZ general solution principles,

TRIZ general solution principles	Solution descriptions	Specific solution strategy
#2 Taking out	Separate an interfering part or property from an object, or single out the only necessary part (or property) of an object	Cross-sectional of the ARB could be in a hollow shape by taking out unnecessary part while maintaining the performance of the component [6].
#3 Local quality	(a) Change an object's structure from uniform to non-uniform, change an external environment (or external influence from uniform to non-uniform. (b) Make each part of an object function in conditions most suitable for its operation and fulfil a different and useful function	(a) Vary diameter of the component in order to handle the high stress at critical point along the bar. The value depends on the value of stress concentration and safety factor [7]. (b) Outer part of the solid bar or inner part of hollow bar could be designed with ribs to reinforce and strengthened the structure [8].
#40 Composite materials	Change from uniform to composite (multiple) materials	Use hybrid composition where natural fiber is combined with high strength synthetic fiber like glass to increase the strength.

Based on the analysis of Inventive Principles suggested previously, the reinforcement of ribs may improve the ARB stiffness [9]. The reinforcement of ribs with multi diameter of ARB's arms in new design reduces the maximum displacement by 22.5% and improved the stiffness. The new concept design of the ARB is shown in Figure 2.
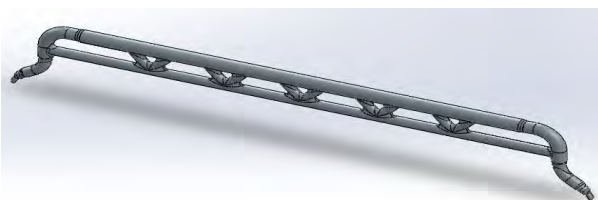
Figure 2 Concept design of hybrid bio-composite ARB.

4. CONCLUSION

In conclusion, to incorporate hybrid natural fiber composite material with design of automotive component, design strategy like in TRIZ could be used in order to develop suitable design for the automotive components without affecting their function and performance. In this case, concept design of hybrid bio-composite automotive ARB had been developed through methods that suggested in TRIZ. The new concept design has been reinforced and strengthened with ribs at bend areas of ARB. In addition, future works will be conducted to evaluate the properties and manufacturability of hybrid bio-composite automotive ARB for comparison with current design of ARB.

REFERENCES

[1] O. Renner, M. Krahl, M. Lepper, and W. Hufenbach, "Stabilizer Bar of Fiber Reinforced Plastic Composite and Method for Its Manufacture," US 8,668,212 B2, 2014.

[2] O. Faruk, A. K. Bledzki, H.-P. Fink, and M. Sain, "Progress Report on Natural Fiber Reinforced Composites," *Macromol. Mater. Eng.*, vol. 299, no. 1, pp. 9–26, 2014.

[3] H. Bayrakceken, S. Tasgetiren, and K. Aslantas, "Fracture of an automobile anti-roll bar," *Eng. Fail. Anal.*, vol. 13, no. 5, pp. 732–738, 2006.

[4] M. Doody, "Design and Development of A Composite Automotive Anti-Roll Bar," 2013.

[5] T.-S. Li and H.-H. Huang, "Applying TRIZ and Fuzzy AHP to develop innovative design for automated manufacturing systems," *Expert Syst. Appl.*, vol. 36, no. 4, pp. 8302–8312, May 2009.

[6] K. Sharma, P. M. Bora, and P. K. Sharma, "Hollow Cross-Section vs . Solid Cross-Section & Increasing the Diameter of Solid Cross-Section by using finite element Analysis of Anti-Roll Bar," *Int. J. Adv. Res. Sci. Eng.*, vol. 1, no. 1, pp. 1–11, 2012.

[7] P. M. Bora, "Vehicle Anti-Roll Bar Analyzed Using FEA Tool ANSYS," *Int. J. Adv. Technol. Eng. Sci.*, vol. 2, no. 7, pp. 130–136, 2014.

[8] M. R. Mansor, S. M. Sapuan, E. S. Zainudin, A. A. Nuraini, and A. Hambali, "Conceptual design of kenaf fiber polymer composite automotive parking brake lever using integrated TRIZ–Morphological Chart–Analytic Hierarchy Process method," *Mater. Des.*, vol. 54, no. 0, pp. 473–482, Feb. 2014.

[9] A. Kobayashi, "Torsion Beam Type Rear Wheel Suspension System," US 7,946,600 B2, 2011.

Development of a rotary axis mechanism for wire EDM turning (WEDT)

M. Akmal[1,*], R. Izamshah[1,2], M.S. Kasim[1,2], M. Hadzley[1,2], M. Amran[1,2], A. Ramli[1]

[1] Faculty of Manufacturing Engineering, Universiti Teknikal Malaysia Melaka,
Hang Tuah Jaya, 76100 Durian Tunggal, Melaka, Malaysia
[2] Centre of Excellence for Advanced Manufacturing, Universiti Teknikal Malaysia Melaka,
Hang Tuah Jaya, 76100 Durian Tunggal, Melaka, Malaysia

*Corresponding e-mail: akmalzak@student.utem.edu.my

Keywords: WEDT; hybrid machining; micro cylindrical part

ABSTRACT - Wire electro discharge turning (WEDT) is a non- conventional machining process that takes advantage of electrical discharge machining (EDM) sparking phenomenon assisted by rotary axis. Incorporating the additional axis increase the wire electrical discharge machining (WEDM) capability for machining hardened and intricate cylindrical parts especially when conventional machining have failed to perform. This research emphasizes on the development of additional rotary axis mechanism in WEDT as well as evaluation for machining capabilities in blending of macro- micro feasible dimension and shapes.

1. INTRODUCTION

Wire EDM turning (WEDT) is a process that employs basis technology of the wire electrical discharge machining (WEDM) fundamentally based on the electrical discharge machining (EDM) sparking phenomenon. A benefit of WEDT is it allows to produces free- form cylindrical geometries of symmetrical parts with minimal diameters and complex shapes without concerning electrode wear. Most of the current works on WEDT only focusing on macro size cylindrical parts and development of rotary axis mechanism. The rotary mechanism were basically formed by assembling of centring chuck or collet, carbon brush, bearing, pulley and belt, worm gear also driven by electrical motor either AC or DC [1-3].

2. METHODOLOGY

2.1 Design and working principle

As shown in Figure 1, the rotational motion that rotates the workpieces is simply transfer from electrical DC motor by tooth pulley and belt. The workpieces is clamped on straight shank collet holder which serves as spindle shaft and works with ER16M adapter as clamping devices. A pair of deep groove Si3N4 ball bearings with ABEC grade 5 was used to support and guide a rotating of spindle shaft. To prevent the excess melted material (debris) and dielectric fluid from enter to the bearing, radial oil seal is used. Carbon brush is used and held by using the carbon brush holder to transmit the electrical current from a static to a spindle shaft. In this WEDT, the rotating of the workpieces is interfered by continuous electrode wire that replenished during the machining for ensure the new electrode wire surface available for next sparks. By applying the

rotational motion, the un- machined portion on the workpieces surface is replaced by machined portion, and vice versa. The rotary axis mechanism is mounted on the WEDM machine table (Figure 1). The pulse-width- modulation (PWM) method were used to controlled the rotational spindle speed generated by 24 volts DC brushed electric motor and pre- programmed with PIC16F887 memory with the maximum rotational spindle speed of 3000 rpm.
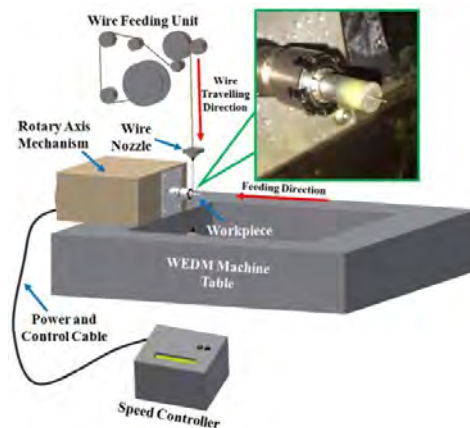
Figure 1 Location of rotary axis mechanism mounted on WEDM machine table.

2.2 Experimental setup

The developed rotary axis are tested in terms of the machining capabilities on Ti6Al4V material with diameter of 9.49 mm. Ti6Al4V was chosen as the workpieces due its low machinability rating by conventional machining [4,5]. The fabricated rotary axis mechanism is installed on Mitsubishi Ra-90 non-submergible WEDM machine. Brass wire with 0.25 mm diameter and single pass cutting condition were employed for all runs.

3. RESULTS AND DISCUSSION

The machining capabilities are tested based on geometries of turning operation and groove profile. As shown in Figure 2, there are four types of geometries feature that were tested and achieved by using this rotary axis mechanism with single pass cutting which are dovetail, cone, ellipse and groove shape. The micro size dovetail shape was successfully machined according to the designated dimension. The successful

of machined down from diameter 9.49 mm of Ti6Al4V to dovetail shape with bottom (neck) diameter as much 163 μm and top diameter 372 μm. Figure 3 shows the comparison in size between machined part of free- form profile and a match.
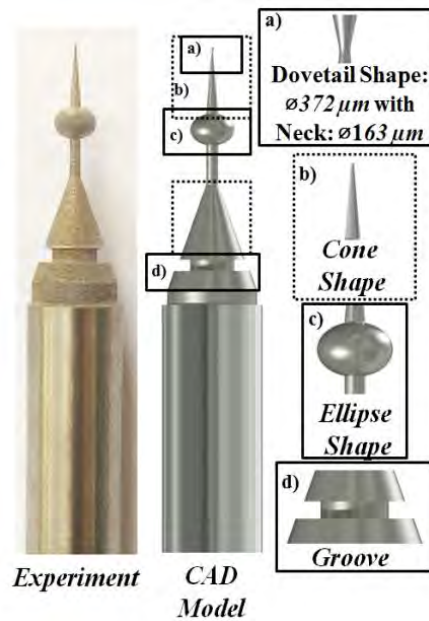
Figure 2 Different geometries in evaluation of machining capability.

Figure 3 WEDT free- form profile machined part.

Figure 4 shows the straight turning machined parts and Table 1 indicates the machined down achieved diameter and length to diameter (L/D) ratio by straight turning operation [6] and WEDT. It is noticable that by incorporating the rotary axis mechanism significantly improved the L/D ratio compared to micro- turning. Basically, the conventional process like micro- turning is well known with its limitation to fabricates parts with large L/D ratio as the workpieces easily deflects by the reacting force with a reduction in rigidity according to the decrease in the diameter.
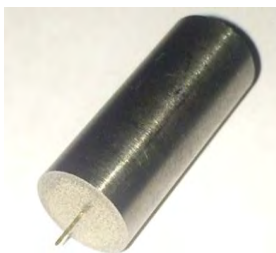
Figure 4 Machined down diameter part to 230 μm by straight turning approach.

Table 1 Comparison of length to diameter ratio (L/D)

Material	Micro- Turning [6]		WEDT	
	Brass	Stainless Steel 316L	Brass	Ti6Al4V
Final Diameter (μm)	80	94	203	230
Final Length (mm)	2	1.46	15	15
Length to diameter ratio (L/D)	25	15.5	73.9	65.2

4. CONCLUSIONS

The developed rotary axis mechanism for WEDT proved to increase the capability in fabricating variation of complex macro and micro dimension geometries. In addition, the improvement on large L/D machining ratio with single pass cutting condition was also observed. This process also has high potential in open new possibilities for blending complex macro- micro geometries components production especially for medical instruments.

REFERENCES

[1] J. Qu, A.J. Shih, and R.O. Scattergood, "Development of the cylindrical wire electrical discharge machining process, part 1: Concept, design, and material removal rate," *Journal of Man. Science and Engineering, Transactions of the ASME,* vol. 124, pp. 702-707, 2002.

[2] M.J. Haddad, and A.F. Tehrani, "Material removal rate (MRR) study in the cylindrical wire electrical discharge turning (CWEDT) process," *Journal of Materials Processing Technology,* vol. 199, pp. 369-378, 2008.

[3] M.T. Yan, and P.H. Hsieh, "Monitoring and adaptive process control of wire electrical discharge turning," *International Journal of Automation Technology,* vol. 8, pp. 468-477, 2014.

[4] R.A. Izamshah, J. Mo, and S. Ding, "Finite element analysis of machining thin-wall parts," *Key Engineering Materials*, vol. 458, pp. 283-288, 2011.

[5] M.S. Kasim, C.H.C. Haron, J.A. Ghani, M.A. Azam, R. Izamshah, M.A.M. Ali, and M.S.A. Aziz, "The Influence of Cutting Parameter on Heat Generation in High-Speed Milling Inconel 718 under MQL Condition," *Journal of Scientific and Industrial Research*, vol. 73, pp. 62-65, 2014.

[6] M.A. Rahman, "CNC microturning: An application to miniaturization," Master of Engineering, Mech. Eng., National University of Singapore, 2004.

Optimal PID sliding surface for sliding mode control based on particle swarm optimization algorithm for an electro-hydraulic actuator system

C.C. Soon[1], R. Ghazali[1,*], H.I. Jaafar[1], S.Y.S Hussien[1]

[1] Faculty of Electrical Engineering, Universiti Teknikal Malaysia Melaka,
Hang Tuah Jaya, 76100 Durian Tunggal, Melaka, Malaysia

*Corresponding e-mail: rozaimi.ghazali@utem.edu.my

Keywords: PID sliding surface; sliding mode control; particle swarm optimization

ABSTRACT – This paper presents the assessment on the sliding mode control (SMC) integrated with proportional-integral-derivative (PID) sliding surface which is optimized through particle swarm optimization (PSO) algorithm. The control scheme is established from the derived dynamic equation which stability is proven through Lyapunov theorem. In the evaluation of PID sliding surface, conventional Ziegler-Nichols (ZN) tuning method has been utilized to obtain the controller parameters and compared with the optimized controller parameters through PSO algorithm which is employed to the electro-hydraulic actuator (EHA) system to evaluate its positioning tracking performances. From the obtained simulation results, it can be concluded that the PSO tuning algorithm outperform the conventional ZN tuning method.

1. INTRODUCTION

In the past decades, electro-hydraulic actuator (EHA) system has been widely used especially in various heavy engineering works. The advanced design of EHA system with the versatile electronic and hydraulic components offers a massive enhancement in an application's performance. The integration of both electronic and hydraulic equipment that absorbed both advantages have been extensively used nowadays.

However, the dynamic features of the EHA system is known to be highly nonlinear in nature and the existing nonlinearities and uncertainties yield to the constraint in the control of EHA system. Such characteristics appeared in the system degrade its performance significantly. These disturbances simultaneously influence the position tracking accuracy and commonly affected by the occurrences of leakage and friction in the system.

Various control strategies have been reported and proposed in the literature to overcome the difficulties in the EHA control system. The raised numbers of works dealing with EHA system ranged from linear, nonlinear to intelligent control approaches have been proposed over the past decades. In the literature study of [1], sliding mode controller (SMC) nonlinear control strategy is found to be efficient and extensively applied to the nonlinear EHA system.

The SMC nonlinear control is verified to have a capability to maintain the control stability of various model classes that exposes to the disturbances and variations in the system parameters. In [2], the sliding surface has been improved by adding an integral action which is simultaneously enhanced the tracking performance of the SMC control on the electromechanical plant.

In this paper, the SMC control has been augmented with PID sliding surface for the purpose of enhancing the position tracking performance of the EHA system. The servo valve and hydraulic actuator integrating with the nonlinear dynamics model has been derived. Afterward, the SMC control scheme has been implemented in the system which stability of the control system is theoretically proven by Lyapunov theorem. Subsequently, the controller tracking performance has been compared to the optimized controller to demonstrate the significant improvement of the controller through the proposed technique.

2. MODELING EHA SYSTEM

The block diagram of the EHS system is described in Figure 1 below.
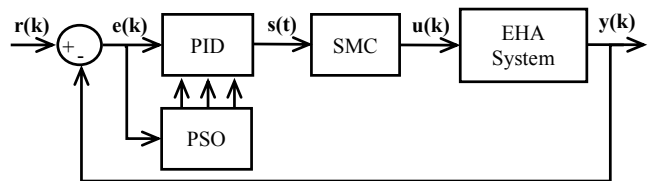
Figure 1 EHA system block diagram.

The dynamics of the servo valve are represented by a second order differential equation that related to an electric current drive from the torque of the motor as expressed in equation (1).

$$\frac{d^2 x_v}{dt^2} + 2\xi\omega_n \frac{dx_v}{dt} + \omega_n{}^2 = I\omega_n{}^2 \tag{1}$$

Where ξ is the damping ratio while ω is the natural frequency of the servo valve.

Through the overall dynamics equation of moving mass, damper, and spring, the total force produced from hydraulic actuator can be evinced in equation (2).

$$F_p = A_p(P_1 - P_2)$$

$$= M_p \frac{d^2 x_p}{dt^2} + B_s \frac{dx_p}{dt} + K_s x_p + F_f \tag{2}$$

3.   SLIDING MODE CONTROL DESIGN

The PID sliding surface for the SMC design implemented into third-order EHA system can be indicated by using the following equation where k_p, k_i, and k_d are referred to the PID parameters [3].

$$s(t) = k_p e(t) + k_i \int_0^t e(\tau)d\tau + k_d \dot{e}(t) \qquad (3)$$

The general expression of SMC control structure consist of switching control and equivalent control as denotes in equation (4). Where the switching control, u_{sw} corresponding to the reaching phase when $s(t) \neq 0$. While the equivalent control u_{eq} corresponding to the sliding phase when $s(t) = 0$.

$$u_{smc}(t) = u_{eq}(t) + u_{sw}(t) \qquad (4)$$

The tracking error will be confined in the sliding surface and converge to the equilibrium point where $s(t) = \dot{s}(t) = \ddot{s}(t) = 0$, where the second derivative of sliding surface is expressed as:

$$\ddot{s}(t) = k_p \ddot{e}(t) + k_i \dot{e}(t) + k_d \dddot{e}(t) \qquad (5)$$

Assume that the lumped uncertainty is neglected (L=0), the equivalent control of the SMC control can be defined as:

$$u_{eq}(t) = (k_d C_n)^{-1}(k_p \ddot{e}(t) + k_i \dot{e}(t) + \cdots$$
$$\cdots + k_d(\dddot{x}_r + A_n \ddot{x}_p + B_n \dot{x}_p)) \qquad (6)$$

By applying the sign function to the sliding surface, the switching control can be determined as:

$$u_{sw}(t) = k_s sign(s) \qquad (7)$$

To ensure the stability of the switching control based on Lyapunov theorem, the chattering effect for the discontinuous function in (7) has been reduced by replace the function of hyperbolic tangent with the boundary layer of φ as proposed in [3].

$$u_{sw}(t) = k_s \tanh(\frac{s}{\varphi}) \qquad (8)$$

4.   RESULTS AND DISCUSSION

In order to evaluate the position tracking performance of the conventional tuning method and the optimization algorithm employed to the PID sliding surface, the step reference input signal has been fed into the plant and observe the controller tracking ability as shown in Figure 2. The PID controller parameters obtained through ZN conventional tuning method provide high overshoot and long settling time denoted in green dotted output signal. It can be clearly seen through Figure 2, the overshoot and settling time has been reduced when the SMC controller with PID sliding surface that utilized ZN parameter as its controller parameters denoted in the blue dotted output signal. By utilizing the PSO algorithm, an optimal PID parameters was obtained which applied to the PID sliding surface and produced the result as represented by the red dotted output signal. The value of $k_s = 10$ and $\varphi = 15$ has been applied in the switching control and the PID controller parameters obtained through two different tuning methods were tabulated in Table 1.

Table 1 Parameters value of the PID controller.

PID	Parameters Values	
	Ziegler-Nichols	PSO Algorithm
K_p	1020	1118.2151
K_i	0.0150	7.3249e-06
K_d	0.0038	4.0391
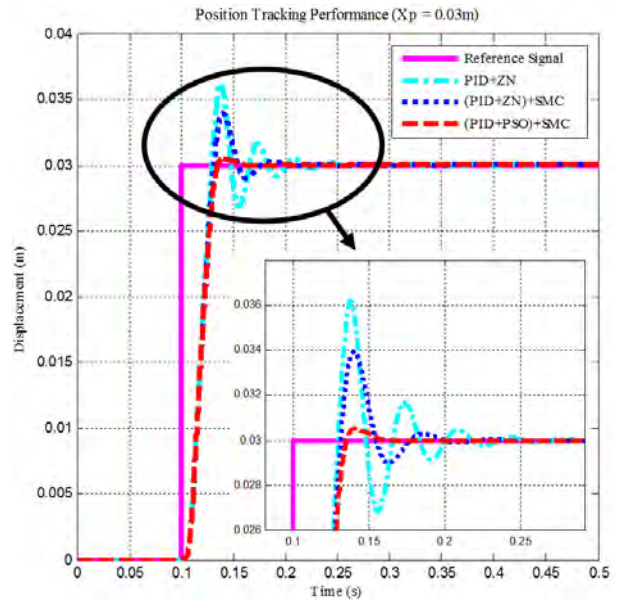
Figure 2 The output for step reference input signal.

5.   CONCLUSION

In this paper, the performance of PID sliding surface for the SMC controller has been evaluated by considering the conventional ZN tuning technique and the PSO tuning algorithm that applied to the controller. The numerical simulation shows that the PSO optimization technique provides significant improvement to the controller and produced more precise position trajectory tracking.

REFERENCES

[1]   R. Ghazali, Y. M. Sam, M. F. Rahmat, D. Hanafi, R. Ngadengon, and Zulfatman, "Point-to-point trajectory tracking with discrete sliding mode control of an electro-hydraulic actuator system," *Proc. - 2011 IEEE Student Conf. Res. Dev. SCOReD 2011*, pp. 148–153, 2011.

[2]   İ. Eker, "Second-order sliding mode control with experimental application," *ISA Trans.*, vol. 49, no. 3, pp. 394–405, 2010.

[3]   R. Ghazali, Y. M. Sam, M. F. Rahmat, A. W. I. M. Hashim, and Zulfatman, "Performance Comparison between Sliding Mode Control with PID Sliding Surface and PID Controller for an Electro-hydraulic Positioning System," *Int. J. Adv. Sci. Eng. Inf. Technol.*, vol. 1, no. 4, pp. 447–452, 2011.

Experimental analysis of 3D gantry crane system via optimal PID and PD controller by PSO

S.Y.S. Hussien[1,2], R. Ghazali[1,2,*], H.I. Jaafar[1,2], C.C. Soon[1, 2]

[1] Faculty of Electrical Engineering, Universiti Teknikal Malaysia Melaka,
Hang Tuah Jaya, 76100 Durian Tunggal, Melaka, Malaysia
[2] Center for Robotics and Industrial and Automation, Universiti Teknikal Malaysia Melaka,
Hang Tuah Jaya, 76100 Durian Tunggal, Melaka, Malaysia

*Corresponding e-mail: rozaimi.ghazali@utem.edu.my

ABSTRACT – A 3D INTECO gantry crane system is used for lifting and moving loads horizontally, lowering and releasing the gripper to the original position. There are two main problems which occurred in the system which are positioning the desired position and minimize the payload oscillation. In order to overcome this problem, a controller is implemented. In this paper, a control strategy of PID and PD controller tuned by Particle Swarm Optimization (PSO) is presented. PID controller is used to control the trolley movement to reach at the precise desired position and PD controller is used to control the undesired oscillation from the payload while moving the load. The results shown that through the experimental platform, the trolley reached the desired position with low payload oscillation.

1. INTRODUCTION

A crane system is used frequently to move load in factories and harbours. The trolley at the crane is used to move the load to the desired target without causing any undesired oscillation. However, controlling the crane manually by human will tend to excite sway angles of the hoisting line and degrade the overall performance of the system.

In this paper, the implementation of Proportional-Integral-Derivative (PID) and Proportional-Derivative (PD) controller in the 3D INTECO gantry crane system had been proposed. PID controller as feed-back structure aims to control the trolley movement in order to achieve the desired position whereas PD controller as the feed-forward structure used to minimize the oscillation during the movement. The parameters of these controllers are obtained by tuning via Particle Swarm Optimization (PSO). Performances of the proposed control schemes are discussed in terms of the precise positioning of payload and reduction in the payload oscillation.

2. 3D GANTRY CRANE DESCRIPTION

Figure 1 shows the experimental of 3D gantry crane system. The crane consists of a payload hanging on a cable, wound by a motor mounted on a trolley. The payload is lifted and lowered in the z-direction. The horizontal motion in x-direction are capable for the rail and trolley. Not only that, the trolley is able to move in horizontal along the rail in the y-direction. There are

three DC motors in the system which used for travelling, traversing and hoisting in x, y and z axes respectively. The system is controlled directly by a PC with RT-DAC4/PCI multipurpose digital I/O board.
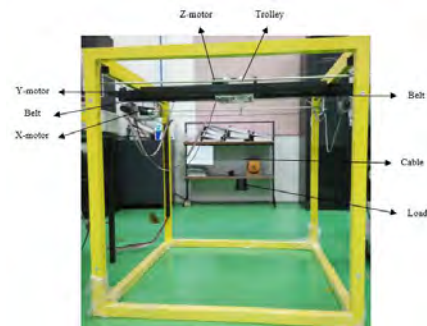
Figure 1 3D INTECO gantry crane.

Figure 2 shows the schematic representation of 3D gantry crane system [1,2]. There are five identical encoders measuring five state variables; x_w represents the distance of the rail with the cart from the center of the construction frame; y_w is the distance of the cart from the center of the rail; R denotes the length of the lift-line; α represents the angle between the y axis and the lift-line; β is the angle between the negative direction on the z-axis and the projection of the lift-line onto the xz-plane.
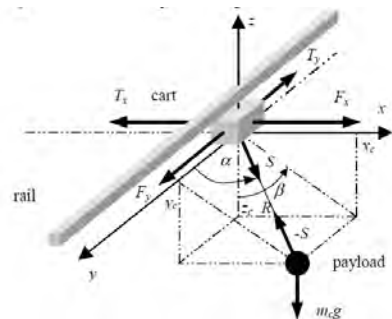
Figure 2 Schematics of 3D gantry crane system.

The dynamic equations of motion in gantry crane system in the y-direction obtained as [1] where y_t is position of trolley and y_p is position of payload oscillation. Parameters of the gantry crane system are tabulated as in Table 1.

$$\ddot{y}_t = \left(\frac{F_x}{m_w} - \frac{T_x}{m_w} \right) + \left(\frac{m_c}{m_w} \right) \left(\frac{F_z}{m_c} - \frac{T_z}{m_c} \right) \cos\alpha \qquad (1)$$

$$\ddot{y}_p = \ddot{y}_t + \left(\ddot{R} - R\dot{\alpha}^2 \right) \cos\alpha - \left(2\dot{R}\dot{\alpha} + R\ddot{\alpha} \right) \sin\alpha \qquad (2)$$

Table 1 Parameters of gantry crane system [1].

Parameters	Unit	Values
Payload mass	m_c	1.0 kg
Trolley mass	m_w	1.155 kg
Moving rail mass	m_s	2.20 kg
Gravity	g	9.81 ms^{-2}
Friction force at x-axis	T_x	100 Nsm^{-1}
Friction force at y-axis	T_y	82 Nsm^{-1}
Friction force at z-axis	T_z	75 Nsm^{-1}
Length of cable	R	0.5 m

3. CONTROL SCHEME

Figure 3 illustrated the block diagram of control scheme in the gantry crane system. There are two types of controllers which are PID and PD controller. PID controller is designed in feed-back structure which is implemented to control the trolley in order to reach the desired position. Besides, PD controller is constructed as feed-forward structure used to control the oscillation of the angle which created from the system while moving the payload to the desired position. The parameters in these controllers are optimized by the meta-heuristics method which is PSO with 20 agents and 100 iterations. The optimized parameters of PID (K_P, K_I and K_D) and PD (K_{Ps} and K_{Ds}) controller is tabulated in Table 2.
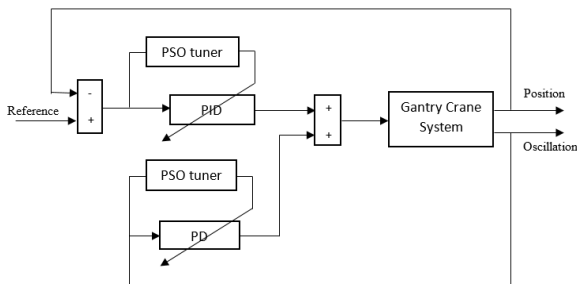
Figure 3 Block diagram of control scheme.

Table 2 Optimized PID and PD Parameters.

Parameters	Values
K_P	20.9716
K_I	10.8455
K_D	4.4700
K_{Ps}	5.0092
K_{Ds}	0.0704

4. RESULTS AND DISCUSSION

4.1 Trolley position

Figure 4 shows the trolley position in the gantry crane system which controlled by the PID controller. After having an overshoot of 19.63%, the system started to settle down at 6.90 seconds and reached the desired position of 0.30 meters with zero steady state error.
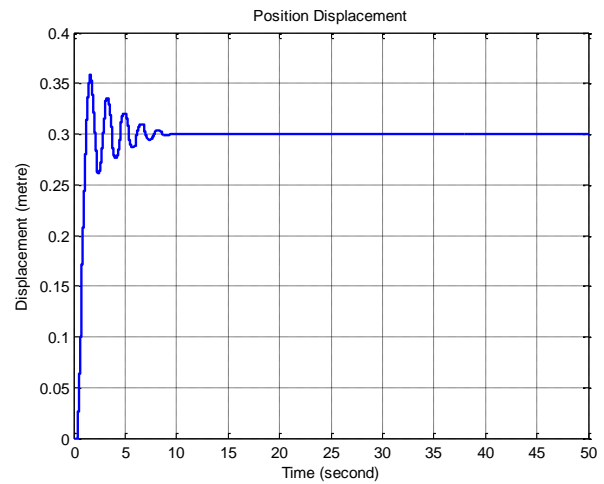
Figure 4 Response of trolley position.

4.2 Payload oscillation

Figure 5 shows the payload oscillation in the gantry crane system which controlled by the PD. It shows that the maximum payload oscillation is 1.1526 radian at 1.4 seconds. Then, the oscillation is slow down and reached the minimized oscillation of 0.0077 radian, which is approximate to zero radian.
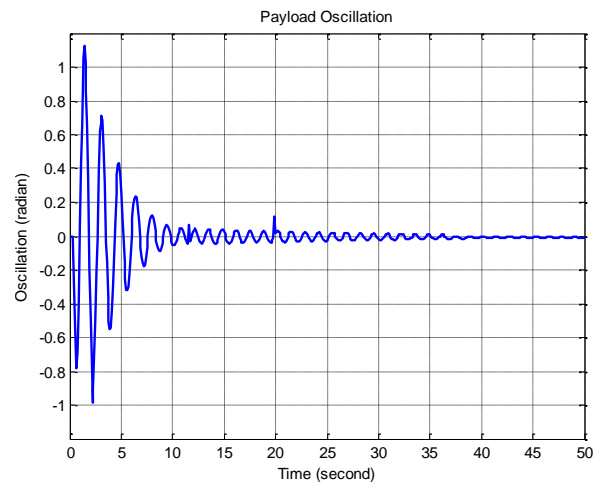
Figure 5 Response of payload oscillation

5. CONCLUSION

This paper is presented a control strategy of PID and PD controller which tuned by PSO in the 3D INTECO gantry crane. The controller is proposed to control the trolley movement with minimize oscillation. The results shown that with the implementation of the PSO, the system able to reach the desired position with low payload oscillation. Therefore, the controller works effectively in experimental platform.

REFERENCES

[1] M. J. Maghsoudi, Z. Mohamed, A. R. Husain, and H. I. Jaafar, "Improved input shaping technique for a nonlinear system," in *2014 IEEE International Conference on Control System, Computing and Engineering*, November 2014, pp. 261–266.

[2] D. Antic, Z. Jovanovic, S. Peric, S. Nikolic, M. Milojkovic and M. Milosevic, "Anti-swing fuzzy controller applied in a 3D crane system," *Engineering Technology and Applied Science Research*, vol. 2, no. 2, pp. 196-200, 2012.

Strength and porosity of additively manufactured PLA using a low cost 3D printing

H.A. Habeeb[1,3], M.R. Alkahari[1,2,*], F.R. Ramli[1,2] , R. Hasan[1,2], S. Maidin[2,4]

[1] Faculty of Mechanical Engineering, Universiti Teknikal Malaysia Melaka,
Hang Tuah Jaya, 76100 Durian Tunggal, Melaka, Malaysia
[2] Centre for Advanced Research on Energy, Universiti Teknikal Malaysia Melaka,
Hang Tuah Jaya, 76100 Durian Tunggal, Melaka, Malaysia
[3] Middle Euphrates University / AL –Mussaib Technical College, Babel, Iraq
[4] Faculty of Manufacturing Engineering, Universiti Teknikal Malaysia Melaka,
Hang Tuah Jaya, 76100 Durian Tunggal, Melaka, Malaysia

*Corresponding e-mail: rizalalkahari@utem.edu.my

Keywords: 3D printing; additive manufacturing; rapid prototyping; porosity

ABSTRACT – Nowadays, with rapid advancement in 3D printing, a relatively low cost 3D for polymer based printers using an open-source self-replicating prototype has increasingly been used in many applications. The printer variants can fabricate any complex parts. In this study, the tensile strength and porosity of PLA and its utilization in 3D printing for standard usage of low cost 3D printers using open-source has been investigated. It was found that, the parts printed from a low cost 3D printer produce relatively acceptable tensile strength and porosity as those from mid-range commercial manufacturer.

1. INTRODUCTION

Three dimension (3D) printing or also can referred as additive manufacturing (AM) process is the method of creating three-dimension rigid item from a digital data. This process of making of product is accomplished by layering down layer by layer of material until the complete product is created. The working principle of the 3D printer starts by creating the object desired to be printed with Computer Aided Design (CAD) for a new object or 3D scanner to make digital copy of an existing 3D object [1]. The materials being utilized for 3D printing possess long history of usage since the early decades of technological revolution [2]. There are many different types of materials that can be used in 3D printing. One of commonly used materials is polylactic acid (PLA) due to its competitive price and more environmental friendly. With the rapid development of low cost 3D printer, it is necessary to study the mechanical properties of these printer. The mechanical properties of 3D printed product is very much influenced by the porosity and mechanical structure during layer formation [3]. This study concentrates on strength and porosity of a low cost 3D printed material by using PLA material. In this study, the relationship between layer height, porosity and tensile strength are studied and presented.

2. METHODOLOGY

In order to determine the mechanical properties of 3D printed materials at different setting, the parameter during the 3D printing and slicing are varied. In this study, samples with the layer height from 0.1mm to 0.4mm was produced and their tensile strength and porosity are determined. Table 1 shows the printing parameters being utilized in this investigation. Tensile test specimen (as shown in Fig. 1) which is based on the ASTM: D638 [4] were produced. During fabrication, CAD data was prepared in which later Slic3r and Cura software were used for slicing the STL files and converting it to machine readable G-code respectively. All specimens were printed solid with a setting of 100% infill; the actual positive or negative air gaps vary among printers due to printer differences. This affects the part as air gap has been shown to be an important contributing factor to tensile strength [5]. Testing was performed on Instron machine. The machine was controlled by the Bluehill Software. Stress, strain, and modulus calculations were performed. Moreover, the porosity of PLA at different layer height was determined using Archimedes principles and observed using optical microscope (Zeiss Axiovert 200 Matt).

Table 1 RepRap 3-D printer slicing variables.

Pattern orientation (º)	90
Layer height (mm)	0.1, 0.2, 0.3, 0.4
Infill (%)	100
Printer type	Kossel RepRap

(a)	(b)
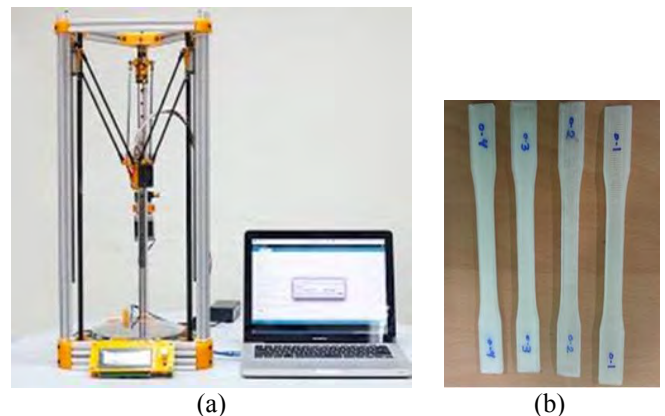
Figure 1 (a) Kossel mini printer and (b) printed PLA specimen according to ASTM: D638.

3. RESULTS AND DISCUSSION

The average values of tensile strength were obtained at different values of layer height. Based on the tabulated results in Table 2 and Figure 2, it is shown that, the greatest tensile strength of PLA is 45.56 MPa were recorded at 0.2mm layer height, while the lowest tensile strength is 32.01 MPa at 0.4 mm layer height. The results indicate that a low cost 3D printer has a comparable tensile strength to mid-range commercial 3D printer which is at 46.77 MPa based on the manufacturer data [6].

Table 2 Average tensile strength and average elastic modulus at 90 ° orientation.

Layer height (mm)	Average tensile strength (MPa)	Average elastic modulus (MPa)
0.1	35.90	1005
0.2	45.56	1125
0.3	45.04	1090
0.4	32.01	725
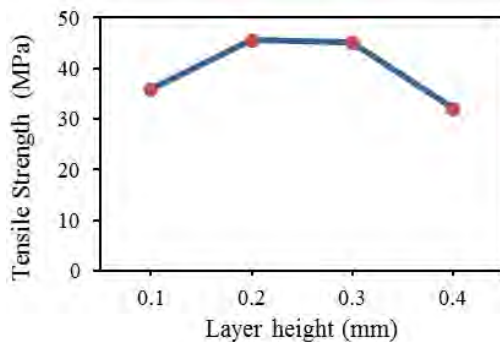
Figure 2 Effect of layer height on the tensile strength of PLA.
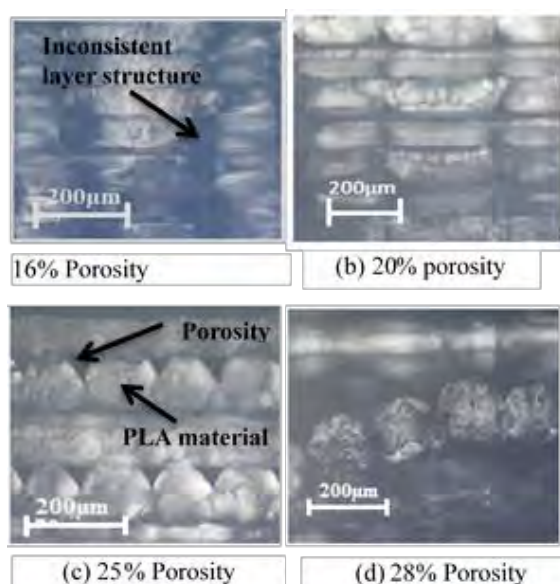
Figure 3 Layer structure and porosity at various layer height, (a) 0.1mm layer height, (b) 0.2 mm layer height, (c) 0.3 mm layer height, (d) 0.4 mm layer height.

The obtained results of porosity testing are shown in Figure 3. The results show the porosity percent increases as the layer height increases. The porosity was the highest percent at 28% when the layer height was set at 0.4 mm. This explain why the tensile was the lowest at 32.01 MPa. The lowest porosity percentage was found at 16% when it is at 0.1 mm height layer. Whereas, the percentage of porosity at 0.2 and 0.3 mm layer height are 20% and 25% respectively. The porosity of PLA is the lowest at 0.1 mm layer height but the tensile strength was a bit lower compared to when the layer height was 0.2 mm. This is because of the disorganized and inconsistent layer structure formed at a very low layer height. During layer formation and nozzle movement, the material deposited on the top layer may cause damage to the previous layer due to very small clearance between the layers. Furthermore, material that is extruded through the nozzle is not consistent at low layer height. As a result, inconsistent layer structure as shown in Figure 3 (a) was produced.

4. SUMMARY

The study shows relationship between the strength and porosity of PLA material in 3D printing through standard tensile tests. The results show that the highest average tensile strength of the printed parts is 45.56 MPa at 0.2 mm height layer for PLA. Porosity of PLA increases with the increase of layer height. Lowest percent of 16% at 0.1 mm layer height and highest percent porosity of 28% at 0.4 mm layer height. The study also demonstrated, at the setting parameter that was used in the study, only a slight drop in the value of tensile strength between the 3D printers. Hence, a relatively comparable strength to mid-range commercial printer can be obtained by a low cost 3D printer using an open source system.

REFERENCES

[1] T. Wohlers, *Additive manufacturing and 3D printing state of the industry*, Wohlers Report, 2013.

[2] L. Hod. C. Francis, J.H. Moon and P. Carlo, "3-D printing the history of mechanisms," *Journal of Mechanical Design*, vol. 127, pp. 1029-1033, 2005.

[3] M.R. Alkahari, T. Furumoto, T. Ueda and A. Hosokawa, "Consolidation characteristics of ferrous-based metal powder in additive manufacturing," *Journal of Adv. Mech. Design, Systems, and Manufacturing*, vol. 8, no. 1, 2014.

[4] Revised ASTM standard method of tensile properties of plastic D638-14 (2014- 2015): 1-17.

[5] J.F. Rodriguez, J.P. Thomas, J.E. Renard, "Design of fused-deposition ABS components for stiffness and strength", *J Mech Des*, vol. 125, no. 3, pp. 545–51, 2003.

[6] Makerbot, https://eu.makerbot.com/fileadmin/ Inhalte/Support/Datenblatt/MakerBot_R__PLA_an d_ABS_Strength_Data.pdf

Optimization of warping deformation in open source 3d printer using response surface method

M.A. Nazan[1,*], F.R. Ramli[1,2], M.R. Alkahari[1,2], M.N. Sudin[1, 2], M.A. Abdullah[1, 2]

[1) Faculty of Mechanical Engineering, Universiti Teknikal Malaysia Melaka,
Hang Tuah Jaya, 76100 Durian Tunggal, Melaka, Malaysia
[2) Centre for Advanced Research on Energy, Universiti Teknikal Malaysia Melaka,
Hang Tuah Jaya, 76100 Durian Tunggal, Melaka, Malaysia

[*]Corresponding e-mail: muhd_afdhal@hotmail.com

Keywords: Open source 3D printer; warping deformation; Response Surface Method

ABSTRACT – The purpose of this paper is to minimize the warp deformation that usually occurs in plastic part produced by open source 3D printer. The process involved 3D solid modeling design, 3D printing with coated adhesive applied on the printing platform, warping deformation measurement and statistical analysis. The optimization processes involved Design on Experiment (DOE) technique where Responses Surface Methodology (RSM) by using Minitab software was applied. The experiment produced the minimum result of warping deformation value when layer temperature, infill density, first layer height and other layer height is 192°C, 13%, 0.20mm and 0.30mm respectively.

1. INTRODUCTION

Open source 3D printer is an additive manufacturing technology that has revolutionized the production of plastic component and has been slowly replacing the conventional subtractive manufacturing process. However, one of the drawback of open source 3D printer is the plastic filament that comes out from its nozzle tends to shrink and warp and sometimes peel away from the bed platform. This warping deformation issues in 3D printer have been highlighted by several researchers [1-2] Additional surface preparation by applying synthetic polymer adhesive between the first layer and the bed platform had been performed to counter this problem [3]. However, due to the different 3D printer process parameter settings, warping deformation may still occur and because of that, the best 3D printer parameters setting need to be figure out to obtain the best printing quality. Hence, the purpose of this paper is to investigate how the 3D printer parameters affected the warping deformation and what are the best process parameters values to minimize the warping deformation.

2. METHODOLOGY

The experiment started with 3D modeling design that was prepared by using CATIA solid modeling software. A cuboid model was designed with size of 100mm in length, 30mm in width and total height of 5mm as shown in Figure 1. This digital model is then converted into printing instruction for the open source 3D printer by using Slic3r software.
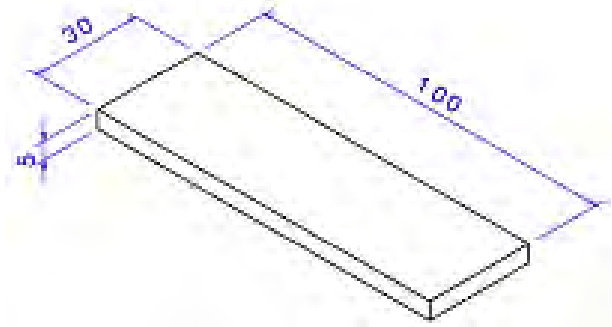
Figure 1 Size of cuboid model in millimeter unit.

Table 1 The parameter of independent variables.

Symbol	Independent variables	Parameters
T	Layer temperature (°c)	180°C - 200°C
ρ	Fill density (%)	10% - 30%
h_1	First layer height (mm)	0.2mm - 0.4mm
h_2	Other layer height (mm)	0.2mm - 0.3mm

By using the DOE techniques, four parameters which are layer temperature, infill density, first layer height and the other layer height were varied and a total of 16 samples were prepared as summarized in Table 1. The Kossel Mini Delta 3D printer without existing heating bed was used to fabricate the cuboid model. The bed platform of the 3D printer was coated by a layer of synthetic polymer adhesive, *poyvinylpyrrolidone* (PVP) to reduce warping deformation of the first layer.

In order to measure the warping deformation, vernier height gauge was utilized. Figure 2 and Eq. (1) shows the method to measure the warping deformation.

Figure 2 Method of measurement at each sample's corner

Warping deformation, $y = y_1 - y_2$ (1)

By referring to the Eq. (1), the value of warping deformation, y is obtained by subtracting the value of y_1, value of total height and y_2, the deflected total height. Four corners of the cuboid part with five attempts each were measured and the average value of warping deformation, y_{avg} were calculated.

By using Minitab software, DOE and RSM was applied to in order to minimize the warping deformations. A sample with optimize parameter value was then produced by 3D printer to checked for its accuracy of the RSM and the optimization process.

3. RESULTS AND DISCUSSION

Fig.3 shows a cuboid printed sample where warping deformation occurs at its corners as in circles. All samples taken in this experiment have more or less deformation around their corners.
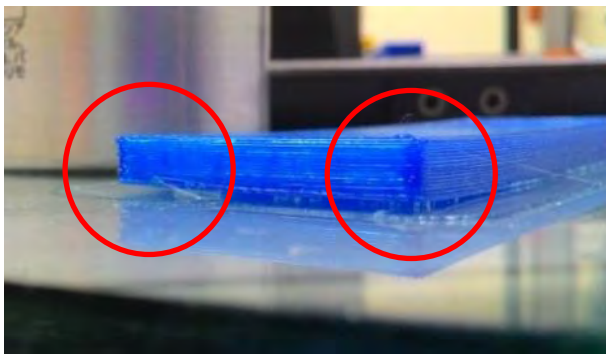
Figure 3 Deflected sample by warping deformation problem shown in the circles.

Table 2 DOE result of warping deformation.

Part No.	Independent variables				Response
	T (ºC)	ρ (%)	h_1 (mm)	h_2 (mm)	y_{avg} (mm)
1	180	10	0.20	0.20	0.08
2	180	10	0.40	0.20	0.13
3	180	30	0.20	0.20	0.20
4	180	30	0.40	0.20	0.14
5	180	10	0.20	0.30	0.09
6	180	10	0.40	0.30	0.08
7	180	30	0.20	0.30	0.09
8	180	30	0.40	0.30	0.07
9	200	10	0.20	0.20	0.23
10	200	10	0.40	0.20	0.26
11	200	30	0.20	0.20	0.23
12	200	30	0.40	0.20	0.27
13	200	10	0.20	0.30	0.08
14	200	10	0.40	0.30	0.08
15	200	30	0.20	0.30	0.12
16	200	30	0.40	0.30	0.17

Table 2 shows the DOE results with average warping deformation, y_{avg} for four corners and T, ρ, h_1 and h_2 is represented by layer temperature, infill density, first layer height and other layer height. The obtained main effect plot in Fig.4 shows that the temperature and other layer height have high influence to the deformation value compared to the infill density parameter. The first layer height does not show any major effect to the warping deformation.
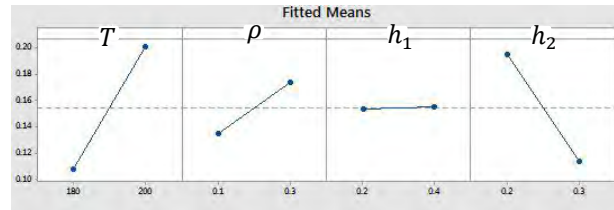
Figure 4 Main effect plot correspond to warping deformation.

Table 3 Optimized result of the Response Surface Method calculated by Minitab software.

Independent variables				Response
T (ºC)	ρ (%)	h_1 (mm)	h_2 (mm)	y_{avg} (mm)
192	13	0.20	0.32	0.03

Table 3 shows the result of optimization obtained by using *Minitab* software where the minimum warping deformation, y_{avg} of 0.03mm was achieved. Sample of experimental with optimized parameter was proved the accuracy of the RSM and the optimization result where y_{avg} is equal to 0.04mm.

4. CONCLUSIONS

It is concluded that the optimum value for the independent variables are 192°C of layer temperature, 0.13% of fill density, 0.2mm of first layer height and 0.3mm of other layer height with minimum deformation of 0.03mm. The accuracy of RSM and optimization resulted a small percentages of error of are 33%.

REFERENCES

[1] W.Z. Wu, P. Geng, J. Zhao, Y. Zhang, D. W. Rosen and H. B. Zhang. "Manufacture and thermal deformation analysis of semicrystalline polymer polyether ether ketone by 3D printing," *Materials Research Innovations*, vol. 18, no. 5, pp. S5-12-S5-16, 2014.

[2] F. Ramli, M. Jailani, H. Unjar, M. Alkahari and M. Abdullah, "Integrated recycle system concept for low cost 3D-printer sustainability," in *Proceedings of Mechanical Engineering Research Day 2015*, 2015, pp. 77-78.

[3] A.H. Peng and X.M. Xiao, "Investigation on reasons inducing error and measures improving accuracy in fused deposition modelling," *Advances in Information Sciences and Service Sciences*, vol. 4 no.5, 2012

Dimensional inspection of 3D laser scanner, coordinate measuring machine and image processing

M.K. Sued[1,2,*], M.Z. Mohd Noh[1], M.F. Dimin[1,2]

[1] Faculty of Manufacturing Engineering, Universiti Teknikal Malaysia Melaka,
Hang Tuah Jaya, 76100 Durian Tunggal, Melaka, Malaysia
[2] Advanced Manufacturing Centre, Universiti Teknikal Malaysia Melaka,
Hang Tuah Jaya, 76100 Durian Tunggal, Melaka, Malaysia

[*]Corresponding e-mail: kamil@utem.edu.my

ABSTRACT – Measurement can be conducted either using contact or non-contact methods. Production components can be small, soft and fragile. Therefore a non-contact method such as 3D laser scanner is preferred due to no contact force and not affecting production time. This makes the technology tempting and has been widespread used by industries due to reverse engineering capability. However, the accuracy of the measurement is dependent on the quality of the digitization. Therefore, this study is to report dimensional measurement comparison between 3D laser scanner with a coordinate measuring machine (CMM) and image processing. The errors are calculated and the best measurement method is proposed. It is found that contact method using CMM produced the least error.

1. INTRODUCTION

Nowadays, measurements are quite demanding because of size and complexity of consumer products. In some cases parts can be flexible, soft and fragile thus, the contact methods are less significant compared to non-contact method. 3D laser scanner is one of the non-contact measuring methods. It is widely spread technology accepted by the industries because of the reverse engineering and prototyping capability. Additionally, the laser scanners in known to be fast compared to the contact methods. 3D laser scanner is able to produce 200 000 points/sec [1], while the CMM touch probe, it is stated to be around 400 to 2 000 points/sec [2]. Other technique of non-contact method is image processing using programming language such as Matlab. This method is well established which capable of producing accurate measurement. The technology is also low in cost which makes it a competitive technology. However, at current stage it has long processing time and limited capability. Image is lack of details and required high programming skills.

Therefore, 3D laser scanner is more preferred. However, all non-contact methods dependent on the quality of the digitisation which is strongly influence by surface quality, orientation and scanning depth [3-5]. It is very difficult to measure shiny and dark surfaces because diffuse reflection is needed in order to capture the projected laser line by the camera. The scanner has a limited field of view and can be easily affected by the geometries of the products such as angle feature. In the case of 3D laser scanner, false data points or no detection can be occurring. Therefore, the accuracy of the 3D laser scanner is found dependent to many factors [6].

It can be noted that each measurement technology has its own limitation. This study is to compare the best scanning strategies for 3D laser scanner and with other with other measuring methods that are CMM and image processing. This will provides clear identification of measurement accuracy which help practice engineer to select their measuring equipment suitable for their application.

2. METHODOLOGY

In this study, the workpiece used to be measured are 50mm gauge block and 32mm ring gauge. The first measurement method is by using CMM bridge type model LH54 manufactured by Wenzel. The second measurement method is conducted by using Faro Laser ScanArm V3 platinum 6 feet model. This is an articulated arm which has 3D laser scanner model attachment. The best scanning approached of the scanner has been explained in [3]. It is based on scanning angles and distances which are illustrated in Figure 1.
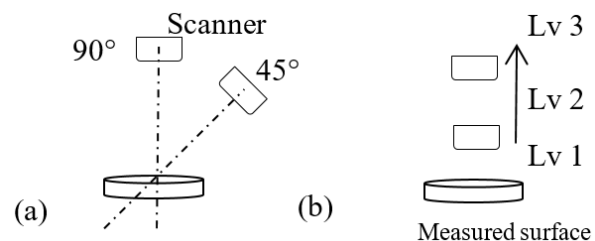
Figure 1 Scanning approach: (a) angle and (b) distance.

The test found that scanning at 45° at a distance of level 2 produced less error. Thus, in the empirical work this setting is adopted. Before scanning is performed, the workpiece is coated with a power based white coat. A light application of the coating is used in order to minimize the buildup error. In obtaining the dimension of the scan parts, Geomagic Studio and Qualify are used in facilitating and extracting the information captured by the scanner. In Geomagic Studio, the workpiece is digitized and editing can be done. In this study, the

editing is minimized by only removing isolated points, false reflection or scanning noise. After using the Geomagic studio, the edited scan image is then inspected by using Geomagic qualify in obtaining the dimensions. The measurement is done by using cross section plane cut through the clouds of points. The points which located on the cross section plane are then fit together by using best fit formula. Triplicate of cross section planes are selected at the interest area for the average measurements dimension value.

The third measurement method is the image processing using MATLAB software. Image is captured using 8 megapixel camera. A program has been developed using canny edge detection. The develop program consist of input selector, image converter from RGB format to Gray Scale format and from Gray Scale format to Black and White (BW), resizing, edge detection, feature extraction, and measurement element.

In each measurement methods, calibration was conducted before actual measurements are carried out. During the measurement, 30 readings are collected. Error is calculated by deducting the measured valued from the actual reading. The mean of error is the computed representing the errors produced by each method.

A simple test is also conducted by using the best approach of laser scanning to represent potential errors that can be produced when scanning complex production components.

3. RESULTS AND DISCUSSION

The error comparison is to determine the most accurate method. The minimum error is the value near to zero, and it's been used as a benchmark for determining the accuracy of measurement methods. Table 1 and Table 2 shows the measurement error of CMM, Geomagic and MATLAB program. For specimen gauge block size of 50mm, the error value of, CMM is -6.9µm, Geomagic is -298.3µm and MATLAB Develop Program is -3.3µm. The lowest displacement value is made by MATLAB, followed by CMM and Geomagic software.

Table 1 Measurement for 50mm gauge block.

Method	CMM	Geomagic	MATLAB
Error (mm)	-0.0069	-0.2983	-0.0033

Table 2 Measurement for 32mm ring gauge.

Method	CMM	Geomagic	MATLAB
Error (mm)	0.0019	-0.2981	-0.2387

However, for ring gauge specimen size of 32mm, the error value for CMM is 1.9 µm, Geomagic is -298.1µm and MATLAB is -238.7. The lowest displacement value is made by CMM, followed by MATLAB and Geomagic. This shows that, the image processing measurement is better than Geomagic software and comparable with the CMM measurement.

Further testing is then conducted for scanning complete object using the best scanning approach. Figure 2 shows the results that typically used for reverse engineering. It can be clearly seen that incomplete

scanning and noise can be present in the results. This reduces the accuracy of the laser scanner due to no detection or false detection occurred. Although this result can be acceptable for this type of application due to lost information can be built using the software, but it is required to be aware by practice engineer that the size produced will be not accurate as the actual components. In [6] the researcher has identified the error propagation that can be present in the measurement of 3D laser scanner. This explains the reason of manufacturer specification accuracy could not be achieved.
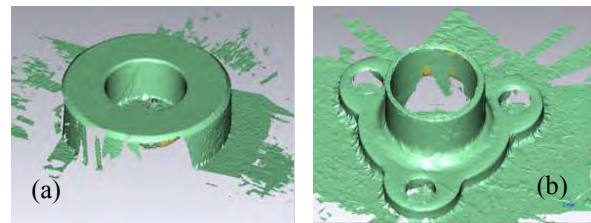
Figure 2 Scanning results: (a) incomplete scan (b) noise.

4. SUMMARY

The work has presented measurement attempt by using different measuring methods. 3D laser scanner is found to produce the highest error, but repeatable, although different complexities of workpieces were used. This is as expected due to the potential of many factors affecting the measurements compared to contact method. Factors like edge features, reflectivity, deep features can affect the registered points. The error recorded is higher than the specified by the manufacturer thus, practice engineer should expect that results for real application. It can be concluding that contact method that is using CMM produced the least error followed by image processing in Matlab.

REFERENCES

[1] Nikon Metrology "3D laser scanning accelerates design-through-manufacturing by providing full geometry feedback",http://www.nikonmetrology. com/en_EU/Products/Laser-Scanning/ (December 2015).

[2] W. Jinwen, C. Yanling,"The geometric dynamic errors of CMMs in fast scanning-probing", *Measurement,* vol. 44, no.3, pp. 511-517, 2011.

[3] M.K. Sued, T. Paul and P.A. Perumal, "The evaluation study on FaroArm laser scanner", *International Conference on Design and Concurrent Engineering*, 20-21 September 2010.

[4] M.K. Sued and S. Mekid, "Dimensional inspection of small and mesoscale components using laser scanner", *International Conference on Advances in Mechanical Engineering,* 16 – 18 November 2009.

[5] N.V. Gastel, S. Cuypers, P. Bleys and J.P. Kruth, "A Performance Evaluation Test for Laser Line Scanners on CMMs", *Optics and Lasers in Engineering*, vol. 47, no. 3-4, pp. 336 – 342, 2009.

[6] S. Mekid and H.D. Luna, "Error propagation in laser scanning of dimensional metrology", *International Journal of Metrology*, vol. 14, no. 2, pp.44-50, 2007.

Studying air flow distribution in a tray dryer through CFD simulation

S. Misha[1,2,*], S. Mat[3], M.H. Ruslan[3], E. Salleh[3], K. Sopian[3]

[1] Faculty of Mechanical Engineering, Universiti Teknikal Malaysia Melaka,
Hang Tuah Jaya, 76100 Durian Tunggal, Melaka, Malaysia
[2] Centre for Advanced Research on Energy, Universiti Teknikal Malaysia Melaka,
Hang Tuah Jaya, 76100 Durian Tunggal, Melaka, Malaysia
[3] Solar Energy Research Institute, Universiti Kebangsaan Malaysia,
43600 UKM Bangi, Selangor, Malaysia

*Corresponding e-mail: suhaimimisha@utem.edu.my

Keywords: Tray dryer; drying simulation

ABSTRACT – Application of tray dryer is widely used in agricultural drying because of its simple design and capability to dry products at high volume. However, the greatest drawback of the tray dryer is uneven drying because of poor airflow distribution in the drying chamber. Implementing the proper design of a tray dryer system may eliminate or reduce non-uniformity of drying and improves drying performance. This study investigates kenaf core drying uniformity in a tray dryer through Computational Fluid Dynamics (CFD) simulation. The result shows that, the higher the average air velocity above the product, the higher the drying rate.

1. INTRODUCTION

Tray dryers are the most widely used dryers for various drying applications because of their simple design and low cost. Generally, a tray dryer consists of several stacks of trays placed in an insulated chamber in which hot air is distributed by a fan or natural flow. The uniformity of airflow distribution over the trays is crucial to obtain uniform product quality. The variation of the final moisture content of the dried product at different tray positions is commonly encountered because of poor airflow distribution [1]. Generally, drying air temperature and velocity significantly affect drying rate [2,3].

Measuring the drying parameters in the drying chamber is expensive, difficult, and time consuming because sensors and data loggers have to be installed in several positions, particularly in a large-scale dryer. Therefore, CFD simulation is used extensively in drying analysis because of its ability to solve systems of differential equations for the conservation of mass, momentum, and energy with the use of advanced numerical methods to predict temperature, velocity, and pressure profiles in the drying chamber

2. METHOD AND SIMULATION

The industrial scale of solar assisted solid desiccant dryer was designed and developed to investigate system performance and drying uniformity in the drying chamber. The experiment setup has been discussed by Misha et al. [4]. The details experimental setup was not discussed in this paper since the focus of

this paper to study the airflow distribution in the drying chamber. Kenaf core was used as a sample for drying.

The design of the drying chamber is shown in Figure 1, and includes seven layers of trays, with each layer comprising six trays with dimensions of 64 cm x 92 cm each, for a total of 42 trays. The drying chamber is designed symmetrically from the top view. The sensors are installed only at the right side, assuming that values from the left side are the same, owing to this symmetry. The volume of the drying chamber is 1.7 m (height) x 2 m (width) x 3 m (length). The wall of the dryer system was constructed using 6-cm thick hollow polycarbonate with a hollow space in the middle, 4 cm deep. The top roof is made of glass.
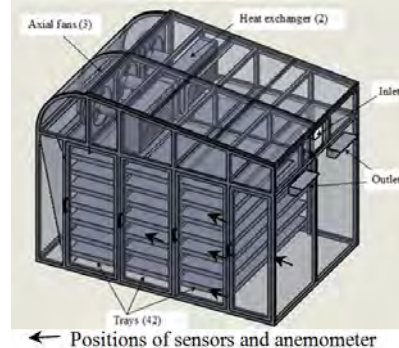
Figure 1 Drying chamber.

The numerical finite volume method used in Fluent 14.0 was used to build a numerical model based on an unstructured 3D mesh using tetrahedral cells. The boundary conditions were set up as follows (Figure 2):

- Inlet 1: The air mass flow rate was 0.58 kg/s (3 m/s), and the air temperature was 44 °C.
- Inlet 2: The air mass flow rate was 0.29 kg/s, and the air temperature was 44 °C.
- Outlet: The gauge pressure was assumed to be equal to 0 at the outlet.
- Porous media: The trays were assumed to be porous with 10% porosity.
- Wall: The heat transfer coefficient of the chamber wall is 4 W/(m^2.K). The environmental temperature is 32 °C, and the temperature at the top roof is 38 °C. The bottom surface was assumed no heat loss. Only half of the drying chamber was analyzed.

Figure 2 Boundary condition.

Figure 3 Drying rate against velocity from simulation.
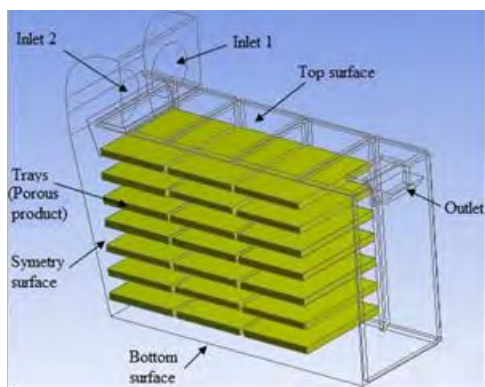
3. RESULTS AND DISCUSSION

Seven positions in the drying chamber were installed with anemometer to validate the CFD simulation. The simulation values for all points were within the range of anemometer accuracy. Therefore, the simulation results are highly consistent with the experimental data. A plane was created 2 cm above each tray to find the average air velocity for each tray. The velocity at this region was necessary to carry the moisture from the product. In general, as the air velocity increased, the drying rate also increased. The drying rate of the product at trays 4, 9, 11, 13, and 18 was determined. The graph in Figure 3 shows the drying rate and velocity from the simulation data. A strong correlation existed between drying rate and air velocity. The straight line represents the relation between these two parameters. The equation for the straight line is given by:

$$y = 0.527x + 0.029 \qquad (1)$$

Where y is the predicted drying rate and x is the air velocity from the simulation result.

The graph in Figure 4 shows the air velocity from the simulation and the predicted drying rate. The simulation result shows that the 0.24 m/s air velocity above tray 18 was the lowest, and that the drying rate in this region was 0.15 kg/h. The highest air velocity was at tray 1 because of the additional baffle that channels the air to the top tray. Without the baffle, less air was channeled to the top tray and lower air velocity was produced. The simulation without an additional baffle was conducted to predict air flow. The 3D simulation result of the air stream is shown in Figure 5.

4. CONCLUSIONS

CFD simulation was used to predict air flow distribution in the drying chamber by considering the product as porous media. The experimental and simulation data were in excellent agreement. The average air velocity above each tray was predicted through simulation. The drying rate of the product was found to be significantly influenced by the average air velocity above the tray, which carried moisture away from the product. In view of the correlation between the experimental and simulation results, the uniformity of the drying for the products at different levels but at the same column was considered acceptable.
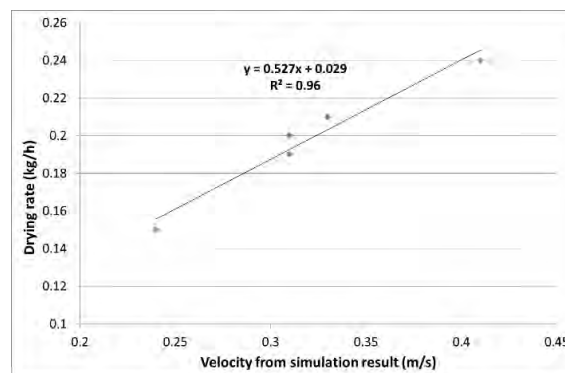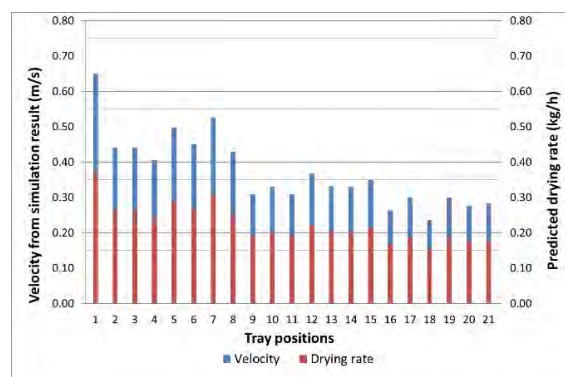
Figure 4 Velocity from simulation and drying rate.
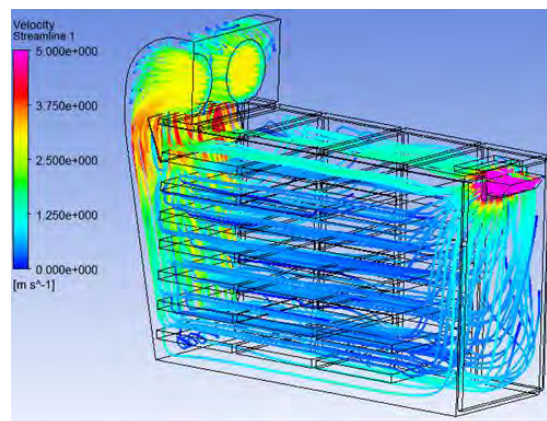
Figure 5 Streamline in the drying chamber.

REFERENCES

[1] S. Misha, S. Mat, M.H. Ruslan, K. Sopian and E. Salleh, "Review on the Application of a Tray Dryer System for Agricultural Products," *World Applied Sciences Journal*, vol. 22, no. 3, pp. 424–433, 2013.

[2] F. Pinaga, A. Mulet, A. Berna and M. Borras, "Effect of air flow rate on carrot drying," *Drying Technology*, vol. 5, no. 2, pp. 245–258, 1987.

[3] V.G. Belessiotis, and V.T. Karathanos, "Sun and artificial air drying kinetics of some agricultural products," *Journal of Food Engineering*, vol. 31, no. 1, pp. 35–46, 1997.

[4] S. Misha, S. Mat, M.H. Ruslan, E. Salleh, and K. Sopian, "Performance of a solar assisted solid desiccant dryer for kenaf core fiber drying under low solar radiation," *Solar Energy*, no. 112, pp. 194-204, 2015.

Evaluation of impact based energy harvesting using a piezoelectric ceramic disc

Ali Mohammed abdal-Kadhim, Kok Swee Leong[*]

Faculty of Electronic and Computer Engineering, Universiti Teknikal Malaysia Melaka,
76100 Durian Tunggal, Melaka, Malaysia

*Corresponding e-mail: sweeleong@utem.edu.my

Keywords: Piezoceramic application; impact to electrical energy transformer; energy scavenging

ABSTRACT - This paper reports an impact based energy harvesting using a piezoelectric ceramic disc, whereby a useful electrical power is generated via the impact of the human weight on the piezoelectric plate transducer. A prototyping of a single human step piezoelectric plate based impact harvester consisting of a piezoelectric transducer was tested on a hydraulic pressing machine with variable forces and impact velocity. In this experiment a piezoelectric ceramic disc with a size of pallet 44mm in diameter and 10mm in thickness was able to generate an average output power of up to 14.5µW across a resistive load of 500KΩ when a force of 0.75 kN of force with a velocity of 600mm/min is applied on it.

1. INTRODUCTION

Energy harvesting using piezoelectric has attracted many interest as a meant for powering up low-power electronic devices which have been reported but mainly in harvesting energy from both vibration sources [1,2]. These offer an advantage for systems in which battery replacement is challenging which limiting the system's life time. Kinetic energies derive from vibration as well as impact are ubiquitous from ambient environment which can easily be found from available energy sources, such as in industrial environments, transportations, and human life activities which has led to rapid development of energy harvesters to scavenge energy from vibration/impact for the past few years. Commonly, there are four types of transduction mechanisms which are suitable for vibrations are electromagnetic, electrostatic, magnetostriction and piezoelectric. Among these energy harvesters, piezoelectric have received more attention because it has the ability of converting the kinetic energy into useful electrical energy with high power density and high conversion efficiency. Beside that it is able to be miniaturized with simple structure and mass manufacturability [3]

However, compared to the vibration or resonance type piezoelectric generation mechanism, the impact type is not broadly available due to its low interaction chances with external impact and hence generating less averaging electrical power and therefore this paper objective is to evaluate the performance of a piezoelectric ceramic disc when an average human weight is applied on the device.

Recently, mechanical to electrical energy conversion technique based on impact, have been investigated in [4]. Amat and Bunji in [5] presents a study to characterize the effect of two mechanical impact parameters (velocity and mass) on impact mode piezoelectric power generation, they have been proven that the instantaneous output voltage is proportional to the impact velocity and for output power it is in a straight line relationship with the same parameter. For this paper, a series of experiments has been conducted to evaluate the amount of voltage and power generated via piezoelectric ceramic disc when it is excited by different forces and velocity.

2. EXPERIMENT SET-UP

For the experiment a human single step piezoelectric generator prototype is designed as shown in Figure 1.
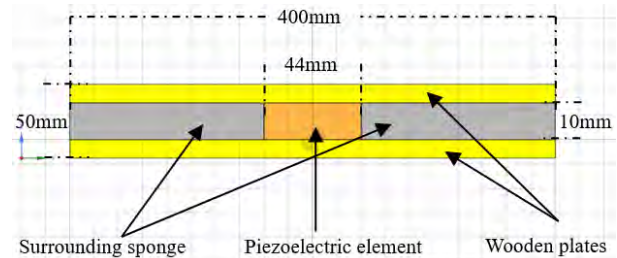
Figure 1 Schematic diagram of a human single step piezoelectric generator prototype.

The construction of the human single step prototype consisted of a piezoelectric ceramic disc with a diameter of 44mm and thickness of 10mm was sandwiched between two wooden plates, surrounded by a sponge, and then covered with a nylon in order to make it more compact and prevent it to be smashed by excessive mechanical load. The final measurement of the prototype is 400mm diameter by 50mm height.

Various impacts/velocities were generated by using AUTOGRAPH AG-I 100KN hydraulic pressing machine to simulate a single human step as shown in Figure 2.

3. EXPERIMENTAL RESULTS AND DISCUSSION

An AC voltage generated from the single step prototype is being measured with varying velocity with a fixed amount of applied impact force of 0.5KN. The peak-to-peak AC voltage shows an exponential

increment as the velocity of the force is increased as shown in Figure 3. An AC peak-to-peak voltage of 27 V is recorded when the speed of the force is at 1000mm/min.
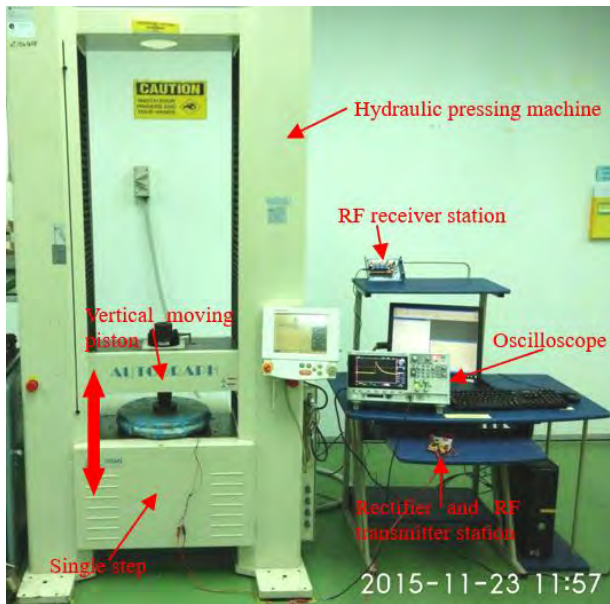
Figure 2 Experimental setup.
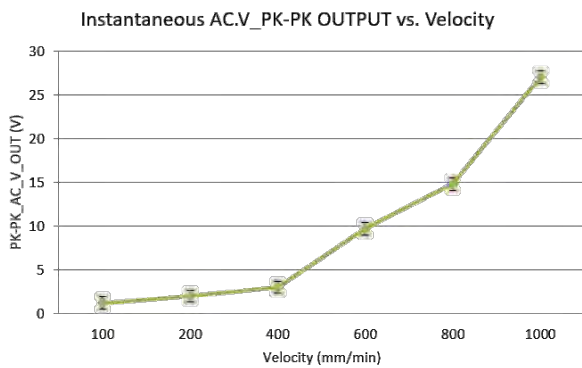
Figure 3 Instantaneous AC.V_PK-PK OUTPUT vs. velocity.

Next experiment is varying the amount of force up to 3 kN at a fixed velocity at 700mm/min. A voltage of 16 V is being measured when 3 kN of force is being applied to the prototype as shown in Figure 4. Figure 5 shows the electrical output power and electrical output current when the output terminal of the piezoelectric is connected to a series of external electrical resistive loads. The force is fixed at 0.75 kN mimicking an average human weight. A maximum output power of 14.5 µW is being measured across an external load of 500 kΩ while the maximum current is measured at around 12 µA when connected to an external resistive load of 65 kΩ.

4.   CONCLUSION

A human single step prototype based on a piezoelectric powered device has been presented. It shows a potential of powering low electrical devices with a power of 14.5 µW.
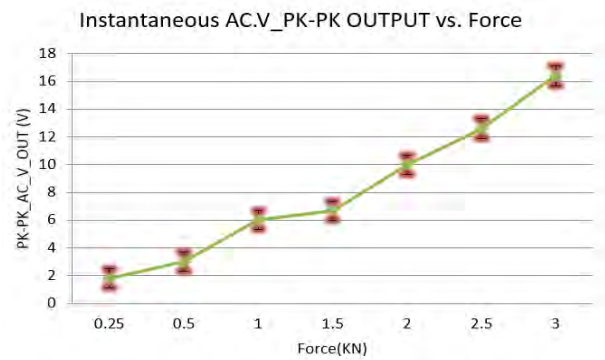
Figure 4 Instantaneous AC.V_PK-PK OUTPUT vs. force.
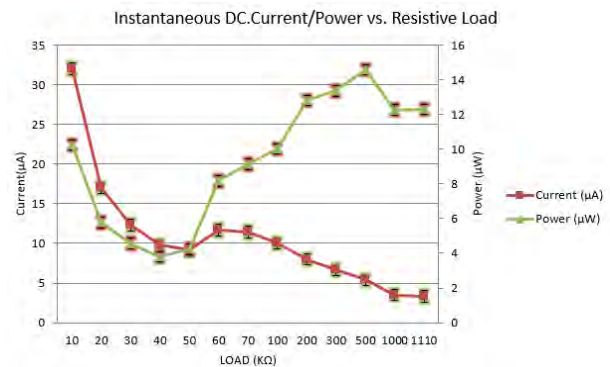
Figure 5 Instantaneous DC.V Current and Power vs. Resistive load.

REFERENCES

[1] D.F. Berdy, B. Jung, J.F. Rhoads, D. Peroulis, "Wide-bandwidth, meandering vibration energy harvester with distributed circuit board inertial mass", *Sens. Actuators A*, Vol. 188, pp. 148-157, 2012.

[2] D. Zhu, M.J. Tudor, S.P. Beeby, "Strategies for increasing the operating frequency range of vibration energy harvesters: a review". *Meas. Sci. Technol*, Vol.21 (2), 022001, pp. 29, 2010.

[3] S. Roundy, P.K. Wright, "A piezoelectric vibration based generator for wireless electronics", *SmartMater. Struct.*, Vol.13, pp. 1131-1142, 2004.

[4] M. Ferrari, M. Baù, F. Cerini, V. Ferrari, "Impact-Enhanced Multi-Beam Piezoelectric Converter for Energy Harvesting in Autonomous Sensors", in *Procedia Engineering*, Vol. 47, pp. 418-421, 2012.

[5] A.B. Amat, H. Bunji, K. Suto, et al, "Evaluation on mechanical impact parameters in piezoelectric power generation", *10th Asian Control Conference* (ASCC), 2015.

Performance analysis of portable power generator by using TEG module

Siti Halma Johari[*], Mohd Faiz Che Pa, Khalil Azha Mohd Annuar, Suziana Ahmad, Madiha Zahari

Faculty of Engineering Technology, Universiti Teknikal Malaysia Melaka,
Hang Tuah Jaya, 76100 Durian Tunggal, Melaka, Malaysia

[*]Corresponding e-mail: siti.halma@utem.edu.my

ABSTRACT – This paper presents the development of portable thermoelectric power generator by using heat as a main source. The aimed groups of this project are hikers and campers those need a portable power generator that can charge their small electronic gadgets while doing their activity. The generation of electricity is based on the Seebeck Effect of Thermoelectric Generator (TEG) module. The developed power generator is consisting of TEG module, heatsink and boost converter. The hot side of the TEG module was mounted on an opposite of the heat source. Then, the heatsink is installed on the cold side of the module with a cooling fans to provide a forced air cooling. Boost converters are used to step up and constant the output voltage from TEG module. Result from the experiment shows that the power generator can produce constant output voltage of 5V and the handphone was successfully charged. This portable power generator can be an alternative power supply while the power source cannot be reached.

1. INTRODUCTION

In present times, small electronic gadgets such as smartphone, camera, GPS device and others become a widely deployed and useful tools. The limitations of these gadgets are power reserve where the battery of these gadgets cannot stand for a long time when it was used extensively. This become a major problem for people who always go out for camping trips, hiking or backpacking. The foundation of the thermoelectric generator (TEG) is based on the Seebeck effect which was discovered by Thomas Seebeck in 1821. Thermoelectric energy production which is one of the many processes of changing heat flow directly into electrical energy, promises a long life working without maintenance due to its reliability, silence, simplicity and the non-existence of moving parts [1]. Applying this TE effect enables thermal energy in waste heat to be converted into electrical energy so as to retrieve the energy [2]. For any type of TEG employed, the output increases depending upon the clamping force in addition to maximum permissible temperature gradient Peltier effect is the existence of cooling or heating at a junction of two different conductors [3]. An electric current is generated in the two dissimilar materials by the Peltier effect as long as one of the two temperature reservoirs are hotter than the other [4].

2. METHODOLOGY

Bunsen burner was used to generate heat energy as shown in Figure 1. This heat energy will be converted into an electrical energy by using a peltier or TEG module. Then, thermoelectricity, seebeck effect and peltier effect was applied where the process involved in the operation of device is related to the project development. After that, the input of DC boost converter circuit is connected to the output wire of TEG module to step up and maintain the voltage and current generated by the TEG module. Figure 2 demonstrates the testing setup to charge a handphone using portable power generator.

Figure 1 Heating process.

Figure 2 Testing setup to charge a handphone.

3. RESULTS AND DISCUSSION

Figure 3 and 4 show the relationship between current and voltage against the temperature. Both graph

displays that each current and voltage is directly proportional with the temperature. For Figure 3, the current is increasing as the temperature is increased until it reached 90˚C then the current remains constant at 700mA up to 139˚C.
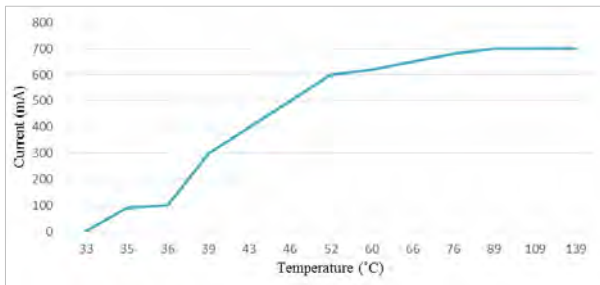
Figure 3 TEG Module Output (Current Vs Temperature).

In Figure 4, the voltage also increases when the temperature is increased. When the temperature reached 139˚C, the voltage measured is 3.31V. The maximum output voltage can reach up to 5.6V based on the explanation in the TEG module datasheet.
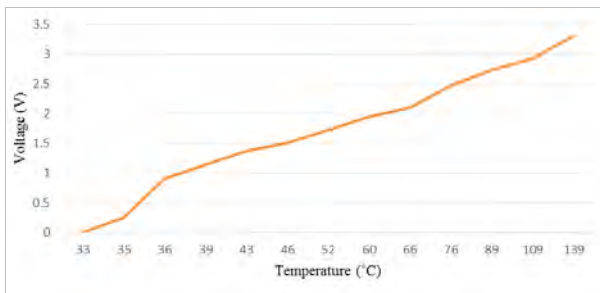
Figure 4 TEG module output (voltage vs. temperature).

The output voltage measured from TEG module will boost up the voltage until 5V. The purpose of getting 5V is used to charge a mobile handphone. Figure 5 and 6 show the current and voltage output of boost converter reacts with the temperature. In Figure 5, the current increases when the temperature is greater than 36˚C and become constant at 400mA after 46˚C. The current remains even the temperature is risen up and reach 139˚C. In Figure 6, shows that the voltage is boosted up to 5V after the TEG module being heated just up to 39˚C. And the voltage remains stable even the temperature is still increasing up to 139˚C.
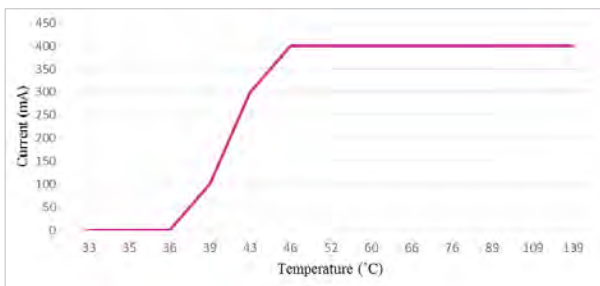
Figure 5 Boost converter output (current vs. temperature).
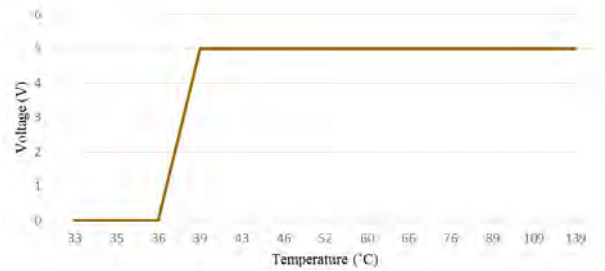
Figure 6 Boost converter output (voltage vs. temperature).

4. CONCLUSIONS

This research is conducted to examine bunsen burner and others thermal source is effective enough to be use to generate an electricity. The voltage produced by the thermal energy reaction is enough to generate a small electricity with value in the range of 1V – 3.75V. From the analysis, the voltage and current is directly proportional with temperature. For the power generated, the TEG module produced more power the longer it being exposed to the heat. Then, the boost converter used to achieve the desired voltage 5V and stabilize the voltage to constant and able to use charge a small gadget.

REFERENCES

[1] J.A.B. Vieira and A.M. Mota, "Thermoelectric generator using water gas heater energy for battery charging," *2009 IEEE Int. Conf. Control Appl.*, pp. 1477–1482, 2009.

[2] I. Biológico, "Efficient Reuse of Waste Energy," *IEEE Nanotechnol. Mag.*, no. June, pp. 28–33, 2009.

[3] A.A. Anitha and J. Jayakumar, "Analysis of (Bi 2 Te 3 -PbTe) hybrid thermoelectric generator for effective power generation," *IEEE Spons. 2nd Int. Conf. Innov. Inf. Embed. Commun. Syst. ICIIECS'15*, 2015.

[4] G.L. Solbrekken, K. Yazawa and A. Bar-Cohen, "Thermal management of portable electronic equipment using thermoelectric energy conversion," *Ninth Intersoc. Conf. Therm. Thermomechanical Phenom. Electron. Syst. (IEEE Cat. No.04CH37543)*, pp. 276–283, 2004.

Peltier and seebeck efficacy of hot and cold air system for portable O-REF (oven & refrigerator) application

M.H. Harun[1,*], K.A.M. Annuar[1], M.F.M.A. Halim[1], M.H.C. Hasan[1], M.S.M. Aras[2], M.F. Yaakub[1]

1) Faculty of Engineering Technology, Universiti Teknikal Malaysia Melaka,
Hang Tuah Jaya, 76100 Durian Tunggal, Melaka, Malaysia
2) Faculty of Electrical Engineering, Universiti Teknikal Malaysia Melaka,
Hang Tuah Jaya, 76100 Durian Tunggal, Melaka, Malaysia

*Corresponding e-mail: haniff@utem.edu.my

Keywords: Seebeck effect; peltier effect; thermo-electric heat pump

ABSTRACT – The main motivation in using Peltier Module is due to the uniqueness of producing hot and cold air at the same time besides able to generate electricity using Seebeck Effect. The generating system theoretically can recycle the heat loss to produce additional electricity for other usage. The efficacy of this system tested using two types of experimental using Peltier and Seebeck Effect. Both experimental is conducted using 3 specific volumes; 1) $1000cm^3$; 2) $4000cm^3$; and 3) $9000cm^3$. As a result, temperature for heating and cooling systems achieve around $14 – 56°C$ while the voltage generated around 12V in 50 minutes.

1. INTRODUCTION

Thermoelectric refrigeration is achieved when a direct current is passed through one or more pairs of n- and p-type of semiconductor materials. Figure 1 is a diagram of a single pair consisting of n- and p-type semiconductor materials. In the cooling mode, direct current is allowed to passes through n and p junction of a semiconductor material. The temperature, denoted as T_C (Cold Temperature) of the interconnecting conductor is decreased while heat is absorbed from the environment. This heat absorption from the environment (cooling) occurs when electrons pass from a low energy level in the p-type material through the interconnecting conductor to a higher energy level in the n-type material. The absorbed heat is transferred through the semiconductor materials through electrons to the other end of the junction, denoted as T_H (Hot Temperature) where the electron are liberated once it return to a lower energy level in the p-type material. This phenomenon is called the Peltier effect [1-3].

A second phenomenon is also important in thermoelectric refrigeration known as Seebeck Effect. When a temperature differential is established between the hot and cold ends of the semiconductor material, a voltage is generated. This voltage is called the Seebeck voltage, and it is directly proportional to the temperature differential. The constant of proportionality is referred to as the Seebeck coefficient.

The Peltier effect is controlled by the Peltier coefficient, defined as the product of Seebeck coefficient of the semiconductor material and the absolute temperature. The Peltier coefficient relates to a cooling effect as current passes through the semiconductor junction n to p, and a heating effect when current passes through p to n junction, as shown in Figure 1. Reversing the direction of the current reverses the temperature of the hot and cold ends [2].
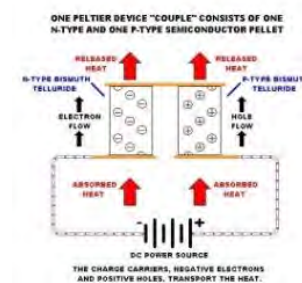
Figure 1 Schematic of thermoelectric module operation for cooling and heating.

2. METHODOLOGY

The Peltier effect is being measured using several volumes which are 1000 cm³, 4000 cm³ and 9000 cm³ by making partition on the area of the product as shown in Figure 2. The Peltier cells inside is cold so small heat sink unit is mounted at the cold side of the Peltier cells to increase the rate of releasing heat outside of unit. Heat sink is simulated using Comsole Multiphysics to study the fin arrangement in order to optimize heat transfer area [4-5]. The blower fan attach to the heat sink has the role to distribute the cold air equally at maximum rate in the container.

Figure 2 Portable O-REF System.

The temperature of the Peltier cell inside is high so small heat sink is mounted on top of the hot side of the Peltier cells to increase absorption rate of heat from the unit. The blower fan attach to the heat sink has the role to distribute the hot air equally at maximum rate within

the container. The other function of the blower fan is to circulate the hot air so that the hot temperature within the within the container remains hot.

By generating the hot and cold temperature, the heat transfer occur in the system can be used for generating current using Seebeck Effect that when the junctions of two different metals are maintained at different temperature, the emf is produced in the circuit. Thermoelectric power generation (TEG) devices typically use special semiconductor materials, which are optimized for the Seebeck Effect.

By referring to Peltier electric generating calculation, the potential electricity generated by the Peltier device can be calculated by,

$$V = \alpha(T_h - T_c) \tag{1}$$

Where

V = Thermoelectric material figure of merit
α = Seebeck coefficient
T_h = Temperature at hot side
T_c = Temperature at cold side

The Seebeck coefficient can be calculated by,

$$\alpha = \frac{\overline{x}V}{\overline{x}T} \tag{2}$$

Where

$\overline{x}V$ = average voltage generated
$\overline{x}T$ = average temperature difference

The magnitudes of voltage generated are affected by the temperature difference 1 °C across the Peltier device, as stated the Seebeck effect. Material with high Seebeck effect is the main factor to increase the efficiency of the Peltier device.

3.   RESULTS AND DISCUSSION

Generally, from the result obtained as shown in Figure 3 that the system can achieve about 14°C for cold system and about 56°C for hot system which enables it for operating in both conditions. From the result, it shows that The Peltier devices itself is dominant to hot temperature, apart from this to spreading the hot temperature within the container is faster compare to cold temperature.

For the Seebeck operation, the data used to use the temperature difference from small container generate the Seebeck coefficient, α=302 mV/ °C. Table 1 shows the relationship between temperature differences with Seebeck coefficient.

According to the result, it shows that the calculated and measured voltages are almost the same that makes this system able to generate power in order to recharging back the battery.

4.   CONCLUSIONS

In conclusion, Portable OREF System can be used in dual mode operation, heating and cooling also can generate electricity using heat transfer occur in the system. This system achieves minimum temperature 14°C and maximum around 56°C and maximum voltage occur in 50 minutes.
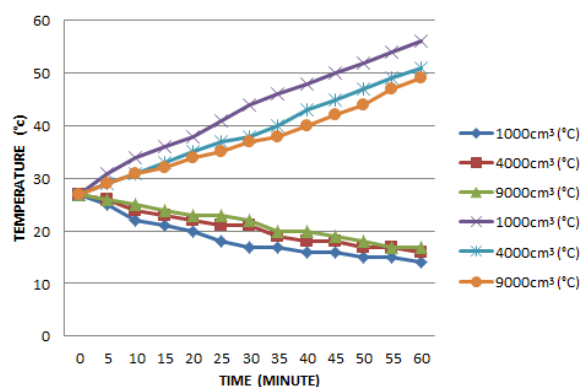
Figure 3 Graph temperature versus time for hot and cold testing in an hour.

Table 1 Result from Seebeck coefficient, α.

Time (min)	$T_{Difference}$ (°C)	$V_{Calculated}$ (V)	$V_{Measured}$ (V)
5	6	1.81	1.67
10	12	3.62	2.84
15	15	4.53	4.16
20	18	5.44	5.37
25	23	6.95	6.08
30	27	8.15	7.59
35	29	8.76	8.36
40	32	9.66	9.76
45	34	10.27	11.24
50	37	11.17	12.24
55	39	11.78	12.76
60	42	12.68	12.76

REFERENCES

[1]   S.B. Riffat and X. Ma, "Thermoelectrics: a review of present and potential applications." *Applied Thermal Engineering*, vol. 23(8), pp. 913-935. 2003.

[2]   S. Mukhopadhyay, S.P. Datta, et al. "Performance of an off-board test rig for an automotive air conditioning system." *International Journal Of Air-Conditioning And Refrigeration*, vol. 21(03), 2014.

[3]   X. Gou, H. Xiao, et al. "Modeling, experimental study and optimization on low-temperature waste heat thermoelectric generator system." *Applied Energy*, vol.87(10), pp. 3131-3136, 2010.

[4]   K.A.M. Annuar, F.S. Ismail, M.H. Harun and M.F. M.A. Halim, "Inline pin fin heat sink model and thermal performance analysis for central processing unit," in *Proceedings of Mechanical Engineering Research Day 2015*, 2015, pp. 35-36.

[5]   K.A.M. Annuar, M.F.M A. Halim, F.S. Ismail, M. Zahari, S.H. Johari and M.H. Harun, "Thermal analysis of staggered pin fin heat sink for central processing unit" *Australian Journal of Basic and Applied Sciences*, vol.9(19), pp. 68-73, 2015.

Potential co-processing of coconut shell and sugarcane residue as a solid biofuel

Nona Merry M. Mitan[1,*], Mohd Nur Shafiq Ahmad Razimi[2]

1) Faculty of Engineering Technology, Universiti Teknikal Malaysia Melaka,
Hang Tuah Jaya, 76100 Durian Tunggal, Melaka, Malaysia
2) Department of Mechanical Engineering, University of Malaya,
50603, Kuala Lumpur, Malaysia

*Corresponding e-mail: nona.merry@utem.edu.my

Keywords: Briquette; coconut shell; sugarcane residue

ABSTRACT – This research reported co-processing of coconut shell and sugarcane residue as a solid biofuel by briquetting process. The aim of the current research is to determine the optimum ratio between coconut shell and sugarcane residue for briquetting. Various ratios of coconut shell to sugarcane are 1:1, 1:3, 1:5 by weight. The briquettes were formed into cylindrical shapes. The carbonization process took place at 370℃. Proximate analysis, compressive test and theoretical heating value are observed on the produced briquette. The results indicated that C 1:5 briquette has the lowest moisture content and highest theoretical heating value.

1. INTRODUCTION

Biomass energy has received attention from entire world since the energy crisis in the mid-1970s. The research and development regarding this type of energy have been done widely. As a store sun energy, biomass gives economical and environmental benefits.

Ferńandez et al. [1] stated that biomass has several advantages compared to fossil fuel which is produce much lower NO_x and SO_2 emission to the atmosphere than fossil fuel. However, the carbon composition in biomass is lower than coal which is result in lower heating value. Furthermore, the volatile content of lignocellulosic fuels (80-90%) is twice than coal.

In coconut, about 15-20% part of coconut is coconut shell which is mainly consists of carbohydrates component such as cellulose, hemicelluloses and lignin. Coconut shell is classified as a hard lignocellulosic. The higher carbon content in coconut shell is making it suitable to be used in charcoal production [2].

Sugarcane is a potential source of ethanol and sugar. The by-product of sugarcane such as bagasse consists of 54.3 % of cellulose, 29.7 % of hemicelluloses and 24.4 % of lignin [3].

As agricultural waste, coconut shell and sugarcane have significant amount of hemicelluloses, cellulose and lignin which are potential to convert it as biofuel. The utilization of these types of biomass is seen as solution to reduce the waste disposal. Therefore, the main focus of this research is to modify these agricultural residues in order to obtain appropriate ratio for producing high quality of briquette. It is expected that this results will be useful in treatment of coconut shell and sugarcane residue as an energy source.

2. METHODOLOGY

2.1 Preparation of coconut shell and sugarcane bagasse samples

The raw materials of coconut shell (CS) and sugarcane residue (S) waste were obtained from Malacca area. The samples are first cleaned before crushing into smaller pieces.

The crushed coconut shell is dried at 104°C for 24 hours while crushed sugarcane undergone drying process at 70°C for 8 hours in a conventional oven. The dried samples were milled by a centrifugal milling machine (Retsch ZM 200) with 0.75 mm of mesh size. Furthermore, the milled samples were carbonized in the electrical furnace at 370°C for 60 min.

In briquetting process, the carbonized samples are separated into three ratios as shown in Table 1. The CS and S were mixed physically until homogeneous mixture formed. 10.0 g of carbonized samples with decided ratio were densified into briquette with cylindrical mould by hydraulic press (Hsin-Chi Machinery HL 200). The mould has inner diameter of 35 mm and 10 mm of thickness.

Table 1 Ratio of coconut shell (CS) and sugarcane residue (S).

Ratio	CS (g)	S (g)	Sample codes	
			Non-carbonization	Carbonization
1:1	5.0	5.0	NC 1:1	C 1:1
1:3	2.5	7.5	NC 1:3	C 1:3
1:5	1.7	8.3	NC 1:5	C 1:5

2.2 Characterization of the coconut shell-sugarcane (CSS) briquette

A proximate analysis of CSS was conducted to determine the moisture content, volatile matter, ash content and fixed carbon. These analyses were carried out according to the American Society for Testing Materials (ASTM) D 3173-03, ASTM D 3174-02 and ASTM D 3175-02 standards [4]. Total organic matter is obtained by deduction the ash content from dry basis. The heating value of CSS briquette was estimated

theoretically based on established Equation (1) founded by Erol et. al. [5]. To determine the compressive strength of briquette, compressive test is performed with Universal Testing Machine Instron 5583.

$$NHV = -116 - 1.33[Ash] - 0.005[VM] + 1.92[VM+Ash] - 0.0227[VM \times Ash] - 0.0122[VM]^2 + 0.0299[Ash]^2 + 6133[OM]^{-1} - 0.82[Ash]^{-1} \qquad (1)$$

3. RESULTS AND DISCUSSION

Figure 1 provides the proximate analysis of CSS briquette. Proximate analysis covers the volatile matter, fixed carbon, moisture and ash content.

Volatile matter is gaseous products which is releasing during combustion. Both carbonized and non carbonized briquettes have almost constant value of volatile matter. The higher volatile matter content in briquette will produce more smoke during burning

The value of fixed carbon from NC and C briquettes is increasing with increasing the ratio as well. The C briquettes have fixed carbon values vary from 13.12, 13.90 and 14.25 % for C 1:1, C 1:3 and C 1:5 respectively.

It is crucial to determine the moisture content of the briquette sample because the moisture content affect quality of the produced briquette. The value of moisture content is decreasing when the ratio of coconut shell and sugarcane is increasing. It was found that the carbonization and non carbonization process affects the moisture content in briquette. The moisture content of carbonized samples is lower than non-carbonized samples. The highest moisture content was founded in NC 1:1 briquette (8.4 %).
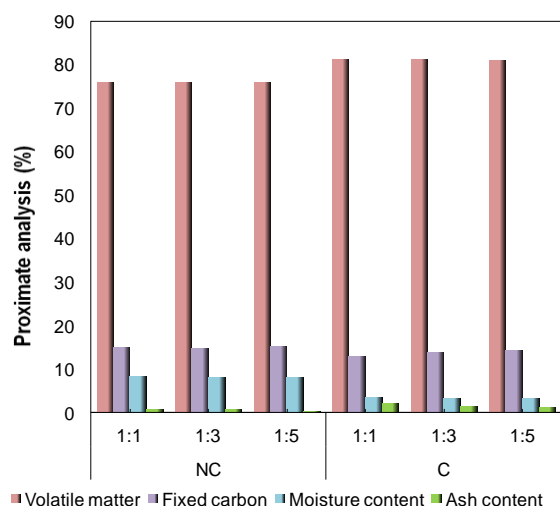
Table 2 Compressive test and theoretical value results of CSS briquettes.

Samples	Theoretical heating value (MJ/kg)	Compressive strength (kN)
NC 1:1	18.98	NA
NC 1:3	18.94	NA
NC 1:5	18.39	NA
C 1:1	18.80	18.20
C 1:3	18.97	10.60
C 1:5	19.00	10.30

Ash play important role in determining the quality of produced briquette. Ash content is the remaining residue that left after combustion and does not have any carbon content. Ash content for both carbonized and non-carbonized shows decreasing value as the ratio coconut shell is increasing in the briquette About 2.12 % of ash content in C 1:1 and the value is decreasing to 1.18 % for C 1:5. Moreover, the NC 1:5 has the lowest ash content.

In order to obtain the higher heating value, the briquette must have lower moisture content and higher ash content and fixed carbon.

Based on Equation (1), the highest heating value is 19.00 MJ/kg from C 1:5 briquette as shown in Table 2. The heating value increases as the ratio of coconut shell and sugarcane in briquette increased. However, the C 1:5 briquette has the lowest compressive strength.

4. CONCLUSION

The co-processing of coconut shell and sugarcane produced C 1:5 with theoretically highest heating value than non-carbonized briquettes. Presence of sugarcane residue also plays a role in heating value. However, due to the lowest compressive strength, the produced briquette required the further modification in future.

REFERENCES

[1] R.G. Ferńandez, C.P. García. A.G. Lavin, J.L. Bueno de lasHeras, Study of main combustion characteristics for biomass fuels used in boilers," *Fuel Processing Technology*, vol. 103, pp. 16-26, 2012.

[2] J. Sarki, S.B. Hassan, V.S. Aigbodion, J.E. Oghenevweta, "Potential of using coconut shell particle fillers in eco-composite materials," *Journal of Alloys and Compounds,* vol. 509, no. 5, pp. 2381–2385, 2011.

[3] K. Hofsetz and M.A. Silva, "Brazilian sugarcane bagasse: Energy and non-energy consumption," *Biomass and Bioenergy*, vol. 46, pp. 564-573, 2012.

[4] American Society for Testing and Materials, Annual Book of ASTM Standards, Designation D 3173-03, D 3174-02 and D 3175-02, 2002.

[5] M. Erol, H. Haykiri-Acma and S. Kűçűkbayrak, "Calorific value estimation of biomass from their proximate analysis data," *Renewable Energy,* vol. 35, pp. 170-173, 2010.

Figure 1 Proximate analysis of non-carbonized (NC) and carbonized (C) of CSS briquettes.

Application of limestone as based catalyst in transesterification of rubber seed oil in biodiesel production

M.M. Zamberi[1,2,3], I.A.K.M. Safari[1,2], N.H. Razak[1,2], F.N. Ani[3,*], M.F.B. Abdollah[1,2]

[1] Faculty of Mechanical Engineering, Universiti Teknikal Malaysia Melaka,
Hang Tuah Jaya, 76100 Durian Tunggal, Melaka, Malaysia

[2] Centre for Advanced Research on Energy, Universiti Teknikal Malaysia Melaka,
Hang Tuah Jaya, 76100 Durian Tunggal, Melaka, Malaysia

[3] Department of Thermodynamics and Fluid Mechanics, Faculty of Mechanical Engineering, Universiti Teknologi Malaysia, 81310 Skudai, Johor, Malaysia

*Corresponding e-mail: farid@mail.fkm.utm.my

Keywords: Limestone; rubber seed oil; biodiesel

ABSTRACT – The effect of using natural limestone as heterogeneous catalyst on the transesterification of high free fatty acid rubber seed oil with methanol was carried out to produce a quality biodiesel. Affecting variables such as methanol to oil molar ratio and catalyst concentration were investigated. The catalyst was calcined at 900°C and were characterized using XRD, SEM and XRF. The results revealed that the CaO catalyst derived from limestone was very clean, easy to used and can maintain a good catalytic activity after being used for several times and can reached up to 88.06% biodiesel yield.

1. INTRODUCTION

Biodiesel feedstock from non-edible plants is now gaining much attention due to the great concern of food demand when opting edible plants as raw feedstock especially in the developing countries. The option of non-edible oil over edible oils can overcome the problems of environmental, economic issues and high cost feedstock related to edible vegetables [1]. Calcium oxide (CaO) catalyst is one among the most promising heterogeneous catalyst that can be classified having an eco-friendly characteristic and value added to the green biodiesel process [2]. Natural limestone is one of the good CaO resources where its major component, calcium carbonate ($CaCO_3$) will convert into calcium oxide and carbon dioxide under very high temperature.

This study was undertaken to investigate the performances of the heterogeneous catalyst derived from natural limestone on the production of biodiesel from high free fatty acid (FFA) rubber seed oil (RSO) with methanol to boost up the process performances.

2. METHODOLOGY

2.1 Material selection and catalyst preparation

Crude rubber seed oil (RSO) was purchased from Kinetics Chemical (M) Sdn Bhd, Malaysia. The physical characteristics of the RSO were conducted and the test result was tabulated as in Table 1. The limestones were purchased from Damai Kuari, Sdn Bhd, Kelantan, Malaysia. The limestones were later crushed and grounded using pestle and mortar and sieves into different particles sizes (2 mm- 4mm). Then it was calcined in a furnace at 900°C with a heating rate of 10°C/min for 4 hours to convert calcium carbonate, $CaCO_3$ into calcium oxide, CaO. The calcined samples were then kept in desiccators to prevent from any contamination.

Table 1 Properties of methyl ester of crude RSO.

Test	Unit	Method	Results
Acid Value	mg KOH/g	ASTM D664	78.9
Iodine Value	(g I_2/100 g)	AOCS Id 3-92	129.8
Water Content	%wt	EN ISO 12937	0.44
Kinematic viscosity @ 40°C	mm^2/s	ASTM D7042	32.96
Density@ 15°C	kg/L	ASTM D4052	0.9248

The chemical composition of cockle was observed using X-ray fluorescence in- build XRD (ARL 8660S) and scanning electron microscopy with energy dispersive X-ray detector (SEM-EDS) technique. The SEM-EDS technique was used to obtain the information of the morphology and elemental composition of the samples.

3.1 Esterification and transesterification

The esterification process is needed in order to reduce the high FFA content of the crude RSO. The process is prepared in the presence of 10 wt% sulphuric acid (H_2SO_4) in reference to the mass of oil and methanol. The treated oil was separated and collected and the amount of FFA content remaining is determined before conducting the transesterification process.

The acid value of crude RSO reduced from 78.9 mg KOH/g to 1.45 mg KOH/g after conducting the esterification process. Transesterification process is carried out by heating 50g of rubber seed oil to ±64°C on a constant temperature with magnetic stirrer. At the same time, methanol and the catalyst were added, mixed and heated up to 60°C and was stirred at all-time throughout the transesterification process. Upon the reaction completion, the catalyst is filtered out and the end product was poured into a separation funnel and was left overnight for separation process. The lower layer which is glycerol is drawn out and the excessive

amount of methanol was evaporated. The product obtained which is the biodiesel was taken out for further properties analysis. The yield obtained was calculated using the formula shown below:

$$\text{FAME Yield (\%)} = \frac{\text{Total weight of FAME}}{\text{Total weight of oil}} \times 100 \quad (1)$$

3. RESULTS AND DISCUSSION

3.1 Characterization of calcined limestones

The elemental composition analysis of the calcined sample with XRF spectroscopy was tabulated as shown in Table-2. XRF analysis showed that the sample was composed mainly of calcium oxide with 58.41wt.%. These results indicated that all calcium carbonate ($CaCO_3$) in the samples was completely transformed to CaO. Typically, plenty of Calcium (Ca) and Oxygen (O_2) were observed.

Figure 1 show the surface morphologies of the calcined heterogeneous catalyst which gave an irregular in shape and some of them bonded together as aggregate. Spot of analyzed (EDS) consists plenty of calcium and oxygen.
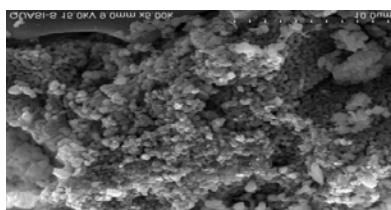
Figure 1 SEM images of the heterogeneous limestones calcined at 900°C for 4 h.

Table 2 Chemical composition of calcined limestone with XRF-XRD.

Formula	CaO	SiO_2	Al_2O_3	MgO	Fe_2O_3	SO_3
Concentration (%)	58.41	21.81	0.21	1.43	1.04	0.64

3.2 Effect of variables on transesterification process

As shown in Figure 2, the yield conversion was increased from 66.82% at 6:1 molar ratio to 88.06% at 16:1 molar ratio. This result is consistent with previous findings [3] which found that the amount of molar ratio of methanol to oil at the ratio of 10 or lower than that is not sufficient enough to dissolve the oil and catalyst phase.
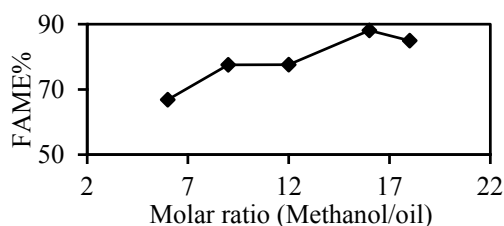
Figure 2 Effect of methanol to oil molar ratio on the biodiesel yield.

Figure 3 show the effects of catalyst loading. The highest yield of 88.06% was obtained within 3h reaction

time by using 9 wt.% of catalyst. However, the yield conversion was decreased to 64.22% after amount of the catalyst increased up to 25 wt.%. This is in line with previous study [4] which reported that the catalyst concentration levels greater than 9 wt% may not able to promote the reaction to form more products because it is already achieved the equilibrium state. The fuel properties of the biodiesel produced from heterogeneous RSO methyl esters are compared with biodiesel and petro diesel standards and most of the physico-chemical properties of RSO methyl ester are comparable to those of biodiesel standard and petro-diesel.
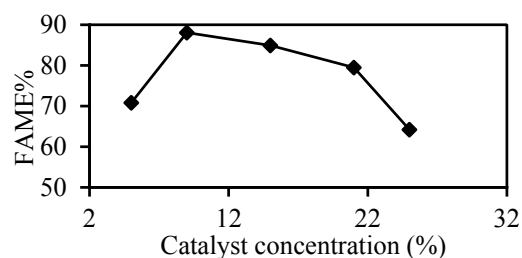
Figure 3 Effect of catalyst concentration on the biodiesel yield.

4. CONCLUSIONS

Overall biodiesel yield conversion was found as high as 88.06%. Molar ratio of methanol to oil and catalyst loading played major role in the production process. Using ratio of 16:1 methanol/oil, catalyst percentage about 9 wt.% and about 3 h reaction time the optimum yield was achieved. Limestones was found had high potential to be commercialized as a green low cost heterogeneous catalyst.

REFERENCES

[1] M.M. Gui, K.T. Lee and S. Bhatia, "Feasibility of edible oil vs. non-edible oil vs. waste edible oil as biodiesel feedstock, "*Energy,* vol. 33, pp.1646-1653, 2008.

[2] F.N.Ani and A.E. Bakheit, "Heterogeneous Microwave Irradiation Biodiesel Processing of Jatropha Oil," *Applied Mechanics and Materials,* vol.554, pp. 500-504, 2014.

[3] C. Ngamcharussrivichai, W. Wiwatnimit and S.Wangnoi, "Modified dolomites as catalysts for palm kernel oil transesterification," *Journal of Molecular Catalysis A: Chemical*, vol. 276(1-2), pp.24-33, 2007.

[4] J.Gimbun, S.Ali, C.C.S. Charan Kanwal, C.C.S., L. Amer Shah, N.H.M.Ghazali, K.C. Chin and S. Nurdin, "Biodiesel Production from Rubber Seed Oil Using Activated Cement Clinker as Catalyst,"*Procedia Engineering*, vol. 53, pp. 13-19, 2013.

Energy audit and analysis in UTeM: Library

A.N. Nasaruddin [1,2,*], M.Z. Akop[1,2], M.A. Salim[1,2], M.R. Mansur[1,2], M.T. Musthafah[1,2], M. Adrinata[1,2]

[1] Faculty of Mechanical Engineering, UniversitiTeknikal Malaysia Melaka,
Hang Tuah Jaya, 76100 Durian Tunggal, Melaka, Malaysia
[2] Centre for Advanced Research on Energy, UniversitiTeknikal Malaysia Melaka,
Hang Tuah Jaya, 76100 Durian Tunggal, Melaka, Malaysia

*Corresponding e-mail: afiqah_ngahn@yahoo.com

Keywords: Energy; cooling load; thermal comfort

ABSTRACT – This paper presents the study on auditing energy consumption at UTeM's main library. By investigating the building energy profile such as analysing previous utilities bill, using instrument and calculation using major energy consumption equation such as cooling load equation and sub-meter reading. The detail on part to be audit will give a perspective for what and how the energy audit will be performed. At the end of this paper is the recommendation for energy conservation step that can be implemented based on suggestion by the Energy Commission policies and Malaysian Standard along with the visitation to the case studies site. The result shows that that the maximum power consumption per day is 2141.35 kWh and the minimum is 1912.28 kWh.

1. INTRODUCTION

The case study is conducted on the UTeM's Main Campus library located on Durian Tunggal. This building has started its operation on 29 September 2009 may provides a seating capacity of 500 users at one time. This building consists of four levels including the ground level and for every level it have different layout depend on the purpose it served. Total area of the building is 10063.68m^2. On average, the energy consumption in office building is 70-300 kWh/m2 which is 10-20 times bigger than residential sectors as previous study [1].

The combustion of fossil fuels from electricity generation for commercial and domestic use somehow contributed to the increasing atmospheric carbon dioxide (CO_2) concentration. Thus, increase energy demand will consequently increase carbon dioxide concentration in the atmosphere as previous study [2].

Based on the previous data shows that energy consumption needs to be used wisely and monitored. For that purpose, energy audit is one of the ways that can keep track on distribution of energy in building which for this case is UTeM's library itself. For instance, with every saving made can be channel to increase the productivity and some improvement in term of the service consequently, students of UTeM may benefit from it indirectly.

2. METHODOLOGY

This case study focussed more on the main energy consumption part by obtaining the information from building blueprint and room data of air conditioning, lighting and plug load and potential heat load contributor. Moreover, a survey on thermal environment and comfort in UTeM's Library was conducted to gather information from the perspective of regular occupant and make a conclusion based on real condition out of it. Basically, several steps in performing energy audit will begin with pre-audit by having a discussion with building occupant and technical staff in charge to understand the energy usage. Then, audit phase consists of collecting plant data and electric bill, and taking measurement to find irregularities. Eventually, the post-audit to present the data from the audit and analyzed it for the purpose of proposing an energy saving recommendation as previous study [3].

Other method such as the data collection procedure and estimation of energy use intensity and detailed audited-age of building which consist of the types of building, weekly hours, air conditioned area, number of occupancy and the appliances specification was being considered thoroughly. As audit complexity increases, so does thoroughness of the site assessment as previous study. A huge amount of energy and it cost can be saved thus the emission of greenhouse gasses can be reduced by introducing different energy savings option including installing insulation and glazing at appropriate part of building [4].

2.1 Parameter analysis for cooling load calculation

The value for the parameter accounted for the whole equation for this case study is mostly resources from the ASHARE Fundamental Handbook 1997 [5], ASHRAE Standard 62 and the latest weather condition. The calculation will be divided to external and internal load where external load consists of calculation for wall, roof and glass surface while for internal load consist of light, people equipment and ventilation component.

(a) The heat conduction through exterior surface is through the wall and the roof of the building.

$$Q_{wall} = U \text{ x } A \text{ x } (t_o - t_i) \tag{1}$$

(b) The second component of the heat gain come from the solar heat load which will be divided into two that is solar heat load through conduction and through transmission radiation through the glass window. Its value varies with time, orientation, shading and storage effect.

$$Q_{glass,\ conduction} = U \times A \times (CLTD)_c \qquad (2)$$
$$Q_{glass,\ radiation} = SHGF \times A \times SC \times CLF \qquad (3)$$

(b) The instantaneous rate of heat gain from electric lighting.

$$Q_{el} = 3.41 \times W \times F_{ul} \times F_{sa} \qquad (4)$$

(d) Heat gain from the occupant can be calculated as the equation below and it is divided by latent heat and sensible heat.

$$Q_{sensible} = N \times Q_s \qquad (5)$$
$$Q_{latent} = N \times Q_l \qquad (6)$$

(e) Obtain the outside air sensible heat (OASH) and outside air latent heat (OALH) with equation below.

$$V_{ventilation} = cfm/person \times N \qquad (7)$$
$$OASH = 0.02044 \times V_{ventilation} \times (t_{db1} - t_{db2}) \qquad (8)$$
$$OALH = 50 \times V_{ventilation} \times (w_1 - w_2) \qquad (9)$$

3. RESULTS AND DISCUSSION

3.1 Cooling load calculation

The estimation made based on the calculation provides an appropriate total value of the cooling load that supposed to be able to provide by the current HVAC system which is about 937.54 kW.

Table 1 cooling load at each level of library at 12pm.

Level	Total, (kW)
G	67.17
1	460.63
2	217.88
3	137.88
R	53.98
TOTAL	937.54

3.2 Thermal microclimate analysis

It can be concluded from the thermal environment analysis that the condition inside the library is proved to be within a comfort zone since the resulting PMV value generated is within a recommended range which is -0.16 for level 1, -0.14 for level 2 and 0.35 for level 3. For PPD the value is 5.77 for level 1, 5.46 for level 2 and 7.73 for level 3. Overall the thermal condition inside the library is consider of neutral and proved that the HVAC system is work accordingly well to provide comfort for the occupant.

3.3 Estimation of power consumption

Below show an estimation of maximum and minimum power consumption by HVAC system, lighting and other several electrical equipment:
Maximum power consumption per day: 2141.35 kWh
Minimum power consumption per day: 1912.28 kWh

3.4 Estimation of water consumption

For the water consumption calculation will be made by the assumption that the library occupant per day is the full capacity of the library itself which is about 500 occupants and about 65 staff:
Total watr consumption =8.63 m³

3.5 Luminousity

Overall the library provide more than 400 lux at various location and may reach up to 1199 lux even at night. The ground floor however is an exceptional since it is rarely having an occupant.

3.6 Survey analysis

The survey questions more on thermal comfort aspect that may influenced the sample occupant decision of their state of mind about the thermal environment. It is because normally muscle activity is converted to heat in the body which might be release to the surrounding to achieve comfort. Whereas sometimes insulation from unpleasant environment an individual made is by optimizing their own thermal comfort with clothing to reduce the body's heat loss. The PMV (Predicted Mean Vote) index predicts the mean value of the subjective ratings of a thermal comfort for group of people in a given environment. Thus, it might differ from person to person. for library environment 3 % experienced hot, 3% warm condition, 7% is slightly warm, 30% is neutral, 27% is slightly cool, 13% is cool and 17% cold condition as in Figure 1.
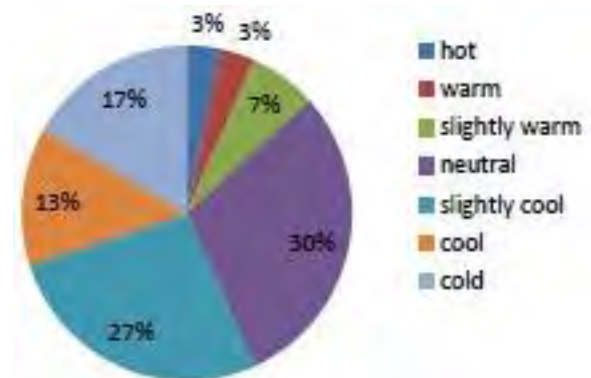
Figure 1 Graph of thermal comfort experiences by the occupant.

4. CONCLUSION

Keeping track, the consumption of energy regularly may help monitoring the performance of equipment that contribute to the energy wastage. To get a better result with a large scale investment but long term benefits is by starting a new process and technology installation that proven to be high in efficiency. By upgrading to variable refrigerant system (VRF), precise retrofitting the lamp and applying energy saving appliance may contribute to energy saving.

REFERENCES

[1] L. Yang, C. Joseph, C.L. Lam, T. Sang, "Energy performance of building envelopes in different

climate zones in China," *Applied Energy*, Vol.85, pp.800-817. 2008.

[2] Anon, Ninth Malaysian Plane 2006 – 2010, The economic planning unit prime minister's department, Putrajaya, Malaysia, 2006.

[3] S. Shashank, K. Sandip, and M.K. Jeentendra, "Improving industrial efficiency by energy audit,"

International Journal of Scientific Engineering and Technology, vol.2 (4), pp 291-294, 2013.

[4] R. Saidur, and H.H. Masjuki, "Energy and associated emission analysis in office buildings," *International Journal of Mechanical and Materials Engineering*, vol.3(1), pp 90-91, 2008.

[5] R. Parson, "ASHRAE Fundamental Handbook 1997," SI Ed, Chapter 28, 1997.

Separate analysis of wind speed and direction for Mersing, Malaysia

N. Sanusi[1,2,*], A. Zaharim[1], S. Mat[1]

[1] Solar Energy Research Institute (SERI), Universiti Kebangsaan Malaysia,
43600 UKM Bangi, Selangor, Malaysia
[2] Faculty of Mechanical Engineering, Universiti Teknikal Malaysia Melaka,
Hang Tuah Jaya, 76100 Durian Tunggal, Melaka, Malaysia

[*]Corresponding e-mail: azami.zaharim@gmail.com

ABSTRACT – This research is conducted purposely to study the effect of wind speed and wind direction in generating wind power. Although the scope is extensive, but this paper will only discuss on the density probability distribution, numerical and graphical presentation of both. A Weibull and finite mixture model of von Mises distribution is used in this paper to represent data of Mersing (Malaysia). The suitability of the distributions was examined by the coefficient determination of R^2. The analysis reveals that the selected models fit with the data.

1. INTRODUCTION

The nature of wind with variant wind speed and direction leads to a broad spectrum of wind research. The importance of wind speed behaviour has widely studied by researchers all over the world including Malaysia.

While research in wind direction is far behind compare to wind speed. The nature of it circular data has limits the interest of investigation. This type of data cannot be treated as an ordinary (linear) data. Despite normal distribution for a linear data, von Mises or a Circular Normal (CN) distribution is the model of choice for circular data in most applied problems [1].

This paper will only discuss on von Mises distribution or Finite mixture von Mises to be exact. This chosen is basically depend on the nature of data which is circular with multi modal that best explain with this type of probability distribution [2-4].

2. METHODOLOGY

2.1 Weibull distribution

The probability density function (pdf) for Weibull is presented in equation (1):

$$h(v) = \left(\frac{k}{c}\right)\left(\frac{v}{c}\right)^{(k-1)} e^{-\left(\frac{v}{c}\right)^k} \quad for\ 0 < v < \infty \quad (1)$$

Where:
k= shape parameter; c= scale parameter;
v= wind speed

The Weibull shape and scale parameters are estimated using Maximum Likelihood method which is given by:

$$k = \left[\frac{\sum_{i=1}^n v_i{}^k ln(v_i)}{\sum_{i=1}^n v_i{}^k} - \frac{\sum_{i=1}^n ln(v_i)}{n}\right]^{-1} \quad (2)$$

Where:
v_i= wind speed in time step, I;
n= number of data points

The value of k is evaluates by using an iterative technique. In this study the Newton Raphson method [5] has been used. The scale parameter, c is obtained by:

$$c = \left[\frac{1}{n}\sum_{i=1}^n v_i{}^k\right]^{1/k} \quad (3)$$

2.2 Finite mixture von Mises (mvM)

$$f_\theta(\theta) = \sum_{j=1}^{H} \frac{\omega_j}{2\pi I_0(\kappa_j)} \exp\left(\kappa_j \cos(\theta - \mu_j)\right) \quad (4)$$

For;

$$0 \leq \theta < 2\pi, \quad 0 \leq \mu_j < 2\pi, \quad \kappa_j \geq 0,$$

$$0 \leq \omega_j < 1 \quad for\ j = 1,2,\ldots .H \quad and \sum_{j=1}^{H} \omega_j = 1$$

$$I_0(\kappa_j) = \frac{1}{\sqrt{2\pi}} \int_0^{2\pi} \exp\left(\kappa_j \cos\theta\right) d\theta$$

$$= \sum_{\kappa=0}^{\infty} \frac{1}{(\kappa!)^2} \left(\frac{\kappa_j}{2}\right)^{2\theta}$$

3. RESULTS AND DISCUSSION

For this study, appropriate distributions have been determined by fitting Weibull probability distribution. Parameter estimations is verifying by using maximum likelihood method. The maximum likelihood estimator (MLE) for the parameters of each can be determined numerically by using Newton Raphson method. Table 1 below shows the result on parameter estimation for Weibull and Gama distribution. These parameter estimation values are then being used in the respective probability distribution function.

Table 1 Estimation parameter.

	Weibull distribution	
Year	Shape parameter k	Scale parameter c
2007	2.10758	3.05830
2008	2.09565	3.29368
2009	2.16443	3.19343
2010	2.14770	2.95556
2011	2.08609	3.24657
2012	2.06077	2.91111
2013	2.08768	3.10305

For the wind direction analysis, the appropriate distribution will best explain the prevailing wind direction in such area. This study chooses finite mixture von Mises distribution to explain its wind direction regime. The parameter estimates for the finite mixture von Mises distribution (H=1,2…8) at Mersing station is first to be calculated. This parameter estimates are important in model fitting.

This study uses R^2 correlation coefficient as the numerical evaluation and determined that the best number of component that represents Mersing data is H=6. By using the parameter estimates, estimation for density probability function of finite mixture von Mises (H=6) model is then derived as:

$$f_\theta(\theta) = \frac{0.276666}{2\pi I_0(12.25072)}\exp\left(12.25072\ \cos(\theta - \mu_1)\right) +$$

$$\frac{0.065021}{2\pi I_0(14.95576)}\exp\left(14.95576\ \cos(\theta - \mu_2)\right) +$$

$$\frac{0.046866}{2\pi I_0(10.62431)}\exp\left(10.62431\ \cos(\theta - \mu_3)\right) +$$

$$\frac{0.317662}{2\pi I_0(19.55538)}\exp\left(19.55538\ \cos(\theta - \mu_4)\right) +$$

$$\frac{0.16176}{2\pi I_0(14.04048)}\exp\left(14.04048\ \cos(\theta - \mu_2)\right) +$$

$$\frac{0.132026}{2\pi I_0(14.95576)}\exp\left(14.95576\ \cos(\theta - \mu_2)\right)$$

With the parameter of mean directions:

$$\begin{bmatrix}\mu_1\\\mu_2\\\mu_3\\\mu_4\\\mu_5\\\mu_6\end{bmatrix}^T = \begin{bmatrix}0.90195 & 0.431841\\-0.21838 & 0.975863\\-0.87079 & 0.491656\\-0.66725 & -0.74484\\-0.09333 & -0.99564\\0.931101 & -0.36476\end{bmatrix}^T$$

The parameter of mean directions refer to mean for circular data in rectangular coordinates:

$$X^T = \begin{bmatrix}\cos\theta & \sin\theta\end{bmatrix}$$

This result reveals that density probability function of finite mixture von Mises (H=6) is the best model that represent the wind direction data for Mersing.

4. CONCLUSION

In this study, Weibull and finite mixture von Mises with H=6 are used to be the best models that represent wind speed and direction data for Mersing. With more than 99% in its R^2 coefficient test, variation in the data can be explained by the selected model. This study gives the idea of how wind speed and direction are typically distributed. Results from this study might be significant for advance studies of wind energy potential in Mersing.

REFERENCES

[1] S.R. Jammalamadaka and A. SenGupta, *Topics in Circular Statistics*. World Scientific Publishing Co.Pte.Ltd; 2001.

[2] N.A.B. Kamisan, A. G. Hussin, and Y. Z. Zubairi, "Finding the best circular distribution for southwesterly monsoon wind direction in Malaysia," *Sains Malaysiana*, vol. 39, no. 3, pp. 387–393, 2010.

[3] N.A.B. Kamisan, A.G. Hussin, Y.Z. Zubairi, and S.F. Hassan, "Distribution of wind direction recorded at maximum wind speed : A case study of Malaysian wind data for," *International Journal of Physical Sciences*, vol. 6(7), pp. 1840–1850, 2011.

[4] N. Masseran, A.M. Razali, K. Ibrahim, and M.T. Latif, "Fitting a mixture of von Mises distributions in order to model data on wind direction in Peninsular Malaysia," *Energy Convers. Manag.*, vol. 72, pp. 94–102, Aug. 2013.

[5] A. Schworer and P. Hovey, "Use of the Newton-Raphson Algorithm in calculating Maximum Likelihood Estimates," in *Electronic Proceedings of Undergraduate Mathematics Day 2004*, pp. 1–11, 2004.

Study of breakdown behaviour of ester oil with suspended cellulose particles under direct current voltage

M.H.S. Zainoddin[*], H. Zainuddin, A. Aman

Research Laboratory of High Voltage Engineering, Faculty of Electrical Engineering,
Universiti Teknikal Malaysia Melaka, Hang Tuah Jaya, 76100 Durian Tunggal, Melaka, Malaysia

[*]Corresponding e-mail: hafiyzainoddin@gmail.com

Keywords: Ester oil; bridging; dielectrophoresis

ABSTRACT – Nowadays, ester oil has become a potential replacement for mineral oil due to biodegradable and renewable factors. Due to the increasing demand for High Voltage Direct Current (HVDC) system to meet the energy requirement, further studies on the performance of ester oil under Direct Current (DC) electric field is sensible. For an HVDC system, a phenomenon called dielectrophoresis (DEP) may occur if the oil-filled equipment such as the HVDC converter transformer is contaminated with suspended solid particles. This paper investigates the breakdown behavior of ester oil with the presence of DEP phenomenon under non-uniform DC electric field.

1. INTRODUCTION

Most of high voltage transformers are oil-immersed and the primary function of the oil are to dissipate heat and to serve as an insulator. The insulation oil is also useful as carrier information in power transformers for diagnostic purposes [1]. For decades, the insulation oil used in high voltage transformer is petroleum-based (mineral oil). Nowadays, due to stringent environmental protection regulations, future scarcity and environmental effect, ester oil has been regarded as a potential replacement for mineral oil in high voltage application. Nevertheless, their dielectric properties and performance are still unknown in the case of DC energization. In response to that, further studies concerning the dielectric behavior of ester oil under DC electric stress are necessary.

It has been reported that the rate of failure of HVDC converter transformer is 5-10 times higher compared to the normal HVAC transformers [2]. Previous studies have shown that cellulose bridging may happen in mineral oil in HVDC converter transformers [3]. The formation of cellulose bridge is due to the non-uniform electric field that leads to the motion of particles. Such phenomenon is called dielectrophoresis (DEP). DEP tends to force the particles into a high field region during a normal transformer operation and this force will form cellulose bridge conduction between two different potentials after certain period of time [4]. To make it worse, transformer failure may occur due to the formation of conducting path between two different potentials. Hence, this project is conducted to study the breakdown behavior of ester oil contaminated with cellulose particles.

2. EXPERIMENTAL SETUP

Figure 1 shows the experimental setup for this study. The test cell is a rectangular glass filled with 1 litre of synthetic ester oil (MIDEL 7131). A pair of spherical brass metal electrodes with 13 mm diameter is immersed in the oil. One of the spherical electrodes is attached to the HVDC and the other one is grounded. Nikon D5300 digital camera was used for throughout the experiment for monitoring and recording purposes.
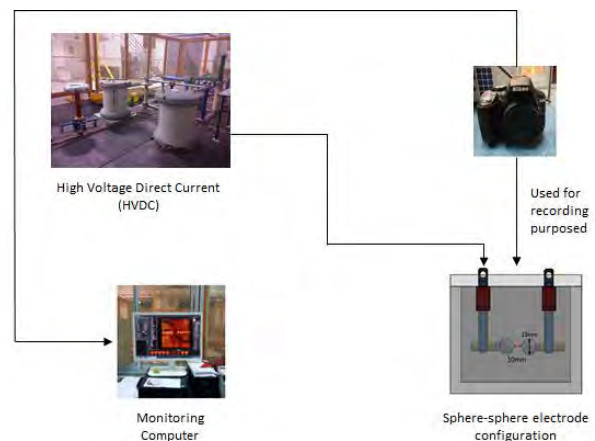
Figure 1 Experimental setup for bridging experiment.

3. EXPERIMENTAL PROCEDURE

The experiment was conducted by applying HVDC in steps of 5 kV with 1 minute interval for each step until breakdown occurs. The breakdown occurs when the high voltage test system tripped. However, for the first 3 steps, the voltage was increased to 2 kV, 7 kV and 10 kV. In order to simulate the presence of cellulose contaminants, a piece of new cellulose pressboard is scraped and the dust obtained from this action is inserted into the oil sample. The breakdown behaviour of three different distances, i.e. 10 mm, 15 mm and 20 mm had been investigated by measuring the bridging time and the values of breakdown voltage. The experiment was repeated three times for validity and reliability in obtaining the results.

4. RESULTS AND DISCUSSION

Figure 2 shows the images obtained from the experiment. Figure 2 (a) depicts the experiment condition without cellulose particles. For samples with cellulose particles, cellulose bridging is observed for all

Optimized guiding vane for propeller turbine

J. Ab Razak[1,2,*], M. Musa[1,2], M.F. Abdul Razak[3]

[1] Faculty of Mechanical Engineering, Universiti Teknikal Malaysia Melaka,
Hang Tuah Jaya, 76100 Durian Tunggal, Melaka, Malaysia
[2] EFFECTS Research Group, Centre for Advanced Research on Energy, Universiti Teknikal Malaysia Melaka,
Hang Tuah Jaya, 76100 Durian Tunggal, Melaka, Malaysia
[3] Linatex Rubber Products Sdn Bhd, Lot Pt 19245, Lorong Haji Abdul Manan 2,
Batu 5, Off Jalan Meru, 41050 Klang, Selangor, Malaysia

*Corresponding e-mail: juhari@utem.edu.my

ABSTRACT – Small scale hydro turbine is used for off-grid villages near the river. Pico hydro is usually selected for this purpose. One the efficiency criteria for this turbine is the velocity of water intake to the blade. The water enters the propeller turbine via the guide vane. Several parameters of the guide vane, which include number of guide vanes, and attack, inlet and outlet angles, are simulated in computer fluid dynamic (CFD) software. The optimized guide vane is further tested with varied flow rate. The simulation result shows a significant increase of water velocity intake to the blades.

1. INTRODUCTION

Most of current rural electrification program is using generator set to provide light and power to the off-grid villages. The problems of escalating fuel prices and its availability to these rural areas are making the generator set to be unattainable for long period usage [1]. In most villages the duration its operation is rationed to several hours at night. Concerns of the effect this type of fuel to the environment drive the authority to change to renewable energy alternatives. The location of off-grid villages usually near river, which make hydro power to be a suitable option for rural electrification.

Small scale turbine, a Micro or a Pico, can be utilized for this purpose, depending on the power produced and the load demand [2]. A micro turbine could produce up to 100 kW and a Pico turbine has a maximum capacity of 5 kW power. Pelton, propeller and cross-flow turbines can be used for micro hydro while Pico hydro can utilize propeller and cross-flow turbines [3][4]. The power production depending on two main variables; the head and the flow rate of water.

$$P = \eta \rho g H Q \qquad (1)$$

P	Power	(Watt)
η	Efficiency	
ρ	Density	(kg/m^3)
g	Gravitational constant	(m/s^2)
H	Net Head	(m)
Q	Volumetric Flow Rate	(m^3/s)

The head is the vertical height from the water intake into the penstock to the water intake to the turbine. The flow rate is in the form of volumetric flow rate at the inlet of the turbine. In certain cases both of the head and flow rate can be low, which require a good judgement in the selection of turbine type.

This research is intended to look at the effects of guide vane parameters to the propeller turbine performance. These parameters are expected to influence the water intake velocity to the blades. The water flow rate will be varied to ensure the consistency of the results.

2. METHODOLOGY

Guide vane parameters which most likely to effect the water inlet velocity to the blade are [5]:

a. Number of guide vane
b. Attack angle
c. Inlet angle
d. Outlet angle

It is important to determine the influence of the guide vanes parameters on water velocity since the kinetic energy of the water from the guide vanes affected the speed rotation of the turbine's blades [6]. Indirectly, this scenario will influence the overall performance of the propeller turbine. Other guide vane's parameters such as length, width and the height are fixed. Table 1 shows about the values of guide vane's parameters that involved in the investigation.

Table 1 Guide vanes parameters for the investigation.

	Standard	New guide vane 1	New guide vane 2	New guide vane 3	New guide vane 4
Length of guide vane			55 mm		
Width of guide vane			6 mm		
Height of guide vane			74 mm		
Number of guide vane	12	3	5	5	5
Angle of attack	67.5^0	14.09^0	22.23^0	42.72^0	10.3^0
Inlet angle	67.5^0	9.5^0	9.11^0	32.48^0	10.3^0
Outlet angle	67.5^0	67.51^0	45^0	69.56^0	69.08^0

3. RESULTS AND DISCUSSION

The final overall design of the guide vane is as shown in Figure 1.
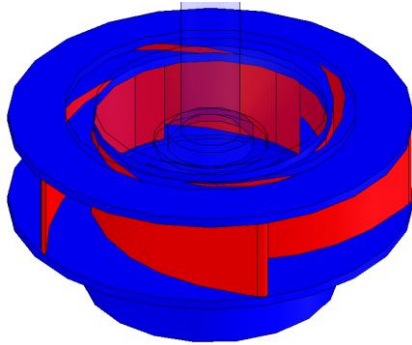
Figure 1 3-D representation of the guide vane.

The simulation indicated the flows of the stream velocity which occurred between the guide vanes. Figure 2 shows an example of CFD image for the related activities. The colours represent the values of the velocity where red colour is the highest value while the blue colour is the lowest.
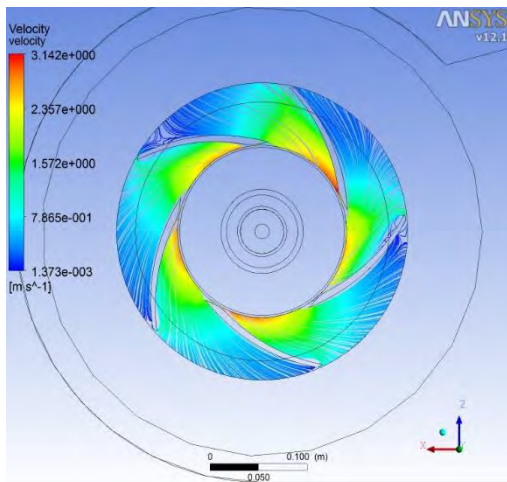
Figure 2 Stream velocity between the guide vanes.

Table 2 Maximum velocities for related guide vanes and water flow rates.

	Standard	New guide vane 1	New guide vane 2	New guide vane 3	New guide vane 4
Maximum velocity at 25 kg/s	2.27 m/s	3.93 m/s	3.14 m/s	5.67 m/s	5.81 m/s
Maximum velocity at 50 kg/s	4.52 m/s	7.87 m/s	6.32 m/s	11.33 m/s	11.63 m/s

For both water flow rate at 25 kg/s and 50 kg/s, the combination of guide vane's parameters for new guide vane 4 produced the highest amount of water velocity (Table 2 and Figure 3). The increment of the velocities for each flow rates were more than 50%. The reduction of angle of attack and inlet angle of the guide vanes from 67.5^0 to 10.3^0 contributed high significant impact on the values of the water velocity. However, in order to achieve this kind of result, the outlet angle must be increased from 67.5^0 to 69.08^0. In addition, number of the guide vane was to be decreased from 12 pieces to 5 pieces. Therefore, in order to obtain high amount of water stream velocity, the angle of attack and inlet angle should be lower than outlet angle. From the results for the flow rates of 25 kg/s and 50 kg/s, the maximum velocity are 5.81 m/s and 11.63 m/s respectively.
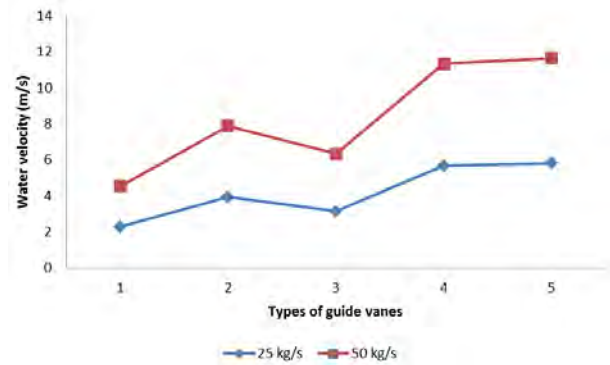
Figure 3 Graph of water velocity vs type of guide vanes.

4. CONCLUSION

Guide vane is one of the main component in propeller turbine that functions as a guide for water stream to flow through it before the water strikes the turbine's blades. This process is very important to provide high velocity impact of water stream (kinetic energy) to ensure the speed of the turbine rotates faster.

It can be concluded that the guide vanes angles and number of guide vanes will influence the stream velocity of the water in the turbine. The best combination of guide vane's parameters for both cases was new guide vane 4. The best combination of guide vane's parameters for both cases was new guide vane 4.

REFERENCES

[1] P. Maher, N.P.A. Smith, A.A. Williams, "Assessment of Pico hydro as an option for off-grid electrification in Kenya", Renewable Energy, pp. 1359-1369, 2002.

[2] Mohibullah, M.A.M. Radzi, M.I.A Hakim," Basic design aspect of micro hydro power plant and its potential in Malaysia", in Proceedings of National Power & Energy Conference (PECon), pp. 220-223, 2004.

[3] O. Paish, "Crossflow Turbine", Renewable and Sustainable Energy Reviews, vol. 6, pp. 537–556, 2002.

[4] V. Nunes, J.L. Genta, "Micro and mini hydroelectric power assessment in Uruguay", in Proceedings of WREC 1996. pp 1235-1328, 1996.

[5] P. Ausoni, "Turbulent vortex shedding from a blunt trailing edge hydrofoil", Ph.D. Thesis, Ecole Polytechnique Federale de Lausanne, 2009.

[6] C. Alatorre-Frenk,"Cost minimisation in Micro-hydro systems using Pumps-as- turbines", PhD Thesis, University of Warwick, U, 1994.

A study on the potential of Peltier in generating electricity using heat loss at engine system

N.M.H. Shalsam, M.H. Harun[*], M.S. Yahaya, K.A.M. Annuar, M.F.M.A. Halim, M.H.C. Hasan, M.F. Yaakub

Faculty of Technology Engineering, Universiti Teknikal Malaysia Melaka,
Hang Tuah Jaya, 76100 Durian Tunggal, Melaka, Malaysia

[*]Corresponding e-mail: haniff@utem.edu.my

ABSTRACT – In the era of globalisation, the electrical energy usage is the main priority in order to do our job and daily activity. Unfortunately, limited power supply for the electrical energy usage makes it hard to continuously provide electrical energy for 24 hours. By using Peltier device, it is possible to develop a portable generating system using heat loss in machines and vehicles. The generating system theoretically can recycle the heat loss to produce additional electricity for other usage. Generally, the objective of the generating system is to study on the potential of Peltier device to generate useful electricity for additional power supply using heat loss. This generating system can be applied on many types of machines and other type of mechanism such as vehicle that release heat loss. Therefore, the result obtain in term of voltage can be generated by the generating system. As a result, this system has higher efficiency which 12.59% compared to 6% using proper heat sink using the same module.

1.   INTRODUCTION

Generally, a Peltier device is an intelligence device that can operate for cooling system by supplying voltage to the device to eject hot and cold air. The cold air will be used for cooling system. Reversely, the device can generate electricity by absorbing heat without supplying any voltage to power up the Peltier device based on W. Thomson in 1851 rewrite Thomas Johann Seebeck foundation on "Seebeck effect" in 1821. In Seebeck effect theory, the electrons in the semiconductor act as transferring agent to transfer the heat from one medium to another medium according to the law of thermodynamics. In this case, the application where the energy conversion system applied is on vehicle engines and exhaust system. Based on Electrical Energy Conversion (E2C) past research at the KTH School of Electrical Engineering 2011, all machines are not working 100% effectively, most appears to work only 70% to 80% effectively as shown in Figure 1 [1].

Meanwhile, the other 30% to 20% are released into energy loss in term of heat. In order to recover the heat loss, this project will design a portable generating system using Peltier device to produce electricity by absorbing heat loss.

2.   METHODOLOGY

The basic operations for the device have been discovered for many years by Thomas Seebeck in 1821 where the temperature difference is established between hot and cold npn junction type semiconductors. Heat loss will be absorb on the hot side and leaving to the cold side of the Peltier device as shown in Figure 2. During the process, the electrons in the npn semiconductor will active and vibrate due to heat then collides with each other in order to release the heat to the cold side. The result is voltage will be produced due to Seebeck effect.
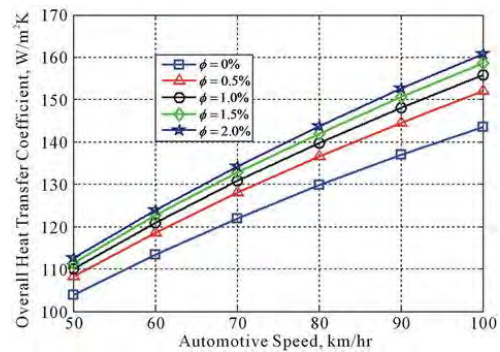
Figure 1 Heat loss in car engine.
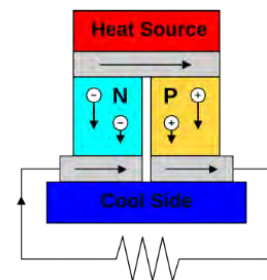
Figure 2 Heat transfer from hot to cold side.

The hot side absorbs heat loss at rate of T_H high temperature ejected by the system and transfer the heat to the cold side to be released at a rate of T_L low temperature. By referring to Seebeck effect, the heat loss absorbed at the hot junction causes electrons to be active and electric current then flow in the npn semiconductor and electrical energy is generated. Using the thermodynamics first law energy conservation principle, the difference between T_H and T_L will generate the electrical energy output power, W_e. The heat released then enter cooling agent which is to maximize the efficiency or the output voltage generated by the device in order to achieve higher temperature gradient between both hot and cold side. The increasing

temperature difference between two junctions will increase voltage generation. The generated voltage will flow to the control circuit to provide 12V output voltage to charge battery for other usage [2].

The experimental data are tested at the engine system in order to determine the maximum efficiency for Seebeck Effect. Figure 3 shows the experimental conducted at the engine system.

Figure 3 Generating system on car engine system.

The maximum efficiency, η of a Peltier device can be defined using the figure of merit, temperatures of the hot side and cold side [3]. For this system the heat loss assume zero.

$$N = n_{carnot} \left[\frac{\sqrt{1 + Z\bar{T}} - 1}{\sqrt{1 + Z\bar{T}} + \frac{T_L}{T_H}} \right] \quad (1)$$

Where:
T_L = Temperature Low
T_H = Temperature High

3. RESULTS AND DISCUSSION

The tests have been carried on the exhaust system and engine system to study the potential of a Peltier device to generate electricity using heat loss. Therefore, experiments have been conducted using:

- Four TEC1-12706 module connected in series
- Short fin heat sink
- Fin heat sink
- High efficient series PWM controller charging
- 12V 1.2Ah battery

The reading was taken at every 5 minutes with total of 30 minutes by considering temperature difference between hot side and cold side is being considered as shown in Table 1. The data was taken when the car stop for every 5 minutes. The car speed was limited to approximately 50 kmh. Temperature of the surrounding are 32-34 ºC which is unstable. Table 1 shows the data collected at the engine system.

Based on the data collected, the generating system with four number of TEC1-12706 modules able to generate voltage up to 12.76 V maximum. As the car engine system become hotter, the temperature difference between hot and cold side of the generating system increases. From the Figure 3, the value of voltage generated and temperature difference are increasing over time then voltage generated reach its maximum value 12.76V due to the maximum operating for four Peltier device.

Table 1 Voltage generated by four Peltier modules at engine system with temperature difference.

Time (min)	Voltage (V)	$T_{Difference}$ (ºC)
0	0	0
5	2.16	16
10	5.34	33
15	7.82	49
20	9.63	67
25	12.58	86
30	12.76	98
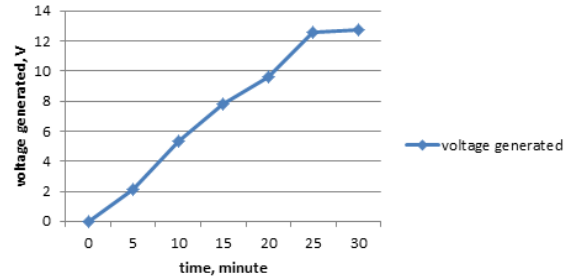
Figure 3 Voltage generated at engine system.

From the efficiency of Carnot, the maximum efficiency of the Peltier TEC1-12706 using equation (1) calculated as shown below.

$$N = n_{carnot} \left[\frac{\sqrt{1 + Z\bar{T}} - 1}{\sqrt{1 + Z\bar{T}} + \frac{T_L}{T_H}} \right]$$

$$N = 0.7481 \left[\frac{\sqrt{1 + 0.5711} - 1}{\sqrt{1 + 0.5711} + \frac{33}{131}} \right]$$

$$= 12.59\%$$

By comparing the maximum efficiency of this generating system to past research by researcher [3], this generating system has higher efficiency which 12.59% compared to 6% using proper heat sink with the same module TEC1-12706.

4. CONCLUSIONS

In conclusion, Peltier modules TEC1-12706 are able to generate voltage from the heat loss at engine system and exhaust system of the car. Therefore, the potential of Peltier in generating electricity is accepted and the generating systems are effectively generates electricity from the heat loss of the vehicle system.

REFERENCES

[1] P. Ramade, P. Patil, M. Shelar, S. Chaudhary, S. Yadav, S. Trimbake, "A research on Automobile Exhaust Thermo-Electric Generator Design & Performance Analysis", *International Journal of Emerging Technology and Advanced Engineering*, 4(5), pp. 682-691, 2014.

[2] M. Ozollapins, A. Kakitis, "Thermoelectric Generators As Alternate Energy Source In Heating Systems. Engineering For Rural Development", 24, pp. 673-677, 2012.

[3] A. Jacks delightus peter, D. Balaji, D. Gowrishankar, "Waste Heat Energy Harvesting Using Thermo Electric Generator", *Journal of Engineering* (IOSRJEN), pp 01-04, 2013.

Flexible piezoelectric micro-power generator based on P(VDF-TrFE)

Khoon Keat Chow[1], Swee Leong Kok[2,*], Kok-Tee Lau[3]

[1] Department of Electrical Engineering, Politeknik Ungku Omar,
Jalan Raja Musa Mahadi, 31400 Ipoh, Perak, Malaysia
[2] Faculty of Electronics and Computer Engineering, Universiti Teknikal Malaysia Melaka,
Hang Tuah Jaya, 76100 Durian Tunggal, Melaka, Malaysia
[3] Faculty of Manufacturing Engineering, Universiti Teknikal Malaysia Melaka,
Hang Tuah Jaya, 76100 Durian Tunggal, Melaka, Malaysia

*Corresponding e-mail: sweeleong@utem.edu.my

Keywords: Polymer; piezoelectric sensor; energy harvester

ABSTRACT − In this paper, we have successfully demonstrated the fabrication of poly(vinylidene fluoride) trifluoroethyleneP(VDF-TrFE) thick films on flexible substrate using rod mayer method. The flexible piezoelectric transducer was able to generate a maximum output power of 0.552μWat an external load of 1MΩ with a maximum peak voltage of 743mV when pinching between two fingers with a force of 5N.

1. INTRODUCTION

Piezoelectric materials have been widely used for various energy harvester applications such as biomedical engineering, smart sensor detection, and flexible electronic applications [1]. Poly(vinylidene fluoride) (PVDF) and PVDF-trifluoroethylene (PVDF-TrFE) are piezoelectric polymers with lower piezoelectricity compared to ceramic based piezoelectric material such as PZT but can conform to complex structuralsurfaces due to their polymeric nature. PVDF and PVDF-TrFE is a highly non-reactive, flexible,inexpensive, and leading polymer with good piezoelectric property [2].

The disadvantage of the PVDF piezoelectric materials is that it requires mechanical stretching, which is not suitable for conventional microfabrication processes [3]. PVDF-TrFE in another hand consists of crystalline structure andtherefore the piezoelectric properties depend on the molecular proportion x of vinyledene fluoride in P(VDFxTrFE1−x).The presence of TrFE in the copolymer of the PVDF-TrFE film introduces significant features to the PVDF homo-polymer.One of the advantages of PVDF-TrFE is that it increases the tendency to crystallize in the polarβ-phase without the requirement of mechanical stretching totransform the nonpolar α-phase to the polar β-phase as in the case of PVDF, when $0.6 < x < 0.85$ [4].

Among the PVDF-TrFE copolymers, the copolymer at composition near 75/25 mol.% exhibits the highest ferroelectric responses [5-6]; hence, in this paper, the PVDF-TrFE copolymer with a molar ratio of 75/25 was used to fabricate as a thick-film on a flexible substrate. The voltage signalresponses to finger pinching of the piezoelectric PVDF-TrFE structures was studied.

2. METHODOLOGY

P(VDF-TrFE) thick films in this work was prepared using Poly(vinylidene fluoride-trifluoroethylene) with a molecular weight of 350,000 gmol^{-1} or [70:25mol%] manufactured by Kureha, Japan. Prior to the thick film fabrication, P(VDF-TrFE) (70:25mol%) powder were dissolved in *N,N*-dimethylformamide (DMF) obtained from Sigma Aldrich, with a concentration of 30ml.

The P(VDF-TrFE) powder was prepared according to the designated weight in percentage of 15wt%. The powder was dissolved in DMF and mechanically stirred at 100 °C for 1 hour. The solution was then immersed in an ultrasonic bath for 20min to ensure that the solution was fully dissolved. Then it was used to deposit a thick film to an approximation of 250μm thick by using mayer rod coating method (RDS #44 wire size, R.D. Specialties) on a flexible polymer (Melinex 723) substrate with thickness of 75 μm. The thick film was dried under infra-red light for 15 min with a temperature of 60˚C in order to remove the residual solvent.

Prior to the P(VDF-TrFE) deposition, first palladium-silver electrode layer were screen-printed using screen stencil onto the blank Melinex 723 substrate. The second palladium-silver electrode layer was applied after the infra-red light treatment. The thick film was subsequently annealed in an ambient environment oven at 100˚C for 1 hour to obtain a smooth and crystalline surface with reduced porosity [7]. Electrical poling was performed across the thick films using D.C. power supply at 100 V for 20 min at 100°C (near to Curie temperature of P(VDF-TrFE). This polarization is to align the domain dipole according to the polarity of the DC voltage. The fabricated sensor device of the sandwiched P(VDF-TrFE) thick film is illustrated in Figure 1 which is being used for the experimental testing in next step.

3. RESULTS AND DISCUSSION

A simple experiment setup was conducted to measure the output of the flexible micro-power generator by pinching between two fingers until both end of the flexible substrate meet each other. The force's magnitude applied by the fingers was estimated by substituting the fingers forces with incrementally loaded

mass weights that placed on the flexible substrate until both substrate end touched. The output from the flexible micro-power generator is measured using digital oscilloscope (Agilent Technologies: DSO-X2012A) as shown in Figure 2. The result shows that the peak-to-peak voltage output signal varying between ±2 mV when a force of average 5N is being applied to the polymer sensor due to the bending and stretchingmovement of a finger.

(a)

Top &BottomElectrode

P(VDF-TrFE) Layer

Melinex Substrate

(b)
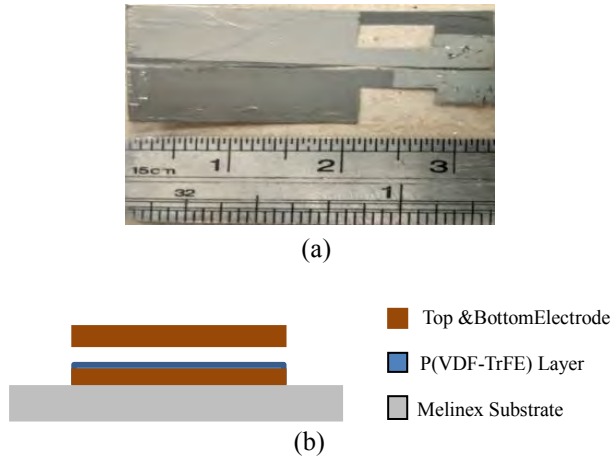
Figure 1 (a) Photograph of a fabricated flexible piezoelectric micro-power generator., (b) the schematic diagram of the sandwiched thick film.
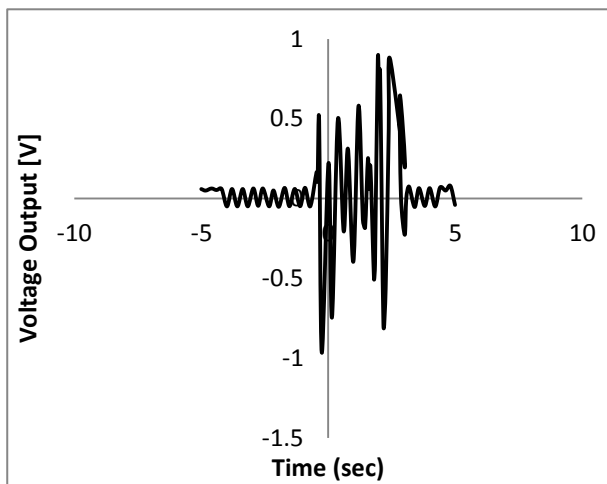
Figure 2 Output voltage from finger movement.

The output power of the flexible sensor is can be evaluated by using equation,

$$P = V^2 / R_L \qquad (1)$$

Where V is the output voltage across a 1MΩ external load resistor R_L. Based on the experimental output voltage, the average output voltage is 843mV and therefore the output power can be calculated as 0.711µW from a single layer P(VDF-TrFE) micro-power generator.

4. CONCLUSION

In this paper, piezoelectric P(VDF-TrFE) thick films were successfully fabricated and polarized simultaneously onto the Melinex polyester substrate as sensor generator using rod mayer method. Repeated and consistent experiment results of output voltage up to 843mV has been generated under bending and stretching movement with an estimated force of 5 N, of which the output power can be calculated as 0.711µW.

REFERENCES

[1] X. P. Qing, H.-L. Chan, S. J. Beard, and A. Kumar, ─An active diagnostic system for structural health monitoring of rocket engines," *J. Intell.Mater. Syst. Struct.*, vol. 17, no. 7, pp. 619–628, Jul. 2006.

[2] Z. L. Wang, ─Zinc oxide nanostructures: Growth, properties and applications," *J. Phys.: Condens. Mat.*, vol. 16, no. 25, pp. R829–R858, 2004.

[3] Chunyan Li, Pei-Ming Wu, Sooh Yun Lee, Andrew Gorton, Mark J. Schulz, and Chong H. Ahn, ─Flexible Dome and Bump Shape Piezoelectric Tactile Sensors Using PVDF-TrFE Copolymer,"*J. MEMS. SYS*, vol. 17, no. 2, pp.334-341, Apr. 2008.

[4] H. Ohigashi, ─Piezoelectric polymers—Materials and manufacture," *Jpn.J. Appl. Phys.*, vol. 24, pp. 23–27, 1985.

[5] H. Nalwa, *Ferroelectric Polymers*. New York: Marcel Dekker, 1995.

[6] T. Furukawa, ─Ferroelectric properties of vinylidene fluoride copolymers," *Phase Transit.*, vol. 18, no. 3/4, pp. 143–211,1989.

[7] Rahman Ismael Mahadi, W.C.Gan and W.H. Abd. Majid, ─Hot Plate Annealing at a Low Temperature of a Thin Ferroelectric P(VDF-TrFE) Film with an Improved CrystallineStructure for Sensors and Actuators," *Sensor*, vol.14, pp.19115-19127,2014.

Effect of samarium concentration on the structural and electrical properties of (K, Na) NbO$_3$ thin films

Nurul Azuwa Azmi[1], Umar Al-Amani Azlan[2,*], Mohd Asyadi „Azam Mohd Abid[1], Mohd Warikh Abd Rashid[1], Maziati Akmal Mohd Hatta[1]

[1)] Faculty of Manufacturing Engineering, Universiti Teknikal Malaysia Melaka,
Hang Tuah Jaya, 76100 Durian Tunggal, Melaka, Malaysia
[2)] Faculty of Engineering Technology, Universiti Teknikal Malaysia Melaka,
Hang Tuah Jaya, 76100 Durian Tunggal, Melaka, Malaysia

[*]Corresponding e-mail: umar@utem.edu.my

Keywords: Samarium; structural; electrical

ABSTRACT – Potassium sodium niobate have been chosen as a new candidate to replace the usage of lead-based materials due to its excellent properties. However, volatilities of K and Na can affect the electrical properties. This problem can be minimized by adding a doping element into A-site ions which is Samarium. A simple sol-gel route was used to produce the thin films with different dopant concentrations. In this work, the structural and electrical properties were determined by using XRD and LCR meter, respectively. It was found that the structure of KNN had a tendency to change from orthorhombic to tetragonal phase, thus resulting in better electrical properties of the KNN thin films.

1. INTRODUCTION

Recent studies on lead-based materials has led to the development of lead-free materials due to the environmental concern on the usage of lead-based materials especially the PbZrTiO$_3$ (PZT). The regulation have been made by the Restriction of Hazardous Substances (RoHS) due to its dangerous effect on human and other living things [1] [2]. Therefore, potassium sodium niobate, (K, Na) NbO$_3$ (KNN) has been a good candidate to replace the high usage of PZT materials. KNN has been recognized recently due to its high Curie temperature (420°C), high dielectric constant (~700), high remanent polarization (14 µC·cm^{-2}), low coercive field (~140 kV·cm^{-1}) and high piezoelectric constant [3]. Nevertheless, the volatilization of K and Na at certain temperature resulted in poor electrical properties of KNN, likely due to defects and oxygen vacancies [3][4]. Therefore, this problem can be minimized by doping of A-site ions, (K$_{0.5}$, Na$_{0.5}$)$^+$ and/or B-site ion Nb^{5+} which happened to be improved its physical and electrical properties [5][6]. Hence, this present study is focusing on the addition of Samarium (Sm), for better electrical properties of KNN with different doping concentrations.

2. METHODOLOGY

Sodium acetate and potassium acetate was used as the starting precursors. Subsequently, samarium nitrate hexahydrate was added with different concentrations of 0.1, 0.3, 0.5, 0.7 and 0.9 mol % as the doping element and mixed into 2-methyloxyethanol. In the meantime, niobium ethoxide and acetyl acetone (chelating agent) were also mixed into 2-methyloxyethanol in different beaker. After continuous stirring for 30 minutes, the solutions were mixed together for an hour with continuous stirring at 60°C. The solution was then deposited on Si-substrate with optimized layer of thickness. The films were spun onto the wafer with 3000 rpm for 1 minute by using spin coater. The pyrolysis was happened between the layers of films for 2 minutes. The films were annealed later on at 650°C for 10 minutes by using rapid thermal processing (RTP) furnace. The crystallization phase of Sm-doped KNN was analyzed by using X-ray diffractometer (XRD). Then, the electrical properties were measured using LCR meter.

3. RESULTS AND DISCUSSION

The XRD patterns of Sm-doped KNN with different concentrations of 0 up to 0.9 mol % Sm are shown in Fig. 1. It was found that the diffraction peak (200) of KNN has been shifted with the addition of dopant element. Moreover, the addition of Sm has changed the structure of KNN from orthorhombic into tetragonal, thus reducing the lattice distortion [6]. As reported in other work, higher piezoelectric properties might be obtained, however, it depends on the ceramic compositions [7].

The LCR meter have been used to measure the tangent loss (tanδ, %) and dielectric constant (ε''), as shown in Fig. 2. The film with above 0.3 mol % of Sm concentration was found to have better electrical properties. It can be clearly seen that the decrement of tan δ and increment of ε'' is attributed due to doping effect. Furthermore, it also indicates that the effectiveness of rare-earth in KNN for better electrical properties in piezoelectric applications.
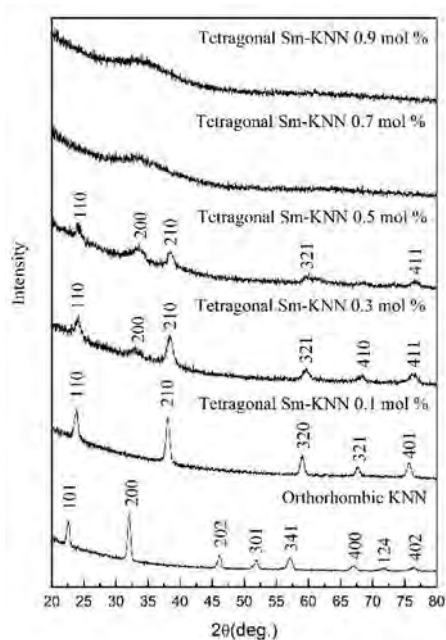
Figure 1 XRD patterns of the KNN thin films with different Sm concentrations of 0, 0.1, 0.3, 0.5, 0.7, and 0.9 mol % deposited on Si substrate and subsequently, annealed at 650°C.
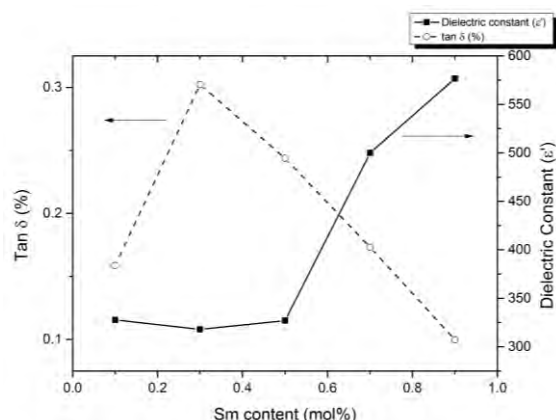
Figure 2 Dielectric constant and tangent loss of KNN thin films with different Sm concentrations.

4. CONCLUSIONS

In this study, the KNN thin films with different Sm concentrations were fabricated to improve its electrical properties. The structure of KNN with higher Sm concentration was found to be transformed from orthorhombic to tetragonal phase, which is also resulted in better electrical properties. This result is believed can contribute in the development of piezoelectric thin films for sensor applications.

REFERENCES

[1] D. Fasquelle, M. Mascot, N. Sama, D. Remiens, and J.-C. Carru, "Lead-free piezoelectric thin films for RoHS devices," *Sensors Actuators A Phys.*, vol. 229, no. 0, pp. 30–35, 2015.

[2] K. Wang and J. Li, "(K, Na)NbO3-based lead-free piezoceramics: Phase transition, sintering and property enhancement," *J. Adv. Ceram.*, vol. 1, no. 1, pp. 24–37, 2012.

[3] M. Akmal, M.A.T. Harttar, M. Warikh, A. B. D. Rashid, U. Al, and A. Azlan, "Physical and electrical properties enhancement of rare-earth doped-potassium sodium niobate (KNN): A review," *Ceramics-Silikaty*, vol. 59, no. 2, pp. 158–163, 2015.

[4] L. Wang, W. Ren, P. Shi, X. Wu, and X. Yao, "Effects of thickness on structures and electrical properties of Mn-doped K0.5Na0.5NbO3 films," *J. Alloys Compd.*, vol. 582, pp. 759–763, 2014.

[5] M.A. Mohd Hatta, U.A. Azlan, M. W. Abd Rashid, and Azmi, Nurul Azuwa, "Enhanced structural and electrical properties of lead-free Y-doped (K, Na) NbO3 thin films," *J. Teknol.*, vol. 21, no. 77, pp. 67–71, 2015.

[6] W. Li, Z. J. Xu, R. Q. Chu, P. Fu, and G. Z. Zang, "Piezoelectric and Dielectric Properties of (Ba1-xCax)(Ti0.95Zr0.05)O3 Lead-Free Ceramics," *J. Am. Ceram. Soc.*, vol. 93, no. 10, pp. 2942–2944, 2010.

[7] C.W. Ahn, C.S. Park, D. Viehland, S. Nahm, D. H. Kang, K. S. Bae, and S. Priya, "Correlation between phase transitions and piezoelectric properties in lead-free (K,Na,Li)NbO3-BaTiO3 ceramics," *Jpn. J. Appl. Phys.*, vol. 47, no. 12, pp. 8880–8883, 2008.

Failure analysis of two serial holes bolted joint hybrid composite

D. Sivakumar [1,2,*], N.S. Salmi[1], M.Z. Selamat[1,2], M.A. Daud[1, 2], C.F. Tan[1, 2]

[1] Faculty of Mechanical Engineering, Universiti Teknikal Malaysia Melaka,
Hang Tuah Jaya, 76100 Durian Tunggal, Melaka, Malaysia
[2] Centre for Advanced Research on Energy, Universiti Teknikal Malaysia Melaka,
Hang Tuah Jaya, 76100 Durian Tunggal, Melaka, Malaysia

*Corresponding e-mail: sivakumard@utem.edu.my

Keywords: Bolted-joint; polypropylene; woven kenaf; hybrid composite

ABSTRACT – This study investigates the effect of different geometry parameters to the behavior of bolted-joint hybrid composites. The hot compression method is used to fabricate the hybrid composite. The composites were fabricated with three layers of woven fibers which are two layers of woven glass fiber and a layer of woven kenaf fiber with polypropylene matrix making a composite panel. The nominal thickness of these composites is 3mm and the bearing test is done by using Universal Testing Machine. The test were conducted according to ASTM D5961. The results show the different geometry parameters affect the behavior of hybrid composites.

1. INTRODUCTION

Natural fiber have many significant advantages over synthetic fiber. Past research state that the advantages of natural fiber over man-made fiber include low density, low cost, recyclability and biodegradability. These advantages make natural fiber potential replacement for glass fiber in composite materials. Mechanical properties of natural fiber are very good and may compete with glass fiber in specific strength and modulus [1]. Natural fiber-reinforced composites can be applied in the plastics, automobile and packaging industries to cut down on material cost [2].

Kenaf, *Hibiscus cannabinus* [3,4], a member of hibiscus family is also a biodegradable and environmentally friendly crop. It has been found to be an important source of fiber for composites and other industrial applications. The fiber is fully biodegradable, is non-toxic and may be recycled. Based on research paper of Abdul Khalil (2010), Malaysian kenaf is composed of two distinct fiber, bast and core, with a makeup of about 35% and 65%, respectively. The usage of the two different fiber is not same. Thus, separation of the fiber produces higher monetary returns over whole-stalk kenaf. Main factors involved in separation of kenaf into its two fractions include size and amount of each portion, type and number of separation machinery, processing rate through separation machinery, moisture content of whole-stalk kenaf and humidity of ambient air [5].

Fiber reinforced composites consist of fiber as reinforcement and a polymer as a matrix. Natural fiber composites such as hemp fiber-epoxy, flax fiber-polypropylene (PP), and China reed fiber-PP are commonly used in automotive applications since it has lower cost and lower density which is 35% to 40% less compared to glass fiber [6].

This study will investigate the behavior of the hybrid composite. The effect of three layers of woven glass/kenaf/PP composite with different geometry parameters which are edge distance-to-upper hole centre/hole diameter (E/D) and distance between centres of two holes/hole diameter (K/D) were tested and the failure was analyzed.

2. METHODOLOGY

The woven glass and kenaf fiber reinforced polypropylene composites panel consists of three layers contain of woven kenaf and glass fiber in polypropylene matrix forming 3 mm thick composite panel.

The fabrication process starts with the production of PP sheet. In mean time, the woven kenaf which already cut to 170×250mm (width × length) are dried in the oven for 24 hours at 40°C. The fiber reinforcements and the matrix then are layered simultaneously glass fiber-PP-kenaf fiber-PP-glass fiber into a picture frame mold 250×170× 3 mm (length ×width ×thickness). The PP sheets is placed in 1-2-1-1 order respectively. The mold is placed in the hot press to reheat it to about 180°C for 5 minutes. Followed by increase in pressure progressively until reaching 30kg/cm2. Finally the pressure is maintained for 4 minutes before cooling it down. The composite panel is cut into specimens and drilled according to ASTM D5961as shown in Figure 1 and Table 1.The crosshead speed used is 2mm/min as recommended in ASTM D5961 for the two serial holes testing.
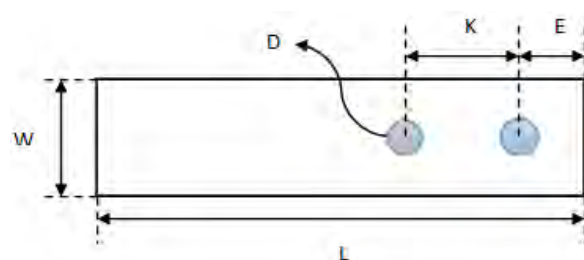
Figure 1 The standard dimension based on ASTM D5961[7].

Table 1 Double-shear and single-shear one-piece test specimen dimensions [7].

Parameter	Standard Dimension (mm)
Fastener or pin diameter, d	6 + 0.00/-0.03
Hole diameter, D	6 + 0.03/-0.00
Length, L	3-5
Width, W	36±1
Edge distance, E	18±1
Countersink	non

3. RESULTS AND DISCUSSION

Based on figure 2, the maximum load of K/D=3 and E/D=3 has a higher maximum load compared to K/D=2 and E/D=3. The higher ratio of E/D and K/D, the failure loads tend to increase[8]. The failure behavior occur during this study are net tension, shear out and bearing. The increasing of E/D ratio causes the composite to shear out become bearing. Meanwhile, the increasing of K/D ratio causes the composites shear out to net tension [9].
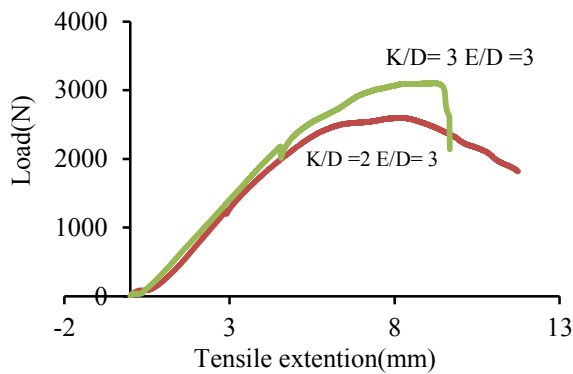
Figure 2 Load-tensile extension graph.

4. CONCLUSION

The different of geometry parameters of bolted joint composites show the different behavior. The larger the ratio of E/D and K/D, the larger the failure load of composite. The bearing occurs when the smaller ratio applied to the specimen, while shear out and net tension occur when the ratio is higher.

REFERENCES

[1] X. Li, L. G. Tabil, and S. Panigrahi, "Chemical Treatments of Natural Fiber for Use in Natural Fiber-Reinforced Composites: A Review," *J. Polym. Environ.*, vol. 15, no. 1, pp. 25–33, 2007.

[2] M. Ammar, B. Che, S. D. Malingam, M. Z. Bin, and R. Bin Said, "A Study on the Mechanical and Forming Performance of Oil Palm Fiber Reinforced," *Am. J. Sustain. Agric.*, vol. 8, no. 4, pp. 141–147, 2014.

[3] H. M. Akil, M. F. Omar, A. A. M. Mazuki, S. Safiee, Z. A. M. Ishak, and A. Abu Bakar, "Kenaf fiber reinforced composites: A review," *Mater. Des.*, vol. 32, no. 8–9, pp. 4107–4121, 2011.

[4] S. Taj, M. A. Munawar, and S. Khan, "Natural Fiber-Reinforced Polymer Composites," *Carbon N. Y.*, vol. 44, no. 2, pp. 129–144, 2007.

[5] H. P. S. Abdul Khalil, A. F. I. Yusra, A. H. Bhat, and M. Jawaid, "Cell wall ultrastructure, anatomy, lignin distribution, and chemical composition of Malaysian cultivated kenaf fiber," *Ind. Crops Prod.*, vol. 31, no. 1, pp. 113–121, 2010.

[6] S. . V Joshi, L. . T. Drzal, a. . K. Mohanty, and S. Arora, "Are natural fiber composites environmentally superior to glass fiber reinforced composites?," *Compos. Part A Appl. Sci. Manuf.*, vol. 35, no. 3, pp. 371–376, 2004.

[7] "ASTM D5961 / D5961M - 13 Standard Test Method for Bearing Response of Polymer Matrix Composite Laminates." .

[8] M. Ozen and O. Sayman, "Failure loads of mechanical fastened pinned and bolted composite joints with two serial holes," *Compos. Part B Eng.*, vol. 42, no. 2, pp. 264–274, 2011.

[9] B. Okutan, Z. Aslan, and R. Karakuzu, "A study of the effects of various geometric parameters on the failure strength of pin-loaded woven-glass-fiber reinforced epoxy laminate," *Compos. Sci. Technol.*, vol. 61, no. 10, pp. 1491–1497, 2001.

Failure analysis on hybrid fiber reinforced plastics for bolted joint under geometric parameters effect

D. Sivakumar [1,2,*], R.M. Chew[1], M.Z. Selamat[1, 2], M.A. Daud[1,2], C.F. Tan[1,2]

[1) Faculty of Mechanical Engineering, Universiti Teknikal Malaysia Melaka,
Hang Tuah Jaya, 76100 Durian Tunggal, Melaka, Malaysia
[2) Centre for Advanced Research on Energy, Universiti Teknikal Malaysia Melaka,
Hang Tuah Jaya, 76100 Durian Tunggal, Melaka, Malaysia

*Corresponding e-mail: sivakumard@utem.edu.my

Keywords: Bolted joint; woven kenaf; hybrid composite

ABSTRACT – In this study, glass fiber and kenaf reinforced thermoplastic hybrid composite were fabricated using compression method. The composite is layout in sandwich structure. Woven glass fiber is sandwiched in between woven kenaf fiber with polypropylene matrix. The nominal thickness of the composite is 3mm. Bolted joint test was conducted according to ASTM D5961 using Universal testing machine. The results confirm geometric parameters affect the failure mode.

1. INTRODUCTION

Composite materials are frequently used in advanced engineering fields such as in aerospace, leisure, automotive, construction and sporting industries. Composite materials have wide application because of their high specific strength and modulus [1,2]. The objective of a composite is to make a component strong and stiff with low density. Thermoplastics are more preferable than thermosetting since they are moldable after initial process whereas thermosetting polymers are permanent and irreversible after solidify. Recently, natural fibers have become a hot topic in composite materials. The advantages of natural fibers are low cost, low density, comparable specific tensile properties, recyclability and bio-degradable, etc. [3]. The application of lightweight, low-cost natural fibers provides the potential to replace a large segment of the glass and mineral fillers in automotive industries [4].

Mechanically fastened joints are frequent and critical elements in composite structure such as aircraft structures. It is important to design the joint properly because if an improper design is used, it may lead to overweight or defective structures. A bolted joint is engaged to hold two or more parts together to form an assembly in a mechanical structure. Since most composite materials display a brittle failure, with little or no margin of safety through ductility, the mechanism of the brittle failure propagation in bolted joint must be fully known [5].

The stress distribution around the hole in the bolted joints is a perplexing phenomenon. The stress distribution is strongly affected by the geometric parameters, clamping force, stacking sequences, and clearance between the hole and the pin. A large part of

the research that has been carried out on bearing strengths had showed that the failure mode is dependent on the width-to-diameter (W/D) and edge distance-to-diameter (E/D) ratios [6]. There are 4 types of common failure modes in bolted composite plates which are cleavage, net-tension, shear-out and bearing.

The present study will investigate the failure analysis of the bolted joint under geometric parameters with a ratio of 3 and 6 on W/D and E/D parameter on glass fiber-kenaf hybrid composite.

2. METHODOLOGY

A custom stainless steel jig is fabricated in order to conduct the bolted joint test. The function of jig is to hold the specimen through the bolt connected to the jig. Figure 1 shows the jig.
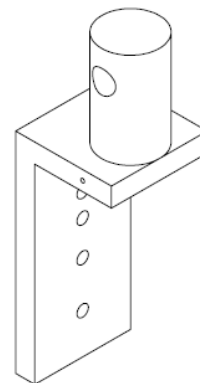
Figure 1 Jig for bolted joint test.

Kenaf and glass fibers are used as reinforcement fibers while PP for the polymer matrix. The layout of the composite structure is sandwich structure, where glass fiber is the central component of the sandwich structure, in between of two woven kenaf layer. A 3mm thick picture frame was used when fabricating the composite in order to get a final nominal composite thickness of 3 mm. The temperature for the compression molding process is 180°C with a pressure of 30 psi.

The composites were cut into appropriate specimen dimension based on ASTM D5961 as shown in Figure 2. The length of the specimen, L = 135 mm. Table 1 shows the specimen dimension ratio used for the test.
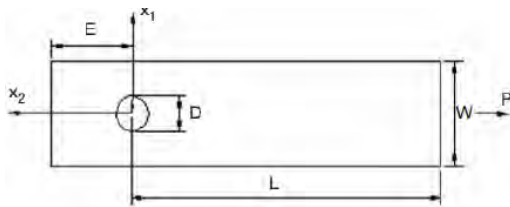
Figure 2 Specimen geometry.

Table 1 Dimension ratio.

D(mm)	E/D	W/D
6.0	3,4,5,6	3,4,5,6

Universal testing machine INSTRON 5969 is used to perform bolted joint test according to ASTM D5961. Three test were conducted for each ratio to obtain the average. The specimen is loaded until a maximum force is reached and force dropped off about 30% from the maximum force. The test is then terminated after the force reached the 30% of the maximum force so the failure mode can be observed.

3. RESULTS AND DISCUSSION

Bolted joint tests were conducted and average maximum load values were computed. According to the test result, some specimens break away suddenly. This failure mode is called net-tension. For a number of specimens, the load then increases with rising damage and reaches the ultimate point. Then, the load decreases with rising damage. However, the specimen continues to hold up loading. This failure mode is called bearing. Net-tension failure occurs to specimen with W/D ratio below than 5 whereas specimen with W/D ratio higher than 4 will experience bearing failure. Figure 3 shows the two extreme results from the test.
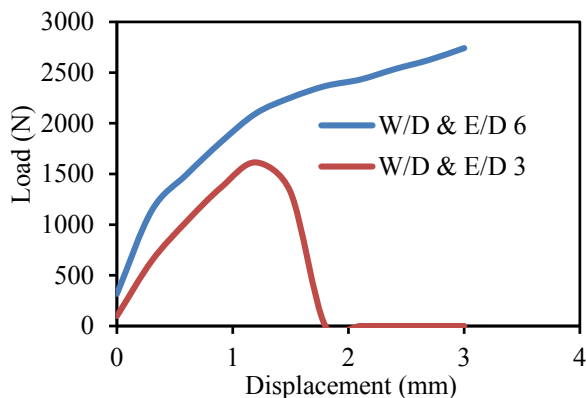
Figure 3 Loads versus displacement graph.

4. CONCLUSION

According to the experimental results, the failure modes of the bolted joint have been investigated experimentally. The effects of changing the geometric parameters were observed. According to the experimental study results, it can be concluded that when W/D ratio is equal and below 4, net-tension failure will occur whereas bearing failure will occur when W/D ratio is equal or more than 5.

ACKNOWLEDGEMENT

REFERENCES

[1] F. Sen, M. Pakdil, O. Sayman, and S. Benli, "Experimental failure analysis of mechanically fastened joints with clearance in composite laminates under preload," *Mater. Des.*, vol. 29, pp. 1159–1169, 2008.

[2] M. Ammar, B. Che, S.D. Malingam, M. Z. Bin, and R. Bin Said, "A Study on the Mechanical and Forming Performance of Oil Palm Fiber Reinforced," *Am. J. Sustain. Agric.*, vol. 8, no. 4, pp. 141–147, 2014.

[3] H. Ku, H. Wang, N. Pattarachaiyakoop, and M. Trada, "A review on the tensile properties of natural fiber reinforced polymer composites," *Compos. Part B Eng.*, vol. 42, no. 4, pp. 856–873, 2011.

[4] J. Holbery and D. Houston, "Natural-fiber-reinforced polymer composites in automotive applications," *Jom*, vol. 58, no. 11, pp. 80–86, 2006.

[5] K.I. Tserpes, G. Labeas, P. Papanikos, and T. Kermanidis, "Strength prediction of bolted joints in graphite / epoxy composite laminates," *Compos. Part B Eng.*, vol. 33, pp. 521–529, 2002.

[6] B.G. Kiral, "Effect of the clearance and interference-fit on failure of the pin-loaded composites," *Mater. Des.*, vol. 31, no. 1, pp. 85–93, 2010.

Thermoplastic matrix selection based on entropy method for importance weight of criteria

N.M. Ishak[1,*], D. Sivakumar[1], M.R. Mansor[1]

1) Faculty of Mechanical Engineering, Universiti Teknikal Malaysia Melaka,
Hang Tuah Jaya, 76100 Durian Tunggal, Melaka, Malaysia

*Corresponding e-mail: diedieku@yahoo.com

Keywords: Thermoplastic matrix; fibre metal laminate; entropy method

ABSTRACT – The purpose of this study is to determine the importance weight of criteria for thermoplastic matrix selection that need to be considered in fibre metal laminate fabrication for car front hood using entropy method, where the information implied using the linguistic terms. The results showed that the tensile strength, impact strength and density are the essential criteria that need to be considered.

1. INTRODUCTION

With the high production of carbon dioxide (CO_2), vehicles are the main source of the air pollution. It is a primary product of combustion and, for this reason, its production is directly connected to fuel consumption and, consequently, to vehicle weight. Hence, to reduce the CO_2 gas emission, the reduction of vehicle weight is highly recommended [1], and one of the strategy is by reducing the front hood weight. Front hood is the broad piece of metal that gives access to the engine compartment. It has an outer and inner panel. The external panel is the hood skin, while the internal panel is the insulator.

To reduce the weight of the front hood the use of fibre metal laminate has been considered which apart from their potential to be lightweight, FML resistance to localized blast events can improve human safety in mass transit and defense applications [2]. Fibre metal laminate is a combining the suitable properties of layering metals with fibre reinforced composites which are bonded by an adhesive layer. One of the familiar adhesive layer is thermoplastic matrix. Mansor et al. [3] used Multiple Attribute Decision Making (MCDM) methods to select thermoset matrix for automotive bumper beam.

Entropy is the most common method used in MCDM and it was introduced as a new concept of information theory. It could generate objective weight and often used for assessing weight with other MCDM method such as TOPSIS, AHP, etc. Entropy also can be combined with multiple MCDM method as it has been used by Jovanovic et al. [4] to evaluate the significance of environmental impacts with multiple methods AHP, AHP Entropy, TOPSIS, VIKOR and Entropy VIKOR. According to Zhou and Guo [5], combination of subjective weighting method (linguistic ratings) and objective weighting method (entropy method) could measure information implied in the index data and consider the essential information. The combination also can embody the conscious tendencies of decision makers.

It is well known that the entropy method is commonly used to determine weight of criteria in any field. Therefore, the aim of this study is to determine the importance weight of criteria for thermoplastic matrix selection that need to be consider in fibre metal laminate fabrication for car front hood using entropy method.

2. RESEARCH METHODOLOGY

For this study, linguistic rating terms and corresponding fuzzy numbers used are as in Table 1.

Table 1 Linguistic terms and corresponding fuzzy numbers.

Linguistic variable	Fuzzy number
Not important	(0.0, 0.0, 0.1)
Low importance	(0.0, 0.1, 0.3)
Slightly important	(0.1, 0.3, 0.5)
Fair	(0.3, 0.5, 0.7)
Medium important	(0.5, 0.7, 0.9)
Important	(0.7, 0.9, 1.0)
Very important	(0.9, 1.0, 1.0)

2.1 Entropy method

The entropy method is capable of being deployed as an objective weight calculation where:

$$X = \left[X_1, X_2, ... X_n \right] \qquad (1)$$

The aggregate weight for each criterion W_j calculated as follow:

$$X_{ij} = \frac{1}{n} \left(\sum_{e=1}^{n} X_{ij}^e \right), i = 1, 2, ... m \qquad (2)$$

The decision matrix need to be normalized to gain projection value of each criterion $C_j (j = 1, 2, ... n)$: P_{ij}

$$P_{ij} = \frac{x_{ij}}{\sum_{j=1}^{m} x_{ij}} \qquad (3)$$

After normalization, the entropy value e_j calculated as,

$$e_j = -k \sum_{j=1}^{n} P_{ij} \ln P_{ij} \qquad (4)$$

k is constant, let $k = (\ln(m))^{-1}$ The degree of divergence d_i of the basic information of each criterion calculated as,

$$d_{ij} = 1 - e_j \qquad (5)$$

The higher the d_j is, the more important the criterion C_j is for the problem.

The objective weight for each criterion can be obtain,

$$W_j = \frac{d_j}{\sum_{k-=1}^{n} d_k} \qquad (6)$$

3. RESULTS AND DISCUSSION

Table 2, Table 3 and Table 4 summarized the overall scores based on the entropy method for the importance of thermoplastic matrix criteria that need to be highly consider on the fibre metal laminate fabrication for car front hood. Criteria that involved in the selection are C1 (tensile strength), C2 (stiffness), C3 (elongation), C4 (impact strength), C5 (density), C6 (water absorption) and C7 (cost).

Table 2 Importance weight of criteria assessed by decision maker.

Criteria	D1	D2	D3
C1	(0.9,1.0,1.0)	(0.9,1.0,1.0)	(0.9,1.0,1.0)
C2	(0.9,1.0,1.0)	(0.7,0.9,1.0)	(0.9,1.0,1.0)
C3	(0.5,0.7,0.9)	(0.5,0.7,0.9)	(0.5,0.7,0.9)
C4	(0.9,1.0,1.0)	(0.9,1.0,1.0)	(0.9,1.0,1.0)
C5	(0.9,1.0,1.0)	(0.9,1.0,1.0)	(0.9,1.0,1.0)
C6	(0.7,0.9,1.0)	(0.9,1.0,1.0)	(0.7,0.9,1.0)
C7	(0.9,1.0,1.0)	(0.9,1.0,1.0)	(0.7,0.9,1.0)

Table 3 Aggregation, normalization and decision maker's weight for each criterion.

Criteria	X_{ij}	P_{ij}	$\widetilde{W}$
C1	(0.9,1.0,1.0)	0.967	0.1519
C2	(0.833,1.967,1.0)	0.933	0.1465
C3	(0.5,0.7,0.9)	0.7	0.1099
C4	(0.9,1.0,1.0)	0.967	0.1519
C5	(0.9,1.0,1.0)	0.967	0.1519
C6	(0.767,0.933,1.0)	0.9	0.1414
C7	(0.833,0.833,1.0)	0.933	0.1465

Table 4 Entropy value, degree of divergence and objective weight for each criterion.

Criteria	e_j	d_j	W_j
C1	0.8266	0.1734	0.1721
C2	0.8429	0.1571	0.1559
C3	0.9690	0.031	0.0307
C4	0.8266	0.1734	0.1721
C5	0.8266	0.1734	0.1721
C6	0.8580	0.142	0.1409
C7	0.8249	0.1571	0.1559

The larger value indicates the important criteria [6]. Based on the results, criteria 1, 4 and 5 have the highest value of weight compared to the other criteria. Second criteria that need to be consider are criteria 2 and 7. While criteria 6 and 3 are at the lowest importance rank.

4. CONCLUSIONS

As a result, through entropy method, it revealed that the three criteria; tensile strength, impact strength and density are the essential criteria that need to be consider during the selection of the thermoplastic matrix for fibre metal laminate fabrication for car front hood. It is crucial to identify the importance weight of criteria before developing any product to prevent failure during fabrication.

REFERENCES

[1] G. S. Cole and a. M. Sherman, "Light weight materials for automotive applications," *Mater. Charact.*, vol. 35, no. 1, pp. 3–9, 1995.

[2] DharMalingam, S., Selamat, Z. B., Said, R. B. and Kalyanasundaram, S., "Effects of process parameters during forming of glass reinforced-pp based," *Advances in Environmental Biology vol.* 8, no. 8, pp. 3143–3150, 2014.

[3] M. R. Mansor, S. M. Sapuan, A. Hambali, E. S. Zainudin, and A. A. Nuraini, "Materials selection of hybrid bio-composites thermoset matrix for automotive," *Adv. Environ. Biol.*, vol. 8, no. 8, pp. 3138–3142, 2014.

[4] J. Jovanovic, H. Shah, A. Vujovic, and Z. Krivokapic, "Comparative analysis of MCDM methods in Evaluation of," pp. 783–796, 2014.

[5] H. Zhao and S. Guo, "External benefit evaluation of renewable energy power in China for sustainability," *Sustainability*, vol. 7, no. 5, pp. 4783–4805, 2015.

[6] L. Abdullah, "A new fuzzy weighted based computation for environmental performance: A case of ASEAN countries," *WSEAS Trans. Environ. Dev.*, vol. 10, pp. 177–185, 2014.

Surface durability of oil palm fiber/epoxy composite at various temperatures

F.F. Shuhimi[1], M.F.B. Abdollah[1,2,*], M.A. Kalam[3], H.H. Masjuki[3], A. Mustafa[1], H. Amiruddin[1,2]

1) Faculty of Mechanical Engineering, Universiti Teknikal Malaysia Melaka,
Hang Tuah Jaya, 76100 Durian Tunggal, Melaka, Malaysia
2) Centre for Advanced Research on Energy, Universiti Teknikal Malaysia Melaka,
Hang Tuah Jaya, 76100 Durian Tunggal, Melaka, Malaysia
3) Department of Mechanical Engineering, Faculty of Engineering, University of Malaya,
50603 Kuala Lumpur, Malaysia

*Corresponding e-mail: mohdfadzli@utem.edu.my

ABSTRACT – The purpose of this work is to study the surface durability of Oil Palm Fiber/Epoxy (OPF/E) composite at different temperatures. The tribological test was carried out by using a pin-on-disc tribometer in dry sliding conditions. Surface durability was determined by the value of specific wear rate with respect to the temperature. The surface morphology was observed by scanning electron microscopy (SEM). It was found that 30 wt.% have high surface durability compared to 50 wt.% and 70 wt.% which can withstand at a maximum of 80°C before transition to severe wear occur.

1. INTRODUCTION

Natural fibre polymer composites have numerous applications in almost all fields of engineering. Natural fibres offer great potential as reinforcement in polymers for various industrial applications and have a greater impact on socio-economic development [1-2]. The development of high-performance engineering products made from natural resources is increasing around the world because of the issues of low cost with their low density, less damage in processing equipment, good relative mechanical properties and renewable resources as apparently environmentally superior alternatives to glass fibers in composites. Hence, in this present work an attempt has been made in order to emerge to be more environmental friendly and appeared as realistic alternative to become an essential factor used in industrial products and applications [3-5].

There are many situations and development of tribological components made of fiber reinforced polymer composites are under tribological loading conditions and having excellent wear and friction [1,6]. In addition, frictional heating must be considered to avoid the failure of tribological components because it has an important influence on the tribological behavior of so many sliding systems [7]. According to several studies that have been done, understanding the tribological behavior of natural fiber/polymer composites has an equal role to be debated with the mechanical attributes of those materials [4].

Although there were many researches about the influence tribological properties of the polymer composite, study on surface durability on temperature is still not considered yet. This motivates the current work to conduct a series of studies on the effect of temperature on OPF/E composite towards surface durability in tribo-performance.

2. METHODOLOGY

For fiber preparations, the fibers were soaked in 6 vol.% natrium hydroxide (NaOH) solution for 48 hours. Then it was rinsed and dried at room temperature. The prepared fibers of 30 wt.%, 50 wt.% and 70 wt.% were mixed with epoxy at a resin to hardener ratio of 4:1 using hot compaction technique. The sample was formed into a pin with diameter of 10mm and pressed at 2MPa, 80°C.

The tribological test was performed using a pin-on-disc tribometer according to ASTM G99-05 standard at a constant applied load of 49.05N and speed of 1000 rpm. The specific wear rate (Ws) was determined as in Equation 1.

$$Ws = \frac{V_{loss}}{FL} \qquad (1)$$

Where, V_{loss} is the volume loss (mm^3), Ws is the specific wear rate (mm^3/Nm), F is the applied load (N), and L is the sliding distance (m).

3. RESULTS AND DISCUSSION

Figure 1 shows the wear rate of OPF/E composite changes with temperature. At certain temperature, the wear rate was sharply increased, which the transitions to severe wear is realized. To be confirmed, the surface morphology was observed at 50°C and 130°C and presented in Figure 2 and Figure 3.

Figure 2 shows the worn surfaces of 30 wt.% OPF/E composite at 50°C and 130°C. It was clearly show that the surface was not highly damaged, as shown in Figure 2(a). Furthermore, it can be seen that the surface is still adhered well and there is a patch of the resin (mark as "R") which is protecting the fiber from severe damage.

As temperature increases to 130°C, debonding of fiber (mark as "De") occurred and micro cracks were observed (mark as "Cr"). According to El-Tayeb et.al

[8], surface heating in sliding contact would influence the extent of surface damage and thus increasing wear rate.
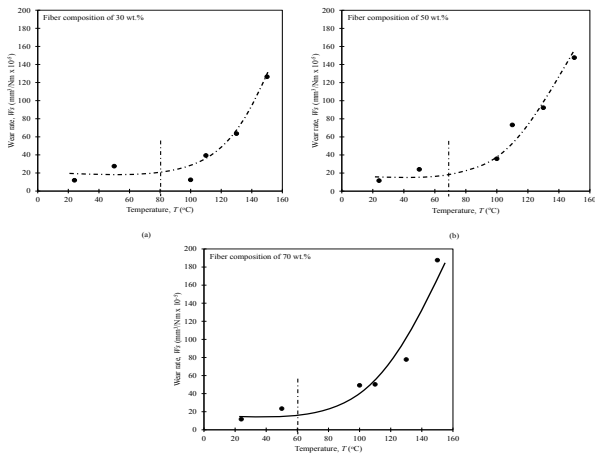
Figure 1 Effect of temperature on the wear rate of OPF/E composite (a) 30 wt.% (b) 50 wt.% (c) 70 wt.%.

Table 1 Mechanical properties of the OPF/E composite pin and disc materials.

Properties	[a]Pin 30wt.%	[a]Pin 50wt.%	[a]Pin 70wt.%	[b]Disc SKD11
Oil Palm Fiber/Epoxy				
Hardness, H [GPa]	7.14	7.13	6.7	7.35
Density, ρ [g/cm3]	1.34	1.336	1.321	7.72

[a] Properties from laboratory measurements.
[b] Properties from manufacturer.

(a)   (b)
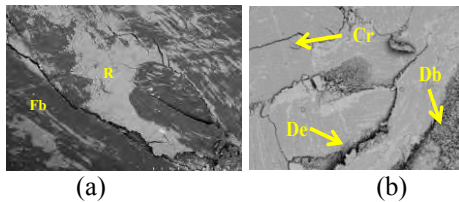
Figure 2 SEM micrographs of worn surface of 30wt.% OPF/E composite at (a)50^{0}C and (b)130^{0}C [De: debonding, Db: Debris, Fr: Small fracture, Cr: Micro-Crack, R: Resin. Fb: Fiber].

(a)   (b)
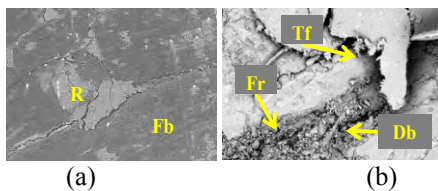
Figure 3 SEM micrographs of worn surface of 50wt.% OPF/E composite at (a)50^{0}C and (b)130^{0}C [Tf: Torn Fiber].

From Figure 3(a), the worn surface of 50 wt.% OPF/E composite is similar with 30 wt.% with less damages are observed. Meanwhile, at the severe region of 130^{0}C, it can be seen the fiber seem to be torn (mark as "Tf") and existed of fracture (mark as "Fr") associated with generated debris (mark as "Db") as

shown in Figure 3(b). This could be the other reason for the higher specific wear rate at higher temperature.

The above observations, 30 wt.% OPF shows lower wear rate than 50 wt.% and 70 wt.%. Chand and Fahim [1] noted that low hardness lead to increase the real area of contact thus increases the wear rate. Hence, the reason is believed due to the high hardness at 30 wt.% as shown in Table 1.

4. CONCLUSION

In summary, the findings provide insights that the OPF/E composite with 30 wt.% fiber has the lowest wear rate. It can be concluded that higher fiber composition in composite is not suitable for application at high temperatures, especially in tribology applications due to the high wear rate.

REFERENCES

[1] N. Chand and M. Fahim, Tribology of natural fiber polymer composites. Elsevier, 2008.

[2] A.N. Kasim, M.Z Selamat, N. Aznan, S.N. Sahadan, M.A.M. Daud, S. Salleh, and R. Jumaidin. "Effect of pineapple leaf fiber loading on the properties of pineapple leaf fiber–polypropylene composite," in *Proceedings of Mechanical Engineering Research Day 2015,* 2015, pp. 3-4.

[3] M.M Davoodi, S.M Sapuan, D. Ahmad, A. Aidy, A. Khalina and M. Janoobi, "Concept selection of car bumper beam with developed hybrid bio-composite material," *Materials & Design,* vol. 32, no.10, pp. 4857-4865, 2011.

[4] A. O'donnell, M.A. Dweib and R.P Wool, "Natural fiber composites with plant oil-based resin," *Composites Science and Technology*, vol.64, no.9, pp. 1135-1145, 2004.

[5] B.F Yousif, S.T. Lau and S. McWilliam, "Polyester composite based on betelnut fibre for tribological applications." *Tribology International*, vol. 43, no.1, pp. 503-511, 2010.

[6] A.K. Mohanty, M. Misra and L.T. Drzal, eds. *Natural fibers, biopolymers, and biocomposites*. CRC Press, 2005.

[7] F.E. Kennedy, "Frictional heating and contact temperatures," *Modern tribology handbook*, vol.1, 235-259, 2001.

[8] N.S.M. El-Tayeb, B.F. Yousif and P.V. Brevern, "On the effect of counterface materials on interface temperature and friction coefficient of GFRE composite under dry sliding contact." *American Journal of Applied Sciences 2*, vol. 11, pp. 1533-1540, 2005.

Estimation of corrugated cardboard strength using tensile test

N.B. Ab Wahab[1,2,*], Ainul Arafah[3], Y. Fukuzawa[3], S. Nagasawa[3]

[1] Faculty of Engineering Technology, Universiti Teknikal Malaysia Melaka,
Hang Tuah Jaya, 76100 Durian Tunggal, Melaka, Malaysia
[2] Advanced Manufacturing Center, Universiti Teknikal Malaysia Melaka,
Hang Tuah Jaya, 76100 Durian Tunggal, Melaka, Malaysia
[3] Department of Mechanical Engineering, Nagaoka University of Technology, 1603-1 Kamitomioka Nagaoka, Niigata 940-2188 Japan

[*]Corresponding e-mail: norfariza@utem.edu.my

Keywords: Corrugated cardboard; strength; tensile

ABSTRACT – The corrugated cardboard is widely used in manufacturing industries as a packaging, transportation material and number of other applications. However, the strength of the corrugated cardboard as a structure is not well understood. The objective of this study is to propose and estimate the strength of corrugated cardboard using tensile test. As a result, new practical tensile test considering the glue bonding strength was proposed and the factory of these test method was investigated.

1. INTRODUCTION

In general, the corrugated cardboard was composed with three layer of paperboard. One is outside liner and inside liner and the other is corrugated medium. The top of corrugated medium is bonded with glue on outside or inside layer surface. The bonded space was decided by company standard. The structure has different properties in its three principal directions as shown in Figure 1 [1].
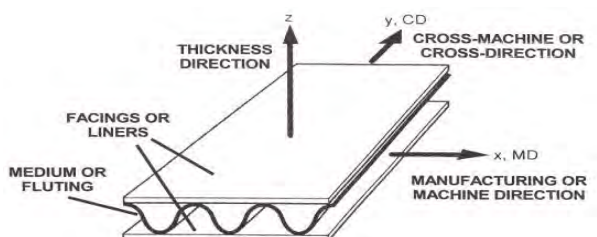
Figure 1 Corrugated cardboard structure showing the three principal axes [1].

Corrugated cardboard is governed by the strength properties of the corrugated medium, which is determined partly by material properties and partly by geometry [2], [3]. The material properties of influence are basis weight, fiber strength and fiber bonding. Geometry properties of influence here are flute shape and flute size.

This research is concern and focus on introducing new method and measuring the strength of corrugated cardboard due to adhesive bond. Measurement the strength of corrugated cardboard using tensile test provides an important parameter in defining the structural properties and for determining the strength of corrugated cardboard panels for end user justify.

2. METHODOLOGY

A flute corrugated cardboard was used as a test piece in the experiment. Cross-sectional size change with dimension of the tensile test specimen with thickness of 5 mm with dumbbell pattern JIS K7217 as shown in Figure 2. Test specimens were fabricated by Yoshizawa Industrial Co., Ltd. using 3 dimension cutting machine. Tensile test was conducted using INSTRON2716-015. In order to suppress the collapse of the specimen by the chuck of the tester, it was decided to insert the aluminum round bar to the corrugated medium as shown in Figure 3. The crosshead speed was set at 20 mm/min in a tensile machine and the experiment was repeated 10 times. All experiments was conducted in humidity 50%RH and constant conditions of temperature 23 degree. The grip distance between the aluminum round bar is approximate 44 mm. Each specimen was subjected to hand fracture pattern observed with a digital microscope. Then, measurement is performed and the computer configuration of Young's modulus were evaluated for mechanical properties by tensile tests. Figure 4 shows the position of corrugated cardboard specimen for tensile test using INSTRON2716-015.
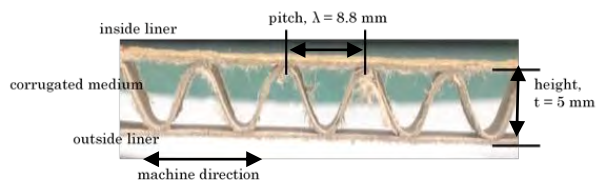
Figure 2 Cross sectional dimension of A flute corrugated cardboard.
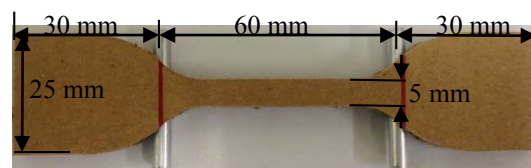
Figure 3 Size of specimen for dumbbell pattern JIS K7217 of corrugated cardboard.
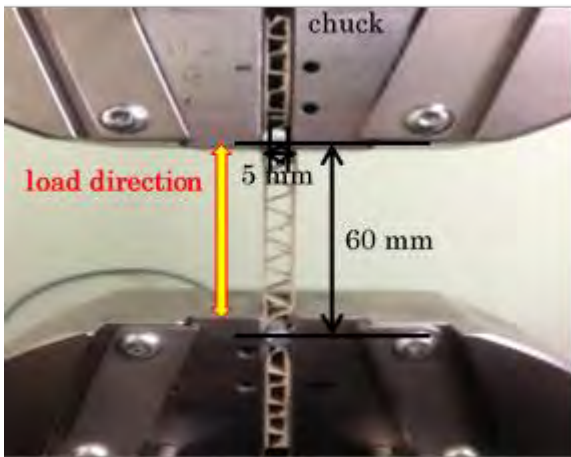
Figure 4 Specimen position during test used INSTRON (2716-015).

3. RESULTS AND DISCUSSION

Figure 5 shows the result for 10 specimen of tensile test on corrugated cardboard. The stress of corrugated cardboard was calculated by Equation (1).

$$Stress = \frac{Load}{Thickness \times 2} \tag{1}$$
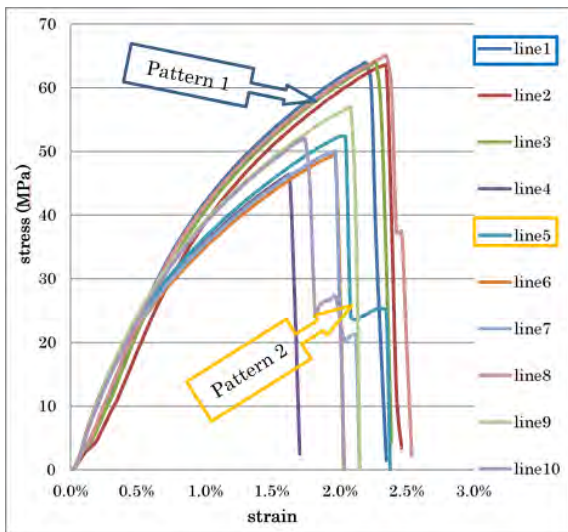
Figure 5 Result of corrugated cardboard on tensile test.

From Figure 5 shows that the fracture pattern of tensile test using this method can be divided into 2 pattern. The average yield breaking was 56.3 MPa and the average strain breaking was 1.7%. In this study, the fracture pattern was addressed as pattern 1 and pattern 2. Pattern 1 of graph is without the effect of change with wavy lines and also for the others and pattern 2 of graph is with the effect of corrugated medium.

For pattern 1, the fracture occurred at both; inside and outside liner as shown in Figure 6. Thus, results show that fracture occurred far from the adhesive bond. Figure 6 show the result that fracture occurred is not in the straight line. This is because the effect of corrugated medium does not appear. For pattern 2, the fracture occurred at both; inside and outside liner. The result show that fracture occurred near from the adhesive bond due to the effect of corrugated medium.
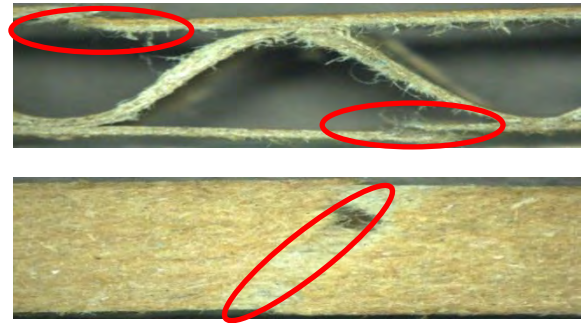
Figure 6 Cross-directional and upper view of pattern 1.

Strength ratio was been calculated by using Equation 2. The average yield breaking was 1.2 times and the average strain breaking was 1.4 times. The range of yield breaking and strain breaking was 18.7 MPa and 1.1% regarding from Figure 5. However, the range for both yield breaking and strain breaking is still huge.

$$Strength\ ratio = \frac{Corrugtaed\ cardboard\ (5\ mm)}{Liner} \tag{2}$$

4. CONCLUSIONS

As conclusions, method to estimate the strength of corrugated cardboard as structural properties had been proposed. Moreover, estimation of corrugated cardboard strength had also been done. However, this proposed method need to be revised for better result or small range different between yield breaking and strain breaking.

REFERENCES

[1] G. Jonson, *Corrugated Board Packaging*, Chap. 14 Leatherhead, England, Pira Int.; 1993.

[2] M. R. M. Rejab, W. J. Cantwell, "The mechanical behaviour of corrugated-core sandwich panels", *Composites: Part B*, vol. 47, pp. 267–277, 2013.

[3] S. Hou, C. Shu, S. Zhao, T. Liu, X. Han, Q. Li, "Experimental and numerical studies on multi-layered corrugated sandwich panels under crushing loading", *Composite structures*, vol. 126, pp. 371-385, 2015.

Influence of size particles of SLS glass on properties of sintered SBE reinforced glass waste composite

Z. Shamsudin[1,*], N. Salleh[1], Z. Mustafa[1], M.A.A. Bakar[1], R. Hasan[2,3]

[1] Faculty of Manufacturing Engineering, Universiti Teknikal Malaysia Melaka,
Hang Tuah Jaya, 76100 Durian Tunggal, Melaka, Malaysia
[2] Faculty of Mechanical Engineering, Universiti Teknikal Malaysia Melaka,
Hang Tuah Jaya, 76100 Durian Tunggal, Melaka, Malaysia
[3] Centre for Advanced Research on Energy, Universiti Teknikal Malaysia Melaka,
Hang Tuah Jaya, 76100 Durian Tunggal, Melaka, Malaysia

[*]Corresponding e-mail: zurina.shamsudin@utem.edu.my

ABSTRACT – The properties of sintered glass waste composite was investigated with two varying size particles of glass waste (SLS) at different loading of spent bleach earth (SBE). The composites were exposed to single step heat treatments in order to produce glass-ceramics condition. This study is focused on physical testing to measure the physical properties combined with microstructural analysis of thev cross section surface using scanning electron microscopy (SEM). ASTM C373-88 analysis was used to assess the variability in density, porosity and water absorption. The results showed that finer size particles in all composition contributed better in physical properties. These properties slightly decreased linearly with increasing SBE loading for both particles sizes and was significantly reduced in 40% of SBE. Microstructure analysis indicated that the present of pores within the glass waste composite was dominated by agglomeration.

1. INTRODUCTION

The fabrication of glass waste can be develop into technical glass ceramic by undergo heat treatment that consist outstanding properties [1]. Moreover, this material also can be transform into a ceramic composite material which glass act as matrix that cause increase in Young's modulus, hardness and fracture toughness depending volume fraction of glasses [1]. The waste glass can be identified in few type of materials such as borosilicate glass, soda lime glass, potash lime glass and others. It has been reported that glass act as matrix in natural fiber composite consists of high durability and non-environmental effect [2,3]. Hence, that cause glasses more favorable and have better properties to be recycle and change into acceptable application. Research based on natural waste had been embarked to transform a useful product as example filler for the composite [4]. Spent bleaching earth, SBE is waste material that origin from edible oil industry and classified as organic waste. Referring to Quesada and Iglesians [5] stated that the SBE has been used clay brick act as pore forming agents indicates that bulk density and mechanical strength is increase but total porosity and water absorption decrease compared to the pure clay brick. Hence, by adding SBE as filler in glass waste matrix, it is expected that the properties of glass waste composite will be improved. Reported by Zhang et al [6], the composite strength increases with decreasing particle size. Smaller particles have a higher total surface area for a given particle loading. This demonstrates that the strength increases with increasing surface area of the filled particles through a more efficient stress transfer mechanism. Therefore, by changing size of particle it is believe that the strength and different properties of glass waste composite will be affected.

2. METHODOLOGY

Glass waste from soda lime glass was collected from the household waste. The preparation of the glass waste undergoes crushing, ball milling, and sieving at 45µm and 75µm. The raw SBE has undergone a cleaning process to extract oil using sonification process followed by filtration and drying process until the SBE was in powdery form. The particle size distribution for SBE was determined using particle size analyzer, Mastersizer 2000 Malvern Instrument Ltd model. The compositions is shown in Table 1. All the samples were produced using conventional powder processing methods involving ball milling and uniaxial pressing before sintering. The obtained green bodies were subjected to sintering treatments using laboratory electric furnace Carbolite 1300 model at 750°C at constant heating rate of 2°C/min and 15 minutes dwelling time. The crystalline phase analysis were conducted using X-ray diffraction (RIGAKU Model MINIFLEX II) operating at 30 kV and 15 mA with Cu Kα radiation. The detector was scanned in the range of 2θ angle from 10° to 80°. Data was collected at room temperature using Cu Kα radiation (α=1.54178 Å). The percentage of bulk density, porosity, water absorption of the sintered glass ceramic was measured following ASTM C373 standards using pellet specimens. The microstructure of the glass waste composites was inspected using SEM EVO 50 (Carl Zeiss SMT, UK) at accelerated 15 kV. Surfaces of the specimens were coated with a conductive gold layer using SC-7620 Mini Sputter Coater (Quorum, UK).

Table 1 The ratio of glass waste composite preparation.

Sample 75µm (wt%)	A1	A2	A3	A4
SLS	60	65	70	100
SBE	40	36	30	-
Sample 45µm (wt%)	B1	B2	B3	B4
SLS	60	65	70	100
SBE	40	35	30	-

3. RESULTS AND DISCUSSION

Figure 1(a, b, c,) shows that the axial shrinkage, bulk density, apparent porosity and water absorption of glass waste composite in relations to the increasing of the SBE content.

(a)

(b)

(c)
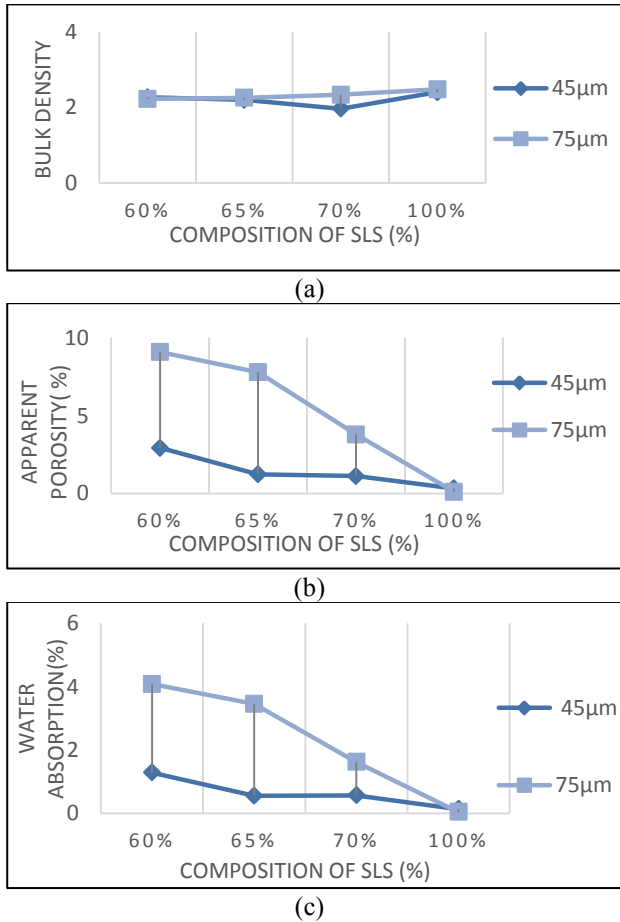
Figure 1 Physical properties of glass waste composite for a) bulk density, b) apparent porosity and c) water absorption.

It can be seen clearly that, in general, as the SBE content increased, porosity and water absorption increased. A significant increase of % porosity was observed in 40 % loading of the SBE content with 75µm of size particle. This finding is coherent with the microscopy observation in Figure 2. Similar trends were also observed in bulk density with finer size. The formation of pores in glass ceramic could be influenced by many factors such as volume of the glass powder, filler [3,4] and others. Works by Juoi [4] on the slug powder (BS) filled glass- ceramic indicated that the porosity increased with increased of the BS content due to lack of glassy form to aid viscous flow. Moreover, it

is also expected that high sintering temperature causes filler such as SBE is burned into gas thus pores present in the process [5].
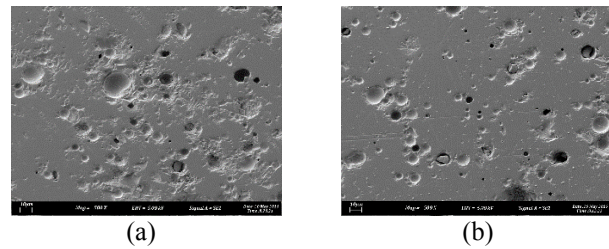
Figure 2 Pores present in glass waste composite for a) 45µm and b) 75µm.

4. CONCLUSION

Glass waste composites incorporating SLS waste glass filled with SBE powder has been produced by sintering at 750^0C at a rate of 2^0C/min and 15 minutes of soaking time. With increasing amount of SBE content, the porosity and water absorption are increased, resulting in reduction of the bulk density values for both size particles. When the particles size increased, morphology of pores changed and appeared to be more open and less dense which reveal the composite dominated by agglomeration of SBE.

REFERENCES

[1] N.F. Ayoob, J.M. Juoi, Z.M. Rosli and N.R. Rosli, "Characterisation and Properties of Sintered Glass-Ceramics Produced from Recycling Glass by Using Pressure-Less Method", Key Engineering Material, no. 471 ,pp 933-938, 2011

[2] M. Erol, S. Küçükbayrak, A. Ersoy-Meriçboyu, "The influence of the binder on the properties of sintered glass ceramics produced from industrial wastes", Ceramic International, vol. 35, pp 2609-2617, 2009

[3] Z. Mustafa, N.F. Ishak, Z. Shamsudin, J.M. Juoi "Porous glass-ceramic composite from recycled soda lime silica glass and charcoal." Journal of Engineering and Technology, vol.6 no 2, pp. 143-150, 2015.

[4] J.M. Juoi, D. Arudra, Z.M. Rosli, A.R. Toibah, S.R. Shamsuri and J.J. Azuraien, "Physical and Mechanical Properties of Glass Composite Material Made from Incinerated Scheduled Waste Slag and SLS Waste Glass" Advance Materials.Reserach, no. 26, pp 280, 2013.

[5] D.E. Quesada, F.A.C. Iglesias, "Utilization of spent filtration earth or spent bleaching earth from the oil refinery industry in clay products" Ceramics International, vol. 40(10), pp 16677-16687, 2014.

[6]   S. Zhang, X.Y. Cao, Y.M. Ma, Y.C. KE, J.K. Zhang and F.S.Wang "The effects of particle size and content on the thermal conductivity and mechanical properties of Al_2O_3/high density polyethylene (HDPE) composites", Express Polymer.Letter, vol5(7), pp581-590, 2011.

Comparative study of polypropylene composites reinforced with pineapple leaf fiber from Josapine and Sarawak cultivar

M.Z. Selamat[1,2,*], A.N. Kasim[1,2], M.A.M. Daud[1,2], M.Y. Yaakob[1], A. Putra[1,2], D. Sivakumar[1,2,]

[1)]Faculty of Mechanical Engineering, UniversitiTeknikal Malaysia Melaka,
Hang Tuah Jaya, 76100 Durian Tunggal, Melaka, Malaysia
[2)]Centre for Advanced Research on Energy, UniversitiTeknikal Malaysia Melaka,
Hang Tuah Jaya, 76100 Durian Tunggal, Melaka, Malaysia

*Corresponding e-mail: zulkeflis@utem.edu.my

Keywords: Pineapple leaf fiber (PLF); polypropylene (PP); biodegradable fiber reinforce polymer (BFRP)

ABSTRACT – This paper presents the comparison of mechanical properties of two difference cultivar pineapple leaf fiber (PLF) (Josapine/PLFJ and Sarawak/PLFS) reinforced polypropylene (PP) (copopolymer/PPC and homopolymer/PPH) composite as a function of fiber loading. The samples of PLFJ/PPC and PLFS/PPH composites were fabricated with 30, 40, 50, 60 and 70 wt.% PLF loading with 100 mm fiber length. The fabrication was made by compression molding techniques. The results revealed that composites utilizing PLFJ/PPC shows superior tensile properties as compared to the PLFS/PPH. However, there are no significant disparities observed in the density and hardness of both composites.

1. INTRODUCTION

Malaysia is one of the world's major producers of pineapple, but only the fruit is use and the leaf was burned or through away, thus will cause pollution and wastage of the best potential sources of fiber [1]. Mohamed et al. in 2009 studied characterization of PLF from selected Malaysia cultivars and discovered that Josapine cultivar have the best mechanical properties and quantity of fiber, finest of fibers, thermal stability, tensile strength and modulus compared with Sarawak and Moris cultivars. Table 1 shows the mechanical properties of difference type cultivars of PLF.

Table 1 Mechanical Properties of of PLF [1].

Property	Cultivars		
	Moris Gajah	Josapine	Sarawak
Tensile Strength (MPa)	174.89	293.08	148.44
Young's Modulus (GPa)	7.45	18.94	10.46
Elongation at Break (%)	0.52	1.41	1.05

Due to exponential interest in the development of Biodegradable Fiber Reinforce Polymer (BFRP) composite as an alternative of conventional material such as metal or plastic in product application, Ayu Natasya Kasim et al. in 2015 had studied effect of pineapple leaf fiber loading on the properties of pineapple leaf fiber /polypropylene composite. Kasim et al. [3] have performed alkaline treated of pineapple leaf fiber from josapine cultivar reinforced polypropylene composites. They have examined the effect of fiber loading on the mechanical properties of PLF/PP

composite. In the present study, the mechanical properties of PLFJ/PPC were compared over the PLFS/PPH composites.

2. METHODOLOGY

Polypropylene (PPC and PPH) in powder form with size of 250μm produced by Lotte Chemical Titan was utilized as the polymer matrix. The PP had excellent chemical and water resistant, light weight and can be recyclable. PLFJ from Josapine cultivars were collected from cultivation areas in Pontian, Johor Malaysia. The PLFJ were produced by novel technology [4], where the PLFJ were extracted by a decortications machine. PLFS from Perak cultivars were collected from cultivation areas in Perak Darul Ridzuan, Malaysia. The leaf was chopped to a length of 100 mm and extracted with a milling machine. Alkaline treatment was conducted with the aim to improve the mechanical properties and surface modification for both PLF [5-8]. The sample of composites was fabricated with 100 mm fiber length with different fiber loading of PLF (30, 40, 50, 60 and 70 wt.%). After the fabrication of PLF/PP composites was made by compression molding techniques, the samples were prepared for tensile test (ASTM D 3039), hardness test (ASTM D1957) and density measurement.

3. RESULTS AND DISCUSSION

The mechanical properties (tensile, hardness and density) of the PLFJ/PPC and PLFP/PPH composites were evaluated and comparative studies of these properties are shown in Figure 1-3. It was found that the tensile behavior of the PLFJ/PPC composites changes considerably with the increments of PLF loading. Maximum tensile strength up to about 70 MPa has been achieved at 70 wt.% of PLF loading. However, this behavior is contrary for the PLFS/PPH composites, in which the tensile behavior drops drastically with the addition of fiber content. In a realistic behavior, improvement of tensile strength due to the addition of fiber content will induce the reduction of strain properties. However, the results obtained for PLFJ/PPC composite exhibits contradicting effect in which the addition of fiber content improves strain properties as shown in Table 2. The occurrence of this phenomenon might be due to the nature of the Josapine cultivar that

---

shows superior strain properties as compared to Sarawak cultivars [1]. From the Table 2, it is observed that at 60 wt.% of PLF loading has the highest value of Young's Modulus for PLFJ/PPC while the PLFS/PPH had the lowest Young's Modulus. The addition of 60 wt.% PLF enhances the Young's modulus by 540% for PLFJ/PPC and diminishes the PLFS/PPH by 83.5% as compared to the Young's modulus of plain PP. Additionally, the usage of the matrix plays an important role in composites properties however the effect of different PP types is only at a disparities of relatively low margin. This can be seen clearly from Figure 2 that the tensile strength of PPC had 4.27% more strength than PPH, where the values are 15.46 and 14.8 MPa respectively. Meanwhile for hardness and density of the PLFJ/PPC composites had shown almost similar pattern with the increment from 30 wt.% up to 70 wt.% PLF loading. While, hardness and density of PLFS/PPH composites had shown increment pattern just from 30 wt.% up to 50 wt.% PLF loading as well as the 60 wt.% and 70 wt.% the properties were reduced but at the small percentage. In this study, PLFJ/PPC composites had shown superior mechanical properties as compared to PLFP/PPH composites especially for tensile properties.

Table 2 Tensile properties of PLFJ/PPC and PLF/PPH.

	PLFJ/PPC		PLFS/PPH	
PLF (wt.%)	Young's Modulus, E (GPa)	Strain, ε (%)	Young's Modulus, E (GPa)	Strain, ε (%)
0	0.76	5.00	1.70	9.00
30	2.98	3.00	0.36	4.59
40	3.30	3.33	0.64	1.72
50	3.93	3.37	0.51	2.01
60	4.87	3.00	0.28	4.49
70	3.08	5.00	0.37	0.95
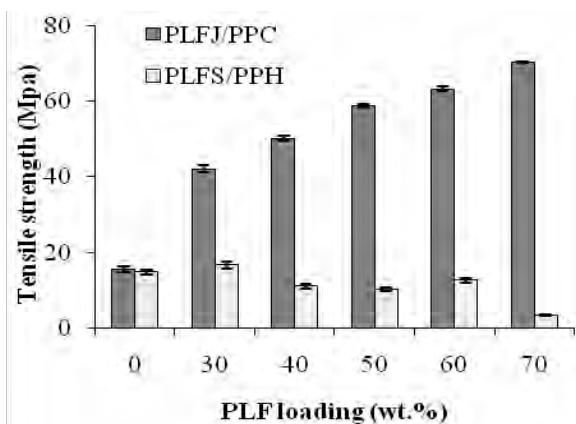
Figure 1 Tensile stress (MPa) vs PLF loading (wt.%).

4.   CONCLUSION

The effects of PLF loading on the mechanical properties of PLFJ/PPC and PLFP/PPH composite have been studied and compared. The tensile strength of PLFJ/PPC is much higher than PLFP/PPH composite. Hardness and density for both of composites have shown almost similar result. In short, the present study revealed that PLF from Josapine cultivar was shown a good contender of natural fiber to be used in fabricate natural composite. With the aim of further

improvement, the mechanical properties of PLFJ/PPC composite, the addition of bonding agent such as maleic anhydride grafted polypropylene (MAPP) will be conduct.
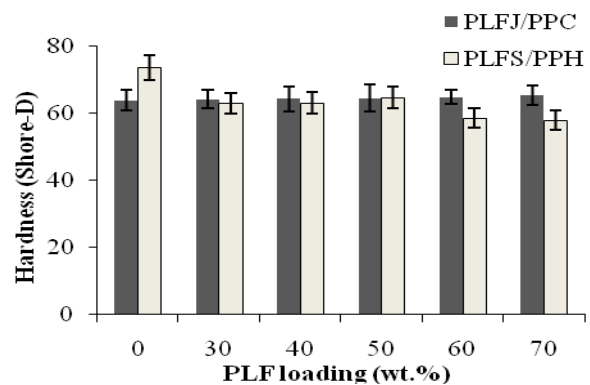
Figure 2 Hardness (Shore-D) vs PLF loading (wt.%).
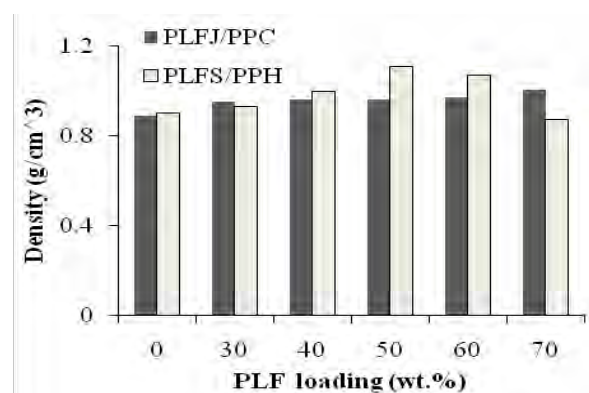
Figure 3 Density (g/cm³) vs PLF loading (wt.%).

ACKNOWLEDGEMENT

REFERENCES

[1] A.R. Mohamed, S.M. Sapuan, M. Shahjahan, A. Khalina, "Characterization of pineapple leaf fibers from selected Malaysian cultivars," *Journal of Food, Agriculture & Environment* 7, 235- 240. 2009.

[2] A.N. Kasim, M.Z. Selamat, N. Aznan, S.N. Sahadan, M.A.M. Daud, S. Salleh, R. Jumaidin, "Effect of pineapple leaf fiber loading on the properties of pineapple leaf fiber – polypropylene composite", *Jurnal Teknologi (Sciences & Engineering),* 77:21 (2015) 117–123. 2015.

[3] A. N. Kasim, M. Z. Selamat, M. A. M. Daud, M. Y. Yaakob, A. Putra, D. Sivakumar, "Mechanical properties of alkaline treated of pineapple leaf fiber from josapine cultivar reinforced polypropylene composites" in *ICMER UMP.* 2015.

[4] Y. Yusuf, S.A. Yahya, A. Adam, "Novel technology for sustainable pineapple leaf fibers productions," *12th Global Conference on Sustainable Manufacturing*, pp. 756-760. 2015.

[5] M.Z. Selamat, A.N. Kasim, S.A. Shamsudin, "Effect of bamboo fibre length on the mechanical

properties of bamboo fiber/polypropylene composite”, in *8thMUCET.* 2014.

[6] D. Chandramohan, Dr.K. Marimuthu, “Tensile and Hardness Tests on Natural Fiber Reinforced Polymer Composite Material”, I*nternational Journal of Advanced Engineering Sciences and Technologies,* Vol. 6, No.1, 097–104. 2011.

[7] N.T Phong, T. Fujii, B. Chuong, K. Okubo. “Study on How to Effectively Extract BFs from Raw Bamboo and Wastewater Treatment”, *Journal of Materials science Research,* Vol.1, No.1, 2012.

[8] B.Vinod, and L.J. Sudev “Effect of Fiber Orientation on the Flexural Properties of PLAF Reinforced Bisphenol composites”, I*nternational Journal of Science and Engineering Applications,* Vol. 2, ISSN-2319-7560, 2013.

Failure analysis on domestic pipeline

N. Adzme[1,*], N.H. Razak[1,2], N.S. Muhammad[1,2]

[1] Faculty of Mechanical Engineering, Universiti Teknikal Malaysia Melaka,
Hang Tuah Jaya, 76100 Durian Tunggal, Melaka, Malaysia
[2] Centre for Advanced Research on Energy, Universiti Teknikal Malaysia Melaka,
Hang Tuah Jaya, 76100 Durian Tunggal, Melaka, Malaysia

*Corresponding e-mail: adzmenasruddin43@gmail.com

ABSTRACT – Today, structural health monitoring is a major concern in the engineering community. Multisite fatigue damage, hidden cracks and corrosion in hard-to-reach locations are among the major flaws encountered in today's extensive diagnosis. In this research, the understanding of non-destructive testing (NDT), thermographic analysis was applied to locate defect as complementary analysis towards the failure analysis of a defect pipe through SEM technique an analysis on specimen morphology and topography.

1. INTRODUCTION

Providing an adequate water supply is a major challenge facing many public water utilities in developing countries, such as Malaysia. A significant part of these challenges is non-revenue water (NRW), which is the difference between the volume of water put into a water distribution system and the volume that is billed to customers. It is estimated that water utilities in developing countries can lose 40-50% of the water they put into their systems and they are unable to bill their customers for this loss. NRW can occur through physical losses from leaking and broken pipes, which failure analysis come in play, to minimize the leakage of domestic water pipeline, by investigating the failure causes through proper analysis and Non-Destructive Technique (NDT) technique [1].

The most powerful technique commonly used for fractographic investigation is the SEM technique. This technique utilizes electron as a source to create high resolution images [2]. Fracture morphology such as fracture sequence, which is at crack initiation, crack propagation, and fast fracture. Revealing marks enable differentiating the different areas and, therefore identify the condition leads to the fracture, such areas are, the fibrous zone, radial zone, and shear lip zone. The fracture also can be future characterize into ductile and brittle fracture [3].

Infrared thermography technique uses an infrared imaging and measurement camera to see and measure invisible infrared energy being emitted from an object. Unlike visible light, in the infrared spectrum, everything with a temperature above absolute zero emits infrared electromagnetic energy. Even cold objects such as ice cubes, emit infrared radiation. The higher the temperature of the object, the greater the infrared radiation emitted. In the industrial/commercial environment, almost everything gets hotter or cooler before it fails, making infrared cameras extremely valuable diagnostic tools with many diverse applications [4].

2. METHODOLOGY

Failure analysis on the domestic pipe line conducted in series of step, to verify the specific fault of the pipe. Two pipe was tested, a good, non defect pipe and bad pipe, the defect pipe. The purpose of conducting analysis on both good and pipe is to create a baseline for comparisons between two results. Both active and passive thermographic analysis approaches are conducted on both pipes, as complementary analysis. Both pipe will be analyzed and compare through string of analysis, visual examination as a preliminary examination and fractography analysis through Scanning Electron Microscope (SEM).

2.1 Scanning Electron Microscopy (SEM)

A scanning electron microscope (SEM) is an electron microscope that produces images samples by scanning it with a focused beam of electrons. The electron beam released from the electron gun travels pass through the electromagnetic field and electromagnetic lenses where it is focused prior to hitting on the specimen surface. Then the X-ray, back scattered electrons, secondary electron and auger electrons are produced. These signals are subsequently collected to produce images and information important for the interpretation of failure analysis. The electrons interact with atoms in the sample, producing various signals that can be detected that contain information about sample's topography and morphology in high resolution ranging from 1000x, 3000x, 6000x, and 12000x pixel resolutions.. The intrados and extrados of the specimen, the pipe, will be scanned.

2.2 Thermographic analysis

All objects, cold or hot, radiate heat in the form of infrared energy. As an object increases in temperature, it radiates more energy, and the wavelength gets shorter. Human eye can only see a narrow range of wavelength in the electromagnetic spectrum. Most of what the eye sees is reflections from objects that high energy from the sun or an incandescent light bulb is striking. However, the infrared camera can detect infrared energy well before we can see it with our eyes. The camera

converts this invisible infrared energy into a two-dimensional visual image. The amount of energy radiated from an object is dependent on its temperature and its emissivity. The emissivity of an object is the ratio of the energy radiated to that which the object would emit if it were a Black Body. Specimens are conducted through active and passive thermographic analysis, to observe the spot of defect and comparing the result.

3.   RESULTS AND DISCUSSION

Thermographic analysis of the pipes shows the location of defect on bad pipe more clearly. The high temperatures reading on the pipe indicate the crack location.
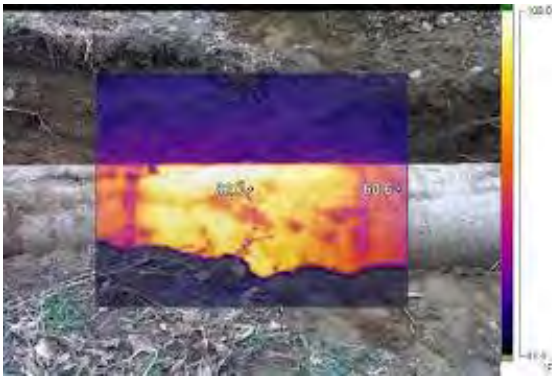
Figure 1 Defect location using thermographic analysis.

Initial observations of fracture failures in bad pipe suggest that in the majority of cases, voids or foreign inclusions in the pipe wall provide localized stress risers which lead to crack initiation under remote stress. However the initial assessment of the fracture surface, inspection, visible light microscopy unable to identify the stress riser at the source of the fracture. More detailed inspection was undertaken using Scanning Electron Microscope (SEM) to provide a higher magnification image and qualitative chemical analysis of any inclusions found. Figure 1 (a) and (b) shows higher magnification of the fracture initiation region.
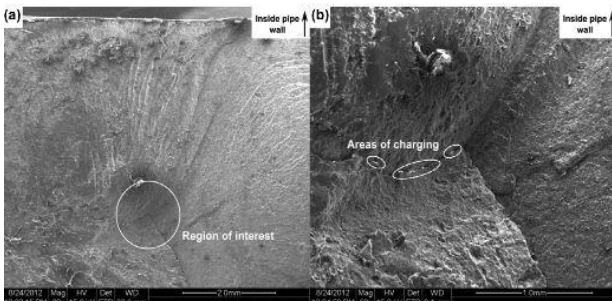
Figure 2 SEM image of cracks (high magnification).

Following exposure of the initiating defect behind the primary fracture surface SEM was again undertaken following the same procedure as used previously. As shown in Figure 2, the defect responsible for crack initiation in this case was a void in the pipe wall, approximately 0.45 mm wide. Three cracks can be seen to radiate out from the void. While this void has been identified as the stress riser that led to crack initiation and eventual failure of the pipe, it is unclear what caused the defect originally. For example, it is possible that the observed void was attributed to a particle or agglomeration of particles that were removed during fracture and subsequent failure. Alternatively, the void may also have been the result of air that was trapped within the pipe during extrusion or uneven shrinkage due to temperature gradients during cooling following pipe extrusion.
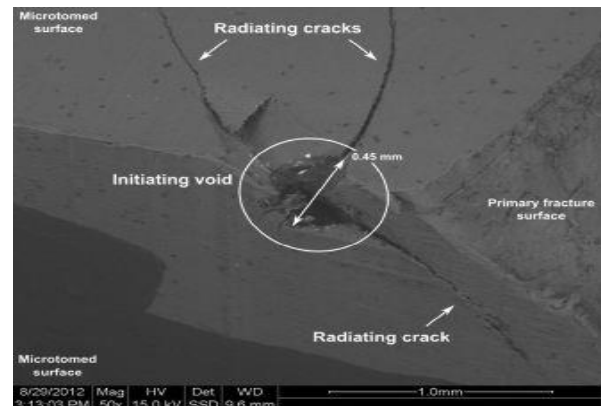
Figure 3 Primary fracture surface.

4.   CONCLUSION

The thermographic analysis of pipe shows the presence of initial crack which then led to the failure analysis of the pipe. Based on the outcome of SEM, it was reasoned that no materials degradation has occurred in contact with domestic sewage. Rather, fracture failure has occurred from an inherent defect in the pipe wall. This study indicates that failure can occur by fracture from inclusions that were built-in during original manufacture.

REFERENCES

[1]   C.T. Kim, *Malaysian Water Sector Reform: Policy and Performance,* Wageningen Academic Publication; 2012

[2]   G.E. Dieter, *Mechanical Metallurgy,* CreateSpace Independent Publishing Platform; 2014.

[3]   C.D. Beachem, *Fractography-Microscopic Cracking Process*, ASTM International; 1976.

[4]   R.S. Kad, "IR thermography is a condition monitor technique in industry". *International Journal of Advanced Research in Electrical, Electronics and Instrumentation Engineering*, vol. 2, no. 3, 2013.

Variations in diameter of struts for micro-lattice structure manufactured using selective laser melting

R. Hasan[1,2,*], R.A.W. Mines[3]

[1] Faculty of Mechanical Engineering, Universiti Teknikal Malaysia Melaka,
Hang Tuah Jaya, 76100 Durian Tunggal, Melaka, Malaysia
[2] Centre for Advanced Research on Energy, Universiti Teknikal Malaysia Melaka,
Hang Tuah Jaya, 76100 Durian Tunggal, Melaka, Malaysia
[3] School of Engineering, University of Liverpool, Liverpool L69 3GH, United Kingdom

*Corresponding e-mail: rafidahhasan@utem.edu.my

ABSTRACT – This paper highlights the dimension of diameter for titanium alloy Ti-6Al-4V micro-lattice structure material with body-centered-cubic (BCC) struts' arrangement, manufactured using additive layer technology, which is selective laser melting (SLM). Direct measurements and simple count analysis were done on the material. Variations in diameters were averaged and the value was compared to that obtained from other formulations. The result shows that there are variations in struts' diameters of micro-lattice structure manufactured using SLM, which can affect the material's performance under load bearing capacity. The finding can be useful to the developments of both micro-lattice structure and additive layer technology researches.

1. INTRODUCTION

The use of the titanium alloy Ti-6Al-4V in the manufacture of micro-lattice structure using the selective laser melting process (SLM) for use as a light-weight load bearing material in sandwich structure cores suggests that this material has a promising future as a candidate of aerospace material. The study of the SLM Ti-6Al-4V micro-lattice structure block is one of the early steps that support the efforts of introducing this novel material into the real aerospace applications [1]. An important performance issue in aerospace sandwich construction is the foreign object impact (FOI) performance such as a result of dropped tools, hail and bird strike [2].

It was observed that the SLM Ti-6Al-4V BCC micro-lattice blocks failed along 45° angle diagonal plane under compression loading [1]. The localized failure in this material has motivated this study to focus specifically at the geometry of the struts. Based on mechanical property of struts which has been reported in other study [3], it can also be concluded that the geometry of the SLM Ti-6Al-4V BCC micro-lattice blocks relates to the structural strength and mechanical properties of the whole micro-lattice structure [4]. Thus, the deliverable of this study is the determination of diameter for BCC micro-lattice structure blocks. The finding is important to be used in FEA analysis on structural performance of this material.

2. METHODOLOGY

The diameter of struts in SLM Ti-6Al-4V BCC micro-lattice blocks was determined using direct measurement as well as shadow measurement method, which the explanation can be found in other report [1]. The surface roughness and circularity of the struts can also be determined using similar procedure. Figure 1 shows an SEM image of the strut arrangements in the 45° angle diagonal plane of the as-received micro-lattice block (with SLM parameter of 160 W x 1000 μs). The struts' diameters can be directly measured from the image.
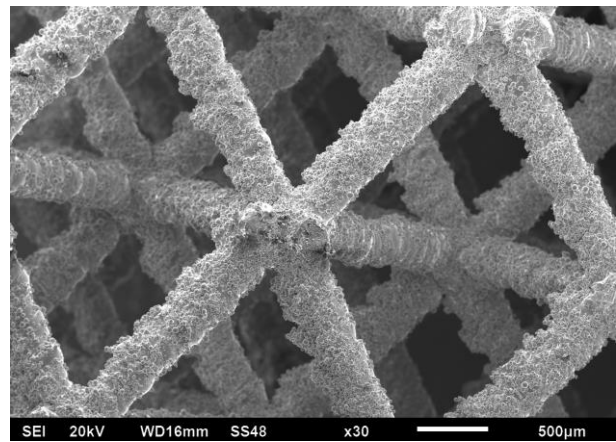
Figure 1 Struts arrangements in 45° angle diagonal plane of the as-received SLM Ti-6Al-4V BCC micro-lattice block (160 W x 1000 μs).

3. RESULTS AND DISCUSSION

For direct measurement, strut diameters for 50 struts (average of three readings per strut) were measured and distributed as shown in Figure 2.

From the figure, it can be seen that most of the strut diameters in the as-received micro-lattice block were between the ranges of 360 to 379 μm. Besides, a noticeable number of strut diameters were between the ranges of 380 to 399 μm. Thus, from direct measurement, the average diameter of the struts was found to be (374.24 ± 17.7) μm. Meanwhile, using the shadow measurement method [1], the average strut

diameter for the as-received micro-lattice blocks was determined as (373.1 ± 29.95) μm, with minimum and maximum values of 321 μm and 429 μm respectively.
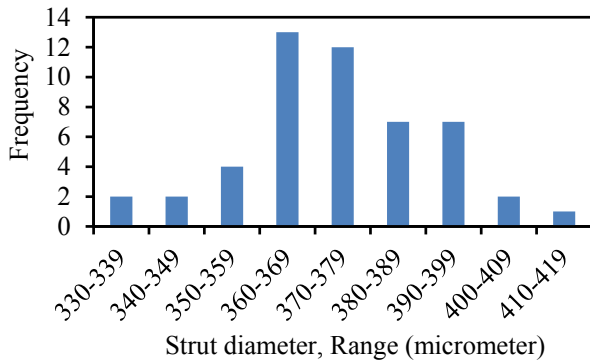
Figure 2 Distribution of strut diameters in as-received SLM Ti-6Al-4V BCC micro-lattice block (160 W x 1000 μs).

The strut diameter values which were determined using direct and shadow measurement methods, were then compared to estimation values obtained from Kude and Khairnar [5] formulation (Equation 1) as well as Tsopanos et al. [6] revised equation (Equation 2).

$$Diameter = 2 \left(\sqrt{\frac{A^2 + B^2}{2}} \right) \qquad (1)$$

$$d = \sqrt{\frac{m_b}{\rho_t . \pi . N_1 \times N_2 \times N_3 . L . \sqrt{3}}} \qquad (2)$$

Where A and B are the maximum and minimum measured radii, respectively; m_b is mass of the block, L is the cell length, ρ_t is density of Ti-6Al-4V taken as 4430 kg/m³, and N_1, N_2 and N_3 were the number of cells along the width, length and height directions.

Table 1 compares the results of struts' diameters which are determined from direct and shadow measurement methods as well as by using the formulation of Kude and Khainar [5] and Tsopanos et al. [6].

Table 1 Diameter of struts in SLM Ti-6Al-4V BCC micro-lattice block from several methods.

Method	Diameter value
Direct measurement	(374.24 ± 17.7) μm
Shadow measurement	(373.1 ± 29.95) μm
Kude and Khairnar [5] formula	378.87 μm
Tsopanos et al. [6] revised equation	339 μm

If the value from direct measurement is being used as a reference, the differences of other values are found to be not more than 10%.

4. SUMMARY

The findings show that there were variations in struts' diameters of SLM Ti-6Al-4V BCC micro-lattice structure blocks, which were due to the selective laser melting process itself [6]. These geometrical variations were eventually affecting the deformation behavior and collapse of the material [1].

ACKNOWLEDGEMENT

REFERENCES

[1] R. Hasan, Progressive collapse of titanium alloy micro-lattice structures manufactured using selective laser melting, University of Liverpool, United Kingdom, 2013.

[2] R.A.W. Mines, C.M. Worrall, A.G. Gibson, "Low velocity perforation behaviour of polymer composite sandwich panels," International Journal of Impact Engineering, vol. 21, no. 10, pp. 855-879, 1998.

[3] R. Hasan, R.A.W. Mines, S. Tsopanos, "Determination of elastic modulus value for selectively laser melted titanium alloy micro strut," Journal of Mechanical Engineering Technology, vol. 2, no. 2, pp. 17-25, 2010.

[4] R.A.W. Mines, S. Tsopanos, Y. Shen, R. Hasan, S.T. McKown, "Drop weight impact behavior of sandwich panels with metallic micro lattice cores," International Journal of Impact Engineering, vol. 60, pp. 120-132, 2013.

[5] V.P. Kude and R.S. Khairnar, "Fabrication of silicon based glass fibres for optimal communication," Bulletin of Material Science, vol. 27, no. 1, pp. 73-77, 2004.

[6] S. Tsopanos, R.A.W. Mines, S. McKown, Y. Shen, W.J. Cantwell, W. Brooks, C.J. Sutcliffe, "The influence of processing parameters on the mechanical properties of selectively laser melted stainless steel microlattice structures," Journal of Manufacturing Science and Engineering, vol. 132, pp. 041011-1 - 140111-12, 2010.

Tensile performance of palm oil fiber metal laminate

F. Hussain[1,2], D. Sivakumar[1,2,*], M.A. Daud[1,2], M.Z. Selamat[1,2]

[1] Faculty of Mechanical Engineering, UniversitiTeknikal Malaysia Melaka,
Hang Tuah Jaya, 76100 Durian Tunggal, Melaka, Malaysia
[2] Centre for Advanced Research on Energy, UniversitiTeknikal Malaysia Melaka,
Hang Tuah Jaya, 76100 Durian Tunggal, Melaka, Malaysia

*Corresponding e-mail: sivakumard@utem.edu.my

ABSTRACT – The effects of palm oil fiber loading on tensile behavior on polypropylene based Palm Oil Fiber Metal Laminate (POFML) was investigates. The testing was conducted on Universal Testing Machine according to ASTM D3039. This type of hybrid materials was fabricated by hand lay-up technique using 2/1configuration where the composite layer is located between two aluminum with 10wt%, 20wt%, and 30wt% and 40wt% fiber content. The results showed the tensile strength increased when fiber loading increase. However, POFML with 20% fiber loading showed a higher modulus of tensile property. The tensile behavior in this study mainly depends on fiber loading.

1. INTRODUCTION

Following the trend of material improvement, the new range of lightweight hybrid materials called fiber metal laminates (FML) had been developed. The usage of lightweight materials such as fiber reinforced composite materials and metal-composite structures can significantly reduce the weight of vehicles[1]. Generally, fiber metal laminates are combination of fiber reinforced polymer composite and metal layers by using adhesive as a bonding agent. FML system also can further improve the mechanical properties of the entire structure compared to their constituent materials. Previous studies reported these materials exhibit excellent impact properties [2], superior fatigue performance [1], good durability, machinability and plastic behaviour of metal [3]. M.Jawaid et al [4] found that tensile and flexural properties of hybrid composite is higher than EFB composite but less than woven jute composite in their research. S.M.R Khalili [2] also found FMLs are superior to BFRE (Basalt Fiber Reinforced Epoxy) composite in energy absorption and the existence of steel layers has a good effect on improving the specific bending and tensile strength. S.E Moussavi-Torshizi et al [5] states that fiber orientation effects the tensile properties of FMLs where fiber sheets with zero orientation in laminate improves modulus of elasticity, yield stress, and ultimate tensile stress considerably. Accordingly, the presents study attempts to investigate the strength behavior of the POFML under tensile test with different fiber loading.

2. METHODOLOGY

The palm oil empty fruit bunch (POEFB) composite based polypropylene as a composite and aluminium 6061-O as the skin was selected for this type of FML. Both of these materials are bonded using modified polypropylene adhesive film. The composite produced with different weight composition (10%wt,20%wt,30%wt and 40%wt) using a granulated POEFB fiber as reinforcement, polypropylene as matrices and maleic anhydride grafted polypropylene (MaPP) as its coupling agent as shown in Table 1.In order to ensure a good level of adhesion, the Al sheet was immersed in 0.1M concentration of sodium hydroxide (NaOH) solution at room temperature for 10 minutes and wiped with ethanol before bonding in order to remove any residual contamination.

Table 1 Composition of material in oil palm composite.

Composition (gram)	10%	20%	30%	40%
Mass of Fiber	5	10	15	20
Mass of PP	43.5	38.5	33.5	28.5
Mass of MaPP	1.5	1.5	1.5	1.5
Total	50	50	50	50

3. RESULTS AND DISCUSSION

Table 2 presents the average data for three specimens after tensile test. It shows that, the tensile strength increase when fiber content increase. Highest percentage of fiber loading which is 40wt% showed the highest tensile strength with 65.99MPa. The reason is, in composites, higher fiber content give a greater tendency for filler-to-filler interaction to take place between fiber and matrix [7]. However, the result of tensile modulus showed irregular trend with 20wt% fiber content, having the highest value. Supposedly, Composites tensile modulus was considerably enhanced by fiber loading at high fiber content because The increased population of fiber leads to agglomeration, which affects the composites' stiffness [7]. Generally, the probable reasons behind this is due to the fiber/matrix interfacial bonding or interaction between palm oil empty fruit bunch fibers and PP matrix for the ability to absorb the stress transfer.

Table 2 Tensile properties of POFML specimens.

Specimens	Tensile Strength (MPa)	Tensile Modulus (GPa)
FML with 10% fiber loading	47.17	30.64
FML with 20% fiber loading	61.73	36.65
FML with 30% fiber loading	62.53	31.48
FML with 40% fiber loading	65.99	32.59

Figure 3(a-d) shows typical failure specimen for 10%, 20wt%, 30wt% and 40wt% fiber content of POFML. The optical micrograph indicates delamination as a failure mechanism between aluminium and composite when both of this constituent's material were separated after testing. Delamination is caused by improper surface preparation. On the others hand, surface contamination will make lack of bond joining between aluminum and palm oil composite. This failure mechanism is called debond.
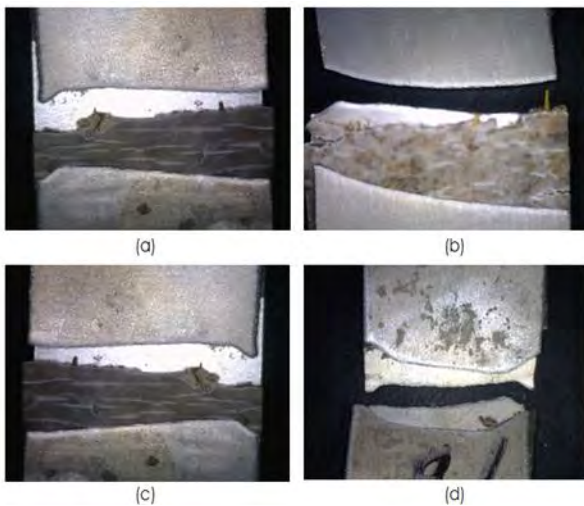
Figure 3 Typical failure mode; (a) 10% fiber loading of POFML, (b) 20% fiber loading of POFML, (c) 30% fiber loading of POFML and (d) 40% fiber loading of POFML.

4. CONCLUSION

A novel Palm Oil Fiber Metal Laminate based polypropylene was fabricated to investigates their tensile performance. The effect of fiber loading on POFML was studied. Based on the result, it was clearly observed that fiber loading in composite laminates affected the tensile properties of POFML. The tensile results showed POFML with 40wt% fiber content had the highest tensile strength with 65.99 MPa, while POFML with 20wt% fiber content had highest tensile modulus with 36.65 GPa.

REFERENCES

[1] S. Kalyanasundaram, S. DharMalingam, S. Venkatesan, and A. Sexton, "Effect of process parameters during forming of self reinforced – PP based Fiber Metal Laminate," *Compos. Struct.*, vol. 97, pp. 332–337, Mar. 2013.

[2] S. M. R. Khalili, V. Daghigh, and R. Eslami Farsani, "Mechanical behavior of basalt fiber-reinforced and basalt fiber metal laminate composites under tensile and bending loads," *J. Reinf. Plast. Compos.*, vol. 30, no. 8, pp. 647–659, May 2011.

[3] R. Santiago, "Impact on thermoplastic fibre-metal laminates : preliminary results and observations on proceding," pp. 1–17.

[4] M. Jawaid, H. P. S. Abdul Khalil, and a. Abu Bakar, "Woven hybrid composites: Tensile and flexural properties of oil palm-woven jute fibres based epoxy composites," *Mater. Sci. Eng. A*, vol. 528, no. 15, pp. 5190–5195, Jun. 2011.

[5] S. M. R. Khalili, V. Daghigh, and R. Eslami Farsani, "Mechanical behavior of basalt fiber-reinforced and basalt fiber metal laminate composites under tensile and bending loads," *J. Reinf. Plast. Compos.*, vol. 30, no. 8, pp. 647–659, May 2011.

[6] S. E. Moussavi-Torshizi, S. Dariushi, M. Sadighi, and P. Safarpour, "A study on tensile properties of a novel fiber/metal laminates," *Mater. Sci. Eng. A*, vol. 527, no. 18–19, pp. 4920–4925, Jul. 2010.

[7] S. Siyamak, N. A. Ibrahim, S. Abdolmohammadi, W. M. Z. W. Yunus, and M. Z. A. Rahman, "Effect of fiber esterification on fundamental properties of oil palm empty fruit bunch fiber/poly(butylene adipate-co-terephthalate) biocomposites.," *Int. J. Mol. Sci.*, vol. 13, no. 2, pp. 1327–46, Jan. 2012.

The effect of fiber length on the mechanical properties of pineapple leaf (PALF) fiber reinforced PLA biocomposites

S.H. Sheikh Md. Fadzullah[1,2,*], Z. Mustafa[3,4], S.N.R. Ramli[1]

1) Faculty of Mechanical Engineering, Universiti Teknikal Malaysia Melaka,
Hang Tuah Jaya, 76100 Durian Tunggal, Melaka, Malaysia
2) Centre for Advanced Research on Energy, Universiti Teknikal Malaysia Melaka,
Hang Tuah Jaya, 76100 Durian Tunggal, Melaka, Malaysia
3) Faculty of Manufacturing Engineering, Universiti Teknikal Malaysia Melaka,
Hang Tuah Jaya, 76100 Durian Tunggal, Melaka, Malaysia
4) Advanced Manufacturing Centre, Universiti Teknikal Malaysia Melaka,
Hang Tuah Jaya, 76100 Durian Tunggal, Melaka, Malaysia

*Corresponding e-mail: hajar@utem.edu.my

ABSTRACT – This research work investigates the effect of fiber length on the mechanical performance of the pineapple leaf fiber (PALF) reinforced poly lactic acid (PLA) biocomposites. Two types of composite systems are considered, these being the short (fiber length of 30 mm) and continuous long pineapple leaf fiber (fiber length greater than 100 mm) reinforced composites. The corresponding fabrication routes are melt-mixing and compression molding via film stacking, respectively. The test samples with nominal thickness of 3 mm were cut to size and subjected to flexural testing via three-point bending set-up, as per ASTM D790. As expected, the continuous long pineapple leaf fiber reinforced composites exhibit greater flexural strength and modulus, with flexural strength and modulus being 30% and 45% than those of the short fiber reinforced composites. These preliminary findings reveal the effect of fiber length on the overall performance of the composites studied.

1. INTRODUCTION

Natural fiber reinforced PLA composites are purely bio-based material with a promising mechanical properties profile in comparison to non-renewable petroleum based products. Nonetheless, this type of material is brittle and has relatively low tensile strength and impact properties in comparison to that of the non-renewable petroleum based polymer [1]. The mechanical properties of such composites depend on the type of fiber used and its homogenization to the matrix. Among the key governing factors that affect the mechanical properties are (i) the content of cellulose in the fiber, (ii) fiber orientation (iii) fiber length and fiber diameter [1].To-date, majority of research studies have focused on physical and mechanical characterization of short-fiber reinforced PLA-based biocomposites with the fiber length of approximately 30 mm or less [2-8].

Thus, this research work aims to contribute in the understanding of influence of the fiber architecture in terms of fiber length on the mechanical properties of the PLA degradable biocomposites, which can provide rigorous input in designing new composite materials (green composites) as a substitute to existing non-renewable petroleum-based products in automotive industry. However, this research paper is focus on the preliminary results obtained from a series of experimental work on the mechanical properties of the biocomposites, using the continuous long fiber as the reinforcement for the plain PLA matrix material.

2. METHODOLOGY

2.1 Raw materials

The biocomposites are fabricated from poly lactic acid (PLA) matrix, supplied by Natureworks (6100D) and pineapple leaf fiber as reinforcement, supplied by Macrocom (M) Sdn Bhd. For this study, all of the test samples are fabricated using an optimum fiber loading, which is at 30 wt. % as reported in the literature [7]. To aid in wetting of the fiber and matrix in the composites, the pineapple leaf fibers were pre-treated using NaOH solution and dried prior to fabrication process. In addition, PLA pellets were also oven dried in the oven at temperature of 60°C for a minimum of 8 hours before proceeding with the fabrication process.

2.2 Fabrication process

There are two types of composites considered for this study; these being the short fiber PALF reinforced PLA biocomposites and the continuous long PALF fiber reinforced PLA biocomposites, with the fiber length of 30 mm and greater than 100 mm for the short and long fiber reinforced composites, respectively.

2.2.1 Short fiber reinforced composites

The short fiber reinforced biocomposites were prepared using a two-step processing. First, the raw materials underwent melt-mixing process using a ThermoHaake machine to form a composites blend. Following these, the composites blend was compression molded to size using a Hot Press machine to produce test samples with nominal thickness of 3 mm each for mechanical characterization.

2.2.2 Continuous long fiber reinforced composites

Continuous long fiber reinforced composites were prepared using a two-step processing, with fiber length and loading of >100 mm each and 30 wt. %. First, the plain PLA material was compression molded into thin films having nominal thickness of 1 mm each. The cured PLA thin films were then stacked together in between the continuous long pineapple leaf fibers using hand lamination and subjected to applied pressure and temperature using a Hot Press machine. The final nominal thickness of the test samples is approximately 3 mm each.

2.3 Mechanical characterization

A flexural test, using a three-point bending set-up was considered to characterize the flexural properties of both types of biocomposites. According to ASTM D790, specimens with dimension of 74 mm x 12 mm x 3 mm were considered. The test samples were then placed on two supports and load were applied.

3. RESULTS AND DISCUSSION

Preliminary results following flexural tests on the PALF reinforced PLA biocomposites as well as data from the literature on PALF reinforced PP composites [7] are listed in Table 1. The continuous long PALF fiber reinforced PLA composites exhibit much greater flexural strength (>30%) and modulus (> 45%) than those of the short fiber reinforced composites of the same fiber loading (30 wt. %). Moreover, these values are also compatible or superior (flexural modulus) to those of the reinforced PP composites [7] of similar fiber loading.

Table 1 Flexural properties of PALF reinforced composites.

Sample	Flexural strength	Flexural Modulus
Short fiber reinforced composites		
PALF reinforced PLA composites	33.6±4.8	2.2 ±0.2
PALF reinforced PP composites [7]	34.8	2.6
Continuous long fiber reinforced composites		
PALF reinforced PLA composites	44.4±15.4	3.17±0.2
PALF reinforced PP composites [7]	68.0	1.94

4. CONCLUSION

In conclusion, the preliminary results following flexural tests on the short and continuous long PALF fiber reinforced PLA biocomposites were assessed as a function of fiber length. As expected, the continuous long fiber exhibit better mechanical properties in comparison to those of the short fiber, demonstrating the effect of fiber length in the mechanical performance of a composite system. However, further works in this area are required to fully characterize the composites

behavior under various loading conditions such as tensile, compression and impact as well as other characterization such as physical and thermal properties to provide an insight into the behavior of PALF reinforced PLA biocomposites.
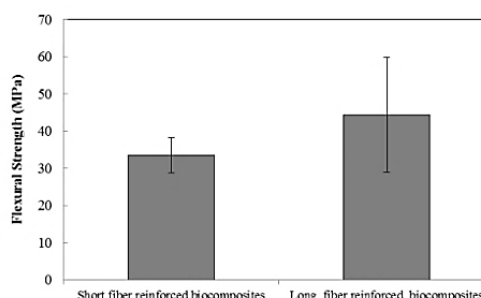
Figure 1 Flexural strength values for the short PALF fiber and continuous long PALF fiber reinforced PLA biocomposites.

REFERENCES

[1] T. Mukherjee and N. Kao, "PLA Based Biopolymer Reinforced with Natural Fiber: A Review," Journal of Polymers and the Environment, pp. 714–725, 2011.

[2] J. George, M. S. Sreekala, and S. Thomas, "A review on interface modification and characterization of natural fiber reinforced plastic composites," Polym. Eng. Sci. Polymer Engineering & Science, pp. 1471–1485, 2001.

[3] A. Leão, B. Cherian, S. Narine, S. Souza, M. Sain, and S. Thomas, "The use of pineapple leaf fibers (PALFs) as reinforcements in composites," Biofiber Reinforcements in Composite Materials, pp. 211–235,2015.

[4] J. George, M. S. Sreekala, and S. Thomas, "A review on interface modification and characterization of natural fiber reinforced plastic composites," Polym. Eng. Sci. Polymer Engineering & Science, pp. 1471–1485, 2005.

[5] N. Lopattananon, K. Panawarangkul, K. Sahakaro, and B. Ellis, "Performance of pineapple leaf fiber–natural rubber composites: The effect of fiber surface treatments," Journal of Applied Polymer Science, pp. 1974–1984, 2006.

[6] S. Luo and A. N. Netravali, "Mechanical and thermal properties of environment-friendly green composites made from pineapple leaf fibers and poly (hydroxybutyrate-co-valerate) resin," Polymer Composites, pp. 367–378, 1999.

[7] M. M, R. AR and H. A, "Characterization and Treatments of Pineapple Leaf Fiber Thermoplastic Composite for Construction Application", Universiti Teknologi Malaysia, 2007.

[8] B. Mitra, "Environment Friendly Composite Materials: Biocomposites and Green Composites", Defence Science Journal, vol. 64, no. 3, pp. 244-261, 2014.

Kinetic study of boron diffusion in powder-pack boronizing

N.H. Omar[1,*], R. Hasan[1,2], N.A.B. Masripan[1,2]

[1] Faculty of Mechanical Engineering, Universiti Teknikal Malaysia Melaka,
Hang Tuah Jaya, 76100 Durian Tunggal, Melaka, Malaysia
[2] Centre for Advanced Research on Energy, Universiti Teknikal Malaysia Melaka,
Hang Tuah Jaya, 76100 Durian Tunggal, Melaka, Malaysia

*Corresponding e-mail: nurulhidayahomar91@gmail.com

Keywords: Boronizing; kinetic; diffusion

ABSTRACT – In this study, boronized properties of AISI 304 ball bearing was investigated using powder-pack boronizing method. The experiment was carried out in temperature range from 850 to 950 ^{0}C with durations 2 – 4 hours. Microstructure of boride layer revealed a smooth surface using SEM micrograph analysis. The thickness of boride layer varied from 17-140 µm while the hardness varied between 470-900 HV. The growth of kinetic rates were plotted using Arrhenius equation and the activation energy measured from the graphical calculation is 126 kJ/mol. From this study, a new knowledge on diffusion of boron atoms on spherical surface is established.

1. INTRODUCTION

Boronizing is a thermochemical heat surface treatment that diffuses the boron atoms into a substrate [1]. It is a diffusion controlled surface hardening treatment in which boron atoms are diffused into the surface of a substrate and form borides with base metal, due to chemical reaction at high temperature [1]. Boronizing can be applied to variety of different materials including ferrous metals, non-ferrous metals and cermet [1]. Boronizing process can be performed in solid, liquid or gaseous medium but powder-pack boronizing (solid) is a process that being used frequently because of the simple method and low cost as well as easily implemented in the industry [1,2]. Besides, the simple powder-pack process can be also combined with other process such as superplastic boronizing [3]. The aim for this present study is to analyze the diffusion of boronizing powder on surface of ball bearing using metallurgraphic technique and to determine the kinetics of boronizing using the Arrhenius equation.

2. METHODOLOGY

2.1 Experimental Setup

The boronizing treatment is carried out in a solid medium using powder-pack boronizing method. 10 mm stainless-steel ball bearing is used as the samples. The sample is buried and packed with boronizing compound (Ekabor 1) in a stainless-steel container then sealed with a lid from the same material as the container. More explanations on the powder-pack boronizing was discussed in other paper [4]. The variables for this experiment are shown in the Table 1. These variables are accordance to the basic boronizing conditions as stated in Davis, 2002 [5]. Stainless-steel is used in this study since the material has shown the ability to perform as superplastic material [4]. However, this ability is not the main concern in this current study.

Table 1 Boronizing parameters.

Boronizing Time (hours)	Boronizing Temperature (^{0}C)
2	850
4	900
6	950

3. RESULTS AND DISCUSSION

3.1 Microstructure

In Figure 1, the SEM micrograph analysis showed the smooth surface of boride layer. This morphology observation is a characteristic property of the boride layer and it depends on the concentration of alloying elements as well as the treatment time and temperature from the boronizing process [2].
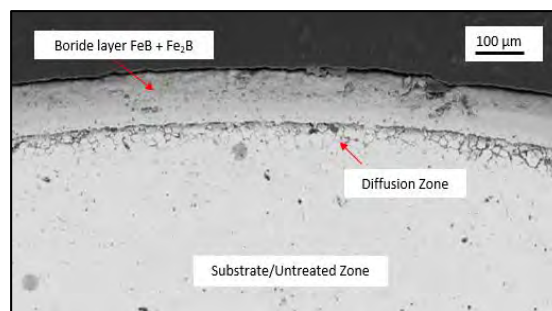
Figure 1 Boride layer morphology.

3.2 Boride layer thickness and hardness

In this present study, the hardness variation of boride layer are between 470 – 900 HV which is higher than untreated specimen (392 – 440 HV). The boride layer thickness varied from 17 to 140 µm. As the boronizing time and temperature increased, the boride layer hardness and thickness also increased as shown in Figure 2 and 3. These results are accordance to the nature of boronizing treatment because of more boron atoms diffused into the substrate with the increment in time and temperature [2].
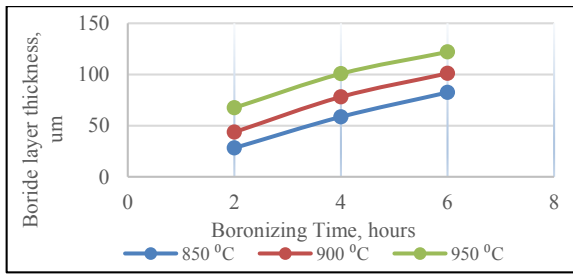
Figure 2 The variation of boride layer thickness as a function of process time.
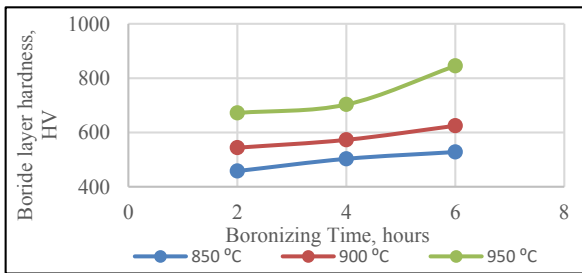
Figure 3 The variation of boride layer hardness as a function of process time.

3.3 Kinetics of atoms diffusion

The kinetics of the layer growth is controlled perpendicularly into the substrate layer [2,6] and it is describing as in Equation 1 and plotted as in Figure 4:

$$D^2 = Kt \tag{1}$$
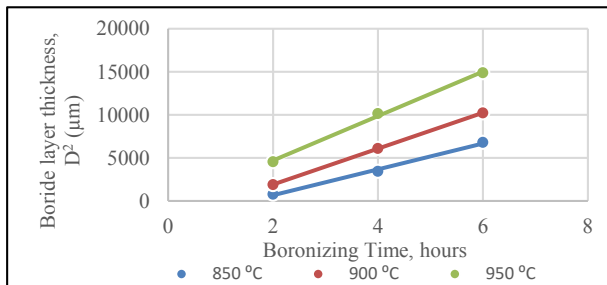
Figure 4 Square of boride layer thickness of borided stainless steel as a function process of time.

The plot of ln K versus 1/T in Figure 5 showed the linear relationship with the temperature and the value of activation energy measured from the slope is 126 kJ/mol using the Arrhenius equation as in Equation 2.
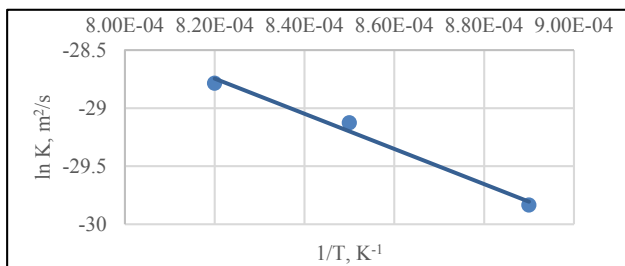
Figure 5 Natural logarithm of growth rate constant as a function of reciprocal boronizing temperature.

$$K = K_o \, e^{-Ea/RT} \tag{2}$$

4. CONCLUSIONS

In conclusion, boronizing time treatment and boronizing temperature influenced the boride layer hardness and thickness. As the boronizing temperature and time increased, the boride layer hardness and thickness also increased. The minimum energy required to start the boronizing process (Activation Energy) is 126 kJ/mol. This study is a part of optimization study for boronizing of stainless-steel ball bearing, in which further explanation can be found in other paper [7]. From this study, a new knowledge on diffusion of boron atoms on spherical surface is established, thus can contribute to the practical engineering applications. This new improved material can be adapted in tribological field due to its high hardness that can reduce friction.

ACKNOWLEDGEMENT

REFERENCES

[1] O. Ozdemir, M.A. Omar, M. Usta, S. Zeytin, C. Bindal, and A.H. Ucisik, "An investigation on boriding kinetics of AISI 316 stainless steel," *Vacuum*, vol. 83, pp. 733–738, 2012.

[2] M. Ipek, G. Celebi Efe, I. Ozbek, S. Zeytin, and C. Bindal, "Investigation of boronizing kinetics of AISI 51100 steel," *Journals of Materials and Engineering Performance*, vol. 21, pp. 733–738, 2012.

[3] R. Hasan, I. Jauhari, H. Ogiyama, and R.D. Ramdan, "Effects of superplasticity in boronizing of duplex stainless steel," *Key Engineering Materials*, vol. 326, pp. 1233–1236, 2006.

[4] N.H. Omar, R. Hasan, S.M.M. Shahidan, N.R. Morjani, and M.H. Kamaludin, "Study on surface diffusion of an effective powder-pack boronizing," in *Proceedings of Mechanical Engineering Research Day 2015*, 2015, pp. 135–136.

[5] J.R. Davis. Surface Hardening of Steels, United States of America: ASM International, 2002.

[6] R. Hasan, I. Jauhari, H. Ogiyama, S.M. Yunus,, R.D. Ramdan, and N.R.N. Masdak, "Kinetic study on boronized duplex stainless steel," in *JSME Material and Processing Conference (MPP)*, 2005.

[7] N.H. Omar, R. Hasan, and N.A.B. Masripan, "A study on powder-pack boronizing of 316 stainless-steel ball bearing," in *Proceedings of Malaysian International Tribology Conference 2015*, 2015, pp. 261–262.

Characterization of nanocarbon particles using nitrogen adsorption analysis: Isotherm, pore type, pore size and BET surface area

S. Zainal Abidin[1,*], I.S. Mohamad[1,2], A.Y. Bani Hashim[3], N. Abdullah[4]

[1] Faculty of Mechanical Engineering, Universiti Teknikal Malaysia Melaka,
Hang Tuah Jaya, 76100 Durian Tunggal, Melaka, Malaysia
[2] Centre for Sustainability and Environment, Universiti Teknikal Malaysia Melaka,
Hang Tuah Jaya, 76100 Durian Tunggal, Melaka, Malaysia
[3] Faculty of Manufacturing Engineering, Universiti Teknikal Malaysia Melaka,
Hang Tuah Jaya, 76100 Durian Tunggal, Melaka, Malaysia
[4] Department of Chemistry, Centre for Foundation Studies, Universiti Pertahanan Nasional Malaysia,
Kem Sungai Besi, 57000, Kuala Lumpur, Malaysia

*Corresponding e-mail: Wanieyza_2792@yahoo.com

Keywords: Nanocarbon; nitrogen adsorption analysis

ABSTRACT – In this research, the characterization of the porous material which is nanocarbon was investigated using nitrogen adsorption technique. The porosity existence of nanocarbon is analysed by using BET method. Then, the surface area is measured from diameter and depth of the existed pores. The BET surface area obtained shows that MWCNT-OH has the largest surface area due to high distribution of micropores and existence of non-porous pore in the sample.

1. INTRODUCTION

Nanoparticles are a great scientific interest as they are effectively a bridge between bulk materials and atomic or molecular structures. The properties of materials change as their size approaches the nano-scale and as the percentage of atoms at the surface of a material becomes significant. Nanoparticles have a very high surface area to volume ratio. This provides a tremendous driving force for diffusion especially at elevated temperatures. The specific atomic structure of nanoparticle make it an interesting chemical and physical properties according to those of graphite and diamond [1]. Generally, the characterization techniques evaluations is done in order to yield important information in studying the effects of surface porosity and particle size for materials engineering. The characterization of the porous materials commonly used gas adsorption as a major technique [2] [3]. Compared to the other gases and vapours available in this earth, nitrogen gas has become a universally pre-eminent gas to be used because of its availability and could be used as adsorptive. Dewar and Ramsay [4] [5] are the one of the earliest researchers that studies the adsorption nitrogen and other gases at liquid air temperature approximately to 88 K by investigating the composition of the atmosphere and the separation of the noble gas. Then, the research regarding adsorption of nitrogen gas and other gases was conducted followed by other researcher but at a low-temperature studies by charcoal, including an extensive series of measurements over varies temperature by Homfray in 1910 [6]. Thus, this research aimed to study the behaviour of nanocarbon structure which using nitrogen adsorption techniques in order to yield essential information in studying the properties of surface porosity and particle size for materials engineering.

2. METHODOLOGY

For this research, Autosorb 6-B surface area and pore size analyser machine manufactured by Quantachrome Instruments were used. The analysis for this characterization testing were made by measuring the volume of nitrogen gas adsorbed at the specific pressures. The characterization testing were performed on these selected nanocarbon which are Multiwalled Carbon Nanotube (MWCNT-OH), functionalized MWCNT and Commercial Carbon Nanofiber (CNF). Table 1 shows the properties of the three nanocarbon particles.

Table 1 Properties of the CNT.

Properties	MWCNT-OH	Functionalized MWCNT	Commercial CNF
Purity (%)	90	95	98
Outer Diameter	10-30nm	30-50nm	100nm
Specific Surface Area (m^2/g)	100	60	43
Form	Powder	Fine Powder	Powder

3. RESULTS AND DISCUSSION

The isotherm plot indicates the distribution of different type of pore which consists of micro, meso and macropores from an adsorption isotherm. The micropore diameter size is between 0 to 2nm, mesopore is between 2 to 50nm and macropore size is more than 50nm. According to Figure 1, MWCNT-OH isotherm can be classified as Type II and Type III. This isotherm type is produced by the non-porous or solid macro pore which showed non-porous solid characteristics. For functionalized MWCNT, the isotherm can be classified

as Type II and Type IV. Commercial CNF can be classified as Type I and Type IV isotherm which means that the sample is mostly microporous with hysteresis loops.
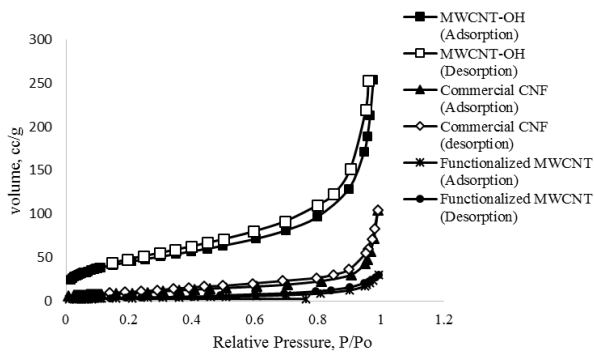
Figure 1 Isotherm comparison for MWCNT-OH, functionalized MWCNT and Commercial CNF.

Referring to the Figure 2, MWCNT-OH shows that the high peak is representing range of micropore type with diameter 1.4nm and depth 2.15×10^{-2} cc/g which shows that it has a high distribution of micropores and average distribution of mesopores. For functionalized MWCNT, the plot shows that high peak is representing range of mesopore type with diameter 3.1nm and depth 5.25×10^{-3} cc/g. Whilst, Commercial CNF shows the high peak with high distribution of micropores which have 0.39nm and depth 2.07×10^{-4} cc/g and moderate distribution of mesopores. Materials with micro-sized pores shows the strong interactions among the narrow pore walls with material adsorbed on the relative pressure which cause the volume of material adsorbed in the pores increases. Pore with meso-sized shows an increase in the volume of the adsorption due to the effect of the occurrence of capillary condensation turn through the establishment of a hysteresis loop. Macro-sized pores indicate the formation of a monolayer on relatively at low pressure and the adsorption layers at relatively high pressure. Material which have bigger pore will result in a weak interaction between materials adsorbed and the adsorbent which causing difficult adsorption.
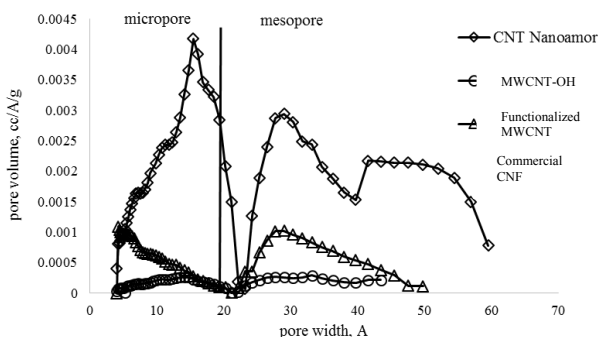
Figure 2 DFT pore size distribution comparison.

Surface area is measured from diameter and depth of existed pores whether it is coming from micro, meso or macro types influencing on surface area reading based on volume of gas adsorbed. Table 2 shows the BET surface area for all sample tested.

Table 2 BET surface area.

Nanocarbon	BET Surface Area (m²/s)
MWCNT-OH	1.610×10^2
Functionalized MWCNT	1.261×10^1
Commercial CNF	3.241×10^1

The BET surface area obtained shows that MWCNT-OH has the largest surface area (MWCNT-OH > Commercial CNF > Functionalized MWCNT). This is due to the high distribution of micropores in the sample which contribute to the high surface area. The functionalized MWCNT has the smallest surface area due to the high distribution of mesopores in the sample.

4. CONCLUSION

Characterization using nitrogen adsorption analysis reveal the pore type of the material tested. From the result, MWCNT-OH nanocarbon has a higher BET surface area which is 1.610×10^2 m²/s due to the non-porous or solid macro pore. Whilst, Functionalized MWCNT has the smallest BET surface area (1.261×10^1 m²/s) due to the high distribution of mesopores in the nanocarbon. For Commercial CNF, the sample shows the microporous pore type with BET surface area 3.241×10^1 m²/s. In conclusion, the BET characterization technique encompasses external area and pore area evaluations to determine the total specific surface area in order to yield important information in studying the effects of surface porosity and particle size for materials engineering.

REFERENCES

[1] L. Sun, Z. Ounaies, X. Gao, C. Whalen, and Z. Yang, "Preparation, Characterization, and Modeling of Carbon Nanofiber/Epoxy Nanocomposites," *Journal of Nanomaterials*, pp 1-8, 2011.

[2] F. Yang, Z. Ning, C. Hu, B. Wang, K. Peng & H. Liu, "Characterization of Microscopic Pore Structures in Shale Reservoirs", *J. Acta Pet. Sin.*, vol. 34, pp. 301-3011, 2013.

[3] C.R. Clarkson, J.L. Jensen & S. Chipperfield, "Unconventional Gas Reservoir Evaluation: What Do We Have to Consider?", *J. Nat. Gas Sci. Eng.*, vol. 8, pp. 9-33, 2012.

[4] J. Dewar, "Physical Constant at Low Temperatures: The Densities of Solid Oxygen, Nitrogen and Hydrogen", *Pro. R. Soc.*, vol. 73, pp. 251-261, 1904.

[5] W. Ramsay, "A Determination of the Amounts of Neon and Helium in Atmospheric Air", *Proc. R. Soc.*, vol. 76, pp. 111-114, 1905.

[6] I.F. Homfray, "On the Absorption of Gases by Charcoal", *Phy. Chem.*, vol. 74, pp. 129, 1910.

Fabrication of polymer lattice structure using additive manufacturing for lightweight material

R. Hasan[1,2,*], M.K. Baharudin[1], M.M. Nasarud'din[1], M.R. Alkahari[1,2]

[1] Faculty of Mechanical Engineering, Universiti Teknikal Malaysia Melaka,
Hang Tuah Jaya, 76100 Durian Tunggal, Melaka, Malaysia
[2] Centre for Advanced Research on Energy, Universiti Teknikal Malaysia Melaka,
Hang Tuah Jaya, 76100 Durian Tunggal, Melaka, Malaysia

[*]Corresponding e-mail: rafidahhasan@utem.edu.my

Keywords: Polymer lattice structure; additive manufacturing

ABSTRACT – This paper reports on the development of polymer lattice structure as lightweight material manufactured using additive manufacturing technology, which is 3D printer. Models of 3D body-centered-cubic (BCC) lattice structure were developed using SolidWorks software for several geometries that match with the capability of CubePro 3D printer. Polymer lattice structure block with dimension 20x20x20 mm^3 has been successfully fabricated. The dimension of a unit cell for the lattice structure is within the range of 10^{-3} meter. The realization of the polymer lattice structure using the 3D printer can contribute to further research in lightweight material with high load-bearing capacity.

1. INTRODUCTION

Lattice structure is a three dimensional periodicity open-cell cellular structure. It contains straight struts of uniform thickness, consistent joint angle, and in symmetrical arrangement. Lattice structure exists in wide range of materials, be it from natural creation such as in wood and bone, as well as from common modern metallic and polymer compounds. It is classified as lightweight material due to its low specific density as compared to the bulk material. There are many methods can be used to fabricate lattice structure from any kind of material, and one of them which receives increasing attention from researchers is by using rapid additive layer technique [1, 2]. An advantage of using the additive layer technique is the formation of lattice structure can be down to 10^{-6} meter scale. Thus, a material with high specific stiffness can be obtained.

One type of popular periodic lattice structure is the body-centered-cubic (BCC) arrangement. Although this type of arrangement has been always discussed in many researches, there are still a lot of new findings that can be explored, especially in terms of process and properties relationship. Thus, the aim of this study is to successfully produce the BCC lattice structure from polymer material which is acrylonitrile-butadiene-styrene (ABS), by utilizing the available additive layer technology which is 3D printer from CubePro. A successfully fabricated polymer BCC lattice structure block is important in order to analyse the performance of the material and compare with other study [1].

2. METHODOLOGY

The stages in this study involve the design of BCC lattice structure, confirmation of struts' diameter size and fabrication of lattice structure block.

2.1 Design of lattice structure

A unit cell of BCC lattice structure is shown in Figure 1, where L = length of unit cell, A = length of strut, H = diagonal distance at surface, θ = angle of strut from surface, α, β, γ = angle of strut from axes x, y, z respectively.
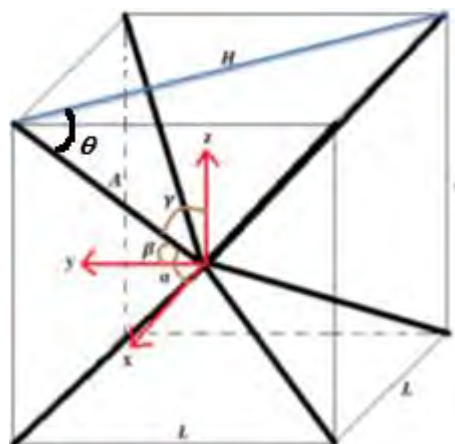
Figure 1 Unit cell of BCC lattice structure.

Model of BCC lattice structure was developed using SolidWorks software, and saved in .STL file.

2.2 Confirmation of strut's diameter size

The capability of CubePro 3D printer to produce lattice structure with as small as possible unit cell was tested. Strut diameter of 0.3 mm or 300 μm was assigned in the confirmation run of the printer.

2.3 Fabrication of lattice structure block

A complete BCC lattice structure block with dimension 20x20x20 mm^3 was fabricated. The layer resolution was 200 μm, the print strength was almost solid and the print pattern was diamond. The default fill spacing was used throughout the fabrication.

3. RESULT AND DISCUSSION

The angle θ of BCC strut was found as 35.26°. Thus, the angle of α, β, γ was 54.74°. The unity of unit cell was further confirmed with Equation (1) [3].

$$cos^2\alpha + cos^2\beta + cos^2\gamma = 1 \qquad (1)$$

After the confirmation run, it was found that the 0.3 mm diameter size was not possible to be fabricated using the CubePro 3D printer. It was realized that the diameter of strut for lattice structure must be larger than 0.5 mm, since the diameter of cartridge wire for the injection process is known to be as 0.5 mm. The scrapped printing of the lattice structure block with 0.3 mm strut diameter size is as shown in Figure 2.

Figure 2 Scrapped printing lattice structure.

The BCC lattice structure block was then designed with 1.0 mm strut diameter size. Due to the enlargement of strut diameter, the number of unit cell in the block was also reduced. Table 1 shows the findings in this study.

Table 1 Details of BCC lattice block fabrication.

Strut diameter	No. of cell	Fabrication status
0.3 mm	8 x 8 x 8	Fail
1.0 mm	4 x 4 x 4	Success

Figure 3 and Figure 4 show the SolidWorks model and the success fabrication of polymer BCC lattice structure block using CubePro 3D printer, respectively.
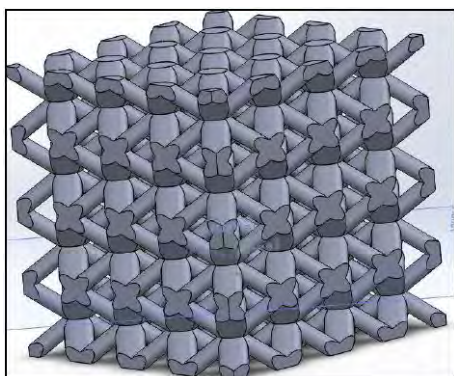
Figure 3 SolidWorks model of BCC lattice block with 1.0 mm strut diameter.
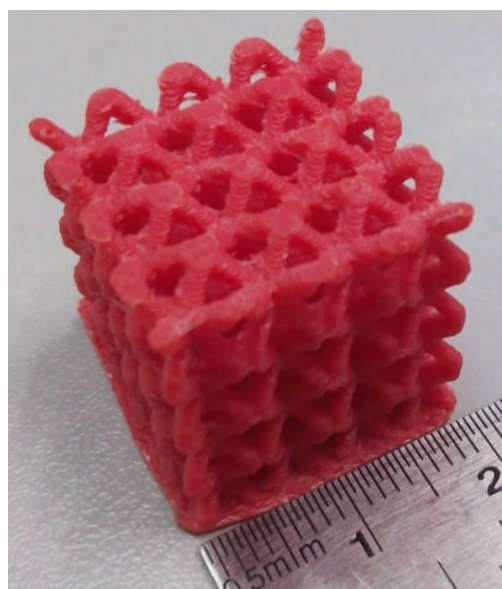
Figure 4 Fabricated ABS polymer BCC lattice structure block with 1.0 mm strut diameter.

4. SUMMARY

The polymer BCC lattice structure block with dimension 20x20x20 mm^3 was successfully fabricated using the CubePro 3D printer. However, the number of cell which is able to be produced is only 4 x 4 x 4 due to the strut diameter size of 1.0 mm. The dimension of a unit cell for the lattice structure is within the range of 10^{-3} meter. Although the CubePro 3D printer machine is not capable to produce lattice structure down to 10^{-6} meter scale, the potential of lightweight material from this study can still be further analyzed. Effects of fabrication parameters on the mechanical properties of the structure will contribute to the knowledge field.

REFERENCES

[1] R. Hasan, "Progressive collapse of titanium alloy micro-lattice structures manufactured using selective laser melting," University of Liverpool, United Kingdom, 2013.
[2] R.E. Doty, J.A Kolodziejska, A.J. Jacobsen, "Hierarchical polymer microlattice structures," *Advanced Engineering Materials*, vol. 14, no. 7, pp. 503, 2012.
[3] R.C. Hibbeler, Engineering Mechanics: Statics, 13th ed. Pearson; 2012.

Mechanical performance of pineapple leaf fiber reinforced poly lactic acid (PLA) biocomposites

S.N.R Ramli[1,2,*], S.H.S.M. Fadzullah[1,2], Z. Mustafa[3,4]

[1) Faculty of Mechanical Engineering, Universiti Teknikal Malaysia Melaka,
Hang Tuah Jaya, 76100 Durian Tunggal, Melaka, Malaysia
[2) Centre for Advanced Research on Energy, Universiti Teknikal Malaysia Melaka,
Hang Tuah Jaya, 76100 Durian Tunggal, Melaka, Malaysia
[3) Faculty of Manufacturing Engineering, Universiti Teknikal Malaysia Melaka,
Hang Tuah Jaya, 76100 Durian Tunggal, Melaka, Malaysia
[4) Advanced Manufacturing Centre, Universiti Teknikal Malaysia Melaka,
Hang Tuah Jaya, 76100 Durian Tunggal, Melaka, Malaysia

*Corresponding e-mail: rabiatutadawiahramli@gmail.com

Keywords: Poly lactic acid; pineapple leaf fibres; mechanical properties

ABSTRACT – Poly lactic acid is a biopolymer that is easily processable and offers goods aesthetics. Biocomposites is prepared by combining poly lactic acid and pineapple leaf fibres (PALF). The aim of this study is to evaluate the mechanical performance of the biocomposites when the fibers are surface treated with alkaline solution (NaOH) prior to fabrication. The fiber length and loading for the composites are 30 mm and 30 wt. %, respectively. The composites were fabricated using a melt mixing process via a ThermoHaake machine before compression molded to produce composite plates with nominal thickness of 3 mm. At preliminary stage, a flexural testing as per ASTMD790 was carried out. As expected, the alkaline-treated composites exhibit much greater flexural strength and modulus in comparison to those of the untreated samples.

1. INTRODUCTION

To-date, with a growing concern and awareness in saving the environment, together with the notion to promote sustainability in manufacturing, *biocomposites* are gaining increasing attention, since they are cost effective and environmental-friendly. Many studies have been done on the use of natural fibers such as kenaf, sisal, jute, ramie and flax to replace the synthetic fibers [1]. However, despite the fact that these materials are low cost and biodegradable, several identified limitations are brittleness, low impact toughness and tensile strength [1–3].

Malaysia is one of the main exporters of pineapple in the world market, after Thailand, Philippine and Brazil [4]. As an example, it has been reported that a total amount of 96, 957 metric tonnes of pineapple have been produced in 2011 [7]. Therefore, to exploit these agricultural wastes, some work has been initiated to extract the pineapple leaf fibers. Pineapple leaf fibre (PALF) exhibit better mechanical properties compared to other naturals fibres are supplied to their high cellulose (70-82 %) and low lignin (5-12 %) content [2, 3].

Polylactic acid (PLA) is a biopolymer, produced by microbial fermentation process of fully renewable resources. Currently, PLA is used in various field of applications such as food packaging, biocompatible medical devices, film and interior automotive parts[2, 3]. PLA is also known for its biodegrability and biocompability features. However, one of the main problems is brittleness. To overcome such problem, one of the common ways is by adding fillers or reinforcement, by means of chemical pre-treatment processes, to improve the brittleness as well as to enhance the overall mechanical and thermal properties of PLA based polymer composites [5].

Previous study in this area has reported that the performance of fibre reinforced composites depend on several factors; these being (i) fibre-matrix adhesion, (ii) fiber volume fraction (iii) fiber orientation and (iv) adhesion at the fiber-matrix interface. The goal is to achieve an efficient stress transfer from the matrix to the fiber when subjected to an applied load [6].

This study reports the result of experimental investigations on the mechanical performance of pineapple leaf fibres reinforced poly lactic acid biocomposites, with fiber pre-treatment using sodium hydroxide (NaOH). At the preliminary stage, the experimental results from flexural testing are presented and discussed for both the treated and untreated PALF reinforced PLA biocomposites.

2. METHODOLOGY

2.1 Material

Polylactic acid, PLA grade 6100D was purchased by NatureWorks, LLC, USA. The main properties of PALF and PLA are given in Tables 1 and 2 respectively. Sodium Hydroxide, (NaOH) was purchase from Merck Chemicals Sdn. Bhd. Pineapple leaf fibres (PALF) from Josapine species.

2.2 Composites preparation

Composites were produced by melt mixing of 30 mm length short PALF fibers and the PLA matrix via melt mixing process in a Thermo Haake machine. Both

---

raw materials were dried overnight to minimise moisture content. Since this machine can feed only 50 g per batch, the same steps were repeated to produce 3 mm thickness of biocomposites. The raw materials, with the ratio of 30/70 for PLA and PALF were feed into the Thermo Haake machine for 15 minutes under temperature 175 °C and rotor speed of 50 min⁻¹. The mixed raw materials were undergoing compression moulding process using a stainless steel mould platen. The raw materials were preheated for 2 minutes and then pressed under pressure of 1.38 MPa and temperature of 175 °C, with a soaking time of 10 minutes, followed by cooling process for 10 minutes prior to demolding of the biocomposites plate. The biocomposites laminates were then cut to size for mechanical characterization.

Table 1 Main properties of PLA (6100D).

Properties	Value
Relative Viscosity	3.1
Specific Gravity	1.24
Crystalline Melt	165-180
Glass Melt	55-60

Table 2 Main properties of PALF fibers.

Properties	PALF
Density (gcm⁻¹)	1.52
Elongation break (%)	3
Young's Modulus (GPa)	6.21
Tensile Strength (MPa)	170

2.3 Mechanical characterizations

Specimens with dimensions of 74 mm x 12 mm x 3 mm were prepared for flexural testing in accordance to ASTM D790. The tests were conducted at crosshead speed of testing of 2 mm/min and maximum load of 1kN. The specimens were placed on two supported stage and load were applied. Universal Testing Machine (UTM) model Instron 5585 was used to conduct the flexural testing.

3. RESULT AND DISCUSSION

3.1 Flexural properties of biocomposites

Table 3 shows the flexural properties of treated and untreated PALF reinforced biocomposites. From the results, treated composites shows higher value for flexural strength and modulus compare to untreated PALF reinforced composites. The flexural modulus is increased from 0.22 GPa for untreated to 0.32 GPa for treated PALF reinforced composites (a 31% increase). This result shows similar trend to the finding from previous work in which the flexural modulus being 4.4 GPa for untreated and 5.6 GPa for treated PALF reinforced composites [5]. In addition, the flexural strength increased by 69% for treated PALF when compared to untreated PALF. These findings are in agreement with the theory that when the PALF fibers

are pre-treated i.e. via an alkaline surface treatment, rougher surface of the fibers results in enhanced interfacial adhesion, therefore inducing better fibre-matrix interlocking and consequently enhance the mechanical performance of the composites [5].

Table 3 Flexural performance of treated and untreated short biocomposite.

Properties	Untreated	Treated
Flexural Strength (MPa)	33.64 ±4.81	107.53 ±10.37
Flexural Modulus (GPa)	0.218 ±0.16	0.32 ±0.02

4. CONCLUSIONS

The preliminary findings obtained from this study have demonstrated the effect of chemical treatment on the mechanical performance of PALF reinforced PLA biocomposites. These observations suggest an improved adhesion achieved by introducing alkaline treatment of the fiber, thereby causing rough surface at the fibre-matrix interface. Consequently, superior mechanical properties of the alkaline-treated PALF fiber reinforced composites in comparison to those of the untreated composites are attained.

REFERENCES

[1] M.S. Huda, L.T. Drzal, A.K. Mohanty, and M. Misra, "Effect of fiber surface-treatments on the properties of laminated biocomposites from poly(lactic acid) (PLA) and kenaf fibers," *Compos. Sci. Technol.*, vol. 68, no. 2, pp. 424–432, 2008.

[2] S. Kaewpirom and C. Worrarat, "Preparation and properties of pineapple leaf fiber reinforced poly(lactic acid) green composites," *Fibers Polym.*, vol. 15, no. 7, pp. 1469–1477, 2014.

[3] F. Carrasco, P. Pagès, J. Gámez-Pérez, O.O. Santana, and M. L. Maspoch, "Processing of poly(lactic acid): Characterization of chemical structure, thermal stability and mechanical properties," *Polym. Degrad. Stab.*, vol. 95, no. 2, pp. 116–125, 2010.

[4] J. De La Cruz Medina and H.S. García, "Post-harvest Operations," *PINEAPPLE Post-harvest Oper.*, 2005.

[5] M.S. Huda, L.T. Drzal, A.K. Mohanty, and M. Misra, "Effect of chemical modifications of the pineapple leaf fiber surfaces on the interfacial and mechanical properties of laminated biocomposites," *Compos. Interfaces*, vol. 15, no. 2–3, pp. 169–191, 2008.

[6] R.M.N. Arib, S.M. Sapuan, M.M.H.M. Ahmad, M. T. Paridah, and H.M.D. Khairul Zaman, "Mechanical properties of pineapple leaf fibre reinforced polypropylene composites," *Mater. Des.*, vol. 27, pp. 391–396, 2006.

[7] Mpib.gov.my. "Portal Rasmi Lembaga Perindustrian Nanas Malaysia". N.p., 2016. Web. 6 Jan. 2016.

The effect of coconut fiber towards impact characteristics

A.R.B.A. Fizal[1], M.A. Shamsudin[1,2,*], M.I.H.C. Abdullah[1,2]

[1] Faculty of Engineering Technology, Universiti Teknikal Malaysia Melaka,
Hang Tuah Jaya, 76100 Durian Tunggal, Melaka, Malaysia
[2] Centre for Advanced Research on Energy, Universiti Teknikal Malaysia Melaka,
Hang Tuah Jaya, 76100 Durian Tunggal, Melaka, Malaysia

*Corresponding e-mail: afdhal@utem.edu.my

ABSTRACT – The aim of this study is to analyze the effect of the coconut fibre composition upon the energy and resilience characteristic. A series of four samples with composition of 15, 30, 45 and 60 vol.% of coconut fiber was prepared by mixing together with polyester resin and were tested using pendulum impact test machine. The energy and resilience were measured according to ASTM D-6110. The sample with 60 vol.% coconut fibre displayed the highest value of energy and resilience. This is due to the proper strength distribution by the fibre matrix. On top of that the coconut fibre itself behaved as a significant adhesion between the matrix and composite. As a conclusion, the higher composition of coconut fibre added to the composite resulted in better impact characteristic.

1. INTRODUCTION

Fibre is one of the elements that been used as reinforcement material to produce composites. This fibre usually present in the filament phase which having an extraordinary mechanical features in term of strength and stiffness properties [1]. A verity type of fibre currently been introduce in developing new composite material such as metallic, aramid, glass, carbon, alumina and ect but yet still limitation awareness on the envirometal friendly aspect [2]. As countermeasure natural fibre tend to be acknowladge nowadays. The natural fibre can be obtained by extraction of plant or animals which can be revolve to filament phase.

Coconut fibre can be classify as one of the natural fibre which is a part of seed fibers. The life spand of the coconut fibre is longer compared to other natural fibre due to high amount of lignin beside the coconut fibre is more cost effective and also biogradable [3].

Currently, the potential of coconut fibre as a reiforcement material to produce new composite material still in slow development stage. A lot of uncertainties raised in term of the peformance of the coconut fibre as reinforcement material especially toward the impact characteristic which is still not yet extensively been study.

The objective of this study is to analyze the effect of the coconut fibre composition on the energy and resilience characteristic toward the impact test.

2. METHODOLOGY

A series of four samples with composition of 15, 30, 45 and 60 vol.% of coconut fibre was prepared according to the Table 1. Each sample was test by using Pendulum Impact Test Machine with 150º angle of hammer, and the impact result was recorded from the machine. The result was verify according to the ASTM D6110- Determining the Charpy Impact Resistance of Notched. Figure 1 illustrate the impact test for each sample.

Table 1 Composition of the sample.

Sample	Composition, Vol.%	
	Coconut fibre	**Polyester Resin**
1	15	85
2	30	70
3	45	55
4	60	40
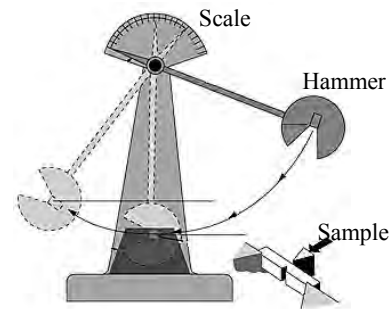
Figure 1 Impact test for each sample [4].

3. RESULTS AND DISCUSSION

Table 2 shows the impact result for overall samples. The fibre compositions of sample 1 which contain of 15 vol.% coconut fibre gave the lowest value of energy and resilience, which are 0.828 J and 5.21 KJ/m², following by another sample that gave an increasing trend. Sample 4 gave the highest value of energy and resilience which are 1.044 J and 6.57 KJ/m. The details comparison for each sample are given by Figure 2.

Table 2 Data obtained from the impact test.

Sample	Coconut fibre, Vol.%	Energy (Joule)	Resilience (KJ/m²)
1	15%	0.828	5.21
2	30%	0.899	5.39
3	45%	0.907	5.71
4	60%	1.044	6.57
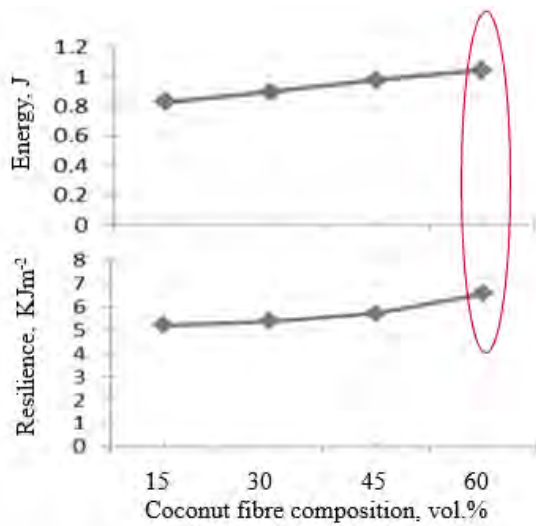
Figure 2 Graph energy and resilience versus coconut fibre composition.

According to some researcher, by adding some of coconut fibre content in sampling, the value of energy and resilience should be increase [5]. The scientific explaination to the increment of the energy and resilience was due to the properties of the coconut fibre where it able to allocate more toughness properties as it dispersed phase in the composites.

Coconut fibre also provided a good and proper adhesion between matrix within the composites. This method is able to stablize the strength distributions and absorption which proportionaly increased the impact energy [6].

Figure 3 shows the image for each sample in term of their cross-sectional area after the impact test was conducted. Refer to the image the more coconut fiber composition the darker the sample which reflected to the color or the coconut fiber itself. The higher content of the coconut fiber able to give better bonding property between resin and the fiber in term of the fiber adhesive support which illustrated by Figure 4.
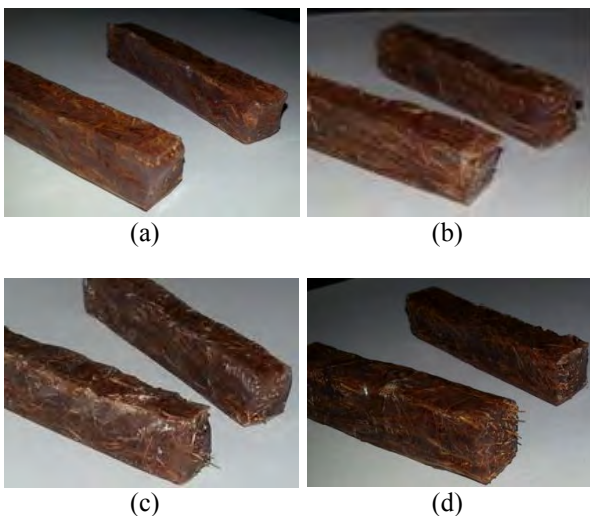
Figure 3 Cross sectional area of each sample with coconut fiber (a) 15 vol.%, (b) 30 vol.%, (c) 45 vol.% and (d) 60 vol.%.
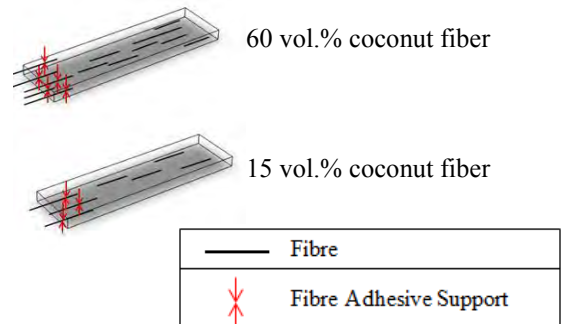
Figure 4 Fiber orientation and fibre adhesive support for sample with 15 and 60 vol.%.

4. CONCLUSION

As conclusion, the higher coconut fiber content the higher result obtained for the resilience and energy absorb which believed due to the physical properties of the coconut fiber itself. Coconut fiber able to provided good adhesion and bonding between the coconut fiber and polyester resin which lead to good strength distributions with balanced absorption of energy.

ACKNOWLEDGMENT

REFERENCES

[1] A.R. Bunsell, and J. Renard, *Fundamental of Fibre Reinforced Composite Material,* UK: Institude of Physics Publishing Bristol and Philadelphia; 2005.

[2] T. Lin, D. Jia, M. Wang, and P.H.D. Liang, "Effects of fiber content on mechanical properties and fracture behavior of short carbon fiber reinforced geopolymer matrix composites," *Bulletin of Materials Science,* vol. 32, no.1, pp. 77-81.

[3] H. N. T. Sen, and J. Reddy, "Application of Sisal, bamboo, Coir and Jute Natural Composites in Structural Upgradation," *International Journal of Innovation, Management and Technology,* pp. 1-6, 2011.

[4] ASTM D6110-10, Standard Test Method for Determining the Charpy Impact Resistance of Notched Specimens of Plastics[1]. April 1, 2010.

[5] S.A. Hussain, D.V. Pandurangadu and D.K. Palanikuamr, "Mechanical Properties of green Coconut Fiber Reinforced HDPE Polymer Composite," *International Journal of Engineering Science and Technology,* vol. 3 no 11, pp. 7942-7952, 2011.

[6] M. Brahmakumar, C. Pavithran and R.M. Pillai, "Coconut fibre reinforced polyethylene composites: effect of natural waxy surface layer of the fibre on fibre/matrix interfacial bonding and strength of composites," *Composites Science and Technology*, vol. 65, issue 3-4, pp. 563-569.

Effect of sintering on the physical properties of porous β-TCP scaffolds

N.F. Ishak[1,2], Z. Mustafa[1,2,*], R. Othman[1, 2], S.H. Sheikh Md. Fadzullah[3], A.R. Mahamad Sahab[4]

[1] Faculty of Manufacturing Engineering, Universiti Teknikal Malaysia Melaka,
Hang Tuah Jaya, 76100 Durian Tunggal, Melaka, Malaysia
[2] Advanced Manufacturing Centre, Universiti Teknikal Malaysia Melaka,
Hang Tuah Jaya, 76100 Durian Tunggal, Melaka, Malaysia
[3] Faculty of Mechanical Engineering, Universiti Teknikal Malaysia Melaka,
Hang Tuah Jaya, 76100 Durian Tunggal, Melaka, Malaysia
[4] Advanced Material Research Centre, SIRIM Berhad, Shah Alam, 40450, Selangor, Malaysia

*Corresponding e-mail: zaleha@utem.edu.my

Keywords: Tricalcium phosphate; scaffold; bioactive

ABSTRACT – This research work investigates the effect of sintering temperatures on the physical properties of porous beta-tricalcium phosphate (β-TCP) scaffolds produced via a template method. A polyurethane (PU) foam was immersed in β-TCP slurry by using a roller infiltration method. The impregnated foam was subsequently sintered to 1400°C, 1450°C and 1500°C. The sintered scaffolds were then characterized by X-ray diffraction (XRD) and scanning electron microscopy (SEM) for evaluation of crystalline phases as well as pore and surface morphology. An increase in sintering temperature reveal an increase in crystallinity as well as the lessening of pores and voids in the struts of the scaffold as a result of progressive sintering.

1. INTRODUCTION

Recent advances in tissue engineering aim to regenerate damaged tissues. It can be accomplished by combining cells from the body with highly porous scaffold biomaterials, which act as templates to guide new tissue regeneration [1]. Hence, the scaffold should mimic the biological bone in order to optimize integration into surrounding tissues. Due to the simplicity of processing technique and inexpensive technology used, the production of scaffolds are favourable. The drawback of this process is the difficulty in specimen handling after sintering due to their brittle and porous structure [2]. Principally, tricalcium phosphate (TCP) exists in many polymorphs but only two phases (α and β) that are commonly used in biomedical materials [3]. β-TCP is greatly biocompatible due to their bioactive nature and ability to set up a resorbable interlocking network within the injury site to encourage healing. One of the most important aspect for successful scaffold application is its porosity, in order to allow nutrient transportation during cell growth. The aim of this work is to investigate the effect of sintering temperature on the phase and microstructure characteristics of β-TCP scaffolds.

2. METHODOLOGY

Tricalcium phosphate (Rekagraph USM, Malaysia) with a Ca:P ratio (1.5) has a mean particle size of $d_{0.5} = 6.03$ μm and a specific surface are of 2.30 m^2g^{-1} .

Polyvinyl alcohol (PVA) (Sigma Aldrich, UK) is used as the binder and polyurethane (PU) foam as the template. The β-TCP powder was mixed in 2% polyvinyl alcohol aqueous solution at a powder to liquid ratio of 40:60. The mixture was then stirred using a magnetic stirrer plate for approximately 2 hours at room temperature to ensure homogenous mixing. PU foam was immersed in the solution and rolled out to ensure full infiltration of the slurry. The foam was then dried in an oven at 60 °C overnight. The samples were subsequently subjected to three different firing protocols with maximum sintering temperatures of 1400 °C, 1450 °C and 1500 °C. The compositional analysis of sintered β-TCP scaffolds were characterized using PANalytical X-ray diffraction unit (model X'Pert Pro MPD PW3060/60) operating at room temperature using Cu Kα radiation (α =1.54178 Å).. For morphological analysis, scanning electron microscopy SEM EVO 50 (Carl Zeiss SMT, UK)) was used at an accelerating voltage of 5 kV.

3. RESULTS AND DISCUSSION

The XRD patterns of sintered TCP scaffolds subjected to three different sintering regimens: 1400 ℃, 1450 ℃ and 1500 ℃ are shown in Figure 1. These XRD patterns match that of pure β-TCP pattern with JCPDS number 55-0898 without any secondary phase formation. It can be seen that all samples sintered at different temperatures show prominent peaks with a preferred orientation at (0 2 10). However, the peak becomes more intense at higher temperatures owing to an increase in the crystallinity of the calcium phosphate. This is consistent with other previous study [4] which reported that the composition of β-TCP was not changed during the sintering process regardless of β-TCP content. Figure 2 shows the microstructures of porous β-TCP at different sintering temperatures in comparison to the microstructure of the PU template (Figure 3). These results reveal that a good pore interconnectivity characteristic. At the two lower sintering temperatures, the scaffolds contain more voids and cracks suggestive of their brittle nature. As the temperature is increased to 1500°C, the surface appears to be smoother and denser suggesting that progressive sintering through diffusion

had taken place.
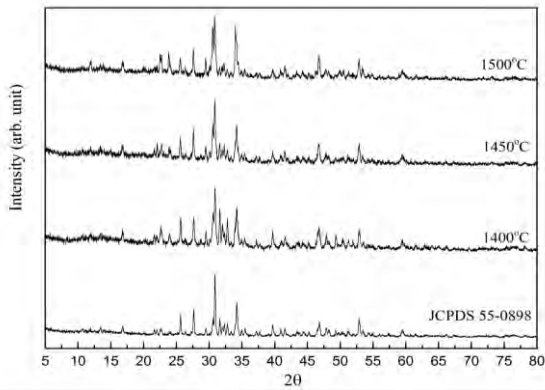
Figure 1 XRD patterns of β-TCP sintered at different temperatures of 1400°C, 1450°C and 1500°C.

Figure 3 SEM image of PU foam.

4. CONCLUSION

In conclusion, the preliminary results showed an increase in the crystallinity of the β-TCP phase as the temperature was increased and no additional phase was identified. Morphological analyses revealed that an interconnected pore structure was successfully produced at all sintering temperatures. The scaffold struts surface appeared to be more dense with less cracks and voids with an increase of sintering temperature suggesting that better diffusion was achieved between the β-TCP particles at 1500°C.

ACKNOWLEDGEMENT

REFERENCES

[1] F.J. O'brien, "Biomaterials & scaffolds for tissue engineering," *Materials Today*, vol. *14*, no.3, pp.88-95, 2011.

[2] T.Y. Yang, W.Y. Kim, S.Y. Yoon, and H.C. Park, "Macroporous silicate ceramics prepared by freeze casting combined with polymer sponge method," *Journal of Physics and Chemistry of Solids*, vol. *71*, no. 4, pp.436-439, 2010.

[3] S.B. Sulaiman, T.K. Keong, C.H. Cheng, A.B. Saim and R.B.H. Idrus, "Tricalcium phosphate/hydroxyapatite (TCP-HA) bone scaffold as potential candidate for the formation of tissue engineered bone," *The Indian Journal of Medical Research*, vol. *137*, no. 6, pp.1093, 2013.

[4] Z.K. Kim, J.J. Oak, H. Kimura, T. Goto, A. Inoue and S.Y. Yoon, "Architecture of porous hydroxyapatite scaffolds using polymer foam process," *Journal of Biomechanical Science and Engineering*, vol. 4, no.3, pp.377-383, 2009.

Figure 2 SEM images of porous scaffolds at different sintering temperatures (A) 1400°C; (B) 1450°C; (C) 1500°C.

Optimization of compression moulding parameters for multi filler polymer composite using Taguchi method

N.A. Jamil[1,2], M.Z. Selamat[1,2,*], R. Hasan[1,2], J. Sahari[1,2], M.A.M. Daud[1,2], M.M. Tahir[1,2]

[1] Faculty of Mechanical Engineering, Universiti Teknikal Malaysia Melaka,
Hang Tuah Jaya, 76100 Durian Tunggal, Melaka, Malaysia
[2] Centre for Advanced Research on Energy, Universiti Teknikal Malaysia Melaka,
Hang Tuah Jaya, 76100 Durian Tunggal, Melaka, Malaysia

*Corresponding e-mail: zulkeflis@utem.edu.my

ABSTRACT – The purpose of this study is to determine the compression moulding parameters on Graphite (G) / Carbon Black (CB) / Carbon Fiber (CF) / Polypropylene (PP) composites through Taguchi method. L_9 Orthogonal Array with four factors and three levels has been choose as a DOE for composition of G/CB/CF/PP with weight percentage of 50/25/5/20. The electrical conductivity value was analysed through Taguchi Method using signal to noise (S/N) ratio to determine the optimum parameters. This result is important to fabricate the potential G/CB/CF/PP composites as conductive polymer composite (CPC), and also very useful for further application as bipolar plate (BP) for PEMFC.

1. INTRODUCTION

Nowadays CPC becomes one of the most attractive options to researchers. CPC can be used in various application such as sensors, batteries, bipolar plates in fuel cell systems, electromagnetic interference (EMI) and radio frequency interference (RFI) [1-2]. CPC with carbon based is the ideal material to be used to produce BP and it is promising a good mechanical properties and low cost. Therefore, in this study G, CB and CF were used as fillers in order to improve the electrical conductivity and mechanical properties of the composites. Meanwhile, PP was selected as the binder.

In this paper the Taguchi Method with L_9 Orthogonal Array was used to optimize the compression moulding parameters and the experimental results are then transformed into S/N ratio. With S/N ratio, the optimum hot compression moulding parameters can be predicted. Then, the confirmation experiment was conducted to determine the optimum parameters obtain from the parameter design. Taguchi Method using S/N ratio proposed a design of experiment (DOE) which minimize the number of experiment to a practical level for optimization process and it is proven to be an effective way in order to produce high quality of composite with low cost and short time [2].

2. METHODOLOGY

A series of nine samples were prepared by using G, CB and CF as fillers and PP as a binder. Nine samples of composites based on the composition of G/CB/CF/PP with a weight percentage of 50/25/5/20 were selected.

The composition of G/CB/CF/PP was mixed by using a ball mill machine for 3 hours and high speed mixer for 10 minutes. The mixture was poured into mould with dimension of 50 mm x 50 mm in square size then being pressed in the hot compression moulding machine. The mould was cooled by air until it reaches room temperature before the sample being released from the mould. The L_9 Orthogonal Arrays which consist of four factors which are temperatures (A), loads (B), preheating times (C) and compressing times (D) with three levels were followed as shown in Table 1. Electrical conductivity test for G/CB/CF/PP composites were measured by Jandel Multi Height Four Point Probe combined with RM3 Test Unit.

Table 1 The compression moulding factors for three levels Taguchi design.

Factors	Variables	Level		
		1	2	3
A	Temperature (°C)	175	180	185
B	Loads (ton)	5	10	15
C	Preheating time (min)	5	7	10
D	Compression times (min)	5	10	15

3. RESULTS AND DISCUSSION

The electrical conductivity of all samples was measured and the results shown in Table 2. Based on requirement from US Department of Energy (DOE) for BP, the electrical conductivity value must be greater than 100 S/cm [3-4]. The result shown in Table 2 shows that the electrical conductivity of this composite was larger than 100 S/cm and it achieved the required value. CB with complex morphology that being used as filler helps to fill the holes and gap in the composite [5]. The electrical conductivity value was analyzed by Taguchi Method using S/N ratio to determine the optimized factor. According to the optimum condition of larger is better for response graph, the levels of the factors that contributed to the highest values are determined as shown in Figure 1. From the response graph as presented in the Figure 1, it shows that the highest electrical conductivity obtained from the combination of optimum condition which are A1 (temperature), B1

(load), C3 (pressing time) and D3 (compressing time). The optimized level of the factors that contributed to the highest value for G/CB/CF/PP composites is shown in Table 3.

Table 2 Results of electrical conductivity for G/CB/CF/PP composite.

No. of Experiment	Electrical Conductivity (S/cm)			
	E1	E2	E3	Average
1	309.99	312.82	334.92	319.24
2	374.79	379.44	357.84	370.69
3	316.62	324.29	338.58	326.50
4	285.20	289.58	289.36	288.05
5	256.49	277.72	241.29	258.50
6	204.04	180.08	195.69	193.27
7	273.11	263.45	256.82	264.46
8	263.13	229.74	236.71	243.19
9	194.15	159.30	199.39	184.28
			Average	272.02
			Maximum	370.69
			Minimum	184.28
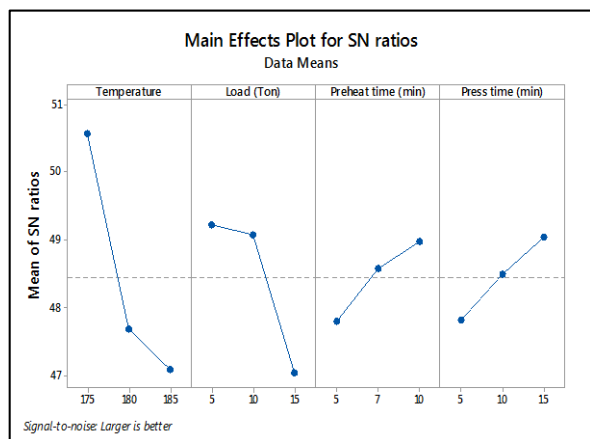
Figure 1 Response graph for S/N ratios.

Table 3 Optimized factors for G/CB/CF/PP composite.

Temperature (°C)	Load (Ton)	Preheating time (min)	Compressing time (min)
175	5	10	15

From the Taguchi Method analysis using S/N ratio, the predicted value for electrical conductivity with optimum condition was 382.40 S/cm and it is higher than any other value from the experimental results. Finally, to confirm the optimum parameters obtain from the Taguchi method analysis, the confirmation experiment has been done based on the optimum parameters and the result shown in Table 4. Based on the result shown in Table 4, it shows that the new electrical conductivity value with optimum parameters had increased which is 393.49 S/cm and 3 % higher than the predicted value from the Taguchi Method analysis. From the results, it is proven that the optimum parameters obtained from the Taguchi Method improved the electrical conductivity of the composite. The process or procedures in order to fabricate the sample is also important to improve the result and it is proven by the result from the confirmation experiment was higher than the predicted value from Taguchi Method analysis.

Table 4 Confirmation experiment of electrical conductivity with optimum condition.

No. of Exp.	Electrical Conductivity (S/cm)			
	E1	E2	E3	Average
1	393.78	397.45	389.23	393.49

4. CONCLUSION

The compression moulding parameters for G/CB/CF/PP composite with 25% of CB and 5% of CF have been studied and determined through Taguchi method using S/N ratio. Based on the result, it can be concluded that the optimum parameters obtained through Taguchi Method improved the electrical conductivity of this composite. The results of this study are important to fabricate the potential G/CB/CF/PP composites as conductive polymer composite, and can very useful for further application as bipolar plate (BP) for PEMFC.

ACKNOWLEDGEMENT

REFERENCES

[1] A. Kasgoz, D. Akın, and A. Durmus, "Rheological and electrical properties of carbon black and carbon fiber filled cyclic olefin copolymer composites," *Compos. Part B Eng.*, vol. 62, pp. 113–120, Jun. 2014.

[2] M.Z. Selamat, J. Sahari, and N. Muhamad, "Simultaneous Optimization for multiple responses on the compression moulding parameters of composite graphite – polypropylene using Taguchi method," vol. 472, *Key Engineering Materials*, pp. 361–366, 2011.

[3] Y. Sadelil, J. W. Soedarsono, B. Prihandoko, and S. Harjanto, "The effects of gompression pressure applied on the manufacture of carbon composite bipolar plate for PEMFC by Utilizing Graphite Waste Products," *Adv. Mater. Res.*, vol. 42, pp. 6–66, 2012.

[4] H. Suherman, J. Sahari, and A.B. Sulong, "Effect of small-sized conductive filler on the properties of an epoxy composite for a bipolar plate in a PEMFC," *Ceram. Int.*, vol. 39, no. 6, pp. 7159–7166, Aug. 2013.

[5] E. Planes, L. Flandin, and N. Alberola, "Polymer composites bipolar plates for PEMFCs," *Energy Procedia*, vol. 20, pp. 311–323, 2012.

Experimental investigation on empty aluminium honeycomb under quasi-static lateral compression

A.J. Chuli[1,2], M.R. Said[1,2,*]

[1] Faculty of Mechanical Engineering, Universiti Teknikal Malaysia Melaka,
Hang Tuah Jaya, 76100 Durian Tunggal, Melaka, Malaysia
[2] Centre for Advanced Research on Energy, Universiti Teknikal Malaysia Melaka,
Hang Tuah Jaya, 76100 Durian Tunggal, Melaka, Malaysia

[*]Corresponding e-mail: radzai@utem.edu.my

ABSTRACT – In the span of last decades, honeycomb structures gained more attention in the field of energy absorption. The honeycomb structures especially made of aluminium has been investigated experimentally, analytically and through simulation in order to study their behavior. In this paper, the honeycomb had undergone a lateral compression. It is found that the honeycomb compressed in x_1 direction produced higher collapse load value, mean crushing value and energy absorption value compared to the honeycomb compressed in x_2 direction.

1. INTRODUCTION

Over the years, extensive research has been conducted on honeycomb structures. In the energy absorption structures, honeycomb cores are very popular as it offers good energy absorbing capability as well as lightweight yet high stiffness properties. Researchers [1-6] had investigated the behaviour of the honeycomb that undergone quasi-static loading. [5] found that during the compression, collapse mode of the honeycomb will be initiated at "top" and lastly forming a "V-shaped" type of deformation.

There are some differences in term of resulting graph of honeycomb compression. In axial loading, the energy absorption value is usually high. In addition, the existence of peak load can be observed. This peak load is one of the important characteristic of energy absorption. It is preferable if the peak load value is reduce the damage to the structure/device. Meanwhile, in the lateral loading, the energy absorption value produced is usually lower compared to the axial loading. However, the peak load does not exist in this situation.

2. METHODOLOGY

The presented result used aluminium honeycomb Al3003-H18 which is also known as Aluminium Commercial Grade (ACG) core with the size of 42 (6x7) cells. The other properties of the honeycomb core are tabulated in Table 1. The specimens were compressed in quasi-static condition with a speed of 5mm/min in two directions of "x_1" and "x_2" as illustrated in Figure 1.

Table 1 Properties of Al3003-H18 honeycomb.

Properties	Data
Young Modulus	69 GPa
Yield stress	115.8 MPa
Poisson's ratio	0.33
Ultimate stress	154.5 MPa
Cell size	12.7 mm
Cell thickness	0.007 mm
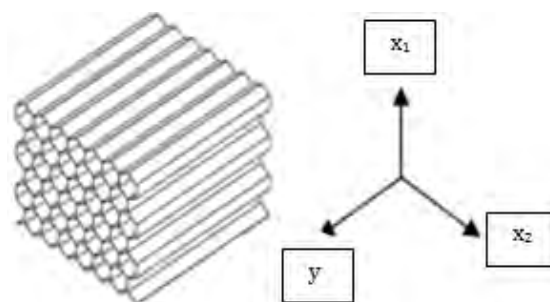
Figure 1 Direction of compression, x_1 and x_2.

3. RESULTS AND DISCUSSION

Based on the present result and previous research, it is found that the specimens undergone three important stages during the compression process. The first stage is known as linear elastic in which the specimen deformed until the critical stress is reached. Next, a plateau stage started in which the load is relatively constant up to certain value of displacement. Densification is the last stage of the compression where the load elevated steeply.

3.1 Lateral compression (x_1-directions)

According to Figure 2, it is observed that the collapse load of the specimen is 73.4 N at the displacement of 16.7 mm. The plateau stage follows afterwards and ended at the displacement of 69.3 mm in which the densification point is achieved. From the observation made, the deforming mode of the specimen started at the middle part (left side) of the specimen. The band then propagated to the opposite side. After the cells in the middle part were completely deformed, the band continued to propagate into the nearby cells.
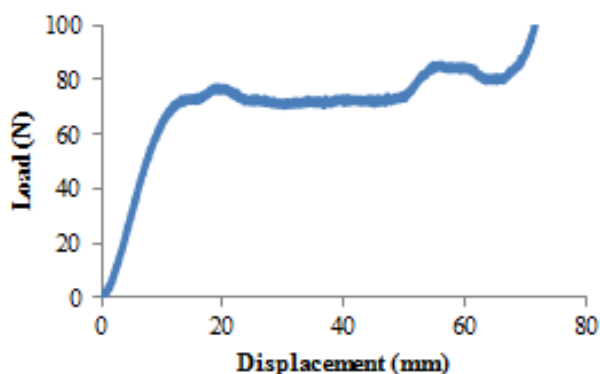
Figure 2 Load-displacement curve for x_1 direction.

3.2 Lateral compression (x_2-direction)

By referring to Figure 3, it is shown that the collapse load for the specimen compressed in this direction is 36.2 N at the displacement of 18.2 mm. The load then becomes steady until the densification stage started at 85.5 mm. The deforming mode of this specimen was started at the top-left side and the band propagated diagonally to the bottom-right side. Next, the band collapse spreads to the nearby cells in progressive way.
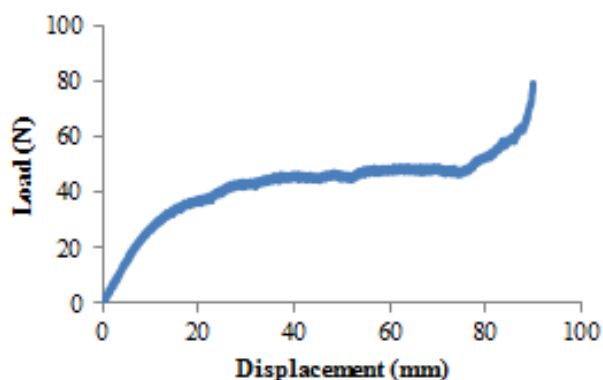
Figure 3 Load-displacement curve for x_2 direction.

Based on the attained result, the energy absorption value for all specimen were found by calculating the area under the graph. Other than that, the value of collapse load and mean crushing load were also calculated as shown in Table 2. Since the honeycomb compressed in x_1 direction has higher collapse load compared to the x_2 direction by a factor of 1.36, it contribute greatly for both mean crushing and energy absorption values. The factor that can contribute to this value is that the specimen in x_1 direction is stiffer than that in x_2 direction. Besides, the cell arrangement of honeycomb in x_2 direction make the cell to collapse easier compared to the cell arrangement in x_1 direction.

Table 2 Collapse load, energy absorption value and mean crushing load for both specimens.

Specimen	X_1 direction	X_2 direction
Collapse load (N)	72.4	42.2
Energy Absorption value (J)	5.2708	3.8815
Mean crushing load (N)	71.28	43.12

4. CONCLUSION

From the experiment, it is found that the cell of honeycomb compressed in x1 direction started to collapse from the left-middle part and propagate to the opposite side of the part (right-middle). Meanwhile, for the honeycomb compressed in x_2 direction, the collapse bands started at the top-left part and propagate diagonally to bottom-right part. In term of collapse load, energy absorption value and mean crushing load, honeycomb compressed in x_1 direction was superior to the honeycomb compressed in x_2 direction. This is largely due to the higher stiffness value and better cell arrangement of the honeycomb in x_1 direction.

ACKNOWLEDGEMENT

REFERENCES

[1] L.J. Gibson and M.F. Ashby. *Cellular solid: Structure and properties*, 2nd Edition. Cambridge University Press, England. 1997.

[2] S.D. Papka and S. Kyriakides, "In-plane compressive response and crushing of honeycomb," *J. Mech. Phy. Solids*, vol. 42, no. 10, pp. 1499-1592, 1994.

[3] S.D. Papka and S. Kyriakides, "Experiments and full-scale simulations of in-plane crushing of a honeycomb," *Acta Mater.*. vol. 46, no. 8, pp. 2765-2776, 1997

[4] L.L. Hu, F.F. You and T.X. Yu, "Effect of cell-wall angle on the in-plane crushing behavior of hexagonal honeycomb," *Mater. Des*. vol. 46, pp. 511-523, 2013.

[5] L.L. Hu and T.X. Yu, " Mechanical behaviour of hexagonal honeycombs under low-velocity impact- theory and simulations," *Int. J. Solids Struct*. vol. 50, pp. 3152-3165, 2013

[6] L.L. Hu, F.F. You and T.X. Yu, "Analyses on the dynamic strength of honeycombs under the y-directional crushing," *Mater. Des*. vol 54, pp. 293-301.

Study of wheel rim impact test using finite element analysis

H.B. Zainuddin[1], M.B. Ali[1,2,*]

[1] Faculty of Mechanical Engineering, Universiti Teknikal Malaysia Melaka,
Hang Tuah Jaya, 76100 Durian Tunggal, Melaka, Malaysia
[2] Centre for Advanced Research on Energy, Universiti Teknikal Malaysia Melaka,
Hang Tuah Jaya, 76100 Durian Tunggal, Melaka, Malaysia

*Corresponding e-mail: basri@utem.edu.my

ABSTRACT – This study measures the impact energy absorbed experienced by the wheel rim under dynamic loading. Computational simulation is time saving, and in contrast the wheel impact experiments involve high cost including the manpower. Alloy wheel is widely used due to its excellent performance and appearance. Wheel rim is modelled using CATIA and imported to ABAQUS for further finite element analysis. Yield strength affects the energy absorbing capacity of a material. Aluminium 6061-T1 is found to have the greatest energy absorption value compared to the other materials.

1. INTRODUCTION

Since the last two decades, vehicle weight has increase about 20%, constituently due to the engine size and safety additional feature [1]. Generally, every 10% of weight reduction allows the reduction of fuel consumption by 5%-7%. One of vital component in a vehicle is wheel. Traditional stone and wood wheel were inefficient with poor traction, low friction, harsh ride and poor load capacity [2]. The wheel nowadays concerns on the durability to endure harsh working condition, fabricated from lightweight material with low manufacturing cost, taking into account the safety requirement as well [3]. Sabri et al. [4] found that alloy wheel allows better performance compared to steel wheel. There are few suitable candidates material in wheel rim manufacturing, which are aluminium alloy [1,4], magnesium alloy [1,5] and steel alloy [5]. Economically, finite element analysis helps to minimize cost and time of experimentation.

Previous study [1,3] has investigated on the 13 degree lateral wheel impact test. However, there are quite few studies on the 90 degree vertical wheel impact. For that reason, this work focuses on the 90 degree vertical impact test using finite element analysis. Impact test is carried out under dynamic loading. Focusing on alloy metallic rim, the objective is to study the energy absorbed by wheel rim with different materials. Different material is expected to give different energy absorbing ability.

2. METHODOLOGY

Reverse engineering has been implemented to get the wheel rim dimension. The wheel 3-dimensional model is done by using CATIA. Modelling of striker and the finite element analysis is executed in the ABAQUS software. The diameter of the wheel rim is 416 mm with 180 mm width. The striker is in rectangular shapes as in the model assembly in Figure 1. The material assigned in the analysis model is isotropic and homogenous. The material used in this analysis is Aluminium (Al) 6061-T1, Magnesium (Mg) AM60 and Stainless Steel (SS) 304L. The properties for the materials are tabulated in Table 1.

Figure 1 Model assembly; undeformed and deformed.

Table 1 Material properties**.**

Component	Material	Young Modulus, E (GPa)	Poisson Ratio, v	Density (kg/m^3)	Yield Strength (MPa)
Striker	Steel	206.9	0.30	8000	-
Rim 1	Aluminium 6061-T1	70	0.33	2700	270
Rim 2	Magnesium AM60	45	0.35	1790	130
Rim 3	Stainless Steel 304L	193	0.25	8000	172

The striker has a simple shaped, but the wheel rim has irregular geometry. Therefore suitable mesh for the striker is hexahedral element and the rim is tetrahedral element [3]. The mesh size used for the wheel rim is varies; 20 mm, 15 mm and 10 mm. Wheel rim is fixed at the four holes, similar to the operating conditions on a vehicle. The striker is set to be displaced in vertical direction with velocity of 22222.2 mm/s, related to the velocity during collision [6].

3.   RESULTS AND DISCUSSION

The measurements were taken at the location where the striker experienced the highest reaction force. Figure 2, Figure 3 and Figure 4 shows the load-displacement curve for all the computational analysis. The mesh size does not affect the results of the analysis. Same pattern is obtained even though different mesh size is assigned. Particularly, if the mesh size is smaller, a more detail analysis is performed by the finite element software and it will increase the number of nodes used.
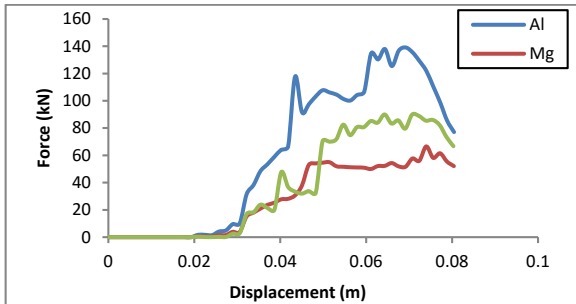
Figure 2 Load-displacement curves for 20mm mesh size**.**
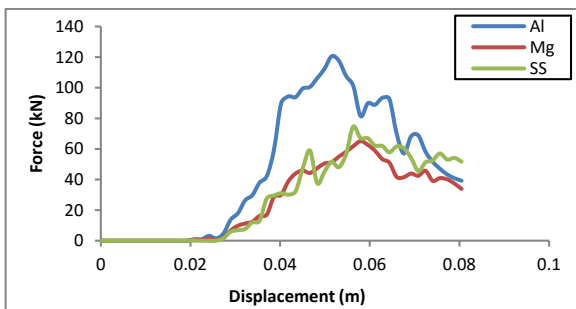
Figure 3 Load-displacement curves for 15mm mesh size**.**
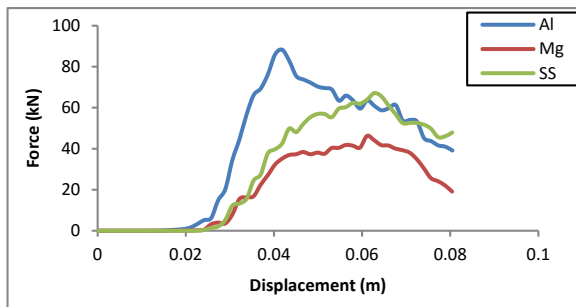
Figure 4 Load-displacement curves for 10mm mesh size**.**

Based on the results, it is observed that if the size of the mesh increased, the peak load of the model increased. The materials behave in similar pattern although different mesh size is assigned. It is observed that the aluminium is having the highest peak load in every case. The energy absorbed for the materials are calculated from the area under the load-displacement curve as shown in Figure 5. Comparing these three materials, Aluminium 6061-T1 absorbed greater impact energy compared to the other two materials, while Magnesium AM60 is found to absorb the least impact energy.
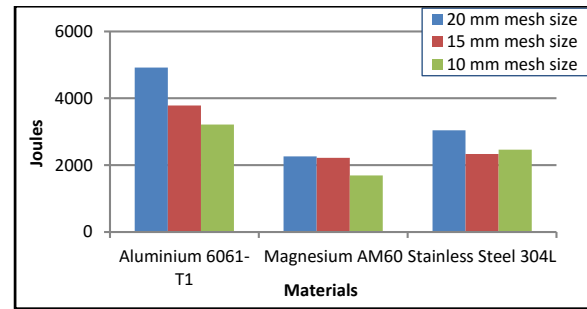
Figure 5 Energy absorbed for different materials**.**

Referring to the material properties in Table 1, Aluminium 6061-T1 has higher yield strength than the Magnesium AM60 and Stainless Steel 304L, with a percentage different of 51.85% and 36.30% respectively. Due to this property, the aluminium possessed greater strength to collapse and thus greater force is produced for the aluminium wheel rim to deform. This explains the high peak load as well as the high energy absorption [7]. High energy absorption capacity represents good structure reliability as well as having the ability to endure the operating condition during services.

4.   CONCLUSIONS

It is found that smaller mesh size produced lower reaction force and lower energy absorbed. In general, the result in a finite element analysis is influenced by the size of mesh applied to the model. Different material shows different energy absorbing capacity. Aluminium 6061-T1 has been found to possess highest energy absorbed. Meanwhile, magnesium AM60 has the least energy absorbed. Hence, it is suggested that the Aluminium 6061-T1 is more reliable and safer to be implemented as wheel rim material.

REFERENCES

[1]   S.K. Bisoyi and M.B. Ashok Kumar, "Analysis and Development Characterisation of Automotive Wheels," *Int. J. Mag. Eng. Technol. Manag. Res.*, vol. 2, pp. 667–671, 2015.

[2]   R.N. Jazar, *Vehicle Dynamics: Theory and Application*. Springer Science & Business Media, 2008.

[3]   C.-L. Chang and S.-H. Yang, "Simulation of wheel impact test using finite element method," *Eng. Fail. Anal.*, vol. 16, no. 5, pp. 1711–1719, 2009.

[4]   M. Sabri, M. Rezal, A. Mu, K. Shahril, and J. Ihsan, "Deformation Behaviour Analysis Of Car Wheel Rim Under Different Loading Using Finite Element Method," *Int. J. Eng. Technol.*, vol. 5, no. 3, pp. 181–184, 2015.

[5]   K.V. Rao and T. Dharmaraju, "Analysis of Wheel Rim Using Finite Element Method," *Int. J. Eng. Res. Technol.*, vol. 3, no. 1, pp. 1259–1263, 2014.

[6]   OUED/ITF, "'Malaysia,'" in *Road Safety Annual Report 2015*, Paris: OECD Publishing, 2015.

[7]   G. Lu and T. Yu, *Energy Absorption of Structures and Materials*. Woodhead Publishing Ltd and CRC Press LLC, 2003.

Characterization of grayscale of the MRI Images for articular cartilage

W.S. Yew[1,*], M.J. Abd. Latif [1,2] , N.H. Mohd.Saad[2,3]

[1] Faculty of Mechanical Engineering, Universiti Teknikal Malaysia Melaka,
Hang Tuah Jaya, 76100 Durian Tunggal, Melaka, Malaysia
[2] Centre of Robotics & Industrial Automation (CERIA) , Universiti Teknikal Malaysia Melaka,
Hang Tuah Jaya, 76100 Durian Tunggal, Melaka, Malaysia
[3] Faculty of Electronics and Computer Engineering, Universiti Teknikal Malaysia Melaka,
Hang Tuah Jaya, 76100 Durian Tunggal, Melaka, Malaysia

[*]Corresponding e-mail: wannnsin721@hotmail.com

Keywords: Articular cartilage; magnetic resonance imaging; grayscale intensity

ABSTRACT – Magnetic resonance imaging (MRI) is a non-invasive potential imaging method to diagnose the cartilage disorder. Degeneration of the articular cartilage has been recognized as the main cause of osteoarthritis (OA). Normally OA refers to the end-stage which is already incurable. Therefore, in this study, a non-invasive method is develop to characterize the grayscale of the MRI images for articular cartilage. To test this, bovine's humeral head cartilage samples (n=7) were selected as models. The primary findings from the results indicated that there was a significant difference in grayscale intensity of the MRI images on the articular cartilage. This could indicate that the composition in the articular cartilage could affect the grayscale of the articular cartilage. This results give a new perspective into the properties of the tissue.

1. INTRODUCTION

Magnetic resonance imaging (MRI) is a non-invasive technique that provides precise imaging visualization on cartilage tissues, bone, synovium and ligaments [1]. Recently, MRI has been known as a tool to characterize the articular cartilage morphology and function [2].

Articular cartilage is a tissue mainly consists of the interstitial water content, collagen and proteoglycan [3]. It comprised of four different layers which can be divided into the superficial zone, middle zone, deep zone and calcified zone. All components in articular cartilage such as proteoglycan, and collagen help in restraining the water content which is very important to remain the unique properties of the articular cartilage [3-4]. Degeneration of the macromolecular constituents in articular cartilage influence the mechanical principle of the tissue [3].

In the present study, a non-invasive method is developed to characterize the grayscale of MRI images on articular cartilage as a potential probe to assess the properties of articular cartilage.

2. METHODOLOGY

2.1 Sample preparation

Articular cartilage from bovine was used in the study as shown in the Figure 1 (a). Humeral head cartilage samples (n=7) were dissected from the 3-4 years old bovine hip joint. All humeral heads were sectioned using electric hand saw to yield samples with four quadrants cross-sectional areas of the articular layer and underlying bone as shown in Figure 1 (b). All samples were kept moist in the phosphate buffered saline (PBS) washes and were observed by visual imaging inspection using MRI.

(a)   (b)
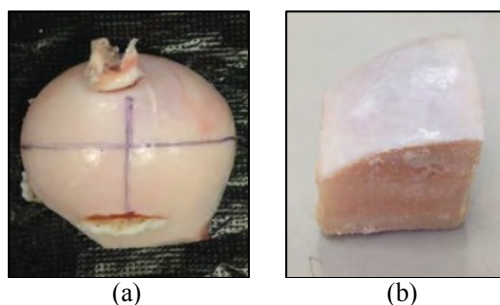
Figure 1 (a) Cartilage specimen of humeral head, (b) One quadrant of the sample was segmented from the humeral head.

2.2 Magnetic resonance imaging (MRI)

Samples were imaged using a low-field magnetic resonance imaging (MRI) with a magnetic field strength of 0.18 Tesla (Genova, Italy) as shown in Figure 2. Scanning of the MRI images of the cartilage was conducted at room temperature (25o). Gradient echo sequence was selected to scan the cartilage [5- 6]. 2mm axial slices of the cartilage were acquired. Field of view was fixed to 200x200mm and the matrix 256x256.

Figure 2 Samples were scanned using Esaote C-Scan low magnetic field magnetic resonance imaging (MRI) from Genova, Italy.

2.3 Data processing

Analysis of MRI images was performed using image processing software, MATLAB. The analysis was performed in the search size of 7x14 pixels throughout the region of interest of the articular layer.

3. RESULTS AND DISCUSSION

The grayscale values in pixels of the MRI images on articular cartilage was determined to observe the range for different zone of the articular cartilage.
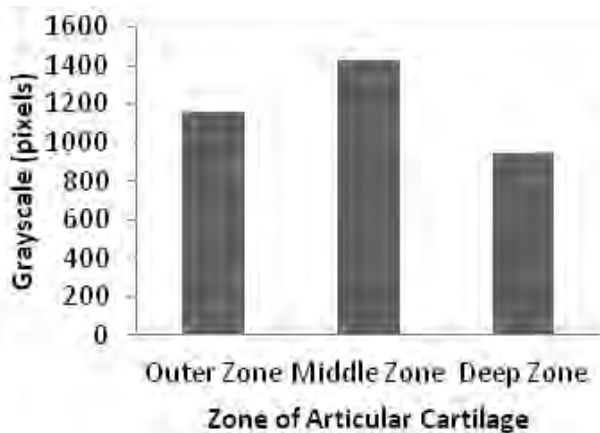
Figure 3 Average grayscale of the MRI images on articular cartilage for different zone.

Figure 3 shows the average grayscale intensity of the MRI images on articular cartilage from one of the samples. Trend for all the samples were the same as it shows a significant difference in grayscale intensity across the different zones of the articular cartilage. Grayscale of the articular cartilage rose gradually from superficial to middle zone until it reach a peak before dropping to the deep zone.

The range of the grayscale intensity for the superficial layer was between 1145.60±10.57 while the middle and the deep zone were between 1411.34±57.50 and 944.48±114.83 respectively. It could be due to the composition in each zone of the articular cartilage that produce a different outcome for the grayscale intensity.

Based on the study, articular cartilage is a complex structure with different composition in each zone that makes the grayscale intensity different across the various zones of the MRI images on articular cartilage [4,6,7]. From superficial to deep subchondral , there is different composition throughout the different layers in regards of the water content, proteoglycan, cellular size and volume and collagen orientation [8].

From the anatomy of the articular cartilage, it shows that water content, proteoglycan and collagen content have an important role in articular cartilage behavior. Deep zone has reduced water content [4, 7]. Subsequently, the grayscale intensity for this zone is the lowest. With this criteria, the water content inherent to the grayscale value among the zones in articular cartilage.

4. CONCLUSION

In this present study, the results of the grayscale intensity of the MRI images on cartilage demonstrated the potential of low-field MRI system to examine the properties of the cartilage. The significant difference in the grayscale intensity across the different zones of the articular cartilage could be reflected mainly based on the composition of the water content, proteoglycan and collagen in different zones. It is also expected that the grayscale intensity could be useful to a new knowledge for further identification of the pre-osteoarthritis and contribute a new insight into the biomechanical environment of the tissues.

REFERENCES

[1] J.P. Raynauld, J. Martel-Pelletier, M.J. Berthiaume, F. Labonté, G. Beaudoin, J.a. De Guise, D.a. Bloch, D. Choquette, B. Haraoui, R.D. Altman, M.C. Hochberg, J.M. Meyer, G.a. Cline, and J.P. Pelletier, "Quantitative Magnetic Resonance Imaging Evaluation of Knee Osteoarthritis Progression over Two Years and Correlation with Clinical Symptoms and Radiologic Changes," *Arthritis Rheum.*, vol. 50, no. 2, pp. 476–487, 2004.

[2] G. Blumenkrantz and S. Majumdar, "Quantitative Magnetic Resonance Imaging Of Articular Cartilage In Osteoarthrtitis," *Eur. Cells Mater.*, vol. 13, pp. 75–86, 2007.

[3] M.J. Nissi, J. Rieppo, J. Töyräs, M.S. Laasanen, I. Kiviranta, M. T. Nieminen, and J. S. Jurvelin, "Estimation of mechanical properties of articular cartilage with MRI – dGEMRIC, T2 and T1 imaging in different species with variable stages of maturation," *Osteoarthr. Cartil.*, vol. 15, no. 10, pp. 1141–1148, 2007.

[4] A.J. Sophia Fox, A. Bedi, and S.a. Rodeo, "The basic science of articular cartilage: structure, composition, and function.," *Sports Health*, vol. 1, no. 6, pp. 461–8, Nov. 2009.

[5] J. Qazi, P.C. Folkesson, M.a. Pettersen, M.a. Karsdal, C. Christiansen, and E.B. Dam, "Separation of healthy and early osteoarthritis by automatic quantification of cartilage homogeneity," *Osteoarthr. Cartil.*, vol. 15, pp. 1199–1206, 2007.

[6] B. Paunipagar and D. Rasalkar, "Imaging of articular cartilage," *Indian J. Radiol. Imaging*, vol. 24, no. 3, p. 237, 2014.

[7] A.D. Pearle, R.F. Warren, and S.a Rodeo, "Basic science of articular cartilage and osteoarthritis.," *Clin. Sports Med.*, vol. 24, no. 1, pp. 1–12, Jan. 2005.

[8] D.Deponti, "Articular Cartilage Morphology and Biomechanics," *J. Orthop.*, vol. 6, no. 2, pp. 75–81, 2014.

Determination of dimple distribution for laser texturing process on cast iron surface

N.A.M. Lazim[1,*], R. Hasan[1,2], S.E.M. Kamal[1,2]

[1] Faculty of Mechanical Engineering, Universiti Teknikal Malaysia Melaka,
Hang Tuah Jaya, 76100 Durian Tunggal, Melaka, Malaysia
[2] Centre for Advanced Research on Energy, Universiti Teknikal Malaysia Melaka,
Hang Tuah Jaya, 76100 Durian Tunggal, Melaka, Malaysia

*Corresponding e-mail: nurulatiqahmohdlazim@gmail.com

Keywords: Dimple distribution; laser texturing

ABSTRACT – The aim of this research is to determine the uniformity distribution of the micro dimples to be textured on cast iron surface by using laser surface texturing method. Distribution of dimples on the surface is important in reducing wear debris amount. Imaginary grid of dimple cell was calculated and certain distance between dimples was determined in order to be located on the surface of cast iron. A uniform dimple's distribution was calculated on the sample surfaces before textured by laser treatment method.

1. INTRODUCTION

Friction and wear produced during engine operation could create heat and reduce performance of engine. Therefore, surface modifications on mechanical components had been studied for contact performance enhancement in order to reduce wear and friction. Laser Surface Texturing (LST) method will be used to create micro dimples on the cast iron surface.

Wakuda et al. [1] has found that the tribological characteristics depend highly on the size and density of the micro dimples. However the dimples shape does affect just a little for the friction coefficient either rounded or angular profiles. Other than size of diameter, depth of micro dimples and shape of micro dimples, the amount of micro dimples on the sample surface also play important roles in order to help reducing wear amount. Too less or too much micro dimples might not give any effect in reducing friction and wear. Wei Tang et al. [2] reported that 5% dimple area fraction resulted 72% less than that of non-textured sample or 0% dimple area fraction after 7 hours test of sliding steel under lubricated condition. According to literature [3] the surface area to density ratio (total dimple area/total surface area) is one of the key parameters for surface texturing. The area density ratio is different according to the variety of dimple's diameter, and sample surface.

Several calculations need to be done to determine the amount and position of micro dimples on the sample surface. This paper is focusing on determination of micro dimple distribution on the cast iron sample for laser texturing. Different percentage from total surface area of sample surface was calculated to determine the volume of micro dimples and grid size on imaginary square of sample surface.

2. METHODOLOGY

2.1 Calculation

A pin sample has diameter 10mm and length of 32mm. An imaginary square is used to calculate the position of dimples on the surface of sample.
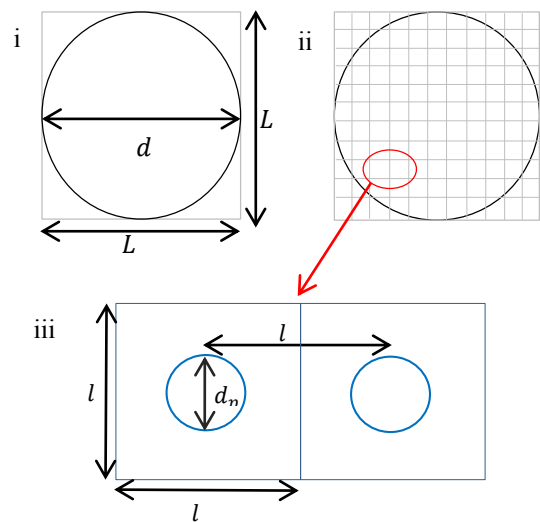
Figure 1 Schematic for (i) pin surface, (ii) imaginary grid and (iii) dimple cell.

Figure 1 (i) show the sample surface with diameter, d 10mm and figure (ii) shows the imaginary grid for $L \times L$. The geometrical model of the dimple is presented in Figure 1 (iii). Each micro dimple is modeled with a diameter, d_p and is located in the center of an imaginary square cell with the length, l which also presented the length between the adjacent cells.

In this study, Equation (1) is used to calculate total surface area of imaginary square of pin sample where L is the length of the square. Equation (2) is used to know the area of how much percentage from the total surface area. The term *value was determined by how many percentage that will be studied in this experiment. Volume of micro dimple can be determined by dividing percentage area with dimple area. Area for micro dimple can be calculated by using Equation (3) where r_p represent the radius of dimple.

$$L \times L = L^2 \tag{1}$$

$$Percentage\ area = \frac{*value}{100} \times L^2 \tag{2}$$

$$Dimple\ area = \pi r_p{}^2 \tag{3}$$

$$Grid\ size = \sqrt{\frac{Percentage\ area}{Dimple\ area}} \tag{4}$$

$$l = \frac{L}{Grid} \tag{5}$$

Equation (4) is used to find the grid size on imaginary square of sample surface by square root the volume of micro dimples. After calculate for the grid size, the distance, l between the micro dimples was determined by using Equation (5) and the size of dimple size can be completed.

3. RESULT AND DISCUSSION

a. Figure of LST of dimples

A real figure of laser surface texturing of dimples by Wakuda et. al [1] and schematic diagram of dimple in this study as in the figure 2 below.
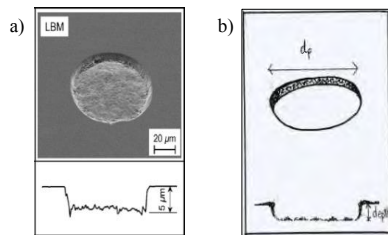
Figure 2 LST of dimple on sample surface from a) previous study [1] and b) schematic diagram.

b. Distribution of dimples

Figure 3 below shows the schematic of micro dimples on cast iron surface following the calculation from Equation (1-5) with diameter 130μm as an example.
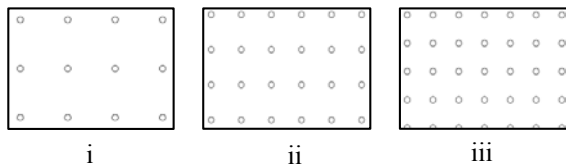
Figure 3 Dimple's distribution for diameter 130um (i) 5%, (ii) 10% and (iii) 15%.

Table 1 shows the diameter of dimples that will be textured on cast iron surface and its surface area. Table 2 shows the total surface area of the sample and area percentage to know how much dimples need to be created on the surface. Table 3 contains a data regarding the size grid on the imaginary square of the sample surface and also the distance between dimples to be located.

The uniformity of the dimple distribution was confirmed with the calculation in this study. However, it does not mean that the method from previous researchers is opposite since each study is conducted with variety

parameters and different values. A suitable amount of dimple's distribution help the existence of micro dimples to act as micro trap of the wear debris effectively during the sliding between two components under lubricated condition.

Table 1 Diameter of dimple and surface area.

Dimple	Diameter (μm)	Surface area (m²)
d_{p1}	70	3.85×10^{-9}
d_{p2}	100	7.85×10^{-9}
d_{p3}	130	1.33×10^{-8}

Table 2 Percentage area of the sample.

Total Surface Area (100%)	$L^2 = 1 \times 10^{-4}$ m²
5%	5×10^{-6} m²
10%	1×10^{-5} m²
15%	1.5×10^{-5} m²

Table 3 Grid and distance for each dimples.

Diameter of dimple, d_p	Percentage area (%)	Grid, $L \times L$	Distance, l (m)
d_{p1}, 70μm	5	36×36	2.78×10^{-4}
	10	51×51	1.97×10^{-4}
	15	62×62	1.61×10^{-4}
d_{p2}, 100μm	5	25×25	4×10^{-4}
	10	36×36	2.78×10^{-4}
	15	44×44	2.27×10^{-4}
d_{p3}, 130μm	5	19×19	5.26×10^{-4}
	10	27×27	3.7×10^{-4}
	15	34×34	2.94×10^{-4}

4. CONCLUSION

From this study, the distribution of dimples on surface has successfully been determined. From the method used, the uniformity of the micro dimples is convincing to be created on the sample surface by laser texturing method. This calculation method is a part from full study on the effect of laser textured piston ring on reducing engine fuel consumption and is important for the next step in this research.

REFERENCES

[1] M. Wakuda, Y. Yamauchi, S. Kanzaki, Y. Yasuda, "Effect of surface texturing on friction reduction between ceramic and steel materials under lubricated sliding contact," *Wear*, vol. 254, pp. 356-363, 2003.

[2] W. Tang, Y. Zhou, H. Zhu, H. Yang, "The effect of surface texturing on reducing the friction and wear of steel under lubricated sliding contact," *Applied Surface Science*, vol. 273, pp. 199-204, 2013.

[3] B. Kim, Y.H. Chae, H.S. Choi, "Effects of surface texturing on the frictional behavior of cast iron surfaces," *Tribology International*, vol. 70, pp. 128-135, 2014.

[4] N.A.M. Lazim, S.E.M. Kamal, R.B. Hasan, "A study on effect of laser textured cast iron surfaces on reducing friction and wear," in *Proceedings of Malaysian International Tribology Conference 2015*, 2015, pp. 273–274.

The effect of PCB surface roughness on the reliability of the SAC405 lead free solder

R.M. Dan[1,2,*], A.H.A. Hamid[1,2], J. Mclaren[1], N.I. Zulkafli[1,2], R.K. Mazlan[1,2]

1) Faculty of Mechanical Engineering, Universiti Teknikal Malaysia Melaka,
Hang Tuah Jaya, 76100 Durian Tunggal, Melaka, Malaysia.
2) Centre for Advanced Research on Energy, Universiti Teknikal Malaysia Melaka,
Hang Tuah Jaya, 76100 Durian Tunggal, Melaka, Malaysia.

*Corresponding e-mail: reduan.dan@utem.edu.my

Keywords: Surface roughness; intermetallic compound; lead free solder

ABSTRACT – The focus of this research is to investigate the surface roughness on the reliability of lead free SAC405 solder material. Surface roughness influences reliability where high reliability improves the bonds of the solder and the substrate. In this study, aluminium and copper substrate is used with 4 different types of surface roughness. Hardness testing is performed using nanoindenter on each of the substrate where the hardness is in increment with the surface roughness. It is discovered that the increase in surface roughness causes increase in wettability and formation of intermetallic compound thus increases the reliability of the solder.

1. INTRODUCTION

Lead (Pb) based solders are the commonly used solders for the electronics industry. Pb based solders poses many negative impact on the machine and consumer [1]. This leads to a safer Tin (Sn) based material that reduces environmental impact as well as satisfies the metallurgy of solder economically [2,3]. Solder alloys subjected to a controlled condition leading to the formation of intermetallic compound (IMC) combined with surface roughness influences the reliability of the solder joints, although IMC is not dependent towards surface roughness. In soldering, surface roughness can affect the quality of wetting and spreading behaviour of filler and reduces the effective contact angle as was discovered in previous research [1, 4].

The objective of this study is to investigate the reliability of the SAC 405 solder joint on different surface roughness of the substrate. The strength of the solder joint is evaluated from its hardness to find the effect of surface roughness using nanoindentation.

2. METHODOLOGY

2.1 Material selection

SAC405 is chosen as the solder material with aluminium and copper plates with dimension of (20 mm × 10 mm) as substrates.

2.2 Sample preparation

The substrates are prepared with 4 different surface roughnesses through 3 different grits of abrasive paper and the substrate initial surface roughness. The surface roughness of the samples is then measured using a calibrated Mitutoyo SJ-301 Portable Surface Roughness Tester.

The SAC405 solder is then formed into balls and attached to the substrate labelled A1, A2, A3, A4, C1, C2, C3 and C4. The samples are then mounted through cold mounting (resin) in which the mounted sample will be grinded and polished for a cross-section cut and analysed through surface profiler.

Hardness of the sample is calculated from the load-displacement measurement of the nanoindentation test through Equation 1:

$$H = \frac{P}{A} \quad (1)$$

where P is the maximum loading and A is the value of h_c from the load-displacement measurement.

3. RESULTS AND DISCUSSION

The surface roughness of the substrate is determined from the value of arithmetic average roughness, Ra shown in Table 1-2.

Table 1 Average value of arithmetic average roughness, R_a for aluminium.

Sample	Type of grits	Average R_a (μm)
A1	-	0.21
A2	240	1.77
A3	800	0.74
A4	1500	0.49

Table 2 Average value of arithmetic average roughness, R_a for copper.

Sample	Type of grits	Average R_a (μm)
C1	-	0.13
C2	240	0.92
C3	800	0.3
C4	1500	0.17

The mechanical properties of copper are far superior than aluminium thus copper is more resilient

towards deformation resulting in a lower surface roughness as compared to aluminium.

3.1 Nanoindentation test

A load-displacement measurement is obtained and for the aluminium samples at maximum loading of 10 mN are 1350.839 nm, 1404.721 nm, 1451.982 nm and 1500.649 nm for sample A2, A3, A4 and A1 respectively. For the copper samples, the displacement values are 1319.417 nm, 1481.304 nm, 1478.730 nm and 1553.384 nm for C2, C3, C4 and C1.

The initial value of displacement shows increments which indicates that the loading applied causes the sample to undergo elastic behaviour until it exceeds the maximum loading of. The unloading process will cause the sample to reach the elastic+plastic behaviour until the sample reaches plastic region where deformation occurs. This behaviour is the result of the formation of IMC between the contact of the attached solder ball and the substrate where at maximum loading the solder behave in the plastic region resulting in no cracking.

The samples shows an increase in hardness as the surface roughness increases with copper slightly superior than aluminium as observed in Figure 1. In previous research, the effect of the material substrate depends on the composition of the solder material and IMC growth condition used and thus varied intermetallic layers formed causing various results of enhancements and also diminishment [5, 6].
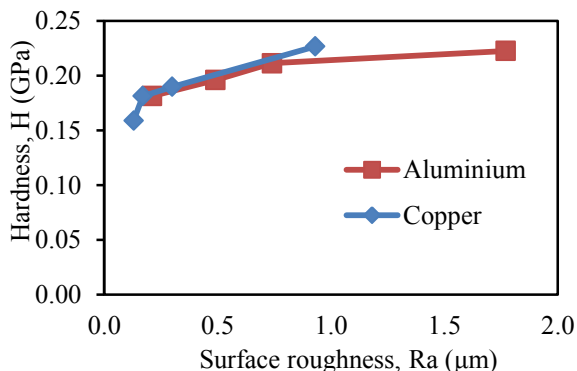
Figure 1 The relationship of surface roughness and hardness value of the sample.

From the results obtained, it is discovered that the value of hardness increases as the value of surface roughness increases. The surface roughness reduces the wettability of the solder causing the increase in the formation of intermetallic compound which in turn affects the hardness value of the attached solder ball. Substrate material is discovered to influence the hardness of the SAC405 by a small margin where copper is superior to aluminium. This is most likely due interaction of SAC405 with the substrate; interlayers of hard intermetallic Ag_3Sn and Cu_6Sn_5 forms for copper while on aluminium substrate the formation of soft particles of AlAg and AlCu were observed resulting in distinguishable hardness strength [7]. The IMC interface is prominently different between the substrate where copper had continuous interlayers while the solder alloy dissolves the substrate along the grain boundaries forming no interlayers for aluminium [8].

4. CONCLUSION

The investigative study leads to various results where it is found that as the surface roughness of the substrate increases, the hardness value of the attached solder ball increases. This suggested that the surface roughness of substrate influence the reliability of lead free SAC 405 solder material. It is also concluded that larger surface roughness of a material specifically aluminium and copper leads a higher reliability for the lead free SAC 405 solder material as well as a slight superiority in for copper substrate as compared to aluminium

ACKNOWLEDGEMENT

REFERENCES

[1] H.Y. Lee, A. Sharma, S.H. Kee, Y.W. Lee, J.T. Moon, and P.J. Jung, "Effect of aluminium addition on wettability and intermetallic compound (IMC) growth of lead free Sn (2 wt% Ag, 5 wt% Bi) soldered joints," *Electron Materials Letters*, vol. 10, no. 5, pp. 997-1004, 2014.

[2] V. Kripesh, P.S. Teo, C.T. Tai, G. Vishwanadam, C.M. Yew, "Development of a lead free chip scale package for wireless applications," in *51th Electron, Component and Technology Conference,* 2001, pp. 665-670.

[3] S.W. Chen, and Y.W. Yen, "Interfacial reactions in Ag-Sn-Cu couples, *"Journal of Electronic Materials,* vol. 28, no. 11, pp. 1203-1208, 1999.

[4] G. Humpston, and D.M. Jacobson, *Principals of soldering,* ASM International. Materials Park: Ohio; 2004.

[5] L.M. Yin, J.W. Xian, and Z.X. Yao, "Comparison of Wettability for Sn-Based Solders on Copper and Aluminum Substrates," *Materials Science Forum*, Vol. 687, pp. 15-20, 2011.

[6] L.P. Lehman, R.K. Kinyanjui, L. Zavalij, A. Zribi, and E.J. Cotts, "Growth and selection of intermetallic species in Sn-Ag-Cu No-Pb solder systems based on pad metallurgies and thermal histories", *In 53rd Electronic Components and Technology Conference*, 2003, pp. 1215-1221.

[7] B. Huang, H.S. Hwang, and N.C.H. Lee, "A Compliant and Crep Resistant SAC-Al(Ni) Alloy", *57th Electronic Components and Technology Conference*, Reno, 2007, pp. 184-191.

[8] P. Fima, J. Pstruś, and T. Gancarz,, "Wetting and interfacial chemistry of SnZnCu alloys with Cu and Al substrates", *Journal of Materials Engineering and Performance*, vol 23, no. 5, pp 1530-1535.

Corrosion analysis of the cold work 316L stainless steel in simulated body fluids

W.M.F.W. Mohamad[1,2,*], M.Z. Selamat[1,2], B. Bundjali[3], M. Musa[1,2], H.M. Dom[4]

[1] Faculty of Mechanical Engineering, Universiti Teknikal Malaysia Melaka,
Hang Tuah Jaya, 76100 Durian Tunggal, Melaka, Malaysia
[2] Centre for Advanced Research on Energy, Universiti Teknikal Malaysia Melaka,
Hang Tuah Jaya, 76100 Durian Tunggal, Melaka, Malaysia
[3] Department of Chemisty, Institut Teknologi Bandung,
Jl. Ganesha 10 Bandung, Jawa Barat-Indonesia
[4] Faculty of Engineering Technology, Universiti Teknikal Malaysia Melaka,
Hang Tuah Jaya, 76100 Durian Tunggal, Melaka, Malaysia

[*]Corresponding e-mail: farid@utem.edu.my

Keywords: 316L stainless steel; simulated body fluids; corrosion resistance

ABSTRACT – The present paper deals with the characteristic of the corrosion failure of the cold work 316L stainless steel in the simulated body fluids. The steel has been cold rolled within the range of 10 to 50% reduction in thickness. The corrosion test was done for 7 days at a temperature of 37°C by immersing the steel in a 0.9% NaCl and phosphate buffered saline (PBS) solution. It was found that the steel with a higher cold reduction tend to increase the corrosion resistance of more than 50% in both simulated environment.

1. INTRODUCTION

A corrosion phenomenon is one of the major problems in any metal-based part or component. Normally, additional costs are required in order to diminish or repair the corroded metal part. If the part was considerably irreversible or too costly, then it will be replaced with a new part. Generally, almost metal alloy are chemically or electrochemically not stable. They suffered with the corrosion phenomena while expose to the environment. This scenario also occurred in the application of medical implants, particularly involving 316L stainless steel. The normal human body is considered as a neutral environment where the pH and temperature are equal to 7.0 and 37°C. However, the nature of the human body that contains of numerous metal and non-metal species contributes to the corrosion of the metal implant. Previous studies have proved that this surgical grade was also suffered to both uniform and localized corrosion [1]. Most of them more focused on the actual failed surgical implant with a less concerning on the cold work process [2-3].

In this study, the corrosion resistance of the cold work 316L stainless steel was analysed experimentally using a cyclic immersion corrosion test. The test was principally referred to ASTM G 31-72 [4] where the corrosive environment was developed to a nearly human body condition.

2. METHODOLOGY

The 316L stainless steel has been used with starting thickness of 2.0 mm with a composition of 16.61% Cr, 10.44% Ni 0.02% C as provided by the manufacturer. This commercial 316L sheet was cold rolled to 10, 30 and 50% reduction in thickness (RT) before preparing to a small test specimen. The specimens, with a three sets for each thickness reduction, have been undergone a process of CNC milling to a dimension of 20.0 x 10.0 mm. Then, the corrosion test was conducted in aerated environment using an OV-445 Gallenkomp wheel test oven. The PBS and 0.9% NaCl were used as the SBF with the initial pH of 7.31 and 6.8. The test duration was set to 7 days with a temperature of about 37°C. All specimens were rinsed with ethanol prior the pre- and post-cleaning.

The corrosion rate (mm/y) was calculated according to the mass loss using the equation [4],

$$Corrosion\ rate = (K \times W)/(A \times T \times D) \quad (1)$$

Where K = constant, W = mass loss in g, A = surface area in cm^2, T = time of exposure in hours and D = density in g/cm^3. The D and K were used 7.98 g/cm^3 and 8.76 x 10^4 mm/y, respectively.

The A for a rectangular specimen was measured by the equation,

$$A = 2(wl) + (2w)t + (2l)t \quad (2)$$

Where w = width, l = length and t = thickness. All dimensions in cm.

The morphology of the corroded steel was analyzed by using a Jeol JSM 6010 plus LV scanning electron microscope (SEM).

3. RESULTS AND DISCUSSION

Figure 1 (a-b) represents the microstructure of the steel in as-received and after 50% cold reduction. The cold-rolling process has modified the steel from polygonal to elongated grains structure. Dislocation twin structures were also appeared in some of the grains after extensive cold reduction. The modifications had strengthened and hardened the steel as it has been proved from previous study [5].
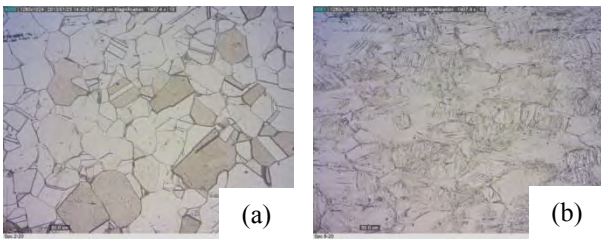
Figure 1 Optical micrograph of 316L steel with (a) 0; and (b) 50 % RT.

These surface modification were greatly affected the corrosion resistance of the mechanically treated steel. Figure 2 shows the average corrosion rate of all specimens obtained from the equation (1) and (2). For specimen with 0% RT, the rate was about 0.22 mm/y and 0.23 mm/y in 0.9% NaCl and PBS solution. However, it has been reduced to 0.11 mm/y and 0.09 mm/y for each SBF solution, after extensive cold reduction.
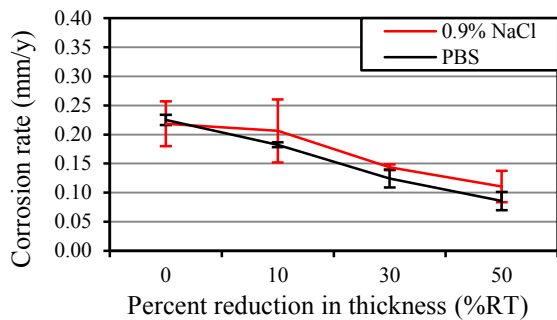
Figure 2 The average corrosion rates of 316L steel in PBS and 0.9% NaCl.

The steel tends to be more corrosive in NaCl rather than PBS for each particular cold reduction. This was possibly due to the presence of a higher concentration of chloride, Cl^- ion, such that an aggressive species in the corrosive environment. In addition, the initial pH of the solution, which more acidic tends to increase the corrosion rates.
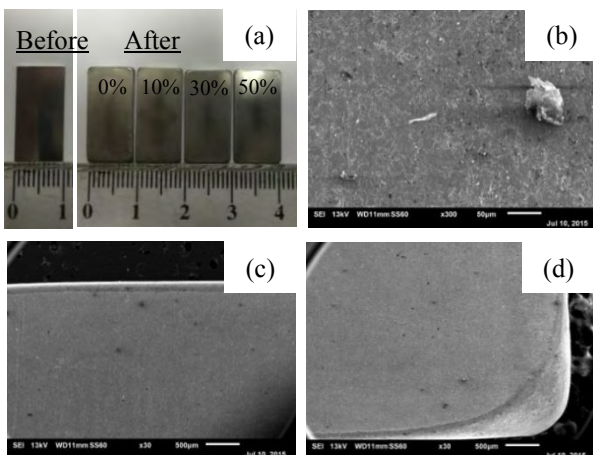
Figure 3 The morphology of the 316L steel (a) before and after the test; and after 10% RT at (b) normal; (c) edge; and (d) corner surface after immersing in PBS.

The corrosion rates obtained from this study was considered higher compare with previous study. The acceptable rate of metal implant in the human body was about 2.5×10^{-4} mm/yr [6]. It can be explained according to the morphology of the corroded steel as shown in Figure 3 (a-d). Generally, the corrosion process was uniformly occurred at the entire surface as shown in Figure 3 (b), without any evidence of the localized corrosion.

However, the corrosive phenomenon was different at the sharp surface as shown in Figure 3 (c-d). It's clearly shows that the surfaces were not only affected with the corrosion but also with a wear process. The wear might occur due to the friction during the cyclic test between the specimens and glass container. Thus, the combinations of both processes were greatly influenced their corrosion resistance. Also, the wear failure tends to be lowered for the steel with extensive cold reduction. This was due to the microstructure changes caused by the cold work process.

4. SUMMARY

The corrosion characteristic of the cold work 316L stainless steel in SBF environment has been analyzed experimentally using the immersion corrosion test. As a result, it can be concluded that:

a. The corrosion resistance was gradually increased for the steel with higher cold reduction. In addition, the resistance slightly low for the steel in 0.9% NaCl compare to PBS solution.
b. The morphology of all corroded steel shows the existence of the uniform corrosion. While, the wear plays a dominant process at the sharp surfaces.

REFERENCES

[1] D.J. Blackwood, "Biomaterials: Past successes and future problems," *Corrosion Reviews*, vol. 21, issue 2-3, pp. 97-124, 2003.

[2] C.M. Shih, Y.Y. Su, S.J. Lin, and C.C. Shih, "Failure analysis of explanted sternal wires," *Biomaterials*, vol. 26, pp. 2053-2059, 2005.

[3] K.V. Sudhakar, "Metallurgical investigation of a failure in 316L stainless steel orthopaedic implant," *Engineering Failure Analysis*, vol. 12, pp. 249-256, 2005.

[4] ASTM G 31-72 Standard Test Methods for Tension Testing of Metallic Materials [Metric], (reapproved 2004), ASTM International: West Conshohocken, PA.

[5] W.M.F. W Mohamad, M.Z. Selamat, B. Bundjali, H.M. Dom, and M. Musa, "Effect of cold mechanical process on the mechanical properties of 316L stainless steel for medical implant application," *International Review of Mechanical Engineering*, vol. 9, no. 4, pp. 353-359, 2015.

[6] M. Geetha, D. Durgalakshmi, and R. Asokamani, "Biomedical implants: corrosion and its prevention - A review," *Recent Patents on Corrosion Science*, vol. 2, pp. 40-54, 2010.

Effect of agitation mechanism on the anodization process of titanium dioxide nanotube arrays

K.A. Khairul, S. Ismail[*]

Faculty of Manufacturing Engineering, Universiti Teknikal Malaysia Melaka,
Hang Tuah Jaya, 76100 Durian Tunggal, Melaka, Malaysia

[*]Corresponding e-mail: syahriza@utem.edu.my

ABSTRACT – Titanium dioxide, TiO_2 nanotubes were fabricated by anodization process of pure titanium substrate in ethylene glycol containing fluoride. The anodization process has been conducted with 2 different agitation mechanisms which are magnetic stirring, and air bubble. The morphology and the structure of the as-anodized TiO_2 was determined using field emission scanning electron microscope and Raman spectroscopy.

1. INTRODUCTION

Nanostructured titanium dioxide, TiO_2 material has been one of the widely investigated metal oxide due to its enormous potential for photocatalysis, photovoltaic, sensing, and electrochromic application. In the form of nanotubes, TiO_2 exhibit semiconductor nature with high surface area and aspect ratio [1]. Several process have been studied to produce highly ordered nanotube arrays such as sol gel, hydrothermal, and anodic oxidation [2]. Apparently amongst other methods, anodization has attracted much attention for their exceptional advantages in fabricating TiO_2 nanotubes. The morphologies of the TiO_2 nanotubes structure can be controlled by adjusting the anodization parameter such as type of electrolyte, applied voltage, time and temperature [3]. Yasuda and Schmuki [4] reported that the nanotube growth is controlled by the ionic species diffusion in the electrolyte. Thus, an agitation mechanism such as magnetic stirring [5] and air bubble [6] is necessary in the anodization process as to increase the rate of ion diffusion. This paper presents the effect of agitation mechanisms which are magnetic stirring and air bubble on the formation of TiO_2 nanotubes.

2. METHODOLOGY

Prior to anodization, titanium foils were degreased by successive ultrasonication in ethanol and distilled water for 5 minutes each and dried using air gun. For all experiments, ethylene glycol solution were used which contains 0.55% NH_4F and 1% H_2O. Anodization was performed in a two-electrode configuration connected to a DC power supply with a titanium foil as the working electrode and graphite rod as the counter electrode. The agitation mechanism was varied using magnetic stirrer and air bubble during anodization process. All the anodization experiments were carried out under a constant 40 V anodic potential for 30 minutes at room temperature. The as formed nanostructures were rinsed using distilled water and dried using air gun.

Subsequently, Raman spectroscopy and FESEM were used to determine the TiO_2 nanotube structure and morphology.

3. RESULTS AND DISCUSSION

Figure 1 shows the current profile of anodization process in different agitation mechanisms which are magnetic stirring and air bubble. It is evident that the current profile present typical curve for highly organized oxide of pore arrangement or formation of nanotubes in both sample [7]. The current density of air bubbling mechanism is higher at the beginning which is 12 mA/cm^2 compared to the current density of magnetic stirring which is 10 mA/cm^2. Both sample reached the stabilization at 6 mA/cm^2. However, the time required for the stabilization of current density with magnetic stirring is faster than air bubbling which is about 6 minutes and 25 minutes respectively.
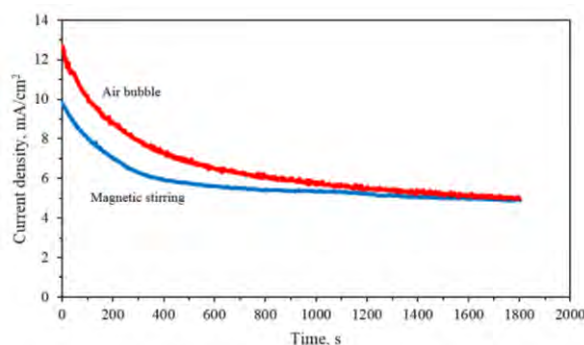
Figure 1 Current profile for nanostructures obtained in EG based electrolytes.

The morphology of the as-anodized TiO_2 grown with air bubble and magnetic stirring is shown in Figure 2 (a) and (b) respectively. Both images indicate the formation of open pores with the diameter of 60 nm for air bubbles and 90 nm for magnetic stirring. Smaller diameter is seen in Figure 2(a) compares with Figure 2(b) which indicates that the dissolution in magnetic stirrer is faster than air bubbles. The tube wall of the nanotubes in magnetic stirrer is vigorously dissolved and hence provide larger diameter. This is also proven by the rapid stabilization of current density for magnetic stirring agitation. As seen from the figures, the top surfaces of the as anodized TiO_2 seem to be covered by some precipitation emanating from the dissolution of barrier layer.
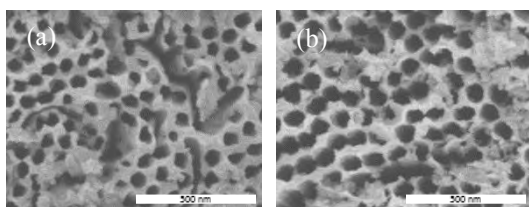
Figure 2: FESEM top images of as-anodized TiO_2 grown with (a) air bubble and (b) magnetic stirring.

Raman spectra of as-anodized TiO_2 nanotubes with different agitation mechanism are shown in Figure 2. The Raman analysis was done over range of 200 to 700 cm^{-1} which is the optimal range for discriminating between crystal phases of TiO_2 [8]. Since titanium has metallic nature, it has free electrons that preventing the lattice vibrations. The Raman spectrum of Ti foil as shown in Figure 2(a). Both Raman spectrum for as-anodized TiO_2 with magnetic stirring and air bubble exhibit broad peaks near 612, 420, 284 cm^{-1} due to amorphous titania, similar results reported in previous study [9].
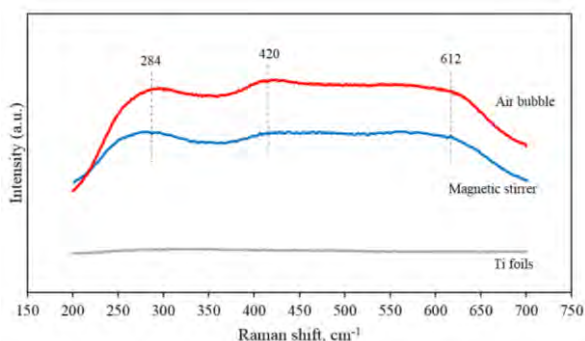
Figure 2 Raman spectra of Ti foils, anodized with magnetic stirring, and air bubble.

4. CONCLUSIONS

The TiO_2 nanotubes were successfully fabricated by anodization process where the formation mechanism of nanotubes can be seen by the current profile. Besides, the investigation of agitation mechanism on the structure of as-anodized TiO_2 nanotubes has been done using Raman spectroscopy. The Raman spectra indicate that the as-anodized TiO_2 nanotubes for both sample of magnetic stirring and air bubble is amorphous since the peak is broad.

REFERENCES

[1] S. Rani, S. C. Roy, M. Paulose, O. K. Varghese, G. K. Mor, S. Kim, S. Yoriya, T. J. LaTempa, and C. A. Grimes, "Synthesis and applications of electrochemically self-assembled titania nanotube arrays," *Phys. Chem. Chem. Phys.*, vol. 12, no. 12, p. 2780, 2010.

[2] H. Liang and X. Li, "This is the Pre-Published Version . Effects of structure of anodic TiO_2 nanotube arrays on photocatalytic activity for the degradation of 2 , 3-dichlorophenol in aqueous solution," pp. 1–29.

[3] H. Omidvar, S. Goodarzi, A. Seif, and A. R. Azadmehr, "Influence of anodization parameters on the morphology of TiO_2 nanotube arrays," *Superlattices Microstruct.*, vol. 50, no. 1, pp. 26–39, 2011.

[4] K. Yasuda and P. Schmuki, "Control of morphology and composition of self-organized zirconium titanate nanotubes formed in $(NH_4)_2$ SO_4/NH_4F electrolytes," vol. 52, pp. 4053–4061, 2007.

[5] D. Kim, F. Schmidt-stein, R. Hahn, and P. Schmuki, "Electrochemistry Communications Gravity assisted growth of self-organized anodic oxide nanotubes on titanium," vol. 10, pp. 1082–1086, 2008.

[6] P. M. Perillo and D. F. Rodriguez, "Growth control of TiO_2 nanotubes in different physical environments," vol. 2311, no. January, 2016.

[7] M. Kulkarni, A. Mazare, P. Schmuki, and A. Iglic, "Influence of anodization parameters on morphology of TiO_2 nanostructured surfaces," vol. 7, no. 1, pp. 23–28, 2016.

[8] D. Regonini, A. Jaroenworaluck, R. Stevens, and C. R. Bowen, "Effect of heat treatment on the properties and structure of TiO_2 nanotubes : phase composition and chemical composition," no. December 2009, pp. 139–144, 2010.

[9] F. D. Hardcastle, H. Ishihara, and A. S. Biris, "Photoelectroactivity and Raman spectroscopy of anodized titania (TiO_2) photoactive water-splitting catalysts as a function of oxygen-annealing temperature," *J. Mater. Chem.*, vol. 21, no. 17, pp. 6337–6345, 2011.

Experimental investigation of buckling behavior of cracked cylindrical shells subjected to axial compression

O. Ifayefunmi[1,2,*], Norehan Kasiman[1], Hazrin Ibrahim Khan[1]

[1] Faculty of Engineering Technology, Universiti Teknikal Malaysia Melaka,
Hang Tuah Jaya, 76100 Durian Tunggal, Melaka, Malaysia
[2] Centre for Advanced Research on Energy, Universiti Teknikal Malaysia Melaka,
Hang Tuah Jaya, 76100 Durian Tunggal, Melaka, Malaysia

*Corresponding e-mail: olawale@utem.edu.my

Keywords: Buckling; cracked cylinder; axial compression

ABSTRACT – The aim of this experimental research work is to investigate the effect of axial crack length on the buckling behavior of cracked cylindrical shells subjected to axial compression loading. The crack on the cylindrical structures is assumed to be a percentage of the axial length of the cylindrical shell structure. The magnitude of the crack length-to-cylinder axial length is varied between 0.05 and 0.15. Cylindrical specimens are made from mild steel with radius-to-thickness ratio, ranging from 25 to 100. The axial length of the specimens was assumed to be constant. Results indicate that the crack length strongly affect the buckling behavior of the axially compressed cylinder. Also, it was revealed that the buckling load of the cylindrical specimens with high value of radius-to-thickness ratio is more sensitive to the effect of change in crack as compared to cylinder with low value of radius-to-thickness ratio.

1. INTRODUCTION

It is a known fact that the presence of defects such as cracks on a shell structures can play the role of geometrical imperfection and thereby reduce the buckling load of the shell structures considerably [1]. Research into buckling behavior of cracked cylindrical shell structures with the presence of crack can be found in Refs [2-5]. Motivation for the presents work originates from the conclusion of Ref [5], where it was reported that for cylindrical shells with axial crack (longitudinal crack), the change in crack length and increasing the crack length-to-circumference of cylinder ratio, has minor effect on the buckling load of the cylinder. This paper investigate the effect of ratio of axial crack length to cylinder axial length ranging from 0 – 0.15 on the bucking behaviour of axially compressed cylinder. This is purely experimental work.

2. METHODOLOGY

2.1 Background

For this research work, circular cylinders with radius-to-thickness ratio, R/t, ranging from 25 to 100 were subjected to axial compressive loading. The cylinder is assumed to have a constant inner diameter, D, of 100 mm, constant axial length, L, of 111.8 mm and wall thickness, t, of (2 mm, 1 mm and 0.5 mm)

respectively. The cylinder has axial crack of various length introduced along its longitudinal axis as illustrated in Figure 1. The magnitude of axial crack, 2a, to the cylinder axial length, 2a/L, was varied between 0.0 to 0.5. Cylindrical shells are assumed to be made from A36 mild steel with material properties presented in Table 1 (see details about material properties extraction in [6]).

Table 1 Average mechanical properties of A36 steel material obtained from uni-axial testing.

Specimen thickness (mm)	E (GPa)	Upper yield (MPa)	UTS (MPa)
0.5	193.7	203.1	305.8
1.0	214.0	256.2	333.2
2.0	241.4	322.1	374.4
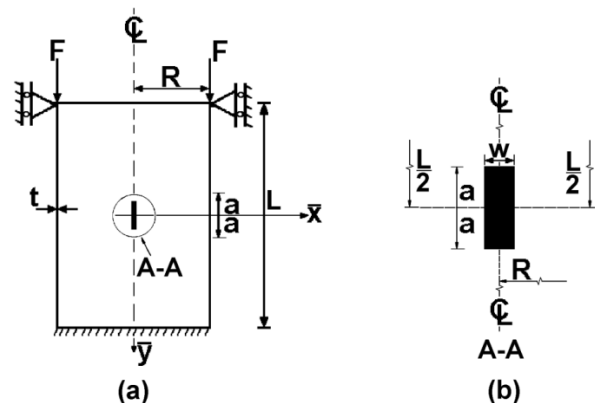
Figure 1 Section through cylindrical shell (Fig. 1a). The insert illustrates the crack region (Fig. 1b).

2.2 Experimentation

For this experiment, cylindrical shells with three different thickness (t = 0.5, 1.0, 2.0 mm) were manufactured and tested. Cylinders were manufactured using Metal Inert Gas (MIG) welding process. During the welding process, axial crack of varying length was introduced on all the specimens. The magnitude of axial crack, 2a, to the cylinder axial length, 2a/L, was varied between 0.0 to 0.15. Then, all cylinders were subjected to axial compression using INSTRON machine. Incremental axial load was applied at the rate of 1.0 mm/min.

3. RESULTS AND DISCUSSION

During the experiment, the buckling load of the cylinder corresponding to the different values of axial crack length was recorded using the machine controller. Figure 2 depicts the plot of buckling load corresponding to different imperfect cylinders having a crack against increasing length of crack for different radius-to-thickness ratio, R/t. The vertical axis is normalized by the respective collapse load for the perfect cylinder for each radius-to-thickness ratio. The corresponding magnitudes of the buckling loads are presented in Table 2.
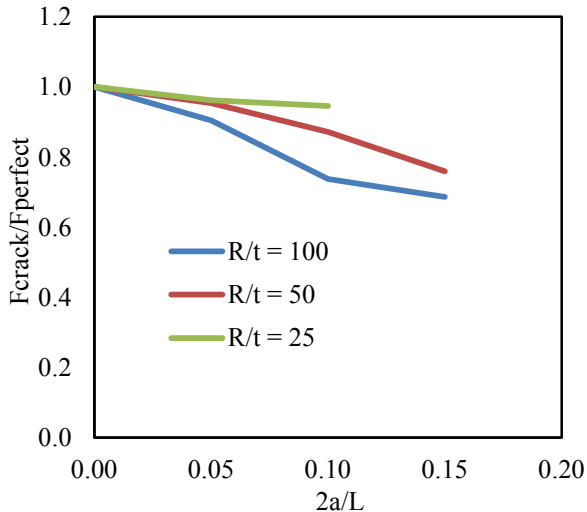
Figure 2 Plot of buckling load versus increasing crack length of axially compressed cylinders with different radius-to-thickness ratio.

Table 2 Magnitude of buckling load obtained with increasing crack length for different radius-to-thickness.

2a/L	Buckling load for different R/t (kN)		
	100	50	25
0	30.13	84.67	208.56
0.05	27.24	80.79	200.69
0.1	22.23	73.81	197.18
0.15	20.67	64.28	-

It can be seen from Figure 2 that increasing the crack length of the cylinder results in decrease in the load carrying capacity of the structures. This result appears to be in agreement with published work in open literature as in Refs [2-4], i.e., load carrying capacity of the cylindrical shell structure reduces as the axial crack length increases.

Also, it is apparent from Figure 2 that the effect of axial crack length is more pronounced for cylinder with higher value of radius-to thickness ratio as compared to cylinder with much lower value. For example, with ratio of crack length of axial length of the cylinder, 2a/L, of 0.05, the percentage drop in buckling loads are 10%, 5% and 4% for radius-to-thickness ratio of 100, 50 and 25, respectively. Whilst, at 2a/L = 0.1, the percentage

reduction for R/t = 100, 50 and 25, are 26%, 13% and 6%, respectively.

In addition, the experimental data complement the work of Ref [5]. In Ref [5], it was reported that for cylindrical shells with axial crack (longitudinal crack), the change in crack length and increasing the crack length-to-circumference of cylinder ratio, has minor effect on the buckling load of the cylinder. From this work, it has been shown that this is not generally true for ratio of axial crack length to axial length of cylinder within the range of 0 – 0.15. However, this might be true for ratio of axial crack length to axial length of the cylinder above 0.2.

4. CONCLUSION

The paper provides additional experimental results into the buckling behavior of imperfect cylindrical shell with axial cracks subjected to axial compressive force. Contrary to Shariati et al. (Ref [5]), it can be concluded that for cylinders with axial crack, change in crack length and increasing the ratio of crack length to axial length of the cylinder will cause a considerable reduction in the load carrying capacity of the cylinders, for crack length-to-axial length of the cylinder ratio ≤ 0.2.

REFERENCES

[1] A. Vafai, H.E. Estekanchi, "A prrologue to the buckling analysis of cracked shells," Iranian Journal of Science and Technology, vol. 20, pp. 137-168–681, 1996.

[2] H.E. Estekanchi, A. Vafai, "On the buckling of cylindrical shells with through cracks under axial load", *Thin-Walled Structures*, **35**, 255-274, 1999.

[3] B.H. Jahromi, A. Vaziri, "Instability of cylindrical shells with single and multiple Cracks under axial compression", *Thin-Walled Structures*, **54**, 35 – 43, 2012.

[4] Y.T. Kim, B. Haghpanah, R. Ghosh, H. Ali, A.M.S. Hamouda, and A. Vaziri, "Instability of a cracked cylindrical shell reinforced by an elastic liner", *Thin-Walled Structures*, **70**, 39- 48, 2013.

[5] M. Shariati, M. Sedighi, J. Saemi, H.R. Eipakchi, and H.R. Allahbakhsh , "Numerical and experimental investigation on ultimate strength of cracked cylindrical shells subjected to combined loading", *Mechanika*, **84**, 12 – 19, 2010.

[6] O. Ifayefunmi, "Buckling behavior of axially compressed cylindrical shells: comparison of theoretical and experimental data", *Thin-Walled Structures*, **98**, 558-564, 2016.

The influence of boundary condition on the deformed shape of axially compressed cones

O. Ifayefunmi[1,2,*], K.L. Chang[1]

[11] Faculty of Engineering Technology, Universiti Teknikal Malaysia Melaka,
Hang Tuah Jaya, 76100 Durian Tunggal, Melaka, Malaysia
[2] Centre for Advanced Research on Energy, Universiti Teknikal Malaysia Melaka,
Hang Tuah Jaya, 76100 Durian Tunggal, Melaka, Malaysia

[*]Corresponding e-mail: olawale@utem.edu.my

ABSTRACT – The aim of this research work is to investigate the influence of boundary condition on the buckling load and deformed shape of axially compressed cone. Two boundary conditions are considered, they are: (i) fully clamped at the bottom and allowed to move in the axial direction at the top ends, and (ii) allow all displacement movement except axial direction at the bottom and restrict all movement at the top except axial direction. Cones were relatively thick with nominal wall thickness of 2 mm and the semi-vertex angle, β is 15°, hence their buckling behavior remains within the elastic-plastic range. The geometry of radius of bigger radius, r_2, to radius of smaller radius, r_1, ($r_2/r_1 = 1.75$), and the ratio of radius-to-thickness (r_2/t) was taken as 35. Results indicate that the change of boundary condition has a strong influence on both the buckling load and the deformed shape.

1. INTRODUCTION

Conical shells structures primarily used in engineering application are susceptible to imperfection. One of the major source of imperfection commonly encountered in the industry is the influence of boundary condition (edge support) when such structures are used. Very few studies have been carried out on the influence of boundary condition on the load carrying capacity of cones. They can be found in Refs [1-6]. Whilst, Refs [1-5] were devoted to elastic buckling, Ref [6] examines the influence of boundary condition on buckling load of cones within the elastic-plastic range. However, the author was silent on the influence of such boundary condition on the deformed shape.

This paper seeks to investigate the influence of boundary condition on the bucking load and deformed shape of axially compressed cone.

2. METHODOLOGY

2.1 Numerical approach

For this research work, numerical analysis was conducted using ABAQUS finite element code. Consider a truncated cone with small radius, r_1, big radius, r_2, cone height, h, cone slant length, L, wall thickness, t and cone semi-vertex angle, β. Assume that cone is subjected to axial compression. The geometry parameters of analyzed cone are: radius of bigger radius, r_2, to radius of smaller radius, r_1, ($r_2/r_1 = 1.75$), the ratio of radius-to-thickness (r_2/t) was taken as 35 and semi-vertex angle of 15 degrees. Cones are assumed to be made from mild steel with material properties presented in Table 1. Two different boundary conditions were employed in this present work as given in Table 2. The notation used above assumes: u $\equiv$ displacements, and $\Phi \equiv$ rotations.

Table 1 Set of mechanical properties of A36 steel material obtained from uni-axial testing.

Sample	E (GPa)	Upper yield (MPa)	UTS (MPa)
1	219.219	367.1	403.6
2	238.253	371.1	409.9
3	201.993	371.6	411.2
Average	219.822	369.9	408.2

Table 2 Boundary conditions employed during numerical calculations.

		u_x	u_y	u_z	ϕ_x	ϕ_y	ϕ_z
Case 1	Top	0	0	$\neq 0$	0	0	0
	Bottom	0	0	0	0	0	0
Case 2	Top	0	0	$\neq 0$	0	0	0
	Bottom	$\neq 0$	$\neq 0$	0	0	0	0

The specimens were modeled using four-node three-dimensional doubly curved shell elements with six degree of freedom (S4R). The material is modeled as elastic perfectly-plastic. Non-linear static analysis was carried out using the modified Riks method algorithm which is implemented in ABAQUS.

2.2 Experimentation

For this experiment, two nominally identical mild steel cones with the same nominal geometry as discussed in Section 2.1 were manufactured and tested. This would provide two experimental data values for cones with nominally the same geometry to ensure repeatability of experimental data. Cones were joined together using Tungsten Inert Gas (TIG) welding process. Conical specimens were subjected to axial compression using Universal Instron Machine. Incremental load was applied at the rate of 1.0 mm/min.

3.   RESULTS AND DISCUSSION

Figure 1 depicts the comparison of deformed shape obtained from ABAQUS analysis of the two boundary conditions considered for relatively thick axially compressed conical shells. For case 1 (Figure 1a) where the big ends of the cone is clamped, it can be seen that there were axisymmetric bulging in the neighborhood of the small radius ends. Whereas, for case 2 (Figure 1b) where the big end of the cone allowed all displacement movement, it is apparent that as a result of change in boundary condition, the deformed shape also changes from bulging in the neighborhood of the small cone ends to a skirt like shape around the cone big ends. In addition, it was observed that the load carrying capacity of the cone reduces from 201.69 kN (for case 1) to 144.56 kN (for case 2) resulting in about 28% drop in the buckling load of the cone.
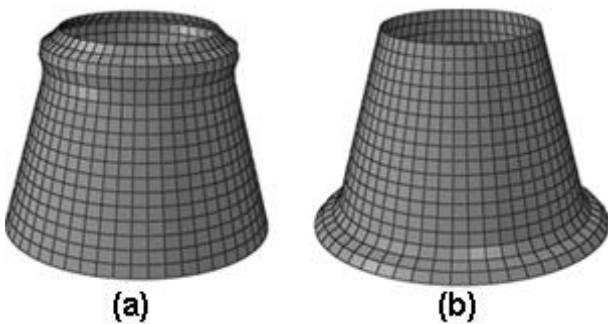
Figure 1 View of FE simulated deformed shape for different boundary conditions.

During the experiment, the axial shortening of the cones were recorded using the machine controller. Figure 2 depicts the plot of axial compressive force against axial shortening for both cones. It is apparent that both curves follow a similar pattern with both cones failing at nearly almost the same buckling load about 2% difference (163.68 kN vs 167.87 kN).
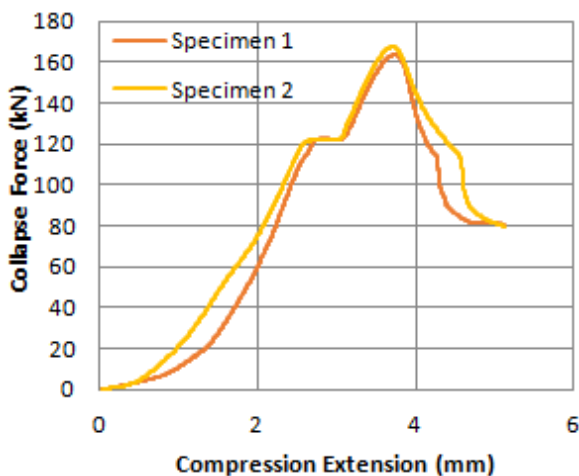
Figure 2 Plot of axial collapse force against compression extension for axially compressed cones.

To validate the deformed shape obtained from numerical simulation, it was decided to compare the experimentally obtained deformed shape with that obtained from ABAQUS using the same boundary condition. Figure 3 depicts the comparison of deformed shape obtain from both experimental and numerical approach. It is evident that there is a good visual comparison of deformed geometries.

Figure 3 View of FE simulated deform shape (Figure 3a) and collapsed cone (Figure 3b) subjected to axial compression.

4.   CONCLUSION

Two nominally identical cones fail at nearly the same collapse load thereby confirming good repeatability of experiment data. Also, it can be concluded that change in boundary conditions has strong influence on both the buckling load and the deformed shape of relatively thick cones subjected to axial compression.

REFERENCES

[1]   M. Baruch, O. Harari, J. Singer, "Effect of in-plane boundary conditions on the stability of conical shells under hydrostatic pressure", in *Proceeding of the 9th Israel Annual Conference on Aviation and Astronautics, Israel Journal of Technology*, vol. 5, no. 1, 12-24, 1967.

[2]   G. A. Thurston, "Effect of boundary conditions on the buckling of conical shells under hydrostatic pressure," *Journal of Applied Mechanics, Transactions of the ASME*, vol. 32, no. 1, pp. 208 – 209, 1965.

[3]   N. Pariatmono, M. K. Chryssanthopoulos, "Asymmetric elastic buckling of axially compressed conical shells with various end conditions," *AIAA Journal*, vol. 33, no. 11, pp. 2218 – 2227, 1995.

[4]   A. Spagnoli, "Koiter circles in the buckling of axially compressed conical shells*," International Journal of Solids and Structures*, vol. 40, no. 22, pp. 6095-6109, 2003.

[5]   M.K. Chryssanthopoulos, A. Spagnoli, "The influence of radial edge constraint on the stability of stiffened conical shells in compression," *Thin-Walled Structures*, vol. 27, no. 2, pp. 147 – 163, 1997.

[6]   O. Ifayefunmi, J. Blachut, "The effect of shape, thickness and boundary imperfections on plastic buckling of cones", in *Proceedings Of The 30th International Conference On Ocean, Offshore and Arctic Engineering*, Rotterdam, 2011.

Effect of polypropylene type on G/CB/CNTs/PP composites properties as bipolar plate for PEM fuel cell

A. Bairan[1,2], M.Z. Selamat[1,2*], S.N. Sahadan[1,2], S.D. Malingam[1, 2], N. Mohamad[3]

[1] Faculty of Mechanical Engineering, Universiti Teknikal Malaysia Melaka,
Hang Tuah Jaya, 76100 Durian Tunggal, Melaka, Malaysia
[2] Centre for Advanced Research on Energy, Universiti Teknikal Malaysia Melaka,
Hang Tuah Jaya, 76100 Durian Tunggal, Melaka, Malaysia
[3] Faculty of Manufacturing Engineering, Universiti Teknikal Malaysia Melaka,
Hang Tuah Jaya, 76100 Durian Tunggal, Melaka, Malaysia

*Corresponding e-mail: zulkeflis@utem.edu.my

Keywords: Nanomaterial fillers; carbon nanotube; conductive polymer composites

ABSTRACT – Investigation of the conductive polymer composites (CPCs) have been carried out using Graphite (G), Carbon Black (CB), Carbon Nanotubes (CNTs) and Polypropylene (PP) as a binder. While, two types of PP which are medium density (MD-PP) and low density (LD-PP) were mixed with multi filler by using a ball mill. The comparison of PP with respect to the resulting electrical conductivity and mechanical properties were investigated. Results indicate that CNTs was dispersed better in MD-PP than LD-PP would cause better electrical conductivity and mechanical properties of G/CB/CNTs/PP composite bipolar plate which are exceeded of the U.S. Department of Energy (DOE) requirement.

1. INTRODUCTION

The development CPCs is a promising and growing field of research due to highly resistant to corrosion, low cost and have low densities that might result in the materials replacing metal bipolar plate in Proton Exchange Membrane Fuel Cell (PEMFC) [1]. The bipolar plate is a main component of PEMFCs stack, which takes a large portion of stack cost [2]. They can contribute 70-80% of the stack weight and up to 45% of the costs. Hence, the investigation on cost/performance materials of bipolar plates has become a critical research issue. In order to obtain the better electrical conductivity of the composite, the combinations of multi fillers have been used as bipolar plate materials [3]. The reinforced fillers used commonly including graphite, carbon nanotube, carbon fiber, and carbon black which has been incorporated into the composites to enhance overall performance of composite bipolar plates by conventional polymer processing technique [3]. There are two different types of polymeric resins including thermoplastics and thermosets in order to fabricate composite bipolar plate. Comparing with this two type material, PP have the advantages of low cost, good processability, well-balance physical and mechanical properties [4]. The aim of this study is to investigate the significant effects of Polypropylene (PP) types on electrical and mechanical properties G/CB/CNTs/PP composite as bipolar plate.

The U.S. DOE has specified requirement (Table 1) regarding the conductivity, gas permeability and material strength which should satisfy for the fabrication of a bipolar plate.

Table 1 Requirement properties for the bipolar plate (DOE target) [2,4,5].

Property	Value
Electrical conductivity	> 100 [Scm^{-1}]
Thermal conductivity	> 10 [W(mK)^1]
Flexural strength	> 25 [MPa]
Shore hardness	> 50
Bulk Density	< 5 [g/cm^3]

2. METHODOLOGY

The multi filler materials are mixed used ball mill as pre-mixing process at a speed of 200 rpm for 1 and half hour. After that, the wt% compositions of G/CB/CNTs/PP are shown in Table 2 has been prepared. Then, a ball mill was used again to mix the materials from the previous stage with binder at a speed of 200 rpm for 1 hour. A hot press machine was used to shape the samples for properties measurements. The mixture of all material was then preheated for 20 min in a mould placed in the hot pressing machine before it pressed at a temperature of 185 ºC and a pressure of 85 kg/cm^2 for 15 min.

Table 2 The composition of composite G/CB/CNTs/PP (Based on weight %).

Filler			Binder
G %	CB%	CNTs%	PP%
52.0	25	3.0	20
51.0	25	4.0	20
50.0	25	5.0	20
49.0	25	6.0	20
48.0	25	7.0	20
47.0	25	8.0	20

3. RESULT AND DISCUSSION

3.1 Effect of CNTs/PP on electrical conductivity

As shown in Figure 1, the electrical conductivity was increased significantly in the order of CNTs/MD-PP>CNTs/LD-PP nanocomposite bipolar plates. At 6 wt% CNTs content, the electrical conductivities of CNTs/LD-PP and CNTs/MD-PP were measured at 125.4 S/cm and 158.32 S/cm respectively. This phenomenon may be attributed to the better dispersion of CNTs in MD-PP than LD-PP [4].
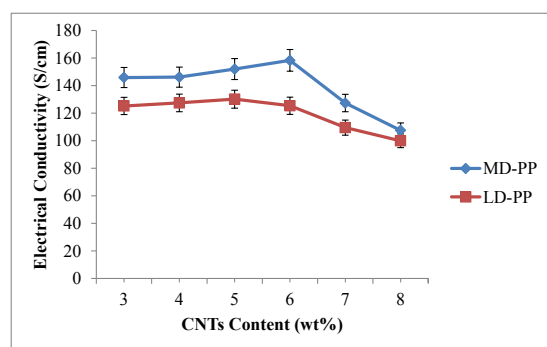
Figure 1 Electrical conductivity with various CNTs contents.

3.2 Effect of CNTs/PP on flexural strength

The flexural strengths of nanocomposite bipolar plates were increased with the increasing of CNTs content as shown in Figure 2. As CNTs content was at 5 wt%, the flexural strength of CNTs/LD-PP and CNTs/MD-PP were increased from 10.6 MPa and 22.95 MPa (3 wt%) to 13.64 MPa and 29.86 MPa (5 wt%), respectively. The CNTs/MD-PP nanocomposites bipolar plates with the better compatibility between fillers and polymer resin have the greater reinforcement of the flexural strength [5].
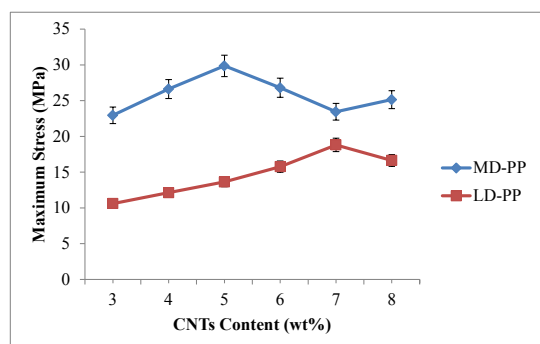
Figure 2 Flexural strength with various CNTs contents.

3.3 Effect of CNTs/PP on shore hardness and density

The value of shore hardness of CNTs/MD-PP nanocomposite bipolar plates were much higher than CNTs/LD-PP as shown in Figure 3. As 8 wt% of CNTs was incorporated into LD-PP and MD-PP nanocomposites bipolar plates, the hardness was increased to 72 (SH) and 81.3 (SH) respectively. These results postulated that better dispersion and good compatibility between CNTs and MD-PP will induce stronger adhesion [5]. However, the density of CNTs/LD-PP and CNTs/MD-PP nanocomposite bipolar plate showing no significant effects of increasing of the CNTs content. An average value of CNTs/LD-PP and CNTs/MD-PP density is 1.616 g/cm3 and 1.635 g/cm3, respectively. It achieves the requirements stated by the U.S. DOE for bipolar plate (<5 g/cm3).
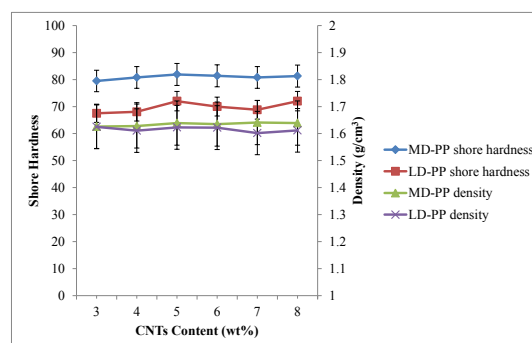
Figure 3 Shore hardness and density with various CNTs contents.

4. CONCLUSIONS

This observation indicates that the addition of CNTs (6 wt%) in MD-PP leads to a significant improvement with high electrical conductivity and mechanical properties which is can be used on the cell performance of the nanocomposite bipolar plate.

REFERENCES

[1] M.C.L de Oliveira, G. Ett, R.A. Antunes, "Materials selection for bipolar plates for polymer electrolyte membrane fuel cells using the Ashby approach," *Journal of Power Sources 206 (2012):* 3-13.

[2] R.B. Mathur, S.R. Dhakate, D.K. Gupta, T.L. Dhami and R. K. Aggarwal, "Effect of different carbon fillers on the properties of graphite composite bipolar plate," *Journal of Materials Processing Technology 203*, no. 1 (2008): 184-192.

[3] B.K. Kakati, K.R. Guptha, A. Verma, "Fabrication of composite bipolar plate for proton exchange membrane fuel cell," J *Environ Res Dev 4 (2009)*: 202-211.

[4] M.Z. Selamat, M.S. Ahmad, M. Daud and N. Ahmad, "Effect of Carbon Nanotubes on Properties of Graphite/Carbon Black/Polypropylene Nanocomposites," *Advanced Materials Research 795 (2013)*: 29-34.

[5] S.H. Liao, C.H. Hung, C.C.M. Ma, C.Y. Yen, Y.F. Lin, "Preparation and properties of carbon nanotube-reinforced vinyl ester/nanocomposite bipolar plates for polymer electrolyte membrane fuel cells," *Journal of Power Sources 176*, no. 1 (2008): 175-182.

Effect of molding temperature on properties of graphite/stannum/polypropylene composites

F. Masron[1,2,*], M.Z. Selamat[1,2], M.M. Tahir[1, 2], M.A.M. Daud[1, 2], J. Sahari[3]

1) Faculty of Mechanical Engineering, Universiti Teknikal Malaysia Melaka,
Hang Tuah Jaya, 76100 Durian Tunggal, Melaka, Malaysia
2) Centre for Advanced Research on Energy, Universiti Teknikal Malaysia Melaka,
Hang Tuah Jaya, 76100 Durian Tunggal, Melaka, Malaysia
3) Institut Sel Fuel, Universiti Kebangsaan Malaysia, 43600 Bangi, Selangor, Malaysia

*Corresponding e-mail: farahmasron@yahoo.com

Keywords: PEMFC; composite bipolar plate; graphite

ABSTRACT – The great efforts have been made over the past decades in developing the advance PEMFC technology especially for bipolar plate sector. Unfortunately, factors such as durability and cost of bipolar still remain as the major barrier to commercialization of high efficiency Polymer Electrolyte Membrane Fuel Cell. In this study, Graphite/Stannum/Polypropylene composite has been fabricated by compression molding process with several different temperatures (170 to 180^0 C), several weight percentage of Stannum (10 to 20 wt%) and have be tested with several mechanical and electrical tests. The result shows that the temperature of 175 ^{0}C with 15 wt% of Stannum give the best properties.

1. INTRODUCTION

One of the most important part in Polymer Electrolyte Membrane Fuel Cell (PEMFC) is bipolar plate. Almost 80% of stack weight and 60% of stack cost depends on bipolar plate. PEMFC is potentially become most promising power source due to its advantages such as high efficiency, large power density, low operating temperature, and quick start-up [1]. Department of Energy (DOE) had specified the requirements that related to electrical, mechanical, thermal and chemical properties of bipolar plate as shown in Table 1.

Table 1 DOE target for bipolar plates [2].

Property	Value
In-plane electrical conductivity	>100 S/cm
Flexural strength	≥25 MPa
Bulk Density	<1.9 [g/cm^3]
Shore hardness	>50

Previously, Graphite (Gr) bipolar plate has been widely used due to excellent chemical, thermal and electrical properties [3]. However, manufacturing cost for Gr bipolar plate become increased due to machining process of the flow channel. Other than that, Gr inherent brittleness, high permeable to gasses and exhibit poor mechanical properties. Due to Gr brittleness, for the channel fabrication process must to be done by machining process which time consuming and costly process [4]. Compared to metallic material bipolar plate,

they offer higher mechanical strength, low permeability, high conductivity manufacturability but exposed to corrosion which highly potential to be at anode and cathode of operating PEMFC.

As material used for steel can's coating, Stannum (Sn) also commonly known as Tin, have been applied as solder materials, bearing materials, alloying elements, super conducting magnet, electromagnetic materials, sodium ion battery and also pewter [5]. However, there is no report about Gr/Sn composite applied as bipolar plate materials yet.

Recently, Polypropylene (PP) has been widely chosen as most favorable resin to be applied as bipolar plate material due to low cost, easy processability and also high mechanical properties. Combining various conductive fillers is one of the effective ways to develop high electrical conductivities and also good mechanical properties. However, the effect of Sn in Gr/Sn/PP composite as bipolar plate still not much reported. The objective of this study is to investigate the effect of molding temperature of Gr/Sn/PP composite as bipolar plate.

2. METHODOLOGY

Three loadings ratio of Gr/Sn composites were prepared by 70/10, 65/15 and 60/20 respectively while loading ratio of PP remain constant, 20% of the composite. These composition will be dry mixed using ball mill machine for four hours. After that, the composite will be placed in mold and hot compression molding begun. Specimens compressed at 65 ton for 8 minutes at three different temperature, 170°C, 175°C and 180°C. The effect of compression molding temperature on the properties of Gr/Sn/PP composites such as electrical conductivity, bulk density and shore hardness were investigated.

3. RESULTS AND DISCUSSION

3.1 Effect of molding temperature on electrical conductivity

The electrical conductivity of Gr/Sn/PP composites with 10, 15 and 20 wt% of Sn loadings are shown in Figure 1. For 170 and 180°C of molding temperatures, electrical conductivity decreased as the Sn loading is

increased. While for 175°C, by adding the 15 wt% of Sn, electrical conductivity has increased (240 S/cm) but finally decreased at 20 wt% of Sn (100 S/cm). According to the result, the highest electrical conductivity shows by the 10 wt% of Sn loading with molding temperature was 170°C (265 S/cm). In the other side, the lowest value of electrical conductivity showed by 180°C of molding temperature at 20 wt% of Sn loading (6.61 S/cm).
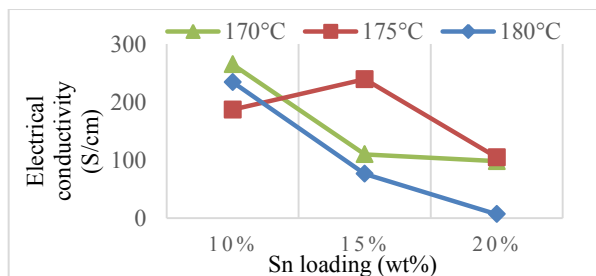
Figure 1 Electrical conductivity (S/cm) versus Sn loadings (wt%).

3.2 Effect of molding temperature on bulk density

Figure 2 showed the bulk density for Gr/Sn/PP composites and the bulk density has decreased with the addition of Sn loadings for 175°C and 180°C of molding temperatures. For 170°C of molding temperature, the bulk density increased with the addition of Sn. The minimum value was 1.46 showed by 10 wt% of Sn loading at 170°C. Besides that, the density value of all samples are meet the DOE requirement which is less than 1.9 g/cm^3. The slightly difference of density value is due to additional of Sn loadings in the composite.
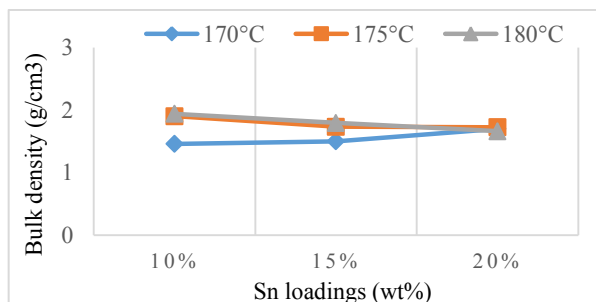
Figure 2 Bulk density (g/cm) versus Sn loadings (wt%).

3.3 Effect of molding temperature on shore hardness

Figure 3 shows the shore hardness results for Gr/Sn/PP composites and for molding temperatures of 175°C and 180^0 C the values of hardness property is quit close as compared to temperature of 170 ^{0}C. The highest value obtained by 15 wt% of Sn at 180°C of molding temperature (63). For the lowest value of hardness obtained by all samples at 170°C of molding temperature (26.8 to 28.2). For 175°C of molding temperature, the hardness decreased by addition of Sn loading to 15 wt% and slightly increased by addition of Sn loading to 20 wt%. As compared to 180°C, the hardness has increased by addition of Sn loading to 15

wt% but then decreased slightly when Sn loading up to 20 wt%. In this study, all specimens for 175°C and 180°C of molding temperatures were achieved the DOE requirement but for 170°C of molding temperature, all specimens were below DOE value.
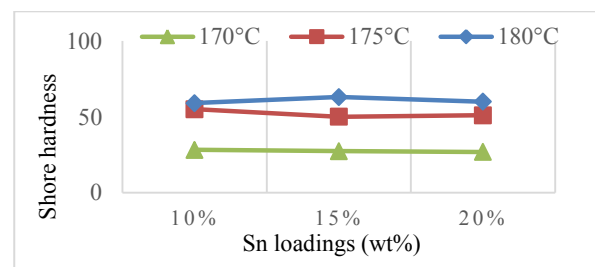
Figure 3 Shore hardness versus Sn loadings (wt%).

4. CONCLUSION

The addition of Sn obviously has a significant effect on electrical, bulk density and shore hardness values. The molding temperature of 175°C was shown as the most suitable temperature in order to produce high electrical conductivity. Other than that, 175°C of molding temperature also showed the results of bulk density and shore hardness that achieved the DOE requirements. A further study about mechanical properties such as flexural strength should be pursued.

REFERENCES

[1] Y. Hung, H. Tawfik, and D. Mahajan, "Effect of terminal design and bipolar plate material on PEM fuel cell performance," *Smart Grid Renew. Energy*, vol. 04, no. 01, pp. 43–47, 2013.

[2] M. C. L. de Oliveira, G. Ett, and R. A. Antunes, "Materials selection for bipolar plates for polymer electrolyte membrane fuel cells using the Ashby approach," *J. Power Sources*, vol. 206, pp. 3–13, May 2012.

[3] M.Z. Selamat, J. Sahari, N. Muhamad, and A. Muchtar, "The effects of thickness reduction and particle sizes on the properties graphite – polypropylene composite," *Composites*, vol. 6, no. 2, pp. 194–200, 2011.

[4] S. Karimi, N. Fraser, B. Roberts, and F.R. Foulkes, "A review of metallic bipolar plates for proton exchange membrane fuel cells: Materials and fabrication methods," *Adv. Mater. Sci. Eng.*, vol. 2012, pp. 1–22, 2012.

[5] M.K. Datta, R. Epur, P. Saha, K. Kadakia, S.K. Park, and P.N. Kumta, "Tin and graphite based nanocomposites: Potential anode for sodium ion batteries," *J. Power Sources*, vol. 225, pp. 316–322, 2013.

Analysis of impact duration from Charpy impact signal

N.B. Muhammad Said[1, 2,*], M.B. Ali[1, 2]

1) Faculty of Mechanical Engineering, Universiti Teknikal Malaysia Melaka,
Hang Tuah Jaya, 76100 Durian Tunggal, Melaka, Malaysia
2) Centre for Advanced Research on Energy, Universiti Teknikal Malaysia Melaka,
Hang Tuah Jaya, 76100 Durian Tunggal, Melaka, Malaysia

*Corresponding e-mail: nurlaelamuhammadsaid@yahoo.com

Keywords: Charpy impact; impact signal; impact duration

ABSTRACT – This paper presents the reviews on impact duration from impact signal due to Charpy test. Charpy impact test is conducted at different material with different thickness but at the same of striker velocity. Impact signal is obtained from strain gauge that has been installed to striker and connected to high frequency data acquisition system. The signal is then analyzed by using software of SoMat eDaQ to identify the time period during impact occurs on materials before fractured. The impact duration from experiment is correlated and compared to the theory or previous study. The result from experiment indicates that Aluminium 6061-T6 has higher impact duration compared to Carbon steel 1050 and it was increased with thickness.

1. INTRODUCTION

Impact on a body is happens in very short period of time with large force is imposed. In impact case, crashworthiness an aspect is always becomes major attention in automotive industry because its ability to protect passengers from harmful during crash event. Vehicle that made from material with high impact duration is safer since there are an extended crush space for car protection which can reduce the damage effect to car structure and occupant.

Some ways may be apply in improving the safety condition of vehicles. Samer et. al [1] recommends that improvements on the security level of vehicle structure need to be achieved in order to enhanced the energy absorption capabilities of vehicles. A good and high quality of energy absorber should be designed to dissipate the impact energy irreversibly via plastic deformation of metallic structure. Most of the energy absorbers were developed using metallic thin-walled structure since they tends to deform plastically due to elasticplastic behavior [2].

Charpy impact test is widely applied for many years in engineering field since it is easy to conduct, reliability and low cost. This test usually implemented to study the failure behaviour and investigate the toughness of a material. Some aspects may influence the failure behaviour of Charpy impact such as temperature, notch position, material properties, impact velocity and others.

According to Jang et al. [3], experimental and numerical studies were performed to examine the effects of notch position on the failure behaviour and energy absorption when the Charpy V-notch impact test is made at 1ºC. Studied by Shende et al. [4] claims ductile-to-brittle transition curves may be obtained when the results of a number of tests presented in different temperatures are plotted. When the temperature is reduced through the transition range, the fracture surface changes from one having a 'fibrous' or 'silky' appearance with much distortion at the sides, to one of completely crystalline appearance with negligible distortion.

The main purpose of this study is to compare the impact duration obtained from Charpy impact strain signal with theory. Based on Ali et al. [5], the total impact duration, t_0 can be calculated from the formula shown as follow.

$$t_o = 2.94(\frac{5}{4Mn^1v^{1/2}})^{2/5} \qquad (1)$$

Where total mass, $M = \frac{1}{m_1} + \frac{1}{m_2}$
m_1 = mass of impactor and m_2 = mass of specimen
v = velocity during impact
and $\qquad n^1 = \frac{4\sqrt{R_1}}{3\pi(k_1 + k_2)}$
Where $k_1 = \frac{1-v_1^2}{\pi E_1}$ and $k_2 = \frac{1-v_2^2}{\pi E_2}$
v_1 and v_2 = poisson ratio of striker and specimen, respectively. E_1 and E_2 = Young Modulus for striker and specimen, respectively.
R_1 = radius of a spherical impactor

2. METHODOLOGY

The geometry of Charpy specimen is prepared according to standard in ASTM E23. In this study, the materials that have been used for Charpy impact test are Aluminium 6061-T6 and Carbon steel 1050. Table 1 shows the material properties for both specimens. The impactor of machine is made from steel and assumed to be rigid body since it is not deformable. Material properties for the impactor are 210 GPa (Young modulus), 7.86×10^3 kg/m³ (density) and 0.32 (Poisson's ratio). Other equipment such as strain gauge and data acquisition system are used in order to collect the impact signal. V-notch Charpy impact test is conducted at 5.18 m/s of striker velocity with different thickness of material (5 mm and 10 mm).

Table 1 Properties of specimens[6].

Properties	Aluminium 6061-T6	Carbon steel 1050
Density (kg/m³)	2700	7860
Young's Modulus (GPa)	70	210
Poisson's Ratio	0.35	0.32
Yield strength (MPa)	292	660
Ultimate strength (MPa)	328	675

3.   RESULT AND DISCUSSION

Obtained signal from Charpy test is analyzed by plotting a graph of strain versus time. The graphs are shown as below.
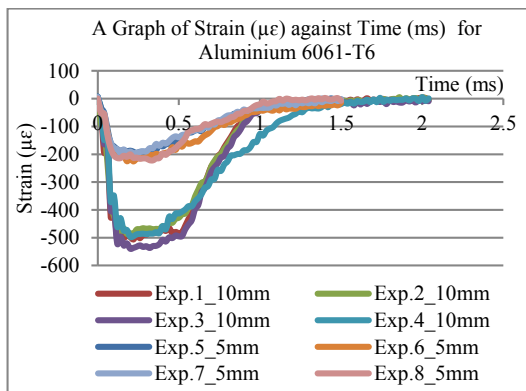
Figure 1: Distribution of strain (μɛ) against time (ms) for Aluminium 6061-T6 at different thickness.
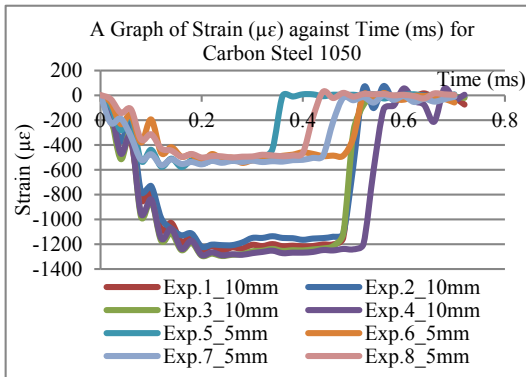
Figure 2: Distribution of strain (μɛ) against time (ms) for Carbon Steel 1050 at different thickness.

Based on the graphs above, the range of impact duration for Aluminium 6061-T6 occurs between 1.1 ms to 1.5 ms and 0.38 ms to 0.60 ms for Carbon steel 1050. For both materials, the highest impact duration was found at the thicker specimen which is at 10 mm. The average impact duration for these specimens is shown in Table 2.

Aluminium 6061-T6 has higher average impact duration compared to Carbon steel 1050. It is because aluminium is more ductile than steel thus it has more elastic and plastic region in stress-strain curve before fracture. Impact duration from theory is calculated by

using equation (1) and the comparison of impact duration between experiment and theory is summarized in Table 3.

Table 2 Average impact duration with different thickness (experiment).

Thickness (mm)	Impact Duration (ms)	
	Aluminium 6061-T6	Carbon Steel 1050
5	1.15	0.49
10	1.43	0.55

Table 3 Impact duration for experiment and theory.

Material	Impact Duration (ms)			
	Experiment		Theory	
	5mm	10mm	5mm	10mm
Aluminium 6061-T6	1.15	1.43	0.0496	0.0654
Carbon Steel 1050	0.49	0.55	0.0597	0.0764

4.   CONCLUSION

The impact duration for Aluminium 6061-T6 and Carbon steel 1050 were identified from both experiment and theory. Experimental result shows that impact duration increased with the increased of specimen thickness. Aluminium 6061-T6 exhibits large impact duration compared to Carbon steel 1050.

REFERENCES

[1] F. Samer, A. Abdullah, and J.O. Sameer, "Enhancement of energy absorption for crashworthiness application : Octagonal-shape longitudinal members," *International Journal of Advanced Engineering and Nano Technology*, no. 2, pp. 1–9, 2015.

[2] L.K.O. K. Hao, A. Radzi, A. Ghani, P. Edi, and K. Yusuf, "Impact energy absorption of concentric circular tubes," *Wseas Transactions On Applied And Theoretical Mechanics*, vol. 4, no. 3, pp. 95–104, 2009.

[3] Y. C. Jang, J. K. Hong, J. H. Park, D. W. Kim, and Y. Lee, "Effects of notch position of the Charpy impact specimen on the failure behavior in heat affected zone," *J. Mater. Process. Technol.*, vol. 201, no. 1–3, pp. 419–424, 2008.

[4] C. J. Shende, A. R. Sahu, A.V. Deshmukh, "Modeling and analysis of hammer of impact testing machine : A review," *Int. J. MEch. & Rob. Res.*, vol. 4, no. 1, pp. 350-354, 2015.

[5] M.B. Ali, S. Abdullah, M.Z. Nuawi, and A.K. Ariffin, "Correlation of absorbed impact with calculated strain energy using an instrumented Charpy impact test," *Indian J. Eng. Mater. Sci.*, vol. 20, no. 6, pp. 504–514, 2013.

[6] M.B. Ali, S.Abdullah, M.Z. Nuawi, and A.K. Ariffin, "Investigation of Energy Absorbed from an Instrumented Charpy Impact on Automotive Specimens," *Appl. Mech. Mater.*, vol. 165, pp. 182–186, 2012.

Cure characteristics and tensile properties of natural rubber vulcanizates modified by tapioca starch

M. Mazliah[1], N. Mohamad[1,*], A.R. Jeefferie[1], A.M. Hairul Effendy[2]

[1] Carbon Research Technology, Faculty of Manufacturing Engineering,
Universiti Teknikal Malaysia Melaka, Hang Tuah Jaya, 76100, Durian Tunggal, Melaka, Malaysia
[2] Faculty of Engineering Technology, Universiti Teknikal Malaysia Melaka,
Hang Tuah Jaya, 76100, Durian Tunggal, Melaka, Malaysia

*Corresponding e-mail: noraiham@utem.edu.my

ABSTRACT – This study focusing on cure characteristics as well as tensile properties of natural rubber (NR) vulcanizates modified with tapioca starch as biodegradability agent. The samples were prepared by melt compounding via a Haake internal mixer. The tapioca starch was varied from 0, 5, 10, 20, 40, and 60 phr in the formulation. Increasing tapioca starch loading was observed to accelerate the curing process meanwhile increases the crosslinks density which depicted by M_H-M_L value. Furthermore, the additional of tapioca starch up to 20 phr increased the elongation of break of the vulcanizate.

1. INTRODUCTION

Over the past few years, the effects of different types of fillers on Natural Rubber compounds have been studied, in search of improvements on their physical and mechanical properties. Recently, the use of fillers from organic nature has been object of interest due to their low cost, light weight, environmentally friendly nature, and because of enhances the mechanical properties of the filled materials [1,2]. Several cellulosic materials such as nut shells, bamboo, ground wood waste, cereal straw and white rice husk have been used as fillers for plastics [3,4] and elastomers [5-6].

Starch is one of the substances most widely found in nature. It is a biopolymer consisting of amylose and amylopectin, present in most plants and in considerable amounts. There are some investigations concerning the reinforcement of elastomers with tapioca starch [7], but only a few report of this material on the physical properties of the elastomers. Thus, the aims of this contribution to assess the potential utilization of tapioca starch in natural rubber formulations, studying the effects of starch content on the rheological and mechanical behaviour of NR composites.

2. METHODOLOGY

2.1 Materials

Composites prepared based on 100 phr of Natural Rubber (NR) SMR-20 and different proportions of Tapioca Starch (TS) at 5, 10, 20, 40 and 60 phr. The NR was obtained from Malaysian Rubber Board and the TS was obtained from a local company. Curing additives for all formulations based on 100 parts of rubber were:

2.5 phr of sulphur (S), 5 phr of Zinc oxide (ZnO), 2 phr of stearic acid, 1 phr of Tetramethyl Thiuram Disulphate (TMTD) and 1 phr of 6PPD. The rubber compound (Figure 1) was prepared using a Haake internal mixer working at 60°C and a rotor speed of 60 rpm for 7 minutes according to ASTM D-3182.

2.2 Testing

The processability of NR compound was the evaluated with cure characteristic assessment in accordance to ASTM D2084 using an oscillating rotorless rheometer model U-CAN Dynatex UR2010 (U-CAN Incorporation, Taiwan). Samples of the respective compounds were tested at 160°C, 4.5 kg cm^{-2} of compression pressure, 1.7 Hz of swing frequency, and 1° swing amplitude within 5 min of curing time. The maximum curing time (t_{c90}), scorch time (t_{s2}), minimum torque (M_L), and the maximum torque (M_H) were determined in this assessment. The torque different (M_H-M_L) were calculated for further analysis of the compound processability. The compounds were subsequently molded with the compression machine 160°C and 150 kgf using hot press model GT7014-A from GoTech (Figure 2).

Figure 1 Rubber compound.

Figure 2 Rubber sheet.

3. RESULTS AND DISCUSSION

3.1 Cure characteristics

Table 1 shows the required time for 90% curing (t_{c90}), the maximum torque (M_H), minimum torque (M_L) and the scorch time (t_{s2}) of the samples. Increasing tapioca starch, shows increasing trend of M_L represents a positive relation of compound viscosity due to solid starch increases compound viscosity. Trends of M_H and crosslink density also increased when increasing in the dosages of starch. This is because solid starch limits the mobility of rubber chains. However, decreasing trends of t_{s2} and t_{c90} shows the compounds become more scorch and shorter in cure time. It may relate to the impurities of starch that accelerate cure and also relates to higher crosslink density.

3.2 Mechanical properties

The experimental data are tabulated in Table 2. The results clearly show that the elongation at break (EB) and modulus at 100, 300 and 500 % of elongation (M100, M300 and M500) increase with an increase in tapioca starch. NR compound with tapioca starch experience a slightly higher result and improvement across all tensile properties. For instance, the EB drastically increased up to 2050 % improvement when 20 phr tapioca starch was added. However, a reduction in TS was encountered for NR compound with higher tapioca starch content due to agglomeration and aggregation of platelets that enables pre-mature failure.

Table 1 Curing parameters of NR/TS.

Sample	M_H dNm)	M_L (dNm)	t_{s2} (min)	t_{c90} (min)	M_H-M_L (dNm)
NR-TS0	26.09	7.92	1.14	1.43	18.17
NR-TS5	26.47	8.25	1.11	1.41	18.22
NR-TS10	28.25	8.36	1.10	1.40	19.89
NR-TS20	32.12	8.83	1.07	1.46	23.29
NR-TS40	33.06	9.43	1.03	1.36	23.63
NR-TS60	35.02	9.47	1.02	1.36	25.55

Table 2 Tensile properties of NR/TS.

Sample	M_{100} (MPa)	M_{300} (MPa)	M_{500} (MPa)	TS (MPa)	ε_r (%)
NR-TS0	5.07	11.38	17.31	17.62	1700
NR-TS5	5.72	11.42	17.62	16.49	1750
NR-TS10	6.00	12.08	17.85	15.58	1800
NR-TS20	6.12	12.44	18.26	14.33	2050
NR-TS40	7.10	12.91	19.52	12.94	1600
NR-TS60	8.05	13.33	20.31	8.60	1450

4. CONCLUSIONS

The curing characteristics and mechanical properties of NR compound were examined as a function of tapioca starch loading. The scorch time, t_{s2} and cure time, t_{c90} decrease with increasing tapioca starch. Tensile modulus increase with increasing tapioca starch in NR compund. However, tensile strength decreases with increasing tapioca starch.

REFERENCES

[1] M.N. Ichazo, M. Hernánde, C. Albano and J. González, "Curing and Physical Properties of Natural Rubber/Wood Flour Composites," *Macromolecular Symposia*, vol. 239, pp. 192-200, 2006.

[2] C. Nakason, A. Kaesman, S. Homsin and S. Kiatkamjornwong, "Rheological and Curing Behavior of Reactive Blending I. Maleated Natural Rubber-Cassava Starch". *Journal Polymer. Science*, vol. 81, pp. 2803-2813, 2001.

[3] G.M. Milena, M.C.B. Radovanovic, and B. Simendic, "Rheological and Mechanical Properties of Wood Flour filled Polyisoprene/ Chlorosulphonated Polyethylene Rubber Blends," *Scientific Paper*, vol. 53, pp. 678-116, 2007.

[4] H. Ismail, M.R. Edyham, and B. Wirjosento, "Bamboo Fibre Filled natural Rubber Composites: The Effects of Filler Loading and Bonding Agent," *Polymer Testing*, vol. 21, pp. 139-144, 2002.

[5] A.W.M. Kahar and H. Ismail, "High-density polyethylene/natural rubber blends filled with thermoplastic tapioca starch: Physical and isothermal crystallization kinetics study," *Journal of Vinyl and Additive Technology*, 2014.

[6] A.W.M. Kahar, H. Ismail, and N.K. Othman," Effects of Dynamic Vulcanization on The Properties of Thermoplastic Tapioca Starch/High Density Polyethylene/Natural Rubber, *Universiti Malaysia Perlis (UniMAP)*, 2012.

[7] A.W.M. Kahar, H. Ismail, and N.K. Othman," Compatibilization Effects of PE-g-MA on Mechanical, Thermal and Swelling properties of High Density Polyethylene/ Natural Rubber/ Thermoplastic Tapioca Starch Blends, *Polymer-Plastics Technology and Engineering*, vol. 51, pp. 298-303, 2012.

A preliminary study of greyscale intensity and deposited electrospun fibres using image analysis technique

F.C. Long[1,*], A.H. Nurfaizey[1,2], M.A.M. Daud[1,2]

[1] Faculty of Mechanical Engineering, Universiti Teknikal Malaysia Melaka,
Hang Tuah Jaya, 76100 Durian Tunggal, Melaka, Malaysia
[2] Centre for Advanced Research on Energy, Universiti Teknikal Malaysia Melaka,
Hang Tuah Jaya, 76100 Durian Tunggal, Melaka, Malaysia

[*]Corresponding e-mail: izah_faizah91@yahoo.com

Keywords: Electrospinning; nanofibres; image analysis

ABSTRACT – The amount of deposited electrospun fibres is difficult to measure due to their extremely small size and mass. In this study, a new method using image analysis technique to predict the amount of deposited fibres is proposed. It is hypothesized that the amount of deposited fibres can be predicted by measuring the greyscale intensity of a sample. Samples were produced and scanned to 8-bit greyscale images and ImageJ software was used to analyze the samples. Preliminary results showed that the greyscale intensities has the potential to be used for measuring the amount of deposited electrospun fibres.

1. INTRODUCTION

Electrospinning is a simple method of producing polymeric nanofibres from polymer solutions using electric charge [1][2]. When an adequate electric potential is applied to the polymer solution (Figure 1) a straight jet of polymer is ejected from the pipette tip before undergoing a spiral looping motion known as the whipping instability [3]. As the jet moves towards the collector, solvent evaporates and fibre stretching continues before landing on the collector as randomly oriented fibres.
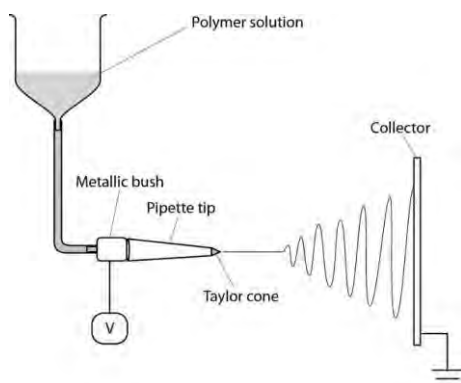
Figure 1 Electrospinning process**.**

Due to the extremely small fibre size and mass, electrospun fibre exhibit unique advantages such as high surface area to volume ratio, light weight, small pore size and high permeability. Electrospun fibres have been proposed in numerous applications such as filtration, tissue engineering scaffolds, drug delivery system and sensors [1]. However, measurements of the deposited fibre amount by means of membrane's physical thickness or mass are difficult to obtain especially at short deposition times. Previously, measurements were made using scanning electron microscope images, digital micrometer and light profilometry. These methods are difficult to manage and could damage the structure of the samples [4]. To overcome the problems, a non-destructive method using image analysis technique to predict the amount of deposited electrospun fibres is proposed.

2. METHODOLOGY

Electrospinning process was carried out using poly (vinyl alcohol) (PVA) with an average molecular weight of 124,000-130,000 g/mol. The PVA was dissolved in distilled water to a final concentration of 8 wt.%. The solution was stirred for approximately 2 hours at 60 ^{0}C using a magnetic stirrer Model C-MAG HS7 (Ika Works, Malaysia). Black A4 papers were used as substrates to aid visibility. These papers were weighed using four figure balance Model AG204 (Mettler Toledo, Switzerland) before and after samples collection. Samples were collected at different deposition times ranging from 1 to 30 minutes. The samples were left overnight to make sure the solvent has fully evaporated. Electrospinning parameters used in this study are summarized in Table 1. Samples were scanned to 8-bit greyscale images using a commercial Canon Model MG5500 scanner and analyzed using ImageJ software (National Institutes of Health, NIH). This software was used to measure the greyscale intensities of the samples. All samples were produced using Model ES1a electrospinning machine (Electrospinz Ltd., New Zealand).

Table 1 Electrospinning parameters.

Parameters	Value
Temperature (^{0}C$^)$	21-24
Humidity (%)	60-75
Voltage (kV)	10
Distance from tip to collector (cm)	10

3. RESULTS AND DISCUSSION

Based on visual observation, the white intensity of the deposition spot increased with deposition time (Figure 2). Furthermore, the size of the white spot also increased as the deposition time increased. A closer examination also revealed that the intensity of the white spot was at a maximum at the centre. These results suggest that the amount of deposited fibres was proportional with deposition time and the densest area was located at the centre of the deposition spot.
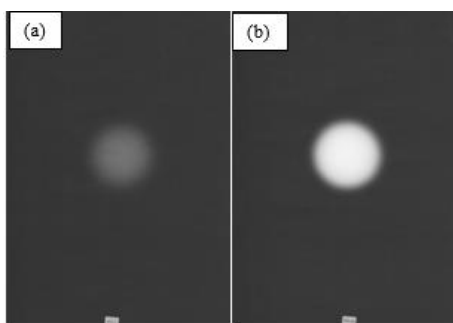

Figure 2 The deposition spot of samples collected at different deposition times (a) 1 minute (b) 15 minutes.

Plots of greyscale intensities from image analysis confirmed the visual findings (Figure 3). The greyscale intensity curves resembling normal distribution curves with minimums at both end of the curves. The peaks of the curves at the centres reasserted the findings that the densest region was located at the centre of the deposition spots. In addition, the peak values of the greyscale intensity curves seem to be proportional with deposition times.
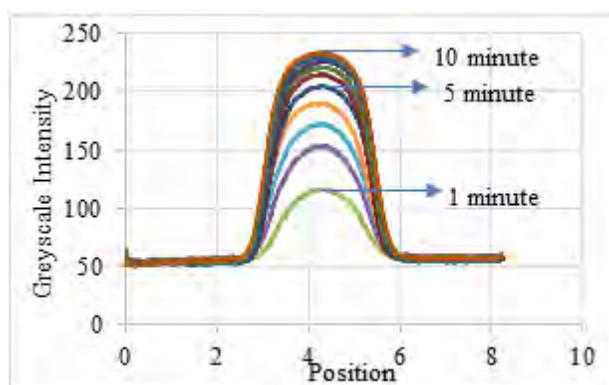
Figure 3 Greyscale intensity curves profiles as a function of position for samples collected at different deposition times.

From Figure 3, the highest peak values of the curves were taken to construct a graph of greyscale intensity versus deposition time (Figure 4). The data produced a curve with a minimum value of 117 for sample of 1 minute deposition time and a maximum value of 233 for sample of 10 minutes. A best fit line was fitted to the data with an R-squared value of 0.88.

Interestingly, a stronger correlation between greyscale intensity and deposition time was found at the lower range of deposition times (inset of Figure 4). This is evidenced by the R-squared value of 0.96. The results suggest that the image analysis technique may be best used at a short deposition times. The inferior result when applying this technique for longer deposition times was most probably caused by the flattening pattern at the higher end of the curve. This was caused by limitations of the scanner in distinguishing the greyscales at the very end of an 8-bit scale.
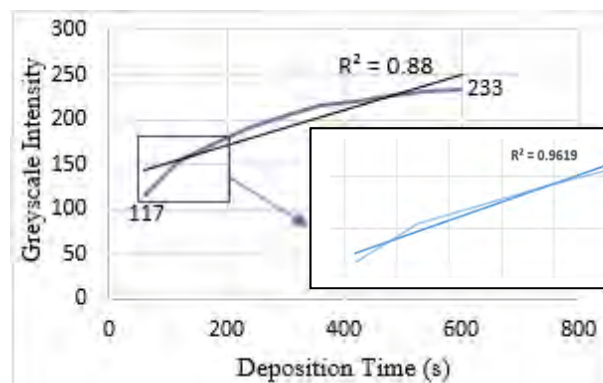
Figure 4 Greyscale intensity as a function of deposition time.

4. CONCLUSION

Visual observations on samples suggested that the amount of deposited fibres increases with time. This finding was confirmed by the greyscale curves obtained from the image analysis. Furthermore, a strong correlation between greyscale intensity and deposition time was found at shorter deposition times. These preliminary results could be an interesting start for a new technique for predicting the amount of deposited electrospun fibres.

REFERENCES

[1] S. Ramakrishna, K. Fujihara, W. E. Teo, T. Yong, Z. Ma, and R. Ramaseshan, "Electrospun nanofibers: Solving global issues," *Mater. Today*, vol. 9, no. 3, pp. 40–50, 2006.

[2] D. H. Reneker and A. L. Yarin, "Electrospinning jets and polymer nanofibers," *Polymer (Guildf).*, vol. 49, no. 10, pp. 2387–2425, 2008.

[3] "Controlling the Spatial Deposition of Electrospun Fibre," 2014.

[4] N. D. N. Affandi, Y. B. Truong, I. L. Kyratzis, R. Padhye, and L. Arnold, "A non-destructive method for thickness measurement of thin electrospun membranes using white light profilometry," *J. Mater. Sci.*, vol. 45, pp. 1411–1418, 2010.

Effect of load on friction and wear of banana peel as an additive

J. Basiron[1], N.A.B. Masripan[1,2,*], M.F.B. Abdollah[1,2], A.H. Husna[1]

[1] Faculty of Mechanical Engineering, Universiti Teknikal Malaysia Melaka,
Hang Tuah Jaya, 76100 Durian Tunggal, Melaka, Malaysia
[2] Centre for Advanced Research on Energy, Universiti Teknikal Malaysia Melaka,
Hang Tuah Jaya, 76100 Durian Tunggal, Melaka, Malaysia

*Corresponding e-mail: norazmmi@utem.edu.my

ABSTRACT – Banana peel is a natural additive which can be used as an additive in the engine oil that can be promotes as a sustainable material development via the usage of renewable resource. In this paper, the preliminary study on the friction and wear of banana peel was mixed into paraffin oil carried out using four ball tester at different load and temperature. Ultrasonic homogenizer was used to mix the banana peel in paraffin oil. Wear scar diameter was measured using inverted microscope. As a yield, the addition of banana peel into paraffin oil has reduced the friction but also increases the wear at different load and temperature.

1. INTRODUCTION

Nowadays, lubrication system is widely being used and it has become the most important part in improving the engine performance and also can reduce friction and wear problems. Lubricant is used to reduce the frictional force between surfaces for most practical usage compared to the surface themselves [1]. Beside, unstable oil prices, the reduction of crude oil reserves in the world and the demand to protect the environment against pollution are all the factors that have attracted interest of researchers in developing alternative lubricant [2].

Vegetable oil is practical and good alternative resource because of their environment friendly, non-toxic and easily biodegradable. The low superior anti-corrosion properties are containing in the vegetable [3]. The banana peel has the capability to be utilised as an alternative lubricant because it could help to reduce the coefficient of friction (COF).

According to research by Mabuchi et al. [4], the frictional coefficient under banana peel as flooring material. They found that, the frictional coefficient was about 0.07 and estimate the polysaccharide follicular gel in banana skin played a dominant role in lubricating effect of banana peel after crush and the alter to homogenous sol. In addition, global production of banana is estimated to be around 48.9 million tons [5]. Hence, it is very essential to investigate the potential of banana peel as an alternative lubricant in terms of friction and wear to ensure it can be adapted by the industry.

2. METHODHOLOGY

In this research, tribology characteristics of lubricant additives (paraffin oil with 5% BP, paraffin oil with 20% BP and paraffin oil with 50% BP) and pure paraffin oil (100%) were conducted utilizing a four ball tester (TR 30L) at different load and temperature as shown in Table 1. The duration period was 30 minutes and the speed was 1000 rpm.

Table 1 Parameters for tribology testing.

Parameter	Value
Load (N)	60, 250, 500
Temperature (°C)	27, 80, 100

The fresh epicarp was ground into small particles by using a blender. Preparation of lubricant sample was determined by using the Equation (1). $V_\%$ is volume percentage $V_{substance}$ is volume of substance and $V_{solution}$ is volume of solution.

$$V_\% = \frac{V_{substance}}{V_{solution}} x100\% \qquad (1)$$

Viscosity index of all lubricants were measured using Brookfield viscometer. Four ball tester was used to determine the friction and wear for all lubricants. Data acquisition system was used to gather the data which generated by four ball tester in form of frictional torque, T (N/mm). The frictional torque was converted to kg/mm in order to utilised in determining the coefficient of friction using equation (2).

$$\mu = \frac{T\sqrt{6}}{3Wxr} \qquad (2)$$

Where, W is the applied load (kg) and r is the distance from center of the contact surfaces on the lower balls to the axis of rotation, namely, 3.67mm.

Wear scar diameter was measured in effort to attain the wear volume losses using inverted microscope.

Equation (3) is expressed to define the wear volume losses. Where, d is the wear scar diameter of ball bearing (mm), R is the radius of ball bearing (mm).

$$V = \frac{\pi(d)^4}{64(R)} \qquad (3)$$

3. RESULTS AND DISCUSION

3.1 Kinematic viscosity index

Table 2 shows the result of kinematic viscosity on four lubricant samples at the different temperatures. From the table, the pure paraffin oil attains higher value of kinematic viscosity than pure paraffin oils. The presence of banana peel as additive in paraffin oil has contributed to the value of kinematic viscosity are lower. This is due to low kinematic viscosity of banana peel.

Table 2 Kinematic viscosity.

Temperature (°C)	Kinematic viscosity (mm²/s)		
	27	80	100
100% PO	24.58	11.20	11.17
PO + 5% BP	24.55	11.00	10.82
PO + 20% BP	24.55	9.23	8.80
PO + 50% BP	24.46	8.76	8.11

3.2 Effect of load on coefficient of friction

Figure 2 depicts the variation of the coefficient of friction (COF) with the load for the various lubricants under different temperatures. There is a decreases of in the COF with the increases in the load. The comparison between pure paraffin oils and lubricant additives is implemented to evaluate the reduction of COF value. Thus, the paraffin oils indicate the higher COF value compared to lubricant additives. The paraffin oils and lubricant additives obtain the lowest value of COF are 0.06 and 0.007 respectively. The reduction of percentage in COF attained of 87.9 %.
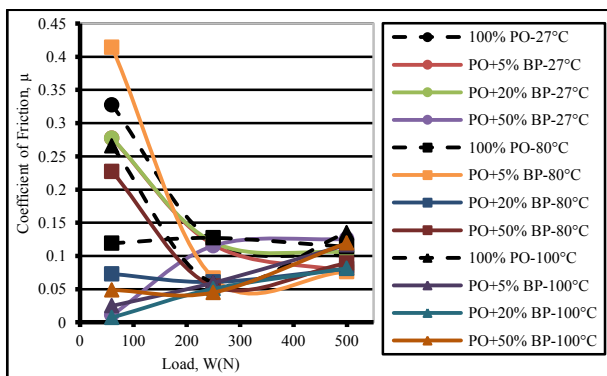
Figure 2 Effect of load on coefficient of friction.

3.3 Effect of load on wear volume losses

Figure 3 shows the effect of different percentage of pure paraffin oils and lubricant additives on the wear volume losses (WVL). The WVL gradually increases with increase in load. The pure paraffin oils and lubricant additives obtain the lowest value of wear volume losses are 3.45 x 10^{-13}m³ and 2.36 x 10^{-12}m³ at 60N respectively. The percentage of WVL by lubricant additives have increased to 85.38%. This result show the use of banana peel as additive is not suitable for reducing wear. This is due to low kinematic viscosity index of banana peel comparing to pure paraffin oil. This will lead to more contact surface during the friction test which increased the wear volume.
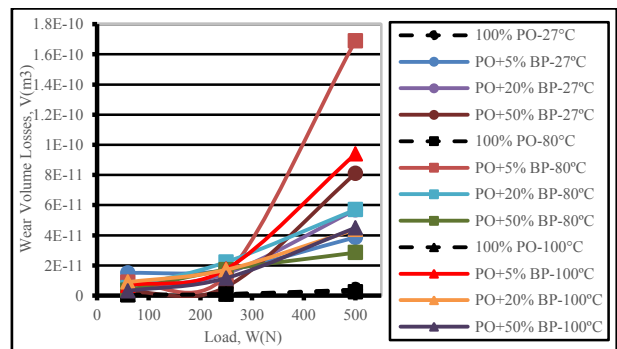
Figure 3 Effect of load on wear volume losses

4. CONCLUSION

The addition of banana peel in paraffin oil significantly affects the tribology characteristics in reducing the friction coefficient at 0.007. However, the wear volume is higher by using banana peel as additive comparing to paraffin based oil.

REFERENCES

[1] I.M. Hutching, Tribology friction and wear engineering material, Cambridge, Butterworth-Heinemann, 1992.

[2] M.A. Delgado, L.A. Quinchia, and C. Galegos, "Viscosity modification of different vegetable oil with EVA copolymer for lubricant applicants," *Industrial Crops and Product*, vol. 32, pp. 607-612, 2010.

[3] J. Salimon, N. Salih, and E. Yousif, "Bio-lubricant: raw material, chemical modification and environmental benefits," *European Journal of Lipid Sciences Technology*, vol. 112, pp. 519-530, 2010.

[4] K. Mabuchi, K. Tanaka, D. Uchijima, and R. Sakai, "Frictional coefficient under banana skin," *Tribology Online*, vol. 7, no. 3, pp. 147-151, 2012.

[5] S.B. Nagarajaiah, and J. Prakash, "Chemical composition and antioxidant potential of peels from three varieties of banana," *Asian Journal of Food and Agro-Industrial*, vol. 4, no. 1, pp. 31-34, 2011.

Friction and wear characteristic of different natural oil-based lubricants with carbon nanotubes as additive

K.F. Yong[1,2,*], B.T. Tee[1,2], M.F.B. Abdollah[1,2], I.S. Mohamad[1,2], C.T. Chong[3]

[1] Faculty of Mechanical Engineering, Universiti Teknikal Malaysia Melaka,
Hang Tuah Jaya, 76100 Durian Tunggal, Melaka, Malaysia
[2] Centre for Advanced Research on Energy, Universiti Teknikal Malaysia Melaka,
Hang Tuah Jaya, 76100 Durian Tunggal, Melaka, Malaysia
[3] Faculty of Mechanical Engineering, Universiti Teknologi Malaysia,
81310 Skudai, Johor, Malaysia

*E-mail: francisyong92@yahoo.com

ABSTRACT – The advantages of natural oil-based lubricant are sustainability and eco-friendly. It is important to study their tribology properties as alternative mineral oils as lubricant. This work investigates the prospects of natural oil-based lubricant for automotive applications in contrast to the available conventional lubricant. The experiment is conducted to obtain the friction and wear characteristics by using four-ball tester set-up. The natural oil-based lubricants involved in this study are refined glycerin and oleic methyl ester with CNT as additive. The results of friction and wear scar diameter for both types of lubricant were shown and compared in this work. From the experiment, refined glycerin with 1% CNT is found to have better friction reduction compared with refined glycerin.
.

1. INTRODUCTION

The tribology study of metal processing has been emphasized nowadays due to the trend is directed toward the machinery world. To increase the life span of machinery system, lubricant is needed. Global environmental awareness encouraged the replacement of mineral lubricant with renewable, sustainability, high biodegradability and eco-friendly lubricant. Palm oil based lubricant constitute as one of the natural oil-based lubricant has the potential to replace the mineral lubricant as alternative lubricant for industrial processes. The performance of lubricants is mainly depending on the friction and wear characteristic [1]. This work investigates the prospects of natural oil-based lubricant for automotive applications in contrast to the available conventional lubricant.

2. METHODOLOGY

To obtain the different characteristics of friction and wear between natural oil-based lubricants with and without the additive, friction and wear test are conducted by using four ball tester. The homogeneous process of lubricant and additive is carried out by using homogenizer instrument. The working principle of four ball tester is that three of the steel ball will be placed at the bottom ball pot and one on the top in the ball chuck. The upper ball is hold in a ball chuck. The bottom three

balls are held in a ball pot containing the test lubricant and pressed against the upper rotating ball. The standard ASTM D-4132 B test condition is as shown in Table 1.

Table 1 Test conditions.

Parameter	Condition
Load (Kg)	40
Duration (Sec)	3600
Temperature (ºC)	75±2ºC
Speed (rpm)	1200±60

For lubricant with carbon nano-tube CNT additive, additive of 1 gram and lubricants of 100 gram are measured by using digital mass measurement instrument. Mixture of lubricant and additive in beaker were put into another metal basin which is filled with water located in the homogeneous instrument. The homogenizer instrument is set to 50 rpm and run for 1 hour. For the four ball tester experiment, all parts in the four-ball were thoroughly cleaned by using acetone and wiped using tissue. Three of the steel ball bearings were placed into the ball pot assembly. The upper spinning ball was locked inside the chuck and tightened into the spindle. The test lubricant was applied into the ball pot assembly with the level which coated all the voids in the test cup assembly. The test lubricants used include refined glycerin (RG) and oleic methyl ester (OME).

The ball pot assembly were fitted in four ball tester machine then connected with the temperature sensor. Once the setting temperature is reached, the drive motor will be operated. After 60 minutes, the heater was turned off and the oil cup assembly was removed from the machine. The test oil in the oil cup was then drained off and cleans it again with acetone. The wear scar area was wiped using a tissue and then viewed by using microscope.

3. RESULTS AND DISCUSSION

After the experiment, the result from four ball tester measurement for Coefficient of Friction (COF) is recorded in Microsoft Excel in computer, the wear scar diameter (WSD) on the three ball-bearings in each experiment was observed and measured using Digital

1

Microscope as shown in Figure 1. The average values of the wear scar diameter were taken. Under the applied conditions, RG with additive delivered the highest average WSD compared to RG without additive. For OME, same result obtained where the WSD for lubricant with additive is higher than the one without additive. The WSD results for both lubricants are shown in Table 3 below. The results show that for both lubricant without additive perform better in forming a thin lubricant film with adsorption of fatty acid which bring to less metal to metal contacts as indicated in previous study [2]. The metallic soap film was rubbed away during the sliding, leading to the production of the non-reactive detergents that increased the wear [3]. The lubricants viscosity was determined under temperature of 40ºC which is as shown in Table 2. From viscosity test, RG show the highest viscosity which show that is perform better compare to OME. Viscosity increase indicates that lubricant has deteriorated by oxidation, while a decrease usually indicates dilution by lower viscosity oil or by fuel [4].

Table 2 Viscosity of Lubricants in cSt.

Parameter	RG	OME
Without additive	404.3	9.5

Table 3 Average WSD on ball bearing in μm.

Parameter	RG	OME
With 1% additive	145.47	173.53
Without additive	136.06	162.51

Figure 1 Sample of measured WSD of RG and SEM.

From friction tests the steady-state condition of the COF is shown in Figure 2. Based on the figure, it indicates that the lubricant layer between ball-bearings was stable and no severe breakdown of lubricant film was occurred. The average values of the COF were calculated for both lubricants with and without adding additive as shown in Table 4.

Table 4 Average of coefficient of friction for different lubricant in μm.

Parameter	RG	OME
With 1% additive	0.059116	0.094960
Without additive	0.071493	0.085170

Referring to table 4, it's shown that, COF of RG with the additive is lower than the one without addictive. This indicates that it perform better than the one without additive in reducing's the friction between two contact surfaces as mentioned in previous study [5].

However for OME it is different case as the one without additive perform better than the sample with with additive. Figure 2 show the COF for OME lubricant with and without additive.
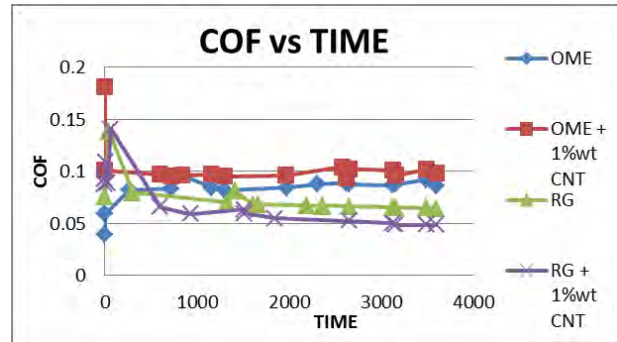

Figure 2 COF of Lubricant.

4. CONCLUSION

The friction and wear characteristic evaluations of natural oil-based lubricants were conducted using a four-ball tester along with lubricants performance analysis with CNT as additive. The addition of additive into lubricating oil has significant influence on the wear mechanism. From the observation on the surface topography of the worn surface, the rough surface that formed helped to create an oil reservoir of the lubricant, and prevented metal-to-metal contact as supported in the previous studied [6-7]. Further tests with different temperature and additive portion will be conducted in future investigation.

REFERENCES

[1] X.Y. Bai, "Theory of tribo-systems," Intech. N.p., 2011, Online access: 6 Oct. 2015.

[2] T. Chiong Ing, A. Mohammed Rafiq, A. and S. Syahrullail, "The effect of temperature on the tribological behavior of RBD palm stearin," *Tribology Transactions*, vol. 55, pp. 539-548, 2012.

[3] F.P. Bowden, D. Tabor, "The Nature of Metallic Wear," *The Friction and Lubrication of Solids*, Oxford University Press, pp. 285-298, 2001.

[4] H.H. Zuidema, the performance of lubricating oil, American Chemical Society, Reinhold Publishing, 1959.

[5] S. Syahrullail, B.M. Zubil, C.S.N. Azwadi, M.J.M. Ridzuan, "Experimental evaluation of palm oil as lubricant in cold forward extrusion process," *International Journal of Mechanical Sciences*, vol. 53, no.7, pp. 549-555, 2011.

[6] N. Zulkifli, M. Kalam, H.H. Masjuki, M. Shahabuddin and R. Yunus, "Wear prevenation characteristic of a palm oil-based TMP(trimethlylolpropane) ester as an engine lubricant," *Energy*, vol. 54, pp. 167-173, 2013.

[7] M.I.R. Azmi, B.T. Tee, N.A.B. Masripan, C.T. Chong, "Preliminary Study of Friction and Wear on Natural-based Lubricants," in *Proceedings of Malaysian International Tribology Conference 2015*, 2015, pp. 220-221.

Effect of duration time of homogenization and sonication on stability of MWCNT-OH in ethylene glycol and deionized water

A. Abdullah[1,*], I.S. Mohamad[1,2], A.Y. Bani Hashim[3], N. Abdullah[4], S. Zainal Abidin[1]

1) Faculty of Mechanical Engineering, Universiti Teknikal Malaysia Melaka,
Hang Tuah Jaya, 76100 Durian Tunggal, Melaka, Malaysia
2) Centre of Sustainability and Environment, Universiti Teknikal Malaysia Melaka,
Hang Tuah Jaya, 76100 Durian Tunggal, Melaka, Malaysia
3) Faculty of Manufacturing Engineering, Universiti Teknikal Malaysia Melaka,
Hang Tuah Jaya, 76100 Durian Tunggal, Melaka, Malaysia
4) Centre for Foundation Studies, Universiti Pertahanan Nasional Malaysia,
Kem Sungai Besi, 5700, Kuala Lumpur, Malaysia

*Corresponding e-mail: amirahabdullah92@yahoo.com.my

ABSTRACT – The limitation of thermal properties in the conventional fluid like ethylene glycol and deionized water can be improved by adding carbon nanotube (CNT) in the solution. However, the dispersion and stability of nanofluid is still a major concerned since CNT is hydrophobic. In this research, functionalized multiwalled carbon nanotube (MWCNT-OH) were used to formulate a nanofluid with additional of polyvinylpyrrolidone (PVP) as dispersing agent and ethylene glycol and deionized water as base fluid. In order to inspect the optimum duration time for ultrasonic homogenizing process which can lead the nanofluid to achieved highest stability, the mixture were inspected at five series of time (1, 3, 5, 10 and 15) minutes. The results show at one minute of synthetisation process of nanofluid already give the stability of t nanofluid.

1. INTRODUCTION

Nanofluid is a suspension of solid nanoparticle of metallic or non-metallic in the base fluid which is ethylene glycol, deionized water or oil. Nanofluids can be used in numerous applications i.e. HVAC, nuclear power plant and electronic cooling system due to its excellent heat transfer performance. However, the dispersion of nanoparticles is yet the main issue while to achieve a very stable nanofluid. In addition, the nature character of CNT itself which is hydrophobic makes it difficult to disperse in the fluid. In the previous research [1], the strong tendency and high aspect ratio of the nanofluid contribute to affect the nanoparticle to have a superior dispersion. Thus, a surfactant or dispersant are used to assist CNT to disperse in the fluid. As previous research [2], the addition of PVP as surfactant in the nanofluid helps to improve the nanoparticles dispersion and offers a better stability. Homogenizer and ultrasonicator used in this research as to stir the nanofluid. The homogenization process can reduce the agglomeration in the nanofluid whilst the sonication can break the intermolecular interaction between the particles. As previous research [3], the high shear rate from homogenization and sonication process can break

the agglomeration particles into single dispersed particles. Furthermore, the higher pressure from the homogenizer makes it the better way to disperse the nanoparticles in the base fluid. Besides, there is no standard time for the sonication process to achieve the stability of nanofluid. For example, the stability of Al_2O_3 nanofluid and CuO nanofluid is achieved on 30 minutes of sonication and titanium-dioxide nanofluid stable at one hour of sonication. In this research, the effect of homogenization and sonication duration time were investigate to inspect the quality of nanoparticles dispersion and stability of MWCNT-OH in ethylene glycol and deionized water.

2. METHODOLOGY

This study used two-step preparation process to synthesis the CNT by mixing of deionized water and ethylene glycol as base fluid with the commercial nanopowder. The nanofluid were formulated using MWCNT-OH develop by Nanostructured & Amorphous Materials, Inc. with additional of PVP produce by Sigma-Aldrich Co. and base fluid (deionized water and ethylene glycol). The mixture were homogenize (Wise Tis HG-15D homogenizer) at 10000 rpm and sonicate (Elma Schidmidbauer GmbH ultrasonicator) at 50 to 60 kHz. The mixture was controlled at room temperature and pH ±9. Five series of times duration for homogenizing and sonicating are setup i.e. (1, 3, 5, 10 and 15) minutes. Next, the behaviour of nanoparticle dispersion and the stability of the nanofluids were monitored for more than 240 hours using Stability Test Rig (STR) as shown in Figure 1 [4].

Figure 1 Stability Test Rig (STR).

3. RESULTS AND DISCUSSION

Based on Figure 2, the result shows that the stability of nanofluids were achieved on the others sample except on NF10 sample. At 15 minutes of synthetisation process (CNT ethylene glycol based nanofluids), the sample shows sedimentation occurs at the bottom of the bottle. The sedimentation only occurs on the ethylene glycol sample. Besides, the stability of nanofluid is achieved in the shorter time. Referring to the Figure 2, synthetisation process of nanofluids at one minutes give the stability. NF1 to NF10 consists of 0.1 wt% CNT and 0.01 wt% PVP. Whilst, the base fluid of the sample NF1 to NF5 is utilizing deionized water and NF6 to NF10 is utilizing ethylene glycol.
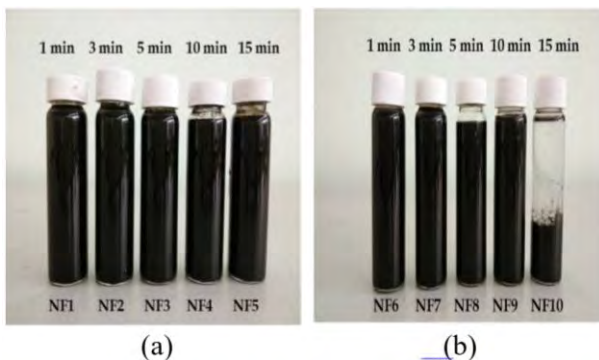

Figure 2 Nanofluids base (a) deionized water and (b) ethylene glycol.

In developing a commercial nanofluid, stability is one of the greatest challenges in the synthetisation of nanofluid. Recent studies [2,4] reveal that the protective role of PVP reduce the agglomeration in the Nnano fluid and resulting to the stability of nanofluids. In addition, the stable nanofluid as surfactants can lower the surface tension of the base fluid and wetting the nanofluids particle. The other factor that can affect the stability of nanofluid is ultrasonic homogenizing. This process is the best method in reducing the nanoparticles agglomeration in the nanofluids. The greater stability of nanofluid is achieved by using the sonicator probe or homogenizer [4]. The higher speed rotation from the homogenizer helps in the dispersion and stability of nanofluid. In addition, the sound waves from the ultrasonicator during the ultrasonic homogenizing process cause the high pressure and low pressure cycle in the nanofluid. Hence, pressures from the ultrasonicator reduce the agglomeration in suspension. The electrostatic or charge from the sonicator contribute to the well dispersion of the CNT in the base fluid. Then, this process contributes in the reducing time of synthesis of nanofluid and make the stability of nanofluid is achieved in the shorter time. Eventhough the ultrasonic homogenizing process help the dispersion of CNT in the base fluid, sedimentation or agglomeration could also occur at the certain times and certain base fluid. As can be seen, the deagglomeration occurs on the CNT ethylene glycol based nanofluid at

15 minutes synthesis process. Thus, the long-time of sonication process also can contribute to the sedimentation in the nanofluid [5]. However, there is no exact or specific sonication time for the sedimentation to occur.

4. CONCLUSION

In conclusion, the ultrasonicating homogenization process giving effect in the stability of CNT in the base fluid (deionized water/ethylene glycol). This process makes the stability of CNT nanofluids were achieved in the shorter time which is one minute. It is because the function of the ultrasonicating homogenization process which reduces and breaks the agglomeration particle in the nanofluids. Therefore it can reduce the time of synthetisation process of CNT nanofluid. But, the long-time of ultrasonicating homogenization process also contribute the sedimentation to occur and it happened on the sample NF10 (15 minutes, CNT ethylene glycol based nanofluids).

REFERENCES

[1] B. Lamas, B. Abreu, A. Fonseca, N. Martins and M. Oliveira, "Assessing colloidal stability of long term MWCNT based nanofluids," *Journal of Colloid and Interface Science,* vol.*381*, pp.17-23, 2012.

[2] S. Mukherjee and S. Paria, "Preparation and stability of nanofluids-A review*," IOSR-Journal of Mechanical and Civil Engineering*, vol.9, no.2, pp. 63-69. 2013.

[3] F.N. Zahari, M.R.H. Noor Salim, I.S. Mohamad, N. Abdullah and S. Thiru, "Thermal properties and heat transfer study of dispersed fluid with functionalized MWCNT particles," *Proceedings of MERD2015*, pp.11-12,2015.

[4] S. N. Syed Idrus, N. S. Zaini, I. S. Mohamad, N. Abdullah and M. H. Mohd Husin, "Comparison of thermal conductivity for HHT-24 CNF based nanofluid using deionized water and ethylene glycol," *Jurnal Teknologi,* vol.77, no.21, pp.85-89, 2015.

[5] D. Rouxel, S. Nguyen, and R. Hadji, "Effect of ultrasonication and dispersion stability on the cluster size alumina nanoscale particle in aqueous solution," *Ultrason Sonochem,* vol.18. pp.382. 2011.

Thermal conductivity enhancement of functionalized multiwalled carbon nanotube and carbon nanofiber based nano-coolant

N.S.N. Abdul Manap[1,*], S.S. Mohd Yunus[1], I.S. Mohamad[1,2], M.H. Mohd Husin[1]

[1] Faculty of Mechanical Engineering, UniversitiTeknikal Malaysia Melaka,
Hang Tuah Jaya, 76100 Durian Tunggal, Melaka, Malaysia
[2] Centre for Sustainability and Environment, UniversitiTeknikal Malaysia Melaka,
Hang Tuah Jaya, 76100 Durian Tunggal, Melaka, Malaysia

*Corresponding e-mail: syahidayatulnisa@yahoo.com

ABSTRACT – Small size and ability to govern high thermal conductivity are the main factor why nanoparticles based coolant has becoming preferable coolant. On this paper, two types of nanocarbon particles were used as a basic material in deionized water named functionalized multiwalled carbon nanotube based nano-coolant (NC1) and carbon nanofiber based nano-coolant (NC2). The weight ratio of the nanocarbon particles is 0.1 wt%, 0.2wt% and 0.3wt% being mixed with deionized water and polyvinylpyrrolidone (PVP). Next, thermal conductivity of NC1, NC2 and standard deionized water (as a reference) was investigated at temperature ranging from 6°C to 40°C. The results show that the thermal conductivity value of NC1 and NC2 are slightly higher than the standard deionized water and increased against the increment of temperature. It also revealed that NC2 with 0.3wt% of CNF at temperature 40°C gives the highest thermal conductivity with a value of 0.661 W/m.K.

1. INTRODUCTION

The low thermal conductivities of conventional heat transfer fluid limit the cooling performance in many industrial applications. The addition of the small amount of nanocarbon in heat transfer fluid contributes to the enhancement of thermal conductivities of the fluid. Commercial coolant with the usage of solid particle such as Cu and Zn might cause the clogging, blockage and corrosion when come to nano-coolant applications due to its sizing. In order to overcome this limitation, nanoparticles such as carbon nanotube and carbon nanofiber were introduced as a based material in nano-coolant since it has very small particles and performs a very good thermal conductivity. Nano-coolant is said to have a better thermal property such as thermal conductivity, heat transfer coefficient and thermal viscosity.

Excellent stability and high thermal conductivity are the two main factors required when preparing a nano-coolant. Since nanocarbon particles surface hydrophobicity limits the nano-coolant to achieved stability, PVP was introduced as dispersing agent which can avoid nanocarbon particles to aggregate and agglomerate [1]. Increase volume of nanoparticles will lead to improve thermal conductivity. Research by Minsta et al. [2] revealed that the increment in particle volume fraction increase the thermal conductivity of the nanofluid as the temperature increased. Thus, this research aimed to study the thermal conductivity pattern of functionalized multiwalled carbon nanotube based nano-coolant (NC1) and carbon nanofiber based nano-coolant (NC2) at various temperatures ranging from 6°C to 40°C.

2. METHODOLOGY

The research were carried out by using two types of nanocarbon which are functionalized multiwalled carbon nanotube (fMWCNT) produced by Nanostructured & Amorphous Materials, Inc. and Pyrograf III High Heat Treated (HHT-24) carbon nanofiber (CNF) manufactured by Pyrograf Products, Inc. Nano-coolant were synthesized with 0.1, 0.2 and 0.3 weight percent (wt%)of nanocarbon particles, mixed with deionized water as a based coolant and polyvinylpyrrolidone (PVP) from Sigma Aldrich which act as dispersing agent.

The mixture then being homogenized at 10000 rpm and undergoes ultrasonication for five minutes. Stability testing is carried out by using the stability test rigs (STR). While the thermal conductivity of the nano-coolant was inspected at various temperature ranging from 6°C to 40°C by using KD2-Pro Thermal Properties Analyzer from Decagon Devices.

3. RESULTS AND DISCUSSION

The result for thermal conductivity against temperature of NC1, NC2 and standard deionized water was presented graphically in Figure 1. The result obtained shows that the trend for the most of the samples for thermal conductivity is increasing steadily with the temperature. Higher thermal conductivity reading is dominated by NC2 sample at all temperatures range. NC2 sample with0.3 wt% gives the highest thermal conductivity value of 0.661 W/m.K at temperature 40°C.

Whilst, the highest thermal conductivity for NC1 sample was recorded at 0.1 wt% with 0.579 W/m.K value at 6°C. However, there is slightly decreasing in thermal conductivity at 0.3wt% of NC1 sample at temperature 40°C. Meanwhile, the highest thermal conductivity for NC1 sample was recorded at 0.3wt% with 0.656W/m.K.
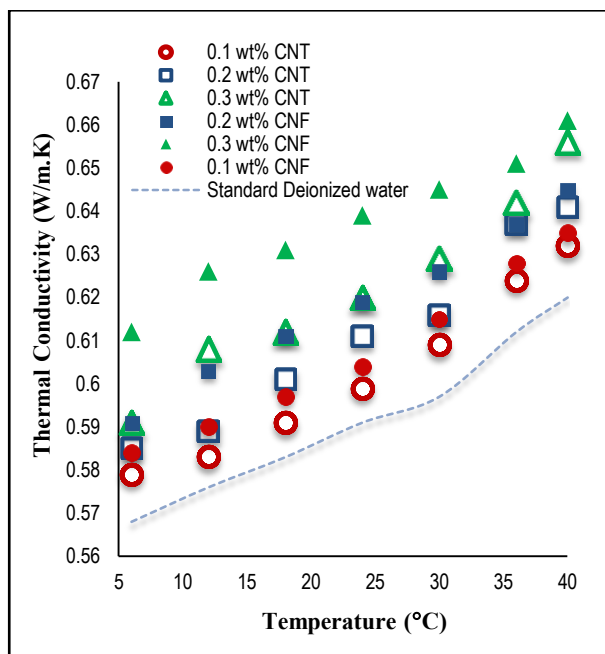
Figure 1 Thermal conductivity of NC1, NC2 and standard deionized water against temperature.

The percentage enhancement (%) of each sample against standard deionized water is calculated using Equation 1 and was tabulated in Table 1.

$$\% \text{ enhancement} = \frac{(\text{T.C of sample} - \text{T.C of based fluid})}{\text{TC of based fluid}} \times 100 \qquad (1)$$

* T.C = thermal conductivity

Table 1 Percentage enhancement (%) of all samples.

Temp (°C)	Percentage enhancement (%)					
	NC1 (wt%)			NC2 (wt%)		
	0.1	0.2	0.3	0.1	0.2	0.3
6	1.94	2.99	4.05	2.82	4.05	7.75
12	1.22	2.26	5.56	2.43	4.69	8.68
18	1.37	3.09	4.97	2.40	4.80	8.23
24	1.35	3.38	4.41	2.2	4.74	8.12
30	2.01	3.18	5.36	3.02	4.86	8.04
36	1.96	4.08	4.90	2.61	4.08	6.37
40	1.94	3.39	5.81	2.42	4.03	6.61

According to the calculation, all samples showed positive enhancement where the enhancing numbers keep increasing as the weight percentage increased. It can be seen that, NC2 shows better enhancement than NC1 with the highest enhancement of 8.68% at 0.3wt% CNF at temperature of 12°C.

As the percentage enhancement depends on the thermal conductivity of nanofluid, thus NC2 leads the enhancement at every temperature ranges compared to NC1. Among the reasons on which NC2 has better thermal conductivity is the bigger surface area. Properties that influenced surface area are number of wall, impurities, hydroxyl and carboxyl functionalized group [3-4]. However, commonly the addition of both CNF and CNT will give superior thermal conductivity compared to any other based fluid due to its characteristics which contributes to physical and chemical properties enhancement of nanofluid. Besides, particle clustering and Brownian motion also affect the thermal conductivity of nano-coolant [5]. Brownian motion occurred due to thermal fluctuation of the solvent, Brownian rates grew stronger resulted more colloidal between nanoparticle thus lead to particle clustering.

4. CONCLUSION

In conclusion, dispersing solid nanoparticles does enhance the thermal conductivity of the based coolant. Temperature as well as weight percentage (wt%) does affected the thermal conductivity of nano-coolant. As the result, thermal conductivity of NC1 and NC2 demonstrate increasing pattern against each temperature, thus resulted better enhancement. A value of 0.661 W/m.K is obtained as the highest thermal conductivity of CNF while 0.656 W/m.K was represent highest thermal conductivity for fMWCNT. NC2 with 0.3 wt% at 40°C showed 8.68% enhancement which stated as highest enhancement among all samples and lowest enhancement throughout this research recorded is 1.22% which represented 0.1wt% of NC1 at 12°C. Thus, additional of CNF in the base coolant showed better thermal conductivity if compared to fMWCNT since the surface area and structure is much higher than fMWCNT.

REFERENCES

[1] S.N. Syed Idrus, N.S. Zaini, I.S. Mohamad, N. Abdullah and M.H.M. Husin, "Comparison of Thermal Conductivity for HHT-24-CNF-Based Nanofluid using Deionized Water and Ethylene Glycol". *Jurnal Teknologi.* eISSN: 2180–3722. vol. 77:21, pp 85-89, 2015.

[2] H.A. Mintsa, G. Roy, C.T. Nguyen and D. Doucet, "Temperature Dependent Thermal Conductivity Data for Water-based Nanoflids", *International Journal of Thermal Sciences.*vol. 48, pp 363-371, 2009.

[3] M.E. Birch, T.A. Ruda-Eberenz, M. Chai, R. Andrews and R.L. Hatfield. "Properties that Influence the Specific Surface Aras of Carbon Nanotubes and Nanofibers". *Oxford Journal: The Annal of Occupational Hygiene.* vol. 57(9). pp 1148-1166, 2013.

[4] N.T. Hung, N.M. Tuong and E.G. Rakov. "Acid Functionalization of Carbon Nanofibers", *Inorganic Material.* vol. 46 (10), pp 1195-1201, 2010.

[5] J. Eapen, R. Rusconi, R.Piazza and S. Yip. "The Classical Nature of Thermal Conducion in Nanofluids", *Journal of Heat Transfer.*vol. 132, pp 1-14, 2010.

Comparison for humidity absorption using various silica gel in experimental chamber

A.A.M. Damanhuri[*], Q.F. Zahmani, A. Ibrahim, S.N. Mokhtar, S.N. Sulaiman, M.R.A. Majid

Faculty of Engineering Technology, Universiti Teknikal Malaysia Melaka,
Hang Tuah Jaya, 76100 Durian Tunggal, Melaka, Malaysia

[*]Corresponding e-mail: amir.abdullah@utem.edu.my

ABSTRACT – Air conditioning are used to absorb humidity. Improper humidity control could affect mold and bacteria growth inside the building. This experiment compare 4 types of desiccant silica which white/ non indicating silica gel, blue indicating silica gel, orange indicating silica gel and calcium chloride. Two sealed experimental chamber $(0.125m^3)$ were used which connected by pipeline. Silica gel are located inside the connection pipelines and result comparison were measured on how effective these silica gel to absorb and reduce humid air by using humidity sensor. Calcium chloride significantly shows the most effective silica gel in absorption of humidity compare to other three types. However, at certain saturated content, solid silica gel of calcium chloride will transform to liquid form. Further investigation are needed to study effectiveness of silica gel for application in real environment either in cases of performance and safety consideration.

1. INTRODUCTION

The acceptable range for specific physical parameter the lead to healthy and comfort for Malaysia typical tropical humid climates are range between 23-26°C while humidity 40-70% [1]. The presence of fungi and bacteria by improper control of relative humidity (RH) may give significant affect to the occupants [2]. Desiccant molecule are hygroscopic substances use for dryness and absorbs moisture which widely used in food product and shoes packaged. The specialized form of desiccant may be in solid form. The use of desiccant in controlling humidity and comfort have been widely used in hotel, office building, medical facilities and homes. Commonly, air conditioning were used to absorb and control space humidity, but this could lead to excessive use of electricity. Meanwhile, the capital cost and initial cost are in decline [3]. Therefore, the aim of this paper are to compare 200 gram desiccant silica gel used to achieve 50-60% of RH based on 4 types solid desiccant silica gel. Meanwhile, referring to Figure 1(b) of blue indicating silica gel that made from cobalt chloride with impregnated and a heavy metal salt. The color will change after the silica gel absorbs moisture and change from blue to pink until desiccant becomes saturated and need to replace. The blue indicate suitable use for electronic equipment with non- dusting packing. Referring to the Figure 1(c) the orange indicating is made from cobalt chloride free organic indicator. Orange indicating silica gel will
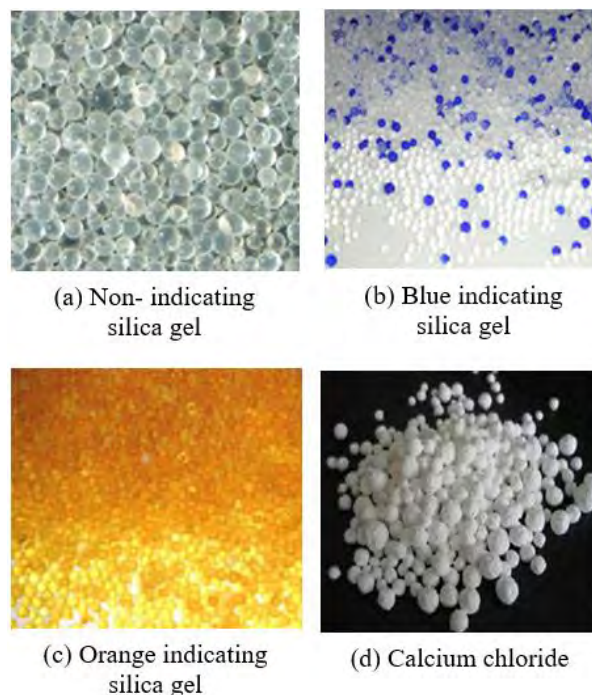
active went absorb moisture and change from orange to yellow color desiccant and change to green when it becomes saturated. This type of silica gel is suitable for food and pharmaceutical products. Meanwhile Figure 1(d) shows calcium chloride that made from ionic compound of calcium chlorine $(CaCl_2)$. The product is common use in refrigeration plants, ice and dust control on road [4] .

(a) Non- indicating silica gel (b) Blue indicating silica gel

(c) Orange indicating silica gel (d) Calcium chloride

Figure 1 Four types of silica gel used.

2. METHODOLOGY

This experiment start with fabrication of small experiment chamber for desiccant testing. Two tightly 0.5m X 0.5 m closed box were selected and connected to each other by using PVC pipe [5].

2.1 Experimental work

Small 50 ft^3/min fan were used to extract the air from the other box [6], and through the silica gel that installed and located inside the PVC pipeline. Figure 2 shows experimental chamber diagram of this experiment carried out. Kettle were put in box A to produce vapor. RH data logger and LEV monitoring device are used to record the through the experiment.

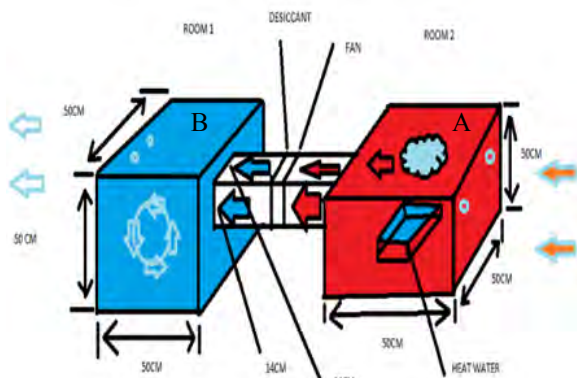Small electric kettle was used to create vapor and located inside box A.

Figure 2 Experimental chamber for silica.

2.2 Experimental procedure

Time interval to record the data is 5 minutes and 3 data were taken. Average data then were tabulated and plotted into graph. Every single changing of silica gel to run the experiment, both box was purged by using mechanical blower to make sure box are really empty and clean. Before running out of this experiment, leak test was performed by using smoke test. Control experiment also runs to compare the readings.

3. RESULTS AND DISCUSSION

Data were recorded through this experiment. Box A were fully vapor which is around 90-100% of RH. Based on Figure 3, after the air through the silica gel that are located at the pipeline, RH at box B were drop to the range between 65-82%. White silica gel/non indicating silica gel and calcium chloride shows significant gradually decrease of RH that are below 70%. This indicate that these type of silica gel could not efficiently absorb humidity. However, only calcium chloride are maintain to be decrease of RH until it reach 51%. Blue silica gel, orange silica gel does not represent good adsorption of humidity compare to calcium chloride. Since calcium chloride to be the most effective silica gel to absorb humidity compare to other three types, calcium chloride however will change to liquid form when it becomes saturated. The solid desiccant then need to be dry using oven at 120 °C for 30 minutes.
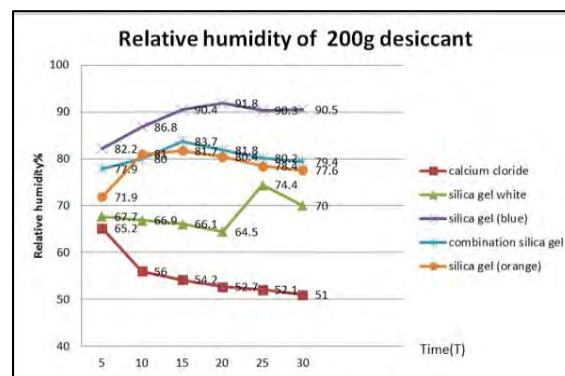

Figure 3 Relative humidity comparison of 200g of 4 types of desiccant.

4. CONCLUSION

In conclusion, solid calcium chloride was effectively absorbing humidity in these small chamber experiment comparing to other three types. However, after fully loaded absorption by humidity process, calcium chloride will change to liquid form and drying process needed to maintain calcium chloride in solid form. Several consideration need to be taken if we want to apply silica gel in dehumidification process depending on the application, material and safety consideration to the human. Further investigation are needed to measure effectiveness of silica gel in real environment.

REFERENCES

[1] DOSH, "Industry Code of Practice on Indoor Air Quality- Department of Occupational Safety and Health Ministry of Human Recources Malaysia," vol. JKKP DP(S), 2010.

[2] A. Chen and V.W.C. Chang, "Human health and thermal comfort of office workers in Singapore," *Build. Environ.*, vol. 58, pp. 172–178, 2012.

[3] A. Pesaran, "A Review of Dessicant Dehumidification Technology," in *Electric Dehumidification: Energy Efficient Humidity Control for Commercial and Industitutional Building Conference*, pp. 1–8, 1993.

[4] L. Moosavi, N. Mahyuddin, N. Ab Ghafar and M.A. Ismail, "Thermal performance of atria : An overview of natural ventilation effective designs," *Renewable and Sustainable Energy Reviews*, vol. 34, pp. 654–670, 2014.

[5] Desicco Pty Ltd T/A Silica Gel Australia, "Sillica Gel Australia," *Available online http://www.silicagel.com.au/Pages/Silica-Gel-Requirement-Guide.Html*, 2013. .

[6] R.W. Haines and C. Lewis Wilson, HVAC System and Design handbook Fourth Edition, McGraw-Hill, 2003.

Preparation and characterization of form-stabilized paraffin/polycaprolactone (PCL) composites as phase change materials

M.S. Aludin[1,2,*], S. Saidatul Akmal[1], Y. Rosiyah[3]

[1] Faculty of Engineering Technology, Universiti Teknikal Malaysia Melaka,
Hang Tuah Jaya, 76100 Durian Tunggal, Melaka, Malaysia
[2] Centre for Advanced Research on Energy, Universiti Teknikal Malaysia Melaka,
Hang Tuah Jaya, 76100 Durian Tunggal, Melaka, Malaysia
[3] Department of Chemistry, Faculty of Science, University of Malaya,
50603 Kuala Lumpur, Malaysia

[*]Corresponding e-mail: aludin@utem.edu.my

ABSTRACT – Paraffinic Phase Change Materials (PCM) possess desirable properties to make it suitable for thermal energy storage applications. However, paraffin has been reported to leak out during the melting process. In this study, composites were prepared by dissolving paraffin and polycaprolactone (PCL) at varied mass compositions in chloroform and then purified through precipitation techniques. The leakage test was conducted by placing the composite samples on a set of four-layer filter papers and left in a furnace at 90°C for 1 hour. By incorporating PCL into paraffin phase, the leakage percentage was drastically reduced. The PCL polymer matrix in the composites may have trapped the paraffin molecules during melting process thus prevent it from leaking.

1. INTRODUCTION

Thermal energy storage (TES) functions as temporary storage of thermal energy in the forms of cold or heat energy. Latent thermal energy storage (LTES) is the most preferred forms of energy storage because it can provide high energy storage density and nearly isothermal heat storage or retrieval processes. Phase change materials (PCM) are materials that can absorb, store and release latent heat of fusion to the environment during melting and freezing processes. Solid-liquid phase change process is shown in Figure 1.
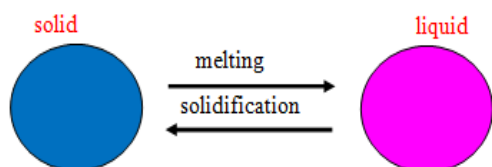

Figure 1 Solid-liquid phase change process.

One of most known PCM is paraffin which possesses desirable properties such as high thermal energy storage and thermal stability to make it the most suitable PCM in thermal energy storage applications. However, the major problem of using paraffin PCMs is leakage during melting process as reported in previous studies [1]. Shape-stabilized PCM, in which the PCM is dispersed in another phase to form a stable composite material, are attracting attention many researchers due their large specific heat, suitable thermal conductivity and the ability to stabilize the shape of PCM during the phase change process [2].

In this study, paraffin/polycaprolactone (PCL) composites were prepared at varied mass compositions in order to obtain form-stabilized PCM composites thus possibly eliminates the leakage problem.

2. METHODOLOGY

2.1 Preparation of paraffin/polycaprolactone composites

The composites were prepared by dissolving paraffin and PCL at varied mass compositions in chloroform and then purified through precipitation techniques by using ethanol solution. The composites were then dried in a fume hood.

2.2 Leakage test

The leakage test was conducted by placing composite samples on a set of four-layer filter papers and left in a furnace at 90°C for 1 hour. Leakage test set-up in a furnace is shown in Figure 2.
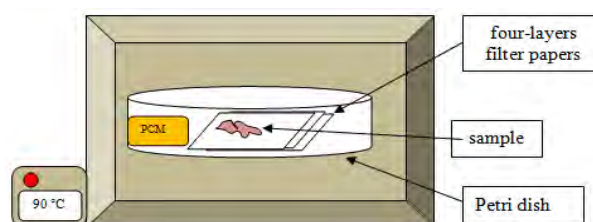

Figure 2 Leakage test set-up.

The leakage percentage was calculated based on the change of sample mass before and after the leakage test.

2.3 Thermal properties of paraffin/PCL composites

The melting temperature and the latent heat of fusion of the composites were measured by Differential Scanning Calorimeter (DSC). The heating rate was set to 10°C per minute.

3. RESULTS AND DISCUSSIONS

The leakage percentage of the composites is significantly lower than that of pure paraffin (leakage percentage 78.4%). Table 1 shows the leakage test results.

Table 1 Leakage test results.

Sample No.	Paraffin/PCL (wt.%)	Leakage Mass	
		(g)	(%)
PCM1	100/0	0.784	78.4
PCM2	80/20	0.251	35.1
PCM3	60/40	0.197	29.7
PCM4	50/50	0.305	30.5
PCM5	40/60	0.001	0.10
PCM6	20/80	0.182	88.2
PCL	0/100	0.000	0.00

The differential scanning calorimeter (DSC) result shows that the melting temperature of the composites did not change much as compared to that of the pure paraffin. Figures 3 shows the DSC curve that indicates the melting temperature and latent heat of fusion of PCM4 (50 mass % paraffin, 50 mass % PCL).
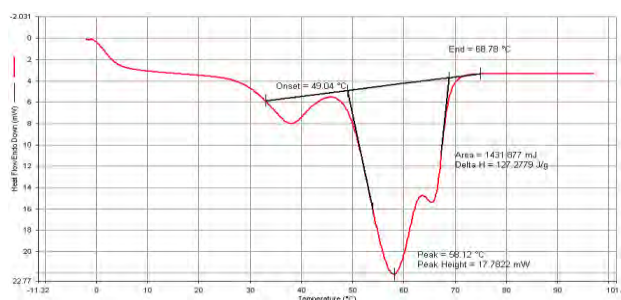

Figure 3 DSC curve of PCM 4.

The melting temperature and latent heat of fusion of the composites that were measured by DSC are shown in Table 2. The heat of fusion of the composites decreased significantly at PCL mass composition 40% to 60%. The composites at these compositions also show the lowest leakage percentage. The composite with 60% PCL shows almost no leakage during the leakage test.

This result indicates that the leakage characteristic of the composites is strongly depends on the heat of fusion of the composites. The lower heat of fusion, the more homogeneous the paraffin phase and the PCL polymer matrix which in turn results in the more stable composite structures.

The PCL polymer matrix in the composites may have trapped the paraffin molecules during melting process thus prevent it from leaking, as illustrated in Figure 4.

Table 2 DSC results of Paraffin/PCL composites.

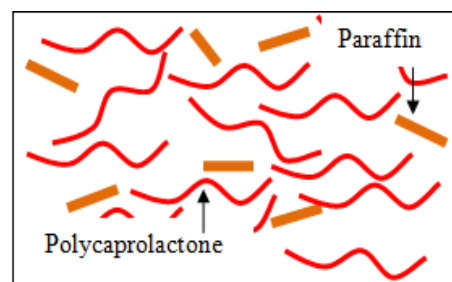| Sample No.	Paraffin/PCL (wt.%)	Melting temp. (°C)	Latent heat of fusion (J/g)
PCM1	100/0	58.97	139.21
PCM2	80/20	59.63	129.06
PCM3	60/40	67.44	85.16
PCM4	50/50	68.78	84.28
PCM5	40/60	67.69	81.44
PCM6	20/80	66.93	102.65
PCL	0/100	64.13	72.13

Figure 4 Paraffin molecules in PCL matrix.

4. CONCLUSIONS

The leakage test results indicated that by incorporating polycaprolactone (PCL) into paraffin phase, the leakage problem that associated to the pure paraffin can be prevented. The leakage characteristic of the composites is strongly depends on the heat of fusion of the composites. These form-stabilized PCMs would potentially become novel candidates of PCM for thermal energy storage applications.

REFERENCES

[1] D. Zhou, C.Y. Zhao and Y. Tian, "Review on the thermal energy storage with phase change materials (PCMs) in building applications," *Applied Energy*, vol. 92, pp. 593-605, 2012.

[2] F. Chen and M. Wolcott,"Polyethylene/paraffin binary composites for phase change material energy storage in building: A morphology, thermal properties, and paraffin leakage study," *Solar Energy Materials and solar Cells*, vol. 137, pp.79-85, 2015.

Investigation of surface breakdown on various solid insulation immersed in ester and mineral oils under ac stress

H. Zainuddin, S.N. Norhan, N.A. Othman*

Research Laboratory of High Voltage Engineering, Faculty of Electrical Engineering,
Universiti Teknikal Malaysia Melaka, Hang Tuah Jaya, 76100 Durian Tunggal, Melaka, Malaysia

*Corresponding e-mail: nadder_zirah91@yahoo.com

Keywords: Creepage discharge; permittivity mismatch; liquid-solid interface

ABSTRACT – Liquid-solid interface is common in high voltage (HV) insulation system. Creepage discharge is a phenomenon that usually occurs along the liquid-solid interface that may cause damage to the surface of solid insulation. This paper presents the effect of various types of solid insulation immersed in liquid insulation on the surface breakdown under AC voltage. In this study, surface discharge experiments were conducted on Eproxy Resin G10, Low Density Polyethylene (LDPE), High Density Polyethylene (HDPE), and Bakelite immersed in Palm Fatty Acid Ester Oil (PFAE) and Mineral oil. Needle-bar method was chosen for the electrode configuration. The results suggest that permittivity mismatch between liquid and solid insulation is an influential factors in creepage discharge among similar materials with different density.

1. INTRODUCTION

Creepage discharge has long been discovered as one of the faults condition found in composite insulation of solid and liquid [1]. The occurrence of creepage discharge promotes a decrease in the value of dielectric strength of the affected liquid-solid interface. There are a few speculated reasons found to be contributing to the occurrence of creepage discharges along a solid insulation, that are, the permittivity mismatch, contamination, surface charging and others.

In previous research [2], pressboard was used as the solid material that impregnated in oil to investigate the partial discharge characteristics at oil-pressboard interface. Oil-pressboard interface is common in high voltage transformer whereby the pressboard serves as the interphase barrier. In [3, 4], the breakdown characteristics of different types of solid materials immersed in mineral oil were studied. This paper on the other hand, investigates the effect of various types of solid insulation immersed in mineral and ester oils on the surface breakdown voltage under AC stress. The electrode configuration is different compared to those reported elsewhere [3, 4].

2. EXPERIMENTAL METHOD

Figure 1 shows the setup for creepage discharge experiment to measure the surface breakdown voltage. The experiment was conducted in an oil bath filled with 4 litres of palm fatty acid ester (PFAE) oil or mineral oil (Gemini-X). A needle-bar electrode configuration as shown in the figure was used with a constant gap distance of 30 mm between the needle tip and earth bar electrode. Epoxy Resin G10, Low Density Polyethylene (LDPE), High Density Polyethylene (HDPE) and Bakelite were used as solid insulation. These solid materials were immersed in the oil to promote liquid-solid interface. AC voltage was applied and increased gradually across the needle electrode and the earth bar until breakdown occurs. All the surface breakdown data were recorded for analysis purposes. The experiment was repeated three times for reliability in obtaining the results.
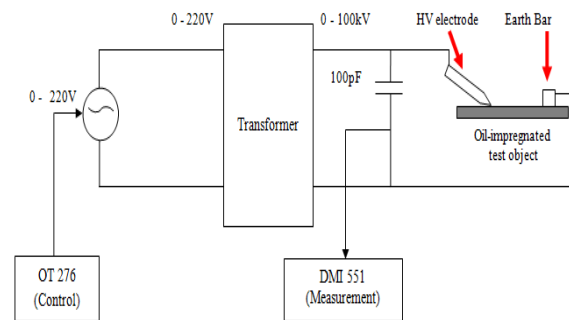

Figure 1 Creepage discharge experiment.

3. RESULTS AND DISCUSSION

Table 1 shows the comparison of average surface breakdown voltage by varying the solid and liquid insulation. The values of permittivity mismatch between oil and solid insulation are also given in the table. The mismatch can be calculated from the permittivity ratio:

$$K = \frac{\varepsilon_{liquid}}{\varepsilon_{solid}} \tag{1}$$

Where, ε_{liquid} and ε_{solid} are the relative permittivity of liquid and solid materials respectively.

From the findings, for a particular solid insulation, it appears that solid immersed in mineral oil has the highest average surface breakdown voltage (BDV) compared to the one that immersed in PFAE oil. This suggests that mineral oil has a better performance compared to PFAE oil regardless the solid materials used in this study and the value of permittivity mismatch.

Generally, for a particular type of oil, the results

show that permittivity matching plays important role in improving the breakdown strength of liquid-solid interface except in the case of Bakelite. This means, the closer the permittivity of solid materials to the liquid permittivity, the higher dielectric strength can be obtained. However, it appears that this rule is invalid when comparison is made with Bakelite suggesting that there are other factors that may influence the breakdown voltage of oil-Bakelite interface. This can be due to the effect of surface roughness, chemical structure, chemical reactions between liquid and solid and etc. which can be further studied. Hence, associating permittivity mismatch among different materials with breakdown strength is inconclusive. On the hand, associating permittivity mismatch among similar material-based like LDPE and HDPE seems more convenient. Both solid materials are differentiated by their density that lead to different permittivity. In the case of mineral oil ($\varepsilon = 2.2$), the BDV value is higher for LDPE ($\varepsilon = 2.3$) as it has a closer permittivity to the mineral oil compared to HDPE ($\varepsilon = 2.35$). However, in the case of PFAE oil ($\varepsilon = 2.95$), the result of BDV is contradict whereby, the BDV value is higher for HDPE since its permittivity is closer to the permittivity of PFAE oil compared to LDPE.

Table 1 Average BDV and Permittivity Mismatch.

Solid Materials	Oil Type	Permittivity Mismatch	Average BDV (kV)
LDPE ($\varepsilon = 2.3$)	PFAE Oil	1.28	31.11
	Mineral Oil	0.956	46.8
HDPE ($\varepsilon = 2.35$)	PFAE Oil	1.25	32.08
	Mineral Oil	0.936	42.89
Epoxy ($\varepsilon = 3.6$)	PFAE Oil	0.82	33.54
	Mineral Oil	0.611	35.77
Bakelite ($\varepsilon = 5.0$)	PFAE Oil	0.59	34.12
	Mineral Oil	0.44	44.64

Note: $\varepsilon_{PFAE} = 2.95$, $\varepsilon_{mineral} = 2.2$

4. CONCLUSIONS

Creepage discharge experiment was conducted in an oil bath under AC voltage. Needle-bar method has been used as the electrode configuration. Several types of solid insulation, i.e. LDPE, HDPE, Epoxy and Bakelite immersed in different insulation oils, i.e. PFAE and mineral oils have been tested. Based on the experimental results, it can be concluded that different types of solid and liquids insulation will affect the surface breakdown voltage at liquid-solid interface. The effects of permittivity mismatch between solid and liquid dielectrics tends to influence the flashover strength of liquid-solid interface. However, this observation is more convenient to be correlated among similar materials with different density. The other factors could be the surface roughness and chemical structure of solid materials as well as chemical reactions that may occur once liquid is in contact with the solid material.

REFERENCES

[1] X. Yi and Z. D. Wang, "Surface tracking on pressboard in natural and synthetic transformer liquids under AC stress", in *IEEE Transactions on Dielectrics and Electrical Insulation*, Vol. 20, No. 5, 2013.

[2] H. Zainuddin, P. L. Lewin, and P. M. Mitchinson, "Partial Discharge Characteristics of Surface Tracking on Oil-impregnated Pressboard under AC Voltage", in *IEEE International Conference on Solid Dielectrics, Bologna, Italy,* June 30- July 4, 2013.

[3] M. Krins, H. Borsi, E. Gockenbach, "Impact of Carbon Particle on The Electrical Strength of Different Solid/Liquid Interface in a Non-Uniform Fields", in *Conference Record of the IEEE International Symposium on Electrical Insulation, Arlington, Virgina, USA,* June 7-10, 1998.

[4] R. J. Taylor, "Effect of Permittivity matching on the Flashover of Solid/Liquid Interface", *Proceedings of the IEEE,* vol. 124, 1977.

Turbulence kinetic energy analysis of a single cylinder engine

A.M.T. Khairil[1], M.T. Musthafah[1,2,*], M.A. Salim[1,2], M.R. Mansor[1,2], M.Z. Akop[1,2], A.M. Saad[1,2], A.M. Mohd Shafei[1]

1) Faculty of Mechanical Engineering, Universiti Teknikal Malaysia Melaka,
Hang Tuah Jaya, 76100 Durian Tunggal, Melaka, Malaysia
2) Centre for Advanced Research on Energy, Universiti Teknikal Malaysia Melaka,
Hang Tuah Jaya, 76100 Durian Tunggal, Melaka, Malaysia

*Corresponding e-mail: musthafah@utem.edu.my

Keywords: Turbulence kinetic energy; computational fluid dynamic (CFD); CNG

ABSTRACT – In the paper show the study of time dependent and turbulence flow inside a cylinder of an alternative engine through the simulation investigation of the distribution of the turbulence kinetic energy in whole chamber. This investigation is carried out during at intake valve. CFD is used to predict the flow behavior in the single cylinder engine. Turbulence model of the inlet air in cylinder has bigger effect into the performance of the engine. Therefore, contours of Turbulence Kinetic Energy are presented to support results. From the results, it is found that the lower valve lifts had better turbulence kinetic energy value.

1. INTRODUCTION

Natural gas is delivered from gas or tied in with unrefined petroleum generation. Natural gas can be compressed and can be stored and use as compressed natural gas (CNG). Furthermore, natural gas is secured than fuel in numerous territory viewpoints. The ignition temperature for natural gas is higher than fuel and diesel. Also, natural gas is lighter than air and will disseminate upward quickly if break happens [1].

This can be accomplished by improving the tumble movement inside the engine cylinder, which upgrades the mean flow and turbulence of the mixture. Producing a huge vortex flows inside the IC engine cylinder amid the intake process generates high turbulence intensity during the later phase of compression stroke prompting quick smoldering rates [2]. In past work clearly delineates that the in-cylinder flows have predominant impact on the engine performance and emission characteristic. Along these lines, a superior comprehension of the in-cylinder flows in an IC engine is all that much crucial for the advancement of the engine parameters [3].

The cylinder speed, the cylinder chamber geometry, fuel utilization, in-cylinder liquid dynamics and ignition devices utilized, speak to distinctive variables that influence the internal combustion [4]. For the most part, the principal air movements were filled into categories such as the rotary movement induced tangentially in the cylinder (swirl) and the rotary movement in the axial plane (tumble) [2]. It is clear that the flow generation with intense vorticity (swirl and/or tumble) in the cylinder during the intake stroke is an efficient tool to obtain a great intensity of turbulence which can be kept up during the compression stroke.

2. METHODOLOGY

The purpose of this study is focused on the flow of the turbulence as well as the method used to analyze the air and fuel flow in the single cylinder engine. The main result obtained were the contours of Turbulence Kinetic Energy.

2.1 CFD simulation analysis

Simulation analysis consists of three elements which are pre-processing, solver and post processing.

2.2 Creation of 3D engine geometry

The geometry was created based on the actual single cylinder engine which is Robin Ey-20D. The process of creating 3D geometry begins with measurements of all parts involved like the intake and exhaust valve, cylinder head, piston, connecting rod and pin and lastly combustion chamber.
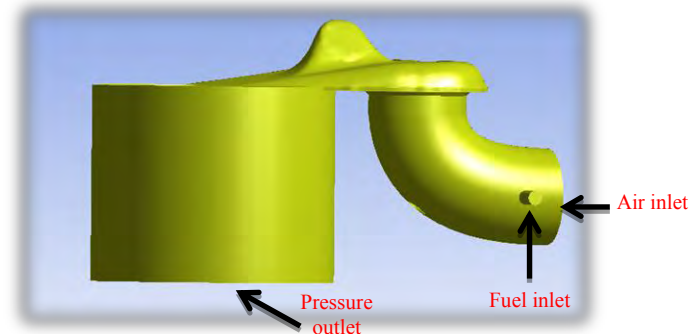

Figure 1 Boundary condition.

2.3 Mole fraction substance of methane, oxygen and nitrogen

The outlet pressure is set to zero in this simulation. The mass fraction at the outlet is calculated. Mass in each mole of the substances and mass fraction are as follows:
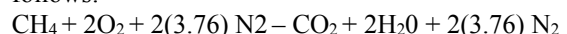
$$CH_4 + 2O_2 + 2(3.76) N2 - CO_2 + 2H_20 + 2(3.76) N_2$$

Table 1 Mass and Mole Fraction.

	Mass in one mole	**Mass fraction**
Methane	16.01	0.05508
Oxygen	64	0.220196
Nitrogen	210.64	0.72472
Total	290.65	

3. RESULTS AND DICUSSION

Results were analyzed and calculated for valve lifts 1.302 mm, 2.604 mm, 3.906 mm, 5.208 mm and 6.51 mm. The results of this simulation were presented in graphical views. Besides, the contour of turbulence kinetic energy, mass fraction and pressure distribution is going to be evaluated.

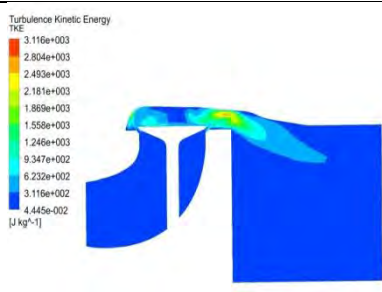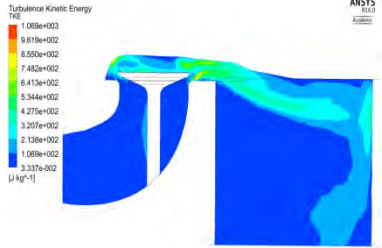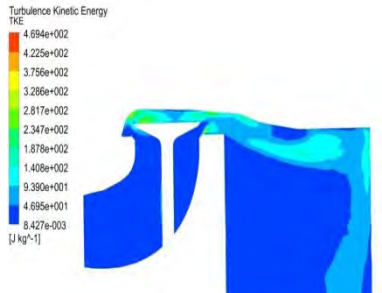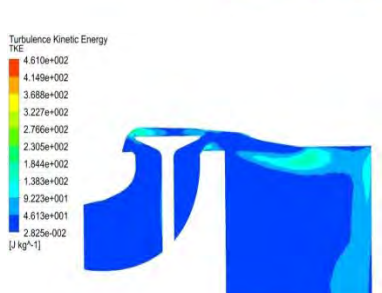Table 2 Turbulence kinetic energy.
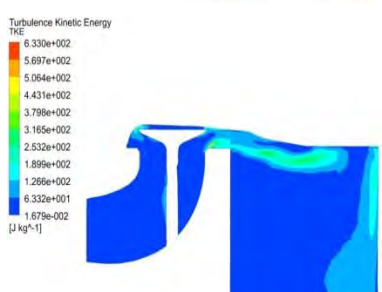
Valve lift	Result	Max. value
1.302 mm		3.116 kJ/kg
2.604 mm		1.069 kJ/kg
3.906 mm		0.4694 kJ/kg
5.208 mm		0.4610 kJ/kg
6.51 mm		0.6300 kJ/kg

Table 2 illustrates the Turbulence Kinetic Energy at the y-z axis at all value lifts. Referring to the table above, the brightest color indicates higher value of Turbulence Kinetic Energy. The brightest colors are more visible at the valve opening. Turbulence represents the irregularity of flows and it is beneficial in gaining the best air-fuel mixing propagation before combustion thus it may increase the combustion rates. Turbulence Kinetic Energy decreases as the value opening is larger due to the decreasing shear rate. For the graph below, it is proven that Turbulence Kinetic Energy is decreasingly as the valve opening increase in value.
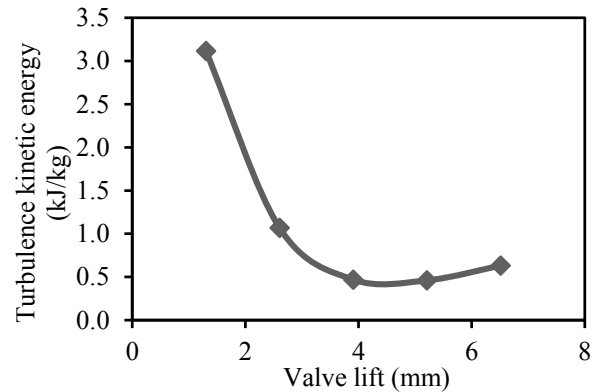

Figure 3 Turbulence kinetic energy for various valve lift.

3. CONCLUSION

At the lower valve lift which is 1.302 mm, the highest turbulence kinetic energy which is 3.116 kJ/kg compared to larger valve lift which is only 0.6300 kJ/kg. Thus, lower valve lift height gives better performance to the engine.

REFERENCES

[1] R.A. Bakar, and Semin, "A Technical Review of Compressed Natural Gas as an Alternative Fuel for Internal Combustion Engine," *Am. J. Engg. & Applied Science*, vol.1 (4), pp. 302-311, 2008.

[2] J.B. Heywood, "Fluid motion within the cylinder of internal combustion engines," *ASME J. Fluids Eng.*, vol.109, pp. 3-35, 1987.

[3] B. Murali Krishna, and J.M. Mallikarjuna, "Tumble Flow Analysis in an Unfired Engine Using Particle Image Velocimetry," *World Academy of Science, Engineering and Technology* vol.54, pp. 430-435, 2009.

[4] Z. Barbouchi, and J. Bessrour, "Turbulence study in the internal combustion engine," *Journal of Engineering and Technology Research*, vol. 1, no. 9, pp. 194-202, 2009.

Friction curve analysis of steel lubricated with jatropha oil

A.M.H.S. Lubis[1,2,*], M.B. Sudin[3], B. Ariwahjoedi[4]

[1] Faculty of Engineering Technology, Universiti Teknikal Malaysia Melaka,
Hang Tuah Jaya, 76100 Durian Tunggal, Melaka, Malaysia
[2] Centre for Advanced Research on Energy, Universiti Teknikal Malaysia Melaka,
Hang Tuah Jaya, 76100 Durian Tunggal, Melaka, Malaysia
[3] Department of Engineering, School of Engineering Science and Technology,
Nilai University, No. 1, Persiaran Kolej, 71800, Nilai, Negeri Sembilan, Malaysia
[4] Department of Fundamental and Applied Science, Universiti Teknologi PETRONAS,
Bandar Seri Iskandar, 31750, Tronoh, Perak, Malaysia

*Corresponding e-mail: munir@utem.edu.my

Keywords: Friction curve; jatropha, four ball test

ABSTRACT – Sliding friction has played a role in many mechanical components such as engines, clutch & brakes, bearings etc.Metal-to-metal contact in sliding motion could results in friction and wear to the metal surfaces. In order to avoid high friction, lubricants are commonly applied to the contacting surface. Although still need to be explored, explanation related to friction process via friction curve is seems to be forgotten. Analysis on the friction curve over the sliding time or sliding distance is important to understand any events during sliding friction. This work is subjected to analyze friction curve of steel lubricated with jatropha oil obtained from four ball-test and propose a sliding friction mechanism under this condition. The friction curve was obtained by four ball testing method under ASTM 4172 method. It is concluded that several friction transition taken place during the sliding friction can be related to the process occurs between the contact asperities.

1. INTRODUCTION

Sliding friction has played a role in many mechanical components such as engines, clutch & brakes, bearings etc. In some application high friction is required and in other application is try to be avoided. Metal-to-metal contact in sliding motion could results in friction and wear to the metal surfaces. In order to avoid high friction, lubricants are commonly applied to the contacting surface. However, there is a condition where the average oil film thickness is about in the same thickness or less than the composite surface roughness thus the contacted surface asperities come into direct contact with each other under relative motion. This condition known as boundary lubrication regime. Therefore, wear and surface damage typically occurs under boundary lubrication. Jatropha oil found to possess good boundary lubrication properties [1], therefore it is considered could

Although still need to be explored, explanation related to friction process via friction curve is seems to be forgotten. Analysis on the friction curve over the sliding time or sliding distance is important to understand any events during sliding friction. This due

to a friction curve transitions is affected not only by the materials involved but also by the applied load and other tribosystem characteristics [2]. Therefore, this study is subjected to analyse friction curve of steel lubricated with jatropha oil obtained from four ball-test so sliding friction process under this condition can be understood.

2. METHODOLOGY

Four AISI E-52100 steel balls with half inch of diameter and 62±2 HRC of hardness were used as solid sample. Jatropha oil obtained from local market was used as lubricants.

Friction and wear preventive characteristics of the lube samples were characterized by four ball method using Ducom TR-701-M6 Multi Specimen Tester unit following ASTM D-4172 standard method. The test was carried out for 60 minutes under 40 kgf of loading. The temperature of oil sample was maintained at 75±3°C and the sliding speed was 1200 rpm. A linear vertical displacement transducer was located between the top and bottom balls to record vertical displacement of both top and bottom steel ball samples. An optical microscope also used to evaluate wear features formed on the sliding surfaces.

3. RESULTS AND DISCUSSION

Friction characteristic of the steel bearing in the presence of jatropha oil as function of sliding time is shown in Figure 1. This figure also shows linear vertical displacement which represent linear wear during the sliding and possible events that were taken place during the sliding.

It is observed that friction of steel in the presence of jatropha oil show a slow increase of friction at the beginning of sliding to its maximum value then after reached the maximum value, the friction slowly decreased.

The behavior of friction show an increases and directly followed by a decreases at the beginning of sliding motion is known as "break-in" period, this behavior is typically followed by a steady friction [3]. This event was taken place for about 15 minute. At this

period, the friction raises were possibly caused by plastic deformation of the surface asperities as the result of loading and sliding. In four-ball testing, the contact is typically categorized as point contact. However the contact action is actually take place on a real area of contact and the load were actually withstand at several tips of asperities. The lubricant layer functioned as connection media which adsorbed to the bearing surface and carried out some part of the load in this situation. When the load was applied and high enough to squeeze the lubricant film, some tip of asperities typically experienced cold weld before the sliding started. The cold weld junction then broken due to shearing action (friction force) whenever the sliding motion started and provides adhesive component of the friction. This event also sequentially and frequently accompanied by engagement and collision of several other tips of asperities, which produce localized elastic and plastic deformation. The dissipation of energy due to these actions typically generate friction and heat [3]. In this event, the point contact has become area contact or it can be said that in microscale diameter of the real contact area were increased due to the cyclic process of friction and wear. Adhesive component from the cold weld action could adhere to other site on the surface and also could chemically react with the oil component to form a new layer so called "tribo-layer" [4,5]. The tribo-layer is a typical thin film that formed due to reaction between the metal surfaces to its surroundings caused by friction. Some deformed asperities may also plow across the surface of the mating surface resulting plastic deformation or elastic hysteresis which contributes to the rise of friction or it also could trapped between the sliding surfaces, abraded both of the mating surface thus give rise in the friction and wear as well. The loosen particle also capable to adhere and scratch other site of the surface and or its counterpart surface with continuation of sliding. The presence of the single hard debris could raise friction, as well as wear, by abrasion mechanism and the adhesion of the particles could increase the friction force by sticking action.
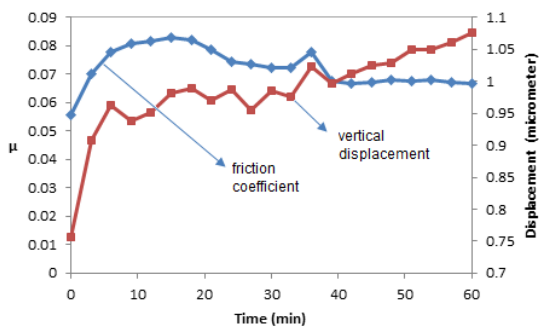

Figure 1 Friction characteristics and vertical displacement of steel in the presence of jatropha oil as function of time obtained by four ball testing.

Figure 2 shows wear scar images obtained by optical microscope. It can be seen scratch marks accompanied by smeared layer observed on the worn surface. This even also observed from the vertical displacement, where around 0.75 μm of the compound thickness already lost at the beginning of sliding and the

fluctuation on the displacement graph is considered related to formation and termination of the tribo-layer. After this event, the steady friction was took places from minutes of 40 to the end of sliding period. The steady friction state was achieved because of tribo-layer was already well maintained and strong enough to withstand the shear from sliding action.
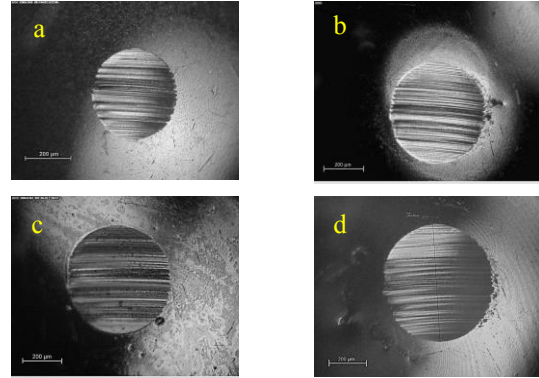

Figure 2 Wear scar feature of worn out bearing in the presence of jatropha at various sliding time; a. 15 minutes, b. 30 minutes, c. 45 minutes, and d. 60 minutes (F: 40 kgf, ω: 1200 rpm, T: 75°C, 100 × mag.)

4. CONCLUSION

It is concluded that several friction transition taken place during the sliding friction can be related to process between contact asperities. Where the process is affected by formation tribo layer, deformation of contact asperities, and capability of the lubricant to flush out wear debris from contact area.

REFERENCES

[1] A.M.H.S. Lubis, M.B. Sudin, and B. Ariewahjoedi, "Four-Ball Study of Tricresyl Phosphate Effect to Jatropha Oil for Transmission Oil Application," *Journal of Applied Science,* vol. 12, pp. 2503 - 2510,, 2012.

[2] P.J. Blau, *Friction Science and Technology; From Concepts to Application*, 2nd ed.: CRC Press, 2009.

[3] S.M. Hsu and R.S. Gates, "Boundary Lubrication and Boundary Lubricating Films," in *Modern Tribology Handbook; Principles of Tribology*. vol. 1, B. Bhusan, Ed., ed: CRC Press, 2001, pp. 455 - 492.

[4] S.M. Hsu and R.S. Gates, "Boundary Lubricating Films: Formation and Lubrication Mechanism," *Tribology International,* vol. 38, pp. 305-312, 2005.

[5] J.-M. Martin, C. Grossiord, T.L. Mogne, and J. Igarashi, "Transfer films and friction under boundary lubrication," *Wear,* vol. 245, pp. 107-115, 2000.

Simulation on comparison of pressure medium in hydraulic hybrid system

Saiful Akmal Sabaruddin[*], Ahmad Anas Yusof, Mohd Noor Asril Saadun

Faculty of Mechanical Engineering, Universiti Teknikal Malaysia Melaka,
Hang Tuah Jaya, 76100 Durian Tunggal, Melaka, Malaysia

[*]Corresponding e-mail: saif_knight90@yahoo.com

ABSTRACT – Natural concerns of fire and safety in hydraulic system promote the uses of water-based hydraulic hybrid system. The main focus of this paper is to simulate the potential of using water hydraulic technology in hydraulic hybrid systems. The research will include an extensive study on the mathematical modeling and simulation by using Matlab/Simulink to determine the feasibility of water compared to oil SAE-30.

1. INTRODUCTION

Typical hydraulic hybrid vehicles depend on petroleum based hydraulic fluid. Typical concerns of fire and safety in hydraulic systems promote the uses of water-based hydraulic system. Mineral oil used in oil hydraulic equipment poses a fire hazard in the event of a spillage or leakage. This is especially critical in vehicle accident scenarios where the oil spillage might trigger fire mishaps as explained in the previous study [1]. Through the usage of water hydraulics, problems related to safety and contamination of oil hydraulics in typical hydraulic hybrid technology can be avoided.

1.1 Hydraulic hybrid system

Hydraulic hybrid system or hydraulic regenerative braking system is a mechanism that store a portion of the kinetic energy that was a momentum as potential energy in the form of pressure. It is stored by a short term storage system, this is done by using a displacement pump to pump hydraulic fluid into an accumulator. That energy is kept until needed by the vehicle, by which the pressure is released from the accumulator as the vehicle accelerates. This pressure will spin the drive shaft while the engine remains idle. As the vehicle achieves the desired speed or the accumulator is emptied, the engine will take over to continue the process that is beyond the capability of accumulator as stated in the previous study [2-3] .

1.2 Hydraulic fluid properties

The implementation of water instead of oils is offers advantages, but certain factors need to be studied in depth in order to match or surpass the current outcome of the oil hydraulics. The specific characteristics of water in term of corrosion, flow erosion, friction, internal and external leakage, lubrication, cavitation, freezing and micro organism are essential prospects that could affect the efficiency of water compared to oil as in previous study [1,4-5].

This project concerns on the effect of novel water-based hydraulic hybrid system. Therefore, the objective of the project is to understand the fundamental knowledge on how to utilize water hydraulics technology. Futhermore, the feasibility of using water as a pressure medium instead of hydraulic oil is analyse.

2. METHODOLOGY

The hydraulic hybrid system is operating in 2 mode which is charge mode and discharge mode. Charge mode occurs while the brake pedal (V1) is pressed that generate the fixed displacement pump which will channel pressurized fluid from low pressure accumulator (AccL) to occupied high pressure accumulator (AccH). Meanwhile, in discharge mode, as the throttle (V2) is pressed, the pressurized fluid stored in the high pressure accumulator (AccH) is release that eventually will operate the fixed displacement motor which will drive the wheel. Besides that, 2 set of 2/2 way directional control valve (V1, V2) are used to control the water flow during charge and discharge mode. Pressure relief valve (PRV) is used to limit pressure in the system. Figure 1 shown fluid circulation as the system in charge mode (red arrow) and discharge mode (green arrow).
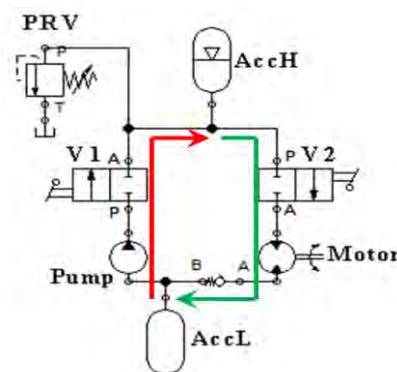

Figure 1 hydraulic hybrid circuit.

The circuit model of water hydraulic is simulate using simulink corresponded to simscape toolbox. Simulation was done by implement water and oil SAE-30 as the pressure medium. Whereas, the output value of torque,T_m and rotational speed,n at motor output shaft are calculated. Torque,T_m and rotational speed,n is given

by the following equation (1,2):

$$n = \frac{q_m \eta_v}{V_g} \tag{1}$$

$$T_m = V_g p \eta_{mech} \tag{2}$$

Where, q_m and p are input flow rate and pressure for hydraulic motor. V_g is volume displacement, η_{mech} is mechanical efficiency and η_v is volumetric efficiency. The following Table 1 and 2 shows the component specification and hydraulic fluid properties that used as the parameter in the simulation.

Table 1 Component specification.

Hydraulic fixed displacement pump	
Max torque (Nm)	500
Max displacement (cm^3/rev)	32
Nominal pressure (bar)	400
Hydraulic fixed displacement motor	
Max displacement (cm3/rev)	107
Nominal pressure (bar)	500
Low pressure accumulator, AccL	
Total accumulator volume (l)	100
Min gas volume (l)	30
Precharge pressure (bar)	5
Initial Fluid Volume (l)	70
High pressure accumulator, AccH	
Total accumulator volume (l)	100
Min gas volume (l)	36.4
Precharge pressure (bar)	100
Initial Fluid Volume (l)	2
Pressure Relief Valve, PRV	
Valve pressure setting (bar)	400

Table 2 Hydraulic fluid properties.

	SAE-30	Water
Parameters		
Relative amount of trapped air	0.005	0.005
System temperature (c)	40	40
Viscosity operating factor	1	1
Fluid Properties		
Nom kinematic viscosity (cSt)	93.9899	0.6572
Nom fluid density (kg/m^3)	878.4	992.6
Bulk modulus (Pa) *	1.68E+9	2.3E+9

* Bulk modulus at atm. Pressure and no gas

3. RESULT AND DISCUSSION

In order to investigate the performance of the system in both medium, a model is implemented in Simulink using corresponded Simscape toolbox as shown in Figure 2.

Simulation results for the comparison of output power produced by the hydraulic motor based on the application of water and oil SAE-30 is showed in Figure 3. The graph indicates that the output power produce by the usage of oil SAE-30 are higher than water which shows 41.3kW are produced at 370.5rpm, meanwhile water produce 34.23kW at 336.2rpm. In other hand, the result shows that water achieve the maximum power at a lower speed compare to SAE-30 due to the occurrence of internal leakage are higher at water, that causes

pressure loss in the system as stated in previous study [1,4]. The condition of internal leakage can be explained by the value of total efficiency in hydraulic motor. The efficiencies of hydraulic components are defined as ratios between its hydraulic power at outlet port and that ones at inlet port. Efficiency of water calculated at the maximum power is 78.7%, whereas SAE-30 is 92.5%.
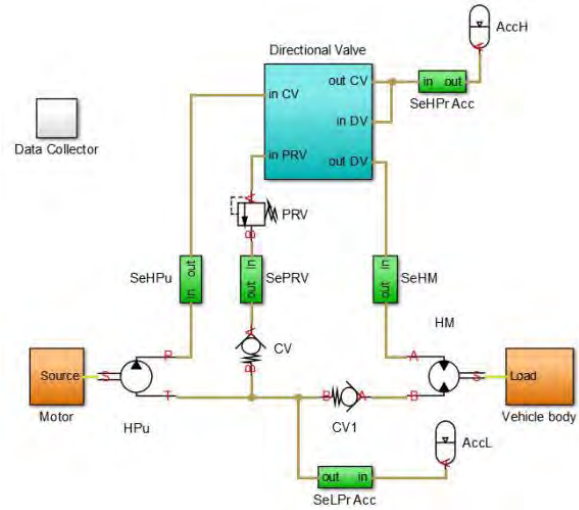

Figure 2 hydraulic hybrid simulation (simscape).

Figure 3 Output power at hydraulic motor.

4. CONCLUSIONS

In this paper, the relationship between oil SAE-30 and water involved in hydraulic hybrid system has been analyzed. Simulation results indicated that oil SAE-30 is more compatible compare to water as the properties which are kinematic viscosity, density and bulk modulus influences the resulted output power and efficiency. In other hand, a small differences of the result should be able to overcome by adjust the diameter of hydraulic hose use in water hydraulic system that eventually will increase the input pressure which will increase the output torque and power.

REFERENCES

[1] G. Krutz and P. Chua, "Water hydraulics—theory and applications 2004," *Proceedings of AETC,* pp. 1–32, 2004.

[2] E. Lindzus and B. R. Ag, "HRB - Hydrostatic Regenerative Braking System : The Hydraulic Hybrid Drive from Bosch Rexroth," 2008.

[3] E.R.A. Kumar, "Hydraulic Regenerative Braking System," *Int. J. Sci. Eng. Res.*, vol. 3, no. 4, pp. 1–12, 2012.

[4] F. Conrad, "Trends in Design of Water Hydraulics - Motion Control and Open-Ended Solutions," *Proc. 6th JFPS Int. Symp. Fluid Power, Tsukuba*, 2005.

[5] K.T. Koskinen, T.Leino, and H. Riipinen, "Sustainable Development With Water Hydraulics-Possibilities and Challenges," *Proc. JFPS Int. Symp. Fluid Power*, vol. 2008, pp. 11–18, 2008.

An experimental study on relation of nonlinearity and transduction coefficient of an electromagnetic energy harvester

P.S. Low[1,2,*], R. Ramlan[1,2], N.S. Muhammad[1,2]

[1] Faculty of Mechanical Engineering, Universiti Teknikal Malaysia Melaka,
Hang Tuah Jaya, 76100 Durian Tunggal, Melaka, Malaysia
[2] Centre for Advanced Research on Energy, Universiti Teknikal Malaysia Melaka,
Hang Tuah Jaya, 76100 Durian Tunggal, Melaka, Malaysia

[*] Corresponding e-mail: lpeising@gmail.com

ABSTRACT – This paper brings about the study of relationship between the degree of nonlinearity and transduction coefficient of an electromagnetic energy harvesting device. The device that exhibit softening nonlinear characteristic is used to perform dynamic test and the transduction coefficient, K across the resonance frequency range is obtained through the relationship of $K = \frac{V}{v}$ where V is the voltage generated per unit of relative velocity, v. Experimental results show that the performance of the transduction coefficient increases as the degree of nonlinearity increases.

1. INTRODUCTION

In an electromagnetic energy harvesting device, the energy conversion performance is greatly reliant on the transduction coefficient, K of the system. According to Challa et al. [1], transduction coefficient defines the relation of mechanical and electrical domains where $K = \frac{V}{v}$ having units of V s m^{-1} with V representing the voltage generated per unit of relative velocity, v. Transduction coefficient is claimed by [1] to have high importance on the coupling strength of an electromagnetic energy harvesting device.

In previous research [1-3], role of linear coupling for electromagnetic energy harvesting device has been studied analytically and experimentally. Sneller and Mann [4] on the other hand studied the performance of nonlinear coupling across the coil axis. In another research, Owens and Mann [5] made comparison of linear and nonlinear coupling with their findings stating that nonlinear coupling performs better under certain circumstances.

However, the relation between coupling strength and degree of nonlinearity is yet to be studied and therefore, in this research, a relation between transduction coefficient and degree of nonlinearity will be studied. Next, the results of transduction coefficient will be used in near future time to draw a relationship between coupling strength and degree of nonlinearity which will not be discussed further in this paper at the moment.

2. METHODOLOGY

An experimental study is carried out in to draw a relationship between degree of nonlinearity and transduction coefficient of an electromagnetic energy harvester device. This device is designed to exhibit the characteristic of a softening nonlinearity.

2.1 Experiment parameter and setup

The nonlinear electromagnetic energy harvesting device is set to parameters listed in Table 1 to undergo the experiment which is known as dynamic test.

Table 1 List of parameter values.

Properties	Data
Coil turn, diameter (mm)	3500, 0.15
Input displacement (mm)	1.0
Length of beam (mm)	50

Figure 1 shows the experimental setup for dynamic test in this research. The device is placed on a LDS V406 shaker and two accelerometer is used during the test, one on the base of the device in order to control the input displacement and another one on the beam of the device to capture the acceleration of the beam across the frequency range of 10Hz to 40Hz. The data from accelerometer is then recorded by a Data Physic analyser. At the same time, an oscilloscope is used to gather the voltage generated from the coil. The nonlinearity of the device is adjusted through magnet gaps of 2mm, 3mm and 8mm representing the decrease in nonlinearity respectively.
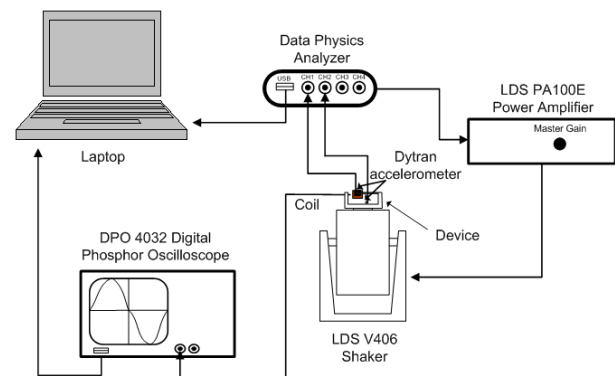

Figure 1 Schematic of dynamic test setup.

3. RESULTS AND DISCUSSION

Transduction coefficient is calculated from the relationship of $K = \frac{V}{v}$ where V is the voltage generated per unit of relative velocity, v across the resonance frequency range of 10Hz to 40Hz. Figure 2 shows graph of transduction coefficient versus frequency for a linear electromagnetic energy harvesting device with an average value of about 3.2 V s m^{-1}.

When a strong nonlinear is applied to the device, that is when the magnet gap is set at 2mm, Figure 3 illustrates the value of K to be about 4.5 V s m^{-1} to 5 V s m^{-1} which is much higher than the linear one. This would justify that a nonlinear electromagnetic energy harvester possess a better K than the linear one. Moving across the decreasing nonlinearity, the value of K decreases to about 3.5 V s m^{-1} and 3.2 V s m^{-1} for 3mm and 8mm magnet gap respectively as shown in Figure 4 and Figure 5.
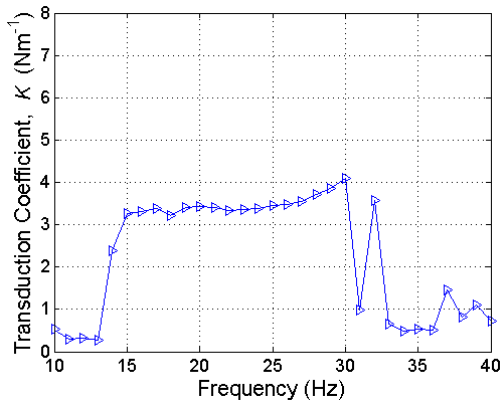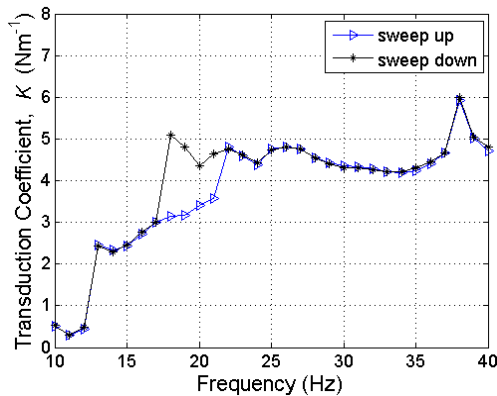

Figure 2 Linear transduction coefficient.

Figure 3 Nonlinear (2mm) transduction coefficient.

4. CONCLUSIONS

An experimental study has been performed to investigate the relation of nonlinearity and transduction coefficient. The results of the experimental study illustrates that the transduction coefficient of a nonlinear electromagnetic energy harvesting device is better than the linear one thus exhibiting that the energy conversion performance of a nonlinear electromagnetic energy harvesting device perform better than the linear harvester. In terms of nonlinearity, the performance of transduction coefficient increases with the degree of nonlinearity. This finding would be beneficial in studying the relation of coupling strength with degree of nonlinearity in near future time.
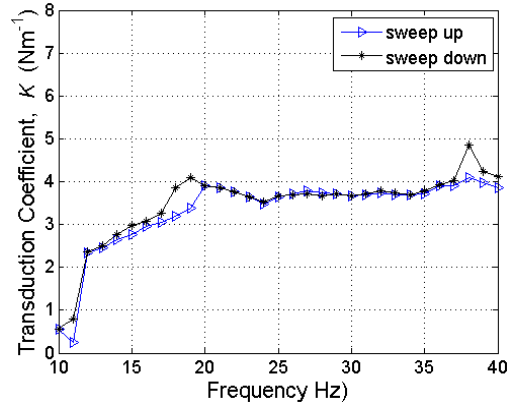

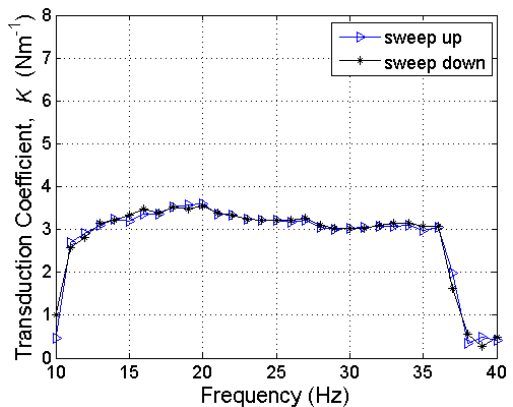Figure 4 Nonlinear (3mm) transduction coefficient.

Figure 5 Nonlinear (8mm) transduction coefficient.

ACKNOWLEDGEMENTS

REFERENCES

[1] V.R. Challa, S. Cheng and D.P. Arnold, "The role of coupling strength in the performance of electrodynamic vibrational energy harvesters," *Smart materials and structures*, vol. 22., pp. 1–11, 2012.

[2] X. Wang, X. Liang, G. Shu and S. Watkins, "Coupling analysis of linear vibration energy harvesting systems," *Mechanical Systems and Signal Processing*, vol. 70-71., pp. 428–444, 2015.

[3] D.F. Berdy, D.J. Valentino and D. Peroulis, "Design and optimization of a magnetically sprung block magnet vibration energy harvester," *Sensors and actuators A:Physical*, vol. 218., pp. 69–79, 2014.

[4] A.J. Sneller and B.P. Mann, "On the nonlinear electromagnetic coupling between a coil and an oscillating magnet," *Journal of Physics D: Applied Physics*, vol. 43., pp. 1–10, 2010.

[5] B.A.M. Owens and B.P. Mann, "Linear and nonlinear electromagnetic coupling models in vibration-based energy harvesting," *Journal of Sound and Vibration*, vol. 331., pp. 922–937, 2011.

Simulation study of high-rise structure model on earthquake movement

M.N. Mustaffa Kamal[1,2], M.A. Salim[1,2,*], A. Md Saad[1,2], M.R. Mansor[1,2], M.Z. Akop[1,2], M.T. Musthafah[1,2], I.R.A. Rosszainily[1,2]

[1] Faculty of Mechanical Engineering, Universiti Teknikal Malaysia Melaka,
Hang Tuah Jaya, 76100 Durian Tunggal, Melaka, Malaysia.
[2] Centre for Advanced Research on Energy, Universiti Teknikal Malaysia Melaka,
Hang Tuah Jaya, 76100 Durian Tunggal, Melaka, Malaysia

*Corresponding e-mail: azli@utem.edu.my

Keywords: High-rise structure model; horizontal vibration; earthquake

ABSTRACT – This paper represents a simulation study of high-rise structure model by exerting horizontal vibration. Three-level of high-rise structure is chosen by referring to Ranau earthquake in 2015. Three analyses were conducted namely stress analysis, strain analysis, and displacement analysis. These analyses were selected as important criteria of horizontal vibration effect on the structure, and finally illustrates the structural behavior of the model. Maximum concentrated stress, maximum strain, and extreme displacement have been recorded. Finally, the conclusion was made, in which all the important criteria were positively proportional to the amount of horizontal vibration energy.

1. INTRODUCTION

Nowadays, modern technologies in seismic and earthquake engineering are very important because many ASEAN countries are affected by recurring events of earthquake. Improvement of material quality, control systems, boundary conditions and many more become mandatory requirements to damp unwanted vibration on high-rise building.

Theoretically, both vertical and horizontal forces appear in high-rise structure. These forces cause the building to sway in multiple directions, from left to the right, and also from top to bottom [1-4]. Many researchers and scientists agreed that new concept and new method of developing high-rise structure are necessary to prevent unwanted behaviors that happened in the past [1-2,5-7].

For instance, this study concentrated in developing new test-rig of high-rise building due to horizontal vibration. It consisted of vertical and horizontal structures. Scatter horizontal forces were applied at every levels, and the response was analyzed by using finite element method.

According to the simulation, three analyses were recorded which were stress analysis, strain analysis, and displacement analysis. Based on these analyses, there were three modes involved to represent the behaviors of the high-rise structure due to horizontal vibration.

2. RESEARCH METHODOLOGY

This section describes the methodology that had been used to analyze the three-level high-rise structure in laboratory scale experiments. The number of levels of

high-rise structures chose in this study was based on the type of structure that were mostly affected during Ranau earthquake [8]. Because of that, this type of structure was selected and referred as baseline model in this study (Berita Harian, 2015).

Initially, this high-rise structure was modeled with horizontal forces exerted at every levels. Three parameters were involved namely height, width, and length with dimension of 800mm, 40mm, and 400mm, respectively.

Additionally, there were five values of forces applied which were 10 newton, 20 newton, 30 newton, 40 newton, and 50 newton. Three modes were involved to demonstrate mechanical behaviors of the high-rise structure when the forces applied to the pillars.

3. RESULTS AND DISCUSSION

Three analyses were recorded which are stress, strain and displacement analysis. Detail discussion of these analyses are necessary because it represents the structural behavior of high-rise structure when horizontal vibration was applied at every levels.

In stress analysis, Figure 1 showed the results in three-dimensional view. According to the results, the concentrated maximum stress occurred when 50 newton of force was applied to the structure. This structure bent at maximum deflection, and it represented in red color. Furthermore, the minimum concentrated stress was recorded when small force was applied. According to this analysis, the concentrated stress of the high-rise structure is positively proportional with the value of the force exerted to the structure.

Figure 2 illustrated the strain analysis for high-rise structure. This analysis was carried out by exerting forces on the structure gradually. Maximum strain occurred when 50 newton of force was applied. Additionally, energy used to expand the material had been applied to develop the high-rise structure model. By using huge amount of forces, it allowed the structure to properly expand. However, this approach can create problem due to huge vibration energy. The structure can easily sway from left to the right, or vice versa because of the huge strain. It increases the potential of the high-rise structure to collapse.

Displacement analysis was the third analysis that was recorded in this study. Three-dimensional results showed in Figure 3. Based on the result, maximum

displacement occurred when 50 newton of horizontal force applied, and located at the top of the high-rise structure. It happened because top of the structure was in free boundary condition, and the structure was free to move at any angles and directions. However, at the bottom of the structure, the displacement was recorded at minimum value because the high-rise structure was embedded into rigid foundation. It can be illustrated as fixed boundary condition, and the structure cannot move easily. Additionally, displacement analysis is an important criterion that needs to be fully understood. Based on this analysis, researchers able to make better judgement on material selection for high-rise structure.
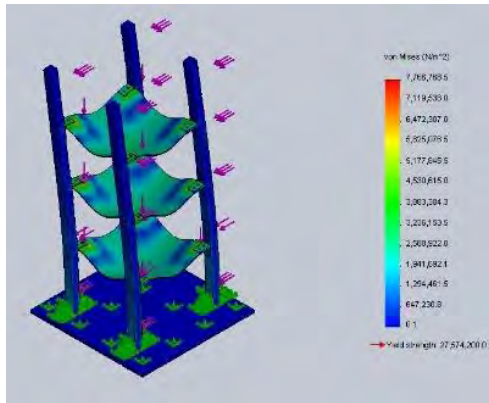

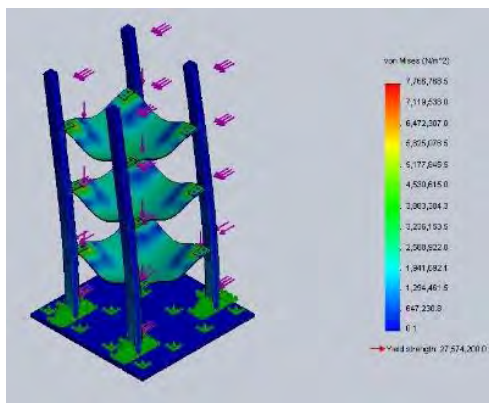Figure 1 Result of concentrated stress for high-rise structure.

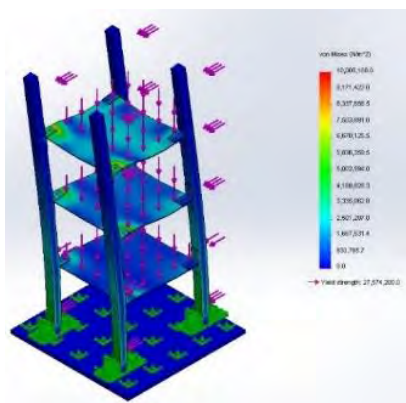Figure 2 Result of strain expanding for high-rise structure.

Figure 3 Result of maximum displacement for high-rise structure.

4. SUMMARY

At the end of the study, the simulation on high-rise structure model has been done. On the other hand, three analyses are accomplished which are stress, strain and displacement analysis to represent the structural behavior of the model. All of these analyses were executed by implementing five fractions of force values which are 10 newton up to 50 newton. One summary can be concluded from all these three analyses. All the studied parameters show positive reaction to the force values, and also proportional to the increasing values of force. According to these analyses, the criteria of the high-rise structure have been examined.

REFERENCES

[1] M.A. Salim, A. Noordin, J. Karjanto, M.Z.M. Rody, "The New Generation of Building Concept to Suppress the Horizontal Vibration During the Earthquake, *Australian Journal of Basic and Applied Sciences*, vol. 5, no. 4, pp. 16–25, 2011.

[2] M. Modirzadeh, S. Tesfamariam, AS. Milani, "Performance based Earthquake Evaluation of Reinforced Concrete Buildings using Design of Experiments", *Expert Systems with Applications*, vol. 39, no. 3, pp. 2919–2926, 2012.

[3] W.W. Sim, I. Towhata, S. Yamada, G.J.M. Moinet, "Shaking Table Tests Modeling Small Diameter Pipes Crossing a Vertical Fault", *Soil Dynamics and Earthquake Engineering*, vol. 35, pp. 59–71, 2012.

[4] H. Tagawa, J. Gao, "Evaluation of Vibration Control System with U-Dampers based on Quasi-Linear Motion Mechanism", *Journal of Constructional Steel Research*, vol. 70, pp. 213–225, 2012.

[5] K. Villarreal, "Effects of MR Damper Placement on Structure Vibration Parameter", in *Proceeding of IEEE Conference Control Engineering*, 2005, pp. 12–44.

[6] M.A. Salim, M.K.M. Nor, M.F. Hassan, "Analysis of Absorption the Level of Vibration Energy in a Building Structure using PID Controller," in *Second International Conference and Workshops on Basics and Basic Applied Sciences & Regional Annual Fundamental Science*, 2009, pp. 99–105.

[7] C. Maniatakis, C.C. Spyrakos, "A New Methodology to Determine Elastic Displacement Spectra in the Near-Fault Region," *Soil Dynamics and Earthquake Engineering*, vol. 35. pp. 41–58, 2012.

[8] http://beritaharian.sg/dunia/54-gegaran-susulan-berlaku-selepas-gempa-di-sabah. Accessed on 21 Oktober 2015.

Enhancement on acoustical performance of reed 'Imperata Cylindrica'

F.A. Khair[1], A. Putra[1,2,*], M.J.M. Nor[1,2], M.Z. Selamat[1,2]

[1] Faculty of Mechanical Engineering, Universiti Teknikal Malaysia Melaka,
Hang Tuah Jaya, 76100 Durian Tunggal, Melaka, Malaysia
[2] Centre for Advanced Research on Energy, Universiti Teknikal Malaysia Melaka,
Hang Tuah Jaya, 76100 Durian Tunggal, Melaka, Malaysia

*Corresponding e-mail: azma.putra@utem.edu.my

ABSTRACT − Common established work on finding the alternative sound absorbing materials are mostly focused on fibrous type of acoustic absorber. Here, the hollow structure of natural reed is utilized as non-fibrous acoustic absorber. This paper study on the acoustic performance of reed when covered with fabric. The sound absorption coefficient is measured using impedance tube method. Result shows that covering sample with fabric enhanced the absorption coefficient above 0.9 for both small and large diameter of length 2 cm and 3 cm.

1. INTRODUCTION

Synthetic fiber are good in sound absorption but it is found that the fabrication process produce carbon dioxide to atmosphere and from Life Cycle Assessment done by Asdrubali [1] also shows high value of global warming potential. This has brought concern of researchers in finding alternative sound absorbing materials made from natural material. Ismail et al. [2] studied Arenga pinnata fiber from palm sugar tree as sound absorber and made comparison with that of the coir and oil palm fibers. Results show that Arenga pinnata has better sound absorption coefficient which is 0.75-0.9 above 2 kHz compared to coir fiber, but slightly lower than the palm oil fiber. Ersoy and Kucuk [3] measured the sound absorption of industrial tea leaf fiber and found that thickness of 10 mm exhibits better sound absorption when backing with a single cotton cloth where the absorption coefficient increases to 0.8 at frequency above 3.5 kHz compared to polyester and polypropylene based non-woven fiber. However, most of the research are focused on the fibrous type of absorber. Thus, this paper presents the non-fibrous acoustic absorber from hollow structure of reed.

2. METHODOLOGY

The stem of the reed is hollow and inside the hollow stem contains porous white pith which can help to absorb the incoming sound energy. The stem of reed is cut into 2 cm and 3 cm and are grouped into small diameter which is between 0.2 cm to 0.4 cm and large diameter between 0.5 cm to 1 cm. The samples were arranged axially in the tube where the cross section of the sample was facing the sound incident as shown in Figure 1(a) tested with single layer of felt fabric with thickness of 0.2 cm that covered either front side or both

sides of the reed as shown in Figure 1(b). The attachment of fabric as a facing surface for sound absorber is common in practice for performance, protection and artistic purposes.

The measurement of the sound absorption coefficient and the experiment setup is done according to ISO 10534-2:2001 [4] as shown in Figure 2. The tube has diameter of 33 mm diameter with sample located at one end of the tube while the other end is a speaker that generates white noise into the tube. Incident and reflected wave signal is recorded by two pre-polarized free field microphone that equipped with pre-amplifier. The sound wave signal is then converted to digital signal by RT Pro Photon analyzer.

(a) (b)

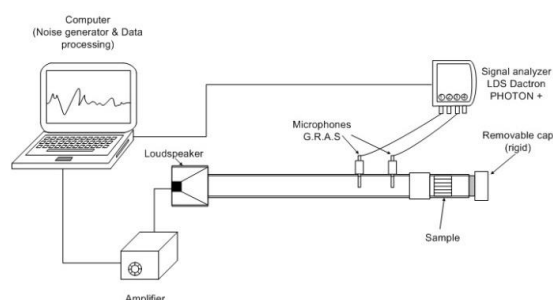Figure 1 Sample of reed (a) in axial arrangement and (b) with attachment of felt fabric.

Figure 2 Experimental setup.

3. RESULTS AND DISCUSSION

In previous study by Khair et al. [5], it is found that reed of length 2 cm and 3 cm with small diameter have absorption coefficient almost 0.9 at frequency 3.6 kHz. Large diameter of reed of length 2 cm have absorption coefficient 0.76 while 0.64 for length of 3 cm. The samples were tested with single layer of felt fabric covered the front and back surface of the reed in order to observed any improvement on sound absorption coefficient. Figure 3 shows the comparison of absorption coefficient reed of small diameter with and

without fabric cover at front side only. Both the 2 cm and 3 cm lengths of reed have the same features of absorption coefficient where the absorption coefficient increase constantly over the frequency with the fabric covering the surface.
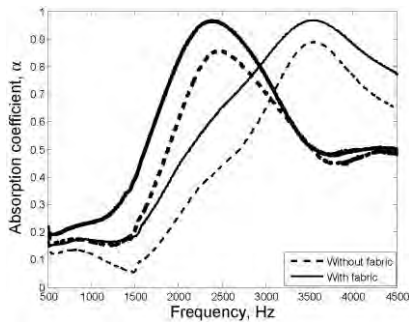

Figure 3 Absorption coefficient of small diameter of reed with attachment of fabric at the front side only with length 2 cm (thin line) and 3 cm (thick line).

Figure 4 shows the effect of sound absorption coefficient of large diameter of reed with attachment of fabric also at front side only which also shows the effect of the fabric to significantly improve the sound absorption. The same treatment has been shown to be successful in the existing works for paddy fiber [6].
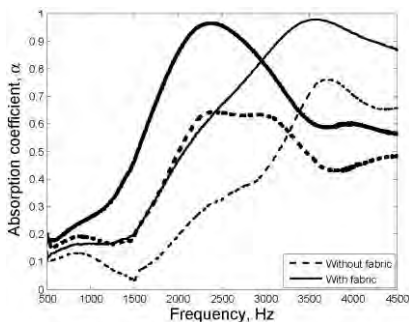

Figure 4 Absorption coefficient of large diameter of reed with attachment of fabric at the front side only with length 2 cm (thin line) and 3 cm (thick line).

Figure 5 shows the results comparing the small and large diameter of reed with attachment of fabric at front side and also at both sides of the sample. It can be seen that no significant improvement can be obtained by adding the fabric to the back layer. Thus only single front layer is sufficient and improvement at lower frequency can be obtained by increasing the air gap between the reed and the back rigid surface.

4. CONCLUSION

Overall, reed itself shows good potential in absorbing sound. By covering the sample with fabric, it improves and enhance the sound absorption performance and also widen the frequency bandwidth. Only covering front side of the sample is sufficient to have absorption coefficient above 0.9.
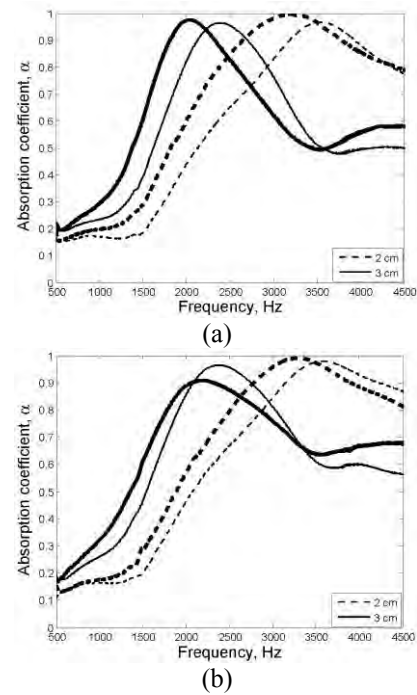

(a)

(b)

Figure 5 Absorption coefficient of reed with attachment of fabric at one side (thin line) and both side (thick line) of sample with reed of (a) small diameter and (b) large diameter.

REFERENCES

[1] F. Asdrubali, S. Schiavoni and K.V. Horoshenkov, "A review of sustainable materials for acoustic applications," *Building Acoustics*, vol. 19, no. 4, pp. 283-312, 2012.

[2] L. Ismail, M.I. Ghazali, S. Mahzan, A.M.A. Zaidi, "Sound absorption of Arenga Pinnata natural fiber," *World Academy of Science, Engineering and Technology*, vol. 67, pp. 601-603, 2010.

[3] S. Ersoy, and H. Kucuk, "Investigation of industrial tea-leaf-fibre waste material for its sound absorption properties," *Applied Acoustics*, vol. 70, no 1, pp. 215–220, 2009.

[4] ISO 10534-2. (2001). Acoustic determination of sound absorption coefficient and impedance tubes part 2: transfer function method, 2001.

[5] F.A. Khair, A. Putra, M.J.M. Nor, and N. Atiqah, "Investigation on reed Imperata Cylindrica as sound absorber," in *Proceedings of Mechanical Engineering Research Day 2015,* 2015, pp. 91-92.

[6] A. Putra, Y. Abdullah, H. Efendy, W.M.F.W. Mohamad, N.I. Salleh, "Biomass from paddy fibers as sustainable acoustic material," *Advances in Acoustics and Vibration*, vol. 2013, pp. 1-7, 2013.

A simulation study on the modal analysis of perforated plates

A.Y. Ismail[1,2,*], A. Ahmad[1]

[1] Faculty of Engineering Technology, Universiti Teknikal Malaysia Melaka,
Hang Tuah Jaya, 76100 Durian Tunggal, Melaka, Malaysia
[2] Centre for Advanced Research on Energy, Universiti Teknikal Malaysia Melaka,
Hang Tuah Jaya, 76100 Durian Tunggal, Melaka, Malaysia

[*]Corresponding e-mail: ahmadyusuf.ismail@utem.edu.my

ABSTRACT – This paper presents a comprehensive modal analysis study of perforated plates with micro and macro size holes as one of the most important aspects in engineering vibration point of view. The Finite Element Method (FEM) in SolidWorks environment is employed to simulate the phenomena and visually present the results. It is found that the presence of holes apparently shifts the natural frequency gradually towards the lower value. As the holes size increases, the natural frequency is proportionally reduced.

1. INTRODUCTION

Perforated plates, either micro or macro size holes, have been widely used in many engineering application [1]. Besides its unique and attractive looks, the perforated panel can also provide many engineering benefits i.e. considerable structural strength and good acoustical performance. Researches on the micro and macro-perforated panel have also been conducted particularly for their acoustical performances [2–4]. Even so, there has been a lack of comprehensive knowledge on the structural mechanical behaviour especially for micro-perforated plate since the existing studies were only conducted in separate ways and for their own particular purposes. Therefore, this paper presents a comprehensive modal analysis study of perforated plates with micro and macro size holes as one of the most important aspects in the structural engineering point of view. This study is an extensive work of Burgemeister and Hansen whereas only macro-holes were considered in the discussion [5]. The Finite Element Method (FEM) in SolidWorks environment is employed to simulate the study and visually present the results.

2. METHODOLOGY

A simply supported square aluminum plate 15 x 15 cm with 2 mm thickness is made in Solid Works environment as a sample. The plate is varied from solid to perforated with gradual holes size increment. Figure 1 shows the initial design of the solid and perforated plate in Solid Works.
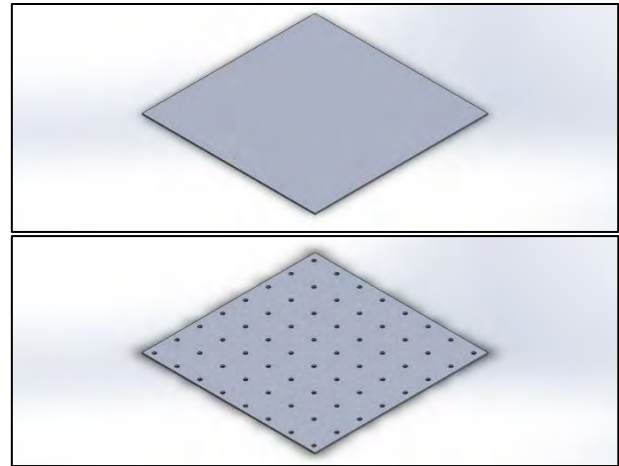

Figure 1 Solid (top) and perforated plates (bottom).

The hole diameter is made to be 0.5 mm to represent micro-holes and 1.5 mm to represent macro-holes. The perforation ratio, however, is kept constant at 0.5% of the plate area. Figure 2 shows the example of finite element models of the perforated plates.
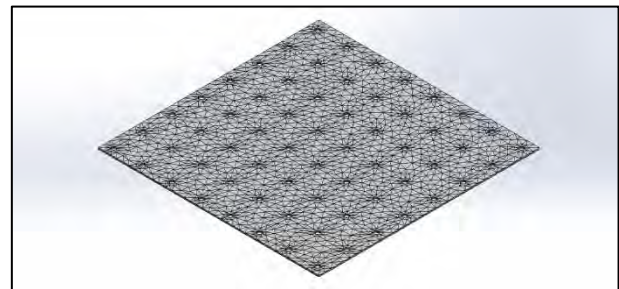

Figure 2 Finite element models of the perforated plate.

3. RESULT AND DISCUSSION

Figure 3 to 7 show the example of FEM result of the perforated plate showing the 1st to the 5th mode shape of both micro and macro-holes. Table 1 shows the frequency value from 1st to 5th mode shape.

It can be seen that the presence of holes gradually shifts the natural frequency to the lower value. For the 1st mode, micro-holes give 9 Hz lower natural frequency than that of solid plate while macro holes shift up to 13 Hz lower. For the 2nd mode and further, the shifting is even higher. Micro-holes shifting is up to 29 Hz while macro-holes is up to 30 Hz. This is happened because

the presence of holes apparently affects the mass of the panels. Micro-holes on the plate reduces the panel mass and macro-holes obviously reduces more. At the same time, the stiffness of the panel is reduced accordingly. As the natural frequency significantly depends on those two parameters, the reduction on both will eventually shifts the natural frequency to the lower level.
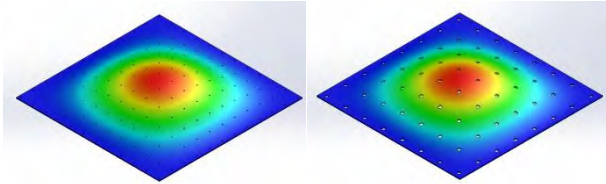
Table 1 Mode shape frequency (Hertz).

Plate	1st	2nd	3rd	4th	5th
Solid	404.14	829.63	830.01	1260.6	1489.9
Micro holes (0.5mm)	393.08	801.69	801.87	1182.2	1437.6
Macro holes (1.5mm)	391.49	799.74	800.14	1181.3	1437.7

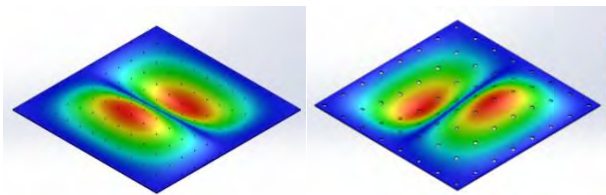

Figure 3 1st mode of the perforated plate.
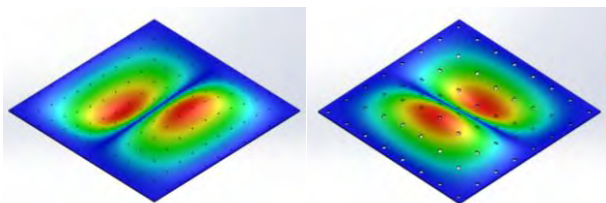

Figure 4 2nd mode of the perforated plate.

Figure 5 3rd mode of the perforated plate.

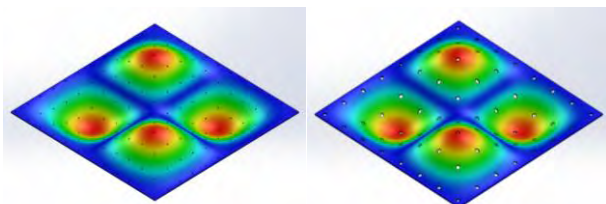
Figure 6 4th mode of the perforated plate.

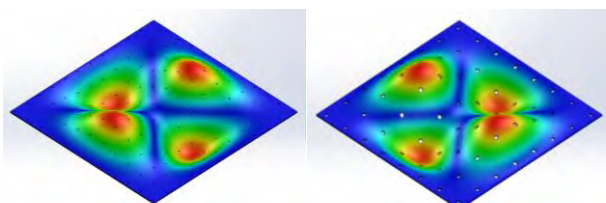Figure 7 5th mode of the perforated plate.

4. SUMMARY

The natural frequency of perforated panels with micro and macro size holes has been studied in the Solid Work environment. The results have been compared to that of solid plate natural frequency. It is found that the holes give significant effect on the mass and stiffness of the panels which proportionally shifts the natural frequency of perforated panel to the lower value. As the holes size increases, the natural frequency accordingly shifts to the lower value.

REFERENCES

[1] D. Herrin, J. Liu, "Properties and Applications of Microperforated Panles" *Sound and Vibration*, vol. July, pp. 6–9, 2011.

[2] A. Putra, A.Y. Ismail, Md. R. Ayob, "Sound transmission loss of a double-leaf partition with micro-perforated plate insertion under diffuse field incidence," *International Journal of Automotive and Mechanical Engineering*, vol. 7, pp. 1086-1095, 2013.

[3] A. Putra, A.Y. Ismail, R. Ramlan, Md. R. Ayob, M.S. Py, "Normal incidence of sound transmission loss of a double-leaf partition inserted with a microperforated panel," *Advances in Acoustics and Vibration*, vol. 2013, pp. 1–8, 2013.

[4] A. Putra, A.Y. Ismail, "Normal incidence of sound transmission loss from perforrated plates with micro and macro size holes," *Advances in Acoustics and Vibration*, vol. 2014, pp. 1–12, 2014.

[5] K.A. Burgemeister, C.H. Hansen, "Calculating resonance frequencies of perforated panels," *Journal of Sound and Vibration*, vol. 196, no. (4), pp. 387–399, 1996.

Nonlinear behavior of a plate with an arbitrarily orientated crack

R. Ismail[1,*], M.P. Cartmell[2], N.S.R. Apandi[1]

[1] Faculty of Mechanical Engineering, Universiti Teknikal Malaysia Melaka,
Hang Tuah Jaya, 76100 Durian Tunggal, Melaka, Malaysia
[2] School of Engineering, College of Science and Engineering, University of Glasgow,
Glasgow, G12 8QQ, Scotland, United Kingdom

*Corresponding e-mail: rainah@utem.edu.my

Keywords: Nonlinear; cracked plate; multiple scale method

ABSTRACT – This paper presents a nonlinear analysis for a thin isotropic plate containing an arbitrarily orientated surface crack. The governing equation of motion of the plate model with enhanced crack modelling and subjected to transverse harmonic excitation is proposed to represent the vibrational response of the plate and is based on classical plate theory into which a developed crack model has been assimilated. An approximate solution method based on the perturbation method of multiple scales is applied and the nonlinear behavior of the cracked plate model is investigated from the amplitude-frequency equation. It is found that the nonlinear characteristics of the cracked plate structure can be greatly affected by the orientation of the crack in the plate.

1. INTRODUCTION

A vibration analysis for a cracked thin isotropic plate has been motivated by the well-known applicability of various vibrational techniques for structural damage detection. Importantly, it is necessary still to develop a deep understanding of the derivation of the model of a cracked plate and it behaviours, especially for nonlinear case. Much research work has been undertaken on linear model, and there are restricted nonlinear models available for vibration problems in cracked plates.

A detailed derivation of the differential equation based on classical plate theory for modelling a crack in a plate for nonlinear model was first initiated by Israr et al. [1]. In these work, the concept of a line-spring model based on Kirchoff's plate bending theories, as first introduced by Rice and Levy [2], was used for the crack formation. Ismail and Cartmell [3] have provided an extension to the development of currently available analytical models of the vibration characteristics of a cracked plate structure, particularly for an alternative geometry in which the crack orientation is variable. Gangadhar et al. [4] presented an analytical model for nonlinear vibration analysis of a thin isotropic by considering two perpendicular, partial surface cracks located at the centre of the plate.

An approximate analytical method based on the perturbation method used in order to study and interpret the physical behaviour of a cracked plate. One of the most widely used perturbation methods is the method of multiple scales [5]. This is frequently used for obtaining close-form solution for nonlinear problems. The basic idea behind this approach is that the single independent variable, T is uniformly split up into several new independent variables for an example T_1, T_2, T_3,…T_n and these independent variables define successively slower dependencies for the dependent variables when expressed in term of a uniformly valid expansion equation. Hence, the aim of this paper is to investigate the nonlinear behaviour of the cracked plate model discussed in paper by [3] in which a plate containing an arbitrarily orientated surface crack is considered.

2. METHODOLOGY

The equation of motion for a plate containing a surface crack of variable angular orientation has been derived by Ismail and Cartmell [3]. Then, by applying the Berger formulation the derived governing equation of motion of this cracked plate is converted into a nonlinear ordinary differential equation model. This Berger formulation can be used to investigate nonlinear vibrations when the strain energy due to second invariant of the strains in the middle surface of the plate can justifiably by ignored. Finally, by considering the system to be under the influence of weak classical linear viscous damping, μ and the load to be harmonic, q leads to the form of a specialized Duffing equation as follows:

$$\ddot{\psi}_{ij}(t) + 2\mu\dot{\psi}_{ij}(t) + \omega_{ij}^2\psi_{ij}(t) + \gamma_{ij}\psi_{ij}^3(t) = \frac{\eta_{ij}}{D}q\cos\Omega_{ij}t \qquad (1)$$

The explanation about each terms in this equation can be found in paper by [3]. Next, the first order multiple scales method is applied for obtain close-form solution in order to investigate the nonlinear behavior of this cracked plate model. So, for the coordinate ψ_{ij}, the dependent variables would typically have this form;

$$\psi_{ij}(t,\varepsilon) = \psi_{0ij}(T_0,T_1) + \varepsilon\psi_{1ij}(T_0,T_1) + o(\varepsilon^2) \qquad (2)$$

Where $T_n = \varepsilon^n t$ and the parameter, ε, is known as a (small) perturbation parameter with $\varepsilon \ll 1$. ψ_{0ij} and ψ_{1ij} are solution functions yet to be determined and T_0 and T_1 are successively slower time scales. Before applying the method of multiple scales to obtain an approximate solution to this problem it is necessary to *order* the cubic term, the damping, and the excitation term. These terms are ordered by means of the small parameter ε according to their perceived relative numerical strength. To accomplish this we assume that the cubic, damping and the excitation terms are a definitionally weak term,

thus these are assumed to become:

$$\gamma = \varepsilon\,\hat{\gamma}; \quad \mu = \varepsilon\,\hat{\mu}; \text{ and } q = \varepsilon\,\hat{q} \tag{3}$$

Finally, uniformly valid expansion for the first order approximate solution can be obtained and after converting the exponent terms into trigonometric forms the full solution to first order ε becomes:

$$\psi_{ij}(t,\varepsilon) = b\cos(\Omega t - \phi) + \frac{\hat{\gamma}_{ij}b^3}{32\omega_{ij}^2}\cos(3\Omega t - 3\phi) + o(\varepsilon^2) \tag{4}$$

Into which numerically calculated values for b can be obtained from the amplitude-frequency equation as follows:

$$\hat{\mu}^2 b^2 + \left(\sigma_{ij} - \frac{3\hat{\gamma}_{ij}b^2}{8\omega_{ij}}\right)^2 b^2 = \frac{\eta_{ij}^2}{4D^2\omega_{ij}^2}\hat{q}^2 \tag{5}$$

3. RESULTS AND DISCUSSION

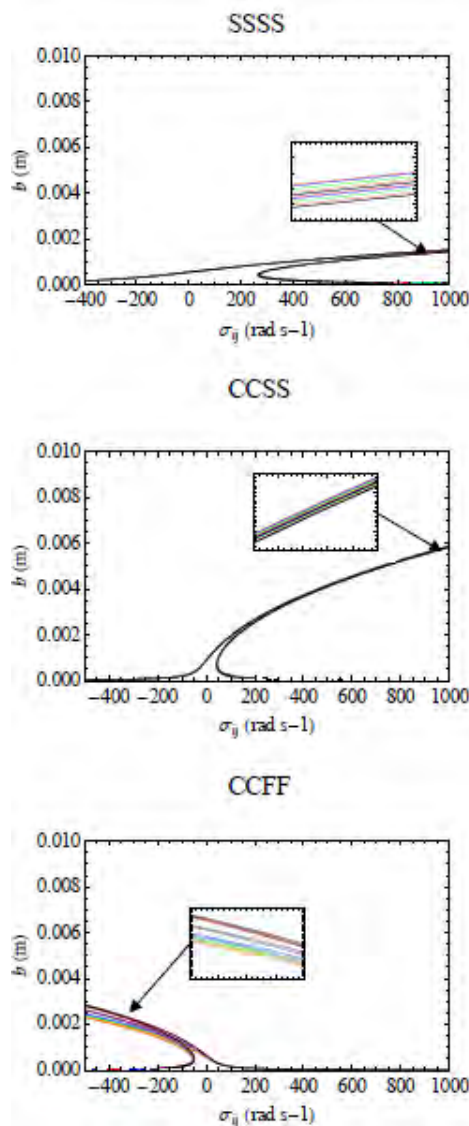The analytical results are shown in Figure 1.

Figure 1 Nonlinear response curves for the cracked plate model for three types of boundary conditions (0º: Red line, 20º: Blue line, 40º: Green line, 60º: Orange line, 80º: Purple line, 90º: Black line).

This Figure show curves for the nonlinear response

which represent the behavior of rectangular plate containing the orientated surface crack for the three different types of boundary conditions. Equation (5) is used to plot these curves and the aspect ratio chosen for the rectangular plate is 1:2. The system displays typical nonlinear characteristics, as evident in the Figure, with characteristic hardening and softening phenomena for a 0.003 m half-crack length. In this Figure, for the cracked plate model with the SSSS and CCSS boundary conditions, the nonlinearity bends the curves to the right, as for a hardening system. In this case the nonlinear hardening effect is clearly much stronger for the SSSS boundary condition. However, for the CCFF boundary condition the nonlinearity bends the curves to the left as for a softening system. The influence of the crack orientation angle on the frequency response is also observed. Cases tested for the SSSS and CCSS boundary conditions show no obvious hardening effects for rectangular plates. For the CCFF boundary condition it can clearly be seen that the nonlinear hardening effect increases up to 60º and then reduces when the crack orientation angles starts to exceed 60º. It should be noted that the amplitude decreases with the increase in frequency.

4. CONCLUSIONS

The nonlinear behavior of the cracked plate model has been investigated from the amplitude-frequency equation and this has showed that the inclusion of a crack within the plate produces a global effect on the nonlinear response of the overall system. As a conclusion, it can be said that the nonlinear characteristics of the plate structure are affected by the orientation of the crack.

5. REFERENCES

[1] A. Israr, M.P. Cartmell, E. Manoach, I. Trendafilova, W.L. Ostachowicz, M. Krawczuk, and Arkadiusz, "Analytical modeling and vibration analysis of partially cracked rectangular plates with different boundary conditions and loading," *Journal of Applied Mechanics,* vol. 76, no. 1, pp. 1-11, 2009.

[2] J.R. Rice, and N. Levy, "The part-through surface crack in an elastic plate," *Journal of Applied Mechanics,* vol. 39, pp. 185-194, 1972.

[3] R. Ismail and M.P. Cartmell, "An investigation into the vibration analysis of a plate with a surface crack of variable angular orientation", *Journal of Sound and Vibration*, vol. 331, no. 12, pp. 2929-2948, 2012.

[4] M.P. Cartmell, S.W. Ziegler, R. Khanin, and D.I.M. Forehand, "Multiple Scales Analysis of the Dynamics of Weakly Nonlinear Mechanical Systems," *Applied Mechanics Reviews*, vol. 56, no. 5, pp. 455-492, 2010.

[5] G.S. Ramtekkar, N.K. Jain, and P.V. Joshi, "Non-linear Vibration Analysis of Isotropic Plate with Perpendicular Surface Cracks," *Advances in Structural Engineering*, pp. 77-94, Springer India; 2014.

Practical controller for positioning control of X-Y ballscrew mechanism

W.K. Hee[1], S.H. Chong[1,*], J.E. Foo[1], A. Che Amran[2]

[1] Faculty of Electrical Engineering, Universiti Teknikal Malaysia Melaka,
Hang Tuah Jaya, 76100 Durian Tunggal, Melaka, Malaysia
[2] Faculty of Engineering Technology, Universiti Teknikal Malaysia Melaka,
Hang Tuah Jaya, 76100 Durian Tunggal, Melaka, Malaysia

*Corresponding e-mail: horng@utem.edu.my

Keywords: *X-Y* ball screw mechanism; CM NCTF; practical controller

ABSTRACT – This paper describes the evaluation of a practical controller performance for point-to-point positioning motion using a *X-Y* ballscrew mechanism. The proposed controller is Continuous Motion Nominal Characteristic Trajectory Following (CM NCTF) controller which is easy to design and having a simple control structure. The performance of the CM NCTF controller is compared with the PI-D controller, which have similar control structure. The experimental result proved that the CM NCTF controller has better positioning performance in point-to-point motion.

1.   INTRODUCTION

Motion control systems play an important role in industrial equipment such as machine tools and robotics. They are required to have not only fast response with little or no overshoot, but also robustness.One type of the motion control systems is point-to-point (PTP) positioning system, which is used to move a plant from one point to another point. The positioning systems generally require a controller to satisfy requirements such as high accuracy, fast response and robust.

In industrial, PID controllers are the most popular and often used for positioning systems. Huang and Chen stated that, the PID gains used performed well in point-to-point (PTP) precision positioning [1]. However, it is difficult to simultaneously satisfy the requirements of fast response and robust. Researchers have changed the structure of PID controller to more advance controller, which is able to overcome the weakness of the classical PID controller.

The advance PID controller have solve the problems stated above, but the control structure of PID controller has become complicated [2]. Besides that, many kinds of controllers such as sliding mode controller (SMC) and disturbance observer (DOB) have been proposed for ballscrew mechanism. However, those controllers require the exact plant model and its parameters which are difficult to be identified [3-4]. The function of the controller increased and the complexity of the control structure will be increased. When the control structure of a controller is complex, the design procedure will become complex because more parameters change needed to be concerned. In these cases, the Continuous Motion Nominal Characteristic Trajectory Following (CM NCTF) controller was proposed. The CM NCTF controller does not require exact model parameters of plant, straightforward design

procedure, simple control structure and does not require deep control knowledge.

2.   NCTF CONTROL SYSTEM DESIGN

Figure 1 shows the structure of the CM NCTF control system. The NCTF controller consists of two important elements which are nominal characteristic trajectory (NCT) and a Proportional Integrator (PI) compensator. The NCT is functioned as a motion path for the object to follow. On the other hand, the PI compensator functions as velocity control and make the mechanism to follow the NCT and finish at origin. The NCT is constructed using the object responses during the open loop experiment while the PI compensator is designed based on a practical stability limit that obtained experimentally [5].
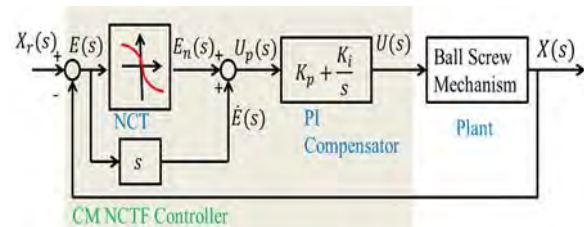

Figure 1 Control structure of CM NCTF controller.

Generally, the design procedure of the CM NCTF controller consists of 3 major steps and it is proved free of friction characteristic [6]. The steps are:

Open loop response:
The mechanism is driven in open-loop and the displacement and velocity are measured
Construction of NCT:
The NCT is constructed on the phase plane using the displacement and velocity of the mechanism during deceleration.
Design of PI compensator:
The PI compensator is designed based on the practical stability limit that determined experimentally.

Figure 2 shows the constructed NCT in the phase plane. The gradient near the origin, $\beta = 87s^{-1}$. Table 1 shows the controller parameter of the CM NCTF controller.

The practical stability limit is obtained by driving the mechanism with the CM NCTF controller using

only the proportional element. The K_p value is increased until continuous oscillations are generated, which denoted as the ultimate proportional gain (K_{pu}). ζ and $\omega_n T$ are selected from the stable region in the practical stability limit graph. K_p and K_i values are calculated using Equation (1) and Equation (2):

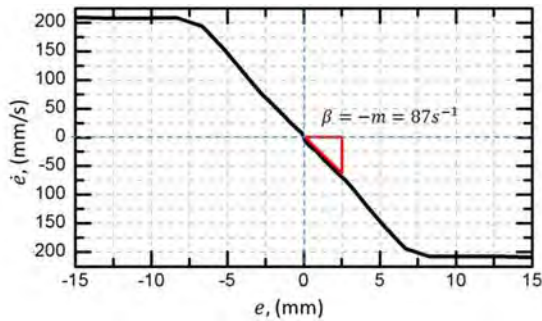$$K_p = \frac{2\xi\omega_n}{K} \qquad (1)$$

$$K_i = \frac{\omega_n^2}{K} \qquad (2)$$

Figure 2 Constructed NCT from open-loop response.

Table 1 Controller parameter.

Parameter	Value
Proportional gain, K_p	0.08
Integrator gain, K_i	1.34
Inclination near origin, β	87s^{-1}

3. PERFORMANCE EVALUATION

A *X-Y* ballscrew mechanism that used to clarify the usefulness of the CM NCTF controller is shown in Figure 3. In this paper, only 1-DOF (*Y*-Axis) which has lighter weight is considered. The positioning performance of the CM NCTF controller is compared with the PI-D controller.
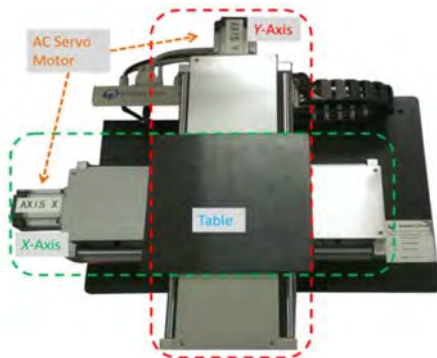

Figure 3 *X-Y* ballscrew mechanism.

Figure 4 shows the comparative experimental positioning performance to step input 5mm and 10mm. The transient responses of the CM NCTF controller and the PI-D controller are shown in error of 0.1%.

Table 2. The CM NCTF controller has showed overshoot 0.76% and 0.94% for step input 5mm and 10mm respectively. Besides that, the CM NCTF controller has succeeded to compensate the steady state error to zero, while the PI-D controller has steady state error of 0.1%.

Table 2 Experiment transient response of CM NCTF and PI-D controller.

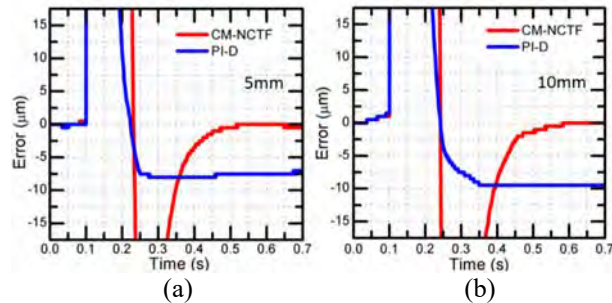| Controller	Amplitude (mm)	Overshoot (%)	Steady state error (%)
CM NCTF	5.00	0.76	0.00
	10.00	0.94	0.00
PI-D	5.00	0.16	0.10
	10.00	0.10	0.10

Figure 4 Experimental PTP performances with step height (a) 5mm and (b) 10mm.

4. CONCLUSION

The CM NCTF controller has demonstrated slightly higher overshoot, but it has succeeded to compensate the steady state error to zero as compared with the PI-D controller. Overall, it can be concluded that the positioning performance of the CM NCTF controller is better than the PI-D controller in point-to-point motion.

REFERENCES

[1] P. Huang and Y. Chen, "Design of PID Controller for Precision Positioning Table Using Genetic Algorithms," in *Proceedings of the 36th Conference on Decision & Control*, 1997, pp. 3–4.

[2] K. Ying-Shieh, W. Ming-Shyan, and C. Tzu-Yao, "FPGA-Based Self-Tuning PID Controller using RBF Neural Network and its Application in X-Y Table," in *ISIE 2009*, 2009, pp. 694–699.

[3] C. H. Lu and Y. R. Hwang, "Hybrid sliding mode position control for a piston air motor ball screw table," *ISA Trans.*, vol. 51, no. 3, pp. 373–385, 2012.

[4] M. Nandayapa, C. Mitsantisuk, Y. Yokokura, and K. Ohishi, "Force sensation improvement in bilateral control of different master-slave mechanism based on high-order disturbance observer," in *IECON 2012 - 38th Annual Conference on IEEE Industrial Electronics Society*, 2012, pp. 4406–4411.

[5] W.K. Hee, S.H. Chong, and A. Che Amran, "Selection of PI Compensator Parameters for NCTF Controller Based on Practical Stability Limit," in *IEEE International Conference on Control System, Computing and Engineering*, 2014, pp.674–679.

[6] S.H. Chong, and K. Sato, "Practical controller design for precision positioning, independent of friction characteristic," *Precision Engineering*, vol. 34, no.2, pp.286–300, 2010.

Radiation efficiency of single beam-stiffened plate

K.H. Lim[1], A. Putra[1,2,*], R. Ramlan[1,2]

[1] Faculty of Mechanical Engineering, Universiti Teknikal Malaysia Melaka,
Hang Tuah Jaya, 76100 Durian Tunggal, Melaka, Malaysia
[2] Centre for Advanced Research on Energy, Universiti Teknikal Malaysia Melaka,
Hang Tuah Jaya, 76100 Durian Tunggal, Melaka, Malaysia

*Corresponding e-mail: azma.putra@utem.edu.my

ABSTRACT – Beam-stiffened method had been used widely in controlling noise problem. However the effect of this technique has not been fully studied and may cause undesired results. This paper studies how different point forces location affect the sound radiation efficiency from beam-stiffened plate. Hybrid mathematical model which comprised of a semi-analytical model and FE model is used to conduct this study. Radiation efficiency by 8 points force location and average radiation efficiency over 8 points force location from single beam-stiffened plate are presented. Besides, range of radiation efficiency variation using 10 and 90 percentile is also presented.

1. INTRODUCTION

Beam-stiffening technique had been used widely in controlling noise problem but it effects on sound radiation have not been fully studied and might lead to undesired noise radiation [1].

Study on sound radiation from beam-stiffened plate was started by Maidanik proposing a statistical method in estimating radiation efficiency of a ribbed panel, followed by Lyon who studied the sound power from an infinite beam attached to an infinite thin plate [2,3]. In later years, several works were published in estimating the sound radiation from beam-stiffened plate structure such as using Fast Fourier Transform and applying the Rayleigh-Ritz formula [4,5].

This paper studies on how different force positions affect by the sound radiation efficiency of beam-stiffened plate using hybrid mathematical modeling.

2. METHODOLOGY

2.1 Hybrid mathematical modeling

In this paper, hybrid mathematical model by Putra et.al is used to conduct the study on sound radiation efficiency of beam-stiffened plate. This mathematical model combines the velocities across the plate from FE model with semi-analytical model. The result from FE will be used with the semi-analytical to calculate the radiated sound pressure through Rayleigh integral [5]. The overview of this mathematical model is shown in Figure 1.
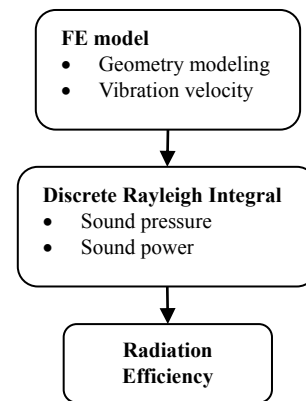

Figure 1 Overview of hybrid mathematical model.

2.2 Governing equation

Consider a rectangular plate lying on xy-plane and excited by a harmonic force. The radiated sound pressure from the plate at the far-field at distance, r is given by [6]

$$p(r) = \frac{jk\rho c}{2\pi} \int_s v(x,y) \frac{e^{-jkr}}{r} dS \qquad (1)$$

Where p is the sound pressure, e^{-jkr}/r is the Green's function, v is the velocity of the plate, ρ is the air density, c is the speed of the sound, k is the acoustic wave number, S is the area of the plate and r is the distance from the plate velocity to the pressure at the air

Assume the plate consists of elementary discrete sources that are vibrating independently, Eq. (1) can be discretized and is written as

$$p(r) = \frac{jk\rho c}{2\pi} \sum_{n=1}^{N} v_n(x,y) \frac{e^{-jkr}}{r} dS \qquad (2)$$

where v_n is the velocity at the n-th element of the plate. This is obtained from the FE model to be the input back in Eq. (2). The radiated sound is given by

$$W = \frac{1}{2} \text{Re} \left\{ \sum p_n v_n(x,y) \right\} dS \qquad (3)$$

and the radiation efficiency, σ of the plate can be obtained by

---

$$\sigma = \frac{W}{\frac{1}{2}\rho c S \left\langle \left| v_n^2 \right| \right\rangle} \tag{4}$$

Where $\left\langle \left| v_n^2 \right| \right\rangle$ is the spatially average squared velocity of the plate.

2.3 *Average radiation efficiency*

In this study, single beam-stiffened plate as shown in Figure 2 having rectangular aluminum base plate with dimension $0.5 \times 0.6 \times 0.003$ m with 0.1 damping is considered. The stiffener dimension is $0.02 \times 0.5 \times 0.01$ m. The Young modulus, density, and Poisson ratio are 7.1×10^{10} Pa, 2700 kg/m^3 and 0.3, respectively. The beam-stiffened plates are excited by 8 points force. The locations of the 8 points force are chosen based on Putra et.al as shown in the Figure 3 [7].
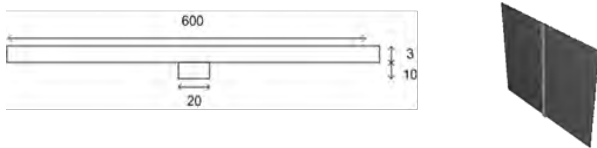

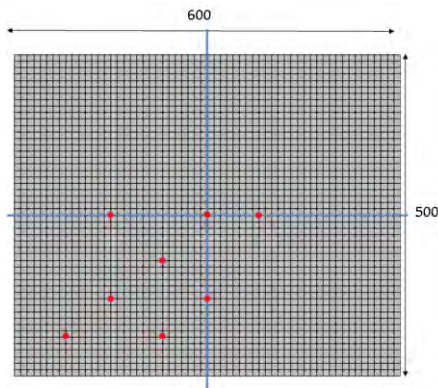Figure 2 Configuration and dimension of single beam-stiffened plate in mm.

Figure 3 Positions of point force on the plate surface.

3. RESULTS AND DISCUSSION

Figure 4 shows the distribution of radiation efficiency and average radiation efficiency over 8 points force. It can be noticed that at 210 Hz, there is a high curve. This high curve is the result of exciting the plate at the center of the plate which does not excite the even mode. Besides, other curves dip at 190 Hz and this is due to (2, 1) mode [7].

Figure 5 shows the range of radiation efficiency using 10 and 90 percentile and average radiation efficiency in one third octave bands. In the monopole region (1-150 Hz) and above critical frequency region (>4000 Hz), radiation efficiency is seen to be unaffected significantly due to force positions. However, it can be seen that force points location affect the radiation efficiency the most in the corner mode region (150 Hz-4000Hz).
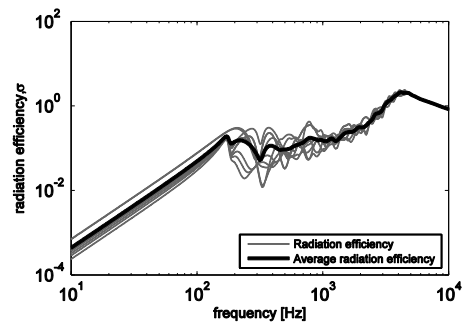

Figure 4 Distribution of radiation efficiency (thin) and average radiation efficiency (thick) over 8 points force locations.
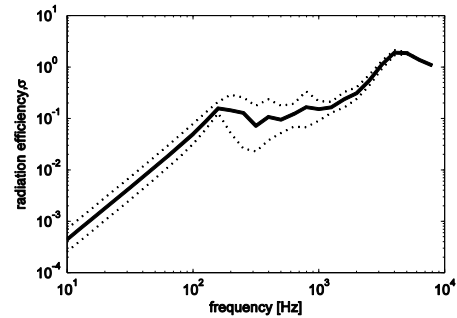

Figure 5 Range of radiation efficiency using 10/90 percentile (dotted) and average radiation efficiency (thick) in one third octave bands.

4. CONCLUSION

Radiation efficiency and average radiation efficiency of single beam-stiffened over 8 points force location has been presented. The position of the point force acted on the plate affect the radiation efficiency in the corner mode region (150-1000 Hz) the most.

REFERENCES

[1] F. Fahy and P. Gardonio, "Sound and structural vibration: radiation transmission and response, Second ed.," *Academic Press*, 2007.

[2] G. Maidanik, "Response of Ribbed Panels to Reverberant Acoustic Fields," in *J. Acoust. Soc. Am.* vol. 34, pp. 809-26, 1962.

[3] R.H. Lyon, "Sound Radiation from a Beam Attached to a Plate". *J.Acoust. Soc. Am.* vol. 34, pp. 1265-1268, 1962.

[4] E.G. Williams and J. D Maynard, "Numerical evaluation of the Rayleigh Intergral for Planar Radiators using FFT," in J. *Acoust. Soc. Am.* vol. 72, no. 6, pp. 2020-2030, 1982.

[5] A. Putra, N. Shyafina, N. Muhammad, H. Bakri, and N. F. Saari, "Development of Hybrid Semi Analytical and Finite Element Analysis to Calculate Sound Radiation from Vibrating Structure," *Advanced Materials Research*, vol. 845, pp. 71-75, 2014.

[6] L. Rayleigh, The Theory of Sound. 2th edition, 1896.

[7] A. Putra and D. J. Thompson, "Sound radiation from rectangular baffled and unbaffled plates," in *Applied Acoustic,* vol. 71, pp. 1113-1125, 2010.

Natural coir fiber and kenaf fiber as multilayer sound absorber

Z.Y. Lim[1], A. Putra[1,*], M.J.M. Nor[1,2], M.Y. Yaakob[3]

1) Faculty of Mechanical Engineering, Universiti Teknikal Malaysia Melaka,
Hang Tuah Jaya, 76100 Durian Tunggal, Melaka, Malaysia
2) Centre for Advanced Research on Energy, Universiti Teknikal Malaysia Melaka,
Hang Tuah Jaya, 76100 Durian Tunggal, Melaka, Malaysia
3) Faculty of Manufacturing Engineering, Universiti Teknikal Malaysia Melaka,
Hang Tuah Jaya, 76100 Durian Tunggal, Melaka, Malaysia

*Corresponding e-mail: azma.putra@utem.edu.my

Keywords: Absorption coefficient; coir fiber; kenaf fiber

ABSTRACT – This paper studies the sound absorption performance of multi-layered natural fibers, particularly coir fiber and kenaf fiber. The effect brought by different layer arrangement these porous materials are studied and it is found that under the same thickness, the low frequency sound absorption is enhanced when kenaf fiber is layered as the first layer to receive the incidence sound. With kenaf fiber layered at the second layer, better absorption performance is seen at high frequency.

1. INTRODUCTION

Synthetic materials such as glass fiber and foam glass are commonly used as sound absorber, these materials are found to be harmful to human health when used as sound absorber. According to a Swiss Life Cycle Assessment (LCA) database, where the entire life history of a product is analysed based on the potential and impacts to the environment, the global warming potential of synthetic materials are seen to be very high [1]. Due to these negative impacts to the environment and human health, attentions are now being shifted to researches on sound absorption performance of natural materials. Fibrous natural materials such as oil palm empty fruit bunch fibers [2], and non-fibrous materials such as reed [3] are among the materials investigated and gave results showing good performance.

Fouladi et al. [4] analyzed the acoustical characteristics of both fresh and industrial treated coir fiber and suggested that approaches such as adding air gap and perforated plate to improve the weak absorption of industrial prepared coir fiber at low frequency. This suggestion was tested by Ayub et al. [5] by studying the effect of implementation of perforated plates and air gaps in coir fiber, low frequency absorption is enhanced through these approaches. Recently, Putra et al. [6] attempted to enhance the sound absorption of hard fiber by using soft fiber, absorption of the coir-kapok fiber hybrid sample with 15% of kapok fiber as content is proved to have achieved unity above 2 kHz with only 10 mm of thickness and 10 mm air gap. Kenaf fiber as soft fiber is previously studied on its sound absorption performance is found to be able to reach unity at 1.5 kHz with thickness of 30 mm [7].

2. METHODOLOGY

2.1 Preparation of sample material

Industrial prepared 10 mm thick coir fiber sheet and 5 mm thick kenaf fiber sheet are being cut into cylindrical shape of diameter 33 mm as shown in Figure 1 in order to fit into the impedance tube for measurement.
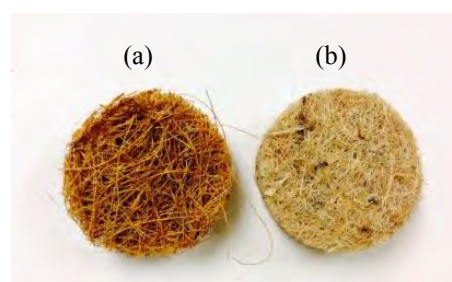

Figure 1 (a) Coir fiber *and* (b) kenaf fiber sample*s*.

2.2 Experimental set up

The impedance tube method was used to measure sound absorption coefficient of the samples. Figure 2 shows the measurement set up using impedance tube.
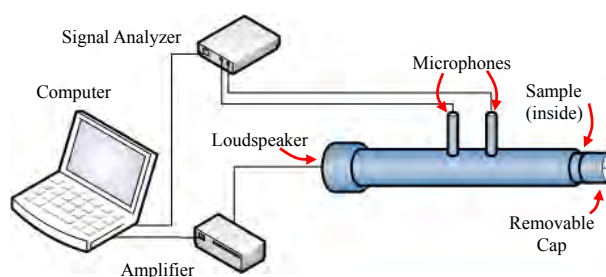

Figure 2 Diagram of absorption coefficient measurement set up.

Fibers were layered in the removable cap according to interested arrangement where the first layer is the surface to first receive the incidence sound, as shown in Figure 3 the first layer is coir fiber, second layer is kenaf fiber and third layer is coir fiber.
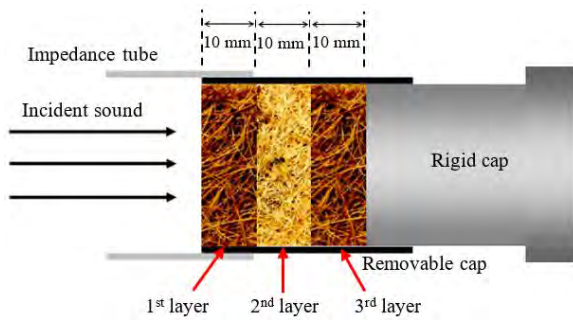
Figure 3 Layering of fiber in removable cap in the impedance tube.

3. RESULTS AND DISCUSSION

The sample layering is indicated with the initial of the fiber type, for example, k-c-c represents kenaf fiber as the first 10 mm layer, followed by 20 mm of coir fiber as the second and third layer.
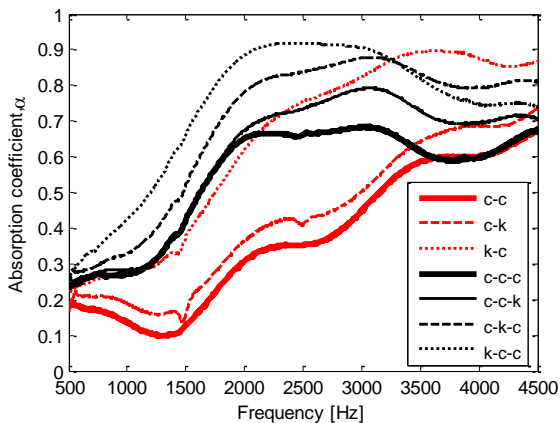

Figure 4 Sound absorption coefficient of 20 mm (red) and 30 mm (black) fiber sample with (thin) and without (thick) 10 mm of kenaf fiber substituted in different layer.

Referring to Figure 4, sample with 20 mm thickness with kenaf fiber substituted as the first layer gave better performance improvement compared to that as second layer. The increased thickness of sample from 20 mm to 30 mm affects the sound absorption by enhancing low frequency sound absorption.

Sound absorption improvement above 2 kHz is seen when kenaf fiber is substituted as third layer in a 30 mm coir fiber sample. As the position of kenaf is brought forward to second and first layer, the sound absorption is further enhanced throughout the frequency range. The sound absorption of 30 mm of sample with coir fiber and kenaf fiber layered at different arrangement is shown in Figure 5. Comparing the sound absorption of samples with coir fiber as first layer with that of samples with kenaf fiber as first, the sound absorption peak of the latter appeared at lower frequency, which is around 2 kHz. The effect of positioning kenaf fiber instead of coir fiber as second layer is improvement of sound absorption above 3.25 kHz.
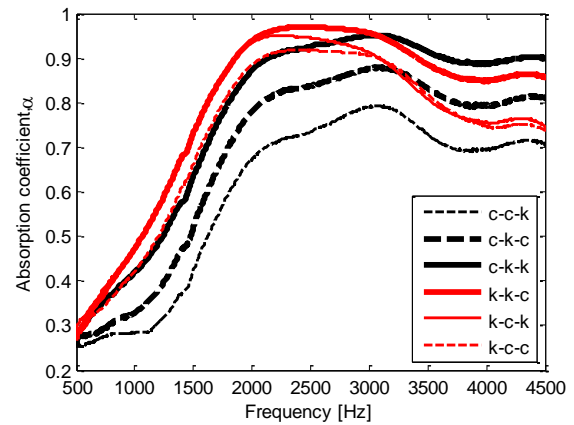

Figure 5 Sound absorption of 30 mm of sample with different layer arrangement of coir fiber and kenaf fiber. (red = kenaf as 1st layer, black = coir as 1st layer, thick = kenaf as 2nd layer, thin = coir as 2nd layer, dotted = one kenaf layer, line = two kenaf layer).

4. CONCLUSION

The implementation of kenaf fiber layer in coir fiber is found to be able to improve low frequency absorption. The peak of absorption is shifted from 3250 Hz to 2000 Hz when kenaf fiber is placed at the first layer. High frequency improvement can be seen when kenaf fiber is substituted as the second layer.

REFERENCES

[1] F. Asdrubali, "Survey on the Acoustical Properties of New Sustainable Materials for Noise Control," in *Euronoise 2006,* 30, 2006.

[2] K.H. Or, A. Putra, and M.Z. Selamat, "Oil palm empty fruit bunch fibers as sustainable acoustic material," in *Proceedings of Mechanical Engineering Research Day 2015*, 2015, pp. 99-100.

[3] F.A. Khair, A. Putra, M.J.M. Nor, and N. Atiqah, "Investigation on reed *Imperata Cylindrica* as sound absorber " in *Proceedings of Mechanical Engineering Research Day 2015*, 2015, pp. 91-92.

[4] M.H. Fouladi, Md. Ayub, and M.J.M. Nor, "Analysis of coir fiber acoustical characteristics," *Applied Acoustics* 72, pp. 35–42, 2011.

[5] Ad. Ayub, M.H.Fouladi, M. Ghassem, M.J.M. Nor, H.S. Najafabadi, N. Amin and R. Zulkifli, "Analysis on Multiple Perforated Plate Sound Absorber Made of Coir Fiber," *International Journal of Acoustics and Vibration*, vol. 19, no. 3, pp. 203-211, 2014.

[6] A. Putra, Z.Y. Lim, M.J.M. Nor and M.Y. Yaakob, "Enhancing Sound Absorption of Coir Fibers Using Kapok Fibers: A Preliminary Study," in *5th International Conference on Noise, Vibration and Comfort*, 2015.

[7] Z.Y. Lim, A. Putra, M.J.M. Nor and M.Y. Yaakob, "Preliminary study on sound absorption of natural kenaf fiber," in *Proceedings of Mechanical Engineering Research Day 2015*, 2015, pp. 95-96.

Positioning control of ball screw mechanism with disturbance observer

J.E. Foo, S.H. Chong*, W.K. Hee, S.L. Loh

Faculty of Electrical Engineering, Universiti Teknikal Malaysia Melaka,
Hang Tuah Jaya, 76100 Durian Tunggal, Melaka, Malaysia

*Corresponding e-mail: horng@utem.edu.my

Keywords: Ball screw; PDDO controller; tracking motion

ABSTRACT – In this paper, a disturbance observer with PD controller (PDDO) is proposed to improve the positioning performance of the ball screw mechanism that is subjected to nonlinearities. The tracking performance of the PDDO controller is examined and compared with a PID controller experimentally. The PDDO controller displays better tracking performance than the PID controller.

1. INTRODUCTION

A ball screw mechanism is a mechanical actuator that is widely applied in different industries due to its high stiffness and efficiency. However, the mechanism often experiences problems such as non-linear frictions and hysteresis that affects the positioning performance of the ball screw mechanism [1]. In order to overcome these problems, various controllers such as H-infinity controllers [2] and Fuzzy Logic Controller [3] were proposed to perform positioning control for ball screw mechanism. Among these controllers, a Disturbance Observer with PD controller (PDDO) has a simpler structure. The PDDO controller does not compensate the system directly [4]; the disturbance observer estimates the disturbances and parameter variations in the system while the PD controller compensates the error.

In this paper, a PDDO controller is proposed for positioning control of ball screw mechanism. This paper is categorized as follow: Section 2 discusses the experimental setup while Section 3 covers the controller design procedures. Section 4 examines and compares the positioning performance of the PDDO controller with PID controller while Section 5 concludes this paper.

2. EXPERIMENTAL SETUP

In this paper, the ball screw mechanism is driven by a rated 24V DC servomotor. The ball screw lead comes in 8mm/rev and a linear encoder of 5µm/pulse is used to measure the displacement of the table. The ball screw mechanism is shown in Figure 1 while its corresponding free body diagram is presented in Figure 2.

A ball screw mechanism consists of two parts: a rotating DC motor that give rise to a driving force drives the table on the lead screw linearly. The transmission ratio of the ball screw is given as $R = r/2\pi$, where r is the radius of the lead screw. The value of parameters of free body diagram is presented in Table 1.
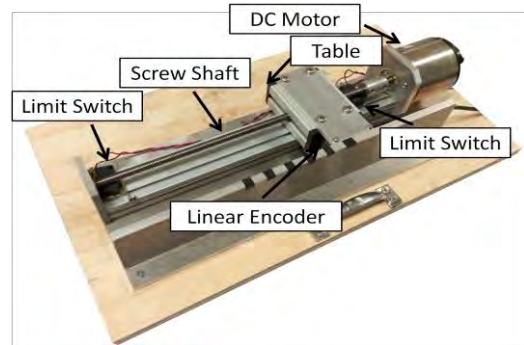

Figure 1 Ball screw mechanism.
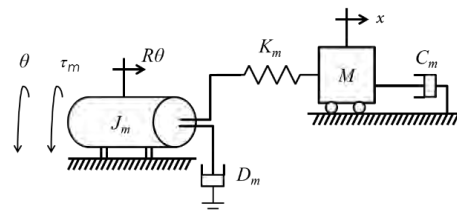

Figure 2 Free body diagram of ball screw mechanism.

The motion of the ball screw mechanism is represented in the equations as follow:

$$J_m\ddot{\theta} + D_m\dot{\theta} + RK_m(R\theta - x) = \tau_m \qquad (1)$$
$$M\ddot{x} + C_m\dot{x} = K_m(R\theta - x) \qquad (2)$$

Table 1 Parameters of the ball screw mechanism.

Parameter	Description	Value	Unit
J_m	Motor inertia	6×10^{-5}	kgm^2
D_m	Motor Viscous Friction	0.385×10^{-3}	Nm/rad/sec
K_m	Stiffness of screw shaft	1.82×10^3	N/m
M	Mass of Table	0.5	kg
R	Ball screw transmission ratio	$1..273\times10^{-3}$	m/rad
C_m	Viscous Friction of mass	50	N/m/sec

3. CONTROLLER DESIGN

To design the PDDO controller, the control structure in Figure 3 is considered. The disturbance observer is made up of an inverse nominal plant, $P_n(s)^{-1}$ and a low pass filter, $Q(s)$. To design the nominal plant,

$P_n(s)$, a general second order transfer function is first considered:

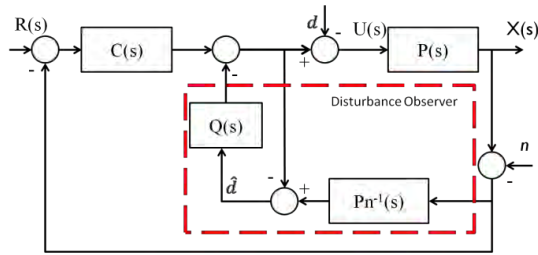$$P_n(s) = \frac{\omega_n^2}{s^2 + 2\varsigma\omega_n s + \omega_n^2} \qquad (3)$$

Figure 3 Control structure of PDDO controller.

To design $Q(s)$, the cut-off frequency, ω_d is determined from the operating frequency of the mechanism, $P(s)$. $Q(s)$ is given as:

$$Q(s) = \frac{\omega_d}{s + \omega_d} \qquad (4)$$

In the PD controller design, root locus approach is adopted. By specifying the desired transient response, the equation of PD controller is obtained as:

$$C(s) = K_p + \frac{K_d s}{T_d s + 1} \qquad (5)$$

The value of T_d was chosen such that the noise picked up by the derivative action is attenuated. The obtained gains are then fine-tuned experimentally.

4. POSITIONING PERFORMANCE

In this paper, the positioning performance of the PDDO controller is examined in tracking motion with sinusoidal input. In order to validate the effectiveness of PDDO controller in positioning control, a PID controller is designed and its performance was compared with PDDO controller. To design a PID controller, three terms are considered: Proportional (P), Integral (I) and derivative (D) of error. By combining these terms, a PID controller equation as shown in Equation (6) is presented.

$$C(s) = K_p + \frac{K_I}{s} + K_D s \qquad (6)$$

In the PID controller design, root locus method is adopted to obtain the gains K_p, K_I and K_d. By setting the desired transient response, the desired poles were obtained. The controller gains are then fine-tuned experimentally.

In the tracking performance validation, a sinusoidal input with frequency of 3Hz and amplitude of 5mm was considered. The tracking motion of the controllers is shown in Figure 4.

When the ball screw mechanism moves in fast motion, the relative viscous frictions increase. Since a PID controller is sensitive towards changes of dynamic, its exhibits large tracking error as it is unable to compensate such changes. A PDDO controller, on the other hand, is capable of estimating such parameter changes, and therefore able to act in reducing the

tracking error of the mechanism. It can be observed that PDDO controller experienced large overshoot at the beginning of the response, but eventually settled down. One conclusion that can be made from this observation is that the PDDO controller has a large observer gain, thus generating the large overshoot.
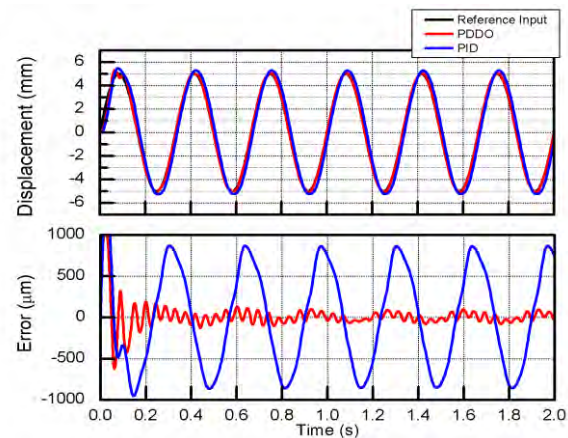

Figure 4 Tracking motion of PDDO and PID controller with sinusoidal input of 3Hz and amplitude 5mm.

5. CONCLUSION

In this paper, the experimental setup of the ball screw mechanism with its corresponding free body diagram was presented. It is concluded that a PDDO controller has better tracking performance than a PID controller. The PDDO controller estimates parameter variations or disturbances in the system, and compensates them such that the mechanism follows the reference input.

REFERENCES

[1] C.L. Chen, M.J. Jang, and K.C. Lin, "Modeling and high-precision control of a ball-screw-driven stage," *Precis. Eng.*, vol. 28, no. 4, pp. 483–495, 2004.

[2] K. Itoh, M. Iwasaki, and N. Matsui, "Robust fast and precise positioning of ball screw-driven table system on machine stand," in *The 8th IEEE International Workshop on Advanced Motion Control, 2004.* 2004, pp. 511–515.

[3] J. Lin and C.H. Chen, "A novel fuzzy friction compensation approach for tracking of a linear motion stage," in *2006 American Control Conference*, 2006, pp. 3188–3193.

[4] X. Li and Z. Mei, "Disturbance-compensation of ball screw servo system," in *2011 International Conference on Electronics, Communications and Control (ICECC)*, 2011, pp. 230–234.

PID control of vertical pneumatic artificial muscle system

M.H. Tan, S.H. Chong[*], T.F. Tang, A.Z. Shukor

Faculty of Electrical Engineering, Universiti Teknikal Malaysia Melaka,
Hang Tuah Jaya, 76100 Durian Tunggal, Melaka, Malaysia

[*]Corresponding e-mail: horng@utem.edu.my

Keywords: Pneumatic artificial muscle; PID; vertical motion

ABSTRACT – Pneumatic Artificial Muscle (PAM) overcome the other common actuators as it has higher power-to-weight ratio. However, the air compressibility and lack of damping ability of PAM brings dynamic delay to the pressure response and causes oscillatory motion to occur. It is not easy to realize the motion with high accuracy and high speed due to all the non-linear characteristics of pneumatic system. A PID control using Ziegler Nichols method for a PAM system in vertical axis to control the tracking motion of the PAM is proposed in this paper. The effectiveness of the proposed control algorithm is demonstrated through experiments.

1. INTRODUCTION

PAM is a rubber tube clothed with a sleeve made of twisted fiber-code, and is fixed at both ends by fixtures. It is an actuator that is able to expand its muscle in radial direction when pressure is supplied and vice versa. PAM has a property like a spring, which enables it to change its own compliance by the inner pressure. The development of actuator system using PAM has been applied to some of the therapy robot and industrial machines. However, PAM has the characteristics such as hysteresis, non-linearity and low damping ability. The air compressibility and lack of damping ability of PAM system cause dynamic delay to the pressure response, which will result in oscillatory motion. Hence, it is not easy to realize the motion with high accuracy and high speed.

Many intelligent control algorithms have been proposed up to now. A simple PID control [1] is applied on a 7 degree of freedom PAM system to power up exoskeleton. Besides, a fuzzy PD+I learning control for a single PAM is done in previous study [2] with the limitation of low accuracy for tracking motion during the starting of operation. The PAM system is vulnerable to parameter changes over time when using fuzzy + PID control in [3]. Tetsuya Kimura applied a method of feedback linearization for a PAM system to handle the non-linear characteristics based on a non-linear model in [4]. Furthermore, a switching algorithm of control parameter using learning vector quantization neural network (LVQNN) was proposed by Kyoung Kwan in [5] on a PAM system.

2. EXPERIMENT SETUP

The experiment setup is shown in Figure 1. The hardware includes a personal computer (i7 4GHz),

which calculates the control input and controls the 5/3 proportional directional valve (FESTO MPYE-5-1/8HF-710B) and two PAM (FESTO DMSP-10-150N-RM-CM) through a data acquisition unit. The pressures in both of the PAM are measured using the pressure sensors (FESTO SDE-10-10). A joint angle θ is detected by using a rotary encoder (3600 pulse/rev). All the signals are fed back to the computer through the data acquisition unit. Two ends of the PAM are connected to the fabricated base, while the other two ends are connected to each other through a timing belt. The timing belt is attached to a timing pulley attaching to a shaft to perform rotational motion. The experiments are conducted under a temperature of 20°C and supply pressure of 5bar.
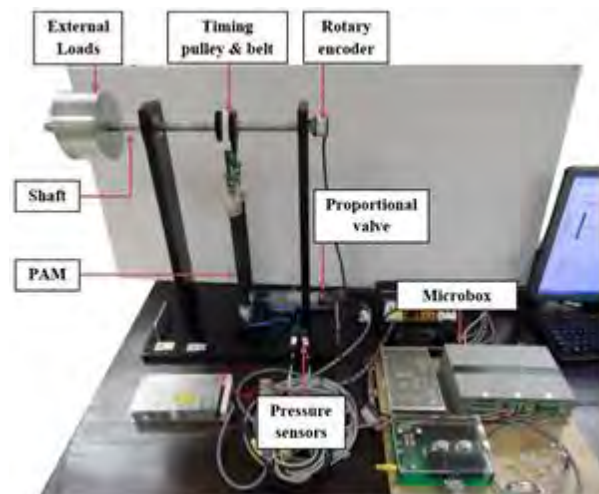

Figure 1 Photograph of the experiment setup.

3. CONTROLLER DESIGN

To design the PID controller for the system, Ziegler Nichols closed-loop tuning method is used to obtain the controller parameters. The ultimate gain value, K_u, and the ultimate period of oscillation, P_u, are obtained in order to calculate K_c by using this method. It is a simple method of tuning the PID controller and can be refined to give a better approximation of the controller parameters. The controller constants K_c, T_i and T_d in the system with feedback are obtained. The obtained gain value K_u is 40, and period of oscillation P_u is 0.6. These values are substituted into the Ziegler Nichols closed-loop equations and the approximated parameters are obtained as shown in Table 1.

Table 1 Ziegler Nichols closed-loop calculation.

Parameters	K_c	T_i	T_d
PID	24	0.3	0.075

For PID controller, we have the general equation of

$$C(s) = K_p(1 + \frac{1}{T_i s} + T_d s) \qquad (1)$$

By substituting the PID parameters into Equation (1), yields

$$C(s) = 24 + \frac{80}{s} + 1.8s \qquad (2)$$

Next, the parameters are fine-tuned to $K_p = 13$, $K_i = 15$ and $K_d = 0.1$ by using trial-and-error through experiments. These values are used as the parameters in the PID controller for sinusoidal input tracking motion as shown in Figure 2.

4. PERFORMANCE EVALUATION

Experiments are carried out using sinusoidal waveform as reference input for uncompensated system and system with PID controller. Figure 2 shows the comparison of the performances between the uncompensated system and PID controller with the sinusoidal input signal to the system at a low frequency of 0.1Hz. The experiments are carried out for 30s. It is shown that the uncompensated system does not reach the desired position angle, meanwhile the PID controller is able to overcome it and enables the system to track the desired input position with minor errors. The error of PID controller is approximately 1.3°, which is 91.7% better than that of uncompensated system. It is clear to show that PID controller is able to control the PAM actuated system in small velocity with minor error.
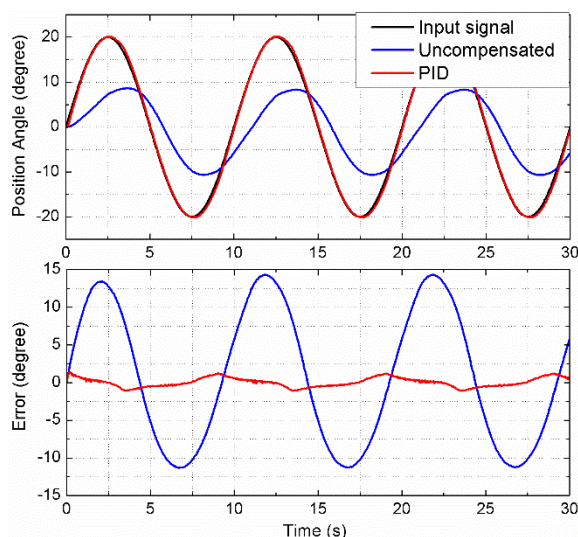

Figure 2 Closed-loop sinusoidal input experiment at f=0.1Hz.

5. CONCLUSIONS

A PID controller is proposed to control the tracking motion of PAM system in vertical axis. It has shown that the proposed method has a good control performance for the nonlinear system, such as PAM system. The PID parameters are designed using Ziegler Nichols tuning method. The controller design by this method does not need any training procedure in advance, but it only requires the input and output of the plant for the adaptation of control parameters. The parameters can be tuned iteratively. From the experiments of the position control of PAM system, the tracking performance is accurate at low frequency. The proposed method is simple and gives satisfactory trajectory tacking.

As future work, a proposed approach can be extended to examine the robust performance in the presence of load change to the PAM system.

REFERENCES

[1] N. Tsagarakis, D.G. Caldwell, and G.A. Medrano-Cerda, "A 7 DOF Pneumatic Muscle Actuator (PMA) Powered Exoskeleton", in *IEEE International Workshop on Robot and Human Interaction*, Pisa, Italy, 1999, pp. 327-333.

[2] S.W. Chan, J.H. Lilly, D.W. Repperger, and J.E. Berlin, "Fuzzy PD+I Learning Control for a Pneumatic Muscle", in *IEEE Int. Conf. Fuzzy Systems*, 2003, pp. 278-283.

[3] K. Balasubramanian, and K.S. Rattan, "Fuzzy Logic Control of a Pneumatic Muscle System Using a Linearizing Control Scheme", in *Int. Conf. North American Fuzzy Information Processing Society*, 2003, pp. 432-436.

[4] T. Kimura, S. Hara, T. Fujita, and T. Kagawa, "Control for pneumatic actuator systems using feedback linearization with disturbance rejection," in *American Control Conference, Proceedings of the 1995*, 1995, vol. 1, pp. 825-829.

[5] K.K. Ahn, T.D.C. Thanh, and Y.K. Ahn, "Intelligent switching control of pneumatic artificial muscle manipulator," *JSME Int. J. Ser. C Mechanical Systems, Machine Elements and Manufacturing*, vol. 48, no. 4, pp. 657-667, 2005.

Identification of noise in room due to HVAC system

Y.M. Cheah[1,2], A. Putra[1,2,*], R. Ramlan[1,2], N. Muhammad[1,2]

[1] Faculty of Mechanical Engineering, Universiti Teknikal Malaysia Melaka,
Hang Tuah Jaya, 76100 Durian Tunggal, Melaka, Malaysia
[2] Centre for Advanced Research on Energy, Universiti Teknikal Malaysia Melaka,
Hang Tuah Jaya, 76100 Durian Tunggal, Melaka, Malaysia

*Corresponding e-mail: azma.putra@utem.edu.my

ABSTRACT – This paper presents noise measurement and noise mapping for two lecture rooms. The results reveal that the background noise level of the empty lecture rooms has exceeded the recommended limit by ANSI 12.2-2008 [1], i.e. above 35 dB(A) due to excessive noise radiated from the structure-borne source coming from the VAV system above the ceiling. Two lecture rooms at the Kampus Teknologi in Universiti Teknikal Malaysia Melaka were used as the case study.

1. INTRODUCTION

Heating, ventilation, and air conditioning system (HVAC) are major sources of interior noise in a building. Vibration from the fan and motor may be transmitted into the structure of the building via transmission along the steel ducts and their hangers and support. The vibration transmitted may activate the building structure to generate noise which causes discomfort and also create secondary radiation of noise from vibrating panels, floors, and roof inside the building [2].

For any learning environment, control of acoustical quality in the room can be divided into three schemes: a) limit transmission of noise from outside the classroom, b) minimize the background noise from the building's HVAC systems, and c) reduce the reverberation time inside the classroom [3]. According to ANSI 12.2-2008, the background noise level of an unoccupied lecture halls and classrooms (volume < 2000 ft^3) should not exceed sound level of 35 dB(A). Excessive background noise level will decrease intelligibility of speech which can affect the understanding of students and uncomfortable for teaching and learning.

Two lecture rooms and one office room at the Technology Campus in Universiti Teknikal Malaysia Melaka were used as the case study. Measurements were carried out for comparison to show the difference of sound pressure levels (SPL) in both room.

2. NOISE MEASUREMENT

The measurement was carried out at two identical lecture rooms on the first floor at Technology Campus in Univerisiti Teknikal Malaysia Melaka. The rooms are located side-by-side separated by gypsum board partition. A variable air volume (VAV) box is located above the ceiling in Room-1 as shown in Figure 1. A VAV box is used to regulate the volume of the air by opening or closing the damper, controlling the air flow to a specific zone. A regular VAV box consists of a motor fan which is triggered to supply air into specific area.
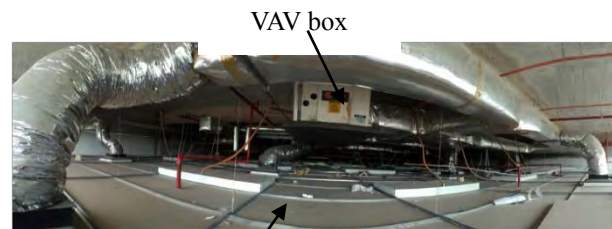
Figure 1 Ventilation layout above the ceiling in Room-1.

The dimension of each room is 70 m^2 and was divided into 135 grids area for the measurement points The sound pressure measurement used RION NA-28 sound level meter calibrated with RION NC-74 sound calibrator. The noise measurement was taken when the lecture room was empty. The microphone is placed at listening position for a person sitting on a chair, roughly 1 m from the floor and not less than 0.03 m from the room walls. Measurement time for each measurement point was set to be 1 minute long. According to Guedes et al. [4], 30 seconds were sufficient to describe the noise events that required observation in their study.

3. RESULT AND DISCUSSION

The SPL in Room-1 taken from 135 measurement points are presented in 2-D contour maps as shown in Figure 3. Figure 3 shows the A-weighted SPL indicating that the background noise level in the lecture room has exceeded the ANSI 12.2-2008 limit of 35 dB(A). The most concentrated area is found to be below the location of the VAV box above the ceiling. It can be seen that this area has noise level at maximum of 60 dB(A). Meanwhile the remaining area can be observed to have an average noise level of 55 dB(A). Strong, rumble-like noise can be heard subjectively in the room, but it is rather difficult to locate the source due to the nature of the low frequency. The VAV box above the ceiling is suspected to transmit the structure-borne noise and also indirect air-borne noise to the classroom.

Measurements in Room-2 were also performed for comparison, and because the low frequency noise level

was observed to be subjectively lower than that in Room-1. The A-weighted noise level shown in Figure 4 also shows that the noise level in the lecture room (Room-2) also exceeds the ANSI 12.2-2008 limit of 35 dB(A). This is due to airborne noise from the air flow at the ventilation which is dominated at higher frequencies [5].
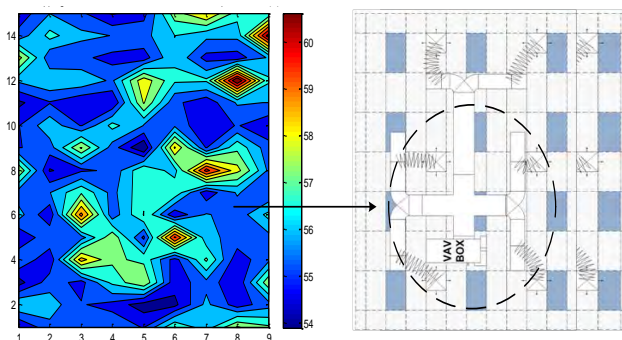

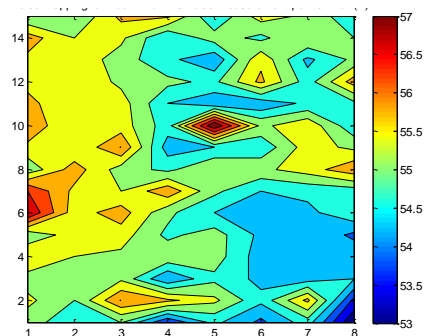Figure 3 Mapping of SPL (dB(A)) in Room-1 corresponds to the HVAC-layout.

Figure 4 Mapping of SPL (dB(A)) in Room-2.

Figure 5 plots together the measured SPL in Room-1 and Room-2. It can be seen that Room-1 is dominated by low frequency noise below 500 Hz having 5 dB differences with SPL from Room-2. Above this frequency, Room-1 and Room-2 have almost the same SPL with 1-3 dB greater SPL for Room-2. Figure 6 again plots together the dB(A) noise distribution in Room-1 and Room-2 now with the same noise level indicator bar. It can be clearly seen that Room-1 has more concentrated noise areas compared to Room-2. The noise contour in Room-2 can be seen to have more uniform colour because the variability of the noise level in dB(A) is smaller than that in Room-1.

As already shown in Figure 6, background noise in Room-1 comes from the radiated noise from the vibrating VAV box. 'Rumble'-like noise can be subjectively heard in this room which is a nature of a low frequency noise.

4. CONCLUSIONS

Noise measurements to identify the structure-borne noise level in lecture rooms have been conducted. The rooms have been found to have the noise level to exceed the recommended maximum background noise level of 35 dB(A) as in ANSI-12.2(2008). However, Room-1 has been identified to have dominant low-medium frequency content due to the structure-borne noise from

the fault VAV unit above the ceiling. The noise is considered to be marginal (roar in nature), but is still acceptable for Room-2, where here the high frequency content is dominant mainly due to the noise from the air conditioning duct ventilation.

Assessment can be more accurate and of interest if vibration measurement can be made on the VAV unit and the ODS of the whole body of the unit, including the hanger rods can be obtained to observe the nature of the vibration mode transmitting the vibration wave to the above floor.
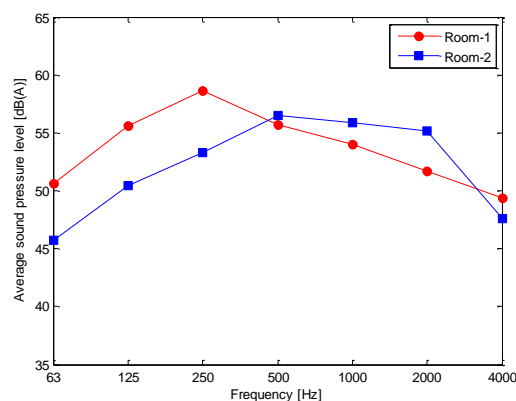
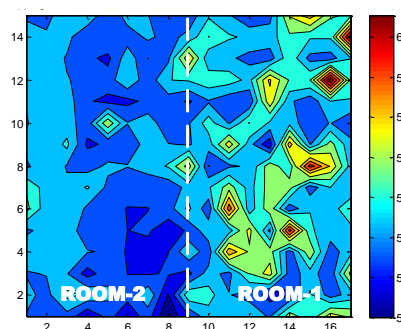

Figure 5 Average SPL in octave band frequencies.

Figure 6 Mapping of SPL (dB(A)) in Room-1 and Room-2.

REFERENCES

[1] ANSI Standard S12.2. *Criteria for Evaluating Room Noise*. Acoustical Society of America, Melville. New York; 2008.

[2] Handbook, ASHRAE., *HVAC Applications: Chapter 48, Noise and Vibration Control*, American Society of Heating, Refrigerating, and Air Conditioning Engineers, Atlanta; 1996.

[3] W. Stewart, "The Components of Good Acoustics in a High Performance School," *Educational Facility Planner 43*, no. 4, pp. 28-30, 2009

[4] I.C.M. Guedes, S.R. Bertoli, and P.H. Zannin, "Influence of urban shapes on environmental noise: a case study in Aracaju—Brazil," *Science of the Total Environment,* vol. 412, pp. 66-76, 2011

[5] A. Putra, F.A. Munir, and C.D. Juis, "On a simple technique to measure the airborne noise in a car interior using substitution source," *International Journal of Vehicle Noise and Vibration*, vol. 8, no. 3, pp. 275-287, 2012

Dynamic analysis of laminated rubber-metal spring using finite element method

S. Norfarizan[1], A. Putra[1,2,*], M.A. Salim[1,2], R. Ramlan[1,2]

[1] Faculty of Mechanical Engineering, Universiti Teknikal Malaysia Melaka,
Hang Tuah Jaya, 76100 Durian Tunggal, Melaka, Malaysia
[2] Centre for Advanced Research on Energy, Universiti Teknikal Malaysia Melaka,
Hang Tuah Jaya, 76100 Durian Tunggal, Melaka, Malaysia

*Corresponding e-mail: azma.putra@utem.edu.my

ABSTRACT – Laminated rubber-metal spring (LRMS) is widely applied in buildings, vehicles and to protect sensitive equipments. In this study, the dynamic performance of such isolator was analyzed. The dynamic analysis was carried out using finite element method. Five models of rubber based isolators with different number of interlayer metal plates was analyzed using Abaqus 6.10 software. Transmissibility ratio was determined from the displacement changes of isolators. The results show the rubber bearing with embedded metal plate layers can improve the transmissibility ratio at high frequency.

1. INTRODUCTION

Rubber based isolators had been widely applied around the world especially for places with high possibility of ground movement such as earthquake. The isolator is used to decouple a structure from the moving component or ground motion. This is important to reduce damages caused by any vibrational force. LRMS was invented to function as an isolation system while withstanding the load applied on it for wide range of periods. It can extend the lifetime of the isolator and prevent bulging effects during the static pre-load[1].

It appears from the aforementioned investigations that most attention has been paid to seismic isolation studies regarding earthquake which is mainly for horizontal and low frequency vibration problems[2], [3]. Furthermore, it can be seen only few studies have discussed the performance measurement focussing on axial vibration. The purpose of this study is to determine the axial vibration transmissibility performance of the solid rubber isolator and LRMSs using dynamic analysis of finite element method. The vibration characteristics of the isolator were defined in term of transmissibility frequency response function which is ratio of output to the input excitation. The Finite Element Analysis (FEA) results will be validated to the experimental results study. The findings of this study will help to use FEA to model future laminated spring products which not only able to sustain large deflection but also demonstrate good isolation performance.

2. METHODOLOGY

The finite element approach is adopted in this paper for various model of isolator from LRMS type.

2.1 Geometrical model

The isolator model studied is a cylindrical sandwiched mounts consisting of alternate layers of steel and rubber discs. All the isolators had the same total length, t_T which was 0.1m and 0.1m for the diameter, D. The flange plate located at both isolator ends is 5mm in thickness. Each metal plate embedded inside the isolator had length, t_S of 3mm and radius of 0.05m. In the whole analysis, the total length of isolators and metal plates were maintained thus only the thickness of rubber discs was varied according to the changes of metal plate number. The rubber sections length, t_R for solid rubber to 4 metal plates isolator were 0.1m, 0.049m, 0.031m, 0.023m and 0.018m respectively. Isolator without metal plate was labeled as solid rubber while LRMS were labeled according to the number of plate layers exist which were LRMS 1 to LRMS 4. Figure 1 shows the example configuration of the LRMS 1 assembly.
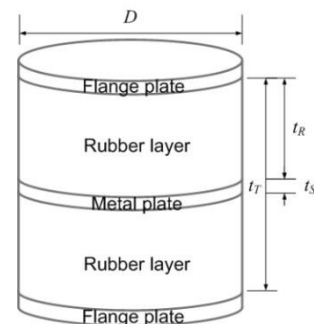

Figure 1 Example of LRMS 1 assembly configuration.

2.2 Finite element model

The finite element modeling of the rubber bearing was carried out using ABAQUS finite element analysis (FEA) software. Both metal end plates were modeled using fully integrated axisymmetric solid elements which is CAX8 while the rubber sections used CAX8H. CAX8H elements are fully integrated axisymmetric solid from hybrid type. Hybrid is formulated for incompressible or nearly incompressible material behavior.

The procedure type used was direct steady state dynamic analysis that provides the steady-state amplitude of the response of a system due to harmonic

excitation at a given frequency. The transmissibility results were obtained from the ratio of the displacement response of the output end plate to the input displacement excitation applied to the input end plate.

2.3 *Material properties*

The material used in the rubber sections were Natural Rubber (NR) which has Young Modulus, E =1.4 MPa and density, ρ=920kgm^{-3}. For the metal plate, the material properties involved are E=211GPa and ρ=7850kgm^{-3}. Rigid mass of 0.3Kg is applied to the metal plate where the part is defined as rigid body.

3. RESULTS AND DISCUSSION

Figure 2 illustrate the results obtained from the FEA done on solid rubber and LRMS isolator. The solid grey line represents the FEA while the dashed black line represents the experimental results. It was observed that the FEA results have good agreement with the experimental data and the presented methodology has good accuracy for analyzing solid rubber and LRMS isolator.
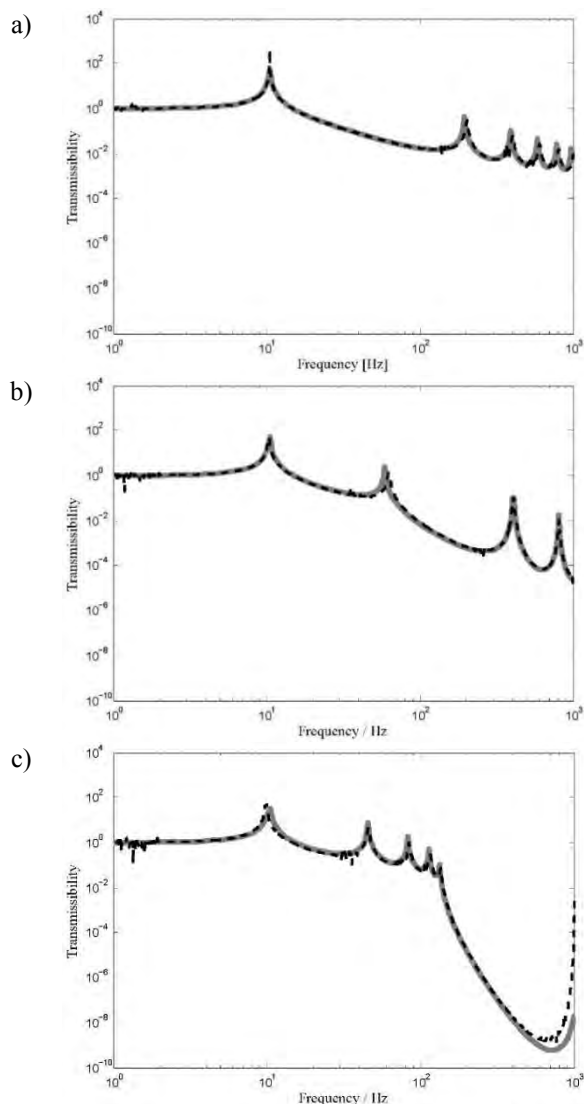

Figure 2 Transmissibility curve for a) solid rubber, b) LRMS 1, c) LRMS 4 (dashed line: experiment, solid line: FEA).

Figure 3 presents all the FEA results in single plot for performance comparison. All isolators maintained the same natural frequency at low frequency while exhibit better high frequency performance for bigger number of metal plates. LRMS 4 had the best dynamic performance among the tested models. This is influenced by stiffness changes of isolator structure with the presents of interlayer metal plates. Greater stiffness results in better isolation performance especially at high frequency.
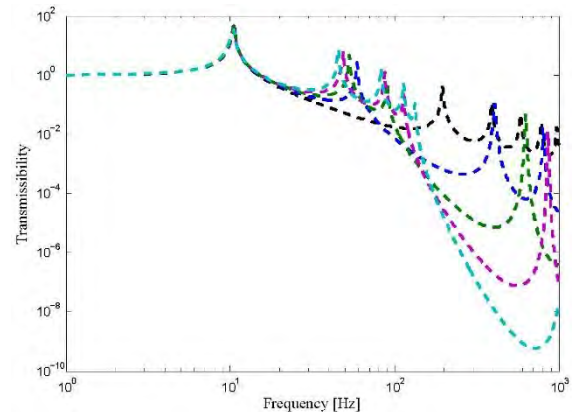

Figure 3 Comparison of transmissibility performance for: solid rubber (black), LRMS 1 (blue), LRMS 2 (green), LRMS 3 (pink) and LRMS 4 (light blue).

4. CONCLUSIONS

The dynamic analysis of solid rubber isolator and LRMSs was carried out using finite element method in Abaqus. The transmissibility curve was successfully validated with the experiment and highlighted few performance characteristics such as:
a) The FEA method has good accuracy for analyzing cylindrical solid rubber and LRMS isolators.
b) More interlayer metal plate inside LRMS has better transmissibility performance at higher frequency.

REFERENCES

[1] J.M. Kelly and D.a. Konstantinidis, *Mechanics of Rubber Bearings for Seismic and Vibration Isolation*. John Wiley & Sons, 2011.
[2] M.C. Kunde and R.S. Jangid, "Seismic behavior of isolated bridges: A-state-of-the-art review," *Technology*, vol. 3, pp. 140–170, 2003.
[3] M.A. Salim, A. Putra, D. Thompson, N. Ahmad, and M. A. Abdullah, "Transmissibility of a Laminated Rubber-Metal Spring: A Preliminary Study," *Appl. Mech. Mater.*, vol. 393, pp. 661–665, 2013.

Experimental investigation of surface roughness using ultrasonic assisted machining of hardened steel

R. Azlan[1,2,*], R. Izamshah[1], M. Hadzley[1], M.S. Kasim[1], M. Arfauz[1], M. Akmal[1]

[1])Faculty of Manufacturing Engineering, Universiti Teknikal Malaysia Melaka,
Hang Tuah Jaya, 76100 Durian Tunggal, Melaka, Malaysia
[2])Department of Mechanical Engineering, Politeknik Melaka, Balai Panjang,
Plaza Pandan Malim, 75250 Melaka, Malaysia

[*]Corresponding e-mail: p051410004@student.utem.edu.my

Keywords: Ultrasonic assisted machining; surface roughness; hardened steel

ABSTRACT – Machining of hardened mould and die material is a very challenging process due to the high strength of the materials. Rough machined surface and premature tool wear are some of the issues that are related when machining with this material. On the other hand, ultrasonic assisted machining (UAM) technique has proven to improve the machined surface and tool life especially for brittle materials such as glass and quartz. Based on the capabilities of UAM technique and to overcome the problem owned by a conventional milling method, this paper evaluate the UAM technique for machining hardened AISI D2 material with the aim to improve the machined surface. Experiments of ultrasonic assisted milling were conducted to investigate the surface roughness of machines surface during slot milling cutting operation. From the conducted investigation, surface roughness values was improved from 0.60 μm (non ultrasonic) to 0.26 μm (ultrasonic) at 37 m/min (cutting speed), 65 mm/min (feed rate) and 0.4 mm (depth of cut). The results from the macroscopic observation shows that the machine surface of slot milling cutting by UAM appeared to be very smooth with consistent scaly and structured.

1.   INTRODUCTION

Work piece surface roughness are the most important criteria for machining hardened steed, D2 to get a mirror surface sculptured profile and good finishing surface of products. Surface roughness is surface texture or surface topography and it's a nature of surfaces.

Modern manufacturing industry currently requires produces a finished products with high product accuracy and good surface quality. The machining hardened steel, ceramics and composites material involve high cost and difficult to machine. To overcome this problem, non-traditional machining with new process and new method is required to replace a traditional machining because traditional machining is more to the metal removal process using the tool that is harder than the work piece.

Ultrasonic machining (USM) is machining operation using vibration tool oscillating at ultrasonic frequencies (18-20 kHz) and aided by abrasive slurry that flows freely between the tool and the work piece to remove material from the work piece. The vibration tool oscillating with amplitude 10 to 40 μm imposes a static pressure on the abrasive grains, hammered into the work piece surface, causing chipping of fine particles and formed the required tool shape. According to [1], ultrasonic machining is non-conventional machining with low material removal rates and operates at ultrasonic frequency range between 20-40 kHz. Investigation by [2] revealed that material removal rate (MRR) and surface roughness (Ra) will increase when amplitude of vibration increase, static load increase and size of abrasive increase when using K-type magnetic ferrite as work piece with using ultrasonic machining. Also, it shown that material removal rate depends on the amount of energy exerted to the materials. Ultrasonic assisted machining also applied in industry for manufacturing process of ceramics components [3]. Experiment by [4] used Rotary Ultrasonic Machining (RUM) based on abrasive removing mechanism and using ultrasonic vibrating diamond particles, which are bonded on the active part of a rotating tool for machining Poly-crystalline cubic boron nitride (PCBN). The result of this experiment shown that Rotary Ultrasonic Machining (RUM) can machining PBCN with a low surface roughness value which Ra 0.24 μm, Rz 2.834 μm and it can be concluded that Rotary Ultrasonic Machining (RUM) is suitable for finishing of hard and brittle material's surface.

In mould and die industry, fine machined surface qualities are necessary and usually are achieved through several processes i.e. roughing, semi roughing and manual polishing which are very costly. To solve this problem, ultrasonic assisted machining is proposed to eliminate the manual polishing process. Thus, this paper attempt to investigate the effectiveness of ultrasonic assisted machining for machining hardened mould and die material. The investigation will taking into accounts on the effect of machining parameters namely cutting speed, feed rate, depth of cut and ultrasonic amplitude on surface roughness magnitudes.

2.   METHODOLOGY

A methodology was carried out to obtain the effects of machining parameters on surface roughness of hardened steel material for slot milling operation as shown in Figure 1. The experiment was conducted to compare the surface roughness magnitudes obtained

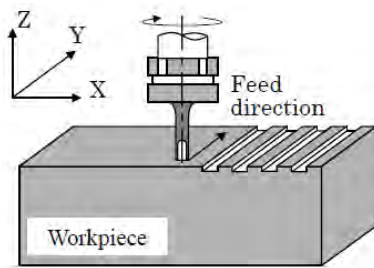through the present of ultrasonic vibration and without ultrasonic.

Figure 1 Slot cutting test.

The study was carried out on CNC Milling Machine, Hass VF 1 model (3axis). Figures 2 and 3 show the cnc machine and ultrasonic tool holder assisted milling setup in this experiment.

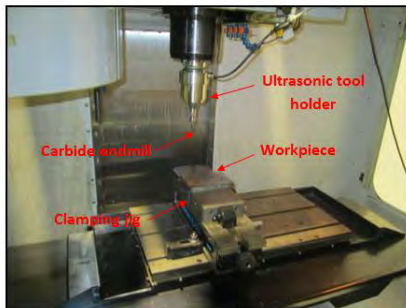Figure 2 Three axis CNC machine used in the experiments.

Figure 3 Ultrasonic assisted milling setup.

The work piece material employed in a study is hardened steel AISI D2 with dimension of 100mm × 100mm × 20mm (W×H×L) in rectangular shape. The cutting tool was used for this experiment (slot milling machining) is solid carbide ball nose mill-K20 micro grain, diameter 5 mm, 2 flutes, 35 degree of helix angle and 50 mm length. The machining parameters are summarized in Table 1.

3. RESULTS AND DISCUSSION

The result of the effect of machining parameters on surface roughness during slot milling cutting of hardened steel, AISI D2 using ultrasonic tool holder assisted milling with solid carbide ball nose mill (2 flutes) are shown at the Table 2.

The maximum value of surface roughness, Ra is 0.60 μm and was obtained at 37 m/min (cutting speed), 65

mm/min (feed rate) and 0.4 mm (depth of cut) at run 1(without ultrasonic tool holder assisted). While, the minimum value and a good of surface roughness, Ra is 0.25 μm at 46 m/min (cutting speed), 145 mm/min (feed rate) and 0.2 mm (depth of cut) at run 4 (ultrasonic tool holder vibration).

The results shown that, the average surface roughness, Ra is decreases when the cutting speed increase, feed rate increase, depth of cut decrease and applying an ultrasonic tool holder assisted milling.

Table 1 Machining parameters.

Cutting speed(m/min)	Feed rate (mm/min)	Depth of cut (mm)	Frequency (kHz)
37	65	0.4	-
46	145	0.2	-
37	65	0.4	23.14
46	145	0.2	23.14

Table 2 The surface roughness of hardened steel using ultrasonic tool assisted milling.

Cutting speed (m/min)	Feed rate (mm/min)	Depth of cut (mm)	Surface roughness, Ra(μm)
37	65	0.4	0.60 (non ultrasonic)
46	145	0.2	0.41 (non ultrasonic)
37	65	0.4	0.26 (ultrasonic)
46	145	0.2	0.25 (ultrasonic)

4. CONCLUSION

Surface roughness of machines surface hardened steel was improved from 0.60 μm (non ultrasonic) to 0.26 μm when apply the ultrasonic tool holder assisted milling. The result shows that the machine surface of slot milling cutting from using ultrasonic tool holder assisted much better compare to non ultrasonic tool holder machine surface. Also, it shows that surface area of slot cutting using ultrasonic very smooth compare to non ultrasonic slot cutting. Machine surface with ultrasonic tool holder assisted milling become consistent scaly, structured and very smooth compare to conventional cutting.

REFERENCES

[1] B.C. Routara, A.K. Sahoo, A.K. Rout, and D.N. Thatoi, "Optimization of Multiple performance characterstic in ultrasonic machining process using grey relational analysis," in *Int. Conf. Mech. Eng.*, 2011, pp. 18–20.

[2] T.C. Lee and C. W. Chan, "Mechanism of the ultrasonic machining of ceramic composites," *J. Mater. Process. Technol.*, vol. 71, no. 2, pp. 195–201, 1997.

[3] R. Izamshah, J.P.T. Mo, M. Arfauz, S. Ding, M.A. Azam, and M.S. Kasim, "Effect of parameter condition on surface roughness for machining AISI D2 hardened tool steel," Journal Of Advanced Manufacturing Technology (Jamt) 8.1, 2014.

[4] M. Kuruc and J. Peterka, "Rotary ultrasonic machining of poly-crystalline cubic boron nitride," *Slovak Univ. Technol. Bratislava J.*, vol. 22, no. 1, pp. 103–108, 2014.

Mathematical modeling on sound absorption of oil palm empty fruit bunch fibers

K.H. Or[1,2], A. Putra[1,2,*], M.Z. Selamat[1,2]

[1] Faculty of Mechanical Engineering, Universiti Teknikal Malaysia Melaka,
Hang Tuah Jaya, 76100 Durian Tunggal, Melaka, Malaysia
[2] Centre for Advanced Research on Energy, Universiti Teknikal Malaysia Melaka,
Hang Tuah Jaya, 76100 Durian Tunggal, Melaka, Malaysia

*Corresponding e-mail: azma.putra@utem.edu.my

Keywords: Oil palm empty fruit bunch fibers; Delany-Bazley model; sound absorption coefficient

ABSTRACT – Oil Palm Empty Fruit Bunch (OPEFB) fibers is an agricultural waste which is available in abundance quantity in Malaysia. This paper discusses the analytical approach used to estimate the sound absorption curve of Oil Palm Empty Fruit Bunch (OPEFB) fibers. Experimental measurement is done by using impedance tube testing to obtain the sound absorption coefficient. The results from the experimental works are validated by comparing with Delany-Bazley model. It is found that the Delany-Bazley model can be used to predict the sound absorption coefficient of OPEFB fibers.

1. INTRODUCTION

The application of 'green' material as acoustic absorber is developing due to its benefits over synthetic materials which are harmful to environment and human's health. Putra et al. employed hollow structure which is bamboo as sound absorber. Addition of fabric at the front surface of bamboo and application of air gap improved absorption at lower frequency region [1]. Researches done by Lim et al. and Or et al. on kenaf fiber sheet and oil palm empty fruit bunch fibers respectively show that increase of thickness and application of air gap improved the peak of absorption coefficient curve and widen the frequency bandwidth of absorption [2,3]. Fouladi et al. analysed the acoustical properties of coir fiber by using two analytical models, namely Delany-Bazley and Biot-Allard [4]. They found out that Delany-Bazley model is easy to use compared to Biot-Allard model. This will be beneficial for the application of fibers in the industry. This paper discusses the application of analytical model, i.e. Delany-Bazley to estimate the sound absorption performance of OPEFB fibers from the experimental works which according to the author's knowledge has not been investigated by other researchers.

2. METHODOLOGY

Samples of OPEFB fibers were fabricated by using hot compression technique without using any binder. The samples were designed based on different densities but same thickness and same density but different thicknesses.

The data on experimental measurement was obtained from the 2-microphones impedance tube testing according to ISO 10534-2 [5].

For the analytical approach, Delany-Bazley model was studied to predict the sound absorption coefficient curve of OPEFB fibers [4,6].

The characteristic impedance Z_o and propagation constant γ of a layer of homogeneous porous material are shown in Equation (1) and Equation (2) [4]. The Z_o and γ are depend on the frequency of the analysis and flow resistivity of the porous material, i.e. OPEFB fibers.

$$Z_o = \rho_o c_o \left\{ \left[1 + c_1 \left(\frac{f\rho_o}{\sigma} \right)^{c_2} \right] - i \left[c_3 \left(\frac{f\rho_o}{\sigma} \right)^{c_4} \right] \right\} \quad (1)$$

$$\gamma = k_o \left\{ c_5 \left(\frac{f\rho_o}{\sigma} \right)^{c_6} + i \left[1 + c_7 \left(\frac{f\rho_o}{\sigma} \right)^{c_8} \right] \right\} \quad (2)$$

where ρ_o is density of air, c_o is speed of sound, $c_1 - c_8$ is Delany-Bazley regression constants [6], f is frequency of sound, σ is flow resistivity and $k_o = 2\pi f / c_o$ is wave number of air.

The surface acoustic impedance Z of a rigidly-backed material of thickness t is shown in Equation (3) [6].

$$Z = Z_o \coth \gamma t \quad (3)$$

The normal incidence sound absorption coefficient of OPEFB fibers based on Delany-Bazley model is derived from Equation (3) and is shown in Equation (4) [6].

$$\alpha = 1 - \left| \frac{Z - \rho_o c_o}{Z + \rho_o c_o} \right|^2 \quad (4)$$

3. RESULTS AND DISCUSSION

Figure 1 shows the graph of sound absorption coefficient versus frequency of OPEFB fibers with different densities but having the same thickness, i.e. 20 mm. From the figure, the Delany-Bazley model can predict the behaviour of the curves with minor deviation from the experimental work.
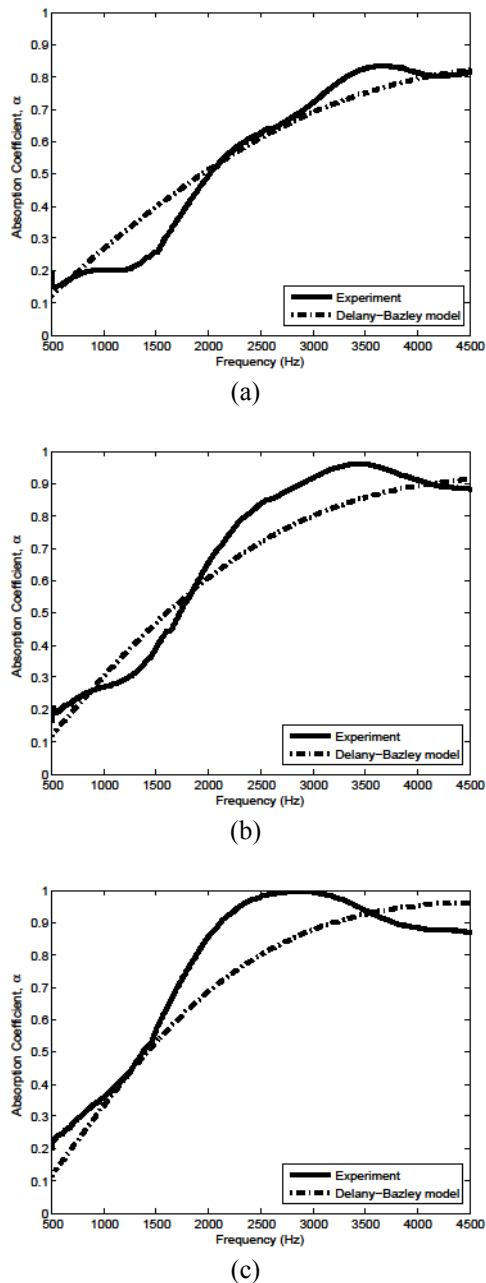
(a)

(b)

(c)

Figure 1 Graph of sound absorption coefficient versus frequency of OPEFB fibers with 20 mm thick and density of (a) 175.4 kg/m^3, (b) 233.8 kg/m^3 and (c) 292.3 kg/m^3.

Figure 2 shows the graph of sound absorption coefficient versus frequency of OPEFB fibers with the same density as Figure 1(c), which is 292.3 kg/m^3 but having thicker sample, i.e. 50 mm. From Figure 2, the Delany-Bazley model can roughly estimate the pattern of the sound absorption coefficient curve. However, this analytical model cannot predict the dips of the curve at 1.5 to 2.3 kHz and 3.8 to 4.5 kHz. This is due to Delany-Bazley model considered the porous layer as bulk material. Thus, in this model, physical characteristic such as flow resistivity alone is considered to predict the sound absorption coefficient of the porous material.

Apart from poor prediction of sound absorption coefficient at the dip of the curve, the Delany-Bazley model is still useful to predict the behaviour of the sound absorption performance of OPEFB fibers due to its simplicity in application.
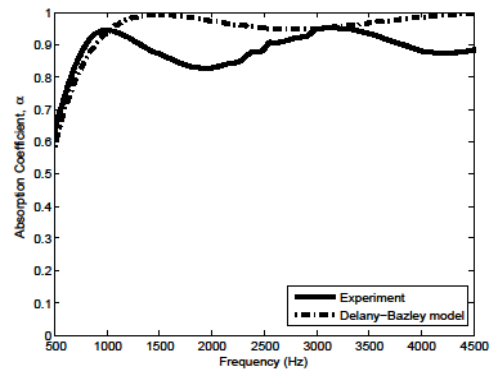

Figure 2 Graph of sound absorption coefficient versus frequency of OPEFB fibers with density of 292.3 kg/m^3 and 50 mm thick.

4. CONCLUSION

The Delany-Bazley model is found to be simple model which is easy to apply and can well-predict the sound absorption coefficient curve for 20 mm thick sample with different densities. Minor deviation between the Delany-Bazley model and the experimental measurement is observed for all the samples. However, the dips of the curve from the experimental measurement for thicker sample are poorly estimated. The study of other analytical models is thus of interest to improve the prediction on the peaks and the dips of the sound absorption coefficient curve.

ACKNOWLEDGEMENT

REFERENCES

[1] A. Putra, F.B.A. Khair, and M.J.M. Nor, "Utilizing Hollow-Structured Bamboo as Natural Sound Absorber," *Archives of Acoustics*, vol. 40, no. 4, pp. 601-608, 2015.

[2] Z.Y. Lim, A. Putra, M.J.M. Nor, and M.Y. Yaakob, "Preliminary study on sound absorption of natural kenaf fiber," in *Proceedings of Mechanical Engineering Research Day 2015*, 2015, pp. 95-96.

[3] K.H. Or, A. Putra, and M.Z. Selamat, "Oil palm empty fruit bunch fibers as sustainable acoustic material," in *Proceedings of Mechanical Engineering Research Day 2015*, 2015, pp. 99-100.

[4] M.H. Fouladi, M. Ayub, and M.J.M. Nor, "Analysis of coir fiber acoustical characteristics," *Applied Acoustics*, vol. 72, no. 1, pp. 35-42, 2011.

[5] Acoustics - Determination of sound absorption coefficient and impedance in impedance tubes - Part 2: Transfer-function method, ISO 10534-2, 2001.

[6] M.E. Delany, and E.N. Bazley, "Acoustical properties of fibrous absorbent materials," *Applied Acoustics*, vol. 3, no. 2, pp. 105-116, 1970.

Designed by